Imperial College London

Department of Materials

Study of the Effect of d-Block and p-Block Dopants on Material and Photocatalytic Properties of $SrTiO_3$.

Dissertation Submitted in the Partial Fulfilment of the Requirements for the Degree of Doctor of Philosophy

October 2024.

Dikshita Bhattacharyya

This thesis is dedicated to all the Ph.D. students in the world!

Declaration

I, Ms. Dikshita Bhattacharyya, hereby declare that this Ph.D. thesis titled, **'Study of the Effect of d-Block and p-Block Dopants on Material and Photocatalytic Properties of $SrTiO_3$'** is entirely my work. This work has not been submitted elsewhere and was produced without any external aid. Sources cited in the work have been duly referenced in the text.

29.09.2024, Cambridge

Date, Place

The copyright of this thesis rests with the author. Unless otherwise indicated, its contents are licensed under a Creative Commons Attribution-Non Commercial-No Derivatives 4.0 International Licence (CC BY-NC-ND). Under this licence, you may copy and redistribute the material in any medium or format on the condition that; you credit the author, do not use it for commercial purposes and do not distribute modified versions of the work. When reusing or sharing this work, ensure you make the licence terms clear to others by naming the licence and linking to the licence text. Please seek permission from the copyright holder for uses of this work that are not included in this licence or permitted under UK Copyright Law.

Abstract

Photoelectrocatalytic and photocatalytic reactions are gaining momentum as a clean method to generate sustainable fuels such as H_2. The Ph.D. study focuses on the identification of suitable d- and p-block dopants and the suitability of doping to enhance the catalytic activity of photochemically stable $SrTiO_3$. In this work, the effect of doping Ga^{3+}, La^{3+}-Ga^{3+}, Cr^{3+}, La^{3+}-Cr^{3+}, and Cs^{1+}-Cr^{3+} on the properties of $SrTiO_3$ has been extensively studied.

Chapter 1 introduces the state-of-the-art research associated with this field and outlines the motivations and aims of the Ph.D. work. Chapter 2 summarizes the synthesis method, and the characterization techniques employed to study the catalysts.

Chapter 3 studies a series of high-temperature synthesized Ga^{3+} doped and La^{3+} co-doped $SrTiO_3$ samples. Accidental exsolutions and anomalous absorption features were observed in some samples. In addition to extrinsic defects, the role of intrinsic defects such as oxygen vacancies in the photoelectrocatalytic performance was investigated.

Chapter 4 studies the Ga^{3+} doped $SrTiO_3$ synthesized at lower temperatures and how these samples differ in properties from those studied in Chapter 3. This chapter highlights the role of intrinsic material properties like electron affinity and ionization potential and defects such as oxygen vacancies.

Chapter 5 investigates the effect of doping $SrTiO_3$ with Cr in its B-site. Cr mono-doping was found to have formed the Cr^{6+} (d^0 configuration) trap states alongside the Cr^{3+} states. The bulk of this chapter investigates the effect of the Cr^{3+}/Cr^{6+} ratio on the material properties and their photoelectrocatalytic performances.

Chapter 6 details the introduction of an additional N_2 annealing step in the standard synthesis route to study its effect on crystallite sizes. Preliminary gas phase photocatalytic CO_2 hydrogenation with the standard sol-gel Pechini synthesized samples showed an increasing trend in CO evolution and a new method to quantify photocatalytic data has been reported.

For Ma and Deuta

Acknowledgments

It is a great honor for me to write the following few lines acknowledging the help and support I received to bring my project to this stage.

I wish to express my sincerest gratitude to my Supervisor, Dr. Ludmilla Steier, for giving me the wonderful opportunity to work on my Ph.D. Thesis at Imperial College London. I have always been in awe of her brilliance and amazing scientific acumen. Indeed, she is an inspiration for all women who want a career in STEM! Her brilliant insight, wisdom, and guidance were of utmost value in steering the course of the Ph.D. Thesis. An exceptional gratitude goes out to Prof. Martyn McLachlan for his excellent counsel and valuable input to my work.

A very special mention to Mr. Ben Bowers, Dr. Florianna Morruzzi, Ms. Baliana Shani, Dr. Arnau Bertran, and the entire Steier Group at the University of Oxford for their unfailing support and encouragement. Thank you for helping with chemistry and making my transition from mechanical engineering a whole lot easier. What awesome people to work with!

I would like to extend my sincere gratitude to Dr. Andrei Berenov, Dr. Manjula Silva, and Dr. Gwilherm Kerherve, Imperial College London for their valuable guidance and insight.

I would like to take this opportunity to thank my parents, my forever cheerleaders, and without whom none of this would have been possible.! To Rimi and Rumon Da for their love and support whenever I needed it! To my little Rimonu, the source of happiness for the entire family. And lastly, the most important person in my life, my husband Dr. Angshuman Kapil. Thank you for teaching me the true meaning of companionship. You are everything I need!

Table of Contents

Abstract..... ii

Acknowledgments..... iv

Chapter 1: Introduction **1**

1.1 Motivation and Literature Review 1

1.2 Semiconductor Physics: A Case Study of $SrTiO_3$ 6

1.2.1 Structural Properties 6

1.2.2 Opto-electronic Properties 8

1.3 Performance Assessment of $SrTiO_3$ 9

1.3.1 Photocatalysis 10

1.3.2 Photoelectrochemistry (PEC) 14

1.4 The Role of Defects in $SrTiO_3$ 15

1.4.1 Understanding the Site and the Charge of Point Defects with the Kröger Vink Notation 17

1.5 Incorporating the Dopants: How Does the Synthesis Route Affect the Final Products? 18

1.6 Aim of the Ph.D. Thesis 21

Reference 21

Chapter 2: Methods **33**

2.1 Catalyst Preparation 33

2.1.2 Synthesis of undoped and doped $SrTiO_3$ 34

2.2 Microstructural Characterization 37

2.2.1 Powder X-ray Diffraction (XRD) 37

2.2.2 Transmission Electron Microscope (TEM) 44

2.3 Optical Measurements 47

2.3.1 UV Vis Spectrophotometer 47

2.3.2 Photoluminescence (PL) Spectroscopy 49

2.3.3 Time-Correlated Single Photon Counting (TCSPC) 50

2.4 Electronic Measurements 52

2.4.1 X-ray Photoelectron Spectroscopy (XPS) 52

2.4.2 Kelvin Probe 54

2.4.3 Electron Paramagnetic Resonance (EPR) 55

2.5 Performance Tests 56

2.5.1 Photoelectrochemical (PEC) Measurements 56

2.5.2 Photocatalytic Set-up 57

2.5.3 Atomic Layer Deposition (ALD) 58

2.5.4 F20 Interferometer 59

2.5.5 Brunauer-Emmett-Teller (BET) Analysis 60

References 60

Chapter 3: Absorption Features, Accidental Exsolution, and Suppression of Ti^{3+} Defects Enhanced Photoelectrochemical Performance in La^{3+}, Ga^{3+} co-doped $SrTiO_3$ 65

3.1 Introduction 65

3.2 Experimental Method: Solution Combustion Synthesis/Sol-Gel Pechini Route for the Synthesis of La, Ga co-doped $SrTiO_3$ 66

3.3 Results and Discussion 67

3.3.1 Microstructural Analysis 67

3.3.2 Elemental Analysis with the XPS 83

3.3.3 Understanding the Role of Defects on the Optoelectronic Properties 91

3.3.4 Performance Evaluation: Photoelectrochemical (PEC) Measurements 111

3.4 Conclusion 115

References 115

Appendix 124

Chapter 4: Enhancements to Sol-Gel Pechini Process- Impact of Annealing Temperatures on Material Properties of Ga^{3+} doped $SrTiO_3$ 125

4.1 Introduction 125

4.2 Results and Discussion 129

4.2.1 Sol-gel Pechini 129

4.2.2 Synthesis of Phase Pure Materials at 500 °C 130

4.2.3 Goldschmidt's Tolerance Factor Consideration in the Structural Stability 131

4.2.4 XRD Analysis 132

4.3 Influence of Temperature on the Microstructural Properties 132

4.3.1 Influence of Temperature on Relative Crystallinity 133

4.3.2 Influence of Temperature on the Coherently Scattering Domain Size 134

4.3.3 Influence of Temperature on the Microstrain 136

4.3.4 Influence of Temperature on the Lattice Parameters and Lattice Volume 138

4.3.5 Effect of the Microstructure on the Time-Correlated Single Photon Counting (TCSPC) Measured Lifetimes 141

4.4 Influence of Temperature on the Opto-electronic Properties of the Samples 144

4.4.1 Influence of Annealing Temperature on Bandgaps 145

4.4.2 Influence of Temperature on the Fermi Level (E_F) and Valence Band Maxima (VB_M) Separation 147

4.4.3 Work Function 149

4.4.4 Correlation between the Electronic Structure and the Microstructure Changes Induced by Temperature Variation via the Formation of Oxygen Vacancies 151

4.4.5 Influence of Temperature on Electron Affinity, Ionization Potential, and Charge Carrier Mobility 153

4.5 Elemental Analysis 159

4.5.1 XPS 159

4.5.2 Doping and the Time-Temperature-Solubility Factor 166
4.5.3 Effect of Temperature on the Surface Composition of the Samples 167
4.6 Performance Assessment 167
4.6.1 Photoluminescence (PL) Analysis 168
4.6.2 Photoelectrochemical Performance of the Doped Samples 172
4.7 Conclusion 174
References 175
Appendix 182
Chapter 5: Investigating the Role of the Cr^{3+}/Cr^{6+} in Determining the Photoactivity in Cr-(co-) doped $SrTiO_3$ 185
5.1 Introduction 185
5.2 Experimental 186
5.3 Goldschmidt's Tolerance Factor Consideration in the Structural Stability of the Samples 187
5.4 Microstructural Analysis with the XRD 188
5.5 Elemental Analysis with X-ray Photoemission Spectroscopy (XPS) and Site of Substitution of the Dopants with EPR 196
5.5.1 XPS Analysis 196
5.5.2 Site of Cr^{3+} doping: EPR Studies 220
5.6 Opto-Electronic Analysis 224
5.6.1 Diffuse Reflectance Spectroscopy (DRS) Analysis 224
5.6.2 Valence Band Analysis 234
5.6.3 Work Function 239
5.6.4 Band Edge Energy Diagrams from the Work Function, the Band Gap, and the Valence Band Analysis 243
5.6.5 Band Edge Alignment for Water Redox Potential 246
5.6.6 Time Co-related Single Photon Counting (TCSPC) 248
5.6.7 Room Temperature Steady State Photoluminescence Analysis (PL) 251
5.7 Performance Assessments 254
5.7.1 Photoelectrochemical Measurements 254
5.8 Conclusion 257
References 258
Appendix 262
Chapter 6: A New Method to Quantify Photocatalysis Data and the Effect of an Intermediate N_2 annealing Before Calcination on the Crystallite Sizes 263
6.1 Introduction 263
6.3 Results and Discussion 264
6.3.1 Preliminary Photocatalytic CO_2 Hydrogenation Results 264
6.4 Conclusion and Future Work 274

References 275
Appendix 276
Chapter 7: Conclusion and Future Work **283**
7.1 Conclusion 283
7.2 Future Work……..….285
Copyright Permissions……..…287

List Of Figures

Chapter 1

Figure 1.1: CO_2 levels and global annual average temperature from 1850 to the present with the black line indicating the rise in CO_2 levels, the red bars indicating temperatures above the average, and the blue bars indicating temperatures below the average [5]. 1
Figure 1.2: A technology readiness level (TRL) based projection of budget allocated to PEC and PC research projects in the European Union as reported in Galushchinskiy, A. et al. [15]. The TRL system is used to measure the maturity of a project on a scale of 1-9 [16]. 2
Figure 1.3: The approaches to solar fuel generation. (a) Photocatalysis setup (PC) (b) Photo(electro-)chemistry setup (PEC) and (c) PV-EC setup[69]. 6
Figure 1.4: Cubic structure of ABO_3 perovskite $SrTiO_3$ with Ti^{4+} (yellow) in the center, Sr^{2+} (dark blue) in the corners and O^{2-} (light blue) forming the octahedron with Ti^{4+} [71]..... 7
Figure 1.5: A schematic of a weak field JTE in d^1 configuration Ti^{3+} in $SrTiO_3$ with the split energy levels t_{2g} and e_g. Both energy levels are separated by 10 Dq. 8
Figure 1.6: The maximum achievable photocurrent of $SrTiO_3$ is close to the anatase TiO_2 at 1.1 mA/cm^2 correlating the solar to hydrogen conversion efficiency (STH) [86]. 9
Figure 1.7: The 6-gear concept depicting the parameters of photocatalysis, and the time scale required to accomplish the associated processes as adopted from the work of Takanabe, K. [101]. 11
Figure 1.8: Schematic showing the Gibb's energy change for an uphill photocatalytic water splitting reaction [106]..... 12
Figure 1.9: Band bending at semiconductor electrolyte junction. (a) n-type semiconductor electrode with a double layer structure. The electrode is in contact with the electrolyte. (b) Energy diagram of n- and p-type semiconductors [110], [112], [113]..... 15
Figure 1.10: Schematic of types of dislocations. (a) Edge dislocations (b) Screw dislocations [119].16

Chapter 2

Figure 2.1: Coarsely ground polyester with a hard glass-like texture after heating the gel to 197 °C before further calcination.....34
Figure 2.2: A Schematic Diagram of Bragg's Diffraction. 37
Figure 2.3: A PANanalytical X'pert MPD XRD housing a goniometer that drives an optical path equipped with an X-ray tube with Cu Kα source, a sample holder, and a detector. 38
Figure 2.4: Sample flattened and loaded on a sample holder before inserting into the diffractometer. 39
Figure 2.5: A TEM micro-graph showing a crystallite adjoined to another crystallite with different orientations separated by a grain boundary highlighted in the white rectangle of a Ga^{3+} doped $SrTiO_3$ sample. 40
Figure 2.6: W-H analysis with the XRD pattern of sample $SrTi_{(0.96)}Ga_{(0.04)}O_3$ (a) Lorentzian fitting of peak (110) (b) Voigt fitting of peak (110) (c) Linear fitting of 4sinθ and ßcosθ with Pearson's r =0.93.....42
Figure 2.7: (a) TEM image of 4 mol% Ga^{3+} doped $SrTiO_3$ nanoparticles (b) Size distribution calculated from the TEM distribution. 43
Figure 2.8: PANanalytical Empyrean high-temperature XRD. 44
Figure 2.9: Principle parts of a TEM housing [17]. 45
Figure 2.10: Samples for TEM analysis dispersed on holey carbon film with Cu grid[18]. ..46

Figure 2.11: TEM analysis on the $SrTi_{(0.96)}Ga_{(0.04)}O_3$ (N_2) to analyze the lattice spacings, the nature of the materials, EDX, and the diffraction pattern. 47
Figure 2.12: (a.) A Shimadzu UV-2600 instrument for UV vis measurements (b.) An integrating sphere. 48
Figure 2.13: Difference between (a) direct and (b) indirect bandgaps with respect to the crystal momentum [24]. 49
Figure 2.14: (a) Fluorolog-2 Spectrofluorometer (Horiba Jobin Yvon) (b) Cary Eclipse (Agilent Technologies. 50
Figure 2.15: A HORIBA DeltaFlex TCSPC setup was used in the Ph.D. study to measure the lifetimes of the synthesized photocatalysts. 51
Figure 2.16: Schematic of the working parts of the XPS [28]. 52
Figure 2.17: XPS sample preparation for (a) Elemental and valence band analysis (b) Work function analysis. 53
Figure 2.18: (a) Principle of the Kelvin Probe setup [41] (b) Sample preparation by doctor-blading samples on FTO glass. 54
Figure 2.19: The cross-section of a H-cell used in photoelectrochemical measurements[43]. 56
Figure 2.20: The photocatalytic set-up used for the CO_2 hydrogenation studies from Prof. Ian McCulloch's group. 57
Figure 2.21: The valves set-up in the ALD, MSRH, Imperial College London. 58
Figure 2.22: Growth per cycle (GPC) measurements of thin films using F20 Interferometer. 59

Chapter 3

Figure 3.1: 900 °C sol-gel Pechini synthesized La^{3+} co-doped samples (0.5 mol% - 10 mol%). 67
Figure 3.2: Comparison of the XRD patterns of 20, 30, and 40 mol% Ga^{3+} doped $SrTiO_3$ which demonstrated secondary phases indicated by *. The motivation to synthesize these batches was to understand the limit of Ga^{3+} doping 68
Figure 3.3: XRD patterns of (a) Ga^{3+} (b) La^{3+}, Ga^{3+} doped $SrTiO_3$ samples with peaks indexed according to $SrTiO_3$ ICSD file. The diffraction patterns were collected between 20° to 80° 2θ values with step size 0.0167113 ° and 24.765 sec per step. 69
Figure 3.4: Lattice volume and relative crystallinity comparison of a.) Ga^{3+} doped b.) La^{3+} co-doped $SrTiO_3$ samples in oxygen-poor annealing conditions. The monodoped samples with shifts to higher angles show a decrease in lattice volumes. The lattice volume increased in the 2 mol% co-doped sample and decreased in the 4 mol% co-doped sample. All the doped samples show lower relative crystallinity compared to the undoped. 73
Figure 3.5: Dislocations present in (100) plane of 4 mol% La^{3+} co-doped samples as observed via TEM analysis. 75
Figure 3.6: (a.) Coalesced nanoparticles due to high-temperature synthesis (b.) Diffraction pattern demonstrating the polycrystalline nature of the region imaged (Sample: 4 mol% La^{3+} co-doped $SrTiO_3$). 77

Figure 3.7: Appearance of grain boundaries due to high-temperature synthesis with differently oriented crystallites (Sample: 4 mol% La^{3+} co-doped $SrTiO_3$).....78
Figure 3.8: Exsolution of nanoparticles in (a, b) Literature comparisons of exsolved NPs to the materials studied in the Ph.D. work [63],[64] (c) 2 mol% (d) 4 mol% La^{3+} co-doped $SrTiO_3$ (e, f) Exsolved particle in 2 mol% La^{3+} co-doped $SrTiO_3$ and the live FFT image of the exsolved particle confirming its crystalline nature (g) Exsolved particles in 4 mol% La^{3+} co-doped $SrTiO_3$. 81
Figure 3.9: (a) Exsolution of NPs near a grain boundary in 4 mol% La^{3+} co-doped sample (c, d) Literature comparisons of exsolved NPs to the materials studied in the Ph.D. work. 81
Figure 3.10: XRD pattern in log intensity scale of the (a) Undoped (b) 0.5 mol% (c) 1 mol% (d) 2 mol% (e) 4 mol% and (f) 10 mol% La^{3+} co-doped $SrTiO_3$ samples. The 2 mol% and 4 mol% La^{3+} co-doped samples show phase segregation.. 82
Figure 3.11: Deconvoluted and charge corrected Sr3d Peaks of Undoped $SrTiO_3$ at 132.77 eV and 134.49 eV with trace amount of $SrCO_3$.The green doublet refers to the presence of $SrCO_3$ confirmed from the 1:1 ratio of the $SrCO_3$ $Sr3d_{5/2}$ and the C1s -C=O. 83
Figure 3.12: Deconvoluted and charge corrected Sr3d Peak of (a) 2 mol% Ga^{3+} (b) 4 mol% Ga^{3+} (c) 2 mol% La^{3+} and (d) 4 mol% La^{3+} co-doped $SrTiO_3$. The 4 mol% co-doped sample shows the highest $SrCO_3$ concentration. 84
Figure 3.13: XPS Ti2p Peak of Undoped $SrTiO_3$ with $Ti2p_{1/2}$ at 464.08 eV. The blue peak indicates the presence of Ti^{3+} defects. 86
Figure 3.14: The XPS $Ti2p_{1/2}$ peaks of (a) 2 mol% Ga^{3+} (b) 4 mol% Ga^{3+} (c) 2 mol% La^{3+} and (d) 4 mol% La^{3+} co-doped $SrTiO_3$. Ti^{3+} decreases upon doping with the co-doped samples showing lowest the concentration. 86
Figure 3.15: XP spectrum of undoped O1s peak with the main component at 529.48 eV. Deconvolution shows the presence of -C=O, -OH and C-O-C. 87
Figure 3.16: Deconvoluted and charge corrected O1s peak of (a) 2 mol% Ga^{3+} (b) 4 mol% Ga^{3+} (c) 2 mol% La^{3+} and (d) 4 mol% La^{3+} co-doped $SrTiO_3$. The 4 mol% co-doped samples show significantly higher -C=O groups and an increase in -OH groups can be observed in all the doped samples. 88
Figure 3.17: (a) The XP spectrum of La3d peak with the main component of $d_{5/2}$ peak at 833.89 eV and the main component of $d_{3/2}$ at 850.87 eV (b, c) La^{3+} and Ga^{3+} incorporation confirmation with EDX in the 4 mol% co-doped sample. The EDX pattern with lower Ti^{4+} could indicate Ti vacancies. 89
Figure 3.18: The XP spectrum of $Ga2p_{3/2}$ and $Ga2p_{1/2}$ of the doped samples showed peaks around 1117.77 eV and 1149.69 eV respectively which matches closely with both Ga_2O_3 and metallic Ga. 90
Figure 3.19: Indirect bandgap (3.17 eV) and reflectance spectrum of undoped $SrTiO_3$. No absorption features were observed for this sample. 92
Figure 3. 21: Indirect Band gap and reflectance spectrum of 2 mol% (a.) Ga^{3+} (3.19 eV) and (b.) La^{3+}, Ga^{3+} (3.21 eV) co-doped $SrTiO_3$. Both samples show a slight increase in the band gap compared to the undoped sample. The co-doped sample shows an absorption feature around 515 nm (2.25 eV) region. 93
Figure 3.21: Indirect Band gap and reflectance spectrum of 4 mol% (a.) Ga^{3+} (3.19 eV) and (b.) La^{3+}, Ga^{3+} (3.23 eV) co-doped $SrTiO_3$. Both samples show similar band gaps as the 2 mol%

co-doped sample. The 4 mol% co-doped sample also shows an absorption feature around 515 nm (2.25 eV) region. 93
Figure 3.22: Comparison of reflectance spectrum of (a) Ga^{3+} (b) La^{3+} and (c) Comparison of La^{3+}, Ga^{3+} co-doped $SrTiO_3$ samples with the undoped $SrTiO_3$. The 2 mol% and the 4 mol% co-doped samples differ from all the samples in exhibiting absorption features at 515 nm. ..94
Figure 3.23: (a.), (b.) Absorption spectrum highlight the absorption feature that is present in the co-doped samples and the extension of the absorption into the NIR region. These features are absent in the undoped and the monodoped samples.(c.), (d.) Blue shifted absorption wavelengths of the Ga^{3+} and La^{3+}, Ga^{3+} doped samples. 96
Figure 3.24: The PL spectrum of (a.) Ga^{3+} (b.) La^{3+} doped $SrTiO_3$ samples were compared with undoped $SrTiO_3$, with the main PL peaks represented by the dotted lines. The 2 mol% (co-) doped samples show higher PL in both cases. In 3.25 (b), the line with the * represents the deconvoluted peak present only in the undoped sample. 97
Figure 3.25: (a.), (c.), (e.), (g.), (i) Direct and (b.),(d.), (f.),(h.), (j.) Indirect band gaps of the samples. In this study, the nature of bandgaps has been determined from the PL with higher intensity indicating more efficient radiative recombinations. 100
Figure 3.26: Average room temperature TCSPC lifetimes of (a) Ga^{3+} (b) La^{3+}, Ga^{3+} doped $SrTiO_3$ samples (c), (d) shows the plots with the time in log scale to highlight the lifetime change in the samples. The 4 mol% co-doped sample shows the highest lifetime. 101
Figure 3.27: VB_M-E_F separation of undoped $SrTiO_3$ at 2.21 eV. The counts/sec on the Y-axis are measured in arbitrary units, a.u. 102
Figure 3.28: VB_M-Fermi level separation of (a) 2 mol% Ga^{3+} (b) 2 mol% La^{3+}, Ga^{3+} (c) 4 mol% Ga^{3+} (d) 2 mol% La^{3+}, Ga^{3+} doped $SrTiO_3$. The monodoped samples show a higher E_F-VB_M separation whereas on co-doping the separation decreases indicating a decrease in n-type nature. The counts/sec on the Y-axis are measured in arbitrary units, (a.u.). 103
Figure 3.29: Measurement of the ϕ of undoped $SrTiO_3$ from the $E_{cut\text{-}off}$ from the XPS. The y-axis is measured in counts/sec with arbitrary units (a.u.). 105
Figure 3.30: Measurement of the work function of (a.) 2 mol% Ga^{3+} (b.) 4 mol% La^{3+} (c.) 4 mol% Ga^{3+} and (d.) 4 mol% La^{3+} doped $SrTiO_3$ showing an increase in the work function in most samples except the 4 mol% Ga^{3+} monodoped sample. 106
Figure 3.31: Band edge energy diagrams of (a) 2 mol% Ga^{3+} (b) Undoped and (c) 2 mol% La^{3+},Ga^{3+} doped $SrTiO_3$. 107
Figure 3.32: Band edge energy diagrams of (a) 4 mol% Ga^{3+} (b) Undoped and (c) 4 mol% La^{3+},Ga^{3+} doped $SrTiO_3$. 108
Figure 3.33: Effect of doping on the (a) -OH species and (b) Ti^{3+} defects as measured with the XPS. The decrease in Ti^{3+} defects aligns with the higher PL intensities in the doped samples which demonstrated a decrease in non-radiative recombination pathways. 108
Figure 3.34: La^{3+} co-doped samples demonstrating higher lifetimes with lower EA and IP. This could be due to lower trapping due to a decrease in defects as observed with the PL intensity which increases the charge carrier mobility. 110
Figure 3.35: Band Edge Alignment to Water Redox Potentials (vacuum) of undoped and doped samples considering direct bandgaps as measured with the DRS. The work function and the E_F-VB_M separation as measured with the XPS were used to calculate the positions of VB and CB. 111

Figure 3.36: Linear sweep voltammetry measurements of La^{3+} co-doped samples under (a) AM1.5G (b) UV (40% intensity) (c) Ga^{3+} doped $SrTiO_3$ samples at 900 °C under UV (40% intensity) with the inset demonstrating the light response towards OER (d) Ga^{3+} doped $SrTiO_3$ samples at 900 °C under UV (40% intensity) with the inset demonstrating the light response towards HER. 112
Figure 3.37: Cyclic voltammetry graph comparing the performance under (a) AM1.5G conditions of La^{3+} co-doped samples (b.) UV irradiation of Ga^{3+} monodoped samples. In both (a) and (b), the doped samples perform better towards OER and HER in the case of the monodoped samples. 113
Figure 3.38: (a) Comparison of light and dark currents in 4 mol% Ga^{3+} doped $SrTiO_3$ showing a small difference (b) Higher photocurrents in 4 mol% La^{3+}, Ga^{3+} co-doped samples (c) Chronoamperometry results showing higher photocurrents in the La co-doped samples….....114

Chapter 4

Figure 4.1: Ga^{3+} doped $SrTiO_3$ nanoparticles coalesced at 900 °C to form bigger particles leading to the formation of grain boundaries. The particles are prone to agglomeration at high temperatures although exhibiting higher crystallinity. 127
Figure 4.2: The possible elongation of one particle and merging with the bigger particle due to high-temperature calcination 2 mol% Ga^{3+}doped sample indicating that at higher temperatures particles undergo sintering and Ostwald ripening. 127
Figure 4.3: HAADF STEM image of 4 mol% Ga^{3+} doped $SrTiO_3$ synthesized at 900 °C demonstrating heterogeneity in Ga distribution. This could be due to local variations in the diffusion rates of the dopant leading to non-uniform doping. 128
Figure 4.4: A Ti^{4+} chelate complex with two deprotonated CA molecules with a charge of -2[25]. CA loses protons (H^+) when it coordinates with Ti^{4+}. 129
Figure 4.5: Samples synthesized at different annealing temperatures from 450 °C to 900 °C. 130
Figure 4.6: Phase pure materials were first obtained at 500 °C. The low-temperature synthesized samples were compared with, and the samples synthesized at 900 °C to check phase purity. The peak at 29.5° 2q is due to kß radiation. 131
Figure 4.7: Phase pure materials as determined from the XRD diffraction patterns of the samples synthesized at different temperatures compared with the standard $SrTiO_3$ sample, ICSD (pink). The XRD pattern of the samples was collected with the same parameters described in Chapters 2 and 3. 132
Figure 4.8: Comparison of XRD peak (110) of (a) Undoped (b) 2 mol% Ga^{3+} doped (c) 4 mol% Ga^{3+} doped $SrTiO_3$ synthesized at 500 °C, 600 °C, 700 °C and 800 °C to demonstrate the effect of calcination temperature on the relative crystallinity of the materials. 133
Figure 4.9: Comparison of XRD (110) peak intensities of doped and undoped samples at different temperatures with the 2 mol% Ga^{3+} doped sample showing the highest crystallinity. Peak (110) as shown in Figure 4.7 is the most intense peak that has been used to compare the relative crystallinity. 134

Figure 4.10: Effect of increasing annealing temperatures on the crystallite sizes as determined by the XRD from the Scherrer equation as analyzed in Figure 4.8. The crystallite sizes increased with an increase in temperature for all the samples. 135
Figure 4.11: Effect of temperature on the microstrain of the undoped and doped samples. The microstrain in this work has been studied as an indicator of localized defects[32]. This parameter decreases monotonically for the undoped samples and for the doped samples increases up to 700 °C. At 800 °C both the doped samples show a decrease. 137
Figure 4.12: XRD peak (110) shifts (a) Undoped (b) 2 mol% Ga Doped (c) 4 mol% Ga doped $SrTiO_3$ as a function of temperature. The 2 mol% doped sample show a monotonic lattice expansion at all temperatures. The undoped and the 4 mol%, samples show a monotonic lattice contraction. 139
Figure 4.13: Comparison of XRD peak (110) between the undoped and the doped samples at (a.) 500 °C (b.) 600 °C (c.) 700 °C (d.) 800 °C demonstrating how the microstructural parameters relating to the size and strain change between the doped samples synthesized at different temperatures. 141
Figure 4.14 : Photoluminescence Decay Time Profile Comparison between undoped mol% doped $SrTiO_3$ at (a) 500 °C (b) 600 °C (c) 700 °C (d) 800 °C. The TCSPC data was fitted with a three exponential decay function as discussed in Chapter 2. The 2 mol% Ga^{3+} at 800 °C show the highest lifetime at 0.68 ns mol% mol% °C. 142
Figure 4.15: The correlation between the lifetimes of the doped samples and the temperature. The lifetimes decrease in all the samples synthesized at 500 °C. to 700 °C. At 800 °C all the samples show an increase in the lifetime with 2 mol% doped sample demonstrating the highest lifetime at 0.68 ns. 144
Figure 4.16: Absorption wavelengths of (a) Undoped (b) 2 mol% Ga^{3+} (c) 4 mol% Ga^{3+} doped $SrTiO_3$. All samples exhibit absorption in the UV region. Doped samples show traces of absorption features which become more prominent with temperature around the 550 nm region indicating the modification of opto-electronic properties due to oxygen vacancies. This phenomenon was also observed in the case of the La^{3+} co-doped samples as discussed in Chapter 3. 145
Figure 4.17: Temperature-dependent bandgaps (a) undoped indirect (b) 2 mol% Ga^{3+} indirect (c) 4 mol% Ga^{3+} doped indirect (d) undoped direct (e) 2 mol% Ga^{3+} doped direct (f) 4 mol% Ga^{3+} doped direct $SrTiO_3$ samples. The absorption features can be observed more prominently with an increase in temperatures in the indirect bandgaps (a-c). 146
Figure 4.18: Temperature-dependent separation of the E_F and the VB_M (a) undoped (b) 2 mol% Ga doped (c) 4 mol% Ga doped $SrTiO_3$ samples. In the undoped series, the E_F-VB_M separation decreases for the samples synthesized at 500 – 600 °C. The separation and therefore, the n-type nature increased at higher temperatures. For the 2 mol% doped series, the 500 and 800 °C samples exhibit a decrease in the E_F-VB_M separation (decrease in n-type nature) whereas, the 4 mol% doped series exhibits only minor differences. 147
Figure 4.19: (a) Band edge alignment of undoped $SrTiO_3$ synthesized at 800 °C. E_F-VB_M separation at all temperatures (b) Undoped samples (c) 2 mol% Ga^{3+} (d) 4 mol% Ga^{3+} doped $SrTiO_3$ demonstrating the highest separation at 700 °C. This aligns with the higher n-type conduction for these samples. 148

Figure 4.20: Work function measurements of the samples with (a.) XPS (b.) Kelvin Probe. Both measurements show a decrease in work function as a function of synthesis temperature. 149
Figure 4.21: (a.) Undoped (b.) 2 mol% Ga (c.) 4 mol% Ga doped $SrTiO_3$ work function spectrum from the secondary electron cut-off measured with the XPS. The work function measured with this method shows slight variation within samples in a series as compared to the Kelvin Probe method. 151
Figure 4.22: Temperature Dependent Correlation between Microstructural (Cell Volume) and Electronic (Work Function) from XPS (a.) Undoped (b.) 2 mol% Ga (c.) 4 mol% Ga doped $SrTiO_3$. The correlation between the two material properties can be linked to the formation of oxygen vacancies. 152
Figure 4.23: Key components of the band edge energy diagram which were calculated from the direct band gap, the E_F- VB_M separation measured from the XPS, and the work function from the XPS. All values were referenced from the vacuum scale. 154
Figure 4.24: (a) Band edge energy diagram of undoped $SrTiO_3$ synthesized at 800 °C. E_F-CB_{Min} separation at all temperatures (b) Undoped samples (c) 2 mol% Ga^{3+} (d) 4 mol% Ga^{3+} doped $SrTiO_3$ demonstrating the relation between the temperatures and n-type conductivity which is highest at 700 °C. 155
Figure 4.25: (a) Band edge energy diagram of the undoped $SrTiO_3$ sample at 800 °C. Comparison of the IP and the EA with the work function at different temperatures. Doped samples show lower IP and EA at 500 °C and 800 °C. For the undoped samples, lower IP and EA are observed at 500 °C. 156
Figure 4.26: Variation of IP, EA, and lifetimes in the samples with temperature (a) undoped (b) 2 mol% Ga doped (c) 4 mol% Ga doped $SrTiO_3$ samples. At 800 °C, both the doped samples show that decrease in the EA and the IP leading to an increase in lifetimes. 157
Figure 4.27: Positions of CB_{Min} and VB_M of the synthesized samples at different temperatures with respect to vacuum. 159
Figure 4.28: Deconvoluted and charge-corrected Sr3d peaks of undoped $SrTiO_3$ at 500 °C at 132.73 eV and 134.49 eV with a trace amount of $SrCO_3$ (green doublet).....160
Figure 4.29: Deconvoluted Sr3d peaks of (a) 2 mol% Ga^{3+} (b) 4 mol% Ga^{3+} doped $SrTiO_3$ synthesized at 800 °C and 500 °C.....160
Figure 4.30: XPS Ti2p Peak of Undoped $SrTiO_3$ with $Ti2p_{1/2}$ at 463.87 eV (orange) and Ti^{3+} (blue) towards lower binding energies. 162
Figure 4.31: XPS Ti2p peaks (orange) of (a) 2 mol% (800 °C) and 4 mol% (500 °C) Ga^{3+} doped samples with $Ti2p_{1/2}$ at lower binding energies as compared to undoped $SrTiO_3$. Deconvolution shows the presence of Ti^{3+} (blue) at varying concentrations. 162
Figure 4.32: XP spectrum of undoped $SrTiO_3$ synthesized at 500 °C peak with the main lattice component at 528.97 eV and surface -OH groups (blue) towards higher binding energies. .163
Figure 4.33: XPS O1s (orange) peak deconvolution of (a) 2 mol% Ga^{3+} at 800 °C and (b) 4 mol% Ga^{3+} at 500 °C doped samples. Both the doped samples exhibit surface -OH groups (violet) and -C=O species (blue) at higher binding energies. 163
Figure 4.34: XPS $Ga2p_{3/2}$ peak of (a) 2 mol% Ga^{3+} and (b) 4 mol% Ga^{3+} doped $SrTiO_3$ confirming the presence of Ga^{3+}. 164

Figure 4.35: Comparison of -OH groups adsorbed on the surface of the (a) undoped, (b) 2 mol%, and (c) 4 mol% Ga^{3+} doped samples synthesized at 500 °C- 800 °C. For the both undoped and the doped series, the sample synthesized at 700 °C shows the highest -OH groups. 165
Figure 4.36: Effect of increase in temperature on the doping levels for the (a) 2 mol% Ga^{3+} (b) 4 mol% Ga^{3+} doped $SrTiO_3$ from XPS. At 500 °C, the dopant concentration is close to the intended mol% doping which could indicate that the solubility of Ga dopant decreases with an increase in temperature in the $SrTiO_3$ matrix.....166
Figure 4.37: Effect of increase in temperature on the doping levels for the (a) 2 mol% Ga^{3+} (b) 4 mol% Ga^{3+} doped $SrTiO_3$ from XPS. The ratio deviates from the 1:1 ratio in the doped samples indicating the incorporation of the dopant in the $SrTiO_3$ matrix. 167
Figure 4.38: Effect of increase in temperature on the (a) 2 mol% Ga^{3+} (b) 4 mol% Ga^{3+} doped $SrTiO_3$ synthesized at 800 °C from the TEM. The samples did not show any exsolution.....167
Figure 4.39: Room temperature PL spectrum comparison of the samples (a) Undoped (b) 2 mol% and (c) 4 mol% Ga^{3+} doped $SrTiO_3$ samples synthesized at different temperatures. The 800 °C samples in the case of the undoped and the doped series show the highest intensity indicating the highest suppression of non-recombination pathways. The dotted lines show the emission peaks upon excitation. 168
Figure 4.40: Dopant dependent PL comparison of undoped and Ga^{3+} doped $SrTiO_3$ samples at (a) 500 °C (b) 600 °C (c) 700 °C (d) 800 °C. The 4 mol% doped samples at all temperatures show the highest PL intensity indicating the better suppression of non-radiative recombination pathways. 169
Figure 4.41: Defect energy level diagram of Ga^{3+} doped $SrTiO_3$ from the PL analysis in Figures 4.39 and 4.40.....170
Figure 4.42: Dopant dependent comparison of Ti^{3+} defects in the samples from the deconvolution of Ti2p peak from the XPS surface characterization at (a) 500 °C (b) 600 °C (c) 700 °C (d) 800 °C. The 4 mol% doped samples showed the highest Ti^{3+} defect suppression at all temperatures. The suppression of Ti^{3+} defects corresponds to the PL analysis in Figure 4.40. 172
Figure 4.43: PEC performance of Ga^{3+} doped $SrTiO_3$ synthesized at (a) 500 °C (b) 600 °C (c) 700 °C (d) 800 °C. At 500 °C, the undoped sample shows a higher performance towards OER and higher photoresponse. The 2 mol% doped samples show higher photoresponse at 600 and 800 °C compared to the other samples at those temperatures.. 173
Figure 4.44: Correlation between the microstrain and lifetimes of the samples for (a) 2 mol% Ga^{3+} (b) 4 mol% Ga^{3+} doped $SrTiO_3$. In the doped samples, the microstrain shows an inverse relation to the lifetimes. 175

Chapter 5

Figure 5.1: Synthesized samples (a) La^{3+} co-doped samples 900 °C (b) La^{3+} co-doped samples 800 °C (c) Serial dilution Cr^{3+} monodoped series (d) Cs^{+1} co-doped sample at 800 °C. 187
Figure 5.2: XRD patterns of (a) La^{3+} co-doped batch at 800 °C (b) La^{3+} co-doped batch at 900 °C (c) Cs^{1+} co-doped batch at 800 °C (d) Cs^{1+} co-doped batch at 900 °C (e) Cr^{3+} monodoped

batch with serial dilution synthesized at 800 °C compared with ICSD reference (pink). All patterns were measured with a PANanalytical X'pert MPD diffractometer with Cu Kα radiation source of λ = 0.15406 nm and were collected between 2θ range 20° to 80° and at 0.3s time/step. 189
Figure 5.3: Comparison of the crystallite sizes (a) Cr monodoped serial dilution samples with the inset comparing the 2 mol% Cr monodoped sample prepared by different methods (b) La^{3+} co-doped (800 °C, 900 °C) (b) La^{3+} co-doped (900 °C) (c) Cs^{1+} co-doped (800 °C, 900 °C). The error bars in the crystallite sizes were added after remeasuring the XRD patterns and applying the Scherrer formula three times. 190
Figure 5.4: Lattice volumes comparison (a) Cr monodoped SD series samples (b) La^{3+} co-doped samples (c) Cs^{1+} co-doped samples. An upward trend in the lattice volumes indicates an expansion and a downward trend indicates a contraction. 191
Figure 5.5: Degree of relative crystallinity comparison w.r.t to (110) in (a) La^{3+} 800 °C co-doped (b) La^{3+} 900 °C co-doped (c) Cs^{1+} 800 °C co-doped (d) Cs^{1+} 900 °C co-doped $SrTiO_3$ samples. The 1 mol% La co-doped sample at 800 °C shows higher relative crystallinity than the undoped and other doped samples. All the Cs doped samples (800 °C) in (c) show higher relative crystallinity as compared to the undoped. 194
Figure 5.6: Microstrain comparison (a) Cr monodoped SD series samples. The inset shows the comparison between the 2 mol% Cr doped samples synthesized with the serial dilution method and the standard sol-gel Pechini method (b) La^{3+} co-doped samples (c) Cs^{1+} co-doped samples. Microstrain is an indirect indicator of defects present in crystal lattices. 195
Figure 5.7: Deconvoluted and charge-corrected Sr3d Peaks of Undoped $SrTiO_3$ (900 °C) at 132.77 eV and 134.49 eV with trace amount of $SrCO_3$. 197
Figure 5.8: Deconvoluted and charge-corrected Sr3d Peaks of 2 mol% Cr^{3+} doped $SrTiO_3$ (900 °C) at 132.59 eV and 134.34 eV with trace amount of $SrCO_3$. 197
Figure 5.9: Deconvoluted and charge-corrected Sr3d Peaks of 2 mol% Cr^{3+} doped $SrTiO_3$ (800 °C) at 133.01 eV and 134.77 eV with trace amount of $SrCO_3$. 198
Figure 5.10: Deconvoluted and charge corrected Sr3d Peak of 1 mol%, 2 mol%, 5 mol% and 10 mol% La, 2 mol% Cr doped $SrTiO_3$ synthesized at 900 °C with additional peaks of $SrCO_3$. 198
Figure 5.11: Deconvoluted and charge corrected Sr3d Peak of (a) 1 mol% (b) 2 mol% (b) 5 mol% and (d) 10 mol% La, 2 mol% Cr doped $SrTiO_3$ synthesized at 800 °C with additional peaks of $SrCO_3$. 199
Figure 5.12: Deconvoluted and charge corrected Sr3d Peak of (a) 0.1 mol% (b) 1 mol% and 2 mol% Cr doped $SrTiO_3$ prepared with the serial dilution method. 200
Figure 5.13: XPS Ti2p Peak of Undoped $SrTiO_3$ with $Ti2p_{1/2}$ at 463.94 eV with Ti^{3+} (blue) at lower binding energies. 201
Figure 5.14: Deconvoluted and charge- corrected $Ti2p_{1/2}$ peaks of 2 mol% Cr^{3+} doped $SrTiO_3$ (900 °C) at 463.78 eV and Ti^{3+} (blue). 202
Figure 5.15: Deconvoluted and charge corrected $Ti2p_{1/2}$ peaks of 2 mol% Cr^{3+} doped $SrTiO_3$ (800 °C) at 464.05 eV with Ti^{3+} defects. 203
Figure 5.16: Deconvoluted and charge corrected $Ti2p_{1/2}$ peaks of (a) 1 mol% (b) 2 mol% (c) 5 mol% and (d) 10 mol% La, 2 mol% Cr doped $SrTiO_3$ at 900 °C. All samples in this exhibit varying concentrations of Ti^{3+}. 203

Figure 5.17: Deconvoluted and charge corrected $Ti2p_{1/2}$ peaks of (a) 1 mol% (b) 2 mol% (c) 5 mol% and (d) 10 mol% La, 2 mol% Cr doped $SrTiO_3$ at 800 °C with Ti^{3+} present in all samples in this batch. 204
Figure 5.18: Deconvoluted and charge corrected $Ti2p_{1/2}$ peaks of (a) 0.1 mol% (b) 1 mol% and (c) 2 mol% Cr doped $SrTiO_3$ synthesized with the serial dilution series. 1 mol% SD samples exhibit the lowest Ti^{3+} in all the Cr (co-) doped samples prepared with different methods. .205
Figure 5.19: XP spectrum of $Cr2p_{1/2}$ and $Cr2p_{3/2}$ of peaks of 2 mol% Cr^{3+} doped $SrTiO_3$ (900 °C). XPS reveals the presence of both Cr^{3+} (orange) around 576 eV binding energy and Cr^{6+} (blue) around 580 eV binding energy. 207
Figure 5.20: XP spectrum of $Cr2p_{1/2}$ and $Cr2p_{3/2}$ of peaks of 2 mol% Cr^{3+} doped $SrTiO_3$ (800 °C) with both Cr^{3+} (orange) and Cr^{6+} (blue). 207
Figure 5.21: XP spectrum of $Cr2p_{1/2}$ and $Cr2p_{3/2}$ of peaks of (a) 1 mol% (b) 2 mol% (c) 5 mol% and (d) 10 mol% La, 2 mol% Cr doped $SrTiO_3$ at 900 °C displaying both Cr^{3+} (orange)and Cr^{6+} (blue). The 2 mol% La co-doped show the highest suppression of the Cr^{6+} states in this batch. 208
Figure 5.22: XP spectrum of $Cr2p_{1/2}$ and $Cr2p_{3/2}$ of peaks of Cr^{3+} (orange) and Cr^{6+} (blue) (a) 1 mol% (b) 2 mol% (c) 5 mol% and (d) 10 mol% La, 2 mol% Cr doped $SrTiO_3$ at 800 °C. In this batch, the suppression of Cr^{6+} states are higher in the 5 mol% (co-) doped sample. 209
Figure 5.23: XP spectrum of $Cr2p_{1/2}$ and $Cr2p_{3/2}$ of peaks of (a) 0.1 mol% (b) 1 mol% and (c) 2 mol% Cr doped $SrTiO_3$ of the SD series. Cr^{6+} states in this batch is prominent at higher mol% doping. The 0.1 and 1 mol% monodoped samples do not exhibit any Cr^{6+} states towards higher binding energies. 210
Figure 5.24: XP spectrum of O1s peak with the main component at 529.36 eV at 900 °C with -C=O (blue) and -OH species (violet). 213
Figure 5.25: XP spectrum of O1s (orange) of peaks of 2 mol% Cr^{3+} doped $SrTiO_3$ at 900 °C and -C=O (blue) and -OH (violet) towards higher binding energies. 214
Figure 5.26: XP spectrum of O1s (orange) of peaks of 2 mol% Cr^{3+} doped $SrTiO_3$ at 800 °C 215
Figure 5.27: XPS O1s (orange) peak deconvolution of (a) 1 mol% (b) 2 mol% (c) 5 mol% (d) 10 mol% La, 2 mol% Cr co-doped $SrTiO_3$ at 900 °C with varying concentrations of -C=O (blue) and -OH (violet). 215
Figure 5.28: XPS O1s peak (orange) deconvolution of (a) 1 mol% (b) 2 mol% (c) 5 mol% (d) 10 mol% La, 2 mol% Cr doped $SrTiO_3$ at 800 °C with 216
Figure 5.29: XPS O1s peak (orange) deconvolution of (a) 0.1 mol% (b) 1 mol% and (c)2 mol% Cr doped $SrTiO_3$ prepared with the SD series with -C=O (blue) and -OH (violet) at higher binding energies. 217
Figure 5.30: XP spectrum of $La3d_{3/2}$ and $La3d_{5/2}$ peaks of 1 mol%, 2 mol%, 5 mol% and 10 mol% La, 2 mol% Cr doped $SrTiO_3$ at 900 °C. 218
Figure 5.31: XP spectrum of $La3d_{3/2}$ and $La3d_{5/2}$ peaks of (a) 1 mol% (b) 2 mol% (c) 5 mol% and (d) 10 mol% La, 2 mol% Cr doped $SrTiO_3$ at 900 °C. 219
Figure 5.32: EPR spectrum of samples 2 mol% Cr-STO 800 °C (black) and 2 mol% Cr-STO 900 °C (red), measured at 100 K with a microwave power of 50 μW and a field modulation amplitude of 0.025 mT. The plot shows only the central part of the measured spectrum, but the

integration was carried out using the full magnetic field range at the edges of which the EPR intensity would go to zero.....221
Figure 5.33: Measurement (black) and simulation (red) of the Cr(III) signal in 2 mol% Cr-STO 800 °C. The spectrum was simulated considering an isotropic Cr(III) (S = 3/2, I = 3/2 (9.5% abun.), I = 0 (90.5% abun.), g = 1.9784, g-Strain = 0.001, A = 48.6 MHz, Lorentzian linewidth = 0.55 mT. The inclusion of zero-field splitting interaction did not improve the agreement with the experiment, and it was therefore neglected, making the simulation identical to that of the corresponding S = 1/2 ion.....222
Figure 5.34: Raw (a) and normalised (b) EPR spectrum of Cr-STO samples prepared with the serial dilution method. (red) 2 mol% Cr-STO 900 °C, (green) 1 mol% Cr-STO 800 °C and (green) 0.1 mol% Cr-STO 800 °C. The spectrum were measured at 100 K with a microwave power of 50 μW and a field modulation amplitude of 0.025 mT for 2 mol% Cr and 0.015 mT for 0.1 mol% Cr and 1 mol% Cr. 222
Figure 5.35: Raw (a) and normalised (b) EPR spectrum of 2 mol% Cr-STO 800 °C (red), 1 mol% Cs,2 mol% Cr-STO 800 °C (magenta), 2 mol% Cs,2 mol% Cr-STO 800 °C (blue) and 5 mol% Cs,2 mol% Cr-STO 800 °C (green). The samples were measured at 100 K with a microwave power of 50 μW and a field modulation amplitude of 0.025 mT. The field modulation for sample for sample 5%Cs,2%Cr-STO 800 °C was 0.01 mT. 223
Figure 5.36: EPR spectrum of the sample sets annealed at 800 °C (a) 900 °C (b), consisting of 2 mol% Cr-$SrTiO_3$ (red), 1 mol% La,2 mol% Cr-$SrTiO_3$ (blue), 2 mol% La, 2 mol %Cr-$SrTiO_3$ (magenta), 5 mol% La,2 mol% Cr-$SrTiO_3$ (purple) and 10 mol% La,2 mol% Cr-$SrTiO_3$ (yellow). The samples were measured at 100 K with a microwave power of 50 μW and a field modulation amplitude of 0.025 mT. (c, d) Normalization of panels and b. 224
Figure 5.37: (a) Suppression of Rh^{4+} states by La^{3+} co-doping which the Rh^{3+} states above the O2p level (VB)[5] (b) Shallow Cr^{6+} states below the CB and Cr^{3+} states above the VB upon site-specific Cr doping in $SrTiO_3$[18]. 225
Figure 5.38: Indirect band gaps of (a) Cr monodoped serial dilution $SrTiO_3$ samples (b) La^{3+} co-doped 800 °C (c) La^{3+} co-doped 900 °C (d) Cs^{1+} co-doped 800 °C (e) Cs^{1+} co-doped 900 °C. All the doped samples show midgap states. These states are suppressed to the maximum for both the 2 mol% La^{3+} (co-) doped samples. Cs co-doping did not show any suppression of these states. 226
Figure 5.39: Direct band gaps with midgap states of (a) Cr monodoped serial dilution $SrTiO_3$ samples (b) La^{3+} co-doped 800 °C (c) La^{3+} co-doped 900 °C (d) Cs^{1+} co-doped 800 °C (e) Cs^{1+} co-doped 900 °C. The midgap state suppression are analogous to the indirect bandgaps.....228
Figure 5.40: Comparison of absorption wavelengths from the Kubelka Munk function of the La^{3+} co-doped samples synthesized at 800 °C with the undoped. These samples show the extension of the absorption into the visible light region and tailing off at 750 nm. The absorption feature around 450 – 500 nm is highly suppressed for the 2 mol% co-doped sample. 230
Figure 5.41: Comparison of absorption wavelength from the Kubelka Munk function of the La^{3+} co-doped samples synthesized at 900 °C with absorption in the doped samples extending beyond 800 nm in most cases. The 2 mol% co-doped sample tails off at 700 nm and shows the highest suppression of the absorption feature around 500 nm.....231
Figure 5.42: Comparison of absorption wavelength from the Kubelka Munk function of the Cs^{+1} samples synthesized at 800 °C with the increase in absorption beyond 800 nm with an

increase in co-doping. No suppression of the absorption feature in any of the co-doped samples. 232
Figure 5.43: Comparison of absorption wavelength from the Kubelka Munk function of the Cs^{+1} samples synthesized at 900 °C behaving similarly to the batch at 800 °C. 232
Figure 5.44: Comparison of absorption wavelength from the Kubelka Munk function of the (a) 0.1 mol% (b) 1 mol% and (c) 2 mol% Cr monodoped serial dilution series synthesized at 800 °C. The absorption into the visible light region and the absorption feature around 550 nm increase with doping. 233
Figure 5.45: VB_M - Fermi level separation of undoped $SrTiO_3$ at (a) 800 °C (2.68 eV) and (b) 900 °C (2.21 eV). 234
Figure 5.46: $VB_M - E_F$ separation decreases for the sol-gel Pechini synthesized 2 mol% Cr^{3+} doped $SrTiO_3$ at (a) 800 °C (2.01 eV) (b) 900 °C (2.05 eV) as compared to the undoped samples. 235
Figure 5.47: VB_M-Fermi level separation further decreases of (a) 1 mol% (1.78 eV) (b) 2 mol% (1.99 eV) (c) 5 mol% (1.91 eV) (d) 10 mol% (1.86 eV) La^{3+} co-doped $SrTiO_3$ synthesized at 800 °C compared to the 2 mol% Cr monodoped and the undoped samples. 236
Figure 5.48: VB_M-Fermi level separation of (a) 1 mol% (1.98 eV) (b) 2 mol% (2.39 eV) (c) 5 mol% (2.39 eV) (d) 10 mol% (1.95 eV) La^{3+} co-doped $SrTiO_3$ synthesized at 900 °C. The 1 mol% and the 10 mol% decrease and the 2 mol% and the 5 mol% increase compared to the 2 Cr monodoped samples. 237
Figure 5.49: (a) Appearance of Cr3d t_{2g} states when Cr is doped at the A-site of $SrTiO_3$ [36](b) 0.1 mol% and 1 mol% Cr^{3+} hinting the presence of Cr3d t_{2g} states in the inset at the edge of the O2p of the VB spectrum. 238
Figure 5.50: VB_M-Fermi level separation decreases of (a) 0.1 mol% (b) 1 mol% (c) 2 mol% Cr doped $SrTiO_3$ synthesized via the serial dilution method at 800 °C compared to the undoped samples. 239
Figure 5.51: Work function of the undoped $SrTiO_3$ synthesized at 900 °C at 4.18 eV. 240
Figure 5.52: Work function of the 2 mol% Cr^{3+} doped sample synthesized at (a) 800 °C (4.34 eV) and (b) 900 °C (4.41 eV) increased compared to the undoped. 240
Figure 5.53: Work function of the (a) 1 mol% (4.26 eV) (b) 2 mol% (4.29 eV) (c) 5 mol% (4.27 eV) (d) 10 mol% La^{3+} co-doped (4.34 eV) samples synthesized at 800 °C decreases in most samples compared to the 2 mol% Cr monodoped sample at the same temperature. 241
Figure 5.54: Work function of these samples decreases with (a) 1 mol% (4.19 eV) (b) 2 mol% (4.33 eV) (c) 5 mol% (4.03 eV) (d) 10 mol% La^{3+} (4.05 eV) co-doped samples synthesized at 900 °C compared to the 2 mol% Cr monodoped sample at 900 °C. 241
Figure 5.55: Work function of the (a) 0.1 mol% (b) 1 mol% (c) 5 mol% Cr^{3+} doped samples synthesized at 800 °C with the serial dilution method increases compared to the undoped. 242
Figure 5.56: Band edge energy diagrams of undoped $SrTiO_3$ synthesized at (a) 800 °C (b) 900 °C. 244
Figure 5.57: Band edge energy diagrams of 2 mol% Cr^{3+} doped $SrTiO_3$ synthesized via sol-gel Pechini at (a) 800 °C for 10 h (b) 900 °C for 6 h. 244
Figure 5.58: Band edge energy diagrams of (a) 1 mol% La^{3+} (b) 2 mol% La^{3+} (c) 5 mol% La^{3+} (d) 10 mol% La^{3+} co-doped $SrTiO_3$ synthesized at 800 °C (10 h). 245

Figure 5.59: Band edge energy diagrams of (a) 1 mol% La^{3+} (b) 2 mol% La^{3+} (c) 5 mol% La^{3+} (d) 10 mol% La^{3+} co-doped $SrTiO_3$ synthesized at 900 °C (6 h).....245
Figure 5.60: Band edge energy diagrams of (a) 0.1 mol% (b) 1 mol% (c) 2 mol% Cr^{3+} doped $SrTiO_3$ synthesized via the serial dilution method at 800 °C (10 h).....245
Figure 5.61: Band Edge Alignment for Water Redox Potentials of (a) undoped and Cr^{3+}-La^{3+} doped samples synthesized at 800 °C and 900 °C (b) Cr monodoped $SrTiO_3$ prepared via the serial dilution method at 800 °C.....247
Figure 5.62: Average Lifetimes of the doped samples (a) La^{3+}, Cr^{3+} samples annealed at 800 °C for 10 h (b) La^{3+}, Cr^{3+} samples annealed at 900 °C for 6 h (c) Cs^{1+}, Cr^{3+} samples annealed at 800 °C for 10 h (d) Cs^{1+}, Cr^{3+} annealed at 900 °C for 6 h. Most of the co-doped samples did not show significant changes in lifetimes compared to the undoped samples.....250
Figure 5.63: Average Lifetimes of the (a) 0.1 mol% (b) 1 mol% (c) 2 mol% (d) 10 mol% monodoped serial dilution series. This batch showed a significant increase in the lifetimes of the doped samples with 1 mol% showing the highest.....251
Figure 5.64: Room temperature PL spectrum of (a) Cr monodoped samples synthesized with the sol-gel Pechini at 800 °C and 900 °C (b) La^{3+} co-doped at 800 °C (c) La^{3+} co-doped at 900 °C (d) Cs^{1+} co-doped at 800 °C (e) Cs^{1+} co-doped at 900 °C (f) Cr monodoped samples synthesized with the serial dilution method at 800 °C. All the (co-) doped samples (a-f) synthesized with the standard sol-gel Pechini showed lower PL intensity indicating higher non-radiative recombination pathways.....252
Figure 5.65: PL Defect Energy Level in Cr: $SrTiO_3$.....254
Figure 5.66: (a) CV of Cr and La co-doped samples synthesized at 800 °C (b) CV of Cr and La co-doped samples synthesized at 900 °C. All the samples were illuminated with chopped AM1.5G light. In both cases, the 2 mol% showed higher anodic OER performance. The doped samples do not show significant photoresponse due to insufficient suppression of the Cr^{6+} and intrinsic defects.....255
Figure 5.67: (a) CV of Cr SD series synthesized at 800 °C (b) LSV of the samples. All the samples were illuminated with AM1.5G light and demonstrated higher anodic performance with an increase in doping the 1 mol% Cr monodoped SD sample (highest TCSPC lifetime, Figure 5.62 (b)) showed the highest photoresponse due to the absence of Cr^{6+} states and maximum suppression of Ti^{3+} states.....255
Figure 5.68: Cr sputtered on TiO_2 nanotubes (a) without UV filter and (b) with UV filter reproduced from the work of Haryński, L. et al. [41].....257

Chapter 6

Figure 6.1: Finely ground charred material after N_2 annealing at 350°C.....264
Figure 6.2: (a) Phase pure XRD pattern of Ga^{3+} monodoped samples compared to the ICSD standard $SrTiO_3$ (pink). The XRD parameters used for the pattern are described in Table 2.2 in Chapter 2. (b) Kubelka Munk spectrum of the doped samples show absorption in the UV region similar to the undoped sample. (c) Decrease in Ti^{3+} defects with increase in mol% doping which is consistent with the findings in Chapters 3 and 4.....265

Figure 6.3: (a) N_2 physisorption curves collected at -195.85 °C for the samples. They are all mesoporous with type IV isotherm with an H1 hysteresis loop (multilayer adsorption and capillary condensation of the nitrogen in the mesopores) according to IUPAC[3]. Pore sizes are in the range between 20 and 37 nm. The BET data obtained aligns with the surface area of $SrTiO_3$ between 8 and 13 m^2/g as reported in literature. (b) CO_2 adsorption isotherms of all samples collected at 25 °C. 266
Figure 6.4: Preliminary CO evolution from photocatalytic CO_2 hydrogenation over Ga^{3+} and La^{3+}, Ga^{3+} co-doped $SrTiO_3$ samples expressed in micromoles normalized per surface area obtained with the BET N_2 physisorption. The photocatalytic setup and sample preparation have been discussed in Chapter 2. 267
Figure 6.5: The CO evolved after photocatalytic reaction expressed as micromoles per gram of catalyst as a function of time for all samples. The synthesized $SrTiO_3$ has an evolution that differs from all the other samples. Therefore, the origin of this behavior is being studied separately and has not been analyzed further. Figure 6.4 compares the doped samples with the commercial $SrTiO_3$. 268
Figure 6.6: XRD pattern of Samples with N_2 annealing intermediate step in the synthesis process compared to the ICSD reference $SrTiO_3$ pattern (pink). The XRD conditions used are discussed in Chapter 2 in Table 2.2....270
Figure 6.7: TEM (a) Nanoparticle cluster (b) Size distribution of 4 mol% Ga^{3+} doped $SrTiO_3$ with N_2 annealing indicating most particles below 25 nm. 271
Figure 6.8: Size comparison of particles with XRD (Scherrer equation and W-H analysis) and the TEM. These methods point towards a common trend of decreasing crystallite sizes with increase in mol% doping. 272
Figure 6.9: XPS Ti2p Peak of undoped $SrTiO_3$ with $Ti2p_{3/2}$ at 458.32 eV with Ti^{3+}(blue) and TiO_2 (violet). 273
Figure 6.10: XPS Ti2p peaks of (a) 1 mol% Ga^{3+} (N_2) (b) 4 mol% Ga^{3+} (N_2) doped samples with $Ti2p_{3/2}$ at lower binding energies compared to undoped $SrTiO_3$ with Ti^{3+}(red) and TiO_2 (violet). 273
Figure 6.11: Kubelka Munk function of the samples annealed under N_2 showing absorption in the UV region and no additional optical features. 274

List of Tables

Chapter 1

Table 1.1: Kröger Vink notations denoting the charges and sites of point defects introduced in $SrTiO_3$ upon doping with acceptor and donor ions 18
Table 1.2: $SrTiO_3$ synthesis methods and some material properties [128]..... 19

Chapter 2

Table 2.1 a: Stoichiometric composition of the doped samples synthesized with the sol-gel Pechini method 35
Table 2.1 b: Stoichiometric composition of the doped samples synthesized with the sol-gel Pechini method 36
Table 2.2: XRD parameters used for data collection……38

Table 2.3: ALD conditions used for 10 nm thick blocking layer on the FTO……...58

Chapter 3

Table 3.1: Goldschmidt's Tolerance Factor for undoped and doped $SrTiO_3$ samples……..68

Table 3.2: Average crystallite sizes, microstrain, lattice volumes, and lattice parameters of the synthesized samples 69
Table 3.3: Dislocation density of the synthesized samples 75
Table 3.4: Position of the $Sr3d_{5/2}$ and the $Sr3d_{3/2}$ of the doped samples..... 83
Table 3.5: Ratio of $SrCO_3$ present in the doped samples as compared to undoped $SrTiO_3$..... 83
Table 3.6: Ratio of A-site: B-site Elements 84
Table 3.7: Peak Positions of the O1s lattice and the secondary peaks 87

Table 3.8 a: Atomic % of Sr^{2+}, Ti^{4+} and O1s in the Synthesized Samples from the XPS 90
Table 3.8 b: Relative mol% doping from the XPS..... 90
Table 3.9: Bandgaps and absorption wavelengths of the synthesized samples……....94

Table 3.10: Average lifetimes of the samples…….……..99

Table 3.11: VB_M-E_F separation of the doped samples…….....…102

Table 3.12: Measurements of Work Function (ϕ), Electron Affinity (χ), Ionisation Potential (IP) and Band Gap (E_g) from the Band Energy diagrams in Figures 3.31 and 3.32….....….106

Chapter 4

Table 4.1: Element distribution from EDX collected from Figure 5 in 4 mol% Ga^{3+} doped $SrTiO_3$ synthesized at 900 °C……...127

Table 4.2: Goldschmidt's Tolerance Factor for undoped and doped $SrTiO_3$ samples 130
Table 4.3: Average Crystallite Sizes and FWHM of the samples deduced from the Debye-Scherrer equation..... 135

Table 4.4: Calculated microstrains of the undoped and the doped samples 136
Table 4.5: Calculated lattice parameters and lattice volumes of the undoped and doped samples prepared at different temperatures 138
Table 4.6: TCSPC decay time constants and the average lifetimes of the temperature-dependent samples..... 142
Table 4.7: Experimental work functions from the Kelvin Probe and the XPS 149
Table 4.8: Position of the $Sr3d_{5/2}$ and the $Sr3d_{3/2}$ of the doped samples..... 160
Table 4.9: Atomic % of elements present in the samples..... 163

Chapter 5

Table 5.1: Goldschmidt's Tolerance Factor for undoped and doped $SrTiO_3$ samples 186
Table 5.2: Ti2p peak position of the (co-) doped samples..... 204
Table 5.3: Binding energies of $Cr2p_{3/2}$ and $Cr2p_{3/2}$ peaks 209
Table 5.4: Calculated Cr^{3+} doping from XPS for the synthesized samples 210
Table 5.5: Amount of Cr^{6+} after La^{3+} co-doping 211
Table 5.6: Binding energies of O1s deconvoluted peaks 212
Table 5.7: -C=O and -OH concentrations comparison 216
Table 5.8: Binding energies of the La3d peaks 218
Table 5.9: Amount of La^{3+} co-doping with respect to Sr^{2+}..... 219
Table 5.10: Indirect, Direct Band Gaps and Absorption Wavelengths of the parent $SrTiO_3$ Edge..... 228
Table 5.11: Measurement of Work Function (ϕ), Ionisation Potential (IP), and VB_M-E_F Separation 242
Table 5.12: Average lifetime of the Cr (co-) doped samples..... 247

Chapter 6

Table 6.1: The crystallite sizes and the BET surface areas from the N_2 and the CO_2 physisorption measurements..... 265
Table 6.2: The μmoles/m^2/h for each fitted sample, the amount of catalyst (mg) loaded, and the N_2 BET-specific surface areas used for the experiments. 267
Table 6.3: Average crystallite sizes, Microstrain, and Lattice Parameters of the synthesized samples with N_2 annealing..... 269

Vitae

Bachelors: *Bachelor of Engineering (Mechanical), India 2016*

Masters: *MSc in Renewable Energy Engineering, Germany 2019*

List of Publications

1.) ***Bhattacharyya, D.****, Shani B., Steier, L., et al., 'Understanding the root cause of the blue color in* La^{3+}*,* Ga^{3+} *co-doped* $SrTiO_3$ *and their performance towards photocatalytic water splitting':* ***Under Preparation***

2.) ***Bhattacharyya, D.****, Shani, B., Steier, L., et al.: 'Specific Surface Area Normalized Photoactivity and the Factors that Enhance the Performances of* Ga^{3+} *Doped* $SrTiO_3$*':* ***Under Preparation***

3.) ***Bhattacharyya, D.****, Shani B., Steier, L., et al.: 'Investigating the Role of* Cr^{3+}/Cr^{6+} *in Determining the Photoactivity of Cr Doped* $SrTiO_3$ *':* ***Under Preparation***

For you a thousand times over!

-The Kite Runner

Chapter 1: Introduction

1.1 Motivation and Literature Review

According to a United Nations Organization report, 90% of the world's crude oil reserves will be depleted within two generations and many other industrial raw materials [1]. Incessant abuse of fossil fuels for rapid industrialization for the expansion of the global economy is the major cause of increased greenhouse gases as reported by the Intergovernmental Panel on Climate Change (IPCC) [2]. The global economy is growing and bound to grow fourfold in the next 25 years. Many developing nations will experience a major economic boom and people's living standards on the rise will increase further. The economic boom will be the result of rapid industrialization based on the use of fossil fuels. The world is therefore in the grasp of a massive energy crisis. Unsustainable strains on natural resources will continue to increase if economic growth and the excessive harnessing of fossil fuels are not segregated. This unprecedented fossil fuel use is one of the leading causes of the increase in the CO_2 levels in the atmosphere that has resulted in the steady rise in global temperatures as shown in Figure 1.1. Zhang, Y. G., et al. [3] report that the 35 gigatons of atmospheric CO_2 resulting from anthropogenic activities pose an alarming threat to the biosphere. One of the solutions to this is a fast and feasible transition to clean fuels as per the guidelines of sustainable development. According to the Brundtland Commission of 1985, sustainable development aims to meet the needs and aspirations of the present generation without compromising the ability of future generations to meet their needs [4]. Therefore, the need of the hour is for a sustainable transition to cleaner and greener energy sources.

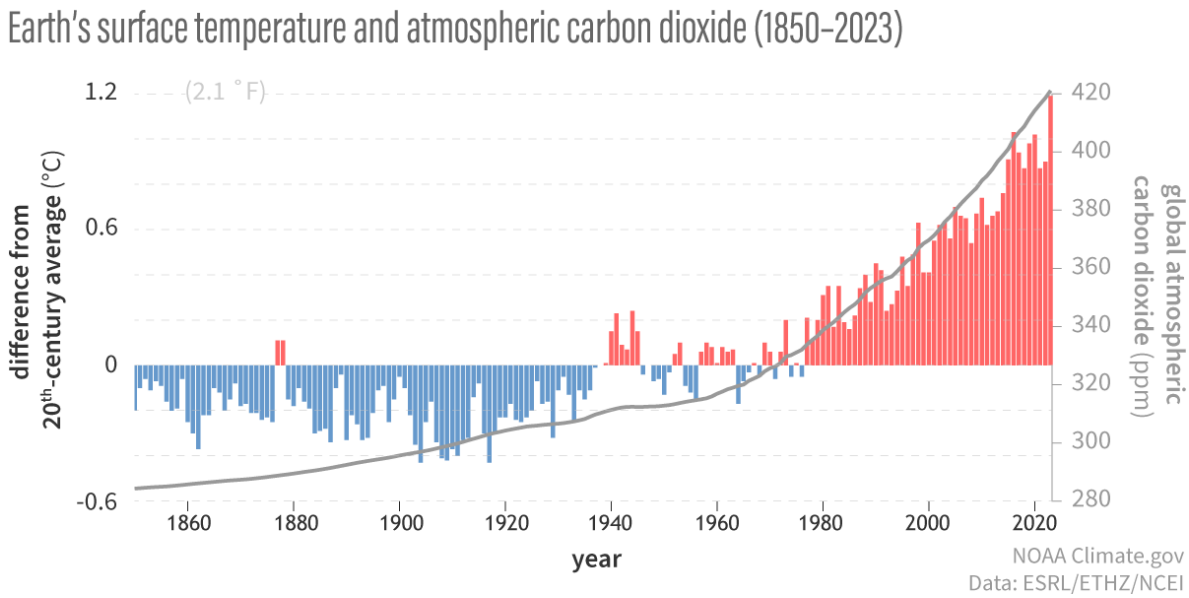


Figure 1.1: *CO_2 levels and global annual average temperature from 1850 to the present with the black line indicating the rise in CO_2 levels, the red bars indicating temperatures above the average, and the blue bars indicating temperatures below the average. Image reproduced from the National Oceanic and Atmospheric Administration (NOAA) Climate.gov website. Accessed on 18.09.2024) [5].*

In recent decades after the pioneering work of Honda and Fujishima in splitting water with a TiO_2-based photo-electrochemical (PEC) system, semiconductor photocatalysts/ photoelectrocatalysts have been in focus for clean fuel generation by harnessing solar radiation [6]. Water splitting and CO_2 reduction are the two most researched avenues for sustainable fuel generation with solar energy [7]–[13]. These technologies aim to produce clean fuels such as H_2, CO, methanol, and methane. Even though this technology has a lot of potential, scalability, and conversion efficiencies are still major issues [14]. From the year 2019, the European Commission has predicted an increase in funding for PEC and photocatalytic (PC) projects with an already allocated budget of 75 million euros [15] as shown in Figure 2.

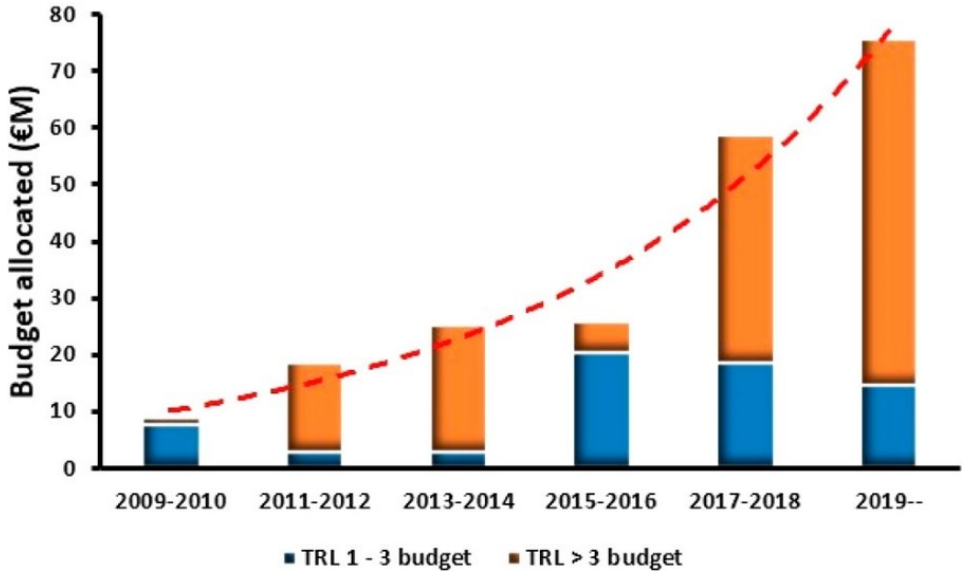


Figure 1.2: *A technology readiness level (TRL) based projection of budget allocated to photoelectrocatalysis (PEC) and photocatalysis (PC) research projects in the European Union as reproduced with permission from Galushchinskiy, A. et al. [15] (Open access, licensed under CC-BY 4.0). The TRL system is used to measure the maturity of a project on a scale of 1-9 [16].*

Photocatalytic and photoelectrocatalytic fuel generation have been studied intensively in recent decades. In their review article, Villa, K. et al. [8] have summarized the key characteristics that an ideal photocatalyst/photoelectrocatalyst should possess for efficient solar fuel generation. These are as follows:

- The conduction band minimum (CB_{Min}) and valence band maximum (VB_M) should be in favorable positions and straddle the redox potentials
- Visible light absorption and bandgap narrowing to maximize light absorption efficiency
- The materials should be photochemically stable
- The materials should be low cost (economic feasibility) and should be earth-abundant

After the revolutionary work of Honda-Fujishima on TiO_2 photoelectrodes, oxide-based photocatalytic materials are highly studied [12]. Since the 1980s, $SrTiO_3$ and TiO_2 are some of the simplest forms of oxide photocatalysts that have been studied for the evolution of H_2 and O_2 upon light absorption which paved the way for the discovery of other materials [12], [17],

[18]. In 1980, overall water splitting on particulate photocatalysts was first reported [19], [20]. Domen, K. et al. [19] and Tomoji, K. et al. [20] reported the photocatalytic decomposition of water vapor with NiO-$SrTiO_3$ and RuO-TiO_2-based catalysts respectively. The work on particulate photocatalysts paved the way for newer oxide materials with layered and tunneled structures. Kudo, A. et al. [21] and Inoue, Y. et al. [22] reported the water decomposition over NiO-$K_4Nb_6O_{17}$ and RuO_x-$BaTi_4O_9$. The presence of tunnels in these catalysts facilitated an interaction with promoters such as RuO_X, leading to a more effective charge separation and higher performance. Tunnels in photocatalysts could increase the surface area for the dispersion of the promoters and provide diffusion pathways to improve mass transport. In overall water splitting, metal cations with d^0 or d^{10} have been reported to show enhanced performances [23]–[27]. In these cited works, the d^0 transition metal cations are Ti^{4+}, Zr^{4+}, Nb^{5+}, Ta^{5+}, and W^{6+}. The d^{10} cations studied are Ga^{3+}, In^{3+}, Ge^{4+}, Sn^{4+}, and Sb^{5+}. Materials such as TiO_2, WO_3, and $SrTiO_3$ are associated with deep-level VB_M (O 2p), increasing the bandgaps, enabling only UV light absorption, and reducing overall efficiency. This has led to increased research in wide bandgap photocatalysts where visible light absorption was introduced upon doping with transition metals with partially filled d-orbitals [28]–[38]. These partially filled d-orbitals can introduce states above the VB_M, narrowing the band gap. Oxides with non-zero d-orbitals such as the Fe_2O_3, even though they exhibit narrow bandgaps and conducive VB_M positions, display several limitations. These limitations in Fe_2O_3 stem from polaronic states inhibiting electron transport, recombinations, and poor hole mobility [39]–[41]. Polaronic states in Fe_2O_3 are electronic states associated with the localization of charge carriers due to their interaction with the surrounding lattice. In 1998, landmark studies were conducted in the field of H_2 and O_2 evolution with Rh-doped $SrTiO_3$ and $BiVO_4$ respectively [42]–[44]. In these photocatalysts, the bandgap was narrowed via the modulation of the VB_M by introducing Rh 4d and Bi 6s filled energy states above it. n-type $BiVO_4$ is another suitable material for water splitting due to its conducive band positions and stability against photochemical corrosion [45]. Studies report the performance of this material due to charge transport properties, small polaron hopping, and oxygen vacancies [45]–[48]. In 2009, the Z-scheme with Rh: $SrTiO_3$ + $BiVO_4$ demonstrated overall water splitting under simulated solar light [49]. The performance observed was due to electron transfer from the CB of the $BiVO_4$ to the impurity level of Rh species in $SrTiO_3$. A Z-scheme combines two separate semiconductor photocatalysts with appropriate energy band structures that can drive H_2 and O_2 evolution half reactions [50]. In most cases, co-catalysts are used along with the photocatalysts, especially in Z-schemes. The role of the cocatalysts such as the $RhCrO_x$ is to facilitate charge separation and transfer, lower the activation energy barrier, provide sites for redox reactions, and prohibit photo-corrosion [50]. In recent years, another photocatalytic material, g-C_3N_4 is gaining momentum in the field of overall water splitting. g-C_3N_4 is characterized by N vacancies and has a band gap of 2.06 eV [51], [52]. However, for oxygen evolution, a larger overpotential has to be overcome being a 4-electron process, g-C_3N_4 is mostly used in a Z-scheme with $BiVO_4$ or WO_3 [53]–[55]. While different photocatalysts have demonstrated promising efficiencies under different conditions, the search for materials with higher stability, cost-effectiveness, and broader application continues. Owing to these factors $SrTiO_3$ is one of the most extensively studied materials for PC and PEC applications [50].

Perovskite type $SrTiO_3$ has become the most researched photocatalyst due to its photochemical stability against corrosion and its conducive band positions to drive overall water splitting favoring effective charge carrier separation and migration [56]. One of the earliest works on $SrTiO_3$ was reported by Domen, K. et al. [57] where they studied the photodecomposition of water vapor catalyzed by NiO-$SrTiO_3$ over 100 h. Overall water splitting can be enhanced by optimizing defects using aliovalent dopants such as Ga^{3+} with the suppression of intrinsic Ti^{3+} defects and increasing oxygen vacancies [58]. In 2020, another landmark achievement was achieved with Al: $SrTiO_3$ loaded with co-catalyst $RhCrO_x$ demonstrating quantum efficiency close to unity [11]. As discussed earlier undoped $SrTiO_3$ is a UV absorber that can absorb in the visible range with bandgap engineering. One such route to increase optical response is through doping and inducing one-step overall water splitting. However, this route has several limitations such as the limited charge extraction [59]. So far the efficiency of such doped systems promoting one-step overall water splitting is quite low including the IrO_2 loaded $SrTiO_3$: Rh, Sb with an apparent quantum yield (AQY) of 0.1% at 420 nm [60]. *Apparent quantum yield (AQY) is a metric to evaluate the efficiency of photocatalytic or photoelectrocatalytic systems. It represents the fraction of incident photons that drive the reactions.* Therefore, this motivated the use of $SrTiO_3$ in Z-schemes with other photocatalysts. Wang, Q. et al. [61] studied the effect of preparation methods, calcination times, and La co-doping on Rh: $SrTiO_3$. They studied how these factors could lead to 3.5-3.8 times higher H_2 evolution from aqueous menthol. They later studied a Z-scheme comprising of $Ir/CoO_x/Ta_3N_5$ and La, Rh: $SrTiO_3$ which demonstrated that the solar to hydrogen (STH) improved by a factor of 3 (AQY of 1.1% at 420 nm). Often an electron mediator such as Fe^{2+}/Fe^{3+}, Au, Pt, or graphene oxide (GO) is required to construct a Z-scheme [49]. Electron mediators facilitate the transfer of electrons between two photocatalysts of the Z-scheme. Sasaki, Y. et al. [49] reported the study of the Z-scheme of Rh: $SrTiO_3$ + $BiVO_4$ via interparticle charge transfer without any electron mediators. Iwase, A. et al. [62] studied the use of reduced GO as an electron mediator in Rh: $SrTiO_3$+ rGO + $BiVO_4$ Z-scheme. Wang, Q. et al. [63] demonstrated that overall water splitting with solar to hydrogen (STH) of 1.2% can be achieved with a particulate photocatalyst sheet of La, Rh: $SrTiO_3$/C/ Mo: $BiVO_4$ Z-scheme.

In recent decades, the rise of CO_2 in the atmosphere from anthropogenic sources such as fossil fuel consumption and industrial activities has raised concerns about climate change. To mitigate these issues, photocatalytic / photoelectrocatalytic CO_2 reduction has gained attention. These technologies offer pathways to convert CO_2 into valuable chemicals and fuels [64]. CO_2 hydrogenation has emerged as a convenient route to reduce CO_2 into high-value products such as CO [64], [65]. CO_2 hydrogenation is a form of CO_2 reduction employing hydrogen to reduce CO_2 to CO and other hydrocarbons. Matsuo, H. et al. [65] have reported the use of Mn-doped $SrTiO_3$ for CO_2 hydrogenation. They report that 20 mol% Mn doped $SrTiO_3$ showed the highest activity towards CO generation due to the highest number of oxygen vacancies. Liu, Y. et al. [66] in their work show the design of Cu-ZnO-$SrTiO_3$ for the optimal performance towards CO_2 hydrogenation to CH_3OH. They also report that oxygen vacancies facilitate the activation of the CO_2.

Even though $SrTiO_3$ has been extensively researched, there are still challenges associated with this material that can limit its performance. The major challenge associated with $SrTiO_3$-based

photocatalysts is charge carrier recombinations and factors such as intrinsic defects that can accelerate recombinations [50]. These challenges can be tackled by optimizing the design conditions. Optimizing morphological parameters, reducing crystallite sizes, and increasing crystallinity are some of the routes to enhance the performance of $SrTiO_3$. A high degree of crystallinity indicates a lesser degree of defects which can reduce charge carrier recombinations and extend the lifetimes of the materials [11]. Takata, T. et al. [58] studied defect engineering that showed the suppression of Ti^{3+} recombination centers with the increase in oxygen vacancies upon doping with aliovalent elements. Co-catalyst loading discussed in the previous paragraph is also an efficient method to enhance performance by facilitating charge extraction. Midgap states that are often associated with transition metal doping in the B-site of $SrTiO_3$ to extend absorption to the visible region, can also act as recombination centers, which can be suppressed by co-doping on the A-site [67],[68]. Therefore, to design a photocatalyst / photoelectrocatalyst it is necessary to optimize its microstructural parameters such as size and crystallinity and opto-electronic properties to suppress recombinations and enhance light harvesting. In this Ph.D. work, $SrTiO_3$ will be investigated to gain a comprehensive understanding of the materials' structural, electrical, and optical properties. Additionally, the thesis also focuses on how doping affects the properties of $SrTiO_3$. *The motivation behind the choice of dopants (Ga^{3+} and Cr^{3+}) are Al^{3+} and Rh^{3+} doped* $SrTiO_3$. *Since Ga and Cr belong to the same block as Al and Rh i.e. p and d block respectively, it would be valuable to investigate if they demonstrate similar behavior in $SrTiO_3$. Both the Ga^{3+} and Cr^{3+}dopings are expected to be in the B-site of $SrTiO_3$ due to similar ionic radii as the Ti^{4+}.*

$SrTiO_3$ can be utilized by three common approaches to produce solar fuels. These are the photocatalysis (PC), the photoelectrocatalysis (PEC), and the photovoltaic-electrochemical routes (PV-EC) [15]. The PC approach to generate solar fuels involves using particulate semiconductor or Z-scheme photocatalysts in setups that on light irradiation generate and separate charge carriers that upon migration to the surface undergo redox reactions to evolve the required products [69], [70]. In PEC systems, the photocatalysts are applied on conductive substrates and constructed as photocathodes or photoanodes in an electrocatalytic cell which drive the reduction and oxidation reactions respectively upon light irradiation and with the application of an external bias [71], [72]. In this setup, the materials can be used as either a photoanode or photocathode with a counter electrode or in a tandem arrangement where photoanodes and photocathodes are used simultaneously. A PV-EC setup consists of a PV cell that converts the solar irradiation and supplies bias to the electrolyzer (EC) [72]. The electrolyzer consists of two electrodes where the redox chemistry takes place. The approaches are demonstrated in Figure 1.3.

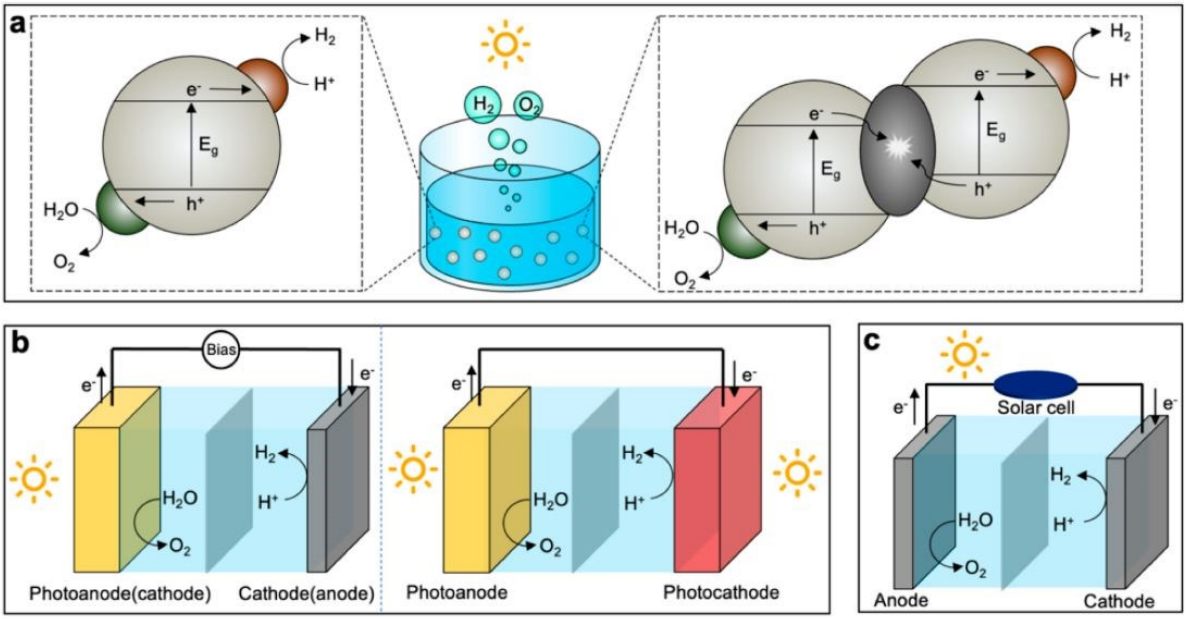


Figure 1.3: *The approaches to solar fuel generation. (a) Photocatalysis setup (PC) (b) Photoelectrochemistry setup (PEC) and (c) PV-EC setup as reproduced with permission from Jiang, C. et al.* [72] *(Open access, licensed by CC-BY-3.0).*

In the scope of the Ph.D. thesis, the PC and the PEC methods are used for performance assessments of the photocatalysts and to understand how the dopants affect the performance of $SrTiO_3$.

Even though the research in the field of photoelectrocatalysts/photocatalysts is vast, the challenges remain due to lower efficiency and stability. Hence, it is crucial to design and study new materials that can scale up this field. This Ph.D. work will attempt to understand the role of p and d block dopants and understand the PEC and the PC performance of $SrTiO_3$ primarily towards hydrogen evolution (HER) / oxygen evolution (OER) reactions and whether doping is a good strategy to address the challenges associated with this field.

1.2 Semiconductor Physics: A Case Study of $SrTiO_3$

1.2.1 Structural Properties

$SrTiO_3$ is one of the most researched photocatalysts due to its high thermo-chemical stability and its conducive conduction and valence band positions [73]. $SrTiO_3$ has a cubic ABO_3 type (pm3m) perovskite structure with Ti^{4+} at the body-centered position (½, ½, ½), Sr^{2+} at the corners (0,0,0) and O^{2-} at the face centers [(½, 0, 0), (0, ½,0), (0, 0, ½)] as shown in Figure 1.4.

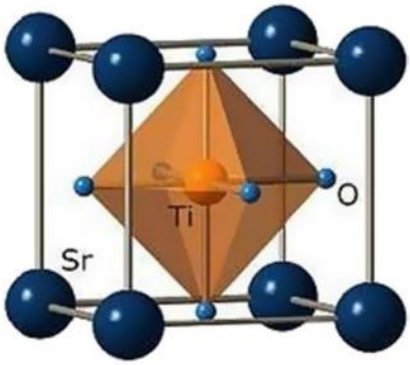


Figure 1.4: *Cubic structure of ABO_3 perovskite $SrTiO_3$ with Ti^{4+} (yellow) in the center, Sr^{2+} (dark blue) in the corners and O^{2-} (light blue) forming the octahedron with Ti^{4+}reproduced with permission from the work of Raturi, A. et al.* [74] (*Copyright © 2022, The Author(s), under exclusive license to Springer Science Business Media, LLC, part of Springer Nature).*

The structural stability of the ABO_3-type perovskites can be predicted with Goldschmidt's tolerance factor, *t* [75]–[77]. The ionic radii of the perovskite materials and their ratios are employed to determine the *t* [78]. Mathematically it is derived as:

$$t = \frac{r_A + r_O}{\sqrt{2}(r_B + r_O)} \quad (1.1)$$

Where,

r_A = Ionic radius of the A-site element in 12 co-ordination with oxygen

r_B = Ionic radius of the B-site element in 6 co-ordination with oxygen

r_O = Ionic radius of the oxide in 1 and 2 co-ordination with Ti and Sr respectively

The radii of the elements used in the Ph.D. have been adopted from the work of Shannon, R. et al. [79]. ABO_3 structures exhibit cubic structures when *t* is between 0.75 to 1[80]. $t < 0.75$ indicates a distortion of the cubic structure with a tilted octahedron and $t > 1$ results in non-perovskite structures [77], [81]. For its structural and chemical stability, cubic perovskite is preferred for various applications including photocatalysts. In the Ph.D. work, the tolerance factors of the doped materials were used as the first step in understanding the limiting concentration of mol% doping when the material ceases to be phase pure. This was correlated with the X-ray diffraction patterns (XRD) of the samples. The details of these analyses are discussed in detail from Chapter 2 onwards. Goldschmidt's tolerance factor tries to theoretically measure the geometric distribution of ions fitting in a perovskite lattice. A *t* value less than or more than 1 indicates a distortion to the ideal structure.

The properties of transition metal oxides such as $SrTiO_3$ are strongly influenced by their d-orbitals with the Jahn-Teller effect (JTE) being a dominant effect that is observed in these compounds. In $SrTiO_3$, this effect could result in distortions to the TiO_6 octahedra. Jahn-Teller effect in transition metal complexes (octahedral) describes the geometrical distortion in non-linear molecules in electronically degenerate states to lower their energy and remove the

degeneracy [82]–[85]. The distortion usually occurs by the elongation or the shortening of the metal-ligand bonds along the z-axis.

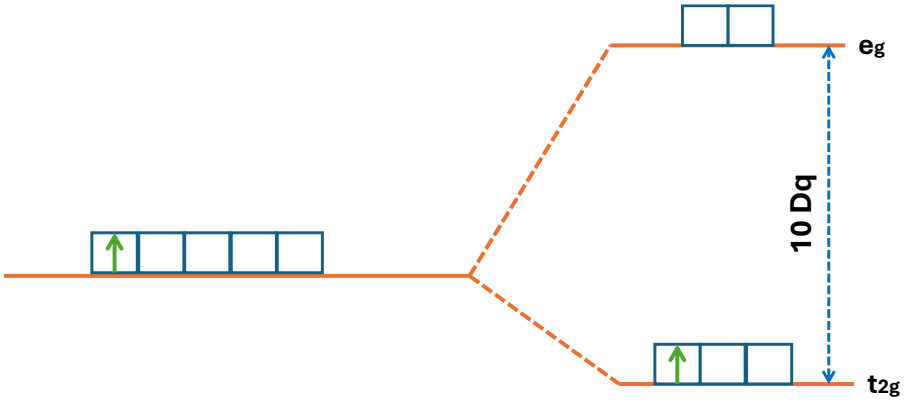


Figure 1.5: *A schematic of a weak field JTE in d^1 configuration Ti^{3+} in $SrTiO_3$ with the split energy levels t_{2g} and e_g. Both energy levels are separated by 10 Dq.*

This effect is prominent in ions with d^1, d^2, d^4, low spin d^5, high spin d^6, d^7 and d^9 configurations [86]. In the scope of the Ph.D. work, this effect is important to understand due to the presence of Ti^{3+} intrinsic defects in undoped and doped $SrTiO_3$. Ti^{3+} with d^1 configuration in undoped $SrTiO_3$ and unevenly occupied t_{2g} levels exhibit weak JTE. In the d^1 electronic configuration in the octahedral field, one electron occupies one of the t_{2g} states (d_{xy}, d_{yz}, d_{zx}) as shown in Figure 1.5. Therefore, the electron-electron repulsion required for JTE is lower. The distortion required to lift the degeneracy due to the single electron is smaller in magnitude which leads to weaker JTE as compared to other configurations. The Ga^{3+}, Cr^{3+}, and Cr^{6+} ions with d^{10}, d^3, and d^0 respectively configurations do not exhibit the Jahn Teller effect. Doping with these ions can induce local structural and electronic changes and hence, affect the intrinsic Ti^{3+} defects in $SrTiO_3$.

Besides the JTE in transition metal complex, another d-orbital related phenomenon central to this Ph.D. thesis is the d-d transitions that were observed in the Cr-doped $SrTiO_3$ which exhibited a clear relation between the optical properties and coordination chemistry. According to the Laporte selection rule, only those electronic transitions that involve a change in parity are allowed whereas those that do not include a change in parity are forbidden. According to this rule, the d-d transitions in a centrosymmetric octahedral field should be forbidden. However, these transitions occur and are responsible for the color of the compounds. These transitions occur in complexes when there is a distortion in the symmetry or when associated with vibronic coupling i.e. the interaction between the electronic states and vibrational modes within a molecule [87], [88]. Vibronic coupling allows forbidden rules by involving phonons that modulate the local environment around dopants such as Cr, breaking symmetry and allowing the d-d transitions.

1.2.2 Opto-electronic Properties

$SrTiO_3$ is one of the most researched photocatalysts due to its conducive opto-electronic properties. The indirect band gap of the photocatalyst is 3.2 eV and the direct band gap is 3.7 eV. Due to its wide band gap nature, $SrTiO_3$ can absorb only in the UV region, constituting 5%

of the total solar spectrum, limiting the PEC and the PC performance. The theoretical maximum achievable photocurrent for $SrTiO_3$ is comparable to TiO_2 at 1.1 mA/cm^2 as shown in Figure 1.6 [89].

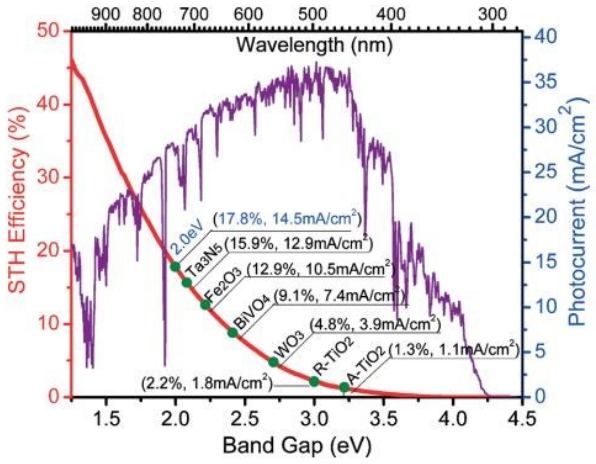


Figure 1.6: *The maximum achievable photocurrent of $SrTiO_3$ is close to the anatase TiO_2 at 1.1 mA/cm^2 correlating the solar to hydrogen conversion efficiency (STH) reproduced with permission from the work of Li, J. and Wu, N.* [89] *(Copyright © 2015, Royal Society of Chemistry, license issued through Copyright Clearance Center, Inc.).*

Doping is a highly researched strategy to increase the efficiency of the photocatalyst by broadening the absorption spectrum to visible light. In this Ph.D. work, doping will be investigated as to whether this route is viable to increase the efficiency of photocatalysts. For defect engineering, the site where the dopant is substituted is equally important, significantly impacting the catalyst behavior. Visible light activity can be introduced by either doping in the A-site or the B-site [90]. B-site doping can affect the electronic structure of $SrTiO_3$ by introducing midgap states. Midgap states are localized states in the bandgap introduced upon doping [91]. These states can act as traps hindering the charge carrier mobility and could negatively affect the photocatalytic performance. A-site doping modulates the oxygen vacancies and facilitates charge compensation [92], [93]. The introduction of dopants such as Cr, Ir, and Rh has been reported to introduce visible light absorption in $SrTiO_3$ [42], [61], [94]–[97]. Visible light absorption is facilitated with the introduction of states above the VB_M. The band alignment of $SrTiO_3$ consists of Ti 3d states forming the conduction band and O 2p states forming the valence band [98], [99]. Hypothetically, the fermi level should be in the middle of the band gap. However, most literatures report n-type conductivity [100], [101]. The n-type nature of $SrTiO_3$ is predominantly from the oxygen vacancy defects intrinsic to the oxide material which add states close to the CB_{Min} [102]. The Ph.D. thesis will attempt to study the effect of dopants with filled d^{10} configuration and partially filled d^3 configuration on the B-site at Ti^{4+} ([Ar]$3d^0 4s^0$ configuration) and how they affect light absorption.

1.3 Performance Assessment of $SrTiO_3$

In the Ph.D. work, two routes assessing the performance of $SrTiO_3$ towards clean fuel generation were studied. The first route was photocatalysis which was used to study CO_2 hydrogenation. The second route was photoelectrochemical measurements that were used to

study the performance of the d^3/d^{10} ion-doped $SrTiO_3$ samples towards OER and HER. The methods are discussed in the subsequent sections.

1.3.1 Photocatalysis

Photocatalysis is a promising method to utilize the intermittent nature of solar energy to generate clean, secondary fuels such as H_2 [103]. $SrTiO_3$ is one of the most extensively researched photocatalysts, especially in water-splitting systems and CO_2 reduction reactions such as CO_2 hydrogenation. Due to the absorption only in the UV region, the applicability of the wide band gap $SrTiO_3$ is limited. Therefore, narrowing the band gap to accommodate visible light absorption has been studied with (co-) doping metals and non-metals. Wang, Q. et al.[63]reported solar to hydrogen (STH) energy conversion efficiency of 1.2% using $SrTiO_3$: La, Rh, and $BiVO_4$: Mo photocatalysts in a Z-scheme. For overall water splitting $RhCrO_x/SrTiO_3$: Al has been reported to have the highest external quantum efficiency of 1 [11]. Takata, T. et al. [11] report that the material properties such as the crystallinity improvement and the defect engineering, are central to the performance observed. Takanabe, K. [104] classifies the photocatalytic process into 6 events which are as follows:

- Photon absorption
- Exciton (e^-/h^+) separation
- Carrier diffusion
- Carrier transport
- Catalytic efficiency
- Mass transfer of reactants and products

Takanabe, K. highlights a 6-gear concept about photocatalytic water splitting in work [104], [105] as shown in Figure 1.7. This concept sequentially depicts the steps associated with the photocatalytic process occurring at different timescales [104]. On the absorption of light, the photocatalyst surface undergoes photophysical and photochemical changes resulting in the excitation of electrons from the valence band to the conduction band. After overcoming the exciton binding energy, the e-/h+ separates after rapid relaxation to the band edges. The separated e^-/h^+ pair influenced by their effective masses are transported through diffusion to the surface where the catalytic reaction occurs.

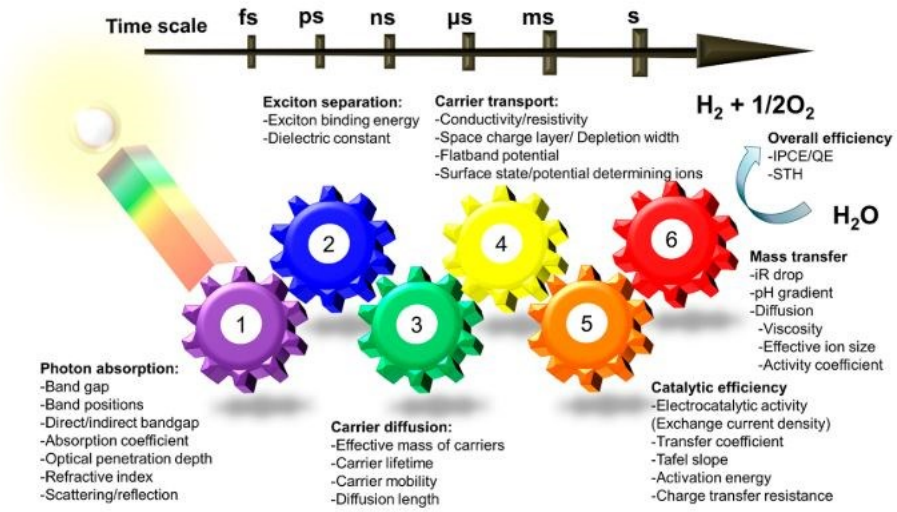


Figure 1.7: *The 6-gear concept depicting the parameters of photocatalysis, and the time scale required to accomplish the associated processes as reproduced with permission from the work of Takanabe, K.* [104] *(Open access, Copyright © 2017 American Chemical Society. Licensed by CC-BY-NC-ND)*

Even though bandgaps are crucial for determining performance, two other factors that should be considered important are the positions of the CB_{Min} and the VB_M. Transition metal dopants with their d-orbitals can hybridize with the states of $SrTiO_3$, bringing the CB_{Min} position closer to the reduction potential. This leads to a decrease in the bandgap. Similarly, the VB_M can also be shifted away from the oxidation potential by suitable dopants. However, this has been reported to be associated with introducing trap states in the forbidden region, which can lead to charge carrier recombinations. In the scope of the Ph.D. thesis, the positions of CB_{Min} and VB_M are fundamental to understanding the performance of the photocatalysts. In some of the doped samples in this work (elaborated in the result chapters 3-5) it has been observed that even if the bandgap did not change much compared to the undoped $SrTiO_3$, the CB_{Min} and VB_M positions vary significantly. This could arise from defect states, dopant-induced changes in the electronic structure, and lattice distortions due to changes in bond lengths. Doping with transition metals with d-orbitals is often associated with midgap states that can deteriorate photocatalysis. A suitable strategy to control the midgap trap states is to use co-dopants that can suppress these states. Co-doping can facilitate band-edge engineering and charge compensation whilst retaining the oxidative and reductive power of the photocatalyst.

Photocatalysis: From a Thermodynamic Point of View

In photocatalysis, the photoreaction occurs on light absorption in the presence of the catalyst which results in the generation and the subsequent separation of charge carriers. Ohtani, B. [106]–[108] in his work describes the photoreaction with the excitation of electrons from the filled valence band to the empty conduction band upon absorbing photons with energy higher than the bandgap. A thermodynamic driving force is required to start the photoreaction. This driving force for photocatalysis can be understood with Gibb's free energy diagram (G). Gibb's energy change (ΔG) for photocatalytic reactions can be both positive (absorbs energy) or negative (releases energy). ΔG is positive for water splitting and CO_2 reduction indicating that

the reaction is non-spontaneous, endothermic, and energetically uphill [103]. An initial activation energy is required to start the photoreaction which is provided by the absorption of light. Therefore, it becomes crucial to understand why such photocatalytic reactions are possible if they are non-spontaneous.

Ohtani, B. [106]–[108] in his work explains that non-spontaneous redox reactions occur when the reduction and oxidation steps are spatially or chemically separate. Without this, no products would form. The total Gibb's free energy change (ΔG) has two components: ΔG_e and ΔG_h attributed to the e^- facilitating the oxidation reaction and the h^+ facilitating the reduction reaction respectively [109]. Both these components should be negative for an uphill photoreaction such as water splitting and CO_2 reduction to occur.

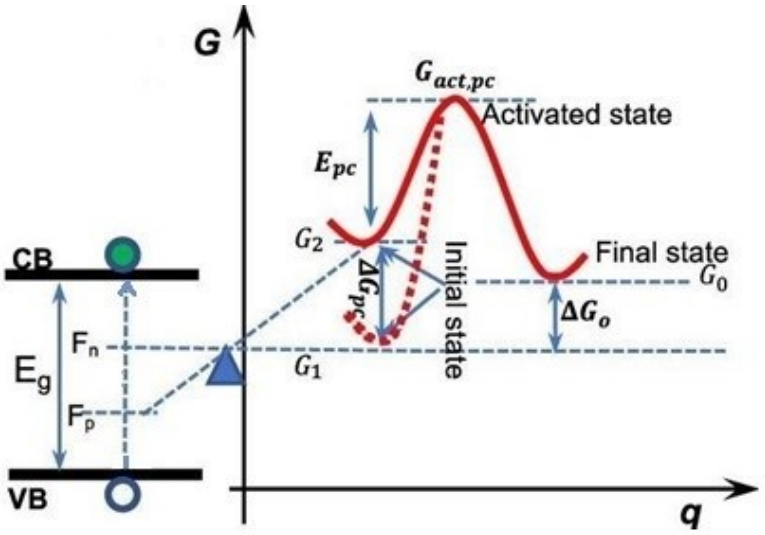


Figure 1.8: *Schematic showing Gibb's energy change for uphill photocatalytic water splitting and CO_2 hydrogenation reactions adapted with permission from the work of Liu, B. et al.* [109] *(Open access, Copyright © 2020, American Chemical Society). The schematic was modified from the original source by reversing the arrow showing the transition from the valence band to the conduction band.*

Figure 1.8 shows Gibb's free energy change for an uphill reaction. Figure 1.8 constitutes two components of a photocatalytic reaction. *The first component (left-hand side) shows the electronic band structure which governs how the electrons are excited by light energy from the valence band (VB) to the conduction band (CB). The second component shows the thermodynamics and the kinetics of the photocatalytic reaction.* A shift in thermodynamic equilibrium to non-equilibrium of excited states occurs on photoexcitation of the catalyst with light energy higher than the bandgap. This causes the electrons and holes in the CB and the VB to disarray. This results in a disturbance in the quasi-fermi levels (F_n, F_p) [110]. The resultant charge carriers cause the excited state to have a higher G position (G_2) than the ground state (G_1). The difference in these states is expressed in Eq. (1.2) and Eq. (1.3). The ΔG_{pc} denotes the change in Gibb's energy from the initial state, G_1 to an intermediate state, G_2. E_{pc} in Figure 1.8 denotes the photocatalytic energy provided upon illumination. The resultant charge carriers cause the excited state to have a higher G position than the ground state. The difference

in these states is expressed in Eq. (1.2) and Eq. (1.3). These conditions yield a positive ΔG with the chemical potential of electron (F_n) being larger than that of the hole (F_p), as expressed in the following Eq (1.4) shows the ΔG of photocatalytic water splitting which is the minimum energy requirement to dissociate water [110]. For the photo-reaction to complete, an activation energy barrier must be crossed from G_2 (reactants, Figure 1.8) to G_O (products, Figure 1.8). To mathematically elaborate on this, we consider $SrTiO_3$ a thermodynamic system.

$$\Delta G = G_{\text{before photoexcitation}} - G_{\text{after photoexcitation}} \quad (1.2)$$

$$\Delta G = - N_A (F_n - F_p) \quad (1.3)$$

$$\Delta G = -N_A E_g - k_B T \ln\frac{np}{NvNc} = 237 \text{ kJ/mol} \quad (1.4)$$

Where,

F_n, F_p = Quasi-equilibrium states denoting electron states with internal equilibrium, and the quasi-fermi level potential of electrons and holes [111].

E_g = Bandgap Energy

k_B = Boltzman's Constant

N_v = Effective Densities of States in Valence Band

N_c = Effective Densities of States in Conduction Band

n, p = Concentration of Electrons and Holes

F_n, F_p = Quasi Fermi Levels of Electrons and Holes

From Eqs 1.2-1.4, it can be observed that Gibb's energy change is the primary charge carrier driver in photocatalysis. For a photoreaction to commence, the thermodynamic driving force is directly proportional to the difference in the number of electrons and holes. When $SrTiO_3$ is at thermal equilibrium, ΔG is zero which indicates zero net force to drive photocatalytic reactions. [112]. From this, it can be inferred that heat is not the driving force for generating electron-hole pairs. Thus, for photo-catalysis, the Gibbs free energy (ΔG) which is supplied by light irradiation is the energy of the reaction that is required to drive the photoreaction.

The experimental setup used in photocatalysis is another important consideration during the measurements. There are two types of setups used in laboratories- closed systems and flow systems [12]. Closed systems are further classified into batch systems and custom-made reactors. A batch-type closed photocatalytic setup comprises a cuvette or a test tube sealed with a rubber septum. This setup is purged with argon gas and irradiated. The gas samples are generally taken with syringes for analysis. The major disadvantage of this system is that O_2 cannot be analyzed accurately due to contamination from air during sampling [12]. Custom-made reactors have an optically transparent part that is illuminated. A typical reactor could consist of stainless steel which houses a Teflon liner and a quartz lid. In both these types of closed systems, the gases produced after photocatalysis are circulated through the system and analyzed with gas chromatography. In flow systems, the liquid phase is continuously flowed with a carrier gas.

1.3.2 Photoelectrochemistry (PEC)

In recent years, PEC measurements have gained popularity as a method to produce solar fuels. Thermodynamically, this method is like photocatalysis in being governed by Gibb's free energy change as the primary driver for the reaction. PEC measurements for water splitting involve 285.8 kJ/mol of energy with 237.2 kJ/mol supplied from Gibb's energy and 48.6 kJ/mol which is the heat released from the reaction[113]. Mathematically, this can be demonstrated by Eq (1.5) [113].

$$2H_2O\ (l) + 285.8\ kJ/mol \longrightarrow 2H_2\ (g) + O_2\ (g) \quad (1.5)$$

The overall potential thermodynamic barrier to be overcome corresponding to 237.2 kJ/mol is 1.23 eV [114]. To dissociate water, the photoelectrode should generate photovoltage greater than 1.23 eV. The entire process of water splitting involves the consumption of 4 electrons for the oxidation reaction (OER) at the anode and 2 electrons for the proton reduction (HER) at the cathode. These can be represented by the equations (1.6) and (1.7) where ΔE^0_{Ox} and ΔE^0_{Red} are the electrode potentials for the oxidation and reduction reactions [113].

$$\text{Anode: } 2H_2O \longrightarrow O_2\ (g) + 4H^+ + 4e^-,\ \Delta E^0_{Ox} = 1.23\ V_{RHE} \quad (1.6)$$

$$\text{Cathode: } 4H^+ + 4e^- \longrightarrow 2H_2\ (g),\ \Delta E^0_{Red} = 0\ V_{RHE} \quad (1.7)$$

The PEC cells consist of a cathode and an anode where reduction and oxidation reactions take place. Due to the favourable band positions of $SrTiO_3$ to the redox potentials of water splitting and CO_2 reduction (or hydrogenation), no external bias is required for the reactions to proceed. The principle of the PEC process involves the generation of charge carriers upon absorbing photon energy higher than the bandgap of the semiconductor catalysts, charge separation and migration to the surface, and surface redox reactions.

In a PEC setup, the electrolyte is an important part of the measurements as electrons can be transferred between the semiconductor electrode and the electrolyte. When the semiconductor and the electrolyte come in contact, it forms the semiconductor-electrolyte junction (SCLJ) [115],[116]. This creates an electrical double layer (shown in Figure 1.9 (a)) due to a difference in the fermi level (E_f) of the semiconductor and the redox potential (E_{redox}) of the electrolyte leading to band bending [113]. The band bending aids the charge carrier separation and migration. When $E_f > E_{redox}$, the band bending is upward in n-type semiconductors, and when $E_f < E_{redox}$, the band bending is downward in p-type semiconductors as shown in Figure 1.9(b).

Band bending leads to a space charge region where the semiconductor is in contact with the electrolyte. In PEC measurements, the minority charge carriers have a dominant role in progressing the redox reactions i.e. the holes lead the oxidation, and the electrons lead the reduction. The electrical double layer at the junction is formed due to the difference in the E_f and the E_{redox} [113]. This is mainly contributed by the Helmholtz and the Gouy layers [113]. A potential drop occurs across the semiconductor-electrolyte junction due to these layers and the space charge region. In the Ph.D. work, the synthesized samples exhibited a n-type character where the fermi level lies closer to the CB. In n-type semiconductors, when the semiconductor is exposed to the electrolyte, the electrons flow to the electrolyte, and the space charge region is positively charged [113]. This leads to the equilibrium fermi level ($E_{f,\,Eq}$) to shift downwards

and remain there till equilibrium is set again. The space charge region at this point is called the depletion region as the electrons and excess holes accumulate at the semiconductor surface. Here, the bands bend upwards.

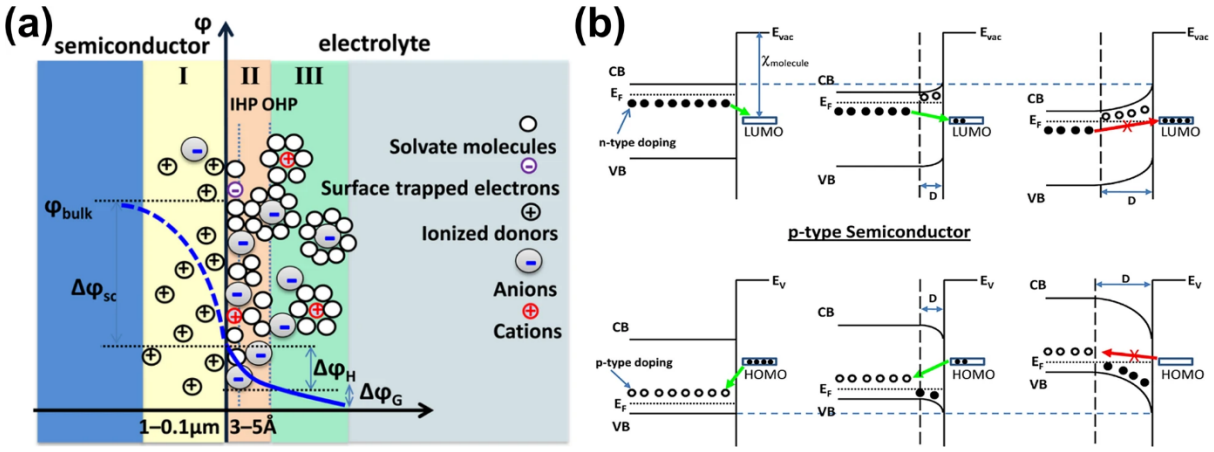


Figure 1.9: *Band bending at semiconductor electrolyte junction. (a) n-type semiconductor electrode with a double layer structure. The electrode is in contact with the electrolyte reproduced with permission from the work of Ding, C. et al. [115] (Copyright © 2016 American Chemical Society). (b) Energy diagram of n- and p-type semiconductors reproduced with permission from the work of Zhang, Z. and Yates, Y. T.* [116] *(Copyright © 2012, American Chemical Society).*

Reported literature often does not differentiate between photocatalytic and photoelectrocatalytic systems and the terms are used interchangeably. Osterloh, F. [117] in his work sets a clear distinction between both cases. He explains that photocatalysts promote reactions with $\Delta G < 0$ without any storage. Whereas photoelectrocatalytic systems harvest light to drive reactions with $\Delta G > 0$, and to do this they must suppress the back reaction.

1.4 The Role of Defects in $SrTiO_3$

Crystallographic and electronic defects in $SrTiO_3$ are closely related to their photocatalytic/ photoelectrocatalytic performances. In the scope of the Ph.D. work, defects in perovskite oxide materials can be classified as 0D, 1D, and 2D. Point defects such as charged anion or cation vacancies are 0D defects contributing to opto-electronic properties [118]. In comparison, 1D and 2D are classified as dislocations or grain boundaries that can facilitate 0D defects by acting as nucleation pathways [119]–[121]. Point defects predominantly exist in the bulk. However, oxygen vacancies can also be on the surface. Defects such as grain boundaries and dislocations are present on the surface.

Grain boundaries are formed during high-temperature annealing when the nucleation process starts. During the nucleation, the grains start growing in random orientations. These randomly oriented grains keep growing and come to points where they and the growth stops. The grain boundary is the point where the two differently oriented grains are joined. Grain boundaries are classified as 2D defects due to their planar characteristic as they extend over an area in a plane. Dislocations on the other hand are classified as 1D defects as they are linear in nature. Dislocations are irregularities in the lattice where atoms are misaligned [122]. These crystal

defects are generally further classified as edge and screw dislocations. Edge dislocations occur when a new half-plane of atoms is inserted into the crystal structure. This causes the dislocation to occur at this half-plane edge and it is perpendicular to the direction of the applied stress. Screw dislocations occur when the crystal lattice undergoes a helical twist along the dislocation line. This type of dislocation is parallel to the applied stress. These crystallographic defects can significantly impact the performance of the catalysts. These dislocations are shown in Figure 1.10. Dislocations are defined by two vectors i.e. the line vector, t which is along the direction of the dislocation line, and Burger's vector which signifies the direction and the distance the dislocation moves. Dislocations and grain boundaries can act as traps and recombination centers for charge carriers [123].

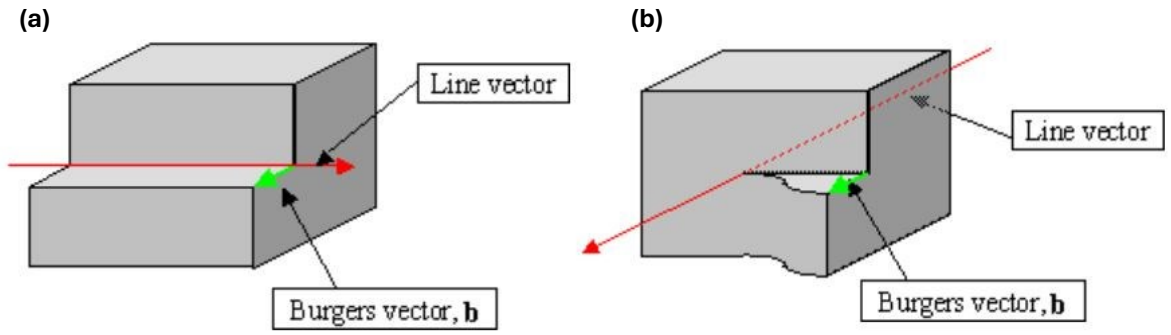


Figure 1.10: *Schematic of types of dislocations. (a) Edge dislocations (b) Screw dislocations. Image reproduced from the Dissemination of IT for the promotion of materials science, DoITPoMS website, University of Cambridge. Accessed on 18.09.2024* [124].

Crystallographic defects such as grain boundaries can act as sinks for point defects such as oxygen vacancies [125]. These vacancies directly impact the photocatalytic/photoelectrocatalytic performances. Photocatalysis involves 6 steps as discussed in section 1.3. In semiconductor photocatalysts, charge separation and transport to the surface involves minority charge diffusion lengths (L_D). These diffusion lengths are dependent on the lifetimes (τ) and the carrier mobilities (μ) as shown in Eq (1.8) [126].

$$L_D = \sqrt{\frac{kT}{e}\tau\mu} \qquad (1.8)$$

Where,

τ = Lifetimes of the generated charge carriers

μ = Charge carrier mobilities

k = Boltzmann's constant = 1.38 x 10^{-23} J/K

T = Absolute temperature

This step in photocatalysis is very sensitive to trapping. Intrinsic defects such as vacancies and Ti^{3+} states can act as traps leading to charge recombinations. Doping is known to introduce oxygen vacancies that can add localized states in the bandgap near the conduction band. These defects act as shallow donors that increase the electron density and enhance the n-type

conductivity [127]. Doping can also induce deep-level traps in the middle of the band gap. Even though these traps can lead to recombinations, they can also be beneficial by promoting charge-selective trapping [128], [129]. Charge selective trapping involves immobilizing either electrons or holes. This can lead to an increase in carrier lifetimes by efficiently separating oppositely charged carriers. Doping in wide-bandgap materials can create sub-band gap levels that extend light absorption in the visible light region. To understand point defects, the Kröger Vink notation is employed. This notation is discussed in the subsequent section.

1.4.1 Understanding the Site and the Charge of Point Defects with the Kröger Vink Notation

Kröger Vink notations identify and represent point defects in crystal lattices such as $SrTiO_3$. These notations help in assigning charges to these defects and the positions they occupy in the lattice [130]. In the scope of this Ph.D., Ga^{3+} and Cr^{3+} doped $SrTiO_3$ were studied. Due to the comparable ionic sizes of these dopants to the ionic size of Ti^{4+}, they are likely to be substituted on the B-site of $SrTiO_3$. When Ga^{3+}/Cr^{3+} is substituted in the B-site, charge neutrality is maintained with the creation of oxygen vacancies [92]. Oxygen vacancies are the most common point defects in perovskite materials. Oxygen vacancies can be neutral, singly ionized, or doubly ionized [131]. Ionized oxygen vacancies can effectively block the incoming holes and reduce surface recombinations. Besides oxygen vacancies, $SrTiO_3$ can also exhibit other intrinsic defects such as cation vacancies or the dopants in interstitial positions. These defects can be represented via the Kröger Vink notation as shown in Table 1.1.

Thermal annealing of doped/undoped $SrTiO_3$ in air or under vacuum can also facilitate the formation of oxygen vacancies in the crystal lattice. The formation of oxygen vacancies is represented by Eq (1.9) which shows oxygen in the oxygen site is lost with the formation of 2 electrons. This leads to a charge imbalance in the lattice that prefers neutrality. To maintain charge neutrality, the loss of each oxide ion is accompanied by the formation of two Ti^{3+} ions as shown in Eq (1.10). Therefore, it can be inferred from here that Ti^{3+} is another intrinsic defect that is associated with $SrTiO_3$ which is formed alongside the oxygen vacancies. Ti^{3+} could be another cause for imparting a n-type conductivity to $SrTiO_3$. In acceptor-type dopants such as Ga^{3+}/Cr^{3+} (denoted as M in Table 1 and Eq (1.11)) doped $SrTiO_3$, the dopants can suppress the reduction of Ti^{4+} to Ti^{3+} and create ionized oxygen vacancies reducing the concentration of the Ti^{3+} defects in an oxygen-rich environment. This can be represented by the Eq (1.7). Eq (1.12) shows a condition when M^{3+} substitutes in the Ti^{4+} site where compensation occurs with doubly ionized oxygen vacancies in an oxygen-poor environment. Doubly ionized oxygen vacancies are more prevalent at higher temperatures. Single ionized oxygen vacancies are formed at lower temperatures when doubly ionized oxygen vacancies trap free electrons shown in Eq (1.13) [132].

$$O^X_O \longrightarrow \ddot{V}_O + \frac{1}{2} O_2 + 2e' \quad (1.9)$$

$$2e' + 2Ti^X_{Ti} \longrightarrow 2Ti'_{Ti} \quad (1.10)$$

$$M_2O_3 + \frac{1}{2} O_2 \longrightarrow 2M'_{Ti} + 4O_O^X \quad (1.11)$$

$$2M_{Ti} + V_O^X \longrightarrow 2M'_{Ti} + \ddot{V}_O \quad (1.12)$$

$$\ddot{V}_O + e' \longrightarrow \dot{V}_O \quad (1.13)$$

Table 1.1: Kröger Vink notations denoting the charges and sites of point defects introduced in $SrTiO_3$ upon doping with trivalent acceptor ions

Kröger Vink Notation	Charge and Site of Point Defects in $SrTiO_3$
Sr^X_{Sr}	Sr at Sr site with a neutral charge
Ti^X_{Ti}	Ti at Ti site with a neutral charge
O^X_O	O at O site with a neutral charge
M'_{Ti}	Single negatively charged acceptor ion at Ti site
$\ddot{G}_{Ti}$	Double positively charged acceptor ion at Ti Site
$\ddot{V}_O$	Double positively charged oxygen vacancy
$\dot{V}_O$	Single positively charged oxygen vacancy
V^x_O	Neutral oxygen vacancy

Intrinsic defects such as cation or anion vacancies can affect the charge carrier dynamics. This is fundamental in understanding how different dopants affect the properties and behavior of $SrTiO_3$.

1.5 Incorporating the Dopants: How Does the Synthesis Route Affect the Final Products?

$SrTiO_3$ has been reported to be synthesized via various synthesis procedures as summarized in Table 1.2 reproduced from the review work of Phoon, B. et al. [133]. Physical characteristics such as crystallinity, morphology, particle size, and shape can be heavily influenced by the synthesis route adopted [134]–[137]. Size and shape are two important parameters that can heavily influence photocatalytic performances [138]. The size and the shape are related to the surface structure of these catalysts. Since photocatalysis/photoelectrocatalysis is a surface phenomenon, therefore the design and the construction of facets are important. These parameters can be optimized with the synthesis route. Different raw materials suitable for various synthesis conditions can be used to synthesize doped/undoped $SrTiO_3$.

Microstructural parameters such as the crystallinity, the specific surface area, and the nanoparticle sizes can determine the performance of the catalysts [138]. In a photocatalyst, the redox reactions occur on the surface, and in the bulk of the material where no electric field exists. Controlling these two aspects i.e. the surface to bulk material is crucial in controlling recombination losses [50]. In photocatalysis/PEC, the photogenerated charges should separate and migrate to the surface for the redox reactions to proceed. However, the transport of these carriers to the surface of oxide materials is limited by (i) the short minority carrier diffusion length of carriers and (ii) the space charge layer width of the semiconductor [139]. Therefore, synthesis methods that result in nanoparticles having a higher surface area to bulk ratio are suitable for photocatalysis. The morphological control of the shape and size of $SrTiO_3$ is also

significant for developing highly efficient photocatalysts. Besides that, the nature of the surface of photocatalysts (facet, traps, step edges etc.) can also influence their photocatalytic activity and selectivity [140].

Table 1.2: $SrTiO_3$ synthesis methods and some material properties [133]

Sr. No.	Synthesis Method	Morphology	Particle Size [nm]
1	Sol-gel with hydrothermal synthesis	Nano-cubes	60-120
2	Polymerized Complex	NPs	25-100
3	Solid state reaction	NPs	110-150
4	Ball milling assisted solid-state reaction	NPs	30
5	Sol-gel combustion	Nano-powders (spherical)	20-30
6	Sol-gel	Nano-powders	-
7	Molten salt reaction	Sub-micron crystallites and nanocrystals	20-184
8	Microwave heating technique	Nano-powders	28-68
9	Solvothermal	NPs	50-80
10	Molten salt reaction	Nano-cubes	64-182
11	Microwave-assisted hydrothermal	Nano-spheres	-
12		Nano-cubes	47-57
13	Sol-gel hydrothermal	NPs	30-150
14	Hydrothermal	Meso-crystals	100-200
15	Solvothermal	Nano-cubes	20
16	Sol-gel combustion	NPs	45-56
17	Hydrothermal	Nano-cubes	20-200
18	Solvothermal	Nano-cubes, Nano-spheres, Nano-flakes	24-43
19	Rapid sol precipitation	Nano-cubes	4-13
20	Hydrothermal	Micro-spheres	30-46
21	Solid state reaction (flux)	Nano-cubes	300
22	Electrospinning	Nano-tubes	100
23	Ultrasound-assisted wet chemical	Nano-crystals	7-17

24	Solid-state crystal growth	Single crystals	-
25	Flux mediated method	Nano-cubes (irregular shape)	200-3000
26	Hydrothermal	Core-shell micro-spheres	700
27	Ultrasound-assisted hydrothermal	Mesoporous nano-powder	8-18
28	Hydrothermal	Nano-cubes	30-56

The most reported route of synthesis of $SrTiO_3$-based photocatalysts is solid-state synthesis. However, particle agglomeration and non-uniform morphology are some severe drawbacks that encourages the use of other synthesis routes [133]. Sol-gel Pechini is a promising method to study the effect of the synthesis route on the performance of the photocatalysts. The Pechini method is a modification of the standard sol-gel method where chelating ligands are used to form a homogenous metal-citrate solution. In the Pechini method, the homogenous metal-citrate solution is converted to a covalent polymer network which entraps and immobilizes the metal ions [141], [142]. This can promote more control over the developing product by delaying the organic matrix decomposition at high temperatures [133]. In this method, a homogenously dissolved starting material of the hydrated metal salt is dissolved in ethylene glycol and citric acid resulting in the metal-citrate chelate complexes. This solution undergoes a polyestrification process upon heating further forming the covalent network. The addition of ethylene glycol ensures that the metal cations are homogenously dispersed, and the segregation of multiple phases is inhibited. The metal citrate network entraps the cations and ethylene glycol makes the solution more viscous which further immobilize the cations. In the Pechini process, the chelating agent i.e. the citric acid suppresses the multiple phases of binary oxides due to different hydrolysis and condensation rates leading to steric immobilization and entrapping the aqueous cations. Ethylene glycol is used in a non-aqueous sol-gel reaction instead of water as ethylene glycol helps in steric immobilization and shape control. The Pechini process thus offers the benefit of homogenously dispersed metal cations in the network and form a polymeric precursor. In their work, Liu, Y. et al. [143] in their work, compared $SrTiO_3$ synthesized with different methods including the Pechini method and the solid-state method. They reported that $SrTiO_3$ which was synthesised by the Pechini method gave a smaller particle size (30 nm) as compared to solid state synthesis (150 nm). The $SrTiO_3$ synthesized with the sol-gel Pechini was reported to have a better photocatalytic performance compared to the solid-state synthesized sample. For sol-gel synthesis, alkoxides are preferred for Ti precursors and nitrates as Sr precursors. Alkoxides are preferred because of the following [143]:

- Physical properties such as the percentage of ionic character of the metal-oxide bond due to electronegativity differences between oxygen and the metal
- Degree of polymerization is an important feature that influences many of the physical and chemical properties of these compounds

Amongst other precursors, nitrates are used mainly to introduce Group I and II elements like Sr since the corresponding alkoxides exhibit limited solubility in alcohols. In this Ph.D. work, sol-gel Pechini method is used to synthesize the catalyst materials. Another advantage of this method compared to the solid-state synthesis is that it is less energy intensive. In this work, phase pure materials were synthesized at temperatures as low as 500 °C.
In the Ph.D. work, doped $SrTiO_3$ samples were synthesized using the sol-gel Pechini method and subsequently studied to investigate their microstructural and opto-electronic properties. This work also aims to understand the influence of doping on the material's structural characteristics such as crystallite size and morphology as well as its optical absorption and electronic behaviour.

1.6 Aim of the Ph.D. Thesis

$SrTiO_3$ exhibits limited photocatalytic performance due to its absorption in the UV region of the solar spectrum. Doping $SrTiO_3$ with trivalent ions at the B-site is often associated with midgap trap states which can negatively affect the catalytic performances. To overcome these challenges, the Ph.D. thesis focuses on understanding doping d^3 (Cr^{3+}) and d^{10} (Ga^{3+}) ions in $SrTiO_3$. A series of samples were synthesized, and their material properties were investigated. In summary, the key research questions the Ph.D. work attempted to address are listed as follows.

- Using low-cost, earth-abundant materials as dopants to modulate the wide band gap of $SrTiO_3$ to understand how light absorption is affected
- Which B-site dopant can facilitate visible light absorption? Can visible light activity be induced without midgap states and co-doping strategies suppress these states?
- Does d^3 and d^{10} doping suppress Ti^{3+} defects and affect the performance of the photocatalysts?
- How are the bulk and surface properties affected by doping?
- How do oxygen vacancies affect the performance of these catalysts?
- How does the synthesis method affect the photocatalyst?
- Is doping a viable strategy to facilitate visible light absorption and enhance the performance of photocatalysts?

Reference

[1] "Climate Action." https://www.un.org/en/climatechange/breaking-fossil-fuels (accessed Sep. 28, 2024).

[2] J. S. P.R. Shukla, M. R. Slade, A. Al Khourdajie, R. van Diemen, D. McCollum, M. Pathak, S. Some, P. Vyas, R. Fradera, and J. M. Belkacemi, A. Hasija, G. Lisboa, S. Luz, "IPCC, 2022: Climate Change 2022: Mitigation of Climate Change. Contribution of Working Group III to the Sixth Assessment Report of the Intergovernmental Panel on Climate Change," 2022. doi: doi:10.1017/9781009157926.

[3] Y. G. Zhang, M. Pagani, Z. Liu, S. M. Bohaty, R. Deconto, and P. T. R. S. A, "A 40-million-year history of atmospheric CO_2 A -million-year history of atmospheric CO," *Phil. Trans. R. Soc. B*, vol. 271, no. 2001, 2013.

[4] N. Kono, “Brundtland Commission (World Commission on Environment and Development) BT - Encyclopedia of Quality of Life and Well-Being Research,” A. C. Michalos, Ed. Dordrecht: Springer Netherlands, 2014, pp. 450–452.

[5] “https://www.climate.gov/media/13840. 18.09.2024.” .

[6] A. Fujishima and K. Honda, “Electrochemical Photolysis of Water at a Semiconductor Electrode,” *Nature*, vol. 238, no. 5358, pp. 37–38, 1972, doi: 10.1038/238037a0.

[7] J. Albero, Y. Peng, and H. García, “Photocatalytic CO_2 Reduction to C2+ Products,” *ACS Catal.*, vol. 10, no. 10, pp. 5734–5749, 2020, doi: 10.1021/acscatal.0c00478.

[8] K. Villa, J. R. Galán-Mascarós, N. López, and E. Palomares, “Photocatalytic water splitting: advantages and challenges,” *Sustain. Energy Fuels*, vol. 5, no. 18, pp. 4560–4569, 2021, doi: 10.1039/d1se00808k.

[9] Ž. Kovačič, B. Likozar, and M. Huš, “Photocatalytic CO_2 reduction: A review of ab initio mechanism, kinetics, and multiscale modeling simulations,” *ACS Catal.*, vol. 10, no. 24, pp. 14984–15007, 2020, doi: 10.1021/acscatal.0c02557.

[10] U. Ulmer, T. Dingle, P.N. Duchesne *et al.*, “Fundamentals and applications of photocatalytic CO_2 methanation,” *Nat. Commun.*, vol. 10, no. 1, pp. 1–12, 2019, doi: 10.1038/s41467-019-10996-2.

[11] T. Takata, J. Jiang, Y. Sakata *et al.*, “Photocatalytic water splitting with a quantum efficiency of almost unity,” *Nature*, vol. 581, no. 7809, pp. 411–414, 2020, doi: 10.1038/s41586-020-2278-9.

[12] S. Nishioka, F. E. Osterloh, X. Wang, T. E. Mallouk, and K. Maeda, “Photocatalytic water splitting,” *Nat. Rev. Methods Prim.*, vol. 3, no. 1, pp. 1–15, 2023, doi: 10.1038/s43586-023-00226-x.

[13] S. Fang, M. Rahaman, J. Bharti *et al.*, “Photocatalytic CO_2 reduction,” *Nat. Rev. Methods Prim.*, vol. 3, no. 1, 2023, doi: 10.1038/s43586-023-00243-w.

[14] T. Takata and K. Domen, “Particulate Photocatalysts for Water Splitting: Recent Advances and Future Prospects,” *ACS Energy Lett.*, vol. 4, no. 2, pp. 542–549, 2019, doi: 10.1021/acsenergylett.8b02209.

[15] A. Galushchinskiy, R. González-Gómez, K. McCarthy, P. Farràs, and A. Savateev, “Progress in Development of Photocatalytic Processes for Synthesis of Fuels and Organic Compounds under Outdoor Solar Light,” *Energy and Fuels*, vol. 36, no. 9, pp. 4625–4639, 2022, doi: 10.1021/acs.energyfuels.2c00178.

[16] John C. Mankins, “Technology Readiness Level – A White Paper,” *22 December* , no. January 1995, 2004, [Online]. Available: https://www.researchgate.net/publication/247705707_Technology_Readiness_Level_-_A_White_Paper.

[17] Q. Wang and K. Domen, “Particulate Photocatalysts for Light-Driven Water Splitting: Mechanisms, Challenges, and Design Strategies,” *Chem. Rev.*, vol. 120, no. 2, pp. 919–985, 2020, doi: 10.1021/acs.chemrev.9b00201.

[18] A. Kudo and Y. Miseki, “Heterogeneous photocatalyst materials for water splitting,” *Chem. Soc. Rev.*, vol. 38, no. 1, pp. 253–278, 2009, doi: 10.1039/b800489g.

[19] K. Domen, S. Naito, M. Soma, T. Onishi, and K. Tamaru, "Photocatalytic decomposition of water vapour on a NiO-$SrTiO_3$ catalyst," *J. Chem. Soc. Chem. Commun.*, no. 12, pp. 543–544, 1980, doi: 10.1039/C39800000543.

[20] T. Kawai and T. Sakata, "Photocatalytic decomposition of gaseous water over TiO2 and TiO_2-RuO_2 surfaces," *Chem. Phys. Lett.*, vol. 72, no. 1, pp. 87–89, 1980, doi: 10.1016/0009-2614(80)80247-8.

[21] A. Kudo, A. Tanaka, K. Domen, K. ichi Maruya, K. ichi Aika, and T. Onishi, "Photocatalytic decomposition of water over $NiOK_4Nb_6O_{17}$ catalyst," *J. Catal.*, vol. 111, no. 1, pp. 67–76, 1988, doi: 10.1016/0021-9517(88)90066-8.

[22] Y. Inoue, T. Niiyama, Y. Asai, and K. Sato, "Stable Photocatalytic Activity of $BaTi_40_9$ Combined with Ruthenium Oxide for Decomposition of Water," *J. Chem. Soc. Chem. Commun.*, no. 7, pp. 579–580, 1992.

[23] J. Sato, N. Saito, H. Nishiyama, and Y. Inoue, "New photocatalyst group for water decomposition of RuO_2-loaded p-block metal (In, Sn, and Sb) oxides with d^{10} configuration," *J. Phys. Chem. B*, vol. 105, no. 26, pp. 6061–6063, 2001, doi: 10.1021/jp010794j.

[24] J. S. Lee, "Photocatalytic water splitting under visible light with particulate semiconductor catalysts," *Catal. Surv. from Asia*, vol. 9, no. 4, pp. 217–227, 2005, doi: 10.1007/s10563-005-9157-0.

[25] F. E. Osterloh, "Inorganic materials as catalysts for photochemical splitting of water," *Chem. Mater.*, vol. 20, no. 1, pp. 35–54, 2008, doi: 10.1021/cm7024203.

[26] K. Ikarashi, J. Sato, H. Kobayashi, N. Saito, H. Nishiyama, and Y. Inoue, "Photocatalysis for water decomposition by RuO_2-dispersed $ZnGa_2O_4$ with d^{10} configuration," *J. Phys. Chem. B*, vol. 106, no. 35, pp. 9048–9053, 2002, doi: 10.1021/jp020539e.

[27] Y. Inoue, "Photocatalytic water splitting by RuO_2-loaded metal oxides and nitrides with d^0- and d^{10} -related electronic configurations," *Energy Environ. Sci.*, vol. 2, no. 4, pp. 364–386, 2009, doi: 10.1039/b816677n.

[28] A. Kudo, K. Domen, Kichi Maruya, and T. Onishi, "Photocatalytic activities of TiO_2 loaded with NiO," *Chem. Phys. Lett.*, vol. 133, no. 6, pp. 517–519, 1987, doi: 10.1016/0009-2614(87)80070-2.

[29] Y. Sakata, T. Yamamoto, T. Okazaki, H. Imamura, and S. Tsuchiya, "Generation of Visible Light Response on the Photocatalyst of a Copper Ion Containing TiO_2," *Chem. Lett.*, vol. 27, no. 12, pp. 1253–1254, 2003, doi: 10.1246/cl.1998.1253.

[30] K. Domen, A. Kudo and T. Onishi, "Mechanism of Photocatalytic Decomposition of Water into H_2 and O_2 over NiO-$SrTiO_3$," *J. Catal. 102, 92-98*, doi: 10.1007/BF00587178.

[31] J. M. Lehn, J. P. Sauvage, R. Zlessel, and L. Hilaire, "Water Photolysis by UV Irradiation of Rhodium Loaded Strontium Titanate Catalysts. Relation between Catalytic Activity and Nature of the Deposit from Combined Photolysis and ESCA Studies," *Isr. J. Chem.*, vol. 22, no. 2, pp. 168–172, 1982, doi: https://doi.org/10.1002/ijch.198200032.

[32] K. Yamaguti and S. Sato, "Photolysis of water over metallized powdered titanium

dioxide," *J. Chem. Soc.{,} Faraday Trans. 1*, vol. 81, no. 5, pp. 1237–1246, 1985, doi: 10.1039/F19858101237.

[33] H. P. Maruska and A. K. Ghosh, "A study of oxide-based heterostructure photoelectrodes," *Sol. Energy Mater.*, vol. 1, no. 5, pp. 411–429, 1979, doi: https://doi.org/10.1016/0165-1633(79)90008-X.

[34] R. U. E. 't Lam, L. G. J. de Haart, A. W. Wiersma, G. Blasse, A. H. A. Tinnemans, and A. Mackor, "The sensitization of $SrTiO_3$ photoanodes by doping with various transition metal ions," *Mater. Res. Bull.*, vol. 16, no. 12, pp. 1593–1600, 1981, doi: https://doi.org/10.1016/0025-5408(81)90032-5.

[35] T. Ishii, H. Kato, and A. Kudo, "H_2 evolution from an aqueous methanol solution on $SrTiO_3$ photocatalysts codoped with chromium and tantalum ions under visible light irradiation," *J. Photochem. Photobiol. A-chemistry*, vol. 163, pp. 181–186, 2004, [Online]. Available: https://api.semanticscholar.org/CorpusID:93326285.

[36] N. Serpone, D. Lawless, J. M. Disdier, and J. M. Herrmann, "Spectroscopic, Photoconductivity, and Photocatalytic Studies of TiO_2 Colloids: Naked and with the Lattice Doped with Cr^{3+}, Fe^{3+}, and V^{5+} Cations," *Langmuir*, vol. 10, pp. 643–652, 1994, [Online]. Available: https://api.semanticscholar.org/CorpusID:96360278.

[37] M. Matsumura, M. Hiramoto, and H. Tsubomura, "Photoelectrolysis of Water under Visible Light with Doped $SrTiO_3$ Electrodes," *J. Electrochem. Soc.*, vol. 130, no. 2, p. 326, Feb. 1983, doi: 10.1149/1.2119704.

[38] H. Kato and A. Kudo, "Visible-Light-Response and Photocatalytic Activities of TiO_2 and $SrTiO_3$ Photocatalysts Codoped with Antimony and Chromium," *J. Phys. Chem. B*, vol. 106, no. 19, pp. 5029–5034, May 2002, doi: 10.1021/jp0255482.

[39] P. S. Bassi, Gurudayal, L. H. Wong, and J. Barber, "Iron based photoanodes for solar fuel production," *Phys. Chem. Chem. Phys.*, vol. 16, no. 24, pp. 11834–11842, 2014, doi: 10.1039/C3CP55174A.

[40] S. R. Pendlebury, X. Wang, F. Le Formal *et al.*, "Ultrafast charge carrier recombination and trapping in hematite photoanodes under applied bias.," *J. Am. Chem. Soc.*, vol. 136, no. 28, pp. 9854–9857, Jul. 2014, doi: 10.1021/ja504473e.

[41] E. Pastor, J. Park, L. Steier *et al.*, "In situ observation of picosecond polaron self-localisation in α-Fe_2O_3 photoelectrochemical cells," *Nat. Commun.*, vol. 10, no. 1, p. 3962, 2019, doi: 10.1038/s41467-019-11767-9.

[42] R. Konta, T. Ishii, H. Kato, and A. Kudo, "Photocatalytic activities of noble metal ion doped $SrTiO_3$ under visible light irradiation," *J. Phys. Chem. B*, vol. 108, no. 26, pp. 8992–8995, 2004, doi: 10.1021/jp049556p.

[43] S. Chen, T. Takata, and K. Domen, "Particulate photocatalysts for overall water splitting," *Nat. Rev. Mater.*, vol. 2, pp. 1–17, 2017, doi: 10.1038/natrevmats.2017.50.

[44] H. K. and I. M. Akihiko Kudo, Kazuhiro Ueda, "Photocatalytic O_2 evolution under visible light irradiation on $BiVO_4$ in aqueous $AgNO_3$ solution," *Appl. Surf. Sci.*, vol. 399, pp. 10–19, 2017, doi: 10.1016/j.apsusc.2016.12.038.

[45] W. Wang, P.L. Strohbeen, D. Lee *et al.*, "The Role of Surface Oxygen Vacancies in $BiVO_4$," *Chem. Mater.*, vol. 32, no. 7, pp. 2899–2909, 2020, doi: 10.1021/acs.chemmater.9b05047.

[46] Q. Zhang, G. Liu, and T. Liu, "Oxygen evolution reaction (OER) active sites in $BiVO_4$ studied using density functional theory and XPS experiments," *Phys. Chem. Chem. Phys.*, vol. 26, no. 3, pp. 2580–2588, 2023, doi: 10.1039/d3cp05579e.

[47] Y. Ma, S. R. Pendlebury, A. Reynal, F. Le Formal, and J. R. Durrant, "Dynamics of photogenerated holes in undoped $BiVO_4$ photoanodes for solar water oxidation," *Chem. Sci.*, vol. 5, no. 8, pp. 2964–2973, 2014, doi: 10.1039/c4sc00469h.

[48] Y. Ma, C. A. Mesa, E. Pastor *et al.*, "Rate Law Analysis of Water Oxidation and Hole Scavenging on a $BiVO_4$ Photoanode," *ACS Energy Lett.*, vol. 1, no. 3, pp. 618–623, 2016, doi: 10.1021/acsenergylett.6b00263.

[49] Y. Sasaki, H. Nemoto, K. Saito, and A. Kudo, "Solar water splitting using powdered photocatalysts driven by Z-schematic interparticle electron transfer without an electron mediator," *J. Phys. Chem. C*, vol. 113, no. 40, pp. 17536–17542, 2009, doi: 10.1021/jp907128k.

[50] C. Avcıoğlu, S. Avcıoğlu, M. F. Bekheet, and A. Gurlo, "Photocatalytic Overall Water Splitting by $SrTiO_3$: Progress Report and Design Strategies," *ACS Appl. Energy Mater.*, vol. 6, no. 3, pp. 1134–1154, 2023, doi: 10.1021/acsaem.2c03280.

[51] S. Cao, J. Low, J. Yu, and M. Jaroniec, "Polymeric Photocatalysts Based on Graphitic Carbon Nitride," *Adv. Mater.*, vol. 27, no. 13, pp. 2150–2176, 2015, doi: 10.1002/adma.201500033.

[52] L. Wang, K. Wang, T. He, Y. Zhao, H. Song, and H. Wang, "Graphitic carbon nitride-based photocatalytic materials: Preparation strategy and application," *ACS Sustain. Chem. Eng.*, vol. 8, no. 43, pp. 16048–16085, 2020, doi: 10.1021/acssuschemeng.0c05246.

[53] G. Z. S. Ling, V. B. Y. Oh, C. Y. Haw, L. L. Tan, and W. J. Ong, "g-C_3N_4 Photocatalysts: Utilizing Electron–Hole Pairs for Boosted Redox Capability in Water Splitting," *Energy Mater. Adv.*, vol. 4, pp. 1–27, 2023, doi: 10.34133/energymatadv.0038.

[54] W. Yu, J. Chen, T. Shang, L. Chen, L. Gu, and T. Peng, "Direct Z-scheme g-C_3N_4/WO_3 photocatalyst with atomically defined junction for H_2 production," *Appl. Catal. B Environ.*, vol. 219, pp. 693–704, 2017, doi: 10.1016/j.apcatb.2017.08.018.

[55] W. Chen, M. Liu, X. Li, and L. Mao, "Synthesis of 3D mesoporous g-C_3N_4 for efficient overall water splitting under a Z-scheme photocatalytic system," *Appl. Surf. Sci.*, vol. 512, no. February, p. 145782, 2020, doi: 10.1016/j.apsusc.2020.145782.

[56] H. Lyu, T. Hisatomi, Y. Goto *et al.*, "An Al-doped $SrTiO_3$ photocatalyst maintaining sunlight-driven overall water splitting activity for over 1000 h of constant illumination," *Chem. Sci.*, vol. 10, no. 11, pp. 3196–3201, 2019, doi: 10.1039/c8sc05757e.

[57] K. Domen, S. Naito, M. Soma, T. Onishi, and K. Tamaru, "Photocatalytic decomposition of water vapour on an NiO–$SrTiO_3$ catalyst," *J. Chem. Soc.{,} Chem. Commun.*, no. 12, pp. 543–544, 1980, doi: 10.1039/C39800000543.

[58] T. Takata and K. Domen, "Defect Engineering of Photocatalysts by Doping of Aliovalent Metal Cations for Efficient Water Splitting," *J. Phys. Chem. C*, vol. 113, no. 45, pp. 19386–19388, Nov. 2009, doi: 10.1021/jp908621e.

[59] X. Ma, X. Cui, Z. Zhao, M. A. Melo, E. J. Roberts, and F. E. Osterloh, "Use of surface photovoltage spectroscopy to probe energy levels and charge carrier dynamics in

transition metal (Ni, Cu, Fe, Mn, Rh) doped $SrTiO_3$ photocatalysts for H_2 evolution from water," *J. Mater. Chem. A*, vol. 6, no. 14, pp. 5774–5781, 2018, doi: 10.1039/c7ta10934b.

[60] R. Asai, H. Nemoto, Q. Jia, K. Saito, A. Iwase, and A. Kudo, "A visible light responsive rhodium and antimony-codoped $SrTiO_3$ powdered photocatalyst loaded with an IrO_2 cocatalyst for solar water splitting," *Chem. Commun.*, vol. 50, no. 19, pp. 2543–2546, 2014, doi: 10.1039/c3cc49279f.

[61] Q. Wang, T. Hisatomi, S. S. K. Ma, Y. Li, and K. Domen, "Core/shell structured La- and Rh-Codoped $SrTiO_3$ as a hydrogen evolution photocatalyst in Z-scheme overall water splitting under visible light irradiation," *Chem. Mater.*, vol. 26, no. 14, pp. 4144–4150, 2014, doi: 10.1021/cm5011983.

[62] A. Iwase, Y. H. Ng, Y. Ishiguro, A. Kudo, and R. Amal, "Reduced graphene oxide as a solid-state electron mediator in Z-scheme photocatalytic water splitting under visible light," *J. Am. Chem. Soc.*, vol. 133, no. 29, pp. 11054–11057, 2011, doi: 10.1021/ja203296z.

[63] Q. Wang, T. Hisatomi, Y. Suzuzki *et al.*, "Particulate photocatalyst sheets based on carbon conductor layer for efficient Z-scheme pure-water splitting at ambient pressure," *J. Am. Chem. Soc.*, vol. 139, no. 4, pp. 1675–1683, 2017, doi: 10.1021/jacs.6b12164.

[64] L. Guo, X. Guo, Y. He, and N. Tsubaki, "CO_2 heterogeneous hydrogenation to carbon-based fuels: recent key developments and perspectives," *J. Mater. Chem. A*, vol. 11, no. 22, pp. 11637–11669, 2023, doi: 10.1039/d3ta01025b.

[65] H. Matsuo, M. Kobayashi, S. Naniwa *et al.*, "Hydrogenation of CO_2 over Mn-Substituted $SrTiO_3$ Based on the Reverse Mars-van Krevelen Mechanism," *J. Phys. Chem. C*, vol. 127, no. 19, pp. 8946–8952, 2023, doi: 10.1021/acs.jpcc.3c01183.

[66] Y. Liu, X. Wang, Z. Wang *et al.*, "Hydrogenation of CO_2 to CH_3OH on the Cu-ZnO-$SrTiO_3$ Catalysts: The Electronic Metal-Support Interaction Induces Oxygen Vacancy Generation," *ACS Catal.*, vol. 14, no. 16, pp. 12610–12622, 2024, doi: 10.1021/acscatal.4c02289.

[67] B. Moss, Q. Wang, K. Butler *et al.*, "Linking in situ charge accumulation to electronic structure in doped $SrTiO_3$ reveals design principles for hydrogen-evolving photocatalysts," *Nat. Mater.*, vol. 20, no. 4, pp. 511–517, 2021, doi: 10.1038/s41563-020-00868-2.

[68] Y. S. Hou, S. Ardo, and R. Q. Wu, "Hybrid density functional study of band gap engineering of $SrTiO_3$ photocatalyst via doping for water splitting," *Phys. Rev. Mater.*, vol. 5, no. 6, pp. 1–9, 2021, doi: 10.1103/PhysRevMaterials.5.065801.

[69] H. Song, S. Luo, H. Huang, B. Deng, and J. Ye, "Solar-Driven Hydrogen Production: Recent Advances, Challenges, and Future Perspectives," *ACS Energy Lett.*, vol. 7, no. 3, pp. 1043–1065, 2022, doi: 10.1021/acsenergylett.1c02591.

[70] C. Xu, J. Hong, P. Sui, M. Zhu, Y. Zhang, and J. L. Luo, "Standalone Solar Carbon-Based Fuel Production Based on Semiconductors," *Cell Reports Phys. Sci.*, vol. 1, no. 7, p. 100101, 2020, doi: 10.1016/j.xcrp.2020.100101.

[71] S. Wang, G. Liu, and L. Wang, "Crystal Facet Engineering of Photoelectrodes for Photoelectrochemical Water Splitting," *Chem. Rev.*, vol. 119, no. 8, pp. 5192–5247,

2019, doi: 10.1021/acs.chemrev.8b00584.

[72] C. Jiang, S. J. A. Moniz, A. Wang, T. Zhang, and J. Tang, "Photoelectrochemical devices for solar water splitting-materials and challenges," *Chem. Soc. Rev.*, vol. 46, no. 15, pp. 4645–4660, 2017, doi: 10.1039/c6cs00306k.

[73] Y. Xu, Y. Liang, Q. He *et al.*, "Review of doping $SrTiO_3$ for photocatalytic applications," *Bull. Mater. Sci.*, vol. 46, no. 1, 2023, doi: 10.1007/s12034-022-02826-x.

[74] A. Raturi, P. Mittal, and S. Choudhary, "Tuning the electronic and optical properties of $SrTiO_3$ for optoelectronic and photocatalytic applications by plasmonic-metal doping: a DFT-computation," *Opt. Quantum Electron.*, vol. 54, no. 10, pp. 1–19, 2022, doi: 10.1007/s11082-022-03995-z.

[75] Z. Liu, S. Xu, T. Li, B. Xie, K. Guo, and J. Lu, "Microstructure and ferroelectric properties of high-entropy perovskite oxides with A-site disorder," *Ceram. Int.*, vol. 47, no. 23, pp. 33039–33046, 2021, doi: 10.1016/j.ceramint.2021.08.204.

[76] S. Jiang, T. Hu, J. Gild *et al.*, "A new class of high-entropy perovskite oxides," *Scr. Mater.*, vol. 142, pp. 116–120, 2018, doi: 10.1016/j.scriptamat.2017.08.040.

[77] Z. Li, M. Yang, J. S. Park, S. H. Wei, J. J. Berry, and K. Zhu, "Stabilizing Perovskite Structures by Tuning Tolerance Factor: Formation of Formamidinium and Cesium Lead Iodide Solid-State Alloys," *Chem. Mater.*, vol. 28, no. 1, pp. 284–292, 2016, doi: 10.1021/acs.chemmater.5b04107.

[78] J. Yao, T. Chen, H. Wang *et al.*, "Stable cubic crystal structures and optimized thermoelectric performance of $SrTiO_3$-based ceramics driven by entropy engineering," *J. Mater. Chem. A*, vol. 10, no. 46, pp. 24561–24572, 2022, doi: 10.1039/d2ta06576b.

[79] R. D. Shannon, "Revised effective ionic radii and systematic studies of interatomic distances in halides and chalcogenides," *Acta Crystallogr. Sect. A*, vol. 32, pp. 751–767, 1976.

[80] L. M. Feng, L. Q. Jiang, M. Zhu, H. B. Liu, X. Zhou, and C. H. Li, "Formability of ABO_3 cubic perovskites," *J. Phys. Chem. Solids*, vol. 69, no. 4, pp. 967–974, 2008, doi: 10.1016/j.jpcs.2007.11.007.

[81] N. Ramadass, "ABO_3-type oxides-Their structure and properties-A bird's eye view," *Mater. Sci. Eng.*, vol. 36, no. 2, pp. 231–239, 1978, doi: 10.1016/0025-5416(78)90076-9.

[82] Y. M. Mukovskii, "Perovskites: Resistivity Behavior," *Encycl. Mater. Sci. Technol.*, pp. 6826–6834, 2001, doi: 10.1016/b0-08-043152-6/01210-9.

[83] A. E. Hughes, " The Jahn–Teller effect in molecules and crystals by R. Englman ," *Acta Crystallogr. Sect. A*, vol. 29, no. 1, pp. 108–109, 1973, doi: 10.1107/s0567739473000288.

[84] H.A. Jahn and E. Teller, "Stability of Polyatomic Molecules in Degenerate Electronic States I-Orbital Degeneracy," *Proc. R. Soc. London*, vol. 161, pp. 220–235, 1937.

[85] I. B. Bersuker, "Jahn-Teller and Pseudo-Jahn-Teller Effects: From Particular Features to General Tools in Exploring Molecular and Solid State Properties," *Chem. Rev.*, vol. 121, no. 3, pp. 1463–1512, 2021, doi: 10.1021/acs.chemrev.0c00718.

[86] R. Ameis, D. Reinen, and S. Kremer, "Jahn-Teller Effect of Ti^{3+} in Octahedral Coordination: A Spectroscopic Study of TiCl63- Complexes," *Inorg. Chem.*, vol. 24, no. 18, pp. 2751–2754, 1985, doi: 10.1021/ic00212a009.

[87] R. G. Burns, *Mineralogical Applications of Crystal Field Theory*, 2nd ed. Cambridge: Cambridge University Press, 1993. Available: https://api.semanticscholar.org/CorpusID:202935531.

[88] M. A. Subramanian and J. Li, "Challenges in the rational design of intense inorganic pigments with desired colours," *Nat. Rev. Mater.*, vol. 8, no. 2, pp. 71–73, 2023, doi: 10.1038/s41578-022-00486-1.

[89] J. Li and N. Wu, "Semiconductor-based photocatalysts and photoelectrochemical cells for solar fuel generation: A review," *Catal. Sci. Technol.*, vol. 5, no. 3, pp. 1360–1384, 2015, doi: 10.1039/c4cy00974f.

[90] H. Sudrajat, M. M. Fadlallah, S. Tao, M. Kitta, N. Ichikuni, and H. Onishi, "Dopant site in indium-doped $SrTiO_3$ photocatalysts," vol. 22, no. 34, pp. 19178–19187, doi: 10.1039/D0CP02822C.

[91] H. Yaghoubi, Z. Li, Y. Chen *et al.*, "Toward a Visible Light-Driven Photocatalyst : The Effect of Midgap- States-Induced Energy Gap of Undoped TiO_2 Nanoparticles," 2015.

[92] C. Cheng and R. Long, "Charge-Compensated Doping Extends Carrier Lifetimes in $SrTiO_3$ by Passivating Oxygen Vacancy Defects," *J. Phys. Chem. Lett.*, vol. 12, no. 50, pp. 12040–12047, 2021, doi: 10.1021/acs.jpclett.1c03775.

[93] G. M. Repa, Z. J. Knepp, and L. A. Fredin, "A-Site Doping to Alter Oxygen Vacancy Diffusion in $SrTiO_3$," *ACS Omega*, 2024, doi: 10.1021/acsomega.4c04099.

[94] Y. Bi, M. F. Ehsan, Y. Huang, J. Jin, and T. He, "Synthesis of Cr-doped $SrTiO_3$ photocatalyst and its application in visible-light-driven transformation of CO_2 into CH_4," *J. CO2 Util.*, vol. 12, pp. 43–48, 2015, doi: https://doi.org/10.1016/j.jcou.2015.10.004.

[95] K. Iwashina and A. Kudo, "Rh-Doped $SrTiO_3$ Photocatalyst Electrode Showing Cathodic," *J. Am. Chem. Soc.*, vol. 133, no. 34, pp. 13272–13275, 2011.

[96] S. Suzuki, H. Matsumoto, A. Iwase, and A. Kudo, "Enhanced H2 evolution over an Ir-doped $SrTiO_3$ photocatalyst by loading of an Ir cocatalyst using visible light up to 800 nm," *Chem. Commun.*, vol. 54, no. 75, pp. 10606–10609, 2018, doi: 10.1039/c8cc05344h.

[97] Z. Jiao, T. Chen, J. Xiong *et al.*, "Visible-light-driven photoelectrochemical and photocatalytic performances of Cr-doped $SrTiO_3/TiO_2$ heterostructured nanotube arrays," *Sci. Rep.*, vol. 3, no. 1, p. 2720, 2013, doi: 10.1038/srep02720.

[98] Y. X. Song, W. Q. Ma, J. J. Chen, J. Xu, Z. Y. Mao, and D. J. Wang, "Photocatalytic activity of perovskite $SrTiO_3$ catalysts doped with variable rare earth ions," *Rare Met.*, vol. 40, no. 5, pp. 1077–1085, 2021, doi: 10.1007/s12598-020-01674-0.

[99] R. Courths, B. Cord, and H. Saalfeld, "Bulk and surface Ti 3d valence and defect states in $SrTiO_3$ (001) from resonant photoemission," *Solid State Commun.*, vol. 70, no. 11, pp. 1047–1051, 1989, doi: https://doi.org/10.1016/0038-1098(89)90190-7.

[100] J. Sun and D. J. Singh, "Thermoelectric properties of n -type $SrTiO_3$," *APL Mater.*, vol.

4, no. 10, 2016, doi: 10.1063/1.4952610.

[101] G. Campet, M. Carrere, C. Puprichitkun, S. Z. Wen, J. Salardenne, and J. Claverie, "n-Type $SrTiO_3$ thin films: Electronic processes and photoelectrochemical behavior," *J. Solid State Chem.*, vol. 69, no. 2, pp. 267–273, 1987, doi: https://doi.org/10.1016/0022-4596(87)90083-1.

[102] C. Mitra, C. Lin, J. Robertson, and A. A. Demkov, "Electronic structure of oxygen vacancies in $SrTiO_3$ and $LaAlO_3$," *Phys. Rev. B - Condens. Matter Mater. Phys.*, vol. 86, no. 15, 2012, doi: 10.1103/PhysRevB.86.155105.

[103] S. Zhu and D. Wang, "Photocatalysis: Basic principles, diverse forms of implementations and emerging scientific opportunities," *Adv. Energy Mater.*, vol. 7, no. 23, pp. 1–24, 2017, doi: 10.1002/aenm.201700841.

[104] K. Takanabe, "Photocatalytic Water Splitting: Quantitative Approaches toward Photocatalyst by Design," *ACS Catal.*, vol. 7, no. 11, pp. 8006–8022, 2017, doi: 10.1021/acscatal.7b02662.

[105] K. Takanabe, "Solar Water Splitting Using Semiconductor Photocatalyst Powders BT - Solar Energy for Fuels," H. Tüysüz and C. K. Chan, Eds. Cham: Springer International Publishing, 2016, pp. 73–103.

[106] B. Ohtani, "Photocatalysis by inorganic solid materials: Revisiting its definition, concepts, and experimental procedures," *Adv. Inorg. Chem.*, vol. 63, pp. 395–430, 2011, doi: 10.1016/B978-0-12-385904-4.00001-9.

[107] B. Ohtani, "Photocatalysis A to Z-What we know and what we do not know in a scientific sense," *J. Photochem. Photobiol. C Photochem. Rev.*, vol. 11, no. 4, pp. 157–178, 2010, doi: 10.1016/j.jphotochemrev.2011.02.001.

[108] B. Ohtani, "Revisiting the fundamental physical chemistry in heterogeneous photocatalysis: its thermodynamics and kinetics.," *Phys. Chem. Chem. Phys.*, vol. 16 5, pp. 1788–1797, 2014, [Online]. Available: https://api.semanticscholar.org/CorpusID:17787252.

[109] B. Liu, H. Wu, and I. P. Parkin, "New Insights into the Fundamental Principle of Semiconductor Photocatalysis," *ACS Omega*, vol. 5, no. 24, pp. 14847–14856, 2020, doi: 10.1021/acsomega.0c02145.

[110] N. Shehzad, M. Tahir, K. Johari, T. Murugesan, and M. Hussain, "A critical review on TiO_2 based photocatalytic CO_2 reduction system: Strategies to improve efficiency," *J. CO_2 Util.*, vol. 26, no. November 2017, pp. 98–122, 2018, doi: 10.1016/j.jcou.2018.04.026.

[111] N. Shehzad, M. Tahir, K. Johari, T. Murugesan, and M. Hussain, "A critical review on TiO_2 based photocatalytic CO_2 reduction system: Strategies to improve efficiency," *J. CO_2 Util.*, vol. 26, pp. 98–122, 2018, doi: https://doi.org/10.1016/j.jcou.2018.04.026.

[112] N. Fajrina and M. Tahir, "A critical review in strategies to improve photocatalytic water splitting towards hydrogen production," *Int. J. Hydrogen Energy*, vol. 44, no. 2, pp. 540–577, 2019, doi: 10.1016/j.ijhydene.2018.10.200.

[113] M. Kumar, B. Meena, P. Subramanyam, D. Suryakala, and C. Subrahmanyam, "Recent trends in photoelectrochemical water splitting: the role of cocatalysts," *NPG Asia Mater.*, vol. 14, no. 1, 2022, doi: 10.1038/s41427-022-00436-x.

[114] D. Liu and Y. Kuang, "Particle-Based Photoelectrodes for PEC Water Splitting: Concepts and Perspectives," *Adv. Mater.*, vol. 19, pp. 1–30, 2024, doi: 10.1002/adma.202311692.

[115] C. Ding, J. Shi, Z. Wang, and C. Li, "Photoelectrocatalytic Water Splitting: Significance of Cocatalysts, Electrolyte, and Interfaces," *ACS Catal.*, vol. 7, no. 1, pp. 675–688, 2017, doi: 10.1021/acscatal.6b03107.

[116] Z. Zhang and J. T. Yates, "Band bending in semiconductors: Chemical and physical consequences at surfaces and interfaces," *Chem. Rev.*, vol. 112, no. 10, pp. 5520–5551, 2012, doi: 10.1021/cr3000626.

[117] F. E. Osterloh, "Photocatalysis versus Photosynthesis: A Sensitivity Analysis of Devices for Solar Energy Conversion and Chemical Transformations," *ACS Energy Lett.*, vol. 2, no. 2, pp. 445–453, 2017, doi: 10.1021/acsenergylett.6b00665.

[118] X. L. Shi *et al.*, "$SrTiO_3$-based thermoelectrics: Progress and challenges," *Nano Energy*, vol. 78, no. May, 2020, doi: 10.1016/j.nanoen.2020.105195.

[119] Z. P. Li, T. Mori, G. J. Auchterlonie, J. Zou, and J. Drennan, "Direct evidence of dopant segregation in Gd-doped ceria," *Appl. Phys. Lett.*, vol. 98, no. 9, pp. 1–4, 2011, doi: 10.1063/1.3556650.

[120] X. Guo and R. Waser, "Electrical properties of the grain boundaries of oxygen ion conductors: Acceptor-doped zirconia and ceria," *Prog. Mater. Sci.*, vol. 51, no. 2, pp. 151–210, 2006, doi: https://doi.org/10.1016/j.pmatsci.2005.07.001.

[121] A. R. Symington, M. Molinari, J. Statham, J. Wu, and S. C. Parker, "The role of dopant segregation on the oxygen vacancy distribution and oxygen diffusion in CeO_2 grain boundaries," *JPhys Energy*, vol. 1, no. 4, 2019, doi: 10.1088/2515-7655/ab28b5.

[122] D. Hull and D. J. Bacon, "Chapter 1 - Defects in Crystals," in *Introduction to Dislocations (Fifth Edition)*, Fifth Edit., D. Hull and D. J. Bacon, Eds. Oxford: Butterworth-Heinemann, 2011, pp. 1–20.

[123] Z. Zafar *et al.*, "Recent Development in Defects Engineered Photocatalysts: An Overview of the Experimental and Theoretical Strategies," *Energy Environ. Mater.*, vol. 5, no. 1, pp. 68–114, 2022, doi: 10.1002/eem2.12171.

[124] "https://www.doitpoms.ac.uk/tlplib/dislocations/dislocations_in_3D.php. 18.09.2024." .

[125] S. Mridha, A. Choudhury, and K. Subramanian, "Effect of grain-boundary character on segregation of vacancies: Thermodynamic aspects," *Phys. Rev. Mater.*, vol. 7, no. 11, pp. 1–12, 2023, doi: 10.1103/PhysRevMaterials.7.113605.

[126] G. Hodes and P. V. Kamat, "Understanding the Implication of Carrier Diffusion Length in Photovoltaic Cells," *J. Phys. Chem. Lett.*, vol. 6, no. 20, pp. 4090–4092, 2015, doi: 10.1021/acs.jpclett.5b02052.

[127] P. Biswas *et al.*, "Tuning of oxygen vacancy-induced electrical conductivity in Ti-doped hematite films and its impact on photoelectrochemical water splitting," *Sci. Rep.*, vol. 10, no. 1, pp. 2–10, 2020, doi: 10.1038/s41598-020-64231-w.

[128] N. A. Koshi, D. H. K. Murthy, S. Chakraborty, S. C. Lee, and S. Bhattacharjee, "Probing Photoexcited Charge Carrier Trapping and Defect Formation in Synergistic Doping of

$SrTiO_3$," *ACS Appl. Energy Mater.*, vol. 5, no. 1, pp. 1159–1168, 2022, doi: 10.1021/acsaem.1c03543.

[129] A. A. Wilson, T. P. Shalvey, A. Kafizas, A. Mumtaz, and J. R. Durrant, "Analysis of charge trapping and long lived hole generation in $SrTiO_3$ photoanodes," *Sustain. Energy Fuels*, vol. 7, no. 20, pp. 5066–5075, 2023, doi: 10.1039/d3se00886j.

[130] U. Guth, "Kröger-Vinks Notation of Point Defects BT - Encyclopedia of Applied Electrochemistry," G. Kreysa, K. Ota, and R. F. Savinell, Eds. New York, NY: Springer New York, 2014, pp. 1159–1160.

[131] J. Gan, X. Lu, J. Wu *et al.*, "Oxygen vacancies promoting photoelectrochemical performance of In_2O_3 nanocubes," *Sci. Rep.*, vol. 3, pp. 1–7, 2013, doi: 10.1038/srep01021.

[132] M. Siebenhofer, F. Baiutti, J.D. Sirvent *et al.*, "Exploring point defects and trap states in undoped $SrTiO_3$ single crystals," *J. Eur. Ceram. Soc.*, vol. 42, no. 4, pp. 1510–1521, 2022, doi: 10.1016/j.jeurceramsoc.2021.10.010.

[133] B. L. Phoon, C. W. Lai, J. C. Juan, P. L. Show, and W. H. Chen, "A review of synthesis and morphology of $SrTiO_3$ for energy and other applications," *Int. J. Energy Res.*, vol. 43, no. 10, pp. 5151–5174, 2019, doi: 10.1002/er.4505.

[134] J. A. Enterkin, K. R. Poeppelmeier, and L. D. Marks, "Oriented catalytic platinum nanoparticles on high surface area strontium titanate nanocuboids," *Nano Lett.*, vol. 11, no. 3, pp. 993–997, 2011, doi: 10.1021/nl104263j.

[135] T. Kimijima, K. Kanie, M. Nakaya, and A. Muramatsu, "Solvothermal synthesis of $SrTiO_3$ nanoparticles precisely controlled in surface crystal planes and their photocatalytic activity," *Appl. Catal. B Environ.*, vol. 144, pp. 462–467, 2014, doi: 10.1016/j.apcatb.2013.07.051.

[136] H. G. Yang, G. Liu, S. Qiao *et al.*, "Solvothermal synthesis and photoreactivity of anatase TiO(2) nanosheets with dominant {001} facets.," *J. Am. Chem. Soc.*, vol. 131, no. 11, pp. 4078–4083, Mar. 2009, doi: 10.1021/ja808790p.

[137] S. T. Huang, W. W. Lee, J. L. Chang, W. S. Huang, S. Y. Chou, and C. C. Chen, "Hydrothermal synthesis of SrTiO3 nanocubes: Characterization, photocatalytic activities, and degradation pathway," *J. Taiwan Inst. Chem. Eng.*, vol. 45, no. 4, pp. 1927–1936, 2014, doi: 10.1016/j.jtice.2014.02.003.

[138] A. Kumar, A. Kumar, and V. Krishnan, "Perovskite Oxide Based Materials for Energy and Environment-Oriented Photocatalysis," *ACS Catal.*, vol. 10, no. 17, pp. 10253–10315, 2020, doi: 10.1021/acscatal.0c02947.

[139] H. Hou, G. Shao, W. Yang, and W. Y. Wong, "One-dimensional mesoporous inorganic nanostructures and their applications in energy, sensor, catalysis and adsorption," *Prog. Mater. Sci.*, vol. 113, no. March, p. 100671, 2020, doi: 10.1016/j.pmatsci.2020.100671.

[140] B. Wang, S. Shen, and L. Guo, "Surface Reconstruction of Facet-Functionalized SrTiO3 Nanocrystals for Photocatalytic Hydrogen Evolution," *ChemCatChem*, vol. 8, no. 4, pp. 798–804, 2016, doi: 10.1002/cctc.201501162.

[141] L.Dimesso, "Pechini Processes: An Alternate Approach of the Sol-Gel Method, Preparation, Properties, and Applications," in *Handbook of Sol-Gel Science and Technology: Processing, Characterization and Applications*, no. January, 2018, p. ix.

[142] A. E. Danks, S. R. Hall, and Z. Schnepp, "The evolution of 'sol-gel' chemistry as a technique for materials synthesis," *Mater. Horizons*, vol. 3, no. 2, pp. 91–112, 2016, doi: 10.1039/c5mh00260e.

[143] Y. Liu, L. Xie, Y. Li *et al.*, "Synthesis and high photocatalytic hydrogen production of $SrTiO_3$ nanoparticles from water splitting under UV irradiation," *J. Power Sources*, vol. 183, no. 2, pp. 701–707, 2008, doi: 10.1016/j.jpowsour.2008.05.057.

Chapter 2: Methods

This chapter discusses the synthesis method and characterization techniques used in the scope of the Ph.D. work. Most techniques were conducted at Imperial College London, and the data analysis was done by the author of this thesis. BET, EPR analysis, and photocatalysis measurements were done at the University of Oxford by Dr. Robert Jacobs, Dr. Arnau Bertran, and Baliana Shani respectively. The photocatalytic set-up used in this Ph.D. work was from Prof. Ian McCulloch Group. *The error bars in the thesis work for the data analysis from the characterization techniques were added from the standard deviations after repeating measurements three times.*

2.1 Catalyst Preparation

The sol-gel Pechini method has been used in this Ph.D. study as an alternative to solid-state synthesis as it leads to the formation of smaller nanoparticles. Smaller particles offer higher specific areas which facilitate enhanced photocatalysis or photoelectrocatalysis. In this work, with sol-gel Pechini the nanoparticles could be synthesized at temperatures as low as 500 °C. This is another advantage over the solid-state synthesis which generally occurs at temperatures higher than 900 °C. In the Ph.D. work, undoped and a series of doped $SrTiO_3$ were synthesized with the sol-gel Pechini method.

2.1.1 Goldschmidt's Tolerance Factor

In the Ph.D. work, before synthesizing the catalysts the Goldschmidt's tolerance factor, t was taken into consideration to determine the range up to which doping leads to single-phase materials. $SrTiO_3$ is an ABO_3 type perovskite structure with a cubic unit cell having a lattice parameter a = 3.905 Å [1]. In $SrTiO_3$, Ti^{4+} is co-ordinated by 6 O^{2-} ions, and each Sr^{2+} ion is co-ordinated by 8 TiO_6 octahedra or 12 O^{2-} ions [1]. In a cubic closed packed $SrTiO_3$, Sr^{2+} cations occupy the body centred position [1/2,1/2,1/2], Ti^{4+} the corners [0,0,0] and O^{2-} ions the [(1/2,0,0);(0,1/2,0);(0,0,1/2)] position [2]. In perovskite structures, Goldschmidt's Tolerance Factor is used to determine the structural stability of the samples [3]. The tolerance factor, t is derived for undoped and doped samples in the following equations [4].

$$t = \frac{r_A + r_O}{\sqrt{2}(r_B + r_O)} \quad (2.1)$$

$$t = \frac{r_A + r_O}{\sqrt{2}((1-x)r_B + x r_{B'} + r_O)} \quad (2.2)$$

where,

r_A = Radius of A-site cation, Sr^{2+}= 1.44 Å

$r_{A'}$ = Radius of co-dopant at A-site, La^{3+}= 1.36 Å

$r_{A'}$ = Radius of Dopant at A site, Cs^{1+}= 1.88 Å

r_B = Radius of B-site cation, Ti^{4+}= 0.605 Å

$r_{B'}$ = Radius of Dopant at B-site, Ga^{3+}= 0.62 Å

$r_{B'}$ = Radius of Dopant at B site, Cr^{3+}= 0.615 Å

r_O = Radius of Oxygen anion, O^{2-}= 1.4 Å

x = Percentage doping

The tolerance factors were calculated from the equations, Eq (2.1) and Eq (2.2) for undoped and doped samples respectively. The tolerance limit of the perovskite materials should be within the range of 0.75<t<(=) 1. If t< (=) 1, it can be inferred, that the doped samples retain the cubic structure with no distortions upon Ga^{3+}/ Cr^{3+} /La^{3+} doping. Takata, T. et al. [5] reported the phase purity of the 5 mol% Ga^{3+} doped $SrTiO_3$ prepared with the solid-state synthesis. This mol% doping was chosen as the starting point for the tolerance factor calculations. Based on the tolerance factors, a series of Ga^{3+} and Cr^{3+} doped were synthesized. Based on this, another series of Cr^{3+}, $La^{3+,}$ and Cs^{1+} co-doped $SrTiO_3$ samples were synthesized. The synthesis process is discussed in the following section.

2.1.2 Synthesis of undoped and doped $SrTiO_3$

Undoped $SrTiO_3$ nano-powders were prepared by adding 2.85 mmol (0.81 g) of titanium (IV) isopropoxide (Sigma Aldrich, 99% pure) to 119.82 mmol (6.7 ml) of ethylene glycol (EG) (Alfa Aeser, 99.5% pure). The mixture was heated in a water bath set to 60 °C and stirred for 1 h. 30 mmol (6.30 g) of citric acid monohydrate (CA) (Alfa Aeser, 99% pure) was added to the mixture as a chelating agent and stirred for another hour. 2.85 mmol (0.60 g) of $Sr(NO_3)_2$ (Sigma Aldrich, 99% pure) were added to the mixture and stirred for a further hour aiming for a 1:1 ratio of Ti: Sr in pure $SrTiO_3$. For the doped samples, the hydrated nitrates of the precursors (Sigma Aldrich, 99% pure) were added to the clear transparent mixture under constant stirring at 60 °C such that the overall B-site: A-site ratio was kept the same (1:1) and the $[Ga^{3+}/Cr^{3+}]$:($[Ga^{3+}/Cr^{3+}]$+$[Ti^{4+}]$) molar ratio was adjusted to the required mol% doping concentration. For the co-doped samples, the mmols of the hydrated nitrates of La^{3+} and Cs^{1+} were added next. After another hour, the metal citrate complex was heated to 197 °C for 6.5 h for polyestrification resulting in a brown resin as shown in Figure 2.1. The 197 °C temperature was selected such that the mixture and resin would dry reasonably well and were set to the boiling point of EG.



Figure 2.1: *Coarsely ground polyester with a hard glass-like texture after heating the gel to 197 °C before further calcination.*

The brown resin was ground to a coarse powder using mortar and pestle. The ground material was then calcined at 450 °C, 500 °C, 600 °C, 700 °C, 800 °C and 900 °C for 6-10 h under airflow 1 (L/min) ramping up from room temperature with a rate of 5 °C/min and natural

cooling after 6-10 h. The calcined material was ground in an agate mortar to obtain the catalyst nanoparticles. Table 2.1 (a) and (b) list the stoichiometric amounts of precursors used for the samples.

In the Pechini method, the stoichiometric amount of the dopant was directly added to the sol. A modification was introduced in a Cr-doped batch where a stoichiometric amount of 10 mol% Cr (114.04 mg) dopant was dissolved in 6.7 ml of EG, and a stock solution was prepared. This stock solution was diluted further with EG to synthesize a serial dilution series of Cr^{3+} monodoped $SrTiO_3$. From the stock, 3.35 ml of the solution was added to 10 ml measuring flash with EG. 1 ml of this solution was then added to the sol prepared as per the Pechini method described above to synthesize 10 mol% Cr doping. Similar dilutions were made by adding 1.34 ml, 0.67 ml, and 0.067 ml to EG in the 10 ml measuring flask to synthesize 2 mol%, 1 mol%, and 0.1 mol% Cr doped $SrTiO_3$. The serial dilution (SD) series was calcined at 800 °C under compressed air for 10 h resulting in faint yellow powders at low doping concentrations to red powders with higher mol% doping. *The undoped* $SrTiO_3$ *was synthesized for all the different doped batches.*

Table 2.1 a: Stoichiometric composition of the doped samples synthesized with the sol-gel Pechini method

Samples	**Mol% Mono-Doping**	**Sr Precursor (g)**	**n(Sr) / mmol**	**Citric Acid Monohydrate (g)**	**n($CAxH_2O$) [mmol]**	**Ethylene Glycol (ml)**	**n(ethylene glycol) [mmol]**
Undoped	0	0.60	2.85	6.30	30.00	6.70	119.82
0.5 Ga	0.5	0.60	2.85	6.30	30.00	6.70	119.82
1Ga	1	0.60	2.85	6.30	30.00	6.70	119.82
2Ga	2	0.60	2.85	6.30	30.00	6.70	119.82
4Ga	4	0.60	2.85	6.30	30.00	6.70	119.82
10Ga	10	0.60	2.85	6.30	30.00	6.70	119.82
0.5 La, Ga	0.5	0.60	2.84	6.30	30.00	6.70	119.82
1La,Ga	1	0.597	2.82	6.30	30.00	6.70	119.82
2La,Ga	2	0.591	2.79	6.30	30.00	6.70	119.82
4La,Ga	4	0.58	2.74	6.30	30.00	6.70	119.82
10La,Ga	10	0.54	2.56	6.30	30.00	6.70	119.82
2Cr	2	0.60	2.85	6.30	30.00	6.70	119.82
1La,2Cr	2	0.597	2.82	6.30	30.00	6.70	119.82
2La,2Cr	2	0.591	2.79	6.30	30.00	6.70	119.82

5La,2Cr	2	0.57	2.71	6.30	30.00	6.70	119.82
10La,2Cr	2	0.54	61.70	6.30	30.00	6.70	119.82
1Cs,2Cr	2	0.597	2.82	6.30	30.00	6.70	119.82
2Cs,2Cr	2	0.591	2.74	6.30	30.00	6.70	119.82
5Cs,2Cr	2	0.57	2.71	6.30	30.00	6.70	119.82
10Cs,2Cr	2	0.54	2.56	6.30	30.00	6.70	119.82

Table 2.1 b: Stoichiometric composition of the doped samples synthesized with the sol-gel Pechini method

Samples	**Mol% Mono-Doping**	**n(Ti) / mmol**	**Ti Precursor [mg]**	**mmol % Mono-doping)**	**M(Mono-dopant) [mg]**	**Mol% Co-Doping**	**Mol% doping)**	**m(Co-dopant) (mg)**
Undoped	0	2.85	810.01	0.00	0.00	-	-	-
0.5 Ga	0.5	2.84	805.96	0.014	5.18	-	-	-
1Ga	1	2.82	801.91	0.028	10.37	-	-	-
2Ga	2	2.79	793.81	0.057	20.74	-	-	-
4Ga	4	2.74	777.61	0.114	41.48	-	-	-
10Ga	10	2.57	729.01	0.285	103.69	-	-	-
0.5 La, Ga	0.5	2.84	805.96	0.014	5.18	0.5	0.01	6.17
1La,Ga	1	2.82	801.91	0.028	10.37	1	0.03	12.34
2La,Ga	2	2.79	793.81	0.057	20.74	2	0.06	24.68
4La,Ga	4	2.74	777.61	0.114	41.48	4	0.11	49.36
10La,Ga	10	2.57	729.01	0.285	103.69	10	0.28	123.41
2Cr	2	2.79	793.81	0.057	22.81			
1La,2Cr	2	2.79	793.81	0.057	22.81	1	0.03	12.34
2La,2Cr	2	2.79	793.81	0.057	22.81	2	0.06	24.68
5La,2Cr	2	2.79	793.81	0.057	22.81	5	0.14	61.70
10La,2Cr	2	2.79	793.81	0.057	22.81	10	0.28	12341
1Cs,2Cr	2	2.79	793.81	0.057	22.81	1	0.03	5.55

2Cs,2Cr	2	2.79	793.81	0.057	22.81	2	0.06	11.11
5Cs,2Cr	2	2.79	793.81	0.057	22.81	5	0.14	27.77
10Cs,2Cr	2	2.79	793.81	0.057	22.81	10	0.28	55.55

In Table 2(a) and (b) 'n' denotes the number of moles

The synthesized samples were characterized with different methods to understand their microstructural and opto-electronic properties. The characterization techniques are discussed in the subsequent sections.

2.2 Microstructural Characterization

2.2.1 Powder X-ray Diffraction (XRD)

In crystallography, XRD is a non-destructive analysis technique that is used to quantify and determine the crystalline forms or phases present in a material. In 1913, William Laurence Bragg built on the observations of Max Laue (1912) about how a crystalline material with its repeated structural order acts as a diffraction grating for X-rays [6]. He then proposed Bragg's law which forms the working principle of XRD [7]. This law is schematically illustrated in Figure 2.2 and can be mathematically expressed as Eq (2.3).

$$n\lambda = 2\, d_{hkl} \sin(\theta) \qquad (2.3)$$

Where,

n = Diffraction order (0, 1, 2….)

d_{hkl} = Interplanar spacings

λ = Wavelength of X-rays

θ = Bragg's angle (X-ray incident angle)

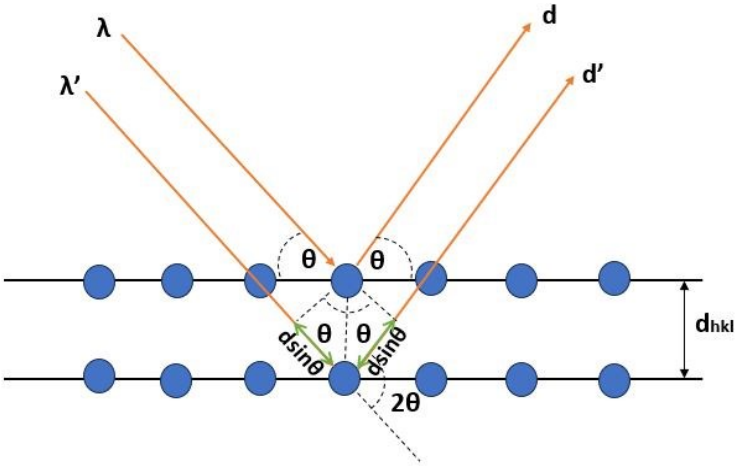


Figure 2.2: *A Schematic Diagram of Bragg's Diffraction.*

Bragg's law states that when X-rays are incident on the crystal surface with an angle θ, they are scattered by the subsequent lattice planes as shown in Figure 2.2. When these scattered waves are in phase, they undergo constructive interference. Bragg's law relates the scattering angle, θ, and the inter-atomic distance, d_{hkl} to the wavelength of a diffraction order (an integer, n).

Bragg's law is a condition that is utilized by X-ray diffractometers to produce diffraction patterns. Diffractometers consist of a cathode ray tube, a goniometer, a sample holder, and a detector as shown in Figure 2.3.

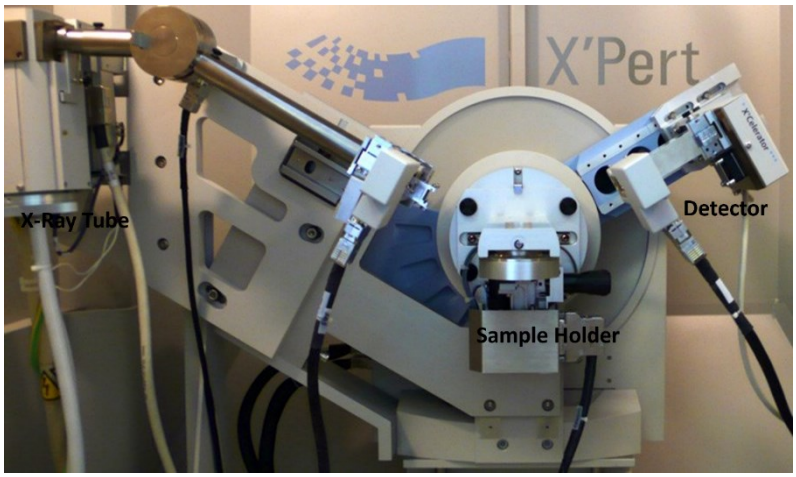


Figure 2.3: *A PANanalytical X'pert MPD XRD housing a goniometer that drives an optical path equipped with an X-ray tube with Cu Kα source, a sample holder, and a detector.*

The cathode ray tube consists of a filament that heats up to produce an electron beam. This electron beam is then bombarded onto the target material by accelerating it with a voltage. When the electron beam collides with the target material then it removes an electron from the inner shell. The vacancy left behind is filled by an electron from the outer shell and emitting X-rays. In the Ph.D. work, XRD diffraction patterns were collected with a PANanalytical X'pert MPD diffractometer**.** The XRD parameters used are consistent with all the materials synthesized. These parameters are recorded in Table 2.2.

Table 2.2: XRD parameters used for data collection

Target Material	Cu Kα (1.5419 Å)
2θ	20° - 80°
X-rays	40 kV, 40 mA
Step Size	0.0167113
Time/Step (s)	24.765
Scan Speed	0.085699

In a diffractometer, the X-rays are collimated and directed towards the sample. The sample is loaded on sample holders and flattened with a glass slide. This ensures that the sample fills the

central part of the holder as shown in Figure 2.4 and the geometry is maintained for impinging the X-rays. Excess samples are removed.

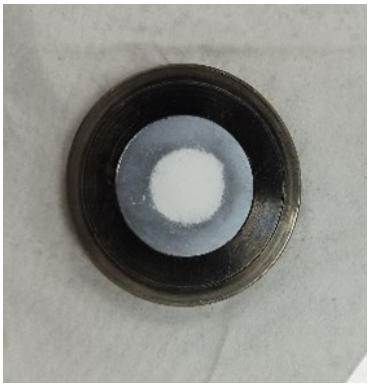


Figure 2.4: *Sample flattened and loaded on a sample holder before inserting into the diffractometer.*

In the diffractometer, the sample is oriented at an angle θ to the collimated X-ray beam and the detector is at angle 2θ to collect the diffracted beam. The emitted X-rays consist of two components- the kα and the kβ radiations. The kα radiation occurs when the electrons transition from the L-shell to the K-shell [8]. Whereas kβ radiation occurs when the electrons transition from the M-shell to the K-shell [8]. A goniometer maintains this orientation and rotates the sample. The diffraction pattern is obtained by scanning through a range of 2θ values. Phase identification is done by comparing the d-spacings and the diffraction peaks with reference patterns from databases such as ICDD.

In material science, XRD is instrumental in identifying the phases, and calculation of crystallite sizes and lattice parameters. In doped semi-conductor materials, XRD analysis can be utilized to study the changes in crystallinity, lattice parameters, crystallite sizes, and microstrains. The studies conducted in the scope of this Ph.D. relating to the XRD are discussed in the succeeding sections.

Lattice Parameters

Doping can lead to a change in lattice parameters of crystal structure [9]. In cubic perovskite structures such as $SrTiO_3$, the lattice parameters, a=b=c form the three dimensions of the unit cell. Hence, the cell volume can be expressed by the Eq (2.4) [10]. With the introduction of dopants, if the structure is maintained without any distortions, the same Eq (2.4) can be applied. Depending on the site of dopant introduction, dopant sizes, and point defects such as vacancies, the parent structure might expand or contract.

$$\text{Volume, } V = a^3 \qquad (2.4)$$

Where,

a = Lattice Parameter

Changes in lattice parameters and the resulting expansions or contractions are fundamental topics of study in this Ph.D. work. The topic will be discussed in detail in Chapter 4. Lattice

parameters of the samples were measured from the XRD diffraction patterns after extracting the hkl values from Rietveld refining with GSAS-II. Rietveld refinement involves a least square method approach where the observed diffraction pattern is fitted with a calculated diffraction pattern. The refinement process involves fitting (pseudo-Voigt) the XRD peaks and refining the structural factors. The factors refined for the samples studied are the zero shift, the scale factor, the peak profile parameters (u, v, w), unit cell parameters, atomic positions, and site occupations. GSAS-II was used to refine the structure and obtain the miller indices which was then used in the UnitCell software to calculate the lattice parameters.

The lattice parameters are fundamental to studying the geometry of the crystal lattices and how they respond to a change whether induced via doping or via any form of treatment like annealing in different atmospheres. In this Ph.D. work, the effect of change in lattice parameters on closely related microstructural components such as the crystallite size and the microstrain will be studied. The methods employed to study these factors are explored in the next sections.

Coherently Scattering Domain Size

Coherently scattering domain sizes are the crystalline domains in a particle. These domains have different orientations separated by grain boundaries as shown in Figure 2.5. Coherently scattering domain size has been used interchangeably with the crystallite size. Since the catalysts are mostly in the form of single crystalline particles, the crystallite size and the particle size are used as the same concept in this thesis.

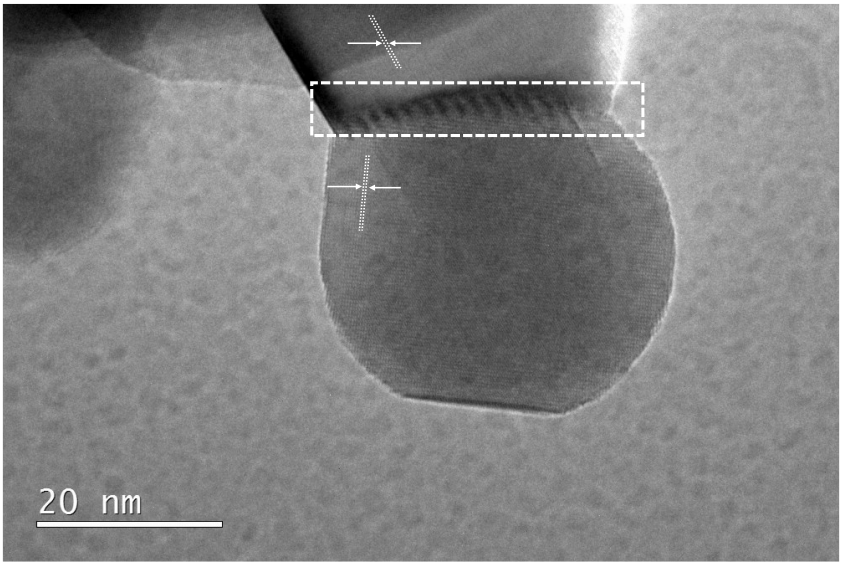


Figure 2.5: *A TEM micro-graph showing a crystallite adjoined to another crystallite with different orientations separated by a grain boundary highlighted in the white rectangle of a* Ga^{3+} *doped* $SrTiO_3$ *sample.*

In photocatalysis, nanoparticle size is one of the fundamental material properties that affect the catalyst performance. With the XRD, two routes- the Scherrer equation and the Williamson-Hall analysis, are undertaken to study crystallite sizes.

Scherrer Equation

The Debye-Scherrer equation correlates the peak broadening (ß, FWHM) to the crystallite size, denoting an inverse relation i.e. broader the peak, smaller the crystallite size. The Eq for this relation is shown in Eq (2.5) [11].

$$D = k\lambda / ß_D \cos\theta \quad (2.5)$$

Where,

$ß_D$ = Peak Broadening in Radians = FWHM

k = Shape Factor = 0.9

λ = 1.5419 Å = Wavelength of X-ray source (Cu Kα)

D = Crystallite Size

θ = Peak Position

In the Scherrer equation, the peak broadening is due to the crystallite size. It does not consider factors such as the microstrain, dislocations, or other lattice defects. In semiconductor physics, the microstrain is an important lattice characteristic to understand defects. This strain is localized to a few lattice spacings and occurs in the vicinity of defects such as dislocations, grain boundaries, or point defects [12]. The microstrain contributes to peak broadening as well. The effect of microstrain will be discussed in detail in Chapter 4. Here, the microstrain is measured with the Williamson-Hall method which is discussed in the succeeding section.

Williamson Hall (W-H) Analysis

In the Williamson Hall analysis of crystallite size, the peak broadening is due to both the crystallite size ($ß_D$) and the microstrain ($ß_e$) [13]. Mathematically, the total peak broadening ($ß_T$) is expressed as Eq (2.6). The strain due to the crystallite size and microstrain are expressed as Eq (2.7) and Eq (2.8).

$$\text{Total Broadening, } (ß_T) = ß_D + ß_e \quad (2.6)$$

$$ß_D = k\lambda / D\cos\theta \quad (2.7)$$

$$ß_\varepsilon = 4\varepsilon\tan\theta \quad (2.8)$$

Inserting Eqs (2.7) and (2.8) into Eq (2.6) gives:

$$ß_T = k\lambda / D\cos\theta + 4\varepsilon\tan\theta \quad (2.9)$$

$$ß_T = k\lambda / D\cos\theta + 4\varepsilon\sin\theta / \cos\theta \quad (2.10)$$

$$ß_T\cos\theta = \varepsilon(4\sin\theta) + k\lambda / D \quad (2.11)$$

For the estimation of the crystallite with W-H analysis, the diffraction pattern is first peak fitted. Two types of peak fittings were tried – Lorentzian and Pseudo-Voigt (PS1) as shown in Figures 2.6(a) and 2.6(b). It was observed that a Pseudo-Voigt (PS1) fitting is more accurate than a Lorentzian fitting. After the peak fitting, the FWHM is extracted along with the 2θ values.

From these two values, the 4sinθ and ßcosθ as expressed in Eq (2.10) were calculated, plotted, and fitted with two linear regressions. The intercepts were extracted as the average crystallite size and the slopes as the microstrain. The presence of two linear regressions indicate the presence of two average size – microstrain regimes which show that the particles are not homogenous in size or strain. In Figure 2.6(c), each point represents the 9 XRD peaks measured from 30° to 90° 2θ values. Eq (2.11) gives a straight-line Eq, y = mx + C. Here, y (= $ß_T cosθ$) and the slope, m gives the microstrain (ε). The x in the straight-line Eq is denoted as 4sinθ and the intercept, C (= kλ/D) gives the average crystallite size. In the scope of this Ph.D., all fittings were done with OriginPro. Instrumental broadening was considered in both cases of the Scherrer and the W-H method, as shown in Eq (2.12).

$$ß_T = \sqrt{ß_S^2 - ß_i^2} \qquad (2.12)$$

Where,

$ß_s$ = Broadening due to the sample

$ß_i$ = Broadening due to instrument

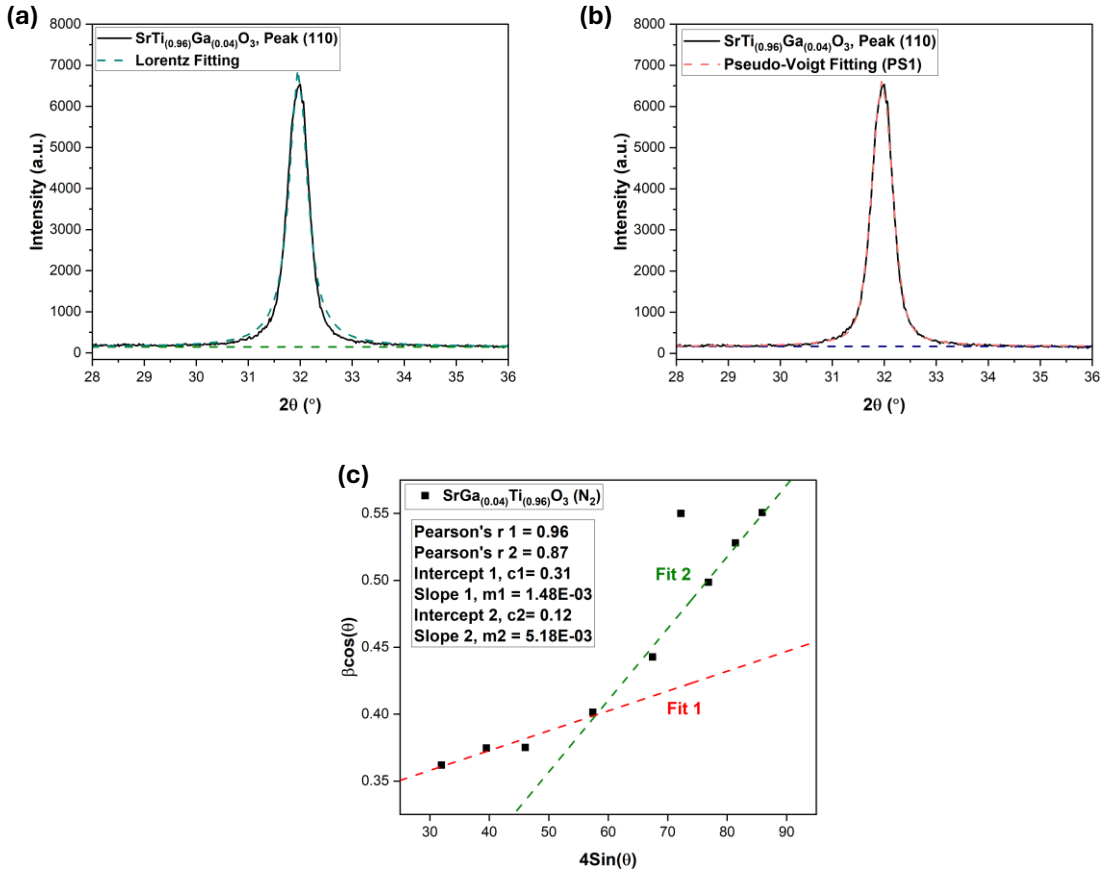


Figure 2.6: *W-H analysis with the XRD pattern of sample $SrTi_{(0.96)}Ga_{(0.04)}O_3$ (a) Lorentzian fitting of peak (110) (b) Voigt fitting of peak (110) (c) Linear fitting of 4sinθ and ßcosθ with*

two lines (Pearson's r =0.96 and 0.87). The different intercepts and slopes of the line indicate the presence of two size-strain regimes.

Eqs (2.7) and (2.8) assume the Uniform Deformation Model (UDM). In the UDM of the W-H analysis, the strain is assumed to be isotropic i.e. it is uniform in all directions[14]. Devesa, S. et al. [14] also argue that in their material, the microstrain influences the size as per Eq(2.7). Ungar, T. et al. [15][16] proposed the use of scaling factors considering dislocations while analyzing peak profiles which reduces the complexities associated with the W-H analysis.

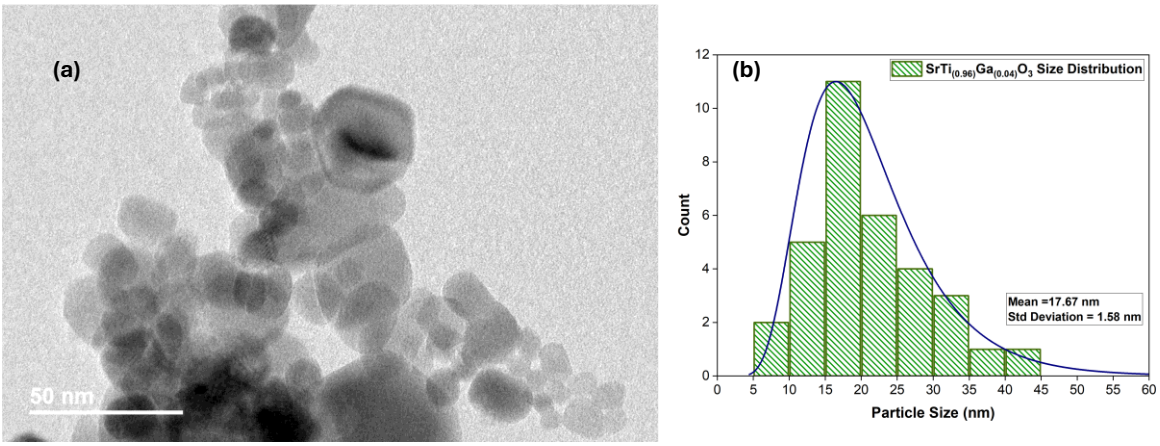


Figure 2.7: *(a) TEM image of 4 mol% Ga^{3+} doped $SrTiO_3$ nanoparticles (b) Size distribution calculated from the TEM distribution.*

Figure 2.7 shows the TEM distribution of 4 mol% Ga^{3+} doped $SrTiO_3$ nanoparticles. The particle sizes were measured with the Scherrer equation, the W-H analysis, and the TEM. The distribution with a mean size of 17.67 nm as shown in Figure 2.7 (b) was closer to the size calculated with the Scherrer equation. Therefore, the particle size was calculated from the XRD data with the Scherrer equation throughout this study. The full discussion on the comparison of techniques i.e. the XRD and the TEM to determine the crystallite size is shown in Chapter 6.

High-Temperature XRD

High-temperature XRD analyses were carried out to study the effect of aging in the catalyst materials. In the materials synthesized during the Ph.D. work, it was observed that secondary oxide phases formed in the samples after a prolonged storage period (over 3 months). With the objective of studying the thermal stability of the oxides formed in the aged photocatalysts and to determine whether these oxides decompose at elevated temperatures in an inert N_2 environment, a study was undertaken with the high-temperature XRD. For this study, experiments were conducted on a PANanalytical Empyrean with Cu kα X-ray tube using an Anton Parr heating chamber as shown in Figure 2.8 (a)**.** The samples were heated from room temperature (25 °C) to 910 °C. The powder samples were placed on an alumina crucible and then loaded in the diffractometer for sample preparation. It was observed that these oxide phases disappeared when heated at 800 °C and above. At these temperature conditions, the phase pure parent cubic crystal structure was regained. There were no observed changes to the cubic perovskite structure upon cooling down to room temperature. Figure 2.8 (b) shows the

XRD pattern of the aged photocatalysts and the decomposition of the oxide phases at elevated temperatures (≥ 800 °C).

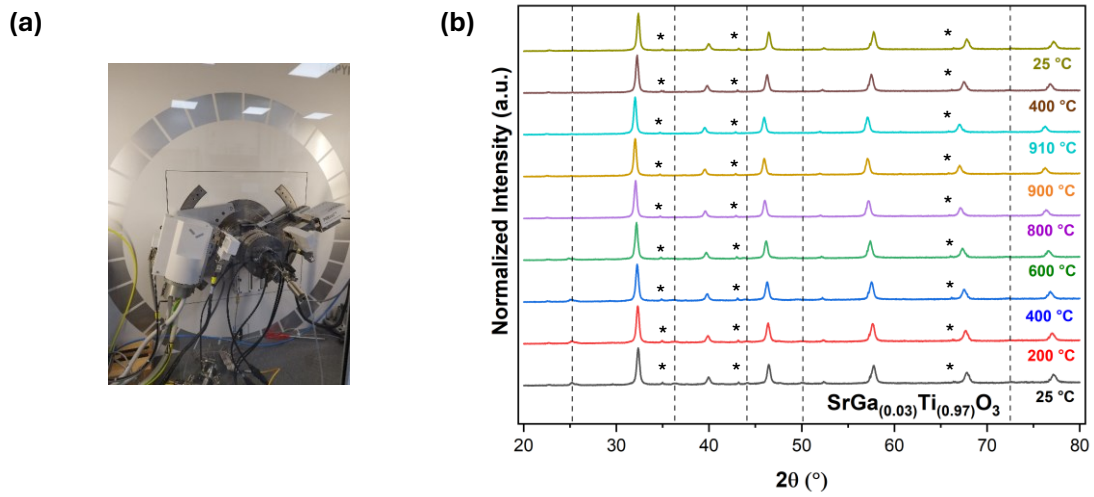


Figure 2.8: *(a) PANanalytical Empyrean high-temperature XRD (b) HT-XRD pattern of 3 mol% Ga^{3+} doped $SrTiO_3$ measured at 25 °C-910 °C-25 °C showing the decomposition of the oxide phases at temperatures ≥ 800 °C and recovery of the phase pure cubic perovskite structure. The oxide phases are demonstrated by the dotted line. * Are the peaks from the alumina crucible.*

Adding dopants in $SrTiO_3$ changes the microstructural properties significantly which affects catalytic activity. The techniques discussed in the following section were employed to study the effect of doping on aspects such as the optical and electronic properties of the materials.

2.2.2 Transmission Electron Microscope (TEM)

The morphology of the nanoparticles was investigated with the transmission electron microscope (TEM). The working principle of the TEM is based on the transmission of an electron beam through a specimen to form an image. It comprises an electron gun which is the source of the electron beam at the top of the TEM housing. The beam is focussed by the condenser system comprising of a condenser lens and aperture and directed towards the specimen. The condenser lens focuses the electron beam onto the specimen by controlling the intensity and convergence. The aperture on the other hand is a small adjustable opening that controls the electron beam passing through the condenser lens. After specimen interaction, the beam passes through the objective lens which focuses the beam to form an image. With high resolutions and high magnifications, TEM is used to study a material at its atomic level. The TEM housing system is illustrated in Figure 2.9.

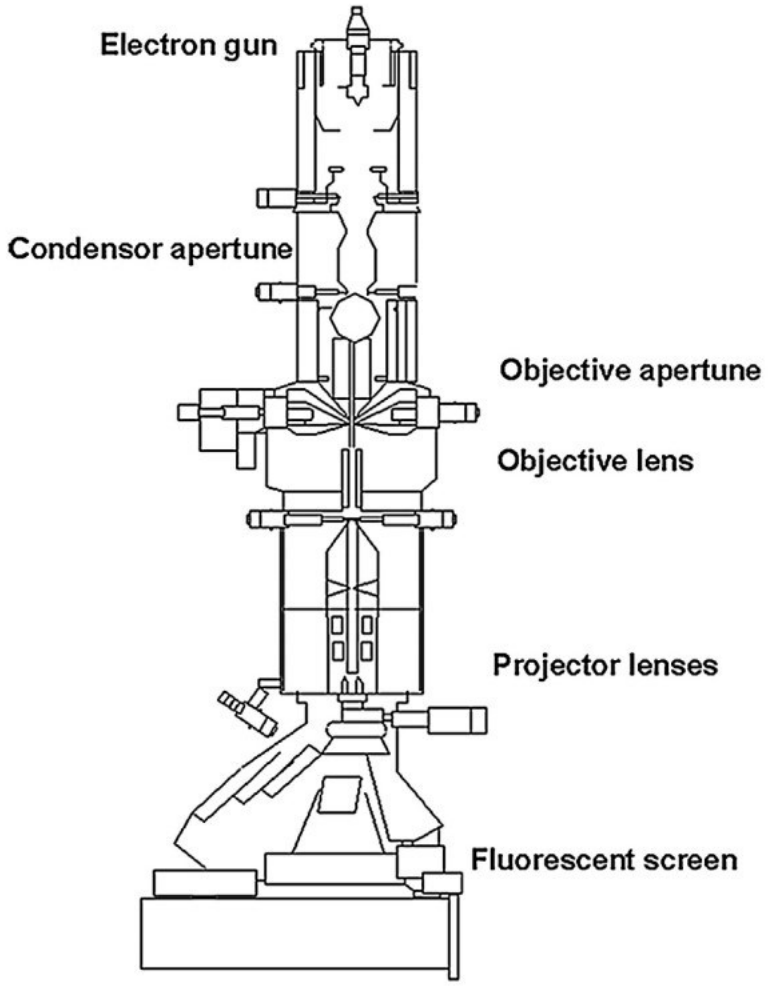


Figure 2.9: *Principle parts of a TEM housing. Image reproduced with permission from the Book: Membrane Characterization, Chapter 8-Transmission Electron Microscope by C. Y. Tang and Z. Yang, Copyright © 2017 Elsevier B.V. All rights reserved [17].*

In the scope of the Ph.D. study, two TEM systems-JEOL2100Plus and JEOL2100F with EDX detectors were used to study the nanoparticles**.** TEM was used to study the nature of the nanoparticles with the diffraction pattern, the lattice spacings, and the particle sizes. The information obtained about the nanoparticle size distribution and crystal plane positions were then compared with the XRD to relate the data obtained from different techniques. For TEM analysis, sample preparation was done by dispersing 1 mg of the nanoparticles in 2 ml isopropanol (IPA) and sonicating for 10 min. The dispersed solution was then loaded on a holey carbon film with a Cu grid (300 mesh) as shown in Figure 2.10. Holey carbon films were used as the perforations to facilitate the electron beam to pass through without any interaction with the samples. This allows for higher-contrast images by reducing background noises. The samples were then loaded on a single tilt specimen holder and guided into the microscope for imaging. The TEM operating conditions employed were 200 kV HT voltage with a beam current of 104-108 μA.

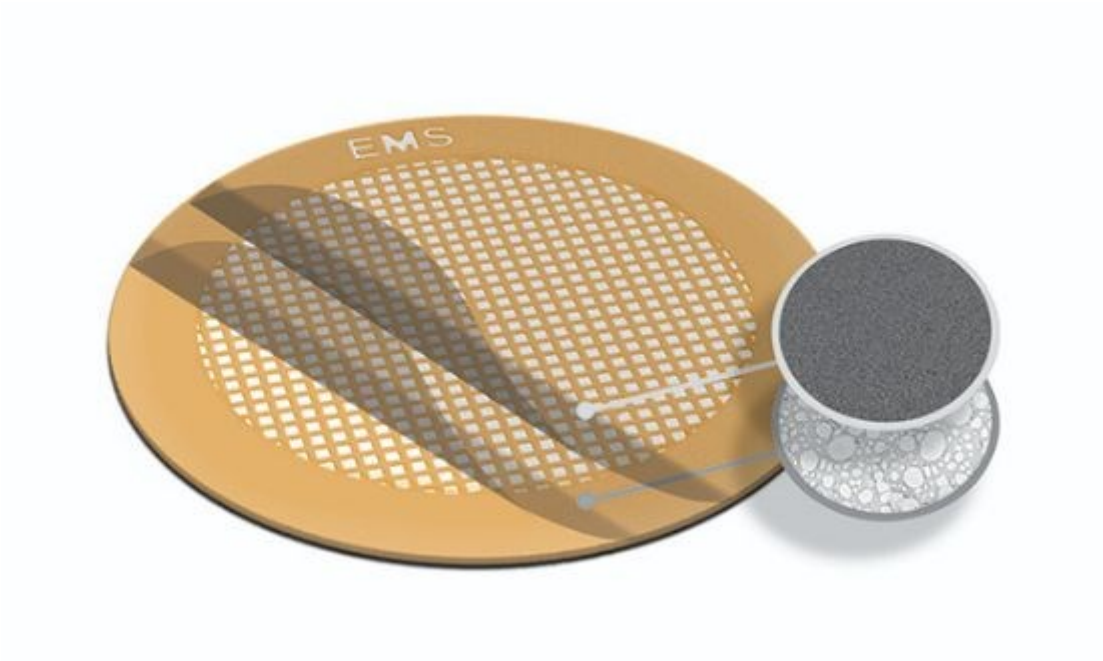


Figure 2.10: *Samples for TEM analysis dispersed on holey carbon film with Cu grid. Image reproduced from the Electron Microscopy Sciences website. Accessed on 27.06.2024) [18].*

The nanoparticles were also studied in the STEM mode with JEOL2100F. In this mode, the electron beam is focused to a narrow point that is used to scan in a raster pattern over a surface. This mode was useful, especially in studying the incorporation of the dopant in the nanoparticles with energy dispersive X-ray spectroscopy (EDX) and how the dopants are distributed in the structure.

Energy Dispersive X-ray Spectroscopy (EDX)

EDX was used in the scope of the Ph.D. to study the extent of incorporation of the dopants, quantification, and element mapping. The EDX system is housed with the JEOL2100F with the sample preparation techniques as discussed in the previous section. The working principle of EDX is based on the emission of X-rays when outer shell electrons fall back into the vacancies created when inner shell electrons are ejected in interaction with the electron beam. The emitted X-rays are detected by the EDX which then gives a spectrum. The peaks in the spectrum correspond to the unique energy levels that each element in the sample possesses. This in turn helps in the identification of the elements present. With the TEM analysis, the microstructural analysis of the nanoparticles was conducted as shown in Figure 2.11 and then correlated with the information gathered from the XRD.

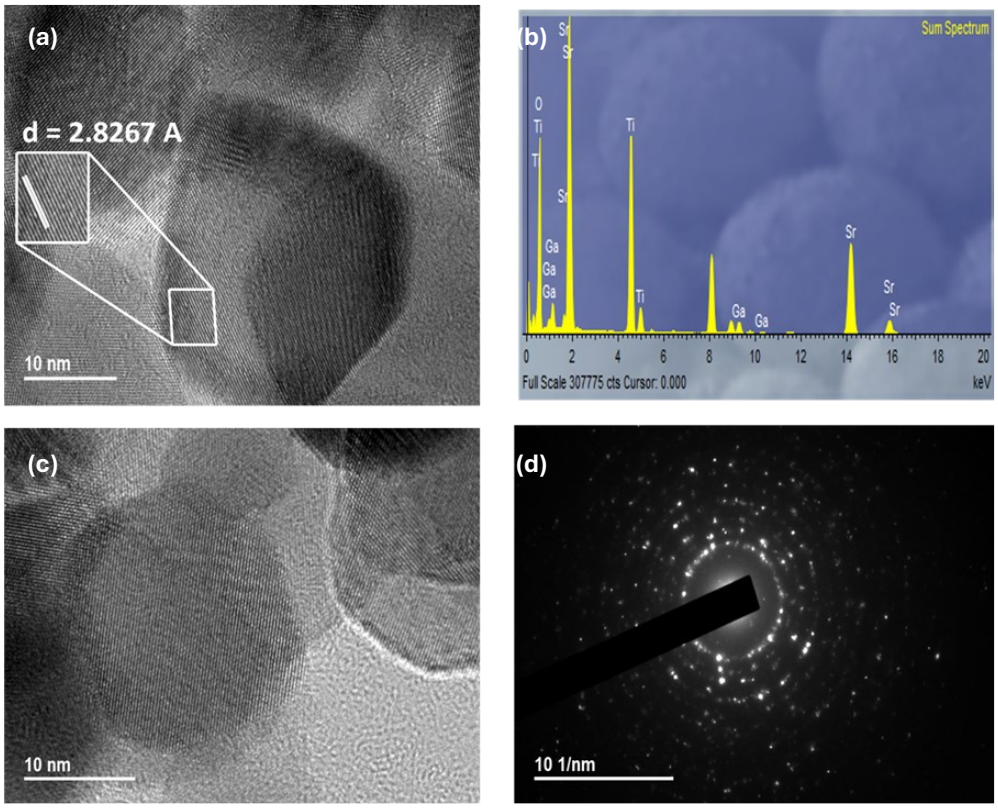


Figure 2.11: *TEM analysis on the $SrTi_{(0.96)}Ga_{(0.04)}O_3$ (N_2) to analyse the lattice spacings, the nature of the materials, EDX, and the diffraction pattern.*

Besides the size, the surface areas of the samples are also an important determinant of the photocatalytic activity. The BET technique probed the surface areas via the N_2 and CO_2 isotherms. The workings of this technique are discussed in section 2.5.5.

2.3 Optical Measurements

2.3.1 UV Vis Spectrophotometer

The working principle of UV vis spectroscopy lies in the transition of electrons from the ground state to an excited state upon light absorption. These transitions upon absorbing certain wavelengths of light produce a unique spectrum for each material. In this Ph.D. work, UV-vis measurements were conducted in reflectance mode to study the band gaps of the photocatalysts, the absorbance wavelengths from the Kubelka Munk function, and the presence of mid-gap states. UV-vis characterization was performed with a Shimadzu UV-2600 instrument with an integrating sphere (ISR-2600, Shimadzu) and with $BaSO_4$ as a scattering reference as shown in Figure 2.12. In the integrating sphere, the light undergoes multiple reflections before entering the detector [19]. For sample preparation, the powder materials were put in a 1 mm thick cuvette and were loaded in the reflectance port of the integrating sphere. Baseline measurements were carried out before the diffuse reflectance measurements with a strongly scattering $BaSO_4$ reference.

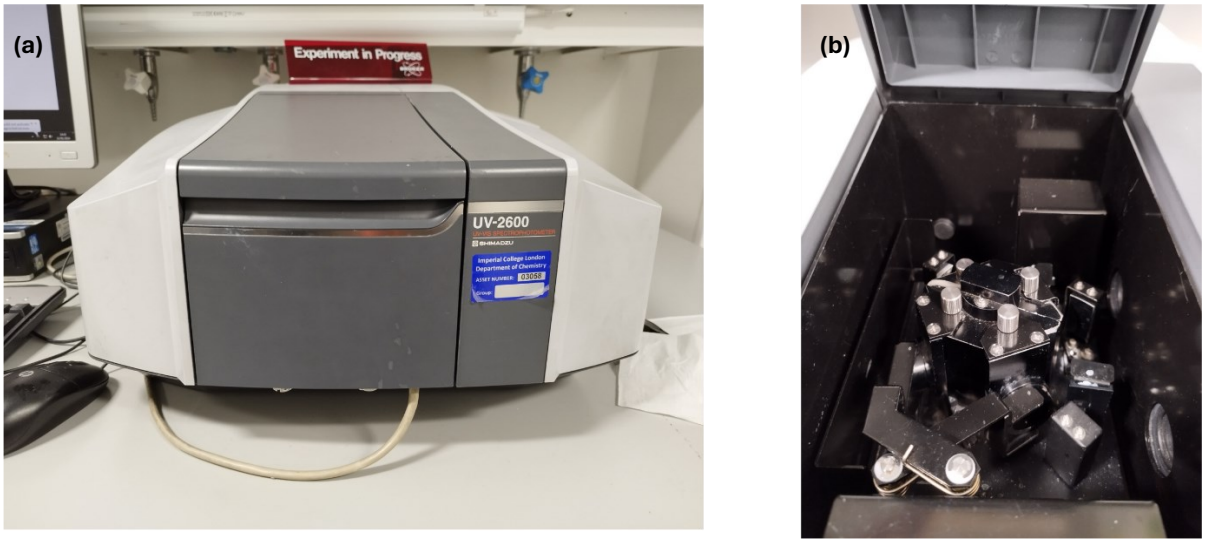


Figure 2.12: *(a.) A Shimadzu UV-2600 instrument for UV vis measurements (b.) An integrating sphere.*

The band gaps are calculated from the Tauc plots i.e. from the intersection of the linear fits of the $(\alpha h\nu)^2$ vs energy plot. The band gap of $SrTiO_3$ lies in the range of 3.2 eV -3.7 eV with the indirect band gap between 3.2 eV -3.4 eV and a direct band gap of about 3.7 eV [20],[21],[22]. In the Tauc plot, the axes denote the terms labelled as Eq (2.13) and Eq (2.14).

X-axis: Energy = $h\nu$ (2.13)

Y- axis : $[F(R)h\nu]^n$ (2.14)

where,

n = ½ for indirect allowed transition

n = 2 for direct allowed transition

Allowed transitions follow symmetry selection rules which determine if an electronic transition between energy levels is permitted. In such cases, the momentum matrix element of the transition is non-zero. These transitions require the conservation of momentum and energy. For the UV-vis experiments related to the doped samples, all measurements were done in the reflectance (diffuse) mode due to the opaque nature of the materials**.** From the diffuse reflectance data, Kubelka Munk function [F{R}] was calculated using the following Eqs[23]:

Absorption Coefficient: $K = (1-R)^2$ (2.15)

Scattering Factor: $S = 2R$ (2.16)

Kubelka Munk Function: $F(R) = K/S$ (2.17)

$F(R) = (1-R)^2/2R$ (2.18)

From the diffuse reflectance UV-vis analysis, both the direct and indirect bandgaps of the materials were calculated via the Kubelka-Munk equation. In the direct allowed bandgaps, the top of the valence band and the bottom of the conduction band lie at the same crystal momentum whereas in the indirect bandgaps, these are at different points as shown in Figure 2.13. In solid state physics, the concept of crystal momentum is defined as the effective momentum of electrons in a crystal lattice.

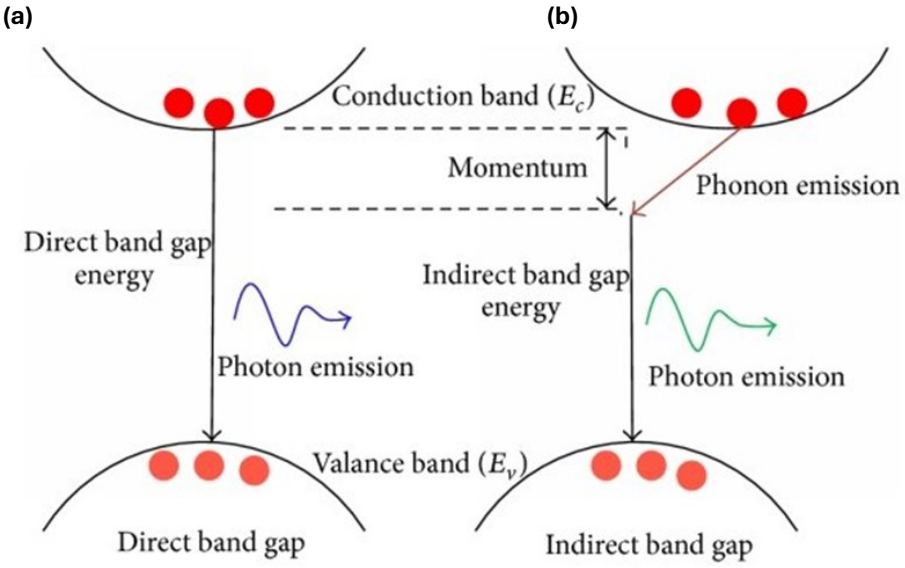


Figure 2.13: *Difference between (a) direct and (b) indirect bandgaps with respect to the crystal momentum reproduced with permission from the work of Singh, A.K. et al. [24] (open access, licensed by CC-BY 3.0).*

2.3.2 Photoluminescence (PL) Spectroscopy

PL measurements were used to study the electronic structure and structural properties with respect to defects present in the materials. The working principle of PL measurement is radiative recombination**.** This occurs when an electron in the conduction band recombines with a hole in the valence band to emit a photon [25]. In PL spectroscopy, photoexcitation takes place by absorbing certain light wavelengths where an electron is excited to a higher state. When this electron relaxes and comes back to its original state, a photon is emitted which results in the PL spectrum [25].

In the scope of the Ph.D. study, two PL instruments were used as shown in Figure 2.14. The instruments used were the Flourolog-3 Spectrofluorometer (Horiba Jobin Yvon) and the Cary Eclipse Fluorescence Spectrophotometer (Agilent Technologies). In both cases, the samples were excited with 295 nm, and a PL spectrum was collected from 350 - 550 nm. Samples were filled in a 1 mm wide quartz cuvette and then loaded into the sample holder of the instrument and the spectrum was measured.

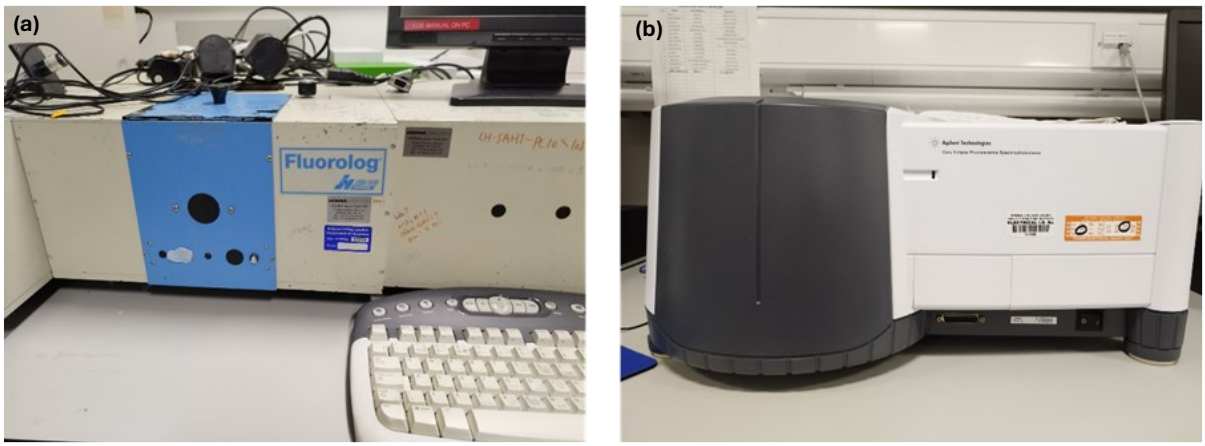


Figure 2.14: *PL measurement instruments used in the Ph.D. work (a) Fluorolog-2 Spectrofluorometer (Horiba Jobin Yvon) (b) Cary Eclipse (Agilent Technologies.*

2.3.3 Time-Correlated Single Photon Counting (TCSPC)

TCSPC was used to study the fluorescence lifetimes of the materials. In this method, a laser diode is used as an excitation source. The working principle of the TCSPC involves the excitation of electrons from the ground to excited states. Like the PL, when the electrons fall back to their original state, a photon is emitted if the recombination path is radiative. The instrument records the time between the pulsed excitation and when a single photon is emitted. In TCSPC, after excitation, the probability of detecting that single photon at an instant (say, t) is proportional to the fluorescence at that instant [26],[27].

Time-resolved PL spectroscopy via TCSPC is essential for measuring the recombination lifetimes of the samples. In this technique, the materials are excited with short laser pulses (282 nm, HORIBA, with a repetition rate of 1 MHz), and the decay of the excited states is monitored. The decay time is the average time the excited states take to decrease 1/e (~ 37%) of its initial value. For all the measurements, an instrument response function (IRF) is measured alongside the sample decay responses. Both these responses are then interpreted to measure the average decay time. To measure the lifetimes of the samples synthesized in the Ph.D. study the IRF and decay time were deconvoluted with a three-exponential fitting according to Eq (2.19).

$$X = A_1+(B_1)e^{(-t/T1)} + A_2+(B_2)e^{(-t/T2)} + A_3+(B_3)e^{(-t/T3)} \quad (2.19)$$

Where,

X = Measured intensity at a given time during the decay process

$A_{(1,2,3)}$ = Baseline value of the signal of any non-decaying background

$B_{(1,2,3)}$ = Magnitude of the decaying signal

$T_{(1,2,3)}$ = Decay time constant

t = The time elapsed during the decay process

The average lifetimes of the samples were measured from the exponential fitting via the HORIBA Da6.8 software and deconvoluted decay time constants were extracted. All samples were excited with λ_{exc} = 282 nm. The average lifetimes were calculated with Eq (2.20).

$$\text{Average Lifetime} = \sum_{i=0}^{n} \frac{A*(t)\hat{}2}{A*t} \qquad (2.20)$$

The IRF was measured with a frosty glass at 282 nm excitation. To measure the decay time, exponential fitting was done with HORIBA DA6.8 fitting software to deconvolute the lifetimes. A 3.2% density filter was used to filter scattering light from the excitation source. The TCSPC setup used in the Ph.D. study is shown in Figure 2.15.

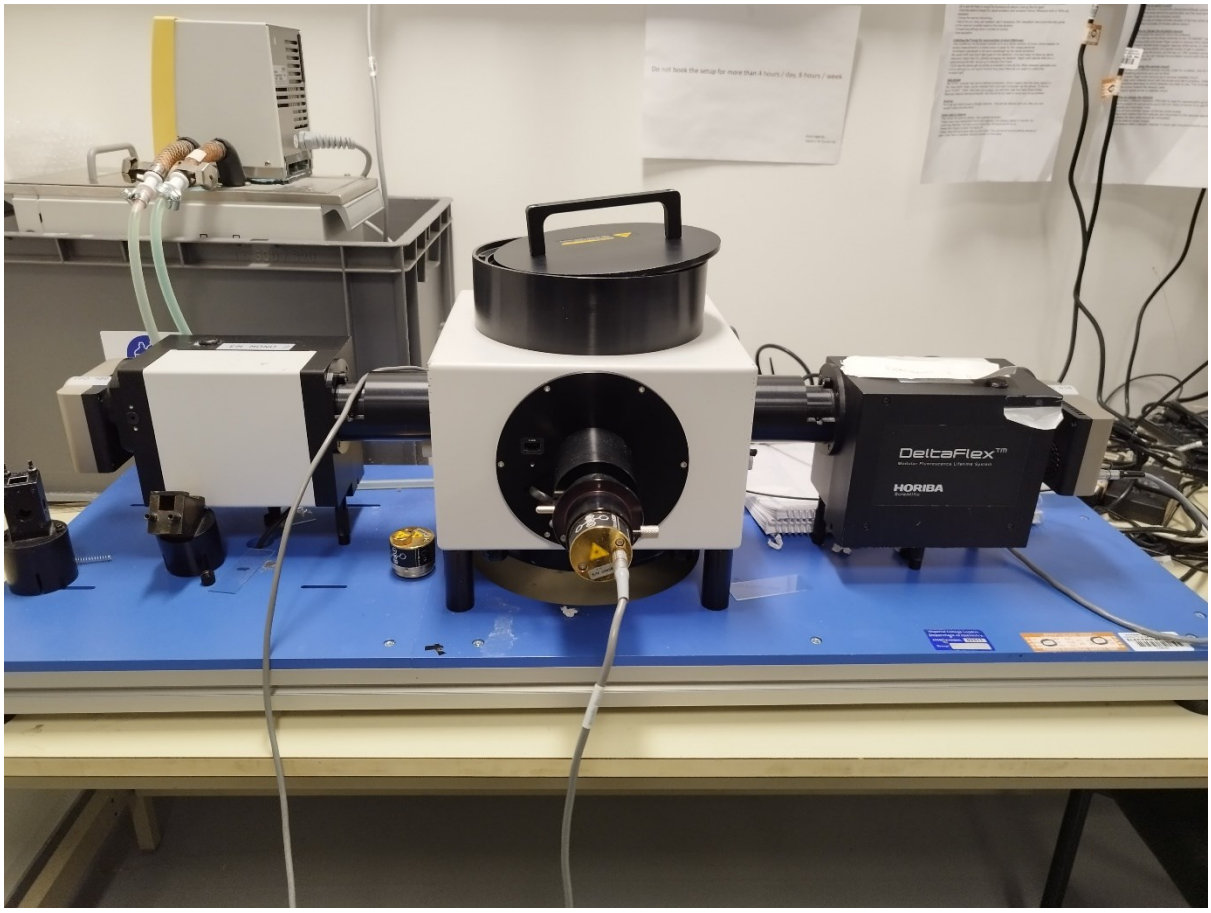


Figure 2.15: *A HORIBA DeltaFlex TCSPC setup was used in the Ph.D. study to measure the lifetimes of the synthesized photocatalysts.*

Sample preparation was like the other optical measurements where a 2 mm quartz cuvette is filled with the samples and then loaded onto the instrument. The TCSPC along with the PL and the UV vis spectroscopy were instrumental in studying the optical properties of the samples and how doping with d^{10} and d^3 elements affect these properties. The changes in the optical properties can be related to the microstructural changes induced by doping. The effects will be discussed in detail in succeeding chapters. Another effect of doping is on the electronic structure of the materials. In the Ph.D. study, the electronic structure was studied in detail with the XPS and the Kelvin Probe which is discussed in the next section.

2.4 Electronic Measurements

2.4.1 X-ray Photoelectron Spectroscopy (XPS)

XPS was used to study the surface chemical composition of the materials and the intrinsic parameters such as the valence band-Fermi level separation and the work function. The working principle of XPS is based on the interaction between the monochromatic, incident X-rays and the sample surface. On absorption of the X-rays, electrons are ejected from the surface with a certain kinetic energy. This energy can be related to the binding energy, the instrumental work function, and photon energy by Eq (2.21) [28].

$$E_k = h\nu - (E_b + \phi) \qquad (2.21)$$

Where,

E_k = Kinetic energy of the ejected electron

E_b = Binding energy

ϕ = Work function of the instrument

$h\nu$ = Incident photon energy

The XPS setup as shown in Figure 2.16 consists of an X-ray source and a vacuum chamber that allow electrons to move freely after emission from the surface. A lens system focuses the electron beam and guides it into the concentric hemispherical analyzer system. This analyzer guides the electrons moving with a given kinetic energy into the detector.

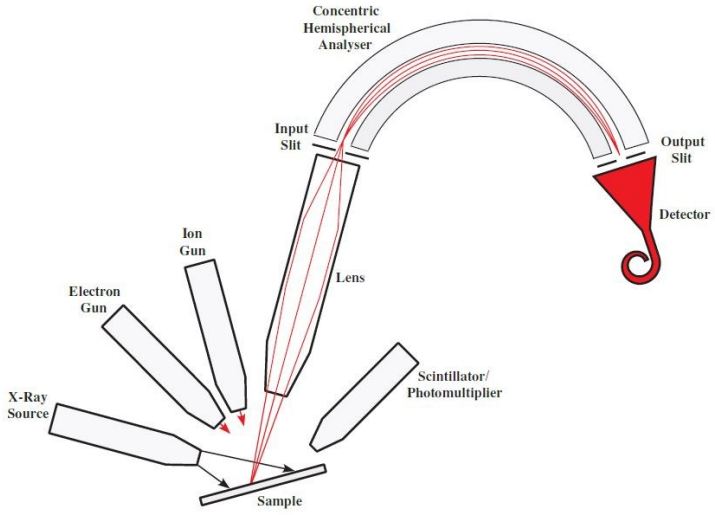


Figure 2.16: *Schematic of the working parts of the XPS reproduced from the book, Microstructural Characterization of Materials by Brandon, D. and Kaplan, W. D. (Copyright © 2008 John Wiley & Sons, Ltd) [28] .*

Samples for elemental analysis and the valence band-fermi level were prepared by loading the samples on carbon tape on a stainless-steel plate of the holder as shown in Figure 2.17 (a). For work function measurements, samples were loaded on conductive copper tape on a stainless-

steel holder with an in-built Au reference (yellow square, *) as shown in Figure 2.17(b). In the Ph.D. work, XPS measurements were carried out on a Thermo Scientific K-alpha+ instrument. Mono-chromated Al Kα X-ray radiation with hν = 1486.6 eV was used to eject electrons from the sample surface. Sample charging was minimized by using a flood gun. Charge correction of the samples was done by referencing to the adventitious carbon in the C1s peak with 284.8 eV binding energy.

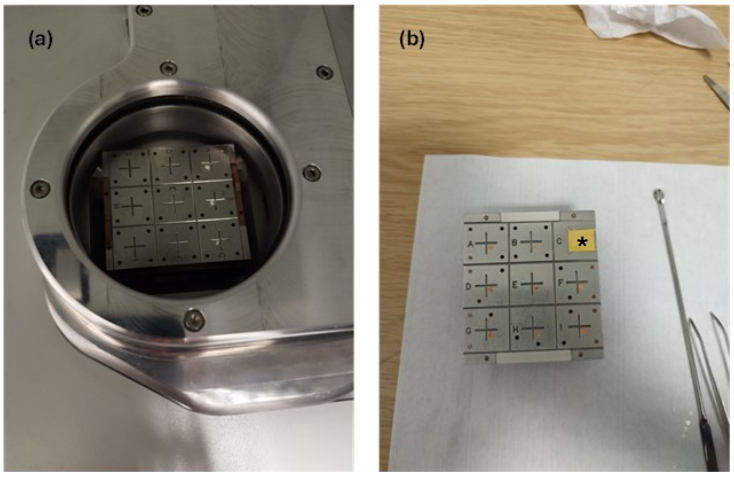


Figure 2.17: *XPS sample preparation for (a) Elemental and valence band analysis (b) Work function analysis holder with the gold patch (*) that is used as the reference before each measurement.*

In the Ph.D. work, XPS was used as one of the techniques to study the work function. Work function is defined as the energy difference between a point in a vacuum and the fermi level. It is the minimum energy required to remove an electron to a point outside the atom [29]. In semiconductor physics, the work function is used to study electron emission [30] and electron flow [31]. The work function has a bulk component and a surface component [32]. In the context of this Ph.D., only the work function of the surface component will be considered. The surface work function of a material arises from two contributions [32]:

1.) Electron chemical potential which gives the fermi level with respect to the vacuum.
2.) Surface dipole is the energy barrier to remove the electron from the surface.

Mathematically, the contributions can be represented by the expression proposed by Wigner and Bardeen [32] which is as follows:

$$\phi = -\mu + D \qquad (2.22)$$

μ = Bulk chemical potential relative to the mean electrostatic potential [33]

D = Energy required to overcome the surface dipole barrier [33]

In literature popular experimental techniques such as the UPS [32],[34],[35], X-ray Photo-electron Spectroscopy (XPS) [36] and Kelvin Probe [37],[38],[39] are used to study work functions. In this Ph.D. two methods were employed to study the surface work function which is as follows:

1.) Kelvin Probe which gives a relative work function based on measuring the Contact Potential Difference (CPD) between the probe tip and the sample surface.
2.) Work Function-XPS to measure the work function from a secondary electron cut-off [40].

For the XPS work function analysis, a different holder was used. This holder has a metal contact that provides the bias during the work function measurement as shown in Figure 2.17 (b). The work function spectrum is convoluted with the instrument work function. To separate these two effects, a negative bias must be applied. To get the final work function, the bias must be subtracted from the extrapolated value of the kinetic energy spectrum recorded by the instrument. The measurements were referenced against a gold sample. The work function of the sample is calculated from the energy cut-off as demonstrated by Eq (2.23).

$$\phi = h\nu - E_{cut\text{-}off} \qquad (2.23)$$

For the bias measurements to give a reading, the contact arm must be rotated so that it contacts the holder, and the voltage is applied. The Kelvin Probe method was the second method used to compare the work functions. This method is discussed in detail in the following section.

2.4.2 Kelvin Probe

The Kelvin probe technique was used to measure the work function. The working principle of the Kelvin probe is based on the contact potential difference (CPD). The Kelvin probe consists of a vibrating tip, a sample stage, and electrical contact as shown in Figure 2.18 (a). It is a non-contact form of work function measurement.

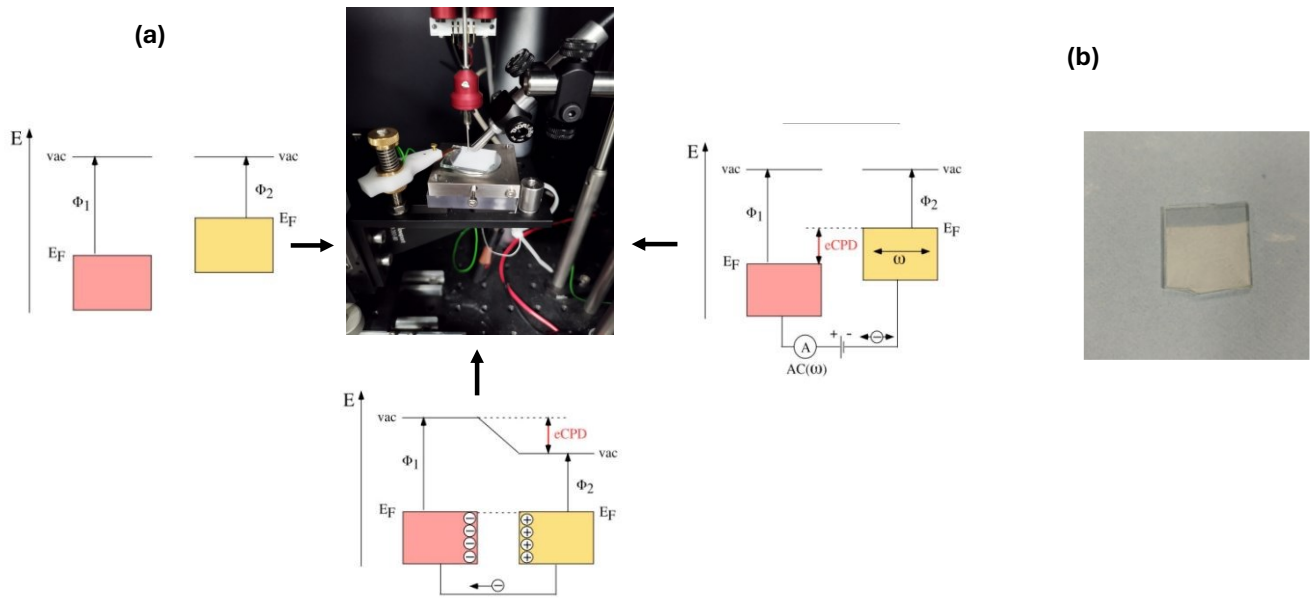


Figure 2.18: *(a) Principle of the Kelvin Probe setup. (Image reproduced from the Tutorial on Kelvin Probe Measurements by Dr. Rudy Schlaf) [41]. The central image is the sample prepared for the Kelvin probe measurements during the Ph.D. work. (b) Sample preparation by doctor-blading samples on FTO glass.*

When two conductors, the KP tip and sample with different work functions (ϕ_{Tip} and ϕ_{Sample}) are kept in close contact with each other, a potential difference is created. In this condition the $\phi_{Tip} > \phi_{Sample}$. When the tip and sample surface are electrically connected then charges are created. Electrons flow from the low work function sample to the high work function tip until equilibrium. The sample becomes positively charged and the tip is negatively charged. The potential difference at equilibrium is equal to the contact potential difference (CPD). There is a distortion of the vacuum level as the fermi level of the sample and the tip are aligned. To realign the vacuum level, an AC bias is applied to counter the CPD. To measure the CPD from the Kelvin probe, an Ag reference is used. This principle is shown in Figure 2.18 (a).

For the Kelvin probe measurements, samples were prepared by drop-casting the catalysts on FTO glass. The catalysts were heated at 400 °C to clean the surface for 30 min. 2 mg of the catalyst was dispersed in 5 ml IPA solution and sonicated for 30 min. The dispersed solution was drop-cast on a clean FTO substrate. The prepared FTO samples were heated at 80 °C for 6 h to dry. The prepared sample is shown in Figure 2.18 (b). All measurements were carried out at ambient temperatures (25% relative humidity) in a KP Technology instrument. The work function measurements are surface sensitive. The Kelvin probe method is carried out in the ambient while the XPS is under vacuum. Therefore, the Kelvin probe method has a higher chance of considering the surface adsorbates in the work function values. Another error that could arise with the Kelvin probe samples is the poor coating of the catalyst films. Therefore, the value obtained with the XPS is considered more accurate in the Ph.D. work.

2.4.3 Electron Paramagnetic Resonance (EPR)

Continuous wave (CW) EPR spectroscopy is a technique that studies materials with unpaired electrons. In this technique when a material is placed in a magnetic field the degeneracy associated with the spin states of the paramagnetic center is removed. This basic principle on which the EPR technique is based is called the Zeeman effect. When the unpaired electrons are placed in the magnetic field, two spin states are created i.e. $m_s = \pm ½$. The energy difference between the two spin states is given by Eq (2.24) [42].

$$\Delta E = h\nu = g ß B \quad (2.24)$$

Where,

g = g-factor

B = Magnetic field

h = Planck's constant = 6.626 x 10^{-34} J/s

ß = Bohr's Magneton

During the EPR measurements, the g-factor in Eq (2.24) changes with the application of the magnetic field. In the EPR measurements, the concept of hyperfine splitting is fundamental. Hyperfine splitting arises due to the interaction between nuclear and electronic spin magnetic moments which result in the splitting of the spectrum into 2nI + 1 lines with n being the number of identical nuclei and I the nuclear spin. Electromagnetic radiations can facilitate the

transitions between the spin states when the resonant condition is met according to Eq (2.25) [42].

$$h\nu = g\text{ß}B_O \quad (2.25)$$

Where,

B_O = Resonant magnetic field where absorption occurs

EPR in the Ph.D. work was used to study the effect of the oxidation state of Cr-doped $SrTiO_3$. This can be elucidated from the g-factor and the hyperfine coupling constants. The samples were flame-sealed under vacuum in 3.8 mm OD 3.0 mm ID quartz tubes. Measurements were carried out at X-band (~9.4 GHz) in a Bruker EMXmicro equipped with a Super High Sensitivity Probehead cavity. Temperature was controlled using an Oxford Instruments cryostat with nitrogen or helium flow. Illumination for the photo-excitation was achieved using an Xe arc lamp coupled to the optical window of the EPR cavity via a liquid waveguide. All spectrum were background corrected by subtracting the signal from an empty tube measured in the same conditions, and the magnetic field offset was corrected using an $N@C_{60}$ standard. Solid-state EPR simulations were carried out using the *pepper* function of the *EasySpin* Matlab toolbox.

2.5 Performance Tests

2.5.1 Photoelectrochemical (PEC) Measurements

To measure the performance of the photocatalysts, PEC analysis was done. The principle of PEC is based on the generation and the separation of e^-/ h^+ pairs upon irradiation followed by the migration of the charges to the catalyst surfaces where the reaction occurs. In the scope of the Ph.D., the PEC testing was done in a H-cell as shown in Figure 2.19.

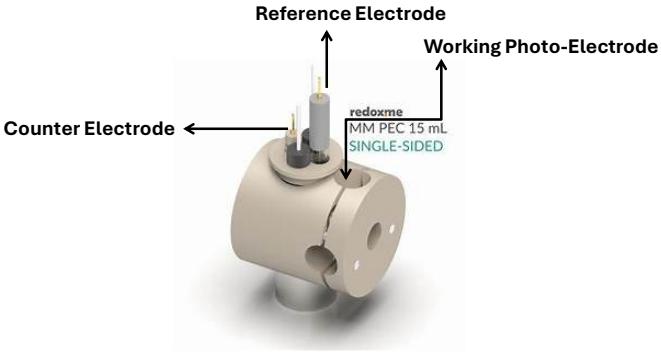


Figure 2.19: *A single compartment of the H-cell. Image reproduced from the Photoelectrochemical cells, Redox.me website. Accessed on 27.06.2024 [43]. The figure demonstrates the arrangement of the electrodes used during the PEC measurements in the Ph.D. work with the reference being placed close to the working electrode.*

The catalysts were tested under both light and dark conditions. The light source used was a WaveLabs SINUS-70 solar simulator. The light conditions utilized were AM1.5G (1 Sun, 100 mW/ cm^2) and UV (40% intensity, 40 mW/cm^2) light. For the experiments, a single compartment of the H-cell was used as a three-electrode system in 1 M KOH (pH= 13.6) with Ag/AgCl (Sat. KCl) as the reference electrode and a Pt wire as the counter electrode. The

reference electrode was placed closer to the working electrode to ensure the minimization of the ohmic losses. For cyclic voltammograms and linear sweeps, a scan rate of 20 mV/s was used. All potentials were converted to the RHE scale with the Nernst Eq (Eq (2.26)).

$$E_{RHE} = E_{Ag/AgCl} + 0.059pH + E_{measured} \quad (2.26)$$

For the sample preparation, the FTO glass slides were cut into 5 cm x 2 cm sizes and cleaned with soap solution, DI water, Acetone, and IPA. 15 mg of the catalyst powders were sonicated in 2 ml IPA solution and the doctor bladed on the FTO glass slides. Post-doctor blading, the slides were annealed at 400 °C for 30 min to remove any contaminations. To improve adhesion and block the metallic FTO surface from interfacing with the electrolyte, a 10 nm thin blocking layer of TiO_2 was deposited by ALD under the following conditions as discussed in section 2.5.3.

2.5.2 Photocatalytic Set-up

In the Ph.D., preliminary work is being carried out on the Ga^{3+} doped $SrTiO_3$ samples in a gas phase loop photocatalytic set-up for CO_2 hydrogenation. The set-up comprises 10 valves to control the flow of gas into the system and 3 mass flow controllers for N_2, H_2, and CO_2. The principle of operation of the setup involves purging the gas lines with N_2 to eliminate any residual gases and injecting H_2 and CO_2 in a controlled ratio (3:1). The catalyst samples were doctor-bladed on quartz glass and placed inside the reactor (volume = 0.0000846 m^3) so the surface is illuminated under simulated solar irradiation for 12 h. The light source was an Asahi 303-Max Xenon lamp with a UV-visible filter with a 300 nm cut-off. The lamp was calibrated to 1 sun with a NEWPORT cell with a KG5 filter. The products were analyzed with a GC 8860 fitted with an FID and TCD detector. For sample preparation, 3 mg of the catalyst powders were dispersed in 3 ml IPA and sonicated for 10 min which were then doctor-bladed on glass slides. The slides were annealed at 450 °C for 30 min and were kept in vacuum prior to measurements.

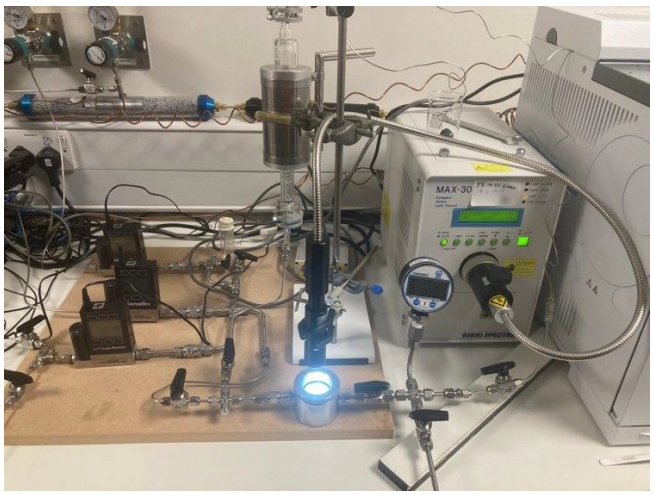


Figure 2.20: *The photocatalytic set-up used for the CO_2 hydrogenation studies from Prof. Ian McCulloch's group.*

2.5.3 Atomic Layer Deposition (ALD)

For the Ph.D. study, a custom thermal ALD setup was used to deposit thin TiO_2 thin films on FTO glass to improve the quality of the photoelectrode. The ALD can be operated safely to deposit thin films up to 200 °C. The heating of the ALD (oven and the furnace) and precursors is controlled by PID- heaters. Before depositing the thin films, the FTO glass (5 cm x 2 cm) was cleaned by sonicating in a soap solution, DI water, Acetone, and IPA for 15 min respectively. The cleaned glass slides were oxygen plasma cleaned. The ALD conditions are tabulated in Table 2.3.

Table 2.3: ALD conditions used for the 10 nm thick blocking layer on the FTO

No. of Cycles	167
TDMAT Pulse	0.1 sec
Ox Pulse	0.02 sec
TDMAT Purge	15 sec
Ox Purge	20 sec
Carrier Gas (N_2) Flow rate (2 MFCs)	5 sscm
Furnace Temperature	100 °C

After the modifications carried out at the start of my Ph.D., the ALD can accommodate four metal precursors and one oxidizer (H_2O). The set-up has 4 three-way valves and 3 two-way valves supplying the precursors and oxidizer as illustrated in Figure 2.21. Two mass flow controllers supply N_2 via the main reactor and to the N_2 supply lines connected to the three-way valves. At the two-way valves, higher vapor pressures will facilitate the movement of the precursors without the requirement of N_2 supply lines. N_2 has two functions in the ALD as a carrier gas and for purging.

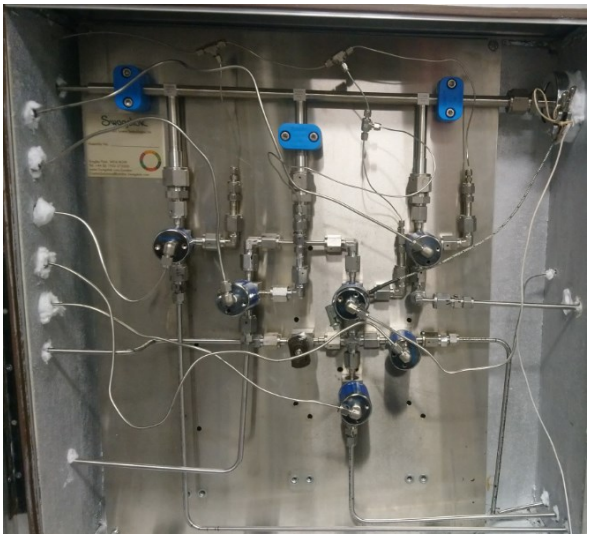


Figure 2.21: *The valves set-up in the atomic layer deposition instrument, MSRH, Imperial College London. The valves are supplied with N_2 which is the carrier gas for the precursors in the set-up.*

The synthesized catalysts were characterized by various techniques to study the material properties such as the morphology, the microstructural properties, and the opto-electronic properties. The characterization technique employed to study the thickness of the ALD deposited materials is discussed in the succeeding section.

2.5.4 F20 Interferometer

An important aspect is the precise control of the thickness of the ALD layers hence measuring the thickness and knowing the growth per cycle (GPC) of the ALD deposition are both crucial. The GPCs were measured with an F20 interferometer (FilmMetrics, Munich). The GPCs or the film thickness is measured via the phase difference of the interference patterns generated by the upper and lower surfaces of the thin films [44]. When the films are too thin, it is difficult to get the phase difference as the interference patterns completely overlap, hence measuring the GPC is more reliable on thicker ALD films.

For the experiments conducted, the ALD TiO_2 layers were deposited on clean Si substrates. n, k data files at different wavelengths were loaded into FilmMetrics software and the thickness was measured at wavelengths 200 nm to 1100 nm and 350 nm to 1400 nm. The parameters n, and k denote the refractive index and the extinction coefficient respectively. Two scenarios based on wavelength regions were seen as shown in Figure 2.22. The goodness of fit in the measurement of 200 nm to 1100 nm was 0.793. Here, the curve did not fit well in the UV region up to 350 nm. The goodness of fit in the measurement of 350 nm to 1400 nm was 0.99. With a band gap of about 3.2 eV, this region recorded the band edge absorption but the n, k data in the database could not fit additional absorption features of the amorphous TiO_2 layers. However, fitting the band edge is typically good enough to estimate the thickness of the films and hence, better fitting laws were not developed which would have required the use of ellipsometry.

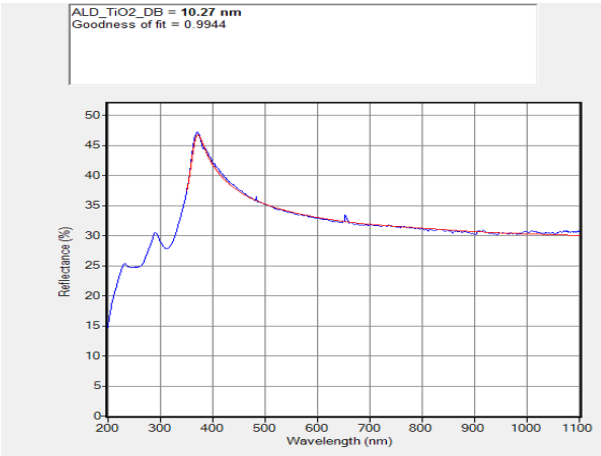


Figure 2.22: *Growth per cycle (GPC) measurements of thin films using F20 Interferometer.*

From Figure 2.21, considering the measurement region 350 nm to 1100 nm with the goodness of fit of 0.99 we can measure the thickness of the TiO_2 layer at 10.27 nm for 167 cycles. From this, we can infer that the ALD GPC of TiO_2 (TDMAT Precursor) is 0.06 nm at 100 °C furnace and 75 °C precursor temperature. New thin film measurements were done on TiO_2 samples for 700 and 1000 cycles at temperatures 75 °C,120 °C, and 80 °C. From the above interferometer analysis, with goodness of fit nearly 1 (approx. 0.99), the GPC of TiO_2 can be measured at

0.052 nm per cycle for 700 cycles at 120 °C and 0.062 nm for 1000 cycles at 80 °C which can be summarized in the following Table 2.4. Abendroth, B. et al. [45] has reported the GPC of ALD TiO_2 between 0.033 nm to 0.067 nm which compares well with the Ph.D. samples.

Table 2.4: Growth per cycle of TiO_2 films at different temperatures

Sr. No	Temperature (°C)	No. of Precursor Cycles	Growth per cycle (nm) (value ± 0.01)[a]
1	75	167	0.06
2	80	1000	0.06
3	100	1000	0.06
4	120	700	0.05

[a] *The error bars were added after refitting the data with the FilmMetrics software.*

2.5.5 Brunauer-Emmett-Teller (BET) Analysis

In catalysis, the specific surface area is a key parameter in determining the reaction rate [46]. To measure the surface area in the Ph.D. study BET was employed. With this technique, the specific surface area along with the pore sizes of the materials was measured with the surface adsorption of an unreactive gas such as N_2 in each cross-sectional area [47]–[49]. The temperature of the catalysts is kept under isothermal conditions and the pressure of the adsorbing gas is varied. The gas molecules form a thin layer on the surface as the pressure is increased from where the volume of the adsorbed gas is calculated. The working principle and the calculation of the specific surface area can be demonstrated with the BET equation as shown below [49].

$$\frac{1}{N[\left(\frac{Po}{P}\right)-1]} = \frac{1}{Nm*C} + \frac{C-1}{Nm*C}\left(\frac{P}{Po}\right) \quad (2.27)$$

Where,

N_m = No. of gas molecules required to form the monolayer

N = No. of gas molecules adsorbed at relative pressure P/P_O

C = Heat of adsorption constant

Eq (2.27) is a straight-line Eq where a linear plot is made between $\frac{1}{N[\left(\frac{Po}{P}\right)-1]}$ and $\frac{P}{Po}$ in BET analysis. From the slope, the intercept, and the measured cross-sectional area of the samples, the specific surface area is calculated.

Chapter 2 provides a detailed discussion of the experimental methods, and the characterization techniques employed to study the doped samples. It includes a comprehensive description of the synthesis process, along with the characterization techniques to understand the structural, opto-electronic, photoelectrochemical, and photocatalytic properties of the doped $SrTiO_3$ materials.

References

[1] A. S. Bhalla, R. Guo, and R. Roy, “The perovskite structure - A review of its role in

ceramic science and technology," *Mater. Res. Innov.*, vol. 4, no. 1, pp. 3–26, 2000, doi: 10.1007/s100190000062.

[2] H. Kronmüller and S. Parkin, *Crystallography and Chemistry of Perovskites*, 1st ed. John Wiley & Sons, Ltd, 2007.

[3] J. Yao, T. Chen, H. Wang *et al.* , "Stable cubic crystal structures and optimized thermoelectric performance of $SrTiO_3$-based ceramics driven by entropy engineering," *J. Mater. Chem. A*, vol. 10, no. 46, pp. 24561–24572, 2022, doi: 10.1039/d2ta06576b.

[4] R. J. D. Tilley, *Perovskites: Structure–Property Relationships*, vol. 42, no. 4. 2016.

[5] T. Takata and K. Domen, "Defect Engineering of Photocatalysts by Doping of Aliovalent Metal Cations for Efficient Water Splitting," *J. Phys. Chem. C*, vol. 113, no. 45, pp. 19386–19388, Nov. 2009, doi: 10.1021/jp908621e.

[6] W. J. Friedrich, P. Knipping, and M. von Laue, "Interferenzerscheinungen bei Röntgenstrahlen," *Ann. Phys.*, vol. 346, pp. 971–988, [Online]. Available: https://api.semanticscholar.org/CorpusID:121915972.

[7] W. L. Bragg, "The structure of some crystals as indicated by their diffraction of X-rays," *Proc. R. Soc. London. Ser. A, Contain. Pap. a Math. Phys. character*, vol. 89, no. 610, pp. 248–277, 1913.

[8] "Characteristic X-ray." https://en.wikipedia.org/wiki/Characteristic_X-ray#:~:text=In Siegbahn notation%2C when an electron falls from,radiation emitted is called a K-beta %28Kβ%29 emission. (accessed Sep. 27, 2024).

[9] Z. Zhang, P. Qian, X. Yang *et al.* , "Manipulating the carrier concentration and phase transition via Nb content in $SrTiO_3$," *Sci. Rep.*, vol. 12, no. 1, pp. 1–7, 2022, doi: 10.1038/s41598-021-03199-7.

[10] P. K. Misra, "Chapter 1 - Basic Properties of Crystals," P. K. B. T.-P. of C. M. Misra, Ed. Boston: Academic Press, 2012, pp. 1–35.

[11] A. L. Patterson, "The scherrer formula for X-ray particle size determination," *Phys. Rev.*, vol. 56, no. 10, pp. 978–982, 1939, doi: 10.1103/PhysRev.56.978.

[12] S. Dolabella, A. Borzì, A. Dommann, and A. Neels, "Lattice Strain and Defects Analysis in Nanostructured Semiconductor Materials and Devices by High-Resolution X-ray Diffraction: Theoretical and Practical Aspects," *Small Methods*, vol. 6, no. 2, 2022, doi: 10.1002/smtd.202100932.

[13] G. K. Williamson and W. H. Hall, "X-ray line broadening from filed aluminium and wolfram," *Acta Metall.*, vol. 1, no. 1, pp. 22–31, 1953, doi: 10.1016/0001-6160(53)90006-6.

[14] S. Devesa, A. P. Rooney, M. P. Graça, D. Cooper, and L. C. Costa, "Williamson-hall analysis in estimation of crystallite size and lattice strain in $Bi_{1.34}Fe_{0.66}Nb_{1.34}O_{6.35}$ prepared by the sol-gel method," *Mater. Sci. Eng. B*, vol. 263, no. June 2019, p. 114830,

2021, doi: 10.1016/j.mseb.2020.114830.

[15] T. Ungár and A. Borbély, “The effect of dislocation contrast on X-ray line broadening: A new approach to line profile analysis,” *Appl. Phys. Lett.*, vol. 69, no. 21, pp. 3173–3175, 1996, doi: 10.1063/1.117951.

[16] T. Ungar, “Dislocation Densities, Arrangements and Character from X-ray Diffraction Experiments,” *Mater. Sci. Eng. A*, vol. 310, no. A309-310, pp. 14–22, 2001.

[17] C. Y. Tang and Z. Yang, “Chapter 8 - Transmission Electron Microscopy (TEM),” N. Hilal, A. F. Ismail, T. Matsuura, and D. B. T.-M. C. Oatley-Radcliffe, EDX. Elsevier, 2017, pp. 145–159.

[18] “https://www.emsdiasum.com/7a-holey-carbon-film-2. Date: 27/06/2024.” .

[19] J. L. Taylor and Perkin Ellmer, “Integrating Sphere Functionality : The Scatter Transmission Measurement,” *Tech. note Perkin Elmer*, pp. 1–6, 2013.

[20] T. Takata and K. Domen, “Defect Engineering of Photocatalysts by Doping of Aliovalent Metal Cations for Efficient Water Splitting,” *J. Phys. Chem. C*, vol. 113, pp. 19386–19388, 2009.

[21] K. Van Benthem, C. Elsässer, and R. H. French, “Bulk electronic structure of $SrTiO_3$: Experiment and theory,” *J. Appl. Phys.*, vol. 90, no. 12, pp. 6156–6164, 2001, doi: 10.1063/1.1415766.

[22] L. Gu, H. Wei, Z. Peng, and H. Wu, “Defects enhanced photocatalytic performances in $SrTiO_3$ using laser-melting treatment,” *J. Mater. Res.*, vol. 32, no. 4, pp. 748–756, 2017, doi: 10.1557/jmr.2016.461.

[23] H. G. Hecht, “Interpretation of Diffuse Reflectance Spectrum.,” *J Res Natl Bur Stand Sect A Phys Chem*, vol. 80 A, no. 4, pp. 567–583, 1976, doi: 10.6028/jres.080A.056.

[24] A. K. Singh, J. Tiwari, A. Yadav, and R. K. Jha, “MATLAB User Interface for Simulation of Silicon Germanium Solar Cell,” *J. Mater.*, vol. 2015, pp. 1–6, 2015, doi: 10.1155/2015/840718.

[25] M. Yoshikawa, “Photoluminescence (PL) Spectroscopy,” in *Advanced Optical Spectroscopy Techniques for Semiconductors: Raman, Infrared, and Cathodoluminescence Spectroscopy*, Cham: Springer International Publishing, 2023, pp. 27–32.

[26] W. Becker, “Advanced Time-Correlated Single Photon Counting Techniques,” *Springer Ser. Chem. Phys.*, vol. 81, pp. I–387, Jan. 2005, doi: 10.1007/3-540-28882-1_9.

[27] T. Korte and A. Herrmann, “Fluorescence Lifetime Imaging Microscopy by TCSPC (TD-FLIM),” *Cold Spring Harb. Protoc.*, pp. 3–17, 2016.

[28] D. Brandon and W. D. Kaplan, *Microstructural Characterization of Materials*. Wiley, 2008.

[29] L. Lin, R. Jacobs, T. Ma, D. Chen, J. Booske, and D. Morgan, "Work Function: Fundamentals, Measurement, Calculation, Engineering, and Applications," *Phys. Rev. Appl.*, vol. 19, no. 3, p. 1, 2023, doi: 10.1103/PhysRevApplied.19.037001.

[30] M. Yoshitake, '*Work Function and Band Alignment of Electrode Materials: The Art of Interface Potential for Electronic Devices, Solar Cells, and Batteries'*, 1st ed. Springer Tokyo.ISBN: 978-4-431-56896-4, 20 December, 2020. DOI: https://doi.org/10.1007/978-4-431-56898-8

.

[31] T. Ma, R. Jacobs, J. Booske, and D. Morgan, "Understanding the interplay of surface structure and work function in oxides: A case study on $SrTiO_3$," *APL Mater.*, vol. 8, no. 7, 2020, doi: 10.1063/1.5143325.

[32] M. T. Greiner, L. Chai, M. G. Helander, W. M. Tang, and Z. H. Lu, "Transition metal oxide work functions: The influence of cation oxidation state and oxygen vacancies," *Adv. Funct. Mater.*, vol. 22, no. 21, pp. 4557–4568, 2012, doi: 10.1002/adfm.201200615.

[33] C. Leung, L. Kao, S. Su, J. Feng, and T. Chan, "Relationship between surface dipole, work function and charge transfer: Some exceptions to an established rule," *Phys. Rev. B - Condens. Matter Mater. Phys.*, vol. 68, no. 19, pp. 1–6, 2003, doi: 10.1103/PhysRevB.68.195408.

[34] S. A. Chambers and P. V. Sushko, "Influence of crystalline order and defects on the absolute work functions and electron affinities of TiO_2 - And SrO-terminated n-SrTi O_3(001)," *Phys. Rev. Mater.*, vol. 3, no. 12, 2019, doi: 10.1103/PhysRevMaterials.3.125803.

[35] Y. W. Chung and W. B. Weissbard, "Surface spectroscopy studies of the $SrTiO_3$ (100) surface and the platinum-$SrTiO_3$ (100) interface," *Phys. Rev. B*, vol. 20, no. 8, pp. 3456–3461, 1979, doi: 10.1103/PhysRevB.20.3456.

[36] O. I. Klyushnikov, "Method to determine the work function using X-ray Photoelectron Spectroscopy," *J. Struct. Chem.*, vol. 39, no. 6, p. 944, 1998.

[37] T. Susaki, A. Makishima, and H. Hosono, "Work function engineering via LaAlO3/$SrTiO_3$ polar interfaces," *Phys. Rev. B - Condens. Matter Mater. Phys.*, vol. 84, no. 11, pp. 2–6, 2011, doi: 10.1103/PhysRevB.84.115456.

[38] C. E. Smith, Z. Xie, I. Bâldea, and C. D. Frisbie, "Work function and temperature dependence of electron tunneling through an N-type perylene diimide molecular junction with isocyanide surface linkers," *Nanoscale*, vol. 10, no. 3, pp. 964–975, 2018, doi: 10.1039/c7nr06461f.

[39] K. Cieślik, D. Wrana, M. Rogala *et al.*, "The Effect of Reduction and Oxidation Processes on the Work Function of Metal Oxide Crystals: TiO_2 (110) and $SrTiO_3$ (001) Case," vol. 2, no. 110, pp. 1–17, 2023.

[40] J. W. Kim and A. Kim, "Absolute work function measurement by using photoelectron spectroscopy," *Curr. Appl. Phys.*, vol. 31, no. July, pp. 52–59, 2021, doi: 10.1016/j.cap.2021.07.018.

[41] R. Schalf, "Tutorial on Kelvin Probe Measurements." http://rsl.eng.usf.edu/Documents/Tutorials/TutorialsKelvinProbe.pdf.

[42]"https://chem.libretexts.org/Bookshelves/Analytical_Chemistry/Physical_Methods_in_Chemistry_and_Nano_Science_(Barron)/04%3A_Chemical_Speciation/4.08%3A_EPR_Spectroscopy. Date: 27/06/2024."

[43] "https://redox.me/collections/photo-electrochemical-cells/products/pec-h-cell-2x15-ml-photo-electrochemical-h-cell. Date: 24/12/2024." .

[44] F. M. Santoyo, "Interferometry: Concepts and Applications," no. February, 2013.

[45] B.Abendroth, T. Moebus, S. Rentrop *et al.* , "Atomic layer deposition of TiO_2 from tetrakis(dimethylamino)titanium and H_2O," *Thin Solid Films*, vol. 545, pp. 176–182, 2013, doi: https://doi.org/10.1016/j.tsf.2013.07.076.

[46] P. Bernard, P. Stelmachowski, P. Broś, W. Makowski, and A. Kotarba, "Demonstration of the Influence of Specific Surface Area on Reaction Rate in Heterogeneous Catalysis," *J. Chem. Educ.*, vol. 98, no. 3, pp. 935–940, 2021, doi: 10.1021/acs.jchemed.0c01101.

[47] S. Brunauer, P. H. Emmett, and E. Teller, "Adsorption of Gases in Multimolecular Layers," *J. Am.Chem.Soc.*, vol. 60, no. 2, pp. 309–319, 1938.

[48] M. Thommes, K. Kaneko, A.V. Neimark *et al.* , "Physisorption of gases, with special reference to the evaluation of surface area and pore size distribution (IUPAC Technical Report)," *Pure Appl. Chem.*, vol. 87, no. 9–10, pp. 1051–1069, 2015, doi: 10.1515/pac-2014-1117.

[49] S. Lowell, J. Shields, M. Thomas, and M. Thommes, *Characterization of Porous Solids and Powders: Surface Area, Pore Size and Density*, vol. 1. 2006.

Chapter 3: Absorption Features, Accidental Exsolution, and Suppression of Ti^{3+} Defects Enhanced Photoelectrochemical Performance in La^{3+}, Ga^{3+} co-doped $SrTiO_3$

Summary

A batch of Ga^{3+} and La^{3+} (co-) doped samples were synthesized at 900 °C. Two co-doped samples stood out in exhibiting absorption features, and exsolution which were found to have impacted their performances. These samples also exhibited higher lifetimes and a decrease in Ti^{3+} defects.

3.1 Introduction

Photoelectrocatalytic water splitting is a promising strategy for producing clean and low-cost fuels by harvesting solar energy. Although H_2 evolution is a highly researched topic, the oxygen evolution reaction due to slow kinetics and high energy consumption is less efficient [1], [2]. Being precious, commercial OER catalysts such as IrO_2 and RuO_2 are not economically feasible[2]. Hence more efficient and low-cost catalysts or catalytic routes should be explored. A prerequisite of highly efficient photocatalytic water splitting is a visible light-responsive catalyst. $SrTiO_3$ although demonstrating excellent performance in photocatalytic water splitting responds only to the UV region of the solar spectrum. Doping transition metal ions in $SrTiO_3$ is an efficient method to introduce visible light activity by creating new absorption edges and band gap narrowing [3]. However, doping with novel transition metal ions often results in mid-gap states, hindering surface catalysis. $SrTiO_3$ is frequently associated with defects such as Ti^{3+} and oxygen vacancies [4]. Defect states such as Ti^{3+} have been reported to be suppressed via low-valence metal ion doping [5]. The photocatalytic activity also depends on the synthesis route of these doped materials which affects the particle size, crystallinity, surface area, and oxygen vacancies. Sol-gel Pechini synthesis route of doped $SrTiO_3$ has been reported to control the particle size with a high specific surface area that aids surface catalysis [6].

The core objective of this work is to study the doping (co-) of novel d^{10} post-transition metal ions such as Ga^{3+} in the Ti^{4+} site of $SrTiO_3$ and how these dopants affect the behavior of $SrTiO_3$. The study focuses on the synthesis of monodoped Ga^{3+} and co-doped La^{3+}, Ga^{3+} $SrTiO_3$ via the sol-gel Pechini process at 900 °C and the corresponding structural and optical characteristics. Highly crystalline particles were observed for all the doped samples and were observed to be less than 50 nm in size. Mid-gap states were not observed in the doped samples. Ti^{3+} defect states observed in undoped $SrTiO_3$ samples were found to be decreased in the doped samples. The Ga^{3+} doped samples demonstrated an n-type nature in contradiction to their expected p-type conductivity. However, it was observed that the n-type nature was reduced with La^{3+} co-doping with the fermi level shifting away from the CB_{Min}. No significant band gap narrowing was observed in the Ga^{3+} doped samples. However, the 2 mol% and the 4 mol% co-doped $SrTiO_3$ samples showed absorption features in the visible light region. A higher photoresponse of the La^{3+} co-doped samples was observed compared to the undoped $SrTiO_3$. The results presented in this work demonstrated the role of defects such as oxygen vacancies in understanding the behavior and performance of doped $SrTiO_3$. Defects were observed to have a profound effect on the Ti^{3+} suppression, exsolution, and the introduction of absorption

features in the visible light region. Overall, this work attempts to understand how defects can affect the material properties which could have a significant effect on the photoelectrocatalytic performances.

Motivation for studying La^{3+} ,Ga^{3+} doped $SrTiO_3$

Recent studies have reported the high quantum yields with Al^{3+} doped $SrTiO_3$ demonstrating the feasibility of overall water splitting [7], [8]. Inspired by the high quantum efficiencies of Al^{3+} doped $SrTiO_3$, this work investigates the Ga^{3+} doping in $SrTiO_3$. Al^{3+} and Ga^{3+} with ionic sizes 0.535 Å and 0.620 Å respectively belong to Group 13 of the periodic table and this work explores whether this dopant has the same effect as Al. Due to similar sizes with the Ti^{4+}, Ga^{3+} is expected to be in the B-site of $SrTiO_3$. Ga^{3+}, an acceptor-type dopant, should push the fermi level toward the valence band, resulting in a p-type conductivity [9]. Sun, S et al. [10] discuss the effect of the relative position of the fermi level vs the doping level on the charge carrier dynamics. This chapter also focuses on the position of the fermi level, and the resulting nature of conductivity, and the factors contributing to this effect. Another important aspect of these materials is maintaining charge neutrality as otherwise, they might be prone to charge accumulation leading to recombination which decreases the performance of the catalysts. In this regard, the effect of co-doping with La^{3+} in the materials will be investigated. La^{3+} in 12 coordination has an ionic radius of 1.36 Å and Sr^{2+} in 12 coordination has an ionic radius of 1.44 Å in $SrTiO_3$ cubic structure [11]. So, it can be assumed that La^{3+} will be in the A site due to the comparable ionic sizes with Sr^{2+}. For every % doping of Ga^{3+} ions in the B site, an equal amount of % doping of La^{3+} in the A site is done thereby aiming to maintain the charge neutrality.

3.2 Experimental Method: Solution Combustion Synthesis/Sol-Gel Pechini Route for the Synthesis of La, Ga co-doped $SrTiO_3$

A series of undoped, Ga monodoped and La, Ga co-doped $SrTiO_3$ samples were prepared by the sol-gel-Pechini route as discussed in Chapter 2. The mol% doping concentration prepared was 0.5-10% for both the mono- and co-doped samples. All synthesized co-doped materials were white except the 2 mol% and 4 mol% co-doped samples which have a blueish tint as shown in Figure 3.1. *The samples were remade 5 times with similar results to verify whether this phenomenon was accidental, and the color was reproducible.*

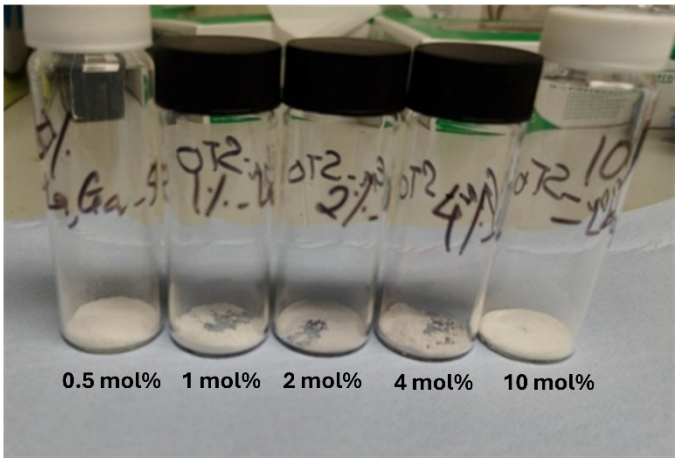


Figure 3.1: *900 °C sol-gel Pechini synthesized La^{3+} co-doped samples (0.5 mol% - 10 mol%).*

3.3 Results and Discussion

The results in this chapter are discussed sequentially starting with the effect of doping on the microstructural properties. Section 3.3.1 analyses the microstructure with the XRD patterns and the TEM. This section correlates the observations with defect chemistry via the Kröger Vink notations. The TEM analysis focuses on the crystallographic defects and the role these defects play in facilitating exsolution. The section ends with re-examining the XRD patterns on a log scale to understand the effect of phase segregation during exsolution.

3.3.1 Microstructural Analysis

Goldschmidt's Tolerance Factor Consideration in the Structural Stability of the Samples

Takata, T. et al. [12] studied the photocatalytic effect of 5 mol% Ga^{3+} doped $SrTiO_3$ prepared with the solid-state synthesis towards water splitting where they reported a higher performance compared to the undoped $SrTiO_3$. Inspired by their work, samples with a range of (0.5 – 10) mol% Ga^{3+} doping were synthesized. To understand further where the limit of doping lies, a batch with 20, 30, and 40 Ga^{3+} mol% doped $SrTiO_3$ was synthesized. All the doped samples in this series were observed to have secondary phases as shown in Figure 3.2.

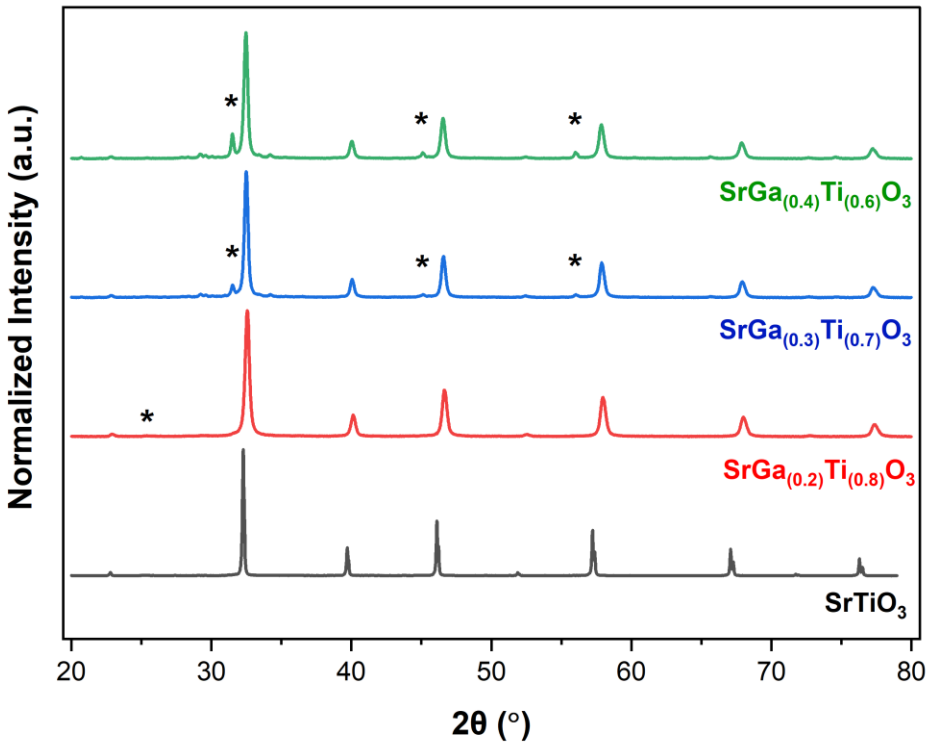


Figure 3.2: *Comparison of the XRD patterns of 20, 30, and 40 mol% Ga^{3+} doped $SrTiO_3$ which demonstrated secondary phases indicated by *. The motivation to synthesize these batches was to understand the limit of Ga^{3+} doping.*

In perovskite structures, Goldschmidt's Tolerance Factor is used to determine the structural stability of the samples [13]. The tolerance factor, t is derived for monodoped and (co)-doped samples in the following equations [14]:

$$t = \frac{r_A + r_O}{\sqrt{2}((1-x)r_B + xr_{B'} + r_O)} \quad (3.1)$$

$$t = \frac{(1-y)r_A + yr_{A'} + r_O}{\sqrt{2}((1-x)r_B + xr_{B'} + r_O)} \quad (3.2)$$

where,
r_A = Radius of A-site cation, Sr^{2+}= 1.44 Å
$r_{A'}$ = Radius of Dopant at A-site, La^{3+}= 1.36 Å
r_B = Radius of B-site cation, Ti^{4+}= 0.605 Å
$r_{B'}$ = Radius of Dopant at B-site, Ga^{3+}= 0.62 Å
r_O = Radius of Oxygen anion, O^{2-}= 1.4 Å
x = Percentage doping at B-site
y = Percentage doping at A-site

The tolerance factors were calculated for doped (co-) samples for 0.5 – 10 mol% from Eqs (3.1) and (3.2) and tabulated in Table 3.1.

Table 3.1: Goldschmidt's Tolerance Factor for undoped and doped $SrTiO_3$ samples

Sr No	Sample	Tolerance Factor, t
1	Undoped $SrTiO_3$	1.0000
2	$SrTi_{(0.995)}Ga_{(0.005)}O_3$	1.0016
3	$SrTi_{(0.98)}Ga_{(0.02)}O_3$	1.0014
4	$SrTi_{(0.96)}Ga_{(0.04)}O_3$	1.0013
5	$SrTi_{(0.9)}Ga_{(0.1)}O_3$	1.0008
6	$La_{(0.005)}Sr_{(0.995)}Ti_{(0.995)}Ga_{(0.005)}O_3$	1.0014
7	$La_{(0.02)}Sr_{(0.98)}Ti_{(0.98)}Ga_{(0.02)}O_3$	1.0009
8	$La_{(0.04)}Sr_{(0.96)}Ti_{(0.96)}Ga_{(0.04)}O_3$	1.0002
9	$La_{(0.1)}Sr_{(0.9)}Ti_{(0.9)}Ga_{(0.1)}O_3$	0.9980

From Table 3.1, the tolerance factor of the samples is close to 1 which is within the tolerance limit of $0.75 < t \leq 1$ for cubic perovskite structures [15]. It can be inferred from Table 1, that the samples retain the cubic structure with no distortions upon doping. This was further validated with the XRD patterns which are discussed in the following sections.

XRD

XRD patterns of the synthesized samples were measured as shown in Figure 3.3. All peaks were indexed after calculation and were found to be consistent with the $SrTiO_3$ ICSD file 23076 [16]–[18]. Figure 3.3 shows the XRD patterns for the sol-gel synthesized undoped $SrTiO_3$ nano-powder samples in comparison to the La, Ga (co)-doped powders. All samples retained the ABO_3 cubic ($Pm\bar{3}m$) perovskite structure and were in good agreement with the ICSD file for $SrTiO_3$, showing no other impurity phases.

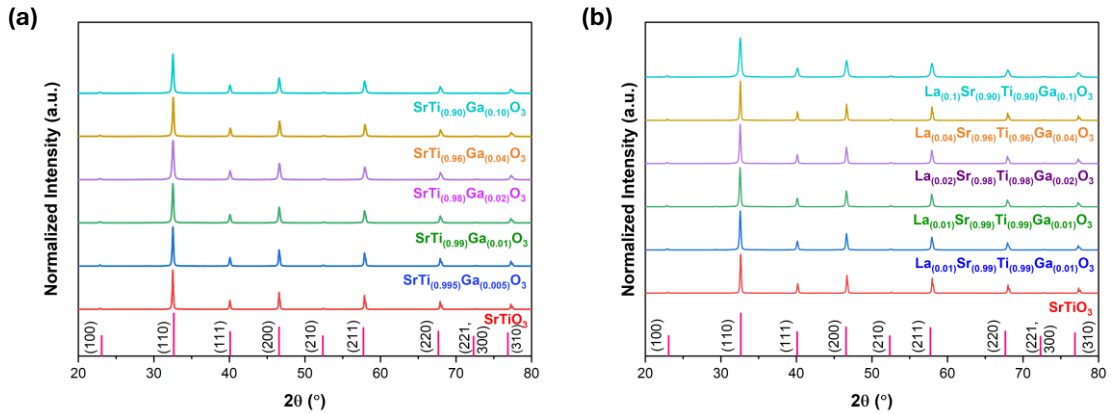


Figure 3.3: *XRD patterns of (a) Ga^{3+} (b) La^{3+}, Ga^{3+} doped $SrTiO_3$ samples with peaks indexed according to $SrTiO_3$ ICSD 23076 file [16]-[18]. The diffraction patterns were collected between 20° to 80° 2θ values with step size 0.0167113 ° and 24.765 sec per step.*

From Figures 3.2 and 3.3, it could be inferred that the limit of doping could lie between 10 mol% and 20 mol%. The synthesized samples were mostly white except for two samples- the 2 mol% and the 4 mol% La^{3+}, Ga^{3+} doped $SrTiO_3$. These samples are bluish-grey. Therefore,

in this report, four samples will be studied comparing their properties. The samples that will be compared are undoped, 2 mol% Ga^{3+}, 2 mol% La^{3+}, Ga^{3+}, 4 mol% Ga^{3+}, and 4 mol% La^{3+}, Ga^{3+}. All synthesized samples were made at 900 °C.

In Chapter 3, the microstructure plays an important role in determining the behavior of the samples. The crystallite size was calculated using the Scherrer equation considering the instrumental correction with LaB_6. The microstrain was calculated via the Williamson-Hall analysis considering the instrumental broadening effect. Lattice parameters of the samples were calculated as discussed in Chapter 2. The microstructural parameters are shown in Table 3.2.

Table 3.2: Average crystallite sizes, microstrain, lattice volumes, and lattice parameters of the synthesized samples

Sr No	% Doping	Average Crystallite Size (nm)	Microstrain (ε)	Lattice Volume ($Å^3$)	Lattice Parameter (Å)
1	$SrTiO_3$	43.02 ± 0.44	1.74E-03 ± 0.32E-03	59.4277 ± 0.09	3.9024 ± 0.002
2	$SrTi_{(0.98)}Ga_{(0.02)}O_3$	23.62 ± 0.82	1.91E-03 ± 0.34E-03	59.4071 ± 0.09	3.9019 ± 0.002
3	$SrTi_{(0.96)}Ga_{(0.04)}O_3$	26.07 ± 0.64	1.55E-03 ± 0.46E-04	59.3596 ± 0.05	3.9009 ± 0.001
4	$La_{(0.02)}Sr_{(0.98)}Ti_{(0.98)}Ga_{(0.02)}O_3$	37.49 ± 0.54	1.41E-03 ± 0.30E-03	59.4318 ± 0.05	3.9025 ± 0.001
5	$La_{(0.04)}Sr_{(0.96)}Ti_{(0.96)}Ga_{(0.04)}O_3$	26.52 ± 0.42	1.37E-03 ± 0.25E-03	59.4010 ± 0.05	3.9018 ± 0.001

The errors in lattice parameters and volumes were added recalculating the lattice parameters and volumes of the samples.

From Table 3.2, it can be observed for both types of dopings that the average crystallite sizes decrease with both mono- and co-doping. For the 4 mol% monodoped sample, the average crystallite size increased as compared to the 2 mol% sample. As highlighted in the previous chapters, the microstrain is an important aspect of microstructural studies indicative of localized areas of defects. This parameter is found to have decreased in the 4 mol% monodoped sample and the co-doped samples. In the 2 mol% Ga^{3+} sample, the microstrain is the highest, and in the 4 mol% La^{3+} co-doped sample is the lowest.

The lattice volumes and parameters decreased for the Ga^{3+} doped samples. In the co-doped samples, the 2 mol% showed an increase in lattice volume. Whereas, the 4 mol% co-doped sample showed a contraction. The results obtained in the Ph.D.. work were compared with other donor-doped $SrTiO_3$ systems in the literature. Kobayashi, S. et al. [19] reported a monotonic expansion in donor-doped Nb, La co-doped $SrTiO_3$ as mol% doping increased. They reported that this phenomenon is due to an electronic compensation mechanism. The electronic compensation mechanism involves the donation of an electron which reduces Ti^{4+} to Ti^{3+}. Pilch, M. et al. [20] reported a contradiction to this trend where they reported a contraction at 0.1 mol% La^{3+} doping. They also reported that the Verneuil method grown 0.1%

La: $SrTiO_3$ was blue indicating electronic compensation [20]. Moos, R. et al. [21] they have reported a similar contraction which they attributed to vacancy compensation.

Vacancy compensation involves maintaining charge neutrality by creating cation ($V_{Sr}^{''}$ or $V_{Ti}^{''''}$) vacancies [20]. The change in the lattice volumes in the synthesized 2 mol% and 4 mol% La^{3+} co-doped samples might indicate a change in the charge compensation mechanism. Change in charge compensation mechanism from electronic to vacancy compensation after a critical mol% doping has been reported in La^{3+}: $BaTiO_3$ [22]. The co-doped samples showed a deeper blue color for the 2 mol% sample compared to the 4 mol% sample. Here it can be argued that as the La^{3+} doping increases, compensation mechanisms might begin to change. In the 4 mol% sample, the charge compensation might be more through vacancy compensation and less through electronic compensation.

Electronic compensation in the La^{3+} co-doped samples can be explained with the Kröger Vink notation as shown in Eq (3.3). La^{3+} when doped in the A-site (SrO plane), forms substitutional defects [23].

$$La_2O_3 + SrO \longrightarrow 2\dot{La}_{Sr} + 2e' + 2O_O^X + \tfrac{1}{2} O_2 \quad (3.3)$$

In the synthesized samples, another substitutional defect may arise with Ga^{3+} substitution in the B-site (TiO_2 plane). This can be denoted by the Kröger Vink notation as shown in Eq (3.4).

$$Ga_2O_3 + 2TiO_2 \longrightarrow 2Ga_{Ti}^{'} + 3O_O^X + \ddot{V}_O \quad (3.4)$$

The ($2\dot{La}_{Sr} + 2e'$) and ($2Ga_{Ti}^{'} + \ddot{V}_O$) defects in the 2 mol% La^{3+} co-doped sample indicate a neutral type of defect that leads to lattice expansion [19]. The observed changes in lattice parameters in the above samples are consistent with the reported literature on $SrTiO_3$ [24], [25]. Lu, D. et al. [26] reported that ($\dot{La}_{Sr} + Tb_{Ti}^{'}$) defect complexes due to the La^{3+} in the A-site ensure that the Tb^{4+} is doped exclusively in the B-site of $BaTiO_3$. They reported that this is crucial for the formation of single-phase materials. XRD patterns of La, Ga doped $SrTiO_3$ in this Ph.D.. work also demonstrated single-phase materials which could be rationalized due to the formation of ($\dot{La}_{Sr} + Ga_{Ti}^{'}$) defect complexes which ensure exclusive doping of La^{3+} and Ga^{3+} in the A- and B-sites respectively. The formation of defect complexes in the co-doped samples is denoted by Eqs (3.3) and (3.4).

High-temperature annealing can also contribute to the formation of oxygen vacancies with the loss of lattice oxygen as demonstrated by Eq (3.5) [27]. The formation of double-ionized oxygen vacancies contributes two electrons to the conduction band [28].

$$O_O^X \longrightarrow \ddot{V}_O + \frac{1}{2} O_2 + 2e' \quad (3.5)$$

An expansion of the local lattice around vacancies in perovskite oxides can occur due to repulsion between neighboring cations [29]. Kobayashi, S. et al. [19] reported this expansion around the oxygen vacancy-containing lattice site can be countered by the lattice contraction around the cations away from the defect site which can lead to an overall contraction. This may be why the 4 mol% La^{3+} co- and monodoped samples showed a contraction. Formation of charged cation vacancies also cannot be excluded in this sample which showed contraction.

The formation of cation vacancies will be probed later in the chapter while discussing the XPS data.

Qin, Y. et al. [30] reported that as the La^{3+} doping increased from 0.4% to 0.6%, the lattice parameters decreased which was explained as La^{3+} substituting in the A site. Liu, J. et al. [31] reported a non-linear trend in the La^{3+} doped $SrTiO_3$ lattice parameters. They observed increased lattice parameters from increasing doping from 2 to 5% and a decrease at 10 %. The lattice parameters varied due to different amounts of oxygen vacancies at different doping % and the decrease in lattice parameters indicated an oxygen deficiency [31]. Peng Peng, S. et al. [32] reported similar lattice shrinkage due to oxygen deficiencies.

Doubly ionized oxygen vacancies, $\ddot{V}_O$ contribute two electrons to the conduction band [28],[19]. In donor-doped $SrTiO_3$, these electrons also lead to the reduction of Ti^{4+} to Ti^{3+} as shown in Eq (3.6). The presence of Ti^{3+} in the La^{3+} co-doped samples was also confirmed with the XPS to be discussed in the subsequent sections. The presence of Ti^{3+} also leads to the expansion of the lattice possibly due to its larger ionic radius (0.67 Å) in 6-coordination [11]. Muta, H. et al. [33] reports the blue color of reduced $SrTiO_3$ and La^{3+} doped $SrTiO_3$ to be due to oxygen vacancies and the generated Ti^{3+} defects. They also reported increased lattice parameters due to these defects which aligns with the theory stated for the synthesized La^{3+} doped $SrTiO_3$ samples. Similar observations about defects and lattice parameters were also reported by Potzger, K. et al. [34] in $SrTiO_3$. Due to the formation of doubly ionized oxygen vacancies, Ti^{3+} defects form in the samples synthesized in this report.

$$2e' + 2Ti_{Ti}^{X} \longrightarrow 2Ti_{Ti}^{'} \qquad (3.6)$$

The presence of Ti^{3+} could be also observed from the XPS analysis (discussed later). Janotti, A. et al. [35] reported that both size differences between the dopants and the parent sites and electronic effects contribute to the change in lattice parameters.

The Kröger Vink notations discussed above apply to the oxygen-poor annealing conditions. This applies to the annealing conditions of the samples synthesized in the Ph.D. work. Eq (3.7) summarizes the defect state when $SrTiO_3$ co-doped with La^{3+}, and Ga^{3+} in oxygen-deficient conditions which leads to more n-type nature. Oxygen is an important parameter during annealing to control oxygen vacancies in oxide materials. In oxygen-rich environments, these vacancies are lost whereas in oxygen deficient conditions more of these vacancies are created.

$$La_2O_3 + 2Ga_2O_3 \longrightarrow 2\dot{La}_{Sr} + 4Ga_{Ti}^{'} + 8O_O^{X} + \tfrac{1}{2}\, O_2 + \ddot{V}_O \qquad (3.7)$$

Eq (3.8) summarizes the defect reaction in oxygen-rich environments which can lead to more p-type materials.

$$La_2O_3 + Ga_2O_3 + \tfrac{1}{2}\, O_2 \longrightarrow 2\dot{La}_{Sr} + 2Ga_{Ti}^{'} + 6O_O^{X} + \tfrac{1}{2}\, O_2 \qquad (3.8)$$

Aidhy, D.S. et al. [36] in their DFT study reports that there is a window of strain where oxygen vacancies are stable. They report that charged oxygen vacancies lead to compression of the lattice and neutral vacancies lead to expansion of the lattice. This observation also holds for the lattice systems of the doped samples synthesized in this study as shown in Figure 3.4.

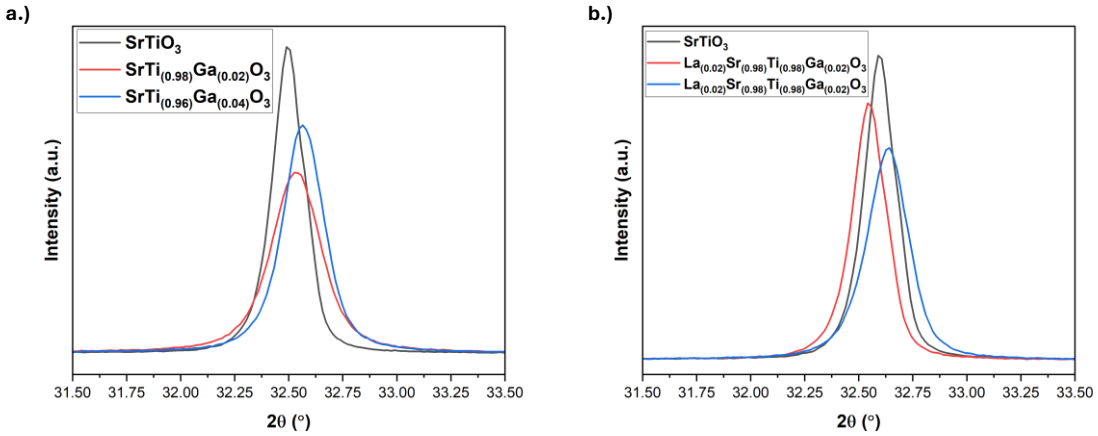


Figure 3.4: *Lattice volume and relative crystallinity comparison of (a) Ga^{3+} doped (b) La^{3+} co-doped $SrTiO_3$ samples in oxygen-poor annealing conditions. The monodoped samples with shifts to higher angles show a decrease in lattice volumes. The lattice volume increased in the 2 mol% co-doped sample and decreased in the 4 mol% co-doped sample. All the doped samples show lower relative crystallinity compared to the undoped.*

Figure 3.4 demonstrates the lattice volume changes in both types of doping. In the Ga^{3+} monodoped samples, the XRD peak (110) shifts to higher 2θ angles. This indicates a compressive strain acting on the lattice leading to the shrinkage. In the La^{3+} co-doped samples, the (110) peak shifts to lower 2θ angles for the 2 mol% sample indicating a tensile stress that expands the volume of the lattice. The shifts to higher 2θ angles for the 4 mol% sample indicate a lattice shrinkage. For both comparisons, synthesized undoped $SrTiO_3$ was used as the reference. The presence of compressive stress in the monodoped samples and 4 mol% La^{3+} co-doped sample could indicate that charged oxygen vacancies might be the dominant defect. Whereas in the 2 mol% co-doped sample, the presence of neutral oxygen vacancies is stable leading to the observed expansion. This is supported by the Kröger-Vink notations in Eqs (3.3)-(3.6).

The degree of crystallinity of materials is measured from the XRD patterns by comparing the areas under the crystalline peaks to the total area of amorphous and crystalline regions. Since Figure 3.3 shows that all the synthesized materials are highly crystalline with no visible amorphous regions, in this work a relative XRD peak intensity and sharpness is used as a measure of crystallinity. Ohtani, B. [37] in his work explains the use of sharpness of XRD peaks as a measure of relative crystallinity. Therefore, henceforth in the Ph.D. work, the XRD peak intensities will be used as a measure of the relative degree of crystallinity. Figure 3.4 demonstrates the effect of doping on the relative crystallinity of the materials. The Ga^{3+} doped samples show lower crystallinity as compared to the undoped. Similarly, for the La^{3+} co-doped samples, both showed lower relative crystallinity. The degree of crystallinity is related to the presence of microstructural defects. From the XRD analysis, the microstrain was studied as an indicator of localized defects (Table 3.2) [38]. Even though most of the doped samples showed lower microstrains, the degree of relative crystallinity is still higher in the undoped sample. This may be due to the doping or the presence of other crystallographic defects such as

dislocations and grain boundaries present in the samples. Micro-structure is an important aspect that affects photocatalytic performances. To further understand the role of microstructural defects, TEM analysis was done. The role of defects such as dislocations and grain boundaries are discussed in the subsequent section.

Dislocations and Grain Boundaries

Defects in metal oxides are a typical occurrence that affects the translational symmetry of the unit cell [39]. These defects can be classified as 0D point defects (vacancies), 1D linear defects (dislocations), 2D planar defects (grain boundaries), and 3D volumetric defects (pores) [40]–[42]. Li, W. et al. [40] report that crystalline transition metal oxides such as $SrTiO_3$ often exhibit defects such as dislocations and grain boundaries that behave differently as compared to the bulk material. These dislocations and grain boundaries may give rise to unique properties mainly due to their charged nature arising from nonstoichiometry [40], [43], [44]. Raizada, P. et al. [45] in their work report that 1D defects such as dislocations have an indirect effect on the electronic properties of metal oxide photocatalysts by acting as sinks for point defects. Ren, P. et al. [46] report that the dislocations induced in their TiO_2 nanowires acted as active Ti^{3+} centers. These centers improved visible light absorption (400-900 nm) and hence, accelerated the photocatalytic degradation by 1.8 times as compared to defect-free TiO_2. These reports concur with the induced defects in the synthesized samples in the Ph.D.. work, observed from the lattice parameters and the XRD in the previous section. Defects can be present in the bulk and on the surface [47]–[49]. 0D defects such as vacancies can be present in both the bulk and the surface of the materials whereas 1D and 2D such as dislocations and grain boundaries are present only on the surface [49]. Yan, J. et al. [47] reported the enhanced photocatalytic performance in TiO_2 due to surface/bulk defects modulated via the hydrothermal synthesis in different calcination temperatures (400 °C-700 °C).

To study how 1D and 2D defects in the lattice affect the microstructural and electronic properties of the synthesized samples, TEM analysis was done. TEM analysis revealed the presence of grain boundaries and dislocations in the samples as shown in Figure 3.5. The samples were synthesized at 900°C. High-temperature synthesis leads to particles coalescing together and hence, the grain boundaries. The samples comprise both single particles and coalesced particles. Figure 3.5 represents a region with coalesced particles with grain boundaries and dislocations.

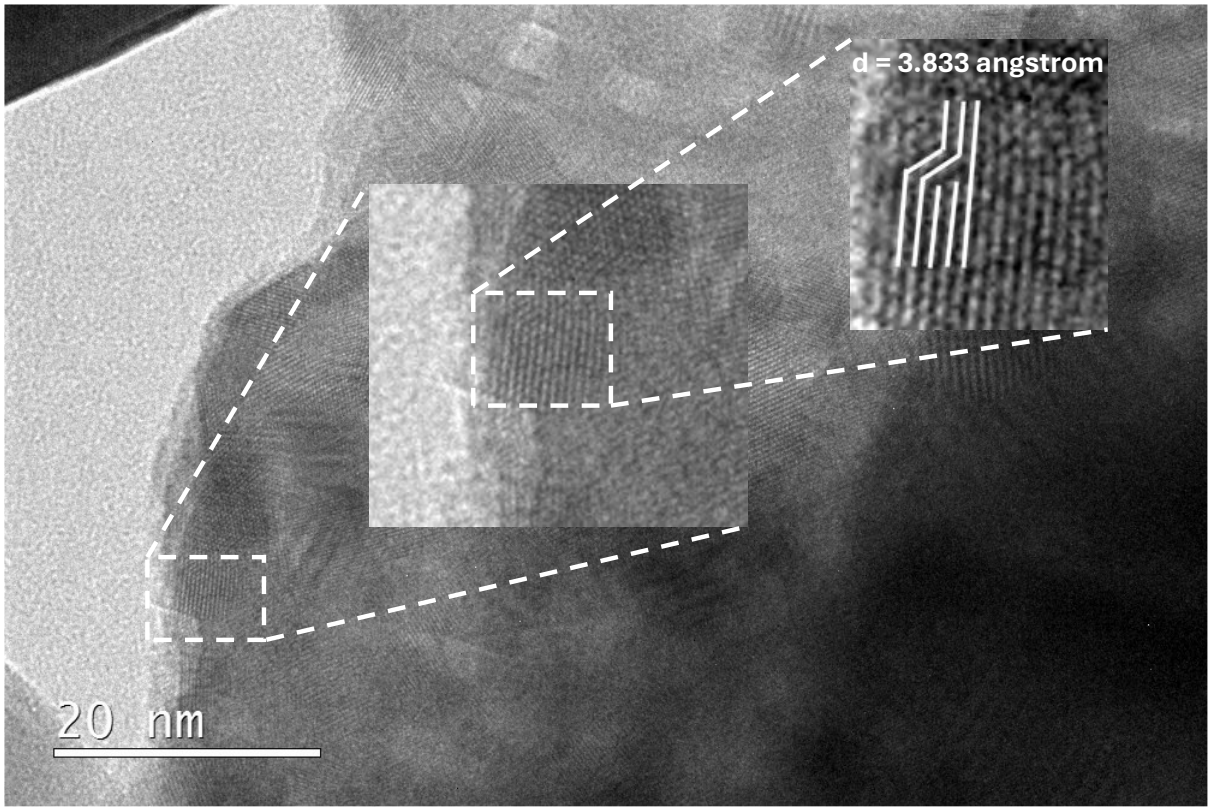


Figure 3.5: *Dislocations present in (100) plane of 4 mol% La^{3+} co-doped samples as observed via TEM analysis.*

The dislocation density in literature has been reported to be measured by various methods such as modified Williamson-Hall methods and modified Warren-Averbach methods [50]–[53]. To calculate the dislocation density, the formula adopted from the work of Laala-Bouali, H. et al. [52] is shown in Eq (3.9). The Eq is based on the use of the modified Warren-Averbach method. Rietveld refinement was used in the work of Laala-Bouali, H. et al. [52] to extract the lattice parameters that are required for the calculation of the Bürger's vector (ß).

$$\rho = 2\sqrt{3}\,\frac{\sqrt{\sigma^2}}{L\text{ß}} \tag{3.9}$$

Where,

ρ = Dislocation density

σ^2 = Microstrain

L = Mean crystallite size

ß = Bürger's vector giving the magnitude and direction of the dislocation

a = Lattice parameter

$$\text{ß} = \frac{a}{2}\sqrt{h^2 + k^2 + l^2} \tag{3.10}$$

The calculated dislocation density and Burger's vector are tabulated in Table 3.3. The direction of the dislocations is along the (100) plane.

Table 3.3: Dislocation density of the synthesized samples

Sr. No	Samples	Bürger's vector	Dislocation density (nm^{-2})	Crystallite Size (nm)
1	$SrTiO_3$	0.1951	1.91E-02	43.02 ± 0.44
2	$SrTi_{(0.98)}Ga_{(0.02)}O_3$	0.1951	3.29E-02	23.62 ± 0.82
3	$SrTi_{(0.96)}Ga_{(0.04)}O_3$	0.1950	3.26E-02	26.07 ± 0.64
4	$La_{(0.02)}Sr_{(0.98)}Ti_{(0.98)}Ga_{(0.02)}O_3$	0.1951	1.78E-02	37.49 ± 0.54
5	$La_{(0.04)}Sr_{(0.96)}Ti_{(0.96)}Ga_{(0.04)}O_3$	0.1951	2.48E-02	26.52 ± 0.42

From Table 3.3, all the Ga^{3+} monodoped samples show higher dislocation densities as compared to the undoped. The amount of microstructural defects affects the degree of crystallinity of the samples. The lower dislocation density of the undoped sample may have resulted in higher relative crystallinity than the Ga^{3+} monodoped samples as confirmed by Figure 3.4(a). Even though the 2 mol% co-doped sample, has lower microstrain and dislocation density, the relative crystallinity is lower than the undoped. This can be attributed to the effect of high doping. Pal, M. et al. [54] reported a similar decrease in crystallinity in Eu^{3+} doped TiO_2. They reported that doping introduced a strain in the lattice that altered lattice periodicity and distorted the crystal symmetry. Jyothi, G. et al. [55] reported that when La^{3+} is co-doped in Eu^{3+}: $SrTiO_3$, then it leads to tilting of the TiO_6 octahedra. The distorted octahedra houses the Ti cations. The introduction of Ga^{3+} and La^{3+} into the $SrTiO_3$ lattice could have similarly affected the periodic arrangement of the lattice planes. Hence, the decrease in relative crystallinity. This shows that the relative crystallinity and the overall microstructural evolution are affected by a combination of factors.

Synthesis temperature is another important parameter that determines the overall crystallographic system. As stated previously, the synthesized materials due to the higher temperatures agglomerated in some regions. The coalesced regions resulted in a polycrystalline area with grain boundaries separating differently oriented crystallites. Figure 3.6 depicts a coalesced region of the 4 mol% La^{3+} co-doped sample.

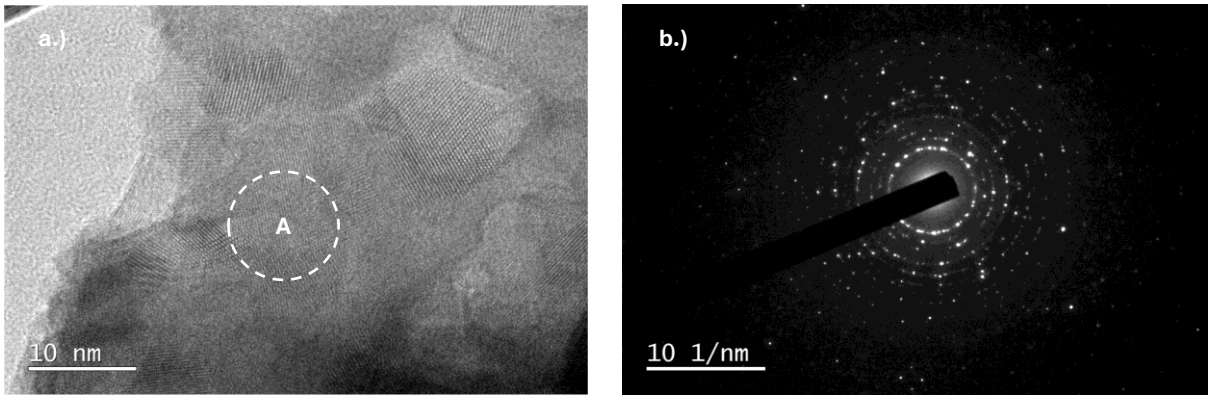


Figure 3.6: *(a.) Coalesced nanoparticles due to high-temperature synthesis (b.) Diffraction pattern demonstrating the polycrystalline nature of the region imaged (Sample: 4 mol% La^{3+} co-doped $SrTiO_3$).*

From the TEM analysis, 2D defects such as grain boundaries can be observed in the coalesced regions. Grain boundaries in photocatalysts can trap charge carriers which lead to recombinations and hence, can be detrimental to their performance [40]. However, grain boundaries are also reported to facilitate photocatalysis. Zhu, Y. et al. [56] have reported that when Rh and Pd nanowires co-catalysts with a high density of grain boundaries are loaded on TiO_2 nanosheets, then an enhanced photocatalytic CO_2 reduction is observed. Grain boundaries can act as sinks for defects such as vacancies [57]–[59]. Figure 3.7 demonstrates the appearance of grain boundaries in the 4 mol% La^{3+} co-doped sample most likely from the high temperature calcination.

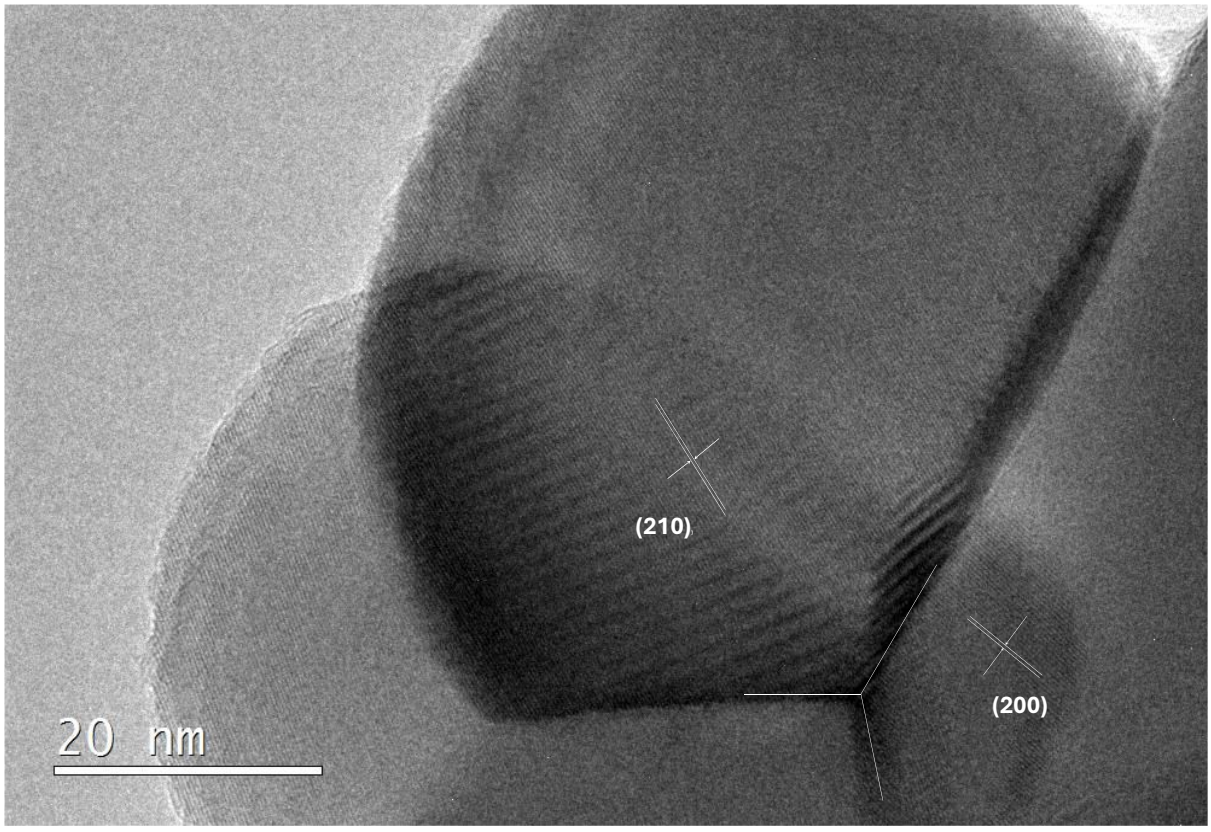


Figure 3.7: *Appearance of grain boundaries due to high-temperature synthesis with differently oriented crystallites (Sample: 4 mol% La^{3+} co-doped $SrTiO_3$).*

Effect of Accidental Exsolution on Material Performance

The catalyst surface of the synthesized samples with TEM shows exsolved particles as seen in Figures 3.9 and 3.10. Exsolution involves the transition metal cations of the B-site cations to leach out of the ABO_3 structure and form metal nanoparticles [60]. These nanoparticles are partially immersed in the perovskite structure. Exsolution happens when a material is subjected to a heat treatment in a reducing environment. This process is reversible as the NPs dissolve into the lattice under oxidative treatment. Such reversibility may be beneficial against agglomeration and can enhance catalyst lifetimes. Singh, S. et al. studied how the presence of 1D and 2D defects such as grain boundaries and stacking faults help in the nucleation of exsolved Ni NPs from $LaNiO_3$ [61]. They report that the 1 nm Ni NPs grow on the Ruddlesen-Popper stacking faults than on the defect-free regions. In the case of the synthesized samples in the Ph.D., the dislocations, and the grain boundaries may have acted as sites of nucleation for the exsolved NPs.

Kousi, K. et al. [62] explain that the exsolution process is a phase decomposition controlled by surface and bulk defects. Metal nanoparticles can exsolve either on the surface or in the bulk which is facilitated by different mechanisms. Surface exsolution can take place due to the presence of crystallographic defects which promotes the nucleation process. Bulk exsolution occurs in reducible materials. Exsolution observed in the 2 mol% and the 4 mol% La^{3+} samples synthesized at 900 °C could be facilitated by the dislocations and grain boundaries present. Besides crystallographic defects, cation or anion vacancies can also facilitate ion diffusion and

promote exsolution [63]. As discussed in the previous section, high-temperature annealing and La^{3+} co-doping could promote deviation from $SrTiO_3$ stoichiometry, leading to exsolution. O'Leary, W. et al. [60] reported the exsolution of Ni from $SrTiO_3$ with the introduction of La^{3+} and Sr vacancies.

Figure 3.8 (a) shows the exsolutions of Ni and CeO_2 from $La_{(0.8)}Ce_{(0.1)}Ni_{(0.4)}Ti_{(0.6)}O_3$ denoted by points 1-4 [64]. Figure 3.8(b) shows the gradual formation of the Ni NPs with time $La_{(0.43)}Ca_{(0.37)}Ni_{(0.06)}Ti_{(0.94)}O_3$ under H_2 reduction at 900°C [64]. The distribution of points (NPs) 2 and 4 are like those observed in the synthesized materials in Figure 3.8 (c-g). This comparison to that observed in the literature confirms the possibility of exsolution in the La^{3+}, Ga^{3+} co-doped samples. The inset in Figure 3.8(d, g) shows the exsolution of NPs on the surface of the 4 mol% co-doped samples. Figure 3.8(c, e) shows the exsolution in the 2 mol% co-doped samples. Figure 3.8 (f) shows the crystalline nature of the single exsolved particle with the live FFT. Due to the tiny exsolved particles, EDX could not be performed with the JEOL2100Plus.

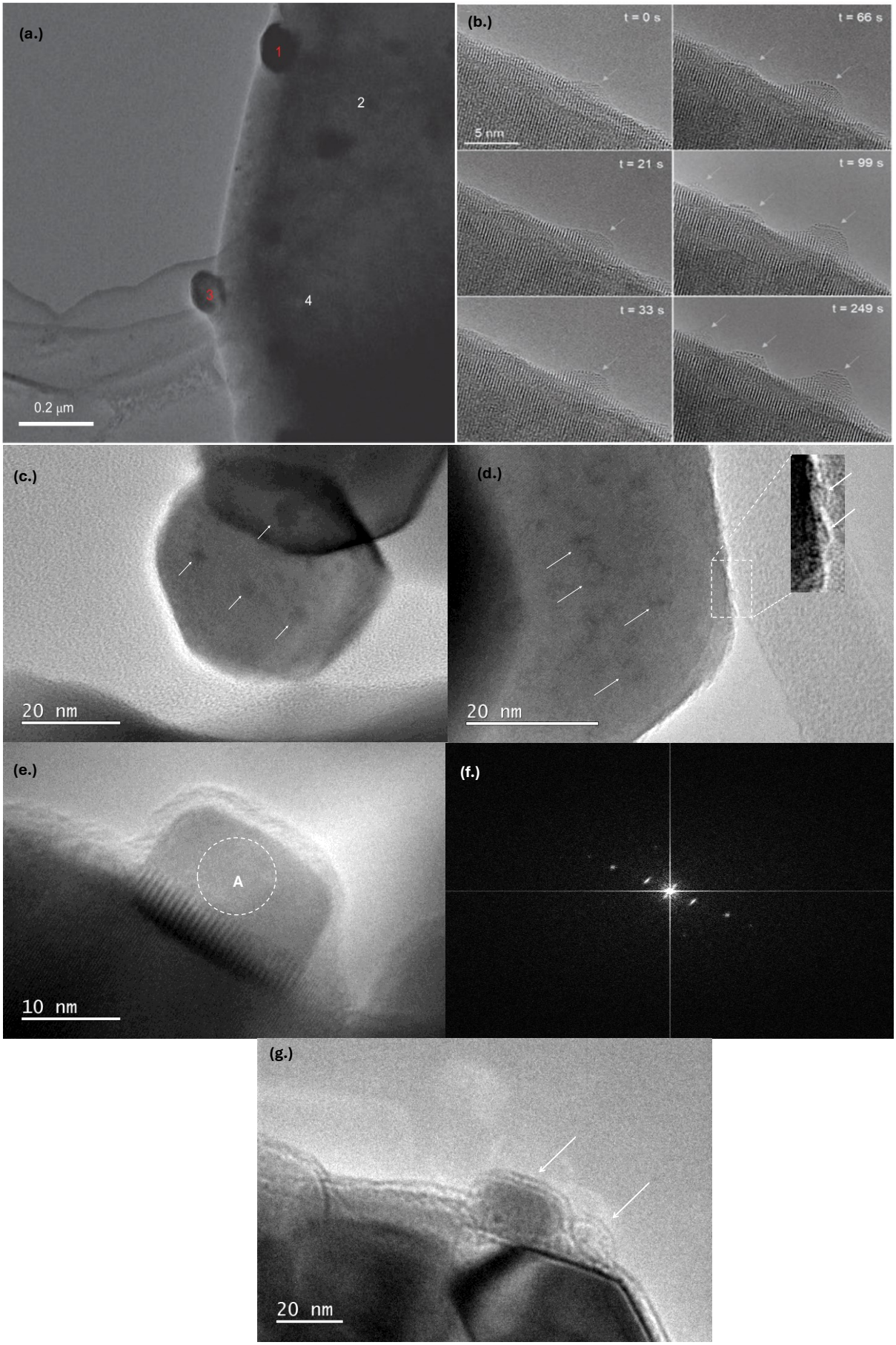

(a.)
1
2
3
4
0.2 μm
(b.)
t = 0 s
t = 66 s
5 nm
t = 21 s
t = 99 s
t = 33 s
t = 249 s
(c.)
20 nm
(d.)
20 nm
(e.)
A
10 nm
(f.)
(g.)
20 nm

Figure 3.8: *Exsolution of nanoparticles in (a, b) Literature comparisons of exsolved NPs to the materials studied in the Ph.D. work reproduced with permission from the works of Neagu, D. et al [63] (Copyright © 2013, Springer Nature Limited and Neagu, D. et al. [64] (Copyright © 2019, American Chemical Society) (c) 2 mol% (d) 4 mol% La^{3+} co-doped $SrTiO_3$ synthesized during the Ph.D. work (e, f) Exsolved particle in the synthesized 2 mol% La^{3+} co-doped $SrTiO_3$ and the live FFT image of the exsolved particle confirming its crystalline nature (g) Exsolved particles in the synthesized 4 mol% La^{3+} co-doped $SrTiO_3$.*

The NPs observed in Figure 3.8 (e) and (g) were about 3nm -5 nm in size. As reported in the literature, La^{3+} co-doping leads to B-site exsolution. So, the exsolved NPs in the doped samples could be metallic Gallium. Figure 3.9 (a.) shows an exsolved NP near a grain boundary in the synthesized 4 mol% La^{3+} co-doped sample. This result aligns with our previous discussion that crystallographic defects such as grain boundaries can facilitate the exsolution process. Figure 3.9 (b) and (c) are literature comparisons of exsolved Ni NPs around grain boundaries [65] and the shape of the Co-Fe exsolved materials [66]. The inset of Figure 3.9 (a) shows the different lattice spacing orientations. From the inset, it can be observed that exsolved NPs are anchored on the perovskite material.

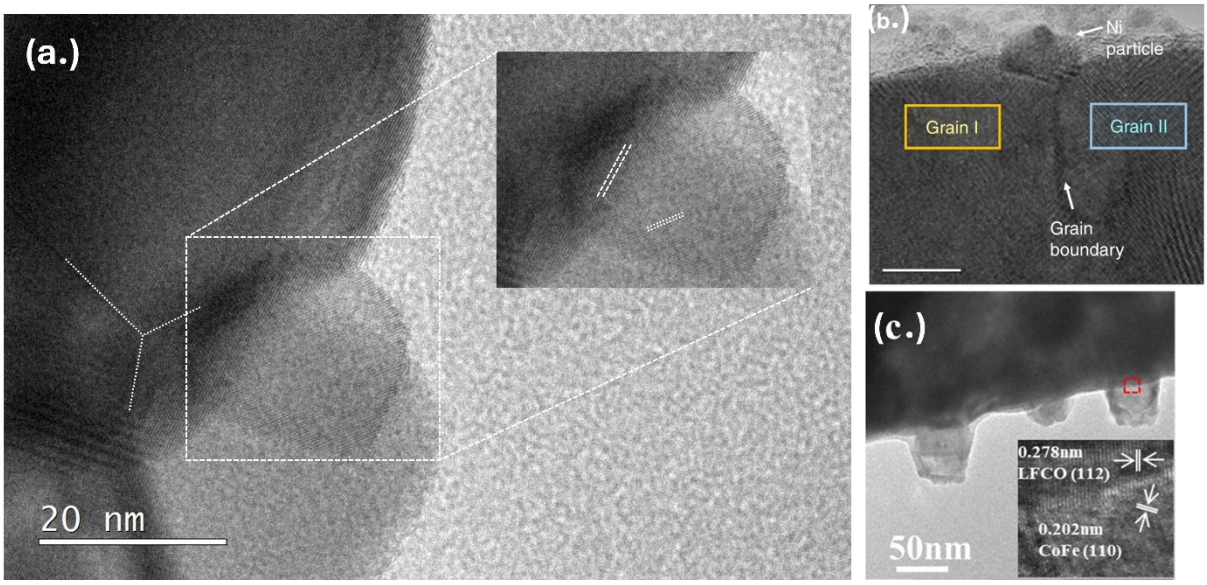


Figure 3.9: *(a) Exsolution of NPs near a grain boundary in 4 mol% La^{3+} co-doped sample synthesized during the Ph.D. work (c, d) Literature comparisons of exsolved NPs to the materials studied in the Ph.D. work reproduced with permission from the works of Kwak, N. W. et al. [65](Open Access, licensed by CC-BY 4.0) and Jiang, Y. et al. [66] (Copyright © 2019 American Chemical Society respectively).*

Rethinking the XRD Pattern due to Exsolution

As discussed earlier, the exsolution involves phase segregation. However, from the XRD analysis in Figure 3.3, no secondary phases were observed in the linear scale. Chattopadhyay, S. et al. [67] reported in their work that the XRD pattern of exsolved CdS nanodots does not show additional XRD peaks due to their small size. They also reported the color change of the titanate perovskite from white to yellow on exsolution. Exsolution can also therefore influence

the blue colour of the La^{3+} co-doped. However, the theory of defects resulting in the blue color also holds as defects and exsolution are closely associated.

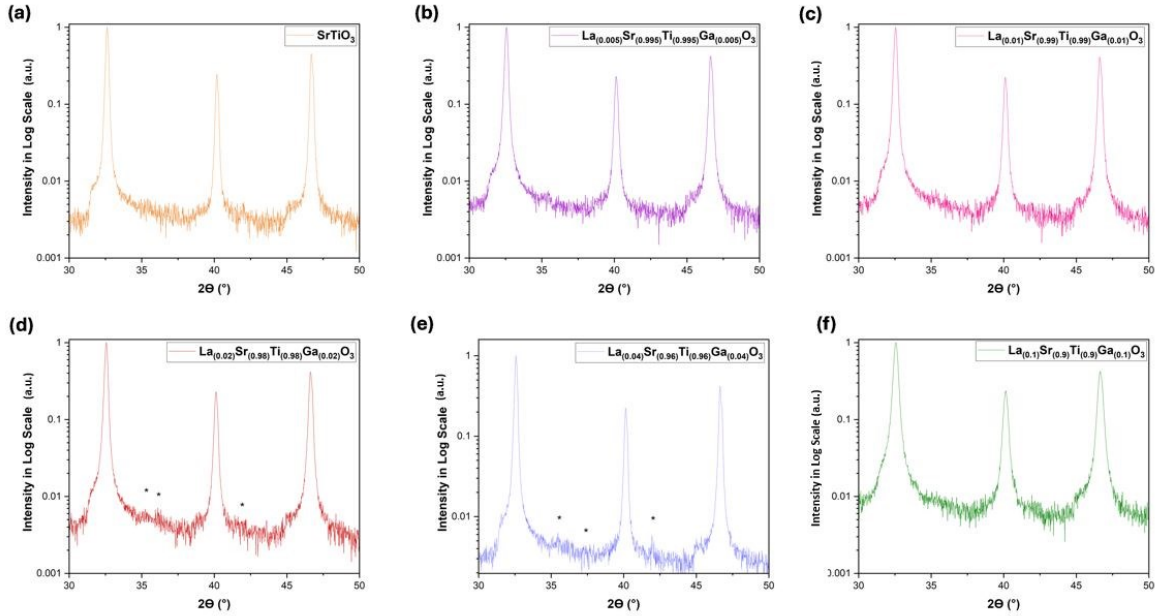


Figure 3.10: *XRD pattern in log intensity scale of the (a) Undoped (b) 0.5 mol% (c) 1 mol% (d) 2 mol% (e) 4 mol% and (f) 10 mol% La^{3+} co-doped $SrTiO_3$ samples. The 2 mol% and 4 mol% La^{3+} co-doped samples show phase segregation.*

Figure 3.10 (a-f) shows the XRD pattern in the log scale to identify phases in small quantities. Most of the co-doped samples were phase pure except the 2 mol% and the 4 mol%. The secondary peaks observed between 30°-50° can be identified to be that of Ga and Ga_2O_3 NPs [68]. The possible exsolution of Ga and Ga_2O_3 is like the exsolution of Ni and CeO_2 observed by Neagu, D. et al. [64]. To further confirm the composition of the NPs, a detailed XPS analysis of the samples was done, which is discussed in the subsequent section. From this section, another hypothesis can be raised regarding the observed trends with dislocation densities (Table 3.2), the microstrains (Table 3.3), and the overall relative crystallinities of the doped samples (Figure 3.4 (a, b)). If Ga/Ga_2O_3 is present as shown in Figure 3.10 (d, e) it could potentially alter the crystallinity of the perovskite structure by introducing more lattice strains which could be also why the relative crystallinity of the undoped sample is higher [69], [70].

From the XRD and the TEM analysis, the presence of defects in the synthesized samples is strongly indicated. As stated above 1D and 2D defects may act as sinks for point defects. These surface defects may form complexes with point defects which drastically affect the properties of materials. Hirel, P. et al. [71] report the possibility of charged dislocations that can attract cation or anion vacancies. It is crucial to understand how these defects interact and affect the optoelectronic and microstructural properties of the photocatalysts. To correlate the microstructural properties of defect-enriched materials to opto-electronic properties various characterization techniques were employed.

3.3.2 Elemental Analysis with the XPS

In this section, the elemental analysis of the catalyst surface was conducted. The section studies the elemental distribution and attempts to correlate it with the microstructural analysis pertaining to the defects and exsolution.

Sr3d

The surface of the undoped, 2 mol% Ga^{3+}, 4 mol% Ga^{3+}, 4 mol% La^{3+}, and 4 mol% La^{3+} co-doped $SrTiO_3$ samples were investigated with XPS. For the samples, Sr3d, Ti2p, Ga2p, La3d and O1s were analysed. All peaks were charge-corrected to C1s at a binding energy of 284.8 eV. Figure 3.11 shows the deconvoluted Sr3d peaks with $Sr3d_{5/2}$ peak at 133.77 eV and $Sr3d_{3/2}$ peak at 134.49eV attributed to Sr^{2+} in $SrTiO_3$ lattice. The split between the $d_{5/2}$ and the $d_{3/2}$ orbital in the case of the undoped $SrTiO_3$ is 1.72 eV. The sample shows two additional peaks at higher binding energies corresponding to $SrCO_3$. For the undoped sample, the ratio between the $SrCO_3$ $Sr3d_{5/2}$ and the C1s C=O is 1:1.15 which is close to the reported 1:1 carbonate ratio in literature consistent with $SrCO_3$ [72].

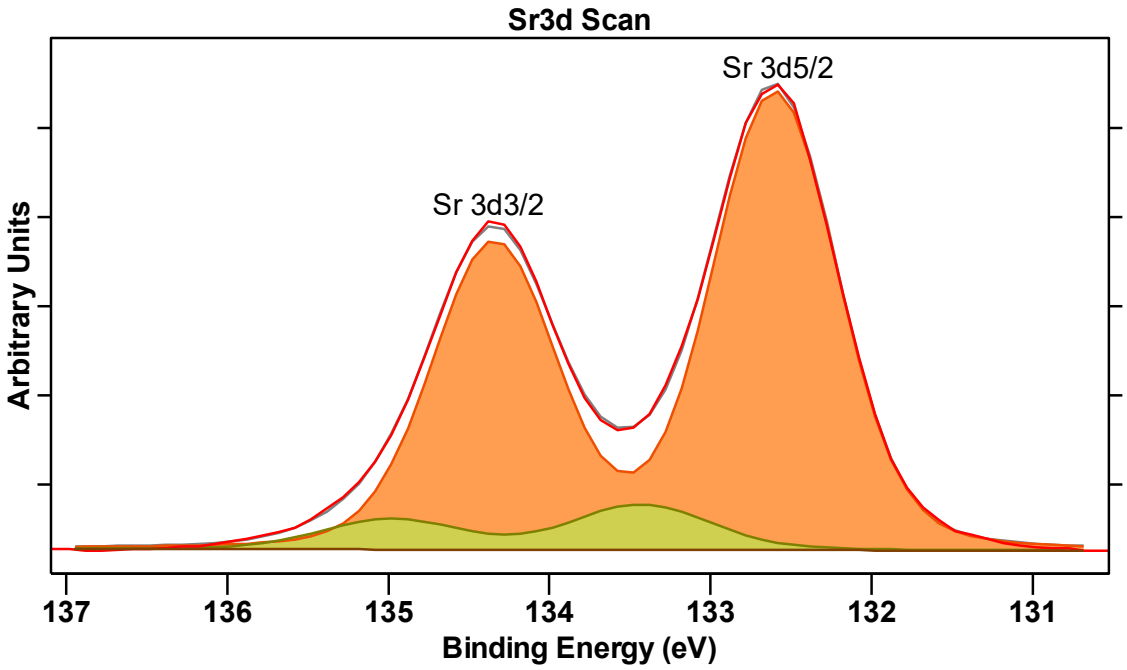


Figure 3.11: *Deconvoluted and charge corrected Sr3d Peaks of Undoped $SrTiO_3$ at 132.77 eV and 134.49 eV with trace amount of $SrCO_3$.The green doublet refers to the presence of $SrCO_3$ confirmed from the 1:1 ratio of the $SrCO_3$ $Sr3d_{5/2}$ and the C1s -C=O.*

From the deconvolution of the Sr3d peaks of the doped samples in Figure 3.12 (a-d), the presence of $SrCO_3$ is evident.

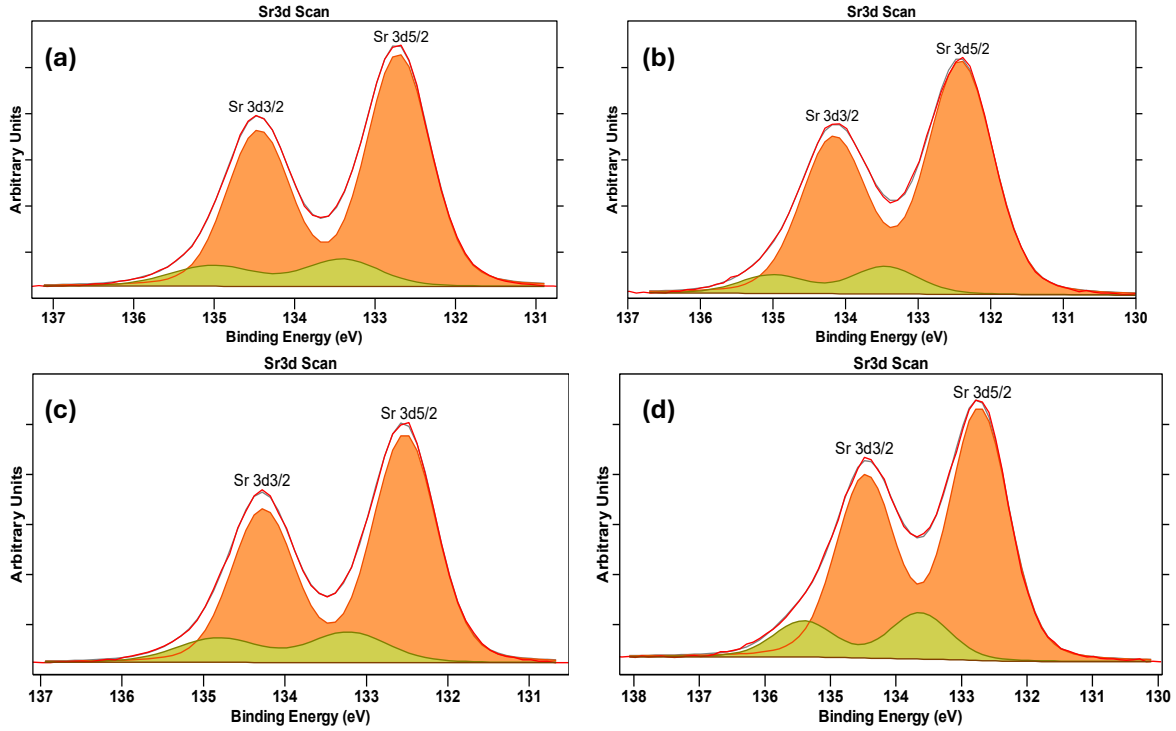


Figure 3.12: *Deconvoluted and charge corrected Sr3d Peak of (a) 2 mol% Ga^{3+} (b) 4 mol% Ga^{3+} (c) 2 mol% La^{3+} and (d) 4 mol% La^{3+} co-doped $SrTiO_3$. The 4 mol% co-doped sample shows the highest $SrCO_3$ concentration.*

The binding energy positions of the $Sr3d_{5/2}$ and the $Sr3d_{3/2}$ of the lattice Sr^{2+} are presented in Table 3.4.

Table 3.4: Position of the $Sr3d_{5/2}$ and the $Sr3d_{3/2}$ of the doped samples

Sr No	Sample	$Sr3d_{5/2}$	$Sr3d_{3/2}$
1	$SrTi_{(0.98)}Ga_{(0.02)}O_3$	132.75	134.46
2	$SrTi_{(0.96)}Ga_{(0.04)}O_3$	132.45	134.12
3	$La_{(0.02)}Sr_{(0.98)}Ti_{(0.98)}Ga_{(0.02)}O_3$	132.65	134.36
4	$La_{(0.04)}Sr_{(0.96)}Ti_{(0.96)}Ga_{(0.04)}O_3$	132.75	134.35

For the doped samples, the ratios between the $SrCO_3$ $Sr3d_{5/2}$ and the C1s C=O are 1:1.06, 1:11, 1:1.03, and 1:1.3 respectively, thereby confirming $SrCO_3$. The ratio of the amount of $SrCO_3$ present in each sample compared to lattice Sr^{2+} is presented in Table 3.5. As observed from Figure 3.12 (d), the 4 mol% co-doped sample has the highest $SrCO_3$ amount.

Table 3.5: Ratio of $SrCO_3$ present in the doped samples as compared to undoped *$SrTiO_3$*

Sr No	Sample	$SrCO_3$: ($SrCO_3$ + $Sr3d_{5/2}$)
1	Undoped	0.08
2	$SrTi_{(0.98)}Ga_{(0.02)}O_3$	0.09
3	$SrTi_{(0.96)}Ga_{(0.04)}O_3$	0.07

4	$La_{(0.02)}Sr_{(0.98)}Ti_{(0.98)}Ga_{(0.02)}O_3$	0.07
5	$La_{(0.04)}Sr_{(0.96)}Ti_{(0.96)}Ga_{(0.04)}O_3$	0.29

Both the $Sr3d_{5/2}$ and the $Sr3d_{3/2}$ peaks in the doped samples show shifts to lower binding energies when compared to undoped $SrTiO_3$. This shift is within error and hence, does not indicate a fermi-level shift. This analogy is borrowed from the work of Chattopadhyay, S et al. [67] who observed similar slight shifts. The split between the $d_{5/2}$ and the $d_{3/2}$ orbital in the case of the doped $SrTiO_3$ samples also shows a decrease at 1.71 eV (2 mol% Ga^{3+}), 1.71 eV (2 mol% La^{3+}, Ga^{3+}), 1.67 eV (4 mol% Ga^{3+}) and 1.6 eV (4 mol% La^{3+}, Ga^{3+}).

Ti2p

The $Ti2p_{3/2}$ peaks for the samples were analyzed and compared with the undoped in Figure 3.13. The deconvolution of the peaks indicates the presence of Ti^{3+} defects. On doping, it has been found that the Ti^{3+} defects decrease. In the undoped sample, the ratio of Ti^{3+}: (Ti^3 + Ti^{4+}) is 0.26:1. In the 2 mol% Ga^{3+} mono and 2 mol% La^{3+} co-doped samples, the ratios are 0.18:1 and 0.11:1 respectively. Similarly in the 4% Ga mono and 4% La, Ga co-doped samples, the ratios are 0.16:1 and 0.09:1 respectively. The 4 mol% La^{3+} co-doped samples had the lowest amount of Ti^{3+} defects among all the samples. This might be indicative of 4 mol% co-doping as the optimal doping to have the least Ti^{3+} defects as compared to the undoped. The main components of the XPS $Ti2p_{3/2}$ and $Ti2p_{1/2}$ peak are at 458.32 eV and 464.08 eV which can be attributed to Ti^{4+}. The ratio of A-site: B-site elements are tabulated in Table 3.6. The undoped $SrTiO_3$ shows a higher Ti^{4+} as seen in Table 3.6. The commercial undoped $SrTiO_3$ shows a ratio of 1.32:1 as shown in Table 3.1A in the Appendix. The $Ti2p_{3/2}$ and $Ti2p_{1/2}$ in all the doped samples show shifts to lower binding energies as compared to undoped samples as shown in Figure 3.14.

Table 3.6: Ratio of A-site: B-site Elements

Sr No	**Samples**	**Sr^{2+}: Ti^{4+}**	**Sr^{2+}: Ti^{4+} + Ga^{3+}**	**Sr^{2+} + La^{3+}: Ti^{4+} + Ga^{3+}**
1	$SrTiO_3$	1:1.25	-	-
2	$SrTi_{(0.98)}Ga_{(0.02)}O_3$	-	1:1.02	-
3	$La_{(0.02)}Sr_{(0.98)}Ti_{(0.98)}Ga_{(0.02)}O_3$	-	-	1:1.07
4	$SrTi_{(0.96)}Ga_{(0.04)}O_3$	-	1:0.99	-
5	$La_{(0.04)}Sr_{(0.96)}Ti_{(0.96)}Ga_{(0.04)}O_3$	-	-	1:1.2

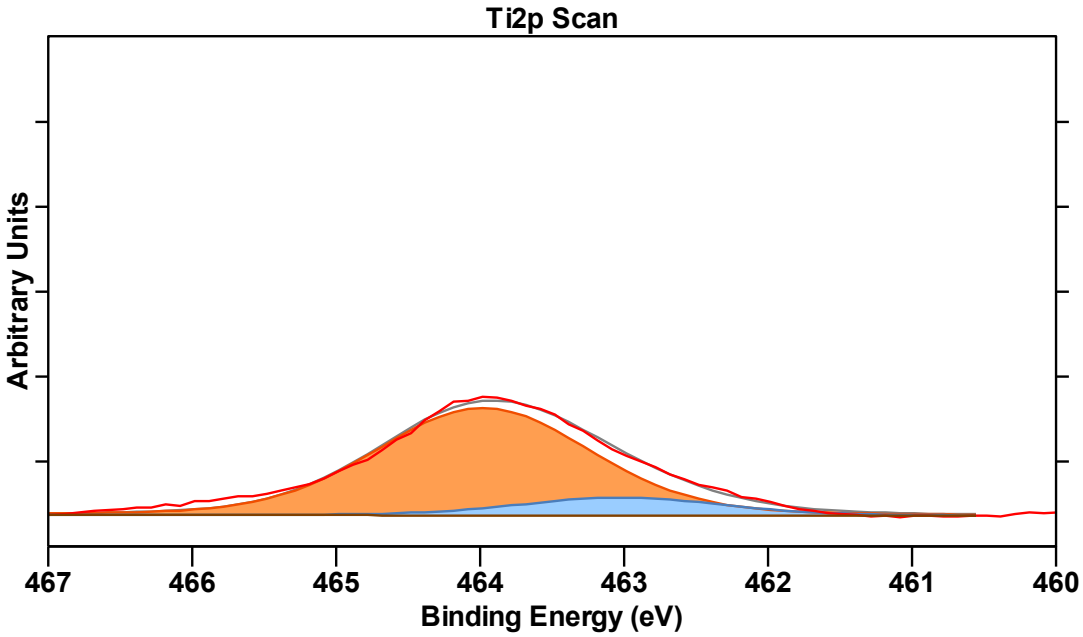


Figure 3.13: *XPS Ti2p Peak of Undoped $SrTiO_3$ with $Ti2p_{1/2}$ at 464.08 eV. The blue peak indicates the presence of Ti^{3+} defects.*

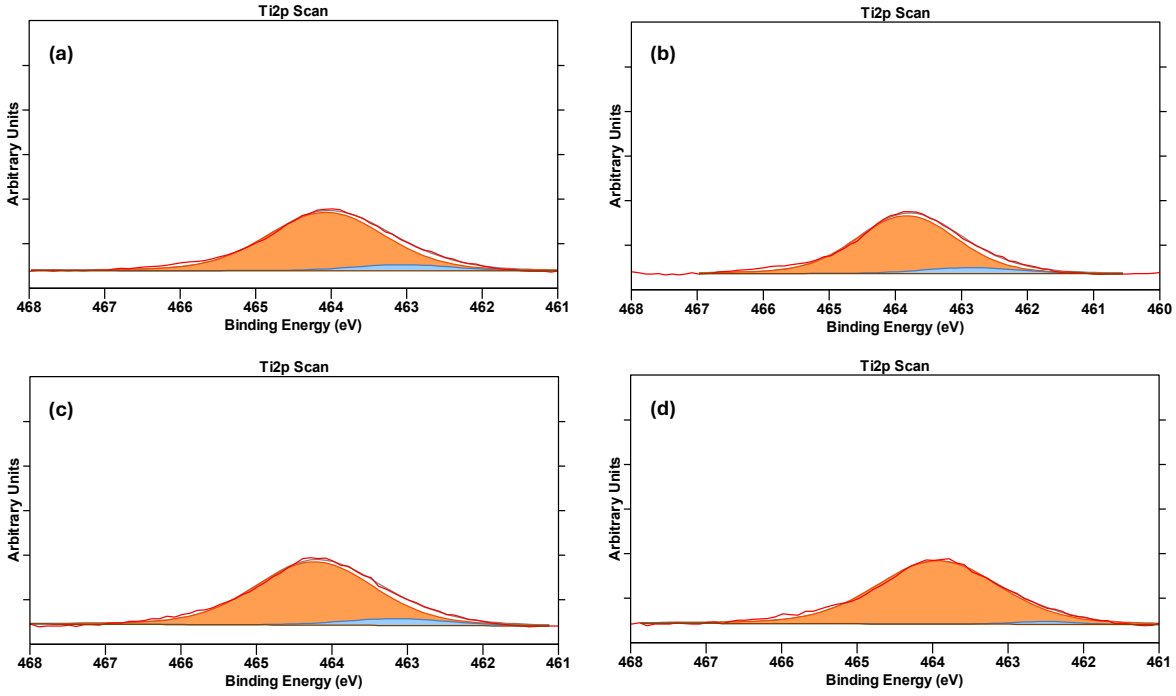


Figure 3.14: *The XPS $Ti2p_{1/2}$ peaks of (a) 2 mol% Ga^{3+} (b) 4 mol% Ga^{3+} (c) 2 mol% La^{3+} and (d) 4 mol% La^{3+} co-doped $SrTiO_3$. Ti^{3+} decreases upon doping with the co-doped samples showing lowest the concentration.*

O1s

The O1s peaks for the samples were analyzed and compared with the undoped in Figures 3.16 and 3.17. The deconvolution of all the samples showed secondary peaks at higher binding

energies. In the case of the undoped sample, the main component of the O1s peak at 529.50 eV can be attributed to lattice oxygen. The spectrum also show other components at higher binding energies of 530.43 eV, 530.91 eV, and 531.68 eV. These features can be attributed to carbonates, hydroxyl groups, and C-O-C groups respectively.

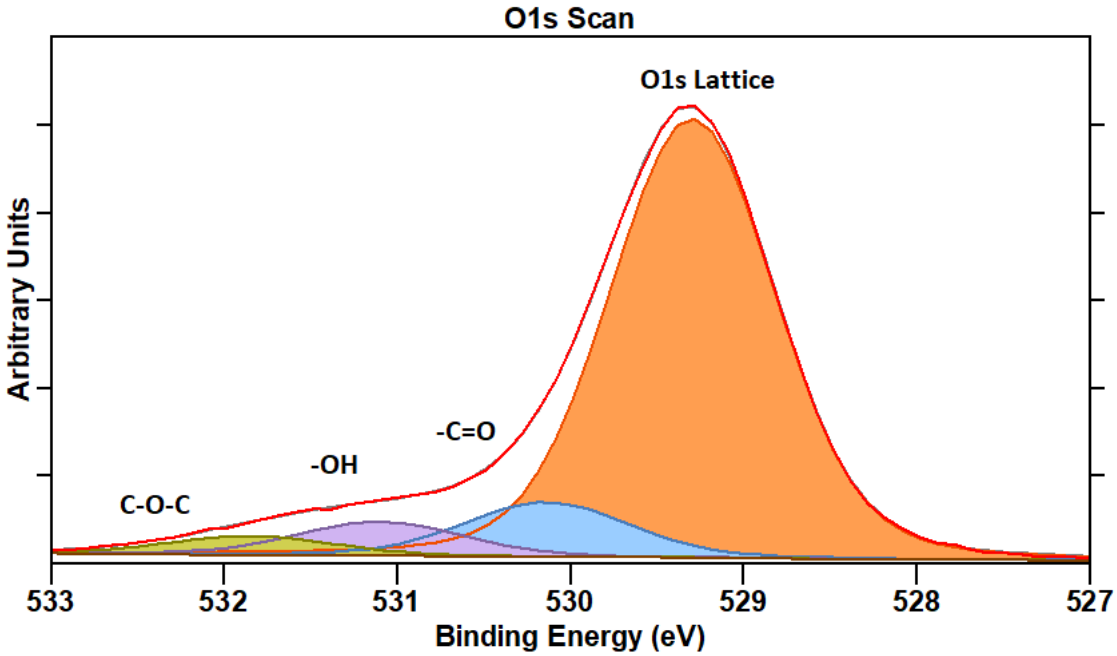


Figure 3.15: *XP spectrum of undoped O1s peak with the main component at 529.48 eV. Deconvolution shows the presence of -C=O, -OH and C-O-C.*

The O1s peak of the doped samples as shown in Figure 3.16 shows similar characteristics i.e., the presence of four peaks. However, all the peaks show shifts to lower binding energies.

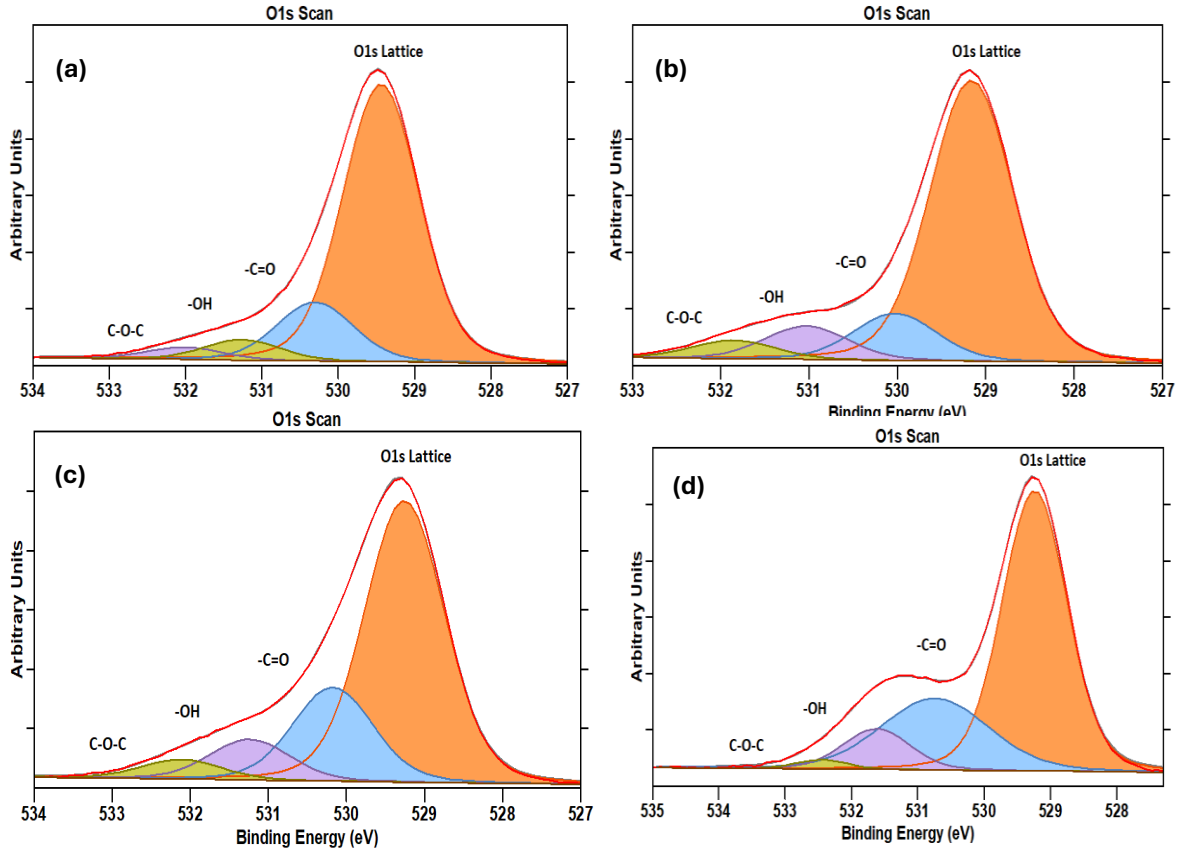


Figure 3.16: *Deconvoluted and charge corrected O1s peak of (a) 2 mol% Ga^{3+} (b) 4 mol% Ga^{3+} (c) 2 mol% La^{3+} and (d) 4 mol% La^{3+} co-doped $SrTiO_3$. The 4 mol% co-doped samples show significantly higher -C=O groups and an increase in -OH groups can be observed in all the doped samples.*

The peak positions of the O1s of the doped samples are given in Table 3.7.

Table 3.7: Peak Positions of the O1s lattice and the secondary peaks

Sr No	Samples	Lattice	-C=O	-OH	C-O-C
1	$SrTiO_3$	529.50 eV	530.40 eV	530.91 eV	531.68 eV
2	$SrTi_{(0.98)}Ga_{(0.02)}O_3$	529.48 eV	530.36 eV	530.86 eV	531.29 eV
3	$La_{(0.02)}Sr_{(0.98)}Ti_{(0.98)}Ga_{(0.02)}O_3$	529.25 eV	530.26 eV	531.02 eV	531.96 eV
4	$SrTi_{(0.96)}Ga_{(0.04)}O_3$	529.30 eV	530.29 eV	531.15 eV	532.22 eV
5	$La_{(0.04)}Sr_{(0.96)}Ti_{(0.96)}Ga_{(0.04)}O_3$	529.23 eV	530.37 eV	531.21 eV	531.81 eV

The presence of carbonate peaks is quite consistent with the Sr3d peaks which showed the presence of $SrCO_3$. The shoulders of the secondary peaks in the samples increase with higher doping % becoming more prominent in the co-doped samples. This could be due to the increased affinity for surface hydroxyls at the vacant oxygen sites introduced with increased %

doping [73]**.** The 4 mol% La^{3+} co-doped sample shows the highest amount of carbonate species consistent with the $SrCO_3$. The 4 mol% Ga shows the highest hydroxyl species.

La3d

From the XPS survey of the surface of 2 mol% and 4 mol% La, Ga co-doped $SrTiO_3$, the presence of La^{3+} is evident as shown in Figure 3.17 (a). The main peak of the $La3d_{5/2}$ and $La3d_{3/2}$ is at 833.89 eV and 847.31 eV for both 2% and 4% La, Ga co-doped $SrTiO_3$. These peaks can be attributed to La^{3+}. The $d_{5/2}$ and $d_{3/2}$ orbital have multiplet splitting values of 4.74 eV and 4.2 eV. Figure 3.17 (b, c) shows the EDX-confirmed dopant incorporation in the samples.

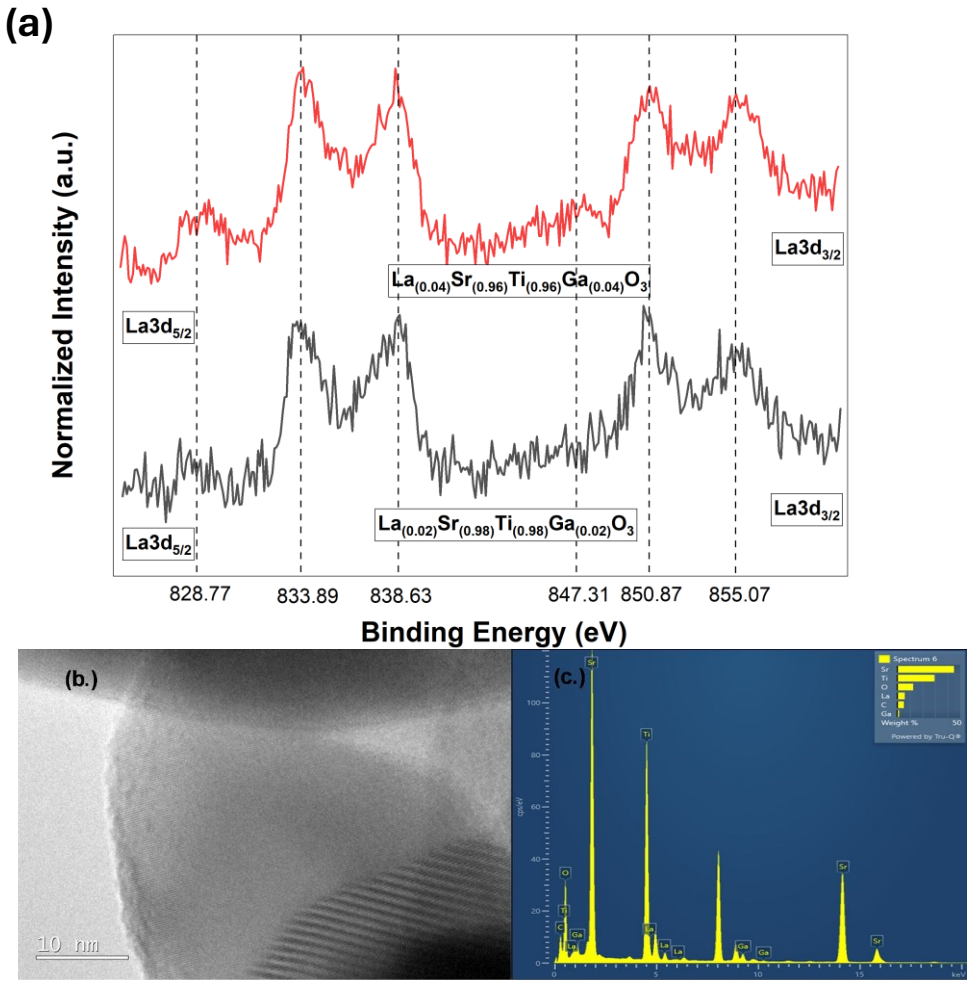


Figure 3.17: *(a) The XP spectrum of La3d peak with the main component of $d_{5/2}$ peak at 833.89 eV and the main component of $d_{3/2}$ at 850.87 eV (b, c) La^{3+} and Ga^{3+} incorporation confirmation with EDX in the 4 mol% co-doped sample. The EDX pattern with lower Ti^{4+} could indicate Ti vacancies.*

The La3d peak shows two satellites at lower binding energies than the $d_{5/2}$ and the $d_{3/2}$ peaks at 828.77eV and 847.31 eV. These satellites are called shake-down satellites as they appear towards lower binding energies of the main peaks. These lower binding energy satellites are

common in Lanthanum compounds and are reported to be due to a photo-electron being ejected from the atom [74]–[76].

Ga2p

From the XPS survey of the surface of 2 mol% Ga^{3+} doped, 2 mol% La^{3+}, Ga^{3+} co-doped, 4 mol% Ga^{3+} doped, and 4 mol% La^{3+}, Ga^{3+} co-doped $SrTiO_3$, the presence of Ga^{3+} is evident as shown in Figure 3.18. The main peaks of the $Ga2p_{3/2}$ and $Ga2p_{1/2}$ are at 1117.77 eV and 1144.69 eV for both mono and co-doped $SrTiO_3$. Metallic Ga has reported a $2p_{3/2}$ peak between 1117 eV-1118.10 eV and Ga_2O_3 has reported peaks in a very similar range between 1117.50 eV - 1117.80 eV [77]–[79]. Hence, XPS is not a useful method to distinguish between the two.

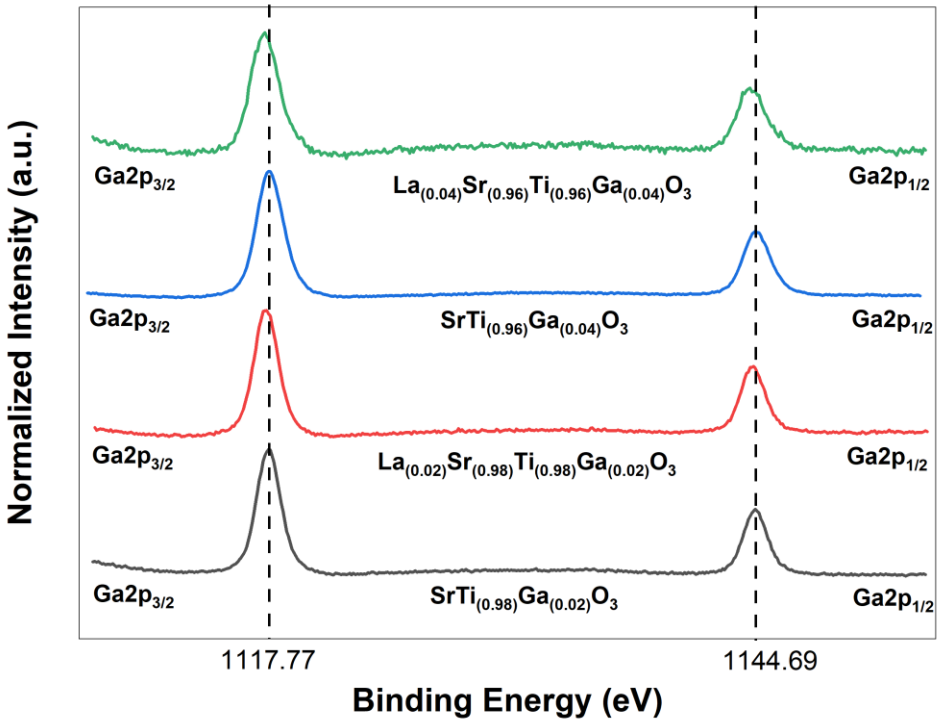


Figure 3.18: *The XP spectrum of $Ga2p_{3/2}$ and $Ga2p_{1/2}$ of the doped samples showed peaks around 1117.77 eV and 1149.69 eV respectively which matches closely with both Ga_2O_3 and metallic Ga.*

Percentage of Doping from the XPS and Time-Temperature-Solubility Factor

Table 3.8 (a) and (b) show the relative doping % to the element at the parent site i.e. Ga^{3+}/ (Ga^{3+} + Ti^{4+}) and La^{3+}/(La^{3+} + Sr^{2+}). Ga^{3+} doping is 10 - 18 times more than the intended 2 mol% and 4 mol%. Similar observations were also made by Dr. Benjamin Moss in his Ph.D. work on Rh: $SrTiO_3$ which was synthesized by high-temperature solid-state synthesis [80]. In his Ph.D. work, Dr. Moss reported that mol% Rh doping was 20 times higher than what was expected (4%) and solubility of Rh in $SrTiO_3$ increased with La^{3+} co-doping. In the case of Ga^{3+}, it could be temperature-time-solubility dependence. This finding will be studied in detail along with

the lower temperature synthesized batches to understand how temperature might affect this. As the synthesis temperature increased from 500°C-800 °C for 10 h, the relative doping increased. At 900 °C (6 h) and above, the solubility of Ga^{3+} could decrease and instead, it could have leached out of the lattice. This observation also can be correlated to the exsolution that was observed in the doped samples. O1s peaks indicate oxygen non-stoichiometry and are positively correlated to Figure 34(a) to be oxygen deficient. The ratio of $Sr3d_{5/2}$: $Ti2p_{3/2}$ is 0.905 and 0.98 respectively for the 2 mol% monodoped and co-doped samples. This indicates that a Sr cation vacancy could also exist in the samples. For the 4 mol% mono- and co-doped samples the ratios are 1.09 and 1.05 respectively. This likely indicates the presence of Ti cation vacancy as indicated by the EDX in Figure 3.17 (c).

Table 3.8 a: Atomic % of Sr^{2+}, Ti^{4+} and O1s in the Synthesized Samples from the XPS

Samples	$Sr3d_{5/2}$ (At %)	$Sr3d_{3/2}$ (At %)	$Ti2p_{3/2}$ (At %)	$Ti2p_{1/2}$ (At %)	O1s (At %)
$SrTiO_3$	11.97	11.98	11.19	4.51	35.35
$SrTi_{(0.98)}Ga_{(0.02)}O_3$	10.20	10.21	11.26	4.93	32.02
$La_{(0.02)}Sr_{(0.98)}Ti_{(0.98)}Ga_{(0.02)}O_3$	9.29	9.30	9.55	3.95	27.62
$SrTi_{(0.96)}Ga_{(0.04)}O_3$	10.65	10.66	9.70	4.34	26.74
$La_{(0.04)}Sr_{(0.96)}Ti_{(0.96)}Ga_{(0.04)}O_3$	8.70	8.70	8.36	4.24	26.33

Table 3.8 b: Relative mol% doping from the XPS

Samples	$Ga2p_{3/2}$ (At %)	$Ga2p_{1/2}$ (At %)	$La3d_{5/2}$ (At %)	$La3d_{3/2}$ (At %)	Ga mol% Doping (Ga^{3+} / $Ga^{3+} + Ti^{4+}$)	La mol% Doping (La^{3+}/ $La^{3+} + Sr^{2+}$)
$SrTiO_3$					-	-
$SrTi_{(0.98)}Ga_{(0.02)}O_3$	2.56	1.47	-	-	19.4%	-
$La_{(0.02)}Sr_{(0.98)}Ti_{(0.98)}Ga_{(0.02)}O_3$	2.95	1.81	0.20 , 0.21	0.22 , 0.22	26%	4.4%
$SrTi_{(0.96)}Ga_{(0.04)}O_3$	4.89	2.81			35%	-
$La_{(0.04)}Sr_{(0.96)}Ti_{(0.96)}Ga_{(0.04)}O_3$	1.29	0.82	0.28 , 0.28	0.28 , 0.28	13.7%	6%

3.3.3 Understanding the Role of Defects on the Optoelectronic Properties

In this section, the opto-electronic properties of the samples were studied. The effect of doping on the bandgap, the reflectance spectrum, the PL, the TCSPC, the valence band and the work function are discussed systematically. The opto-electronic characterizations. The BEA is fundamental in understanding the nature of the conductivity i.e. whether the materials are n- or p-type. Intrinsic material parameters such as the electron affinity and the ionization potential have been studied for their impact on the material properties.

Effect of Doping on the Bandgap

Altering the band gap by narrowing it or by introducing mid-gap states can significantly affect the performance of a photocatalyst. To study the effect of doping Ga^{3+} and La^{3+} in $SrTiO_3$ diffuse reflectance spectroscopy (DRS) measurements were carried out. These measurements were done with a Shimadzu UV Vis instrument with an integrating sphere. The data were analyzed with the Kubelka-Munk function and the Tauc plots as discussed in Chapter 2. Figure 3.19 shows the reflectance spectrum and the indirect bandgap of the undoped $SrTiO_3$. The indirect bandgap of the undoped sample has been calculated from the Tauc plot to be 3.17 eV which is close to the value (3.2 eV) in the literature [81].

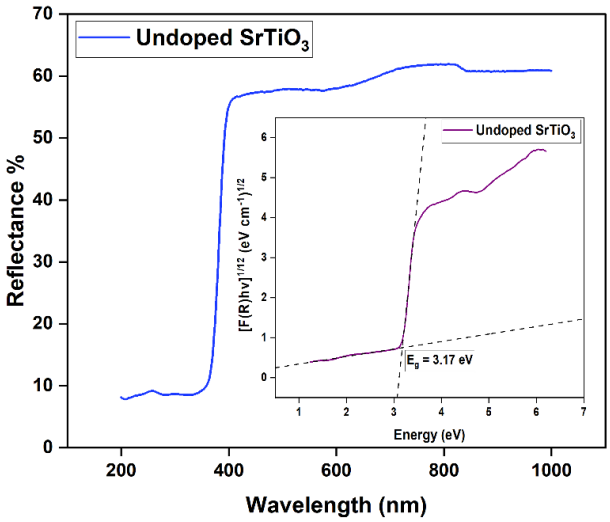


Figure 3.19: *Indirect bandgap (3.17 eV) and reflectance spectrum of undoped $SrTiO_3$. No absorption features were observed for this sample.*

Figure 3.20 demonstrates the difference in the reflectance spectrum and the indirect band gap between the 2 mol% mono- and co-doped samples. The co-doped sample shows an absorption feature and a low energy peak in the reflectance and the indirect bandgap respectively. The indirect bandgap of 2 mol% mono- and co-doped samples are 3.19 eV and 3.21 eV, respectively.

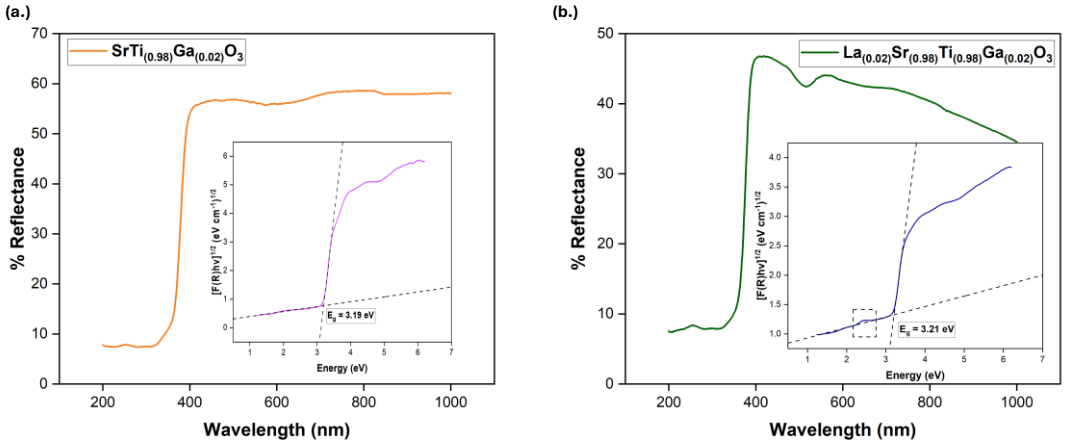


Figure 3.20: *Indirect band gap and reflectance spectrum of 2 mol% (a.) Ga^{3+} (3.19 eV) and (b.) La^{3+}, Ga^{3+} (3.21 eV) co-doped $SrTiO_3$. Both samples show a slight increase in the band gap compared to the undoped sample. The co-doped sample shows an absorption feature around 515 nm (2.25 eV) region.*

Figure 3.21 demonstrates the difference in the reflectance spectrum and the indirect band gap between the 4 mol% mono- and co-doped samples. The co-doped sample too shows an absorption feature in the reflectance spectrum and a low energy feature below the indirect bandgap. The indirect bandgap of 4 mol% mono- and co-doped samples are 3.19 eV and 3.23 eV, respectively.

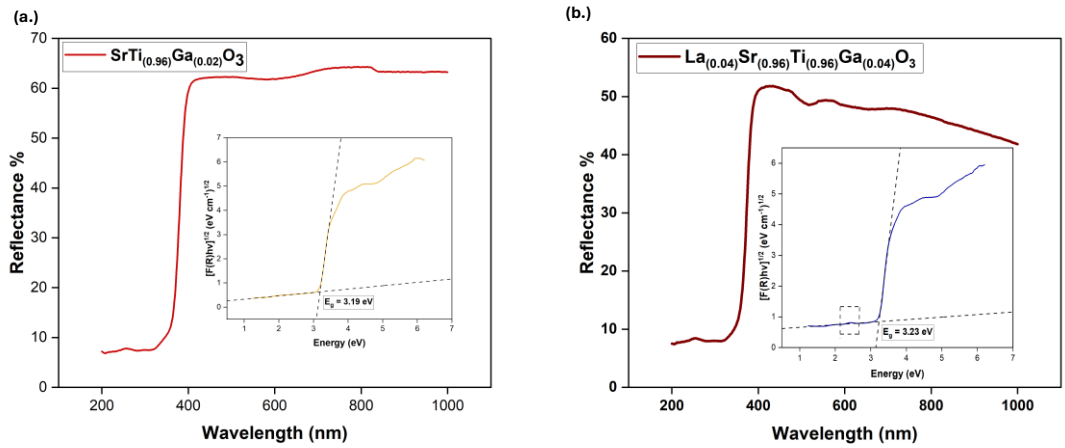


Figure 3.21: *Indirect band gap and reflectance spectrum of 4 mol% (a.) Ga^{3+} (3.19 eV) and (b.) La^{3+}, Ga^{3+} (3.23 eV) co-doped $SrTiO_3$. Both samples show similar band gaps as the 2 mol% co-doped sample. The 4 mol% co-doped sample also shows an absorption feature around 515 nm (2.25 eV) region.*

The indirect bandgaps of the monodoped samples increased slightly as compared to the undoped sample and both 2 mol% and 4 mol% had the same bandgap value. The co-doped samples showed an increase in the bandgap value at 3.21 eV (2 mol%) and 3.23 eV (4 mol%). No mid-gap states or visible light absorption was observed in the Ga^{3+} monodoped samples.

Most of the samples showed a behaviour like the undoped sample without any mid-gap states. However, the 2 mol% and 4 mol% La^{3+} co-doped deviated from the other samples in having a bluish-grey colour. On analysing the reflectance spectrum, these two samples showed dips in the visible light region around 515 nm as shown in Figure 3.22. The dips in the 515 nm region correspond to the blue-cyan region of the visible light spectrum. Compared to the undoped sample, the doped spectrum show a blueshift to lower wavelengths. This indicates a change in the band edge positions.

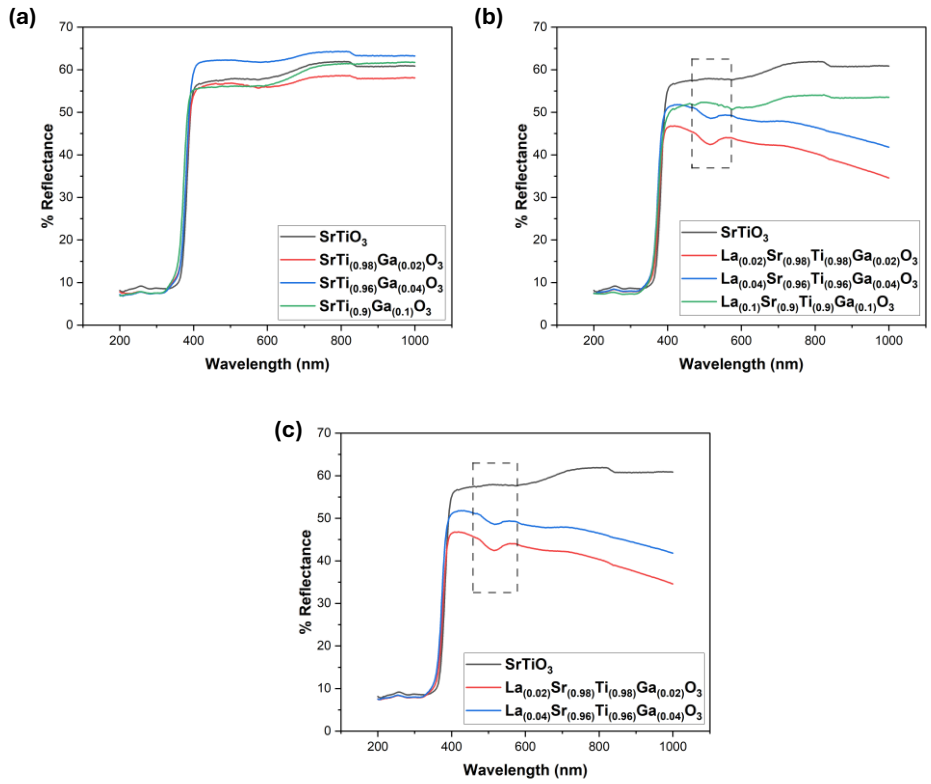


Figure 3.22: *Comparison of reflectance spectra of (a) Ga^{3+} (b) La^{3+} and (c) Comparison of La^{3+}, Ga^{3+} co-doped $SrTiO_3$ samples with the undoped $SrTiO_3$. The 2 mol% and the 4 mol% co-doped samples differ from all the samples in exhibiting absorption features at 515 nm.*

Mishra, V. et al. [82] observed in their study that similar low energy peaks between 1.5 eV and 2.75 eV below the bandgap of their materials- TiO_2, ZnO, and ZrO_2. The fundamental experimental technique they employed was DRS to study the materials. They compared their experimental data with DFT simulations which relate the low energy peak to oxygen vacancies. They report that in TiO_2 oxygen-deficient systems, the states near the fermi level are dominated by both Ti3d (t_{2g} and e_g states) and the O2p, with the p_x orbital having the highest contribution. The formation of doubly ionized oxygen vacancies is accompanied by Ti^{3+} defects. The presence of Ti^{4+} and Ti^{3+} (t_{2g} and e_g) orbitals near the fermi level results in rehybridization between the Ti3d and O2p. This leads to the formation of the low energy peak below the bandgap. This theory aligns with the previous XRD observations about doubly ionized oxygen vacancies and Ti^{3+} defects. Oxygen vacancies are the predominant factor causing the low energy absorption features around 2.4 eV.

Even though the co-doped samples showed absorption features in the visible light region, the absorption edge in these samples showed a blueshift from the undoped $SrTiO_3$ edge indicating that both the mono- and co-doped samples can absorb high-energy UV photons at shorter wavelengths. This indicates a definite change in the opto-electronic properties upon doping. Figure 3.23 demonstrates the absorption spectrum and bandgaps from the Kubelka Munk Function. The absorption wavelengths are listed in Table 3.9. In Figure 3.23 (a) and (b), the absorption spectrum of the La^{3+} co-doped samples shows absorption beyond 1000 nm into the NIR region. This could also influence the bluish-grey colour of the co-doped samples.

Table 3.9: Bandgaps and absorption wavelengths of the synthesized samples

Sr No.	Samples	Wavelengths (nm)	Indirect Bandgap (eV)	Direct Bandgap (eV)
1	$SrTiO_3$	389.60	3.17	3.29
2	$SrTi_{(0.98)}Ga_{(0.02)}O_3$	384	3.19	3.30
3	$SrTi_{(0.96)}Ga_{(0.04)}O_3$	380.70	3.19	3.30
4	$La_{(0.02)}Sr_{(0.98)}Ti_{(0.98)}Ga_{(0.02)}O_3$	385.70	3.21	3.29
5	$La_{(0.04)}Sr_{(0.96)}Ti_{(0.96)}Ga_{(0.04)}O_3$	380	3.23	3.34

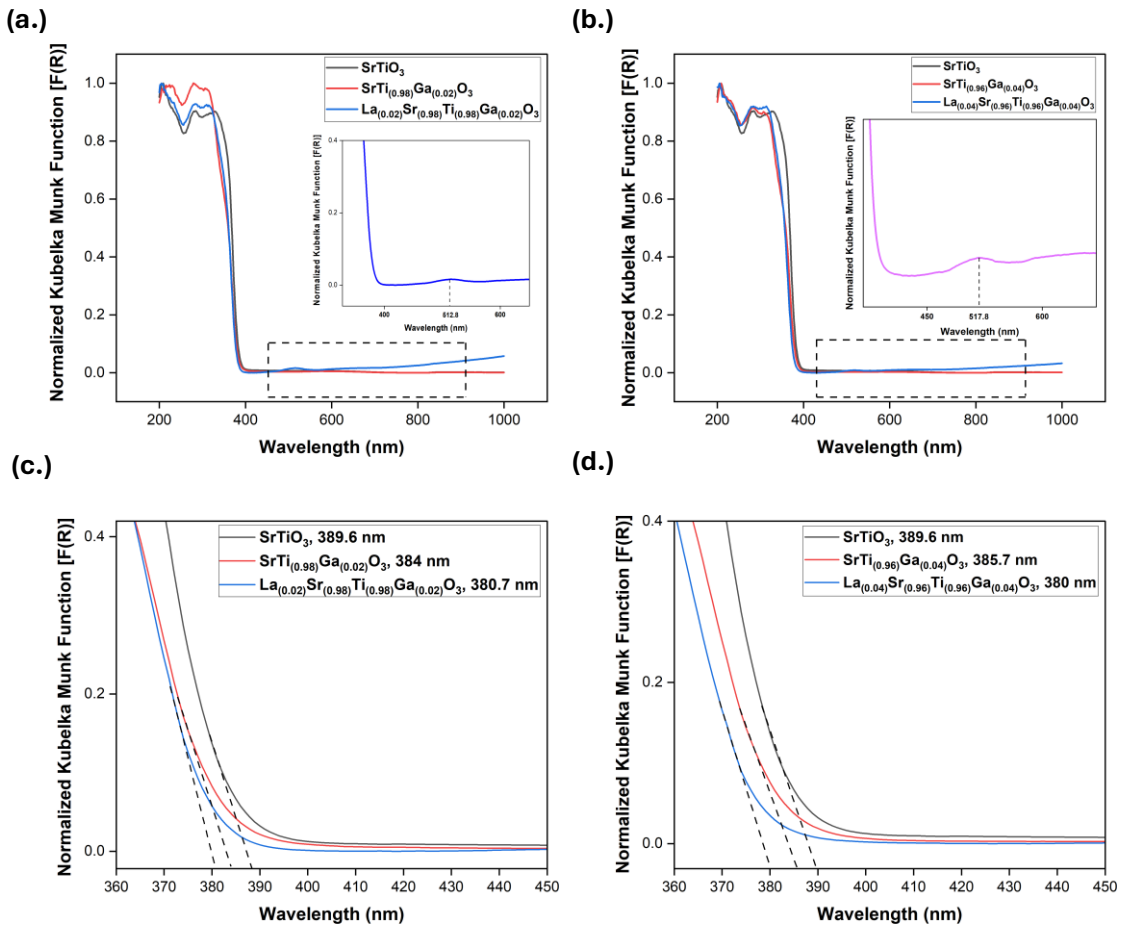


Figure 3.23: *(a.), (b.) Absorption spectrum highlight the absorption feature that is present in the co-doped samples and the extension of the absorption into the NIR region. These features are absent in the undoped and the monodoped samples.(c.), (d.) Blue shifted absorption wavelengths of the Ga^{3+} and La^{3+}, Ga^{3+} doped samples.*

Steady State Photoluminescence (PL) Analysis

Steady-state PL studies facilitate the understanding of shallow and deep-level defects in materials [83]. PL characterization is based on the recombination of e^-/h^+ pairs. This recombination can take place with the emission of a photon (radiative) or loss of energy through interaction with defects in the materials. In PL analysis, the spectrum is observed when the emission of photons occurs on exciting a material with light of a specific wavelength. Figure 3.24 shows the comparison of the PL spectrum of the Ga^{3+} and La^{3+}, Ga^{3+} doped samples. The samples studied in this work were excited with a wavelength of 295 nm at room temperature. A broad peak covering 350 nm to 438 nm with varying intensity can be observed. Two additional low-intensity peaks were observed around 463 nm and 500 nm. A broad peak indicates multiple recombination pathways. These recombination pathways might be from the localized states introduced by point defects such as vacancies [83], [84]. In both cases of doping, the $SrTiO_3$ has a lower PL intensity than the doped samples. This indicates that the non-radiative recombination pathways in the doped samples are getting suppressed. Li, R. et al. [8] reported an increase in the PL intensity of Al^{3+}: $SrTiO_3$ as compared to undoped $SrTiO_3$

due to suppression of deep-level Ti^{3+} trap states. Due to charge compensation mechanisms in La^{3+} co-doped samples, Ti^{3+} defects are prevalent. As discussed earlier, the blue color from dark to lighter as the mol% doping increases. This may be due to the decrease in Ti^{3+} defect content in the materials. La^{3+} co-doping suppresses these defect centres which increases the PL intensity of the samples. Similar suppression of defect-induced trap states results in higher PL intensity of the monodoped samples. In both cases of doping, the 2 mol% doped sample showed the highest PL intensity. The 2 mol% co-doped also has the lowest dislocation density and hence, lesser the possibility of non-radiative trappings.

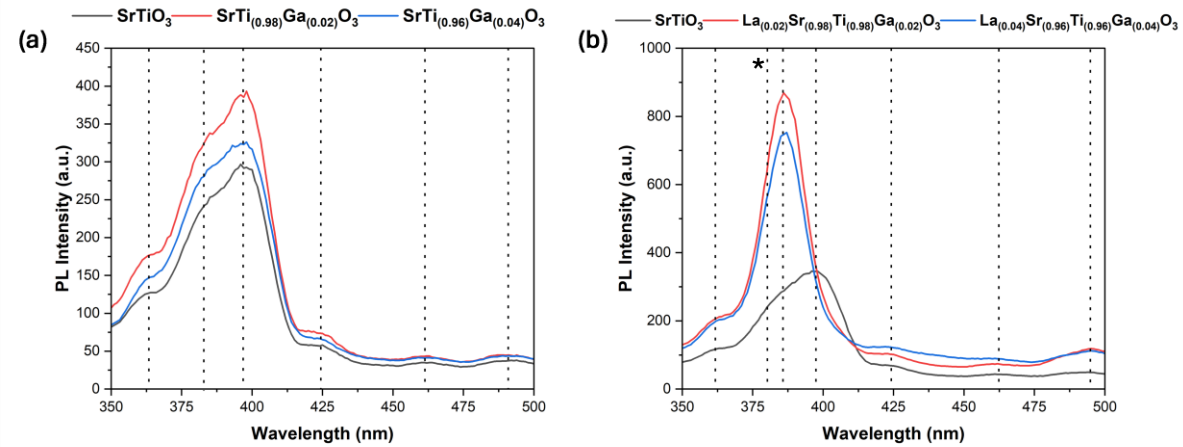


Figure 3.24: *The PL spectrum of (a.) Ga^{3+} (b.) La^{3+} doped $SrTiO_3$ samples were compared with undoped $SrTiO_3$, with the main PL peaks represented by the dotted lines. The 2 mol% (co-) doped samples show higher PL in both cases. In 3.25 (b), the line with the * represents the deconvoluted peak present only in the undoped sample.*

From Figure 3.24 (a) the broad PL peaks can be deconvoluted into multiple peaks at 363 nm (3.43 eV), 385 nm (3.22 eV), 397 nm (3.12 eV), 424 nm (2.93 eV), 463 nm (2.68 eV) and 490 nm (2.53 eV) for the monodoped samples. The La^{3+} co-doped sample exhibits peaks at 363 nm (3.43 eV), 390 nm (3.18 eV), 424 nm (2.93 eV), 463 nm (2.68 eV), and 490 nm (2.53 eV). Each of these peaks represents the transition states. The 397 nm peak is absent in the co-doped samples. The peak around 500 nm present in all the samples could be due to the recombination of electrons and holes coupled in a self-trapped exciton (STE) state [84]–[86]. STE peaks become more prominent at lower temperature PL measurements. At 397 nm and 463 nm, the emission could be linked to $\ddot{V}_O$ and $\dot{V}_O$ [87]. At 363 nm, this emission could be due to the Ti^{3+} t_{2g} states of the TiO_6-octahedra [88]. Alternatively, the transmissions can be from Ga or Ti interstitials or vacancies. The PL emission data aligns with the previous data analysis about the presence of oxygen vacancies. Oxygen vacancies add levels close to the conduction bands which act as shallow donors [8]. The samples were irradiated with 4.2 eV (295 nm) which is higher energy than the band gaps of these materials. Therefore, the most intense peak around 385 nm for the samples could indicate near-band edge (NBE) transitions from the valence to the conduction band. This aligns with the E_g of the samples observed with the DRS. In the samples synthesized in this study, the contributions from oxygen vacancy-related defect energy levels can be observed.

Steady-state PL helped in understanding the recombination suppression of the non-radiative pathways present in the synthesized materials. To better understand the recombination dynamics and carrier lifetimes in the samples, time-resolved PL techniques such as the TCSPC were employed.

Determination of the nature of the doped samples based on the type of bandgap from the DRS-UV Vis and PL

An important aspect of study is the nature of the band gaps of the samples synthesized in the Ph.D. work. Whether a material has a direct or an indirect band gap influences the electron-hole dynamics and photoreactivity [89], [90]. From the DRS analysis, the direct and indirect bandgaps of the materials were measured as shown in Figure 3.25. In direct band gap materials, direct transitions from VB_M to CB_{Min} take place with radiative recombination between e^- and holes [89]. Whereas in indirect bandgap materials, direct recombination cannot take place due to CB_{Min} and VB_M having different momentum in the Brillouin zone [89], [90]. Zanatta, A.R. [91] reports that to identify the nature of the band gap one should look for the plot that exhibits a clear linear region for fitting. In the case of the doped samples in this study, both direct and indirect plots exhibit a well-defined linear region. Therefore, whether the materials exhibit more direct or indirect bandgaps cannot be judged solely on the DRS data. From the PL analysis, both types of doping resulted in higher PL intensity indicating the dominance of radiative recombination processes via the suppression of non-radiative pathways [92], [93]. The higher PL intensity in these samples indicates a dominance of radiative recombinations which are more efficient in direct bandgaps as discussed above. Henceforth, based on this assumption in this study, the materials will be considered to possess a direct bandgap when they show stronger relative PL intensity. The (co-) doped materials exhibited higher PL intensity than the undoped sample and all the band edge alignments were done considering the direct bandgaps.

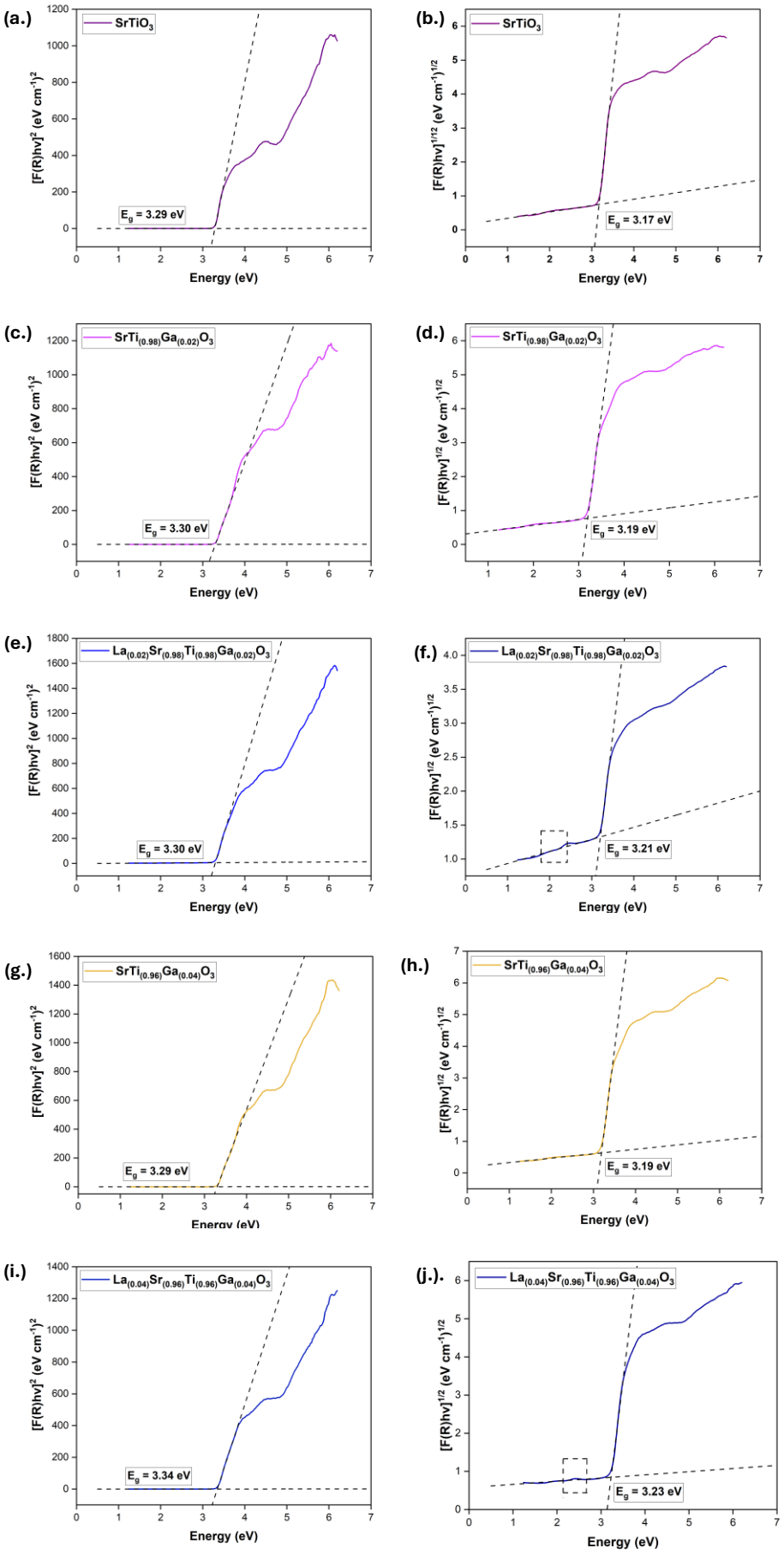

(a.)
SrTiO3
Eg = 3.29 eV
[F(R)hν]2 (eV cm-1)2
Energy (eV)
(b.)
SrTiO3
Eg = 3.17 eV
[F(R)hν]1/2 (eV cm-1)1/2
Energy (eV)
(c.)
SrTi(0.98)Ga(0.02)O3
Eg = 3.30 eV
[F(R)hν]2 (eV cm-1)2
Energy (eV)
(d.)
SrTi(0.98)Ga(0.02)O3
Eg = 3.19 eV
[F(R)hν]1/2 (eV cm-1)1/2
Energy (eV)
(e.)
La(0.02)Sr(0.98)Ti(0.98)Ga(0.02)O3
Eg = 3.30 eV
[F(R)hν]2 (eV cm-1)2
Energy (eV)
(f.)
La(0.02)Sr(0.98)Ti(0.98)Ga(0.02)O3
Eg = 3.21 eV
[F(R)hν]1/2 (eV cm-1)1/2
Energy (eV)
(g.)
SrTi(0.96)Ga(0.04)O3
Eg = 3.29 eV
[F(R)hν]2 (eV cm-1)2
Energy (eV)
(h.)
SrTi(0.96)Ga(0.04)O3
Eg = 3.19 eV
[F(R)hν]1/2 (eV cm-1)1/2
Energy (eV)
(i.)
La(0.04)Sr(0.96)Ti(0.96)Ga(0.04)O3
Eg = 3.34 eV
[F(R)hν]2 (eV cm-1)2
Energy (eV)
(j.).
La(0.04)Sr(0.96)Ti(0.96)Ga(0.04)O3
Eg = 3.23 eV
[F(R)hν]1/2 (eV cm-1)1/2
Energy (eV)

Figure 3.25: *(a.), (c.), (e.), (g.), (i) Direct and (b.),(d.), (f.),(h.), (j.) Indirect band gaps of the samples. In this study, the nature of bandgaps has been determined from the PL with higher intensity indicating more efficient radiative recombinations.*

From Figure 3.25 and Table 3.9, the direct band gaps of the doped materials did not show significant changes except for the 4 mol% La^{3+} co-doped samples with 3.34 eV. From the PL, the nature of the doped materials has been identified as direct and henceforth, this band gap will be used during the band edge alignment. Bandgaps are one of the intrinsic parameters that are important for identifying the band edges and determining the photoactivity towards a reaction. Intrinsic parameters are crucial for understanding the charge carrier dynamics in a photocatalyst. A systematic study of the intrinsic parameters has been undertaken in this work which are discussed in the subsequent sections.

Time-correlated Single Photon Counting (TCSPC)

Time-resolved PL spectroscopy via TCSPC is essential for measuring the recombination lifetimes of the samples. The average lifetimes of the samples shown in Figure 3.26 were measured from the exponential fitting via the HORIBA Da6.8 software and reconvoluted decay time constants are shown in Table 3.10. All samples were measured at λ_{exc} = 282 nm.

The average lifetimes of the samples were measured from the exponential fitting via the TCSPC software which are listed in Table 4 and shown in Figure 3.26.

Table 3.10: Average lifetime of the samples

Sr No	Sample	Average Lifetime, t (ns)[a]
1	Undoped	0.15 ± 0.01
2	2% Ga doped $SrTiO_3$	0.14 ± 0.02
3	2% La, Ga co-doped $SrTiO_3$	0.17 ± 0.01
4	4% Ga doped $SrTiO_3$	0.19 ± 0.02
5	4% La, Ga co-doped $SrTiO_3$	0.22 ± 0.04

[a] *The errors in the lifetimes were added after remeasuring the samples and refitting the data*

From Table 3.10 and Figure 3.26(b), both the co-doped samples have a higher average lifetime as compared to the undoped and the monodoped samples. The 4 mol% La^{3+} co-doped $SrTiO_3$ has the highest average lifetime. Even though the 2 mol% co-doped showed higher PL intensity and lower dislocation density, the 4 mol% co-doped sample exhibited higher lifetimes. Li, R. et al. [8], reported that undoped $SrTiO_3$ has longer lifetimes when measured in air than the Al^{3+} doped $SrTiO_3$. They explained this phenomenon in terms of the surface depletion effect due to the absorption of oxygen species on the sample surfaces. They reported that the surface-adsorbed oxygen captured free electrons resulting in a surface depletion layer that separates photogenerated e^-/h^+. This could lead to a lower lifetime in the 2 mol% co-doped sample as compared to the 4 mol% sample. The amount and the effect of adsorbed oxygen will be discussed in the band energy diagram section with further analysis of the adsorbed -OH groups.

The undoped sample has a lower PL signifying the presence of defects that are detrimental to lifetimes.

Correlating higher PL intensity and higher lifetimes is hard to apply to the monodoped samples. The monodoped samples showed similar lifetimes with the undoped as shown in Figure 3.26(a). This phenomenon can be correlated with the dislocation density calculated in the previous section. The Ga^{3+} monodoped samples exhibit higher dislocation densities as shown in Table 3.3. Due to their presence in higher concentrations, these defects could act as sinks for point defects to act as traps that obstruct charge carrier mobility. These traps lead to faster recombinations lowering the lifetimes of the monodoped samples. A contradiction to this observation has been reported by Blumenau, A. et al. [55]. They reported a higher PL due to interstitial clusters around the dislocations in Si. Alternatively, the surface-adsorbed oxygen could also inhibit the lifetimes in the monodoped samples.

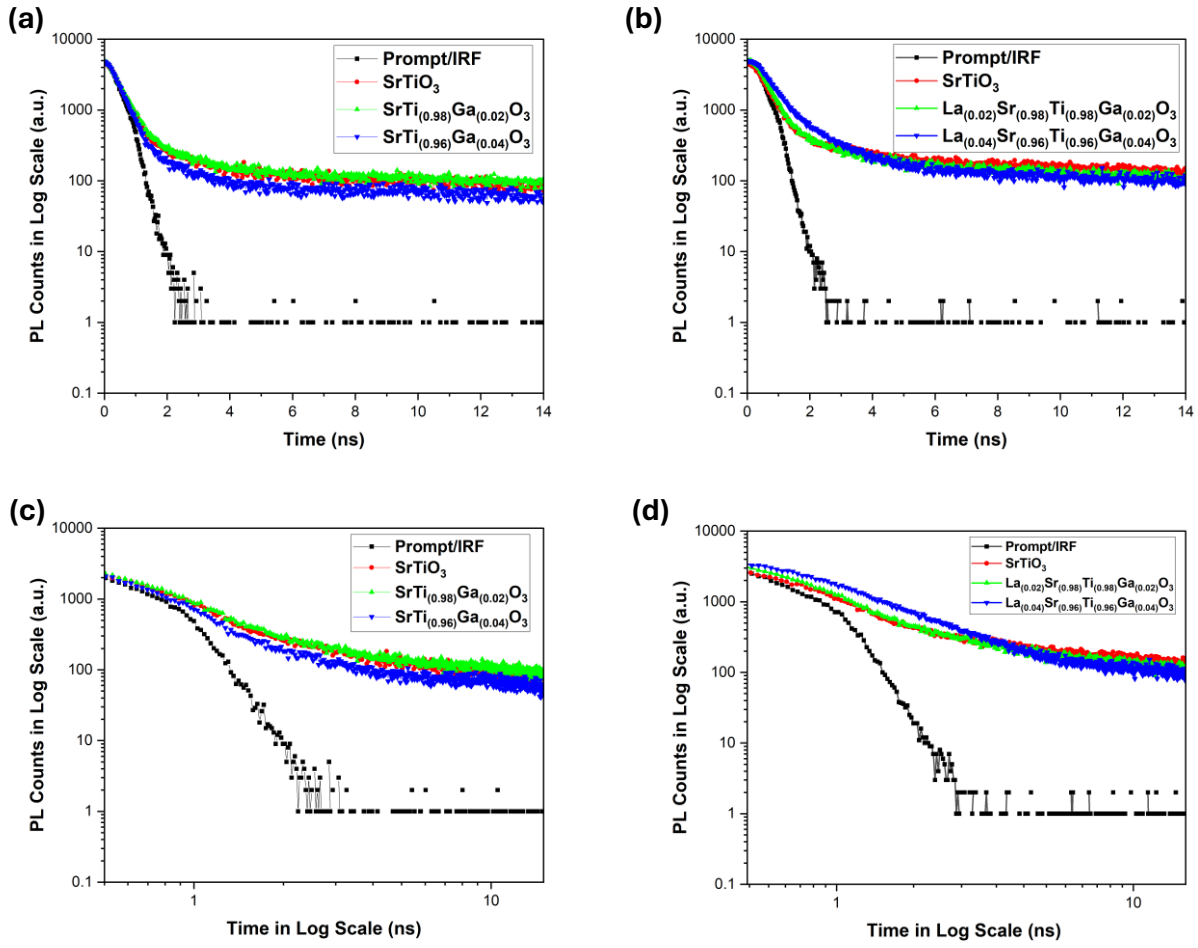


Figure 3.26: *Average room temperature TCSPC lifetimes of (a) Ga^{3+} (b) La^{3+}, Ga^{3+} doped $SrTiO_3$ samples (c), (d) shows the plots with the time in log scale to highlight the lifetime change in the samples. The 4 mol% co-doped sample shows the highest lifetime. The log-log plot is utilized to magnify small differences i.e. by applying logarithmic scaling to both axes, subtle deviations in the decay dynamics become more discernible.*

Charge carrier dynamics is an important aspect of understanding the performance of a photocatalyst. However, as Li, R. et al. [8] in their work reports that higher lifetimes are not always an indicator of the higher quantum efficiency of the catalysts. They emphasize more on the charge extraction methods that determine the efficiency of the photocatalysts. Hence, other material properties should be considered as well while determining the performances. Concerning the other opto-electronic properties of the synthesized materials, the valence band maxima position was studied with the XPS, and the spectrum are discussed in the subsequent section.

Effect of Doping on the Valence Band

Figures 3.28 and 3.29 show the normalized valence band spectrum measured with the XPS. The spectrum show the main peaks between 3 eV to 8 eV which aligns with the literature [94], [95]. The feature between 3 eV to 8 eV is due to the hybridization between the O2p and the Ti3d states. For the undoped sample, the linear extrapolation fittings gave a valence band maximum (VB_M) and the fermi level (E_F) separation at 2.21 eV at the intersection of the two fitted lines as shown in Figure 15. Moss, B. et al. [95] reported the VB_M-E_F separation to be 1.8 eV. This is mainly due to the linear fitting of one edge. Jiang, D. et al. [96] reported a VB_M-E_F separation of 2.12 eV with a double fitting close to the value obtained in this work.

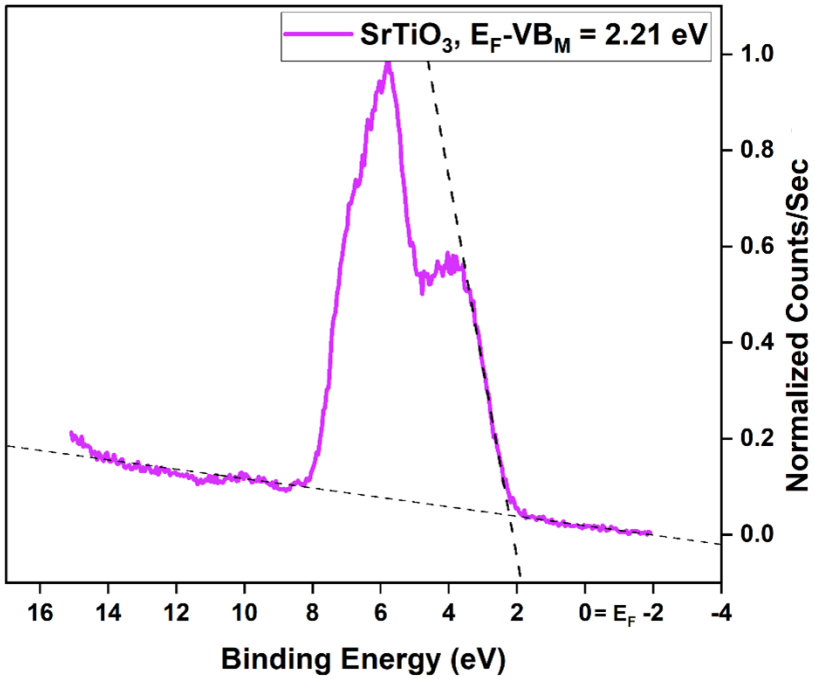


Figure 3.27: *VB_M-E_F separation of undoped $SrTiO_3$ at 2.21 eV. The VB_M-E_F separation was measured at the intersection of the linear fittings. The counts/sec on the Y-axis are measured in arbitrary units, a.u.*

The VB_M analysis of the doped samples showed the main features of the spectrum between 3 eV to 8 eV as the undoped shown in Figure 3.28. Alarab, K. et al. [94] observed additional

states between 2-2.5 eV binding energy of their Ni-doped $SrTiO_3$ which was attributed to additional states being introduced above the VB_M. Moss, B. et al. [95] attributed the visible light absorption in Rh-doped $SrTiO_3$ to doping-induced states introduced above the VB_M. In the samples synthesized in the Ph.D. work, no such states were observed which aligns with the UV Vis data where no additional mid-gap states were observed. Hence, band gap narrowing was not observed for the Ga^{3+} and La^{3+} co-doped samples as no states were introduced in the bandgap. The VB_M-E_F of the doped samples is summarized in Table 3.11.

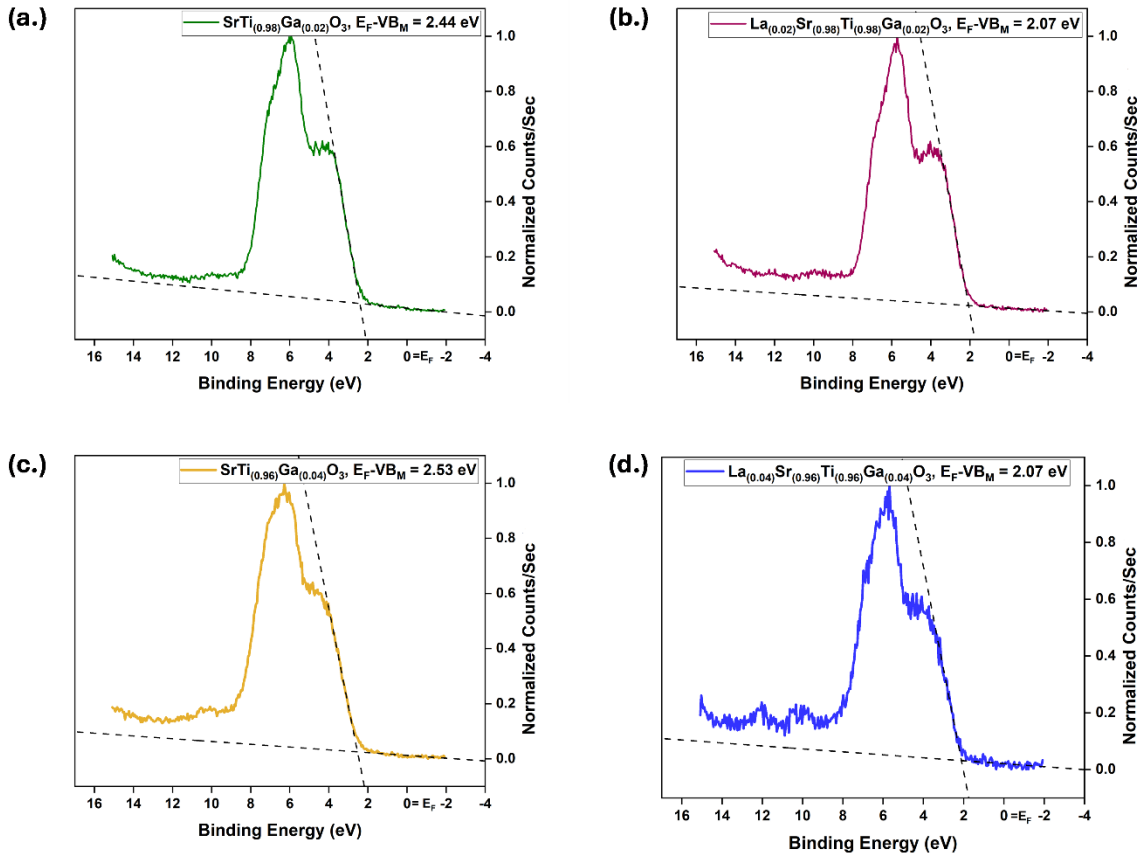


Figure 3.28: *VB_M-Fermi level separation of (a) 2 mol% Ga^{3+} (b) 2 mol% La^{3+}, Ga^{3+} (c) 4 mol% Ga^{3+} (d) 2 mol% La^{3+}, Ga^{3+} doped $SrTiO_3$. The monodoped samples show a higher E_F-VB_M separation whereas on co-doping the separation decreases indicating a decrease in n-type nature. The counts/sec on the Y-axis are measured in arbitrary units, (a.u.).*

Table 3. 11: VB_M-E_F separation of the doped samples

Sr No.	Samples	VB_M-E_F Separation (eV)
1	$SrTiO_3$	2.21
2	$SrTi_{(0.98)}Ga_{(0.02)}O_3$	2.44
3	$SrTi_{(0.96)}Ga_{(0.04)}O_3$	2.53
4	$La_{(0.02)}Sr_{(0.98)}Ti_{(0.98)}Ga_{(0.02)}O_3$	2.07
5	$La_{(0.04)}Sr_{(0.96)}Ti_{(0.96)}Ga_{(0.04)}O_3$	2.07

The VB_M edge of the 2 mol% and the 4 mol% Ga^{3+} monodoped sample shifts to higher binding energy as compared to the undoped indicating a more n-type nature as shown in Table 3.11. The increase in n-type nature with Ga^{3+} doping is consistent with the work of Neagu, D. et al. [97]. The VB_M edge of the 2 mol% and the 4 mol% La^{3+} co-doped sample shifts to lower binding energy as compared to the undoped reducing the n-type nature. Both the observed shifts are counterintuitive as Ga^{3+} is an acceptor and La^{3+} is a donor-type dopant. This can be rationalized through the presence of doubly ionized oxygen vacancies and the electrons as shown in Eq (3.5). These electrons reduce the Ti^{4+} to Ti^{3+} which increases the n-type nature. With the co-doping, the Ti^{3+} reduces as seen in the PL intensity in Figure 3.24(b). The suppression of Ti^{3+} could decrease the n-type nature and therefore, push the fermi level lower in the co-doped samples. In the monodoped samples, higher charge compensation with Ga^{3+} doping could happen with the formation oxygen vacancies (doubly ionized) rather than Ti^{3+}. Therefore, these point defects can act as electron donor to the conduction band increasing the n-type behaviour.

The valence band analysis helps us understand how doping affects the nature of the conductivity of the samples. The positions of the VB_M, the $CB_{Min,}$ and the bandgap help in the band edge alignment from which the photoactivity of the doped materials can be predicted. For the overall band edge alignment, the position of the fermi level is as important. To calculate the position of the fermi level, the work function (ϕ) must be determined. The work function measurement is discussed in detail in the following section.

Effect of Doping on the Work Function

The work function is defined as the minimum energy required to remove an electron from the fermi level to a point in vacuum [98]. As discussed in the previous chapter, the work function arises from two contributions- a surface and a bulk component [99]. Since photocatalysis is a surface phenomenon therefore the surface contribution of the ϕ. The work function in this study was calculated from the secondary electron cut-off measured with the XPS. The Cut-off Energy ($E_{cut\text{-}off}$) is the region in the graph that was linearly fitted as shown in Figures 3.29 and 3.30. The samples were subjected to a photon energy ($h\nu$) of 29.47 eV. The following Eq was used to measure the work function.

$$\text{Work Function, } \phi = h\nu - E_{cut\text{-}off} \qquad (3.11)$$

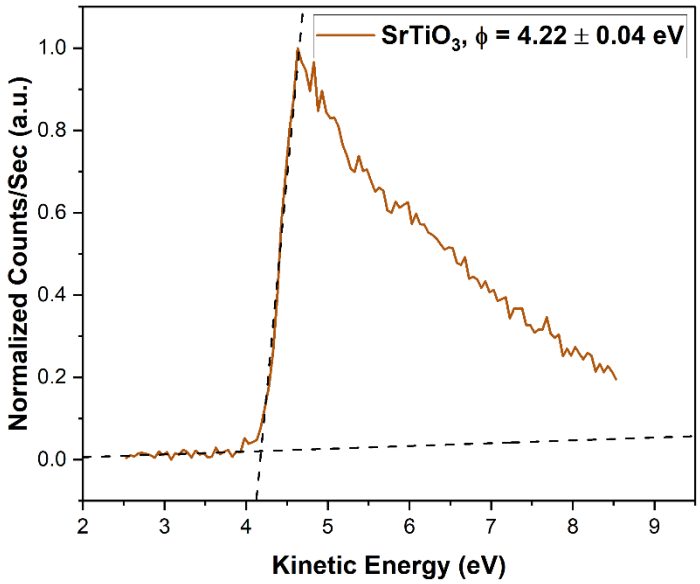


Figure 3.29: *Measurement of the ϕ of undoped $SrTiO_3$ from the $E_{cut\text{-}off}$ from the XPS. The y-axis is measured in counts/sec with arbitrary units (a.u.).*

Figure 3.29 shows the measured work function of the undoped $SrTiO_3$ at 4.22 eV from the XPS. The cut-off spectrum show a single peak for the samples indicating clean surfaces. Figure 3.30 shows the spectrum for the doped samples.

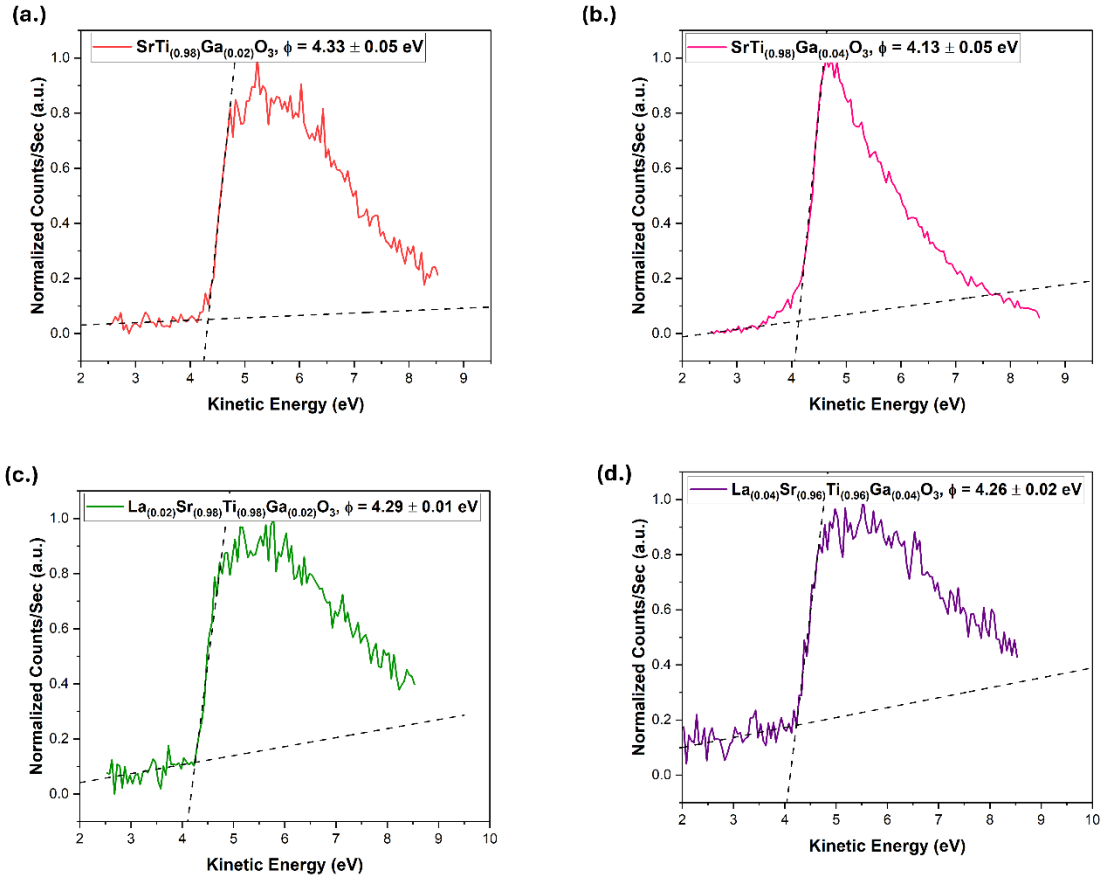


Figure 3.30: *Measurement of the work function of (a) 2 mol% Ga^{3+} (b) 4 mol% La^{3+} (c) 4 mol% Ga^{3+} and (d) 4 mol% La^{3+} doped $SrTiO_3$ showing an increase in the work function in most samples except the 4 mol% Ga^{3+} monodoped sample.*

No trend can be identified in the work function of the samples. The 2 mol% Ga^{3+} monodoped sample showed an increase in ϕ compared to the undoped. In the 4 mol% Ga^{3+} monodoped samples, the work function decreases to 4.13 eV. In the 2 mol% and the 4 mol% La^{3+} co-doped samples, the ϕ increases compared to the undoped. However, it shows a slight decrease with an increase in doping. The ϕ of the samples are listed in Table 3.12 along with other intrinsic parameters that affect the performance of a photocatalyst.

From the valence band and the work function, the band edge alignment (BEA) was done. BEA is instrumental in calculating two fundamental intrinsic parameters- the electron affinity (EA) and the ionization potential (IP). A trend was recognized where the samples with higher charge carrier lifetimes showed lower EA and IP. The EA and the IP are important to ascertain the CB_{Min} and the VB_M respectively. Detailed analysis of the intrinsic parameters is discussed in the following section.

Band Edge Energy Diagrams from the Work Function (ϕ), the Band Gap (E_{gd}), and the Valence Band Analysis

The band edge energy diagrams (Figures 3.32-3.33) of the samples were calculated from the direct band gap (E_{gd}) measurements, work function (ϕ), and valence band analysis. From the energy diagrams the electron affinity (χ), the ionization potential (IP), and the band gap (E_g) are depicted in Table 3.12. All the values were calculated from the vacuum level.

Table 3.12: Measurements of Work Function (ϕ), Electron Affinity (χ), Ionisation Potential (IP), and Band Gap (E_g) from the Band Energy Diagrams in Figures 3.31 and 3.32

Sample	ϕ (eV)	χ (eV)	IP (eV)	E_{gd} (eV)
$SrTiO_3$	4.22	3.13	6.43	3.30
$SrTi_{(0.98)}Ga_{(0.02)}O_3$	4.33	3.47	6.77	3.30
$La_{(0.02)}Sr_{(0.98)}Ti_{(0.98)}Ga_{(0.02)}O_3$	4.29	3.06	6.36	3.30
$SrTi_{(0.96)}Ga_{(0.04)}O_3$	4.13	3.37	6.66	3.29
$La_{(0.04)}Sr_{(0.96)}Ti_{(0.96)}Ga_{(0.04)}O_3$	4.26	2.99	6.33	3.34

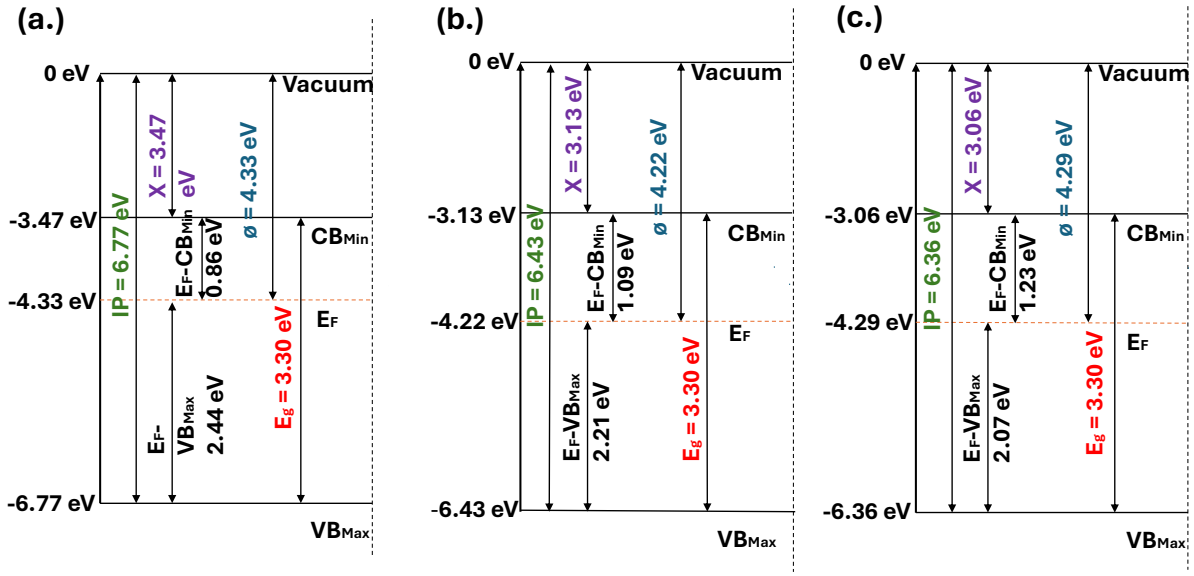


Figure 3.31: *Band edge energy diagrams of (a) 2 mol% Ga^{3+} (b) Undoped and (c) 2 mol% La^{3+},Ga^{3+} doped $SrTiO_3$.*

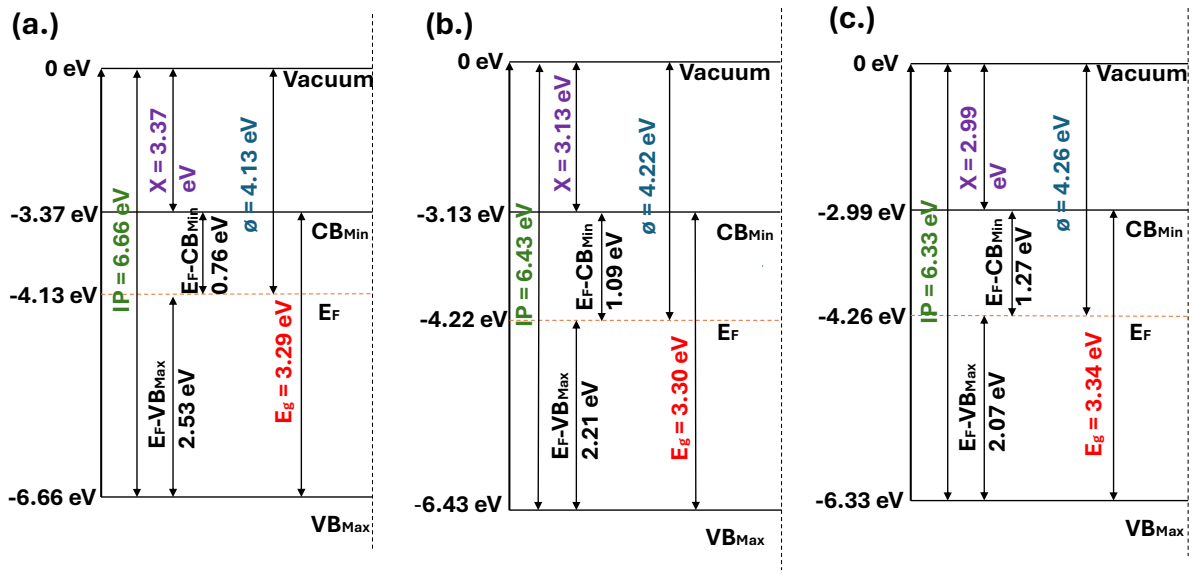


Figure 3.32: *Band edge energy diagrams of (a) 4 mol% Ga^{3+} (b) Undoped and (c) 4 mol% La^{3+},Ga^{3+} doped $SrTiO_3$.*

From Figures 3.31-3.32, Ga^{3+} doping pushes the fermi level closer to the CB_{Min} making the monodoped samples n-type. With La^{3+} the fermi level is pushed back. The position of the fermi level here can be correlated with the presence of the -OH groups and Ti^{3+} defects as discussed in the XPS elemental analysis in section 3.3.2. A comparison of hydroxyl species and Ti^{3+} with mol% doping is shown in Figure 3.33 (a) and (b).

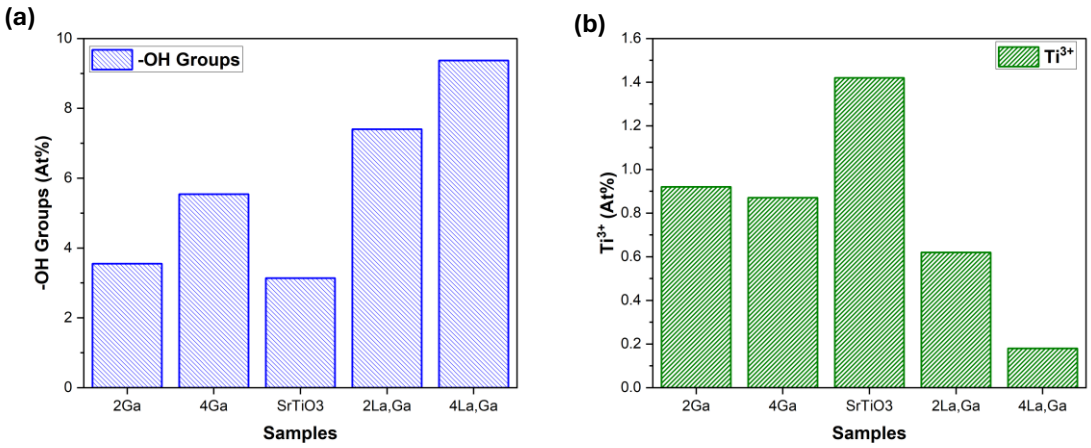


Figure 3.33: *Effect of doping on the (a) -OH species and (b) Ti^{3+} defects as measured with the XPS. The decrease in Ti^{3+} defects aligns with the higher PL intensities in the doped samples which demonstrated a decrease in non-radiative recombination pathways.*

From Figure 3.33 (a), the presence of -OH groups indicates the amount of surface oxygen vacancies where these species adsorb on the vacant sites on the surface. The -OH species were found to be higher in the co-doped samples than their monodoped counterparts. Takata, T. et al. [12] reported the introduction of oxygen vacancies and the suppression of Ti^{3+} that led to higher photocatalytic performance of the Ga^{3+} doped $SrTiO_3$. Similar observations were also

made in this study. The presence of Ti^{3+} in the samples was observed to have decreased with both types of doping as seen in Figure 3.33 (b). Oxygen vacancies as discussed earlier act as shallow electron donors. These could lead to the increase in n-type conductivity in the monodoped samples as observed in the band edge alignment in Figures 3.31-3.32. However, these samples have higher Ti^{3+} than the co-doped samples. This could lead to a higher n-type conductivity observed in the band edge energy diagrams (Figures 3.31-3.32). The co-doped samples show a decrease in n-type conductivity due to a greater suppression of Ti^{3+}. Suppression of Ti^{3+} in Figure 3.33 (b) can be positively correlated to the PL in Figure 7 (a, b) where the doped samples show higher radiative recombination**.**

In the 4 mol% La^{3+} co-doped samples and monodoped samples, suppression of Ti^{3+} can also be positively correlated to the lattice volume changes in Figure 3.4 (a-b). These samples showed volume shrinkage which could be because a lesser amount of Ti^{4+} is reduced to Ti^{3+}. Ti^{3+} in the B-site with a greater ionic radius would promote expansion. In the 2 mol% co-doped sample, a lattice expansion was observed even though Ti^{3+} was suppressed. Two possible reasons for this could be the presence of the type of oxygen vacancies present as discussed in Section 3.3.1. The second more likely reason in this case could be the site of substitution of the dopants. If the La^{3+} with a higher ionic radius gets fully or partially substituted in the smaller B-site an expansion can occur.

Another apparent trend is the decrease in the EA and the IP with La^{3+} co-doping. Here a theory can be proposed that when there is a window of low EA and IP, lifetimes are higher. This could be due to low trapping and higher charge carrier mobility. A similar trend can be seen in the La^{3+} co-doped samples where higher lifetimes are accompanied by lower EA and IP. This correlation is shown in Figure 3.34. Lower traps in the co-doped samples can also be supported by the high PL intensity (lower non-radiative recombination) in Figure 3.24 compared with the monodoped and the undoped samples.

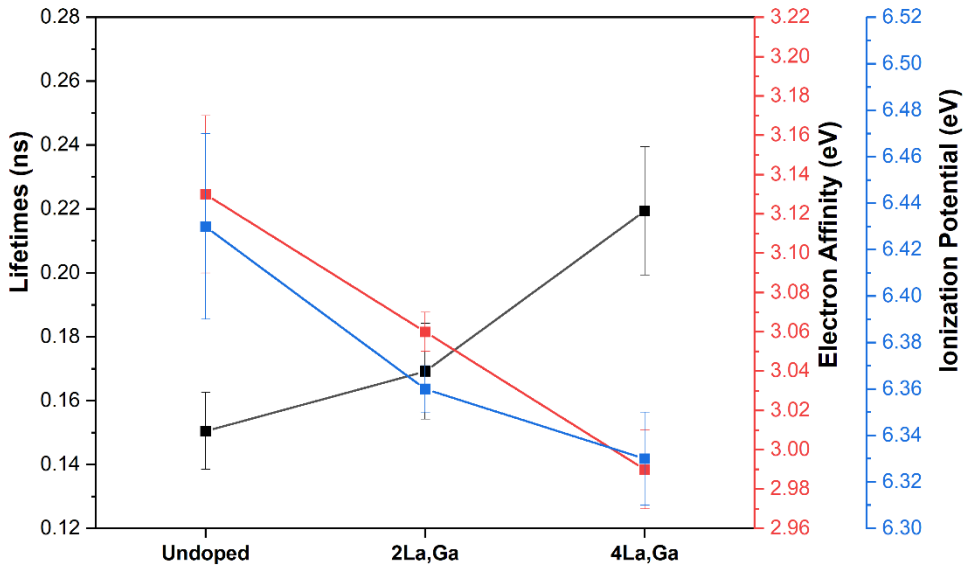


Figure 3.34: *La^{3+} co-doped samples demonstrating higher lifetimes with lower EA and IP. This could be due to lower trapping due to a decrease in defects as observed with the PL intensity which increases the charge carrier mobility. The error in the EA and IP were added from the standard deviations after recalculating the band edge alignment.*

Band Edge Alignment to Water Redox Potential

Band alignment is used to predict the photocatalytic activity towards water splitting. For the best photocatalytic water splitting, the band gap of the material should be straddling the water redox potential of 1.23V [95]. The redox water potentials are at -4.5 eV for $E(H^+/H_2)$ and -5.73 eV for $E(O_2/H_2O)$ on the vacuum scale [95]. The band edge alignment to the water redox potentials was calculated as shown in Figure 3.35 with data from Figures 3.31-3.32. In the case of the samples synthesized, all of them might demonstrate photo-activity.

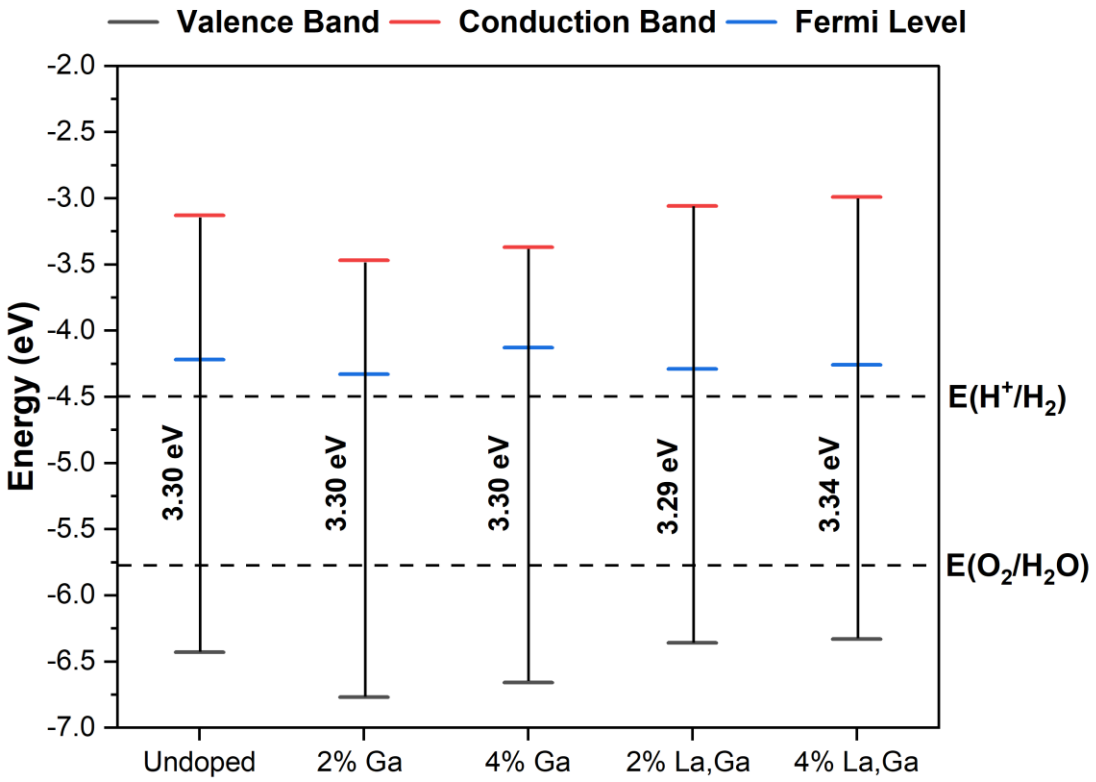


Figure 3.35: *Band Edge Alignment to Water Redox Potentials (vacuum) of undoped and doped samples considering direct bandgaps as measured with the UV-vis diffuse reflectance spectroscopy. The work function and the E_F-VB_M separation as measured with the XPS were used to calculate the positions of VB and CB.*

From Figure 3.35, it can be observed that the fermi level shifts are close to the undoped for the 2 mol% monodoped, 2 mol%, and 4 mol% co-doped samples. At -4.13 eV, the fermi level of the 4 mol% Ga^{3+} doped sample shows a slightly higher shift. For enhanced photoactivity, the CB_{Min} should be more negative to the water reduction potential and the VB_M should be more positive to the water oxidation potential [100]. Comparing the oxidation potentials (VB_M) of the co-doped samples with the undoped, they lie closer to the $E(O_2/H_2O)$. This indicates that a lesser overpotential is required to drive the oxidation reaction. To validate the performance of the La^{3+} co-doped catalysts from the band edge alignment photoelectrochemical analysis was carried out which is discussed in the subsequent section.

3.3.4 Performance Evaluation: Photoelectrochemical (PEC) Measurements

PEC measurements were done on the undoped and Ga^{3+}/La^{3+} (co-) doped samples in 1M KOH, pH = 13.6. The catalyst solutions were doctor-bladed on 2cm x 5cm FTO slides. The catalyst-coated FTO slides (working electrodes) were loaded on the H-cell. The electrical connections to the cell were completed with Pt wire as a counter electrode and Ag/AgCl (Sat. KCl). The irradiated area was 1 cm^2 of the working electrode on the backside (electrode-electrolyte contact). Figure 3.36 (a), (b), and (c) demonstrate the linear sweep voltammetry (LSV)

measurements of the Ga^{3+} doped and La^{3+} co-doped samples under chopped AM1.5G and UV (40% intensity) irradiation at 0.02V/s scan rate. All the measurements were converted to V vs RHE with the Nernst Eq as discussed in the methods chapter.

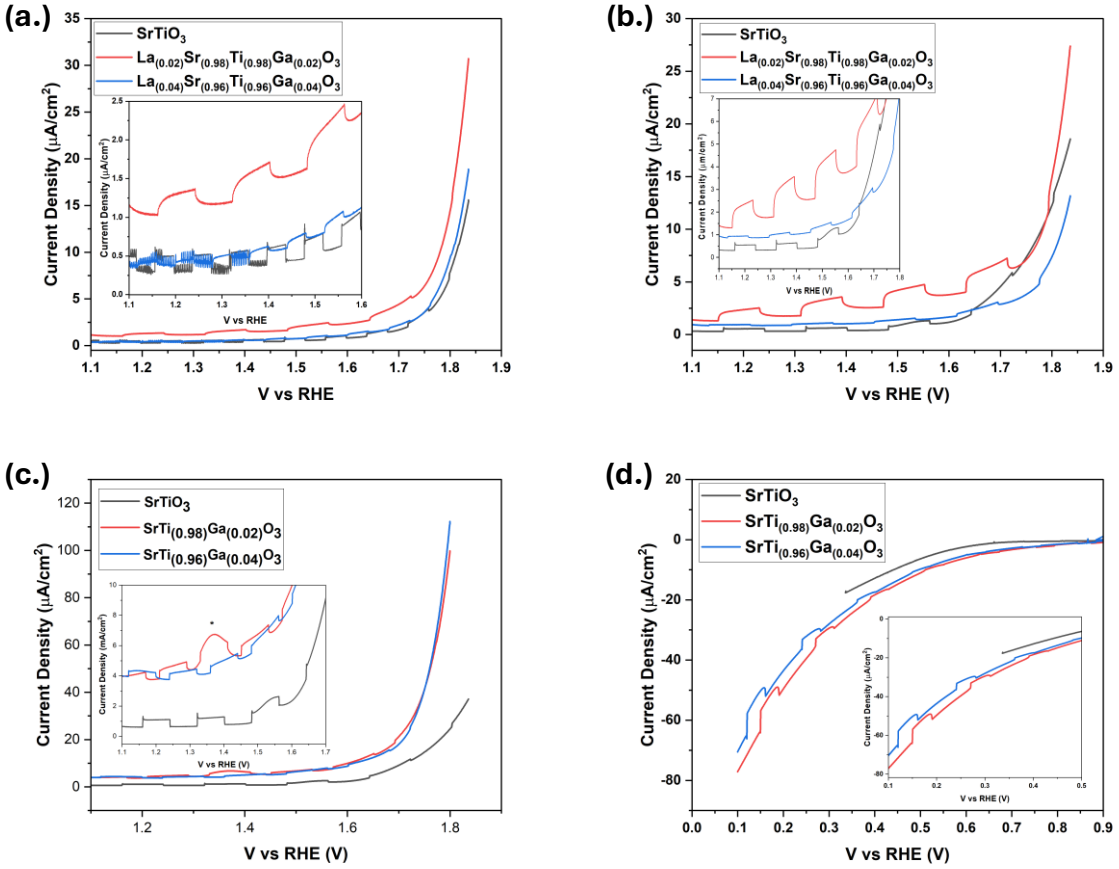


Figure 3.36: *Linear sweep voltammetry measurements of La^{3+} co-doped samples under (a) AM1.5G (b) UV (40% intensity) (c) Ga^{3+} doped $SrTiO_3$ samples at 900 °C under UV (40% intensity) with the inset demonstrating the light response towards OER (d) Ga^{3+} doped $SrTiO_3$ samples at 900 °C under UV (40% intensity) with the inset demonstrating the light response towards HER.*

Under both types of light irradiations- AM1.5G and UV, the 2 mol% La^{3+} co-doped samples show higher light response. Even though under UV irradiation the 2 mol% co-doped sample showed a higher oxidation current density, the undoped sample has an earlier onset potential. Under AM1.5G, the 2 mol% co-doped sample has an earlier onset for both reduction and oxidation potentials as seen in the CV in Figure 3.37(a). Earlier onset indicates how easily reducible or oxidizable the material is. However, the light response is observed only towards the oxidation reaction. The Ga^{3+} monodoped samples show photoresponses towards both HER and OER, as shown in Figures 3.36(c, d) and 3.37 (b). The monodoped samples show a higher decrease in onset potential towards OER.

In the case of Ga^{3+} monodoped samples under UV irradiation, the 4 mol% and 2 mol% samples show much higher oxidation current density than the undoped and the La^{3+} co-doped samples. An oxidation peak can be observed in the 2 mol% Ga^{3+} doped sample at 1.37 V vs RHE shown

in Figure 3.36 (c) inset with *. Sr, Ga, and La are stable as Sr^{2+}, Ga^{3+}, and La^{3+} and are not oxidizable. No such peaks were observed in the 4 mol% monodoped sample or any other synthesized samples which could be an instrumental artifact. The photocurrents were measured from the chopped illumination. Under UV irradiation, the photocurrents measured from light on and off are 0.48, 1.76, and 0.10 µA for the undoped, 2 mol%, and 4 mol% co-doped samples respectively. When illuminated with AM1.5G, the photocurrents are 0.22, 0.51, and 0.06 µA for the undoped, 2 mol%, and 4 mol% co-doped samples respectively. For the Ga^{3+} doped series at 900°C, the 2 mol% and 4 mol% monodoped samples showed 0.58 and 0.43 µA.

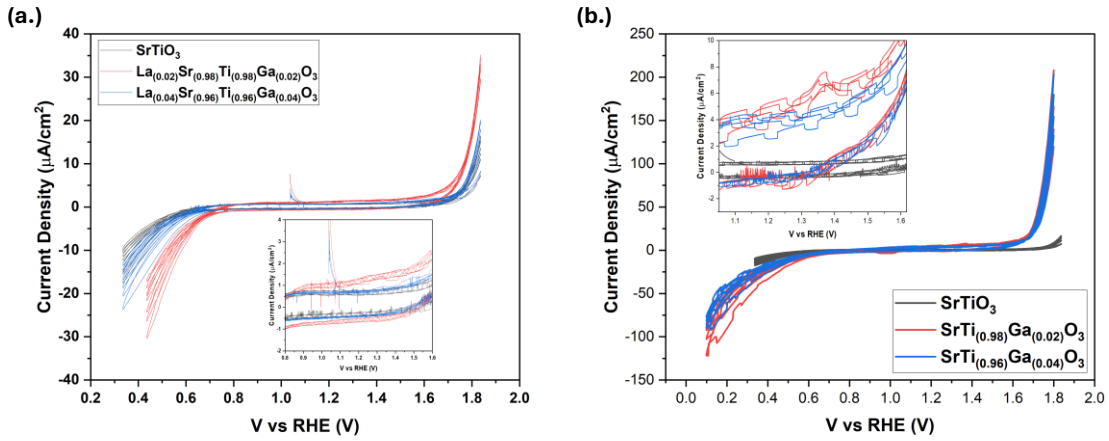


Figure 3.37: *Cyclic voltammetry graph comparing the performance under (a) AM1.5G conditions of La^{3+} co-doped samples (b.) UV irradiation of Ga^{3+} monodoped samples. In both (a) and (b), the doped samples perform better towards OER and HER in the case of the monodoped samples.*

The performance of the monodoped catalysts is higher under UV conditions (Figure 3.37 (b)). Therefore, it can be inferred that Ga^{3+} mono-doping can improve UV absorption. The 2 mol% doped sample shows higher photoresponse than the undoped one and the 4 mol% is slightly lower. The co-doped samples show higher performance under AM1.5G (Figure 3.36 (a)) indicating the ability to absorb in the visible light region. Under UV irradiation in Figure 3.36 (b), the 2 mol% La^{3+} co-doped sample exhibits higher current density than the 4 mol% co-doped and undoped samples. The trend in the doped samples in Figure 3.36 follows the same trend as the PL intensity in Figure 3.24 (b). The higher current density observed under the light conditions in the doped samples can be attributed to the suppression of defects such as Ti^{3+} as seen in Figure 3.33 (b). Under UV illumination, even though the 4 mol% has a lower current density than the undoped, the photo response is better. The dark current in Figure 3.37 (a) and (b) also indicates that the doped samples are more conductive which aligns with the higher suppression of Ti^{3+}. Higher photoresponse in the co-doped samples can also be due to better charge carrier migration as seen from the TCSPC higher lifetimes seen in Figure 3.26 (b). The absorption features in the visible light region in the case of the co-doped samples as seen in Figure 3.22(b) could also have contributed to the performance. The performance under AM1.5G conditions can be validated by the band edge alignment observed in Figures 3.31,

3.32, and 3.35 which shows the favourable position of the VB_M to the oxidation potential. The n-type conductivity of the samples can also facilitate the performance towards OER.

Another set of experiments is being conducted on these samples which are still in their preliminary stages. Here the photoelectrodes with doctor-bladed Ga^{3+} and La^{3+} (co)-doped catalysts were prepared with an ALD-grown 10 nm thick TiO_2 blocking layer in between the FTO and the catalyst layer. The primary function of this layer was to prevent the catalyst from being washed off when dipped in the electrolyte and hence, to improve adhesion. In these experiments, the La^{3+} co-doped showed the highest photocurrent with the PEC analysis followed by the undoped samples. The Ga^{3+} doped samples showed the lowest performances. These results are shown in Figure 3.38. However, these studies are still ongoing, and the results need more detailed analysis.

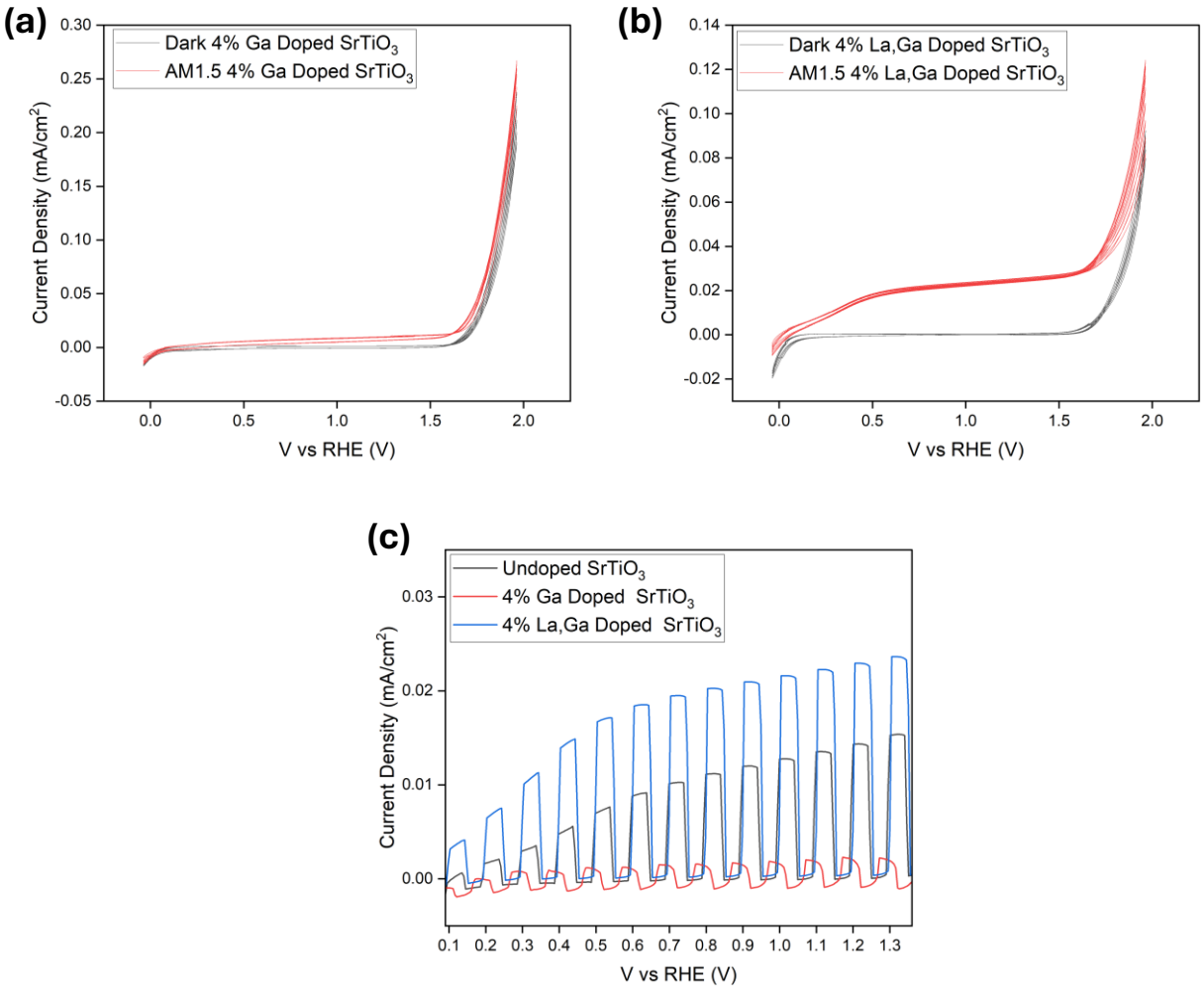


Figure 3.38: *(a) Comparison of light and dark currents in 4 mol% Ga^{3+} doped $SrTiO_3$ showing a small difference (b) Higher photocurrents in 4 mol% La^{3+}, Ga^{3+} co-doped samples (c) Chronoamperometry results showing higher photocurrents in the La co-doped samples.*

The photoresponses of the co-doped samples in the current studies could be attributed to the microstructural and opto-electronic factors observed from the characterization techniques utilized so far. Another behavior that could contribute to the performance of the catalyst is exsolution which was observed with the TEM. The exsolution in this work was unintentional and is speculated to be due to the high-temperature calcination. Exsolution has been reported to facilitate higher photo-(electro)-catalytic rates due to the higher surface area (more active sites) provided for catalytic reactions. With the higher Ga^{3+} content in the 2 mol% co-doped sample, the better performance in the PEC can be justified. As observed from the TEMs, these exsolved particles with their small sizes provide higher surface areas that facilitate higher performances. Another trend that can be recognized here is the surface segregation of the dopants as observed with the T-T-S as discussed in Section 3.3.2. This segregation could also facilitate the doped samples in demonstrating higher performance. From the TCSPC and the PEC results, it is evident that the performance of photo-(electro)-catalysts is dependent on several parameters including the type of defects present. In this study, crystallographic defects such as dislocations and grain boundaries were observed which act as sinks for point defects such as vacancies. The role of 1D defects particularly dislocations and their role in photo-(electro)-catalytic performance is still a very novel field.

3.4 Conclusion

In this work, a series of Ga^{3+} mono- and La^{3+}, Ga^{3+} co-doped samples were synthesized with the sol-gel Pechini method with calcination at 900 °C for 6 h. d^{10} type dopants did not exhibit any bandgap narrowing. The higher PL intensities of the doped samples indicate a more efficient defect suppression. However, the 2 mol% and 4 mol% La^{3+} co-doped samples deviated from the rest of the samples as being bluish-grey compared to the white color. Characterizations revealed anomalous absorption features and exsolution which were found to have affected the performances of the photocatalysts. These anomalous features were closely related to the overall defect chemistry. 1D and 2D defects were observed to have acted as sinks and nucleation pathways for vacancies and exsolution respectively. Oxygen vacancies were found to have affected intrinsic parameters such as the EA, the IP, and the charge carrier dynamics. The Ga^{3+} monodoped samples showed a higher n-type nature which indicates the presence of oxygen vacancies. ***Therefore, the formula of the monodoped samples can be written as*** $\boldsymbol{SrTi_{(1-x)}Ga_xO_{3-y}}$ ***where x is the mol% dopant and y is the missing oxygen.*** Adding La^{3+} was found to have decreased the n-type conductivity by pushing the fermi level away from the CB_{Min} thereby charge compensating. A time-temperature-solubility dependence of the samples was observed with the XPS which indicated surface segregation of the dopants. Preliminary analysis showed this to be one of the factors in facilitating the higher PEC performances of the doped samples. This phenomenon will be studied in detail in the next chapter and a broader conclusion will be drawn for the Ga^{3+} doped samples in terms of properties and performances. In summary, this work attempts to understand the underlying mechanisms and defect suppressions that can affect the performance of photo-electrocatalysts.

References

[1] Y. Lu, A. Ma, Y. Yu, R. Tan *et al.*, "Engineering Oxygen Vacancies into $LaCoO_3$

Perovskite for Efficient Electrocatalytic Oxygen Evolution," *ACS Sustain. Chem. Eng.*, vol. 7, no. 3, pp. 2906–2910, 2019, doi: 10.1021/acssuschemeng.8b05717.

[2] L. L. Deng, X. P. Ma, M. T. Lu, Y. He, R. L. Fan, and Y. Xin, "Accelerated oxygen evolution kinetics on Ir-doped $SrTiO_3$ perovskite by NH3 plasma treatment," *Chinese Phys. B*, vol. 31, no. 11, 2022, doi: 10.1088/1674-1056/ac70b1.

[3] Y. Xu, Y. Liang, Q. He, R. Xu *et al.* , "Review of doping $SrTiO_3$ for photocatalytic applications," *Bull. Mater. Sci.*, vol. 46, no. 1, 2023, doi: 10.1007/s12034-022-02826-x.

[4] Z. Su, F. Fang, X. Li, W. Han, X. Liu, and K. Chang, "Synergistic surface oxygen defect and bulk Ti^{3+} defect engineering on $SrTiO_3$ for enhancing photocatalytic overall water splitting," *J. Colloid Interface Sci.*, vol. 626, pp. 662–673, 2022, doi: 10.1016/j.jcis.2022.06.109.

[5] F. Fang, Z. Su, X. Li, F. Xu *et al.* , "Mechanistic Understanding of Alkali-Metal-Ion Effect on Defect State in $SrTiO_3$ During the Defect Engineering for Boosting Solar Water Splitting," *Adv. Funct. Mater.*, vol. 33, no. 24, p. 2215242, Jun. 2023, doi: https://doi.org/10.1002/adfm.202215242.

[6] V. G. Kessler, "The Synthesis and Solution Stability of Alkoxide Precursors," in *Handbook of Sol-Gel Science and Technology: Processing, Characterization and Applications*, 2nd ed., Springer Cham, 2018, pp. 31–80.

[7] T. Takata, J. Jiang, Y. Sakata, M. Nakabayashi *et al.* , "Photocatalytic water splitting with a quantum efficiency of almost unity," *Nature*, vol. 581, no. 7809, pp. 411–414, 2020, doi: 10.1038/s41586-020-2278-9.

[8] R. Li, T. Takata, B. Zhang, C. Feng *et al.* , "Criteria for Efficient Photocatalytic Water Splitting Revealed by Studying Carrier Dynamics in a Model Al-doped $SrTiO_3$ Photocatalyst," *Angew. Chemie - Int. Ed.*, vol. 62, no. 49, 2023, doi: 10.1002/anie.202313537.

[9] U. Wijesinghe, G. Longo, and O. S. Hutter, "Defect engineering in antimony selenide thin film solar cells," *Energy Adv.*, vol. 2, no. 1, pp. 12–33, 2022, doi: 10.1039/d2ya00232a.

[10] S. Sun, B. Peng, Y. Song, B. Liu, H. Song, and W. Lin, "Boosting photoelectron transfer by Fermi and doping levels regulation in carbon nitride towards efficient solar-driven hydrogen production," *Chem. Eng. J.*, vol. 495, p. 153547, 2024, doi: https://doi.org/10.1016/j.cej.2024.153547.

[11] R. D. Shannon, "Revised effective ionic radii and systematic studies of interatomic distances in halides and chalcogenides," *Acta Crystallogr. Sect. A*, vol. 32, pp. 751–767, 1976.

[12] T. Takata and K. Domen, "Defect Engineering of Photocatalysts by Doping of Aliovalent Metal Cations for Efficient Water Splitting," *J. Phys. Chem. C*, vol. 113, pp. 19386–19388, 2009.

[13] J. Yao, T. Chen, H. Wang, M. Khan *et al.*, "Stable cubic crystal structures and optimized thermoelectric performance of $SrTiO_3$-based ceramics driven by entropy engineering," *J. Mater. Chem. A*, vol. 10, no. 46, pp. 24561–24572, 2022, doi: 10.1039/d2ta06576b.

[14] R. J. D. Tilley, *Perovskites: Structure–Property Relationships*, vol. 42, no. 4. 2016.

[15] J. Lu and Y. Li, "Perovskite-type Li-ion solid electrolytes: a review," *J. Mater. Sci. Mater. Electron.*, vol. 32, no. 8, pp. 9736–9754, 2021, doi: 10.1007/s10854-021-05699-8

[16] M. G. Vergniory, B.J. Wieder, L. Elcoro, S.S.P. Parkin *et al.* , "All topological bands of all nonmagnetic stoichiometric materials," *Science (80-.).*, vol. 376, no. 6595, 2022, doi: 10.1126/science.abg9094.

[17] M. G. Vergniory, L. Elcoro, C. Felser, N. Regnault, B. A. Bernevig, and Z. Wang, "A complete catalogue of high-quality topological materials," *Nature*, vol. 566, no. 7745, pp. 480–485, 2019, doi: 10.1038/s41586-019-0954-4.

[18] B. Bradlyn, L. Elcoro, J. Cano, M.G. Vergniory *et al.* , "Topological quantum chemistry," *Nature*, vol. 547, no. 7663, pp. 298–305, 2017, doi: 10.1038/nature23268.

[19] S. Kobayashi, Y. Ikuhara, and T. Mizoguchi, "Lattice expansion and local lattice distortion in Nb- and La-doped $SrTiO_3$ single crystals investigated by X-ray diffraction and first-principles calculations," *Phys. Rev. B*, vol. 98, no. 13, 2018, doi: 10.1103/PhysRevB.98.134114.

[20] M. M. Pilch, C. Rodenbücher, F. Krok, and K. Szot, "Heterogeneity in La Distribution in Highly La-Doped $SrTiO_3$ Crystals," *Crystals*, vol. 13, no. 11, pp. 1–15, 2023, doi: 10.3390/cryst13111552.

[21] R. Moos and K. H. Härdtl, "Electronic transport properties of Sr1−xLaxTiO3 ceramics," *J. Appl. Phys.*, vol. 80, no. 1, pp. 393–400, Jul. 1996, doi: 10.1063/1.362796.

[22] S. M. Hwang, J.C. Lim, S. Kim, J.Y. Kim *et al.* , "Impact of the change in charge compensation mechanism on the electrical, dielectric, and structural properties of La-doped $BaTiO_3$ ceramics," *J. Eur. Ceram. Soc.*, no. September, 2023, doi: 10.1016/j.jeurceramsoc.2023.12.029.

[23] T. Shi, Y. Chen, and X. Guo, "Defect chemistry of alkaline earth metal (Sr/Ba) titanates," *Prog. Mater. Sci.*, vol. 80, pp. 77–132, 2016, doi: 10.1016/j.pmatsci.2015.10.002.

[24] Y. Kim, A. S. Disa, T. E. Babakol, X. Fang, and J. D. Brock, "Strain and oxygen vacancy ordering in $SrTiO_3$: Diffuse X-ray scattering studies," *Phys. Rev. B - Condens. Matter Mater. Phys.*, vol. 92, no. 6, 2015, doi: 10.1103/PhysRevB.92.064105.

[25] H. Yamada and G. R. Miller, "Point defects in reduced strontium titanate," *J. Solid State Chem.*, vol. 6, no. 1, pp. 169–177, 1973, doi: 10.1016/0022-4596(73)90216-8.

[26] D. Y. Lu, Y. Y. Peng, X. Y. Yu, and X. Y. Sun, "Dielectric properties and defect chemistry of la and Tb co-doped $BaTiO_3$ ceramics," *J. Alloys Compd.*, vol. 681, pp. 128–138, 2016,

doi: 10.1016/j.jallcom.2016.04.119.

[27] C. Rodenbücher, C. Korte, T. Schmitz-Kempen, S. Bette, and K. Szot, "A physical method for investigating defect chemistry in solid metal oxides," *APL Mater.*, vol. 9, no. 1, 2021, doi: 10.1063/5.0033891.

[28] P. Blennow, A. Hagen, K. K. Hansen, L. R. Wallenberg, and M. Mogensen, "Defect and electrical transport properties of Nb-doped $SrTiO_3$," *Solid State Ionics*, vol. 179, no. 35–36, pp. 2047–2058, 2008, doi: 10.1016/j.ssi.2008.06.023.

[29] D. A. Freedman, D. Roundy, and T. A. Arias, "Elastic effects of vacancies in strontium titanate: Short- and long-range strain fields, elastic dipole tensors, and chemical strain," *Phys. Rev. B - Condens. Matter Mater. Phys.*, vol. 80, no. 6, pp. 1–14, 2009, doi: 10.1103/PhysRevB.80.064108.

[30] Y. Qin, F. Fang, Z. Xie, H. Lin *et al.* , "La,Al-Codoped $SrTiO_3$ as a Photocatalyst in Overall Water Splitting: Significant Surface Engineering Effects on Defect Engineering," *ACS Catal.*, vol. 11, no. 18, pp. 11429–11439, 2021, doi: 10.1021/acscatal.1c02874.

[31] J. Liu, C.L. Wang, W.B. Su, H.C. Wang *et al.* , "Enhancement of thermoelectric efficiency in oxygen-deficient Sr 1-x Lax $TiO_{3-\delta}$ ceramics," *Appl. Phys. Lett.*, vol. 95, no. 16, pp. 3–6, 2009, doi: 10.1063/1.3254219.

[32] P. P. Shang, B. P. Zhang, Y. Liu, J. F. Li, and H. M. Zhu, "Preparation and thermoelectric properties of la-doped SrTiO 3 ceramics," *J. Electron. Mater.*, vol. 40, no. 5, pp. 926–931, 2011, doi: 10.1007/s11664-010-1452-5.

[33] H. Muta, K. Kurosaki, and S. Yamanaka, "Thermoelectric properties of reduced and La-doped single-crystalline $SrTiO_3$," *J. Alloys Compd.*, vol. 392, no. 1–2, pp. 306–309, 2005, doi: 10.1016/j.jallcom.2004.09.005.

[34] K. Potzger, J. Osten, A.A. Levin, A. Shalimov *et al.* , "Defect-induced ferromagnetism in crystalline $SrTiO_3$," *J. Magn. Magn. Mater.*, vol. 323, no. 11, pp. 1551–1562, 2011, doi: 10.1016/j.jmmm.2011.01.018.

[35] A. Janotti, B. Jalan, S. Stemmer, and C. G. Van De Walle, "Effects of doping on the lattice parameter of SrTiO 3," *Appl. Phys. Lett.*, vol. 100, no. 26, 2012, doi: 10.1063/1.4730998.

[36] D. S. Aidhy, B. Liu, Y. Zhang, and W. J. Weber, "Chemical expansion affected oxygen vacancy stability in different oxide structures from first principles calculations," *Comput. Mater. Sci.*, vol. 99, pp. 298–305, 2015, doi: 10.1016/j.commatsci.2014.12.030.

[37] B. Ohtani, "Photocatalysis by inorganic solid materials: Revisiting its definition, concepts, and experimental procedures," *Adv. Inorg. Chem.*, vol. 63, pp. 395–430, 2011, doi: 10.1016/B978-0-12-385904-4.00001-9.

[38] S. Dolabella, A. Borzì, A. Dommann, and A. Neels, "Lattice Strain and Defects Analysis in Nanostructured Semiconductor Materials and Devices by High-Resolution X-ray

Diffraction: Theoretical and Practical Aspects," *Small Methods*, vol. 6, no. 2, 2022, doi: 10.1002/smtd.202100932.

[39] E. Pastor, M. Sachs, S. Selim, J. R. Durrant, A. A. Bakulin, and A. Walsh, "Electronic Defects in Metal Oxide Photocatalysts," vol. 0123456789, 2022, doi: 10.1038/s41578-022-00433-0.

[40] W. Li, J. Shi, K. H. L. Zhang, and J. L. Macmanus-Driscoll, "Defects in complex oxide thin films for electronics and energy applications: Challenges and opportunities," *Mater. Horizons*, vol. 7, no. 11, pp. 2832–2859, 2020, doi: 10.1039/d0mh00899k.

[41] E. Pastor, M. Sachs, S. Selim, J. R. Durrant, A. A. Bakulin, and A. Walsh, "Electronic defects in metal oxide photocatalysts," *Nat. Rev. Mater.*, vol. 7, no. 7, pp. 503–521, 2022, doi: 10.1038/s41578-022-00433-0.

[42] W. Hayes and A. M. Stoneham, "Defects and defect processes in nonmetallic solids," 1985, [Online]. Available: https://api.semanticscholar.org/CorpusID:136562522.

[43] Z. Zhang, W. Sigle, W. Kurtz, and M. Rühle, "Electronic and atomic structure of a dissociated dislocation in (formula presented)," *Phys. Rev. B - Condens. Matter Mater. Phys.*, vol. 66, no. 21, pp. 1–7, 2002, doi: 10.1103/PhysRevB.66.214112.

[44] P. Gao, S. Wang, R. Ishikawa, N. Li *et al.* , "Atomic-Scale Measurement of Flexoelectric Polarization at $SrTiO_3$ Dislocations," *Phys. Rev. Lett.*, vol. 120, no. 26, pp. 1–6, 2018, doi: 10.1103/PhysRevLett.120.267601.

[45] P. Raizada, V. Soni, A. Kumar, P. Singh *et al.* , Surface defect engineering of metal oxides photocatalyst for energy application and water treatment, vol. 7, no. 2. Elsevier Ltd, 2021.

[46] P. Ren, M. Song, J. Lee, J. Zheng *et al.* , "Edge Dislocations Induce Improved Photocatalytic Efficiency of Colored TiO_2," *Adv. Mater. Interfaces*, vol. 6, no. 17, pp. 1–6, 2019, doi: 10.1002/admi.201901121.

[47] J. Yan, G. Wu, N. Guan, L. Li, Z. Li, and X. Cao, "Understanding the effect of surface/bulk defects on the photocatalytic activity of TiO_2: Anatase versus rutile," *Phys. Chem. Chem. Phys.*, vol. 15, no. 26, pp. 10978–10988, 2013, doi: 10.1039/c3cp50927c.

[48] Y. Zhao, G. Chen, T. Bian, C. Zhou *et al.* , "Defect-Rich Ultrathin ZnAl-Layered Double Hydroxide Nanosheets for Efficient Photoreduction of CO_2 to CO with Water," *Adv. Mater.*, vol. 27, no. 47, pp. 7824–7831, 2015, doi: 10.1002/adma.201503730.

[49] Z. Zafar, S. Yi, J. Li, C. Li *et al.* , "Recent Development in Defects Engineered Photocatalysts: An Overview of the Experimental and Theoretical Strategies," *Energy Environ. Mater.*, vol. 5, no. 1, pp. 68–114, 2022, doi: 10.1002/eem2.12171.

[50] J. Gallet, M. Perez, R. Guillou, C. Ernould *et al.* , "Experimental measurement of dislocation density in metallic materials: A quantitative comparison between measurements techniques (XRD, R-ECCI, HR-EBSD, TEM)," *Mater. Charact.*, vol. 199, p. 112842, 2023, doi: https://doi.org/10.1016/j.matchar.2023.112842.

[51] A. Muiruri, M. Maringa, and W. du Preez, "Evaluation of dislocation densities in various microstructures of additively manufactured Ti_6Al_4V (Eli) by the method of X-ray diffraction," *Materials (Basel).*, vol. 13, no. 23, pp. 1–23, 2020, doi: 10.3390/ma13235355.

[52] H. Laala-Bouali, F.-Z. Bentayeb, S. Louidi, X. Guo *et al.* , "X-ray line profile analysis of the ball-milled Fe-30Co alloy," *Adv. Powder Technol.*, vol. 24, no. 1, pp. 168–174, 2013, doi: 10.1016/j.apt.2012.04.007.

[53] J. E. Ayers, "The measurement of threading dislocation densities in semiconductor crystals by X-ray diffraction," *J. Cryst. Growth*, vol. 135, no. 1–2, pp. 71–77, 1994, doi: 10.1016/0022-0248(94)90727-7.

[54] M. Pal, U. Pal, J. M. G. Y. Jiménez, and F. Pérez-Rodríguez, "Effects of crystallization and dopant concentration on the emission behavior of TiO_2: Eu nanophosphors," *Nanoscale Res. Lett.*, vol. 7, pp. 1–12, 2012, doi: 10.1186/1556-276X-7-1.

[55] G. Jyothi and K. G. Gopchandran, "Role of La^{3+} ion substitution sites on the photoluminescence properties of the $SrTiO_3$:Eu3+ phosphors," *J. Sci. Adv. Mater. Devices*, vol. 5, no. 2, pp. 233–241, 2020, doi: 10.1016/j.jsamd.2020.04.006.

[56] Y. Zhu, Z. Xu, Q. Lang, W. Jiang *et al.* , "Grain boundary engineered metal nanowire cocatalysts for enhanced photocatalytic reduction of carbon dioxide," *Appl. Catal. B Environ.*, vol. 206, pp. 282–292, 2017, doi: 10.1016/j.apcatb.2017.01.035.

[57] A. Senthamizhan, B. Balusamy, Z. Aytac, and T. Uyar, "Grain boundary engineering in electrospun ZnO nanostructures as promising photocatalysts," *CrystEngComm*, vol. 18, no. 34, pp. 6341–6351, 2016, doi: 10.1039/c6ce00693k.

[58] A. M. Van Der Zande, P.Y. Huang, D.A. Chenet, T. C. Berkelbach *et al.* , "Grains and grain boundaries in highly crystalline monolayer molybdenum disulphide," *Nat. Mater.*, vol. 12, no. 6, pp. 554–561, 2013, doi: 10.1038/nmat3633.

[59] Z. Wang, M. Saito, K.P. McKenna, L. Gu *et al.* , "Atom-resolved imaging of ordered defect superstructures at individual grain boundaries," *Nature*, vol. 479, no. 7373, pp. 380–383, 2011, doi: 10.1038/nature10593.

[60] W. O'Leary, L. Giordano, J. Park, S. S. Nonnenmann, Y. Shao-Horn, and J. L. M. Rupp, "Influence of Sr-Site Deficiency, Ca/Ba/La Doping on the Exsolution of Ni from $SrTiO_3$," *J. Am. Chem. Soc.*, vol. 145, no. 25, pp. 13768–13779, 2023, doi: 10.1021/jacs.2c12011.

[61] S. Singh, E. Prestat, L. F. Huang, J. M. Rondinelli, S. J. Haigh, and B. A. Rosen, "Role of 2D and 3D defects on the reduction of $LaNiO_3$ nanoparticles for catalysis," *Sci. Rep.*, vol. 7, no. 1, pp. 1–7, 2017, doi: 10.1038/s41598-017-10703-5.

[62] K. Kousi, C. Tang, I. S. Metcalfe, and D. Neagu, "Emergence and Future of Exsolved Materials," *Small*, vol. 17, no. 21, 2021, doi: 10.1002/smll.202006479.

[63] D. Neagu, G. Tsekouras, D. N. Miller, H. Ménard, and J. T. S. Irvine, "In situ growth of

nanoparticles through control of non-stoichiometry," *Nat. Chem.*, vol. 5, no. 11, pp. 916–923, 2013, doi: 10.1038/nchem.1773.

[64] D. Neagu, V. Kyriakou, I.-L. Roiban, M. Aouine *et al.* , "In Situ Observation of Nanoparticle Exsolution from Perovskite Oxides: From Atomic Scale Mechanistic Insight to Nanostructure Tailoring," *ACS Nano*, vol. 13, no. 11, pp. 12996–13005, 2019, doi: 10.1021/acsnano.9b05652.

[65] N. W. Kwak, S.J. Jeong, H. G. Seo, S. Lee *et al.* , "In situ synthesis of supported metal nanocatalysts through heterogeneous doping," *Nat. Commun.*, vol. 9, no. 1, pp. 1–8, 2018, doi: 10.1038/s41467-018-07050-y.

[66] Y. Jiang, Z. Geng, Y. Sun, X. Wang *et al.* , "Highly Efficient B-Site Exsolution Assisted by Co Doping in Lanthanum Ferrite toward High-Performance Electrocatalysts for Oxygen Evolution and Oxygen Reduction," *ACS Sustain. Chem. Eng.*, vol. 8, no. 1, pp. 302–310, 2020, doi: 10.1021/acssuschemeng.9b05344.

[67] S. Chattopadhyay, A. B. Naden, W. S. J. Skinner, G. Kerherve, D. J. Payne, and J. T. S. Irvine, "Room Temperature Exsolution of Cds Nanodots on A-site Deficient Cotton-Ball Like Titanate Perovskite Nanoparticles for H_2 Production Under Visible Light," *Adv. Energy Mater.*, vol. 13, no. 47, pp. 1–9, 2023, doi: 10.1002/aenm.202301381.

[68] Y. Takano, Y. Hayashi, J. Fukushima, and H. Takizawa, "Room-temperature synthesis of γ-Ga_2O_3 nanoparticles from gallium metal via ultrasound irradiation," *Adv. Powder Technol.*, vol. 32, no. 3, pp. 860–865, 2021, doi: 10.1016/j.apt.2021.01.032.

[69] Y. H. Kim, H. Jeong, B.-R. Won, H. Jeon *et al.* , Nanoparticle Exsolution on Perovskite Oxides: Insights into Mechanism, Characteristics and Novel Strategies, vol. 16, no. 1. Springer Nature Singapore, 2024.

[70] J. Wang, A. Kumar, J. L. Wardini, Z. Zhang *et al.* , "Exsolution-Driven Surface Transformation in the Host Oxide," *Nano Lett.*, vol. 22, no. 13, pp. 5401–5408, 2022, doi: 10.1021/acs.nanolett.2c01439.

[71] P. Hirel, P. Carrez, E. Clouet, and P. Cordier, "The electric charge and climb of edge dislocations in perovskite oxides: The case of high-pressure $MgSiO_3$ bridgmanite," *Acta Mater.*, vol. 106, pp. 313–321, 2016, doi: 10.1016/j.actamat.2016.01.019.

[72] E. Calì, G. Kerherve, F. Nauhal, K. Kousi *et al.* , "Exsolution of Catalytically Active Iridium Nanoparticles from Strontium Titanate," *ACS Appl. Mater. Interfaces*, vol. 12, no. 33, pp. 37444–37453, 2020, doi: 10.1021/acsami.0c08928.

[73] H. Idriss, "On the wrong assignment of the XPS O1s signal at 531–532 eV attributed to oxygen vacancies in photo- and electro-catalysts for water splitting and other materials applications," *Surf. Sci.*, vol. 712, no. June, pp. 2–7, 2021, doi: 10.1016/j.susc.2021.121894.

[74] S. Sarkar, V.K. Singh, P. Sadhukhan, A. Pariari *et al.* , "X-ray photoelectron spectroscopy study of a layered tri-chalcogenide system $LaTe_3$," *AIP Conf. Proc.*, vol. 2220, no. May,

2020, doi: 10.1063/5.0001764.

[75] D. J. Morgan, "X-ray Photoelectron Spectroscopy (XPS): An Introduction," *SINTEF Mater. Chem.*, no. March, pp. 1–7, 2007, [Online]. Available: http://sites.cardiff.ac.uk/xpsaccess/files/2014/07/AccessXPS_Primer_Paper.pdf.

[76] A. Kotani, T. Jo, and J. C. Parlebas, "Many-body effects in core-level spectroscopy of rare-earth compounds," *Adv. Phys.*, vol. 37, no. 1, pp. 37–85, Feb. 1988, doi: 10.1080/00018738800101359.

[77] M. Romand, M. Roubin, and J.-P. Deloume, "X-ray photoelectron emission studies of mixed selenides $AgGaSe_2$ and Ag_9GaSe_6," *J. Solid State Chem.*, vol. 25, no. 1, pp. 59–64, 1978, doi: https://doi.org/10.1016/0022-4596(78)90043-9.

[78] C. D. Wagner, "Chemical shifts of Auger lines, and the Auger parameter," *Faraday Discuss. Chem. Soc.*, vol. 60, pp. 291–300, 1975, doi: 10.1039/DC9756000291.

[79] G. Schön, "Auger and direct electron spectrum in X-ray photoelectron studies of zinc, zinc oxide, gallium and gallium oxide," *J. Electron Spectros. Relat. Phenomena*, vol. 2, no. 1, pp. 75–86, 1973, doi: https://doi.org/10.1016/0368-2048(73)80049-0.

[80] B. Moss, "'A spectroscopic study of charge separation in photocatalytic and photoelectrochemical water splitting devices'. Ph.D. Thesis. Department of Chemistry, Imperial College London."

[81] D. J. Kok, K. Irmscher, M. Naumann, C. Guguschev, Z. Galazka, and R. Uecker, "Temperature-dependent optical absorption of $SrTiO_3$," *Phys. Status Solidi Appl. Mater. Sci.*, vol. 212, no. 9, pp. 1880–1887, 2015, doi: 10.1002/pssa.201431836.

[82] V. Mishra, M. K. Warshi, A. Sati, A. Kumar *et al.* , "Diffuse reflectance spectroscopy: An effective tool to probe the defect states in wide band gap semiconducting materials," *Mater. Sci. Semicond. Process.*, vol. 86, no. May, pp. 151–156, 2018, doi: 10.1016/j.mssp.2018.06.025.

[83] V. M. Longo, A.T. de Figueiredo, S. de Lázaro, M. F. Gurgel *et al.* , "Structural conditions that leads to photoluminescence emission in $SrTiO_3$: An experimental and theoretical approach," *J. Appl. Phys.*, vol. 104, no. 2, 2008, doi: 10.1063/1.2956741.

[84] D. Kan, T. Terashima, R. Kanda, A. Masuno *et al.* , "Blue-light emission at room temperature from Ar^+-irradiated $SrTiO_3$," *Nat. Mater.*, vol. 4, no. 11, pp. 816–819, 2005, doi: 10.1038/nmat1498.

[85] T. Hasegawa, M. Shirai, and K. Tanaka, "Localizing nature of photo-excited states in $SrTiO_3$," *J. Lumin.*, vol. 87, pp. 1217–1219, 2000, doi: 10.1016/S0022-2313(99)00520-7.

[86] R. Leonelli and J. L. Brebner, "Evidence for bimolecular recombination in the luminescence spectrum of $SrTiO_3$," *Solid State Commun.*, vol. 54, no. 6, pp. 505–507, 1985, doi: 10.1016/0038-1098(85)90657-X.

[87] C. Mitra, C. Lin, J. Robertson, and A. A. Demkov, "Electronic structure of oxygen vacancies in $SrTiO_3$ and $LaAlO_3$," *Phys. Rev. B - Condens. Matter Mater. Phys.*, vol. 86, no. 15, pp. 1–8, 2012, doi: 10.1103/PhysRevB.86.155105.

[88] M. L. Crespillo, J. T. Graham, F. Agulló-López, Y. Zhang, and W. J. Weber, "Isolated oxygen vacancies in strontium titanate shine red: Optical identification of Ti^{3+} polarons," *Appl. Mater. Today*, vol. 12, pp. 131–137, 2018, doi: https://doi.org/10.1016/j.apmt.2018.04.006.

[89] L. D. Yuan, H. X. Deng, S. S. Li, S. H. Wei, and J. W. Luo, "Unified theory of direct or indirect band-gap nature of conventional semiconductors," *Phys. Rev. B*, vol. 98, no. 24, pp. 1–10, 2018, doi: 10.1103/PhysRevB.98.245203.

[90] P. H. M. Andrade, C. Volkringer, T. Loiseau, A. Tejeda, M. Hureau, and A. Moissette, "Band gap analysis in MOF materials: Distinguishing direct and indirect transitions using UV–vis spectroscopy," *Appl. Mater. Today*, vol. 37, no. January, 2024, doi: 10.1016/j.apmt.2024.102094.

[91] A. R. Zanatta, "Revisiting the optical bandgap of semiconductors and the proposal of a unified methodology to its determination," *Sci. Rep.*, vol. 9, no. 1, p. 11225, 2019, doi: 10.1038/s41598-019-47670-y.

[92] X. Wang, J. Li, R. Guo, X. Yin *et al.* , "Regulating phase homogeneity by self-assembled molecules for enhanced efficiency and stability of inverted perovskite solar cells," 2024, doi: 10.1038/s41566-024-01531-x.

[93] V. Campanari, F. Martelli, A. Agresti, S. Pescetelli *et al.* , "Reevaluation of Photoluminescence Intensity as an Indicator of Efficiency in Perovskite Solar Cells," *Sol. RRL*, vol. 6, no. 8, 2022, doi: 10.1002/solr.202200049.

[94] F. Alarab, K. Hricovini, B. Leikert, L. Nicolaï *et al.* , "Photoemission study of pristine and Ni-doped $SrTiO_3$ thin films," *Phys. Rev. B*, vol. 104, no. 16, pp. 1–8, 2021, doi: 10.1103/PhysRevB.104.165129.

[95] B. Moss, Q. Wang, K. Butler, R. Grau-Crespo *et al.*, "Linking in situ charge accumulation to electronic structure in doped $SrTiO_3$ reveals design principles for hydrogen-evolving photocatalysts," *Nat. Mater.*, vol. 20, no. 4, pp. 511–517, 2021, doi: 10.1038/s41563-020-00868-2.

[96] D. Jiang, X. Sun, X. Wu, L. Shi, and F. Du, "Hydrothermal synthesis of single-crystal Cr-doped $SrTiO_3$ for efficient visible-light responsive photocatalytic hydrogen evolution," *Mater. Res. Express*, vol. 7, no. 1, 2020, doi: 10.1088/2053-1591/ab660d.

[97] D. Neagu and J. T. S. Irvine, "Enhancing electronic conductivity in strontium titanates through correlated A and B-site doping," *Chem. Mater.*, vol. 23, no. 6, pp. 1607–1617, 2011, doi: 10.1021/cm103489r.

[98] M. G. Helander, M. T. Greiner, Z. B. Wang, and Z. H. Lu, "Pitfalls in measuring work function using photoelectron spectroscopy," *Appl. Surf. Sci.*, vol. 256, no. 8, pp. 2602–

2605, 2010, doi: 10.1016/j.apsusc.2009.11.002.

[99] M. Yoshitake, 'Work Function and Band Alignment of Electrode Materials: The Art of Interface Potential for Electronic Devices, Solar Cells, and Batteries′, 1st ed. Springer Tokyo.ISBN: 978-4-431-56896-4, 20 December, 2020. DOI: https://doi.org/10.1007/978-4-431-56898-8

[100] M. Kumar, B. Meena, P. Subramanyam, D. Suryakala, and C. Subrahmanyam, "Recent trends in photoelectrochemical water splitting: the role of cocatalysts," *NPG Asia Mater.*, vol. 14, no. 1, 2022, doi: 10.1038/s41427-022-00436-x.

Appendix

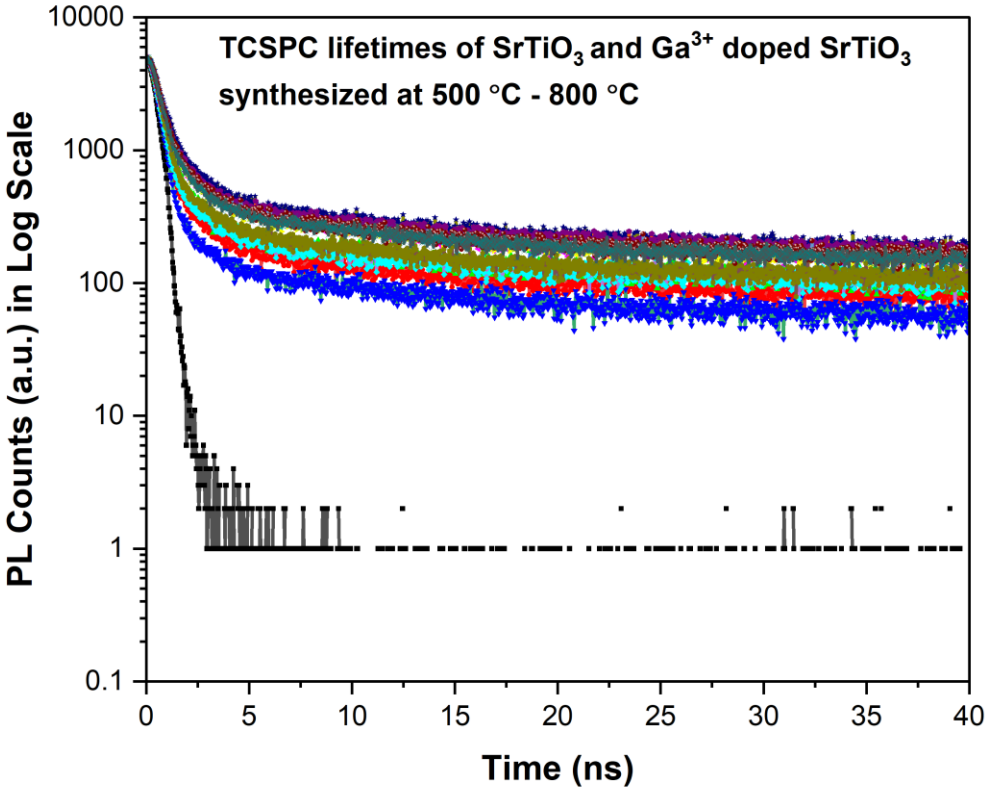
Table 3.1 A: XPS elemental ratios of commercial $SrTiO_3$

Name	Peak BE	FWHM eV	Area (P) CPS eV	Atomic %
C1s C-C	284.75	1.11	379.34	1.2
C1s C-O-C	285.54	1.48	237.45	0.75
C1s CO_3	289.25	2.02	151.65	0.48
O1s Lattice	529.62	1.08	32062.05	41.79
O1s -C=O	530.38	0.69	1314.4	1.71
O1s -OH	531.33	1.86	6648.31	8.68
O1s C-O-C	532.24	1.44	2246.79	2.93
$Sr3d_{5/2}$	133.15	0.92	21584.36	14.63
$Sr3d_{3/2}$	134.9	0.93	14870.83	14.64
$SrCO_3$	134.09	0.93	1577.77	1.07
$SrCO_3$	135.79	0.93	1087.03	1.07
$Ti2p_{3/2}$	458.5	0.96	19801.54	10.88
Ti^{3+} Defects	457.44	0.57	224.55	0.12
TiO_2	459.15	0.49	82.68	0.05

Chapter 4: Enhancements to Sol-Gel Pechini Process- Impact of Annealing Temperatures on Material Properties of Ga^{3+} doped $SrTiO_3$

Summary

In this work, Ga^{3+} doped $SrTiO_3$ was synthesized at 500 °C-800 °C. Microstructural and opto-electronic properties were found to have been affected by the synthesis temperature due to induced defects. These defects were found to affect the charge carrier dynamics. Higher lifetimes were observed for the Ga^{3+} doped $SrTiO_3$ samples synthesized at varying temperatures indicating better charge separation than the undoped $SrTiO_3$ samples.



4.1 Introduction

Photocatalytic reactions are a promising strategy for producing clean and useful fuels by harvesting solar energy [1]. A prerequisite of highly efficient photocatalytic fuel generation is designing catalysts that enhance the conversion to useful fuel products. Owing to the high photochemical stabilities of titanate perovskites, $SrTiO_3$ is a promising candidate for photocatalysis reactions [2]. Doping trivalent metal ions such as Rh^{3+} and Al^{3+} in $SrTiO_3$ has been reported to be an efficient method to increase the photocatalytic activity [3][4]–[6][7]. Doping with trivalent metal cations such as Ga^{3+} with d^{10} configurations has also been reported to enhance photocatalysis [8]. Neagu, D. et al. [9] reported an enhanced n-type conductivity in $SrTiO_3$ when doped with La^{3+} in the A site and with Ga^{3+} in the B site. However, studies on the material properties and the photocatalytic performance of Ga^{3+} doped $SrTiO_3$ are limited.

Doping often introduces trap states and defects such as oxygen vacancies [10], [11]. The role of defects in photocatalysts is an ongoing scientific debate. There is still much to be understood about defects and material properties that are affected by these defects. Therefore, designing and understanding novel catalysts is a crucial step in advancing the field of photocatalysis.

The fundamental step in designing a novel photocatalyst is its synthesis route. The material properties and the subsequent photocatalytic activity depend on the synthesis route [12]. The synthesis route of photocatalytic materials affects their morphological, optical, and electronic properties. The most reported synthesis method is the solid-state synthesis [7],[13]. The major advantage of the solid-state method is the high degree of crystallinity that the synthesized materials exhibit. Crystallinity is one of the important material characteristics that can enhance photocatalysis [5]. The major drawback with the solid-state synthesis is that high temperatures are employed in this route which is energy intensive. Moreover, at higher temperatures, the particles coalesce together to form bigger particles and as a result, decrease their surface areas [14]. Therefore, exploring new synthesis routes that are more energy efficient and retain the characteristic properties of a highly efficient photocatalyst is required.

The conditions such as the annealing temperatures and reducing or oxidizing environments applied during the synthesis process determine the material properties. Varying annealing temperatures have been found to affect microstructural, optical, and electronic properties [15]–[18]. In this study, the sol-gel Pechini route at various annealing temperatures has been employed to synthesize undoped and Ga^{3+} doped $SrTiO_3$ photocatalysts. The core objective is to study the effect of the temperature and doping of novel trivalent d^{10} metal ions in the Ti^{4+} site of $SrTiO_3$. This work focuses on the intrinsic and extrinsic properties that affect the material performance. In this study materials are synthesized at varying temperatures to determine the suitable conditions and properties that result in a highly efficient photocatalyst. Detailed analysis of both the extrinsic and the intrinsic material properties such as the lifetimes, defects, microstructure, electron affinity, and ionization potential has been studied to understand and improve Ga^{3+} doped $SrTiO_3$. This work aims to lay a framework by determining a synthesis method and condition to make photocatalysts and extend our understanding of the material properties that enable this.

Motivation for the Temperature Dependent Studies on Undoped and Ga^{3+}doped samples

In Chapter 3, the samples synthesized at 900 °C showed crystallographic defects such as grain boundaries which could have facilitated the exsolution process by acting as nucleation sites. Figure 4.1 shows the formation of grain boundaries in the Ga^{3+} doped $SrTiO_3$ samples. At higher temperatures, the particles undergo sintering or the Ostwald ripening process that lead to bigger particles. Ostwald ripening involves the smaller particles melting and enlarging upon depositing on a neighboring particle [19]. Figure 4.2 shows the elongation (melting) of a particle and its merging to enlarge. At 900 °C, it was also observed that in some particles the distribution of Ga^{3+} doping was found to be inhomogeneous as shown in Figure 4.3. The distribution of the elements is listed in Table 4.1.

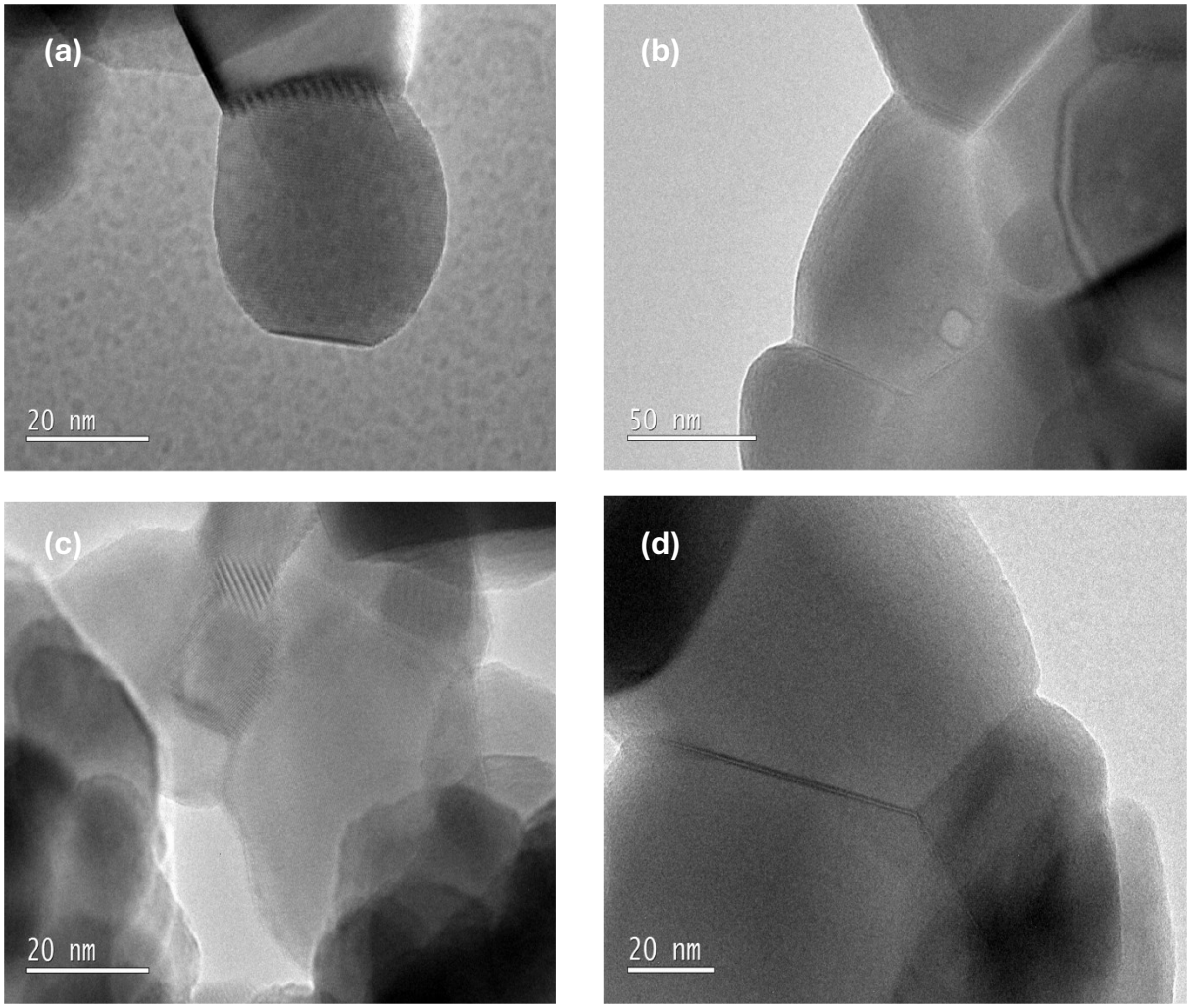


Figure 4.1: *Ga^{3+} doped $SrTiO_3$ nanoparticles coalesced at 900 °C to form bigger particles leading to the formation of grain boundaries. The particles are prone to agglomeration at high temperatures although exhibiting higher crystallinity.*

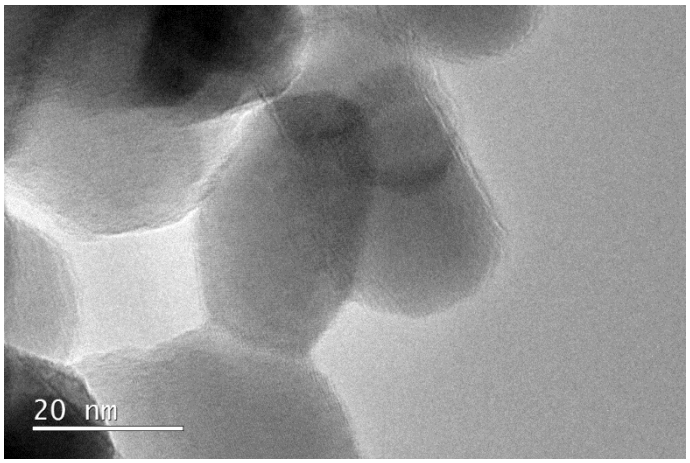


Figure 4.2: *The elongation of a particle and merging with the bigger particle due to high-temperature calcination 2 mol% Ga^{3+} doped sample indicates that particles undergo sintering and Ostwald ripening at higher temperatures.*

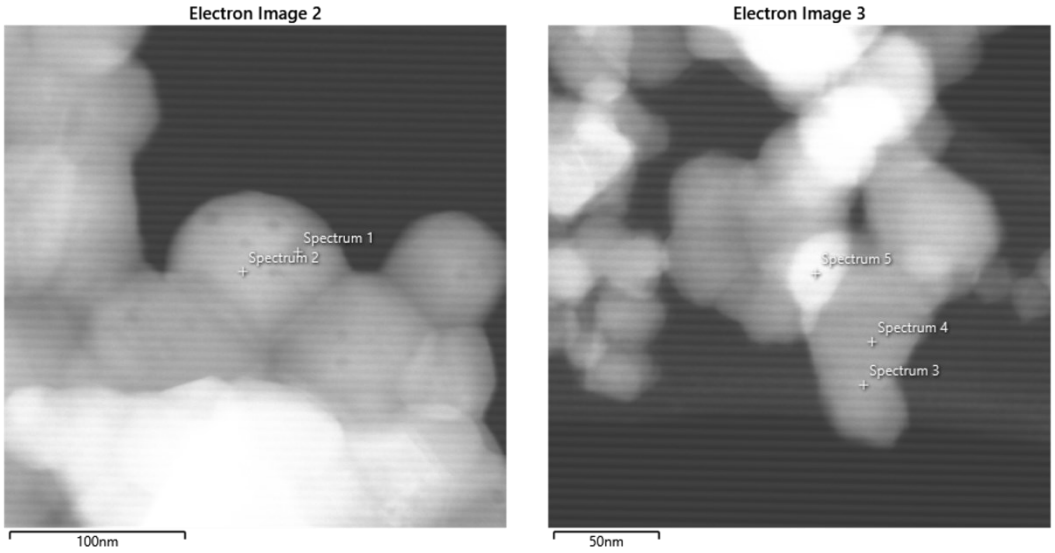


Figure 4.3: *HAADF STEM image of 4 mol% Ga^{3+} doped $SrTiO_3$ synthesized at 900 °C demonstrating heterogeneity in Ga distribution. This could be due to local variations in the diffusion rates of the dopant leading to non-uniform doping.*

Table 4.1 : Element distribution from EDX collected from Figure 5 in 4 mol% Ga^{3+} doped $SrTiO_3$ synthesized at 900 °C

Spectrum	**Sr (At%) (value ± 0.11 At%)[a]**	**Ti (At%) (value ± 0.12 At%)[a]**	**Ga (At%) (value ± 0.05 At%)[a]**	**O (At%) (value ± 0.08 At%)[a]**	**Ga^{3+}/(Ga^{3+} + Ti^{4+}) (At %)**	**(Ga^{3+}+ Ti^{4+}): Sr^{2+}:O^{2-} (At %)**
1 (Area 1)	27.20	20.46	1.19	51.14	5.50	1:1.3:2.4
2 (Area 1)	28.99	21.38	0.91	48.73	4.09	1:1.3: 2.2
3 (Area 2)	23.47	18.05	1.37	57.11	7.05	1:1.2:2.9
4 (Area 2)	24.94	18.94	0.64	55.48	3.27	1:1.3:2.8
5 (Area 2)	23.71	18.84	0.55	56.90	2.84	1:1.2:2.9

[a] *The errors in the At% were added after remeasuring the areas with the EDX*

From Table 4.1 and Figure 4.3, the elements in two areas of the same sample show variation in their distribution at 900 °C. Spectra 1 and 2 are in Area 1 and spectra 3,4 and 5 are in Area 2. The difference in Ga^{3+} distribution is more apparent in Area 2 where the distribution varies between 1.37 atomic % to 0.55 atomic %. This may be speculated to be due to an uneven dopant diffusion at higher temperatures. The primary motivation for this study is to understand whether the observed anomalous behavior pertains only to the high-temperature samples and how the doped samples behave when synthesized at lower temperatures. High-temperature synthesis is energy intensive and therefore, the viability of a lower temperature at which phase purity is achieved was also investigated in this work. In the previous chapter, a time-temperature-solubility factor was discussed which could affect how and in what quantity the dopant is being incorporated into the $SrTiO_3$ matrix. Therefore, to investigate this factor further, the time of

synthesis was increased to 10 h in the low-temperature synthesized samples, and the effect was investigated.

4.2 Results and Discussion

The section starts with a brief discussion of the synthesis process. Phase pure materials were synthesized at temperatures as low as 500 °C. The phase purity is discussed with the Goldschmidt's tolerance factor and the XRD. With the XRD, the microstructural parameters such as the crystallite sizes, the microstrain, and the lattice volumes are discussed. In this section, the effect of oxygen vacancies on the microstructure are studied.

4.2.1 Sol-gel Pechini

In this study, sol-gel Pechini process has been used as the catalyst synthesis route due to the presence of an alkoxide precursor, Titanium (IV) Isopropoxide. This route removes the difficulties associated with conventional alkoxide-based sol-gel processes. Alkoxide precursors are sensitive to moisture and they can undergo rapid hydrolysis and condensations [20], [21]. This in turn can affect reaction kinetics and the final catalyst's morphologies. In the Pechini process, the metal cations from the precursors having different hydrolysis and condensation rates are entrapped in a polymer network by the chelating agent. In this study, citric acid monohydrate has been used as a chelating agent due to its high stability [21]. The ethylene glycol on the other hand aids in polyestrification by forming a polymer network around the metal citrate complex and immobilizes the cations. The cations are homogeneously dispersed in the gel and the segregation of multiple phases is inhibited [22]. The polymer network prevents the thermal decomposition of the metal-citrate complex from controlling the growing product [23]. In this study, citric acid and ethylene glycol in a molar ratio of 4:1 was used to preserve the stoichiometric ratio between the metal cations [24]. Higher CA relative to the EG promotes the formation of a dense polymer network that ensures the uniform dispersion of the metal cations. The higher CA can also ensure that phase segregation is inhibited. In the case of the Ti^{4+} transition metal cation (central atom), the CA molecules will bond through the oxygen atoms through the carboxyl (-COOH) and hydroxyl (-OH) bonds. The formation of the transition metal chelate complex is shown in Figure 4.4.

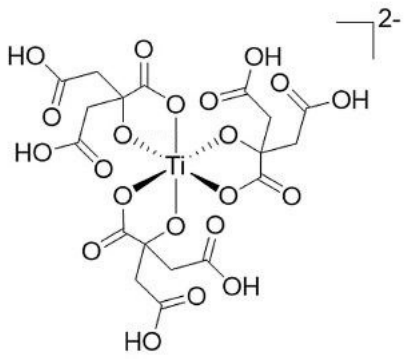


Figure 4.4: *A Ti^{4+} chelate complex with two deprotonated CA molecules with a charge of -2 [25]. CA loses protons (H^+) when it coordinates with Ti^{4+}.*

In the Pechini process or any other solution combustion synthesis process, temperature is an important parameter that determines the crystallite, grain, and particle size. In the work of Can

Li [26], the nanomaterials were calcined at 900 °C with improved crystallinity. In the current Ph.D.. work, there are **two critical temperature steps** in the synthesis route at **197 °C polyestrification** and **calcination at a range of temperatures from 450 °C to 900 °C**.

4.2.2 Synthesis of Phase Pure Materials at 500 °C

Doped and undoped samples were synthesized at 450 °C, 500 °C, 600 °C,700 °C, 800 °C and 900 °C as shown in Figure 4.5. It was observed that white materials were first yielded at 500 °C which was confirmed to be phase pure with the XRD analysis as shown in Figure 4.6. The 500 °C sample was compared with the sample prepared at 900 °C to eliminate any indiscretion regarding the presence of secondary phases as shown in Figure 4.6. The small peak at around 29.5° 2θ angle was confirmed with the Spectral Line Analysis Tool in the Expert High Score+ XRD Analysis Software to be due to kß radiation from the diffractometer.

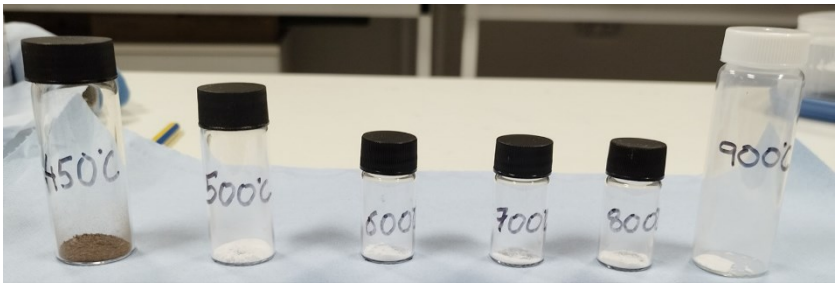


Figure 4.5: *Samples synthesized at different annealing temperatures from 450 °C to 900 °C.*

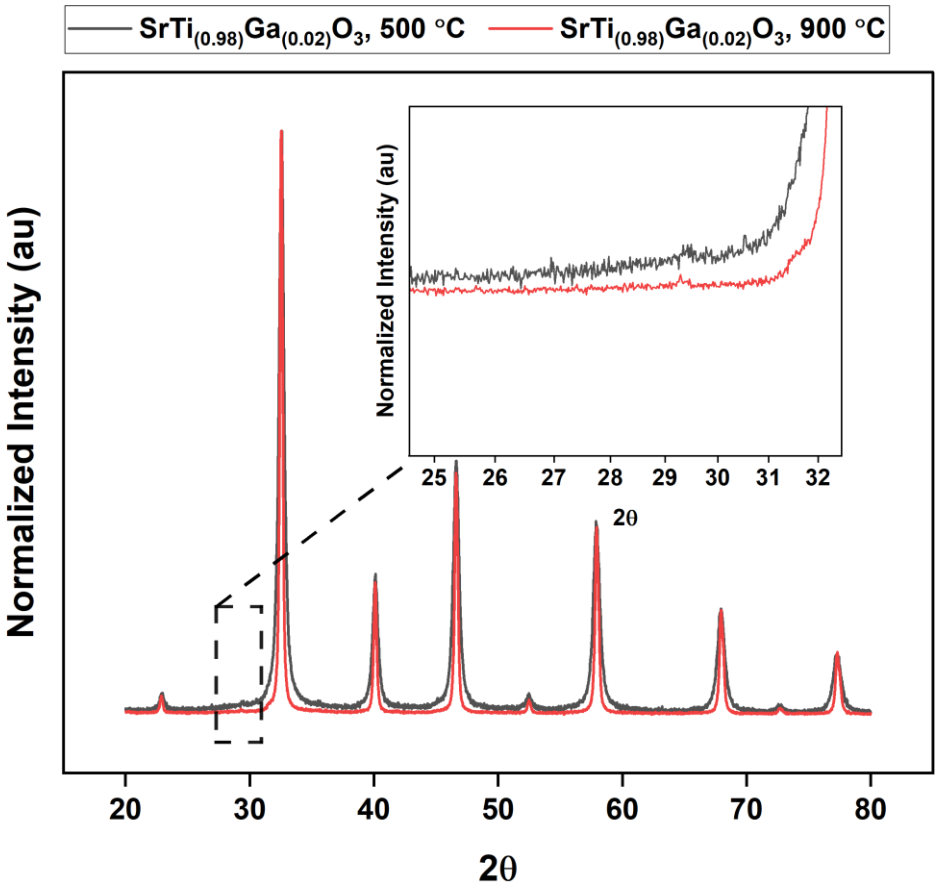


Figure 4.6: *Phase pure materials were first obtained at 500 °C. The low-temperature synthesized samples were compared with, and the samples synthesized at 900 °C to check phase purity. The peak at 29.5° 2θ is due to kß radiation.*

During the synthesis process, the calcination temperature is the key parameter in determining the phase purity, the extent of incorporation of the dopants, and the nature of the materials. During the calcination, the Ga precursor decomposes to Ga_2O_3 and reacts with the $SrTiO_3$ to give the Ga^{3+} doped samples. In this work, we study the effect of different calcination temperatures on the material properties and their potential to be a photocatalyst.

4.2.3 Goldschmidt's Tolerance Factor Consideration in the Structural Stability

The Goldschmidt's tolerance factor, t indicates that the doped samples maintain structural stability and show no secondary phases. Table 4.2 shows the 't' of the samples.

Table 4.2: Goldschmidt's Tolerance Factor for undoped and doped $SrTiO_3$ samples

Sr No	Sample	Tolerance Factor, t
1	Undoped $SrTiO_3$	1
2	2 mol% Ga doped $SrTiO_3$	1.001
3	4 mol% Ga doped $SrTiO_3$	1.001

From Table 4.2, the tolerance factor of the samples is 1 which is within the tolerance limit 0.75<t<(=) 1 as discussed in the previous chapter**.** It can be inferred from Table 4.2, that the samples retain the cubic structure with no distortions upon Ga^{3+} mono-doping. This can be further validated with XRD patterns which showed similar results.

4.2.4 XRD Analysis

XRD patterns of the undoped and doped samples synthesized at different calcination temperatures retain the cubic structure of $SrTiO_3$ as shown in Figure 4.7. Crystallization starts at 500 °C and secondary reflections from impurity phases were not observed. Peak indexing was done according to ICSD 23076 [27]–[29]. In all the samples the (110) peak is the most intense. XRD was repeated for the samples three times and error bars were included for the results.

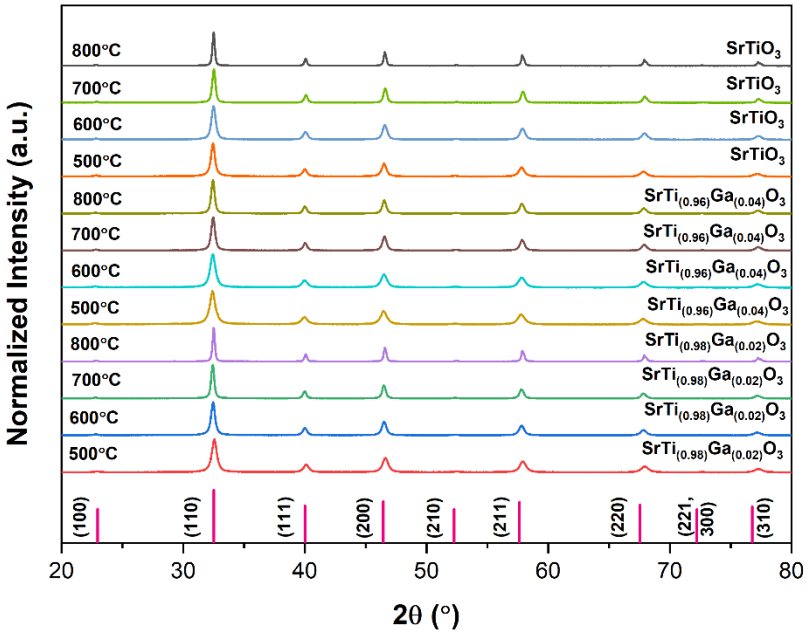


Figure 4.7: *Phase pure materials as determined from the XRD diffraction patterns of the samples synthesized at different temperatures compared with the standard $SrTiO_3$ sample, ICSD (pink) [27]-[29]. The XRD pattern of the samples was collected with the same parameters described in Chapters 2 and 3.*

The analysis of the XRD diffraction pattern in Figure 4.7 shows the broadening of the peaks, indicating a significant effect of temperature on the microstructure of the samples. The influence of different annealing temperatures on the different aspects of the microstructure such as crystallinity, crystallite sizes, and lattice volume are discussed in the following sections.

4.3 Influence of Temperature on the Microstructural Properties

This section discusses the role of temperature in influencing the microstructural properties. The discussion on the properties based on the XRD analysis starts with the relative crystallinity, crystallite sizes, microstrain, and lattice volume. This section tries to correlate the microstrain

and the lattice volumes with defects present in the crystal structure and how these factors can influence the charge carrier lifetimes.

4.3.1 Influence of Temperature on Relative Crystallinity

The crystalline nature of materials increases with temperature. In Figures 4.8 (a, b, c) the (110) peak of the samples calcined at 500 °C, 600 °C,700 °C and 800 °C was compared against their peak intensity and the full width at half maximum (FWHM). Here the peak (110) was chosen for comparison as this peak was the most intense. All the peaks show the same shift trend as the (110). It was observed that at 800 °C, each sample had the most intense peak with the smallest FWHM. This can be attributed to the increase in ordering of the atoms which subsequently results in better crystallinity of the materials. The consideration of relative crystallinity has been discussed in Chapter 3.

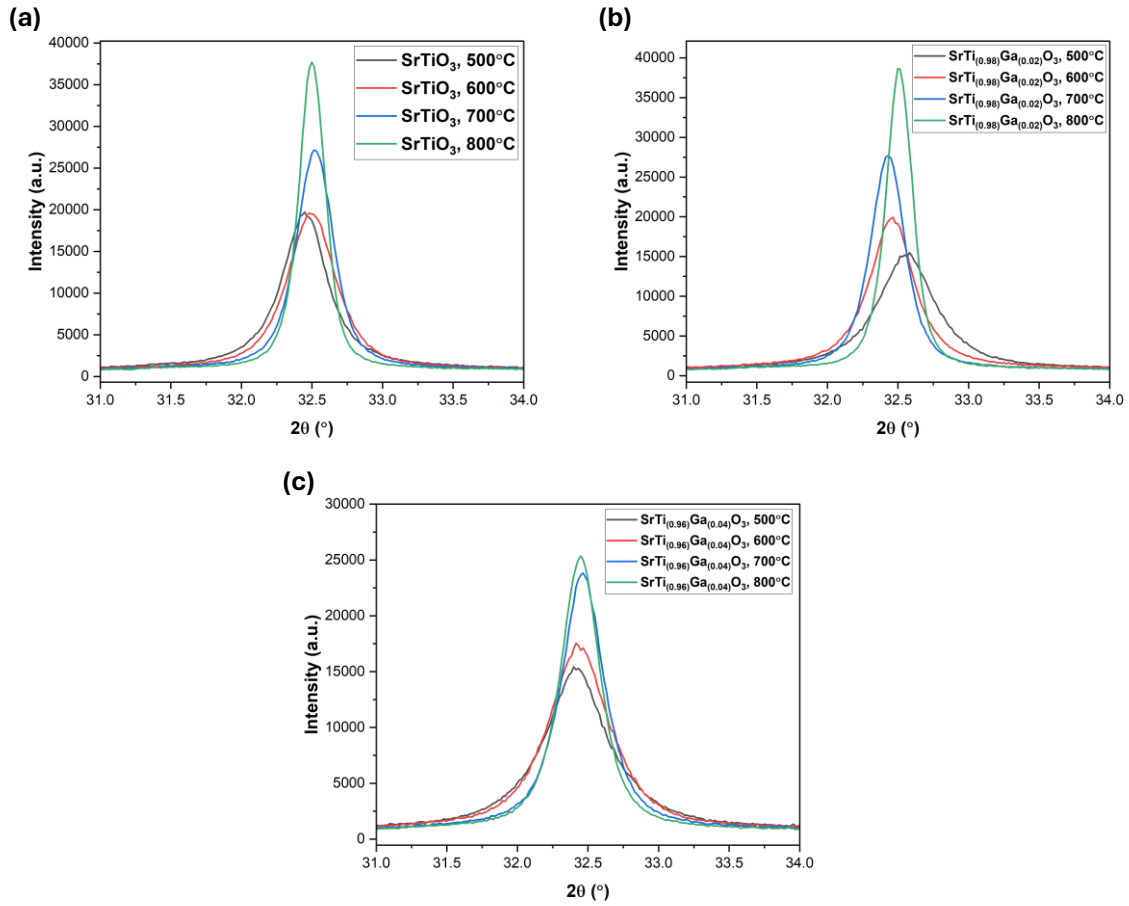


Figure 4.8: *Comparison of XRD peak (110) of (a) Undoped (b) 2 mol% Ga^{3+} doped (c) 4 mol% Ga^{3+} doped $SrTiO_3$ synthesized at 500 °C, 600 °C, 700 °C and 800 °C to demonstrate the effect of calcination temperature on the relative crystallinity of the materials.*

A highly crystalline surface devoid of defects is instrumental for charge carrier migration to the photocatalyst surface for enhanced performance [30], [31]. 2 mol% Ga^{3+} doped $SrTiO_3$ at 800 °C shows a higher degree of crystalline nature as compared to all the other samples as shown in Figure 4.9.

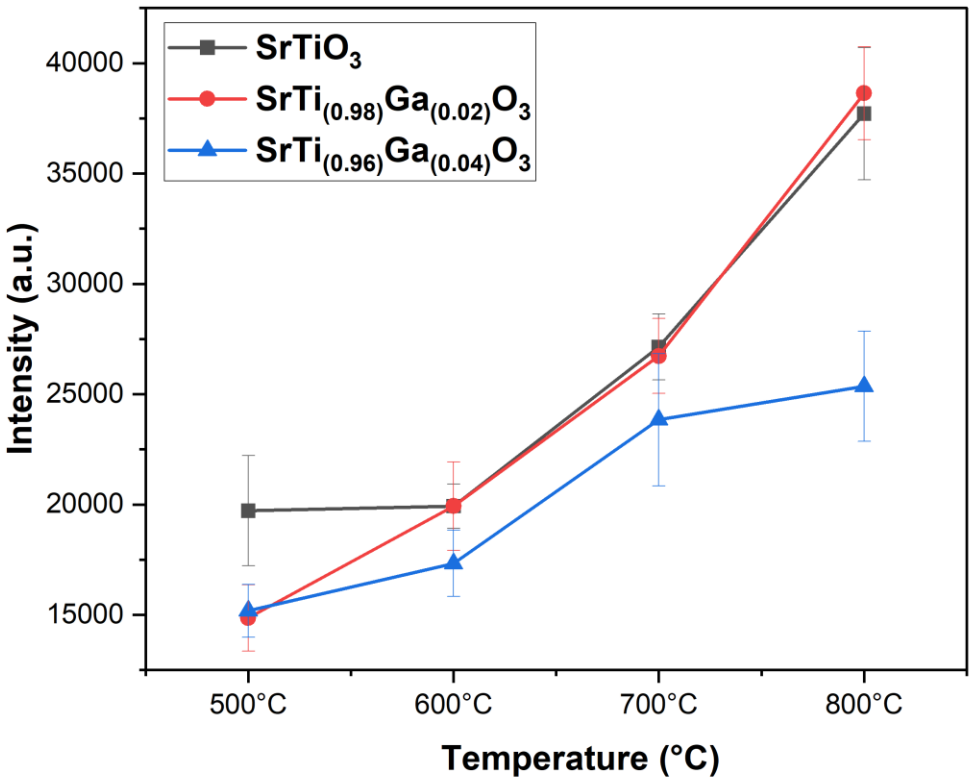


Figure 4.9: *Comparison of XRD (110) peak intensities of doped and undoped samples at different temperatures with the 2 mol% Ga^{3+} doped sample showing the highest crystallinity. Peak (110) as shown in Figure 4.7 is the most intense peak that has been used to compare the relative crystallinity.*

Crystalline nature and smaller particle sizes are desirable characteristics of photocatalysts for enhanced performance as discussed previously. Figures 4.7, 4.8, and 4.9 show that the FWHM of the XRD peaks decreases with increasing temperatures. This can be reflected in the size of the nanoparticles obtained with different calcination temperatures which are discussed in detail in the following section.

4.3.2 Influence of Temperature on the Coherently Scattering Domain Size

The doped and the undoped samples demonstrated that with increasing the calcination temperature, the coherently scattering domain size increases as shown in Figure 4.10. For ease of use, coherently scattering domain size will be referred to as crystallite size henceforth. The increase in crystallite size with temperature can be attributed to the coalescence of the smaller crystallites into larger ones as the temperature increases.

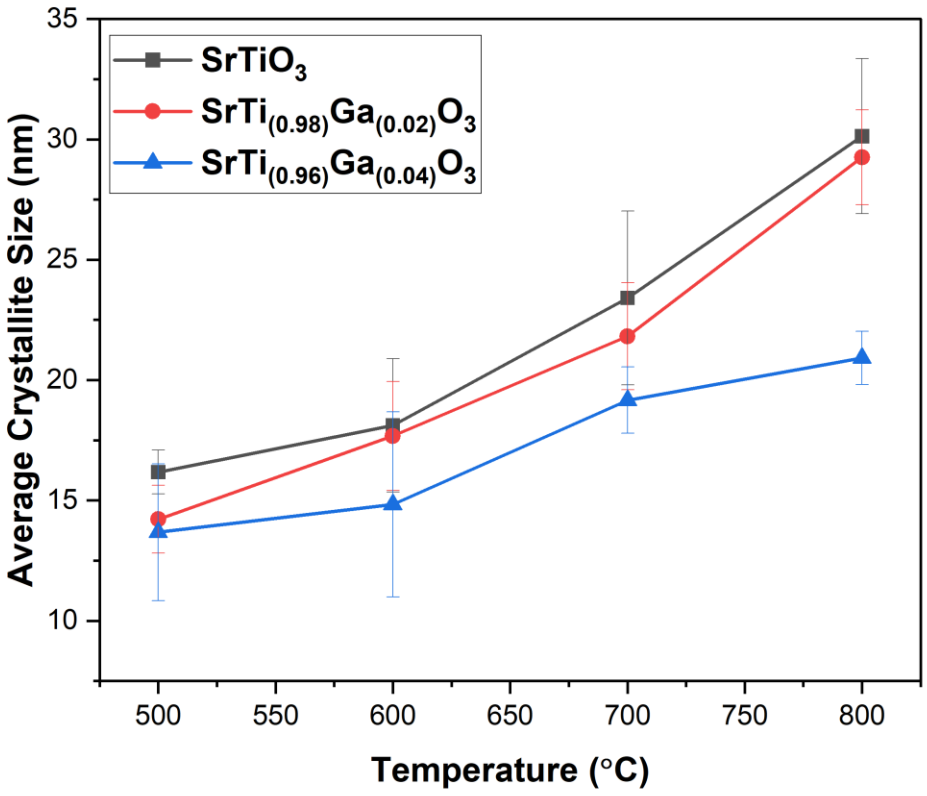


Figure 4.10: *Effect of increasing annealing temperatures on the crystallite sizes as determined by the XRD from the Scherrer equation as analyzed in Figure 4.8. The crystallite sizes increased with an increase in temperature for all the samples.*

According to the Debye-Scherrer equation, as discussed in Chapter 2 (Eq 2.5), the FWHM is the indicator of peak broadening (ß) which can be correlated to the crystallite sizes. The broader the peak or higher FWHM the lower the crystallite size. With the increase in temperature, the FWHM of the peaks decreased indicating an increase in the crystallite size. Figures 4.8 (a,b,c) show the narrowing of the peaks for the undoped and doped samples. The increasing crystallite sizes and the decreasing FWHM w.r.t to the 110 planes of the samples are listed in Table 4.3.

Table 4.3: Average Crystallite Sizes and FWHM of the samples deduced from the Debye-Scherrer equation

Samples	Annealing Temperature	Average Crystallite Size (nm)	FWHM (110)
$SrTiO_3$	500 °C	16.82 ± 0.91	0.41
$SrTiO_3$	600 °C	20.08 ± 2.77	0.38
$SrTiO_3$	700 °C	25.96 ± 3.61	0.31
$SrTiO_3$	800 °C	32.41 ± 3.22	0.22
$SrTi_{(0.98)}Ga_{(0.02)}O_3$	500 °C	13.22 ± 1.41	0.39
$SrTi_{(0.98)}Ga_{(0.02)}O_3$	600 °C	19.28 ± 2.26	0.37
$SrTi_{(0.98)}Ga_{(0.02)}O_3$	700 °C	23.39 ± 2.22	0.29
$SrTi_{(0.98)}Ga_{(0.02)}O_3$	800 °C	30.65 ± 1.97	0.22
$SrTi_{(0.96)}Ga_{(0.04)}O_3$	500 °C	15.68 ± 2.84	0.53
$SrTi_{(0.96)}Ga_{(0.04)}O_3$	600 °C	17.55 ± 3.85	0.51
$SrTi_{(0.96)}Ga_{(0.04)}O_3$	700 °C	19.77 ± 1.38	0.36
$SrTi_{(0.96)}Ga_{(0.04)}O_3$	800 °C	20.12 ± 1.10	0.33

Besides the temperature, crystallite size was also observed to be a function of the doping concentration. From Figure 4.10, as the mol% doping increased for the samples then the crystallite size decreased. This could be speculated to be due to an increase in defect sites. With the introduction of the dopant, more defect sites can be introduced which can act as nucleation sites. As the nucleation rate increases, the smaller nuclei formed will result in smaller particles. At every calcination temperature between 500 °C to 800 °C, the crystallite size decrement for 4 mol% Ga doped $SrTiO_3$ is higher compared to 2 mol% Ga doped and undoped $SrTiO_3$ samples.

In the Scherrer equation, while the peak broadening is associated with the crystallite size it does not consider the microstrain which can also contribute to peak broadening. Microstrain in this study is also another crucial parameter that might be important to understand why the crystallite size decreased with doping. Microstrain is discussed in detail in the following section.

4.3.3 Influence of Temperature on the Microstrain

Microstrain or the local lattice strain is defined as the strain that is localized in some lattice spacings [32]. These types of strains are associated with defects such as dislocations, faults, and grain boundaries [32]. In this work, microstrain is calculated by the Williamson-Hall (W-H) Method based on the uniform deformation model (UDM). The W-H analysis is a mathematical model that takes into consideration the effect of the microstrain on the crystallite size which is overlooked by the Scherrer equation. In both cases of the Scherrer and the W-H method, instrumental broadening was taken into consideration which is shown in Chapter 2 Eq (2.12).

Figure 4.11 shows the effect of temperature on the microstrain. With the increase in temperature in the undoped $SrTiO_3$, the microstrain decreases to nearly zero at 800 °C. In the case of both the doped samples, the microstrain increases between 500 °C and 700° and then decreases at 800 °C. The calculated strains are given in Table 4.4.

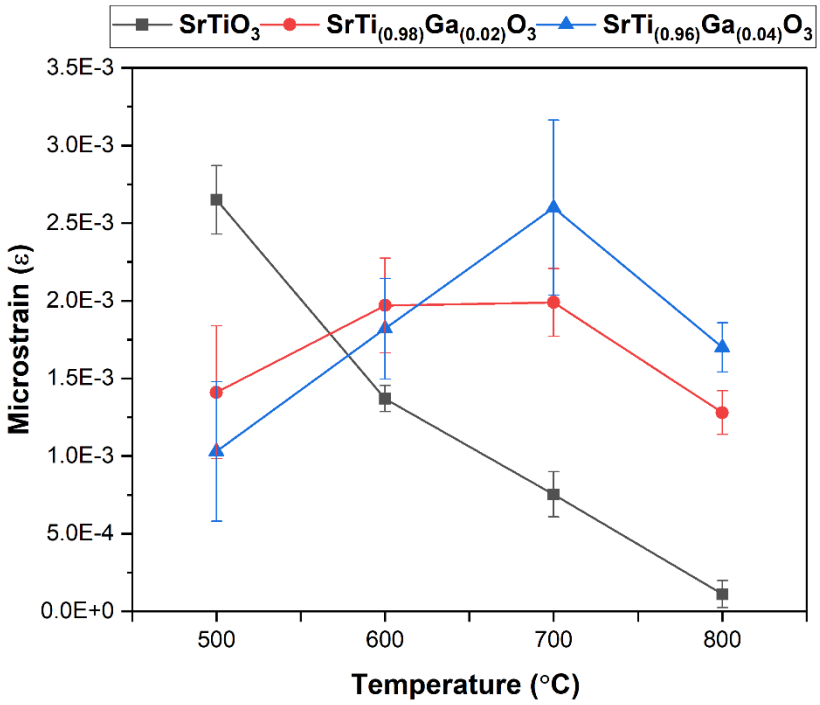


Figure 4.11: *Effect of temperature on the microstrain of the undoped and doped samples. The microstrain in this work has been studied as an indicator of localized defects[32]. This parameter decreases monotonically for the undoped samples and for the doped samples increases up to 700 °C. At 800 °C both the doped samples show a decrease.*

Table 4.4: Calculated microstrains of the undoped and the doped samples

Samples	Annealing Temperature	Microstrain (ε)	Standard Deviation
$SrTiO_3$	500 °C	2.65E-03	± 0.22E-03
$SrTiO_3$	600 °C	1.37E-03	± 0.84E-04
$SrTiO_3$	700 °C	7.54E-04	± 0.15E-03
$SrTiO_3$	800 °C	1.11E-04	± 0.19E-03
$SrTi_{(0.98)}Ga_{(0.02)}O_3$	500 °C	1.41E-03	± 0.43E-03
$SrTi_{(0.98)}Ga_{(0.02)}O_3$	600 °C	1.97E-03	± 0.31E-03
$SrTi_{(0.98)}Ga_{(0.02)}O_3$	700 °C	1.99E-03	± 0.22E-03
$SrTi_{(0.98)}Ga_{(0.02)}O_3$	800 °C	1.28E-03	± 0.14E-03
$SrTi_{(0.96)}Ga_{(0.04)}O_3$	500 °C	1.03E-03	± 0.45E-03
$SrTi_{(0.96)}Ga_{(0.04)}O_3$	600 °C	1.82E-03	± 0.32E-03
$SrTi_{(0.96)}Ga_{(0.04)}O_3$	700 °C	2.60E-03	± 0.56E-03
$SrTi_{(0.96)}Ga_{(0.04)}O_3$	800 °C	1.70E-03	± 0.16E-03

Microstrain arises due to defects in the lattice. The trend in Figure 4.11 with the undoped samples shows the decrease in microstrain with temperature. This indicates that with temperature the defects decrease, and the crystallinity improves. In the case of the doped samples, Ga^{3+} doping might induce some defects at temperatures up to 700 °C which increases the microstrain. At 800 °C, the strain decreases for both the doped samples. This might again be speculated to be an improvement in the crystallinity and decrease in defects as temperatures increase above 700 °C.

In a crystal, two types of strains may affect the microstructure. First is a microstrain which is a localized strain arising from defects contributing to XRD peak broadening. This type of strain does not cause peak shifts. The second type of strain arises when a uniform stress is applied to the entire lattice [32], [33]. The resultant strain causes the XRD peaks to shift. Peak shifts are crucial to understanding the changes the lattice is undergoing as the temperature is varied. The following section gives a detailed analysis of the changes observed from the peak shifts.

4.3.4 Influence of Temperature on the Lattice Parameters and Lattice Volume

XRD peak shifts are due to a uniform stress exerted on all over the lattice. In Figure 4.12(a) and (c), peaks shift towards higher 2θ angles in the undoped samples and 4 mol% Ga doped $SrTiO_3$. This might be due to a compressive stress that acts on the lattice. In Figure 4.12(b), the 2 mol% Ga doped $SrTiO_3$ samples shift to lower 2θ angles. Here, a tensile stress may be acting uniformly over the lattice.

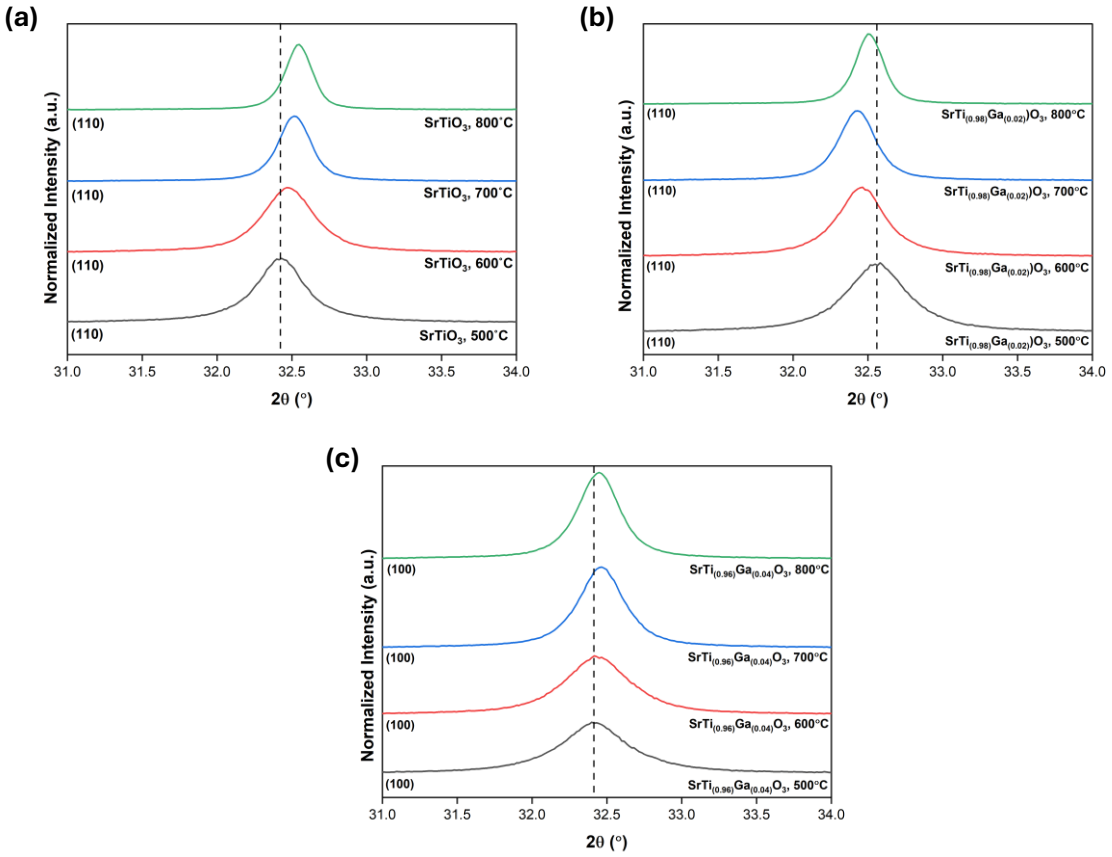


Figure 4.12: *XRD peak (110) shifts (a) Undoped (b) 2 mol% Ga Doped (c) 4 mol% Ga doped $SrTiO_3$ as a function of temperature. The 2 mol% doped sample shows a monotonic lattice expansion at all temperatures. The undoped and the 4 mol%, samples show a monotonic lattice contraction.*

Peak shifts in XRD can also be due to how the samples are loaded on the holder. But in this case, the monotonic peak shifts indicate the changes in the lattice of the samples which can be validated by the change in the lattice parameters and cell volumes of the samples.

The lattice parameters were obtained as per the method discussed in Chapter 2. Since Ga-doped $SrTiO_3$ retained the cubic structure of undoped $SrTiO_3$, the lattice volumes were calculated by Eq 2.4 in Chapter 2.

The calculated lattice parameters and the volumes are mentioned in Table 4.5.

Table 4.5: Calculated lattice parameters and lattice volumes of the undoped and doped samples prepared at different temperatures

Samples	Annealing Temperature	Lattice Parameter (Å) (value ± 0.001 Å)[a]	Lattice Volume (Å^3) (value ± 0.05 Å^3)[b]
$SrTiO_3$	500 °C	3.8954	59.1103
$SrTiO_3$	600 °C	3.8911	58.9118
$SrTiO_3$	700 °C	3.8785	58.3434
$SrTiO_3$	800 °C	3.8778	58.3109

$SrTi_{(0.98)}Ga_{(0.02)}O_3$	500 °C	3.8809	58.4499
$SrTi_{(0.98)}Ga_{(0.02)}O_3$	600 °C	3.8824	58.5172
$SrTi_{(0.98)}Ga_{(0.02)}O_3$	700 °C	3.9082	59.6955
$SrTi_{(0.98)}Ga_{(0.02)}O_3$	800 °C	3.8995	59.2960
$SrTi_{(0.96)}Ga_{(0.04)}O_3$	500 °C	3.9064	59.6113
$SrTi_{(0.96)}Ga_{(0.04)}O_3$	600 °C	3.9020	59.4084
$SrTi_{(0.96)}Ga_{(0.04)}O_3$	700 °C	3.9022	59.4194
$SrTi_{(0.96)}Ga_{(0.04)}O_3$	800 °C	3.9011	59.3710

[a,b] *The errors in lattice parameters and volumes were added after remeasuring the XRD data of the samples and recalculating the lattice parameters and volumes*

For the undoped and the 4 mol% Ga doped samples, the lattice parameters, and the cell volumes decrease/contract respectively with increasing temperatures. The 2 mol% Ga doped $SrTiO_3$ shows the lattice parameters and the cell volume increase/expansion with temperature**.** From Figure 4.13, the theory about the presence of defects as a function of temperature and crystallinity can be hypothesized. The more crystalline the surface is, the lesser the incidence of defects. At 500 °C, the undoped sample has a more intense (110) peak as compared to the doped samples. As the temperature increases, the crystallinity improves but differently for the three types of samples. The undoped and the 2Ga mol% doped $SrTiO_3$, the crystallinity increased more than the 4Ga mol% doped samples at each temperature. At 800 °C, the 2Ga mol% has better crystallinity than the undoped and the 4Ga mol% doped sample. This could be due to doping beyond an optimal level may adversely impact the crystallinity.

The lattice expansion and contraction depend on the types and concentration of the intrinsic defects. Kobayashi, S. et al. [34], reported similar contraction and expansion in Nb, La co-doped $SrTiO_3$. They found that doping led to lattice distortions and the formation of Sr and O vacancies that reduced the lattice expansions. In their monodoped samples, the lattice parameter changed only by a small margin. Similar observations were made in the case of Ga-doped samples in the Ph.D. study. Birkner, N. et al. [35] in their study on Ga^{3+} doping in $Li_7La_3Zr_2O_{12}$ found that increasing doping leads to a decrease in lattice parameters and cell volumes. Doping in the Li site in their study led to defect formation such as Li vacancies which led to the shrinking of the cell volume. Similar observations were also made by Wagner, R. et al. [36]. Li, G. et al. [37] proposed a surface defect dipole model to explain monotonic expansion in cell volumes in rutile TiO_2.

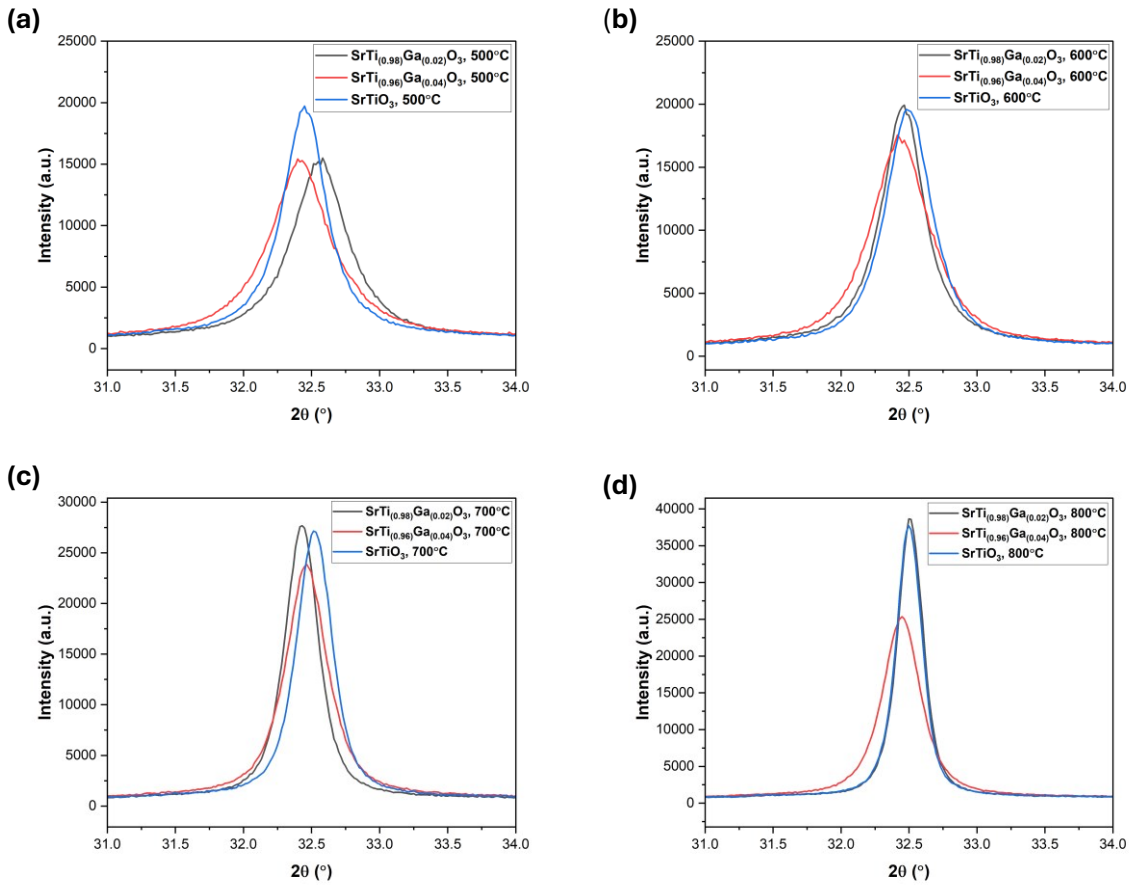


Figure 4.13: *Comparison of XRD peak (110) between the undoped and the doped samples at (a.) 500 °C (b.) 600 °C (c.) 700 °C (d.) 800 °C demonstrating how the microstructural parameters relating to the size and strain change between the doped samples synthesized at different temperatures.*

High crystallinity and low defect concentrations are strongly related to charge carrier dynamics[38]. Recombination of charges is common in semiconductors with a high density of defects. To study the effect of these, TCSPC analysis of the samples was done. The charge carrier dynamics are discussed in detail in the following section.

4.3.5 Effect of the Microstructure on the Time-Correlated Single Photon Counting (TCSPC) Measured Lifetimes

Time-resolved PL spectroscopy via TCSPC is essential for measuring the recombination lifetimes of the samples. The parameters of the TCSPC measurements are discussed in Chapter 2 (2.3.3). The TCSPC data were reconvoluted with a 3-exponential decay fitting according to Eq 2.19 in Chapter 2.

The average lifetimes of the samples shown in Figure 4.14 were measured from the exponential fitting via the HORIBA Da6.8 software and reconvoluted decay time constants are shown in Table 4.6. All samples were measured at λ_{exc} = 282 nm. Table 4.6 shows the average lifetimes of the samples which was calculated with Eq 2.20 in Chapter 2.

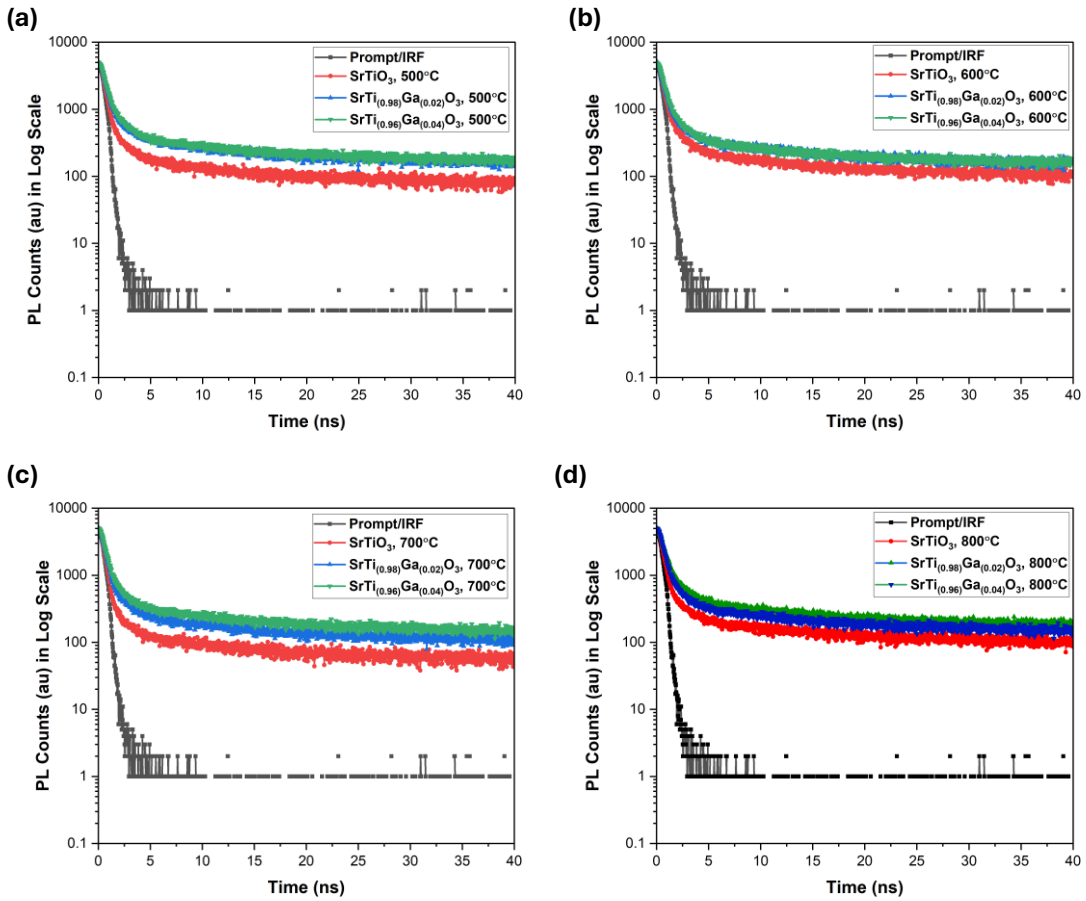


Figure 4.14 : *Photoluminescence Decay Time Profile Comparison between undoped mol% doped $SrTiO_3$ at (a) 500 °C (b) 600 °C (c) 700 °C (d) 800 °C. The TCSPC data was fitted with a three exponential decay function as discussed in Chapter 2. The 2 mol% Ga^{3+} at 800 °C show the highest lifetime at 0.68 ns.*

Table 4.6: TCSPC decay time constants and the average lifetimes of the temperature-dependent samples

Sample	T_1 (s)	T_2 (s)	T_3 (s)	Average Lifetimes (ns)	χ^2
$SrTiO_3$ (500 °C)	2.60E-09	8.59E-08	1.21E-10	0.31 ± 0.01	1.99
$SrTiO_3$ (600 °C)	2.24E-09	5.81E-08	1.14E-10	0.27 ± 0.02	1.43
$SrTiO_3$ (700 °C)	2.33E-12	2.15E-09	5.56E-08	0.23 ± 0.01	1.29
$SrTiO_3$ (800 °C)	2.55E-09	6.36E-08	1.00E-10	0.24 ± 0.04	1.38
$SrTi_{(0.98)}Ga_{(0.02)}O_3$ (500 °C)	2.74E-09	6.34E-08	1.62E-10	0.53 ± 0.01	1.61
$SrTi_{(0.98)}Ga_{(0.02)}O_3$ (600 °C)	2.69E-09	6.18E-08	1.67E-10	0.53 ± 0.02	1.65
$SrTi_{(0.98)}Ga_{(0.02)}O_3$ (700 °C)	2.57E-09	5.79E-08	1.36E-10	0.34 ± 0.03	1.42
$SrTi_{(0.98)}Ga_{(0.02)}O_3$ (800 °C)	2.48E-09	5.84E-08	1.87E-10	0.68 ± 0.01	1.85
$SrTi_{(0.96)}Ga_{(0.04)}O_3$ (500 °C)	2.54E-09	6.20E-08	1.53E-10	0.54 ± 0.02	1.68
$SrTi_{(0.96)}Ga_{(0.04)}O_3$ (600 °C)	1.45E-10	2.07E-09	5.15E-08	0.47 ± 0.02	1.54
$SrTi_{(0.96)}Ga_{(0.04)}O_3$ (700 °C)	1.18E-10	2.17E-09	5.27E-08	0.24 ± 0.01	1.36
$SrTi_{(0.96)}Ga_{(0.04)}O_3$ (800 °C)	2.55E-09	6.03E-08	1.65E-10	0.52 ± 0.01	1.65

From Figure 4.14 and Table 4.6, 2 mol% Ga doped $SrTiO_3$ at 800 °C has a longer lifetime than the other samples at 0.68ns. This sample from Figure 4.9 shows better crystallinity than the other samples. Better crystallinity indicates a more defect-free surface. A defect-free surface has fewer possibilities of charge carrier recombination than a sample with a high concentration of defect density**.** At each temperature, the doped samples showed higher lifetimes than the undoped $SrTiO_3$.

In the case of the undoped and the 4 mol% Ga doped $SrTiO_3$, each showed the highest lifetime at 500 °C. Each sample at 700 °C has the lowest lifetime in their group. The correlation of lifetimes with temperature is shown in Figure 4.15.

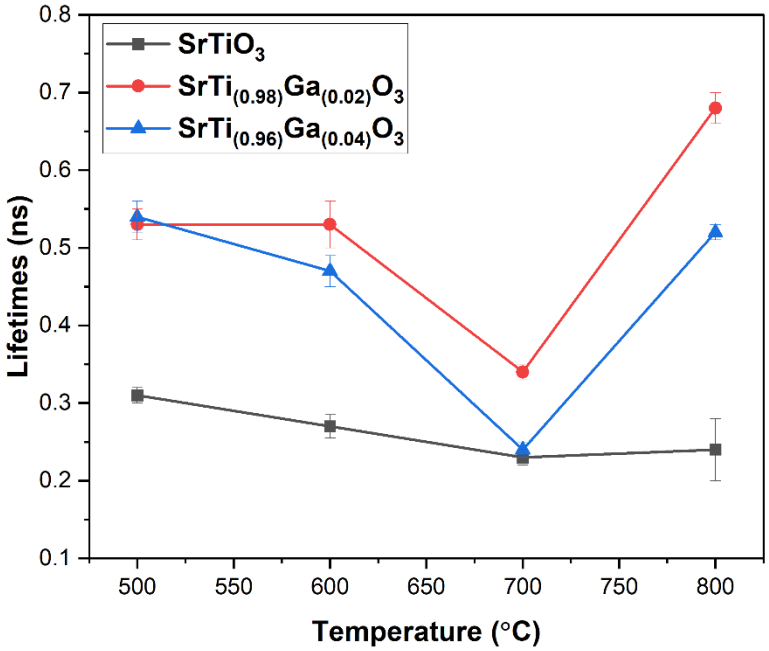


Figure 4.15: *The correlation between the lifetimes of the doped samples and the temperature. The lifetimes decrease in all the samples synthesized at 500 °C. to 700 °C. At 800 °C all the samples show an increase in the lifetime with 2 mol% doped sample demonstrating the highest lifetime at 0.68 ns.*

In the 4 mol% doped samples, a direct relation between the lifetimes and the microstrain can be observed. Here, the lifetimes decrease gradually as the microstrain increases, and at 800 °C as it decreases again the lifetimes increase. Similar conclusions can also be drawn with the 2 mol% sample. In this sample, the lifetimes decrease by a small amount between 500 °C and 600 °C, and then there is a steep decline at 700 °C. At 800 °C, the microstrain is decreased, the lifetimes increase. For the undoped, the opposite trend can be observed where the sample with the highest microstrain has the highest lifetime. At 600 °C and 800 °C, the microstrain decreases with the increase in lifetimes for the undoped samples. An attempt to explain this phenomenon will be made in later sections of the chapter correlating with the opto-electronic properties.

Microstructural parameters such as degree of crystallinity, type, and concentration of defects thus can affect the charge carrier dynamics. In combination with the microstructural parameters, the intrinsic parameters such as the band gap, the work function, the electron affinity, and the ionization potential also affect the charge carrier dynamics [39]. The role of intrinsic parameters will be discussed in the section below.

4.4 Influence of Temperature on the Opto-electronic Properties of the Samples

This section discusses the effect of temperature on the opto-electronic properties of the materials. The discussion starts with the bandgaps, the valence band positions, and the work function. A correlation between the microstructural and opto-electronic properties is attempted

here. Intrinsic properties such as the electron affinity and the ionization potential are calculated to understand the band edge alignment.

4.4.1 Influence of Annealing Temperature on Bandgaps

In Figure 4.16, no significant changes in bandgaps were observed with an increase in temperature for the samples contrary to many reported literature on semiconductor materials [40]–[42]. Ga^{3+} doping did not induce any visible light activity in the samples as seen in Figure 4.16 (a-c).

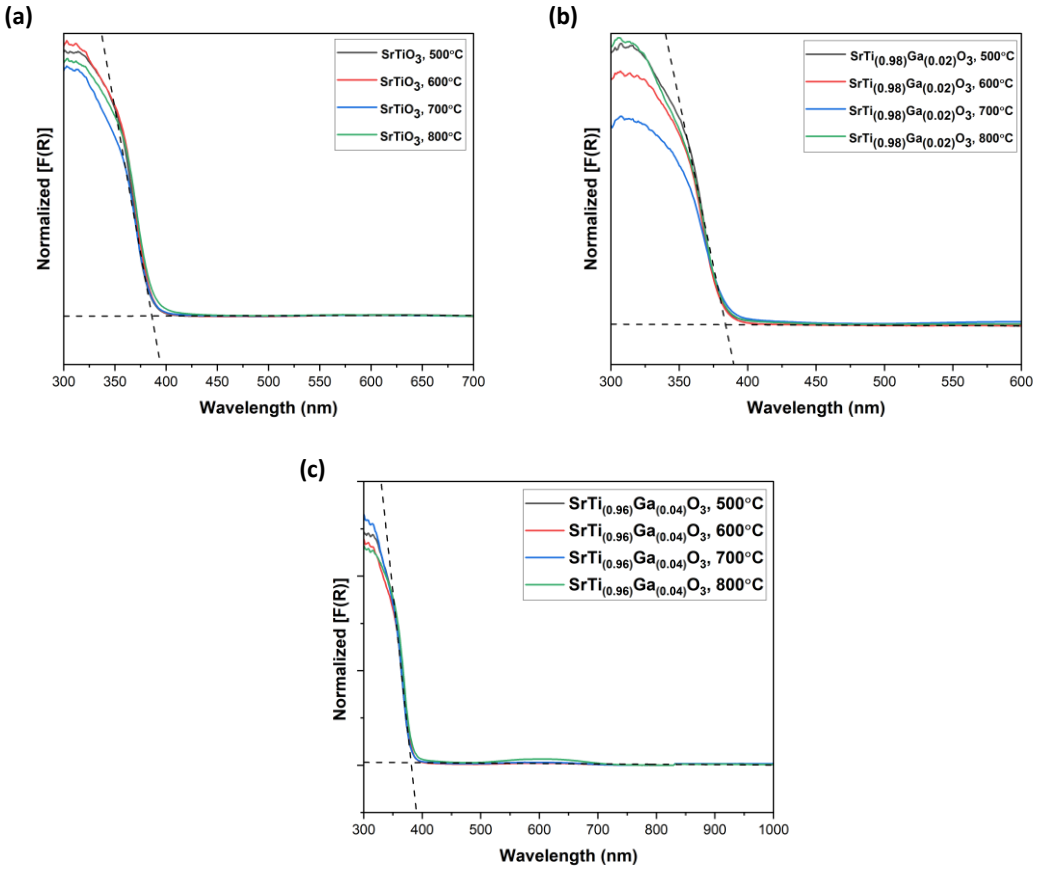


Figure 4.16: *Absorption wavelengths of (a) Undoped (b) 2 mol% Ga^{3+} (c) 4 mol% Ga^{3+} doped $SrTiO_3$. All samples exhibit absorption in the UV region. Doped samples show traces of absorption features which become more prominent with temperature around the 550 nm region indicating the modification of opto-electronic properties due to oxygen vacancies. This phenomenon was also observed in the case of the La^{3+} co-doped samples as discussed in Chapter 3.*

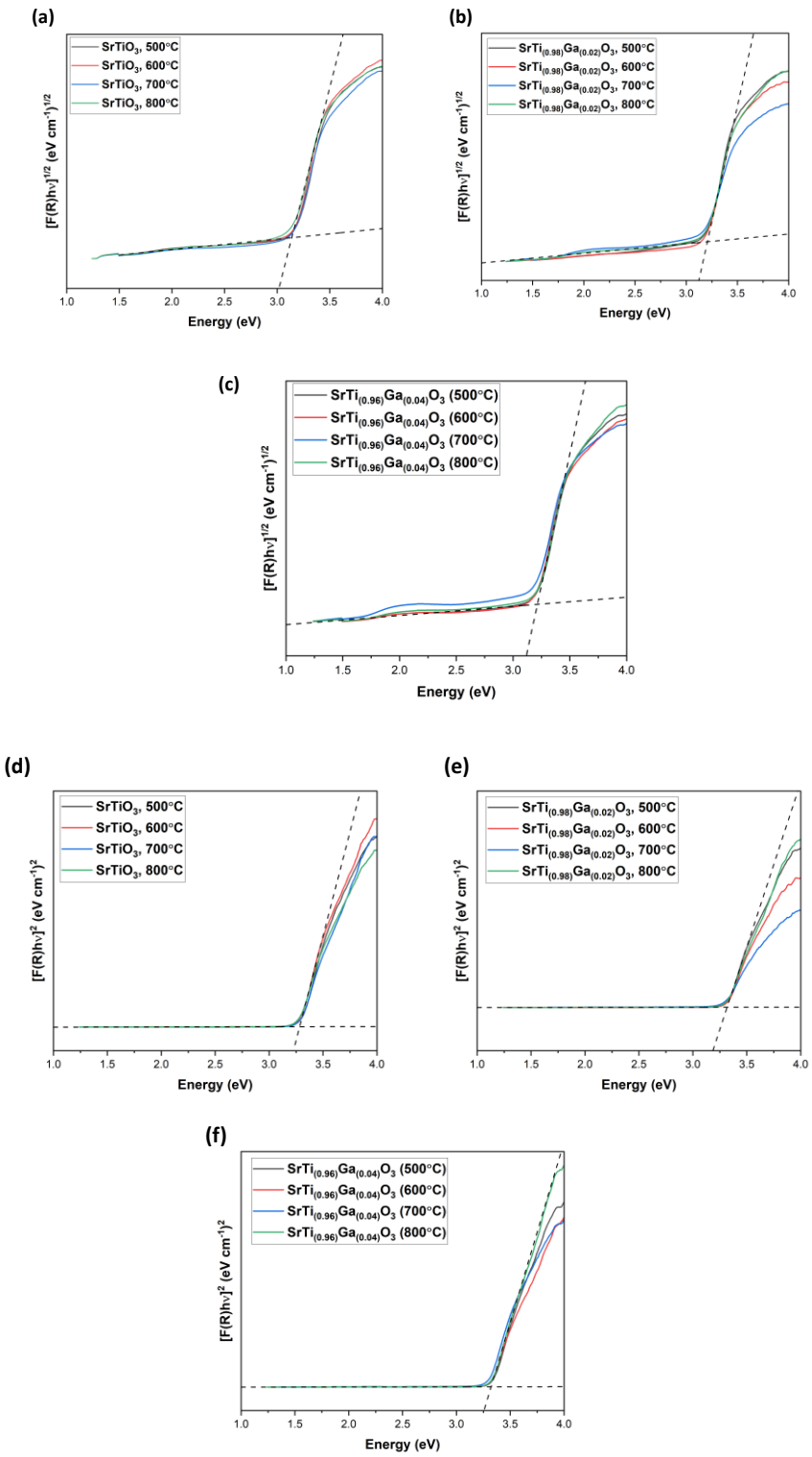


Figure 4.17: *Temperature-dependent bandgaps (a) undoped indirect (b) 2 mol% Ga^{3+} indirect (c) 4 mol% Ga^{3+} doped indirect (d) undoped direct (e) 2 mol% Ga^{3+} doped direct (f) 4 mol% Ga^{3+} doped direct $SrTiO_3$ samples. The absorption features can be observed more prominently with an increase in temperatures in the indirect bandgaps (a-c).*

In the doped samples, absorption features can be observed in the indirect band gaps (Figure 4.17 (b, c)). These features as discussed in detail in Chapter 3, are due to oxygen vacancies.

This aligns with the microstructural and electronic measurements that indicate the presence of oxygen vacancies. Even though the temperature increase did not affect the band gap, it was observed that other opto-electronic properties are affected by temperature. This can be validated from the band energy diagrams in the Appendix Figures 1-6. Temperature was found to have influenced changes in the Fermi level-valence band maxima separation. This is crucial in determining the IP of the samples. Further discussion on this topic is elaborated in the following section.

4.4.2 Influence of Temperature on the Fermi Level (E_F) and Valence Band Maxima (VB_M) Separation

The fermi level and the valence band separation were calculated from the valence band analysis via the XPS as shown in Figure 4.18 (a-c). The position of the valence band maxima is an important parameter to determine the IP of the samples. In the context of this study, IP and EA are two fundamental concepts to understand the trap-limited carrier mobility that affects the performance of the photocatalysts. The fermi level from the XPS is set at zero. The E_F-VB_M separation is shown in Appendix Figures 1-6.

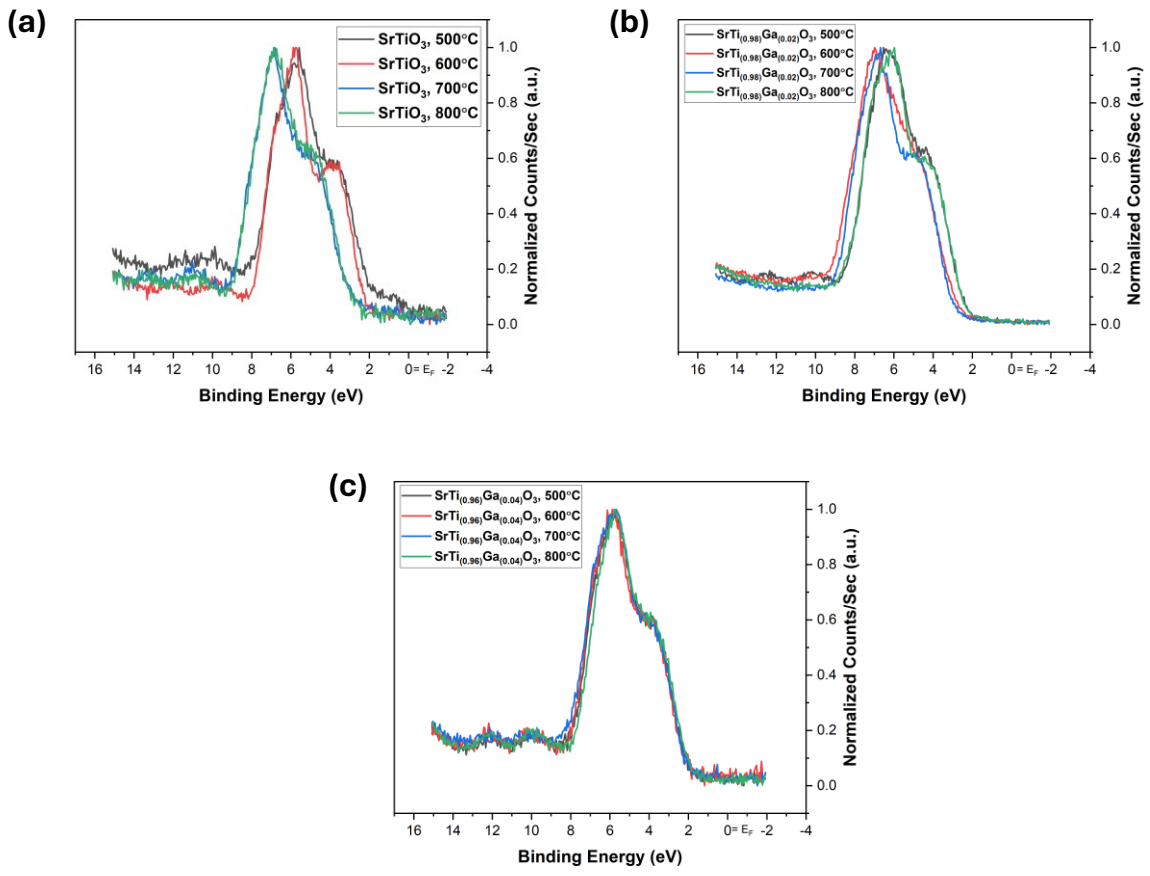


Figure 4.18: *Temperature-dependent separation of the E_F and the VB_M (a) undoped (b) 2 mol% Ga doped (c) 4 mol% Ga doped $SrTiO_3$ samples. In the undoped series, the E_F-VB_M separation decreases for the samples synthesized at 500 – 600 °C. The separation and therefore, the n-type nature increased at higher temperatures. For the 2 mol% doped series,*

the 500 and 800 °C samples exhibit a decrease in the E_F-VB_M separation (decrease in n-type nature) whereas, the 4 mol% doped series exhibits only minor differences.

In the undoped $SrTiO_3$ samples as shown in Figure 4.18 (a-c), the E_F-VB_M increases from 500 °C -700 °C. At 800 °C, the E_F-VB_M decreases. This can be observed in the band edge energy diagrams in Appendix Figures 1-6. From the E_F-VB_M and the bandgap, the E_F-CB_{Min} (i.e. conduction band minimum) can be calculated which together with the E_F position can be crucial to understanding the nature of conductivity of the materials. It was observed that in the undoped $SrTiO_3$ samples, the separation between the E_F-CB_{Min} decreases as the temperature increases peaking at 700 °C for all the types of doped and undoped samples as shown in Figure 4.19 (b-d).

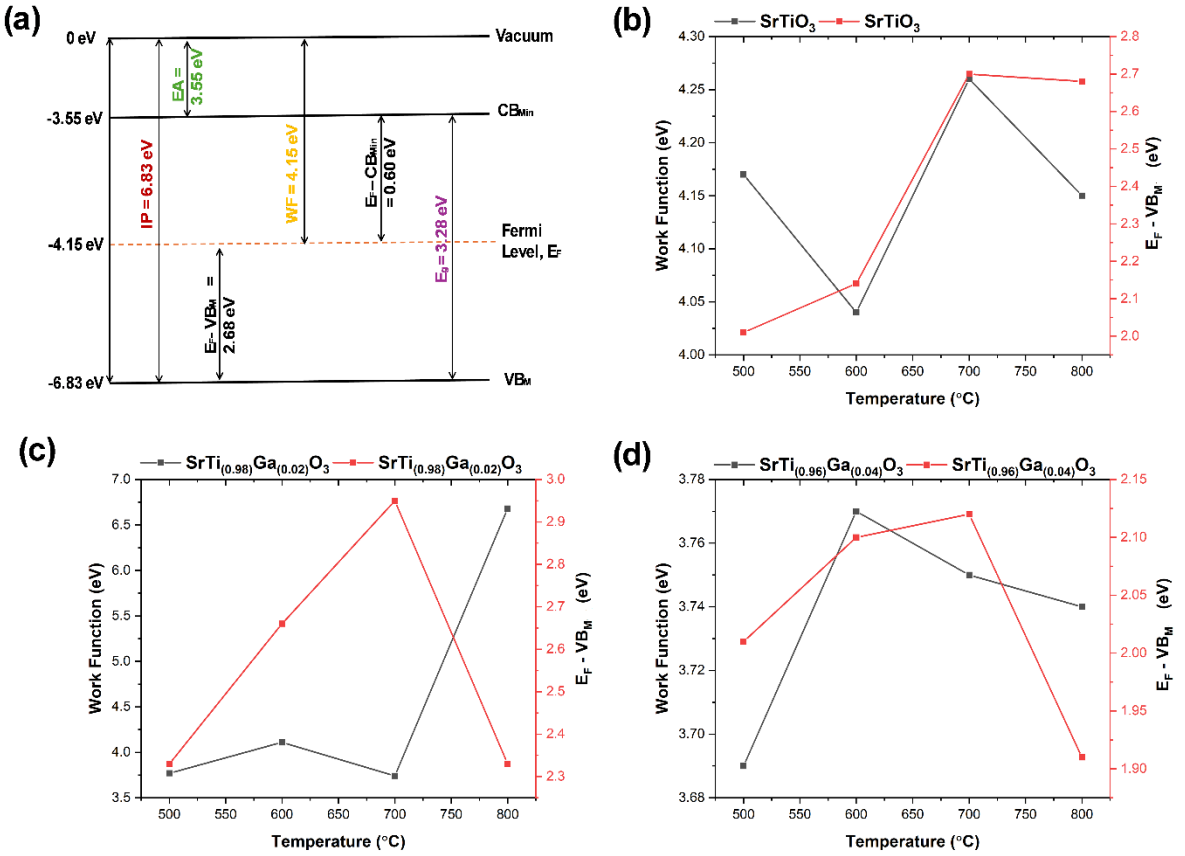


Figure 4.19: *(a) Band edge alignment of undoped $SrTiO_3$ synthesized at 800 °C. E_F-VB_M separation at all temperatures (b) Undoped samples (c) 2 mol% Ga^{3+} (d) 4 mol% Ga^{3+} doped $SrTiO_3$ demonstrating the highest separation at 700 °C. This aligns with the higher n-type conduction for these samples.*

Figure 4.19 (b-d) indicates the n-type nature of the undoped samples increases with temperature and decreases at 800 °C. In the case of the 2 mol% and the 4 mol% Ga doped $SrTiO_3$ samples, the E_F-VB_M increases between 500 °C -700 °C, and the E_F-VB_M decreases at 800 °C. Although this degree of change in the 4 mol% doped samples is small. In the doped samples, the n-type nature increases between 500 °C -700 °C and decreases at 800 °C. As discussed in the previous chapter, the n-type nature could be due to the oxygen vacancies forming shallow vacancies

near the CB.

Another intrinsic parameter that is essential for calculating the position of the fermi level is the work function. The work function in the Ph.D. work has been studied with the XPS and the Kelvin probe. The findings related to this parameter are discussed in detail in the next section.

4.4.3 Work Function

The work function is a surface-sensitive technique. The presence of surface dipoles which is heavily affected by crystallographic orientations, surface adsorbates, surface terminations, and reconstructions makes the study of work functions very challenging [43],[44]. Ma, T. et al. [43] applied DFT to a clean and reconstructed $SrTiO_3$ surface to predict the work function. They studied the effect of surface point defects, reconstructions, adsorbates, and doping (1 at% Nb-doped $SrTiO_3$) on the work function. With doping, they found that the work function decreases whereas the presence of reconstructions and adsorbates either increase or decrease the parameter. Perovskite oxide work function shows a greater dependence on the surface terminations and orientations [45], [46]. Chambers, S.A. et al. [47] reported an experimental work function (Ultraviolet Photoelectron Spectroscopy, UPS) of 3.6 eV for SrO-terminated Nb: $SrTiO_3$ (001) which was close to their DFT calculated work function of 3.6-3.7 eV. For the TiO_2-terminated Nb: $SrTiO_3$ (001), the work function was found to be higher at 4.5eV and 4.7eV. The work function of TiO_2-terminated $SrTiO_3$ has been reported to be 4.2 eV-4.3 eV [48]–[50].

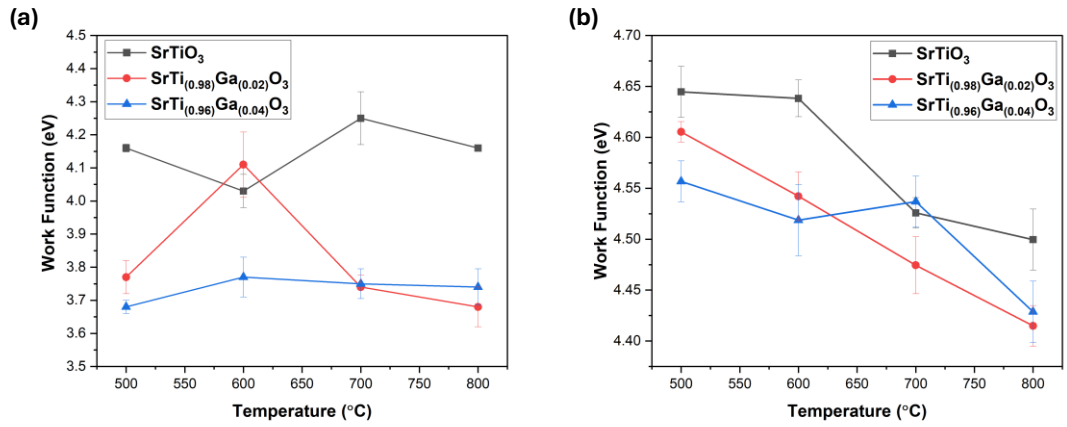


Figure 4.20: *Work function measurements of the samples with (a) XPS (b) Kelvin Probe. Both measurements show a decrease in work function as a function of synthesis temperature.*

In the context of the Ph.D. work, the work function measured with both the techniques (XPS and Kelvin probe) shows a decrease with doping as seen in Figure 4.20 (a, b). From Figure 4.20(b.), the Kelvin Probe method shows a linear decrease in the work function as the temperature increases. Some reports in the literature show such behaviors in metals [51]–[54]. As the temperature of the samples increases, the lattice starts to expand, and electrons are thermally excited. The electrons are more mobile in this state, and it is easier to overcome the work function and hence, be removed from the surface [55]. However, the samples in this study were synthesized at different temperatures and the measurements were done at room temperature. In perovskite oxide materials, the study of work function variation with

temperature is limited. In this Ph.D. study, an attempt is being made to understand how the work function in perovskite oxide materials relates to the synthesis temperature.

A clear relation between the work function and the temperature can be observed from the Kelvin Probe Method in Figure 4.20(b) which shows a decreasing trend with the synthesis temperature. In Figure 4.20(a) the work function from the XPS is shown. In this method, the 2 mol% and 4 mol% Ga doped $SrTiO_3$ show an increase in work function at 600 °C and a linear decrease beyond this point. For the undoped $SrTiO_3$, first decreased at 600 °C and then increased at 700 °C which further decreased at 800 °C. The work functions from both methods are given in Table 4.7.

Table 4.7: Experimental work functions from the Kelvin Probe and the XPS

Samples	Kelvin Probe (eV)	XPS (eV)
$SrTiO_3$ (500 °C)	4.65 ± 0.03	4.17 ± 0.01
$SrTiO_3$ (600 °C)	4.64 ± 0.02	4.04 ± 0.05
$SrTiO_3$ (700 °C)	4.53 ± 0.02	4.26 ± 0.08
$SrTiO_3$ (800 °C)	4.50 ± 0.03	4.15 ± 0.01
$SrTi_{(0.98)}Ga_{(0.02)}O_3$ (500 °C)	4.61 ± 0.01	3.61 ± 0.05
$SrTi_{(0.98)}Ga_{(0.02)}O_3$ (600 °C)	4.54 ± 0.02	4.20 ± 0.10
$SrTi_{(0.98)}Ga_{(0.02)}O_3$ (700 °C)	4.47 ± 0.03	3.86 ± 0.04
$SrTi_{(0.98)}Ga_{(0.02)}O_3$ (800 °C)	4.42 ± 0.02	3.77 ± 0.06
$SrTi_{(0.96)}Ga_{(0.04)}O_3$ (500 °C)	4.56 ± 0.02	3.68 ± 0.02
$SrTi_{(0.96)}Ga_{(0.04)}O_3$ (600 °C)	4.52 ± 0.03	3.77 ± 0.06
$SrTi_{(0.96)}Ga_{(0.04)}O_3$ (700 °C)	4.54 ± 0.03	3.75 ± 0.05
$SrTi_{(0.96)}Ga_{(0.04)}O_3$ (800 °C)	4.43 ± 0.03	3.74 ± 0.06
FTO Substrate	4.82 ± 0.02	-

Figure 4.21 shows the work function spectrum from the XPS. Helander, et al. [56] demonstrated that the work function measured by photoelectron spectroscopy techniques such as UPS and XPS is the minimum work function on a non-uniform surface in contrast to the average work function measured with the Kelvin Probe. The major disadvantage in using the XPS (or UPS) is that if the sample is not perpendicular to the detector i.e. the photoelectron take-off angle is not 90°, it erroneously gives a higher work function [56]. Details about the experimental setup and its workings are discussed in Chapter 2.

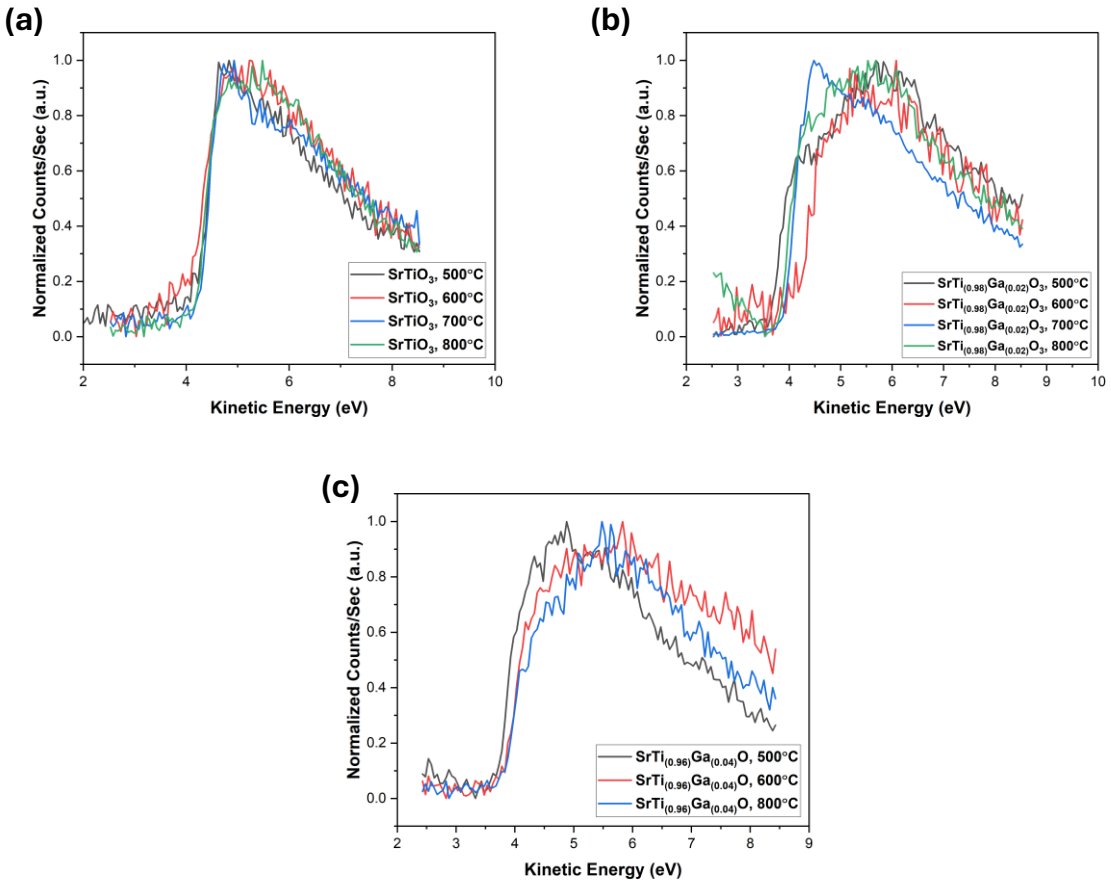


Figure 4.21: *(a.) Undoped (b.) 2 mol% Ga (c.) 4 mol% Ga doped $SrTiO_3$ work function spectrum from the secondary electron cut-off measured with the XPS. The work function measured with this method shows slight variation within samples in a series as compared to the Kelvin Probe method.*

Both the work function measurement methods show a decrease in work function with doping. However, only the Kelvin Probe shows a linear decrease with temperature as expected from the literature. For further analysis of the samples, the XPS will be referred to for further data analysis. The details for this discussion have been provided in Chapter 2.

From the definition of work function and its dependence on the temperature, a relation can be established between microstructural parameters such as the cell volume, and the electronic properties such as the work function. The correlation between these parameters is discussed in the following section. In this section, the role of oxygen vacancies and how they correlate with the effects on different aspects of $SrTiO_3$ is discussed.

4.4.4 Correlation between the Electronic Structure and the Microstructure Changes Induced by Temperature Variation via the Formation of Oxygen Vacancies

Temperature has a significant effect on the lattice parameters [57]. From Eq 2.4 (Chapter 2) lattice parameters are directly proportional to the volume. As the temperature increases the materials undergo thermal expansion which increases the unit cell volume. Ligny, D. et al. [58] observed a trend where $SrTiO_3$ exhibited volume expansion as the temperature increased.

Lattice/cell volumes are inherently also dependent on the annealing atmosphere. Under a controlled atmosphere of oxygen partial pressures, Mizusaki, J. et al. [59] observed that both unit cell volumes and thermal coefficients increased as the oxygen content decreased in $La_{(1-y)}MnO_{(3+d)}$ and $La_{(1-x)}Sr_{(x)}MnO_{(3+d)}$. These volumes can also be influenced by point defects such as oxygen vacancies. Oxygen vacancies are common in perovskite oxide materials, and they are formed during doping and high-temperature synthesis [60]. Aidhy, D.S. et al. [60] did DFT simulations on the effect of charged and neutral oxygen vacancies on the lattice volumes in ten systems including $SrTiO_3$. They found that charged oxygen vacancies lead to volume contraction whereas neutral oxygen vacancies can lead to volume expansion**.** They also reported that charged and neutral oxygen vacancies (vacancy stability) respond to lattice strain differently. This aligns with Figure 4.12 depicting the strains in the samples. The peak shifts indicating tensile and compressive stresses could give rise to strains interacting with the point defects.

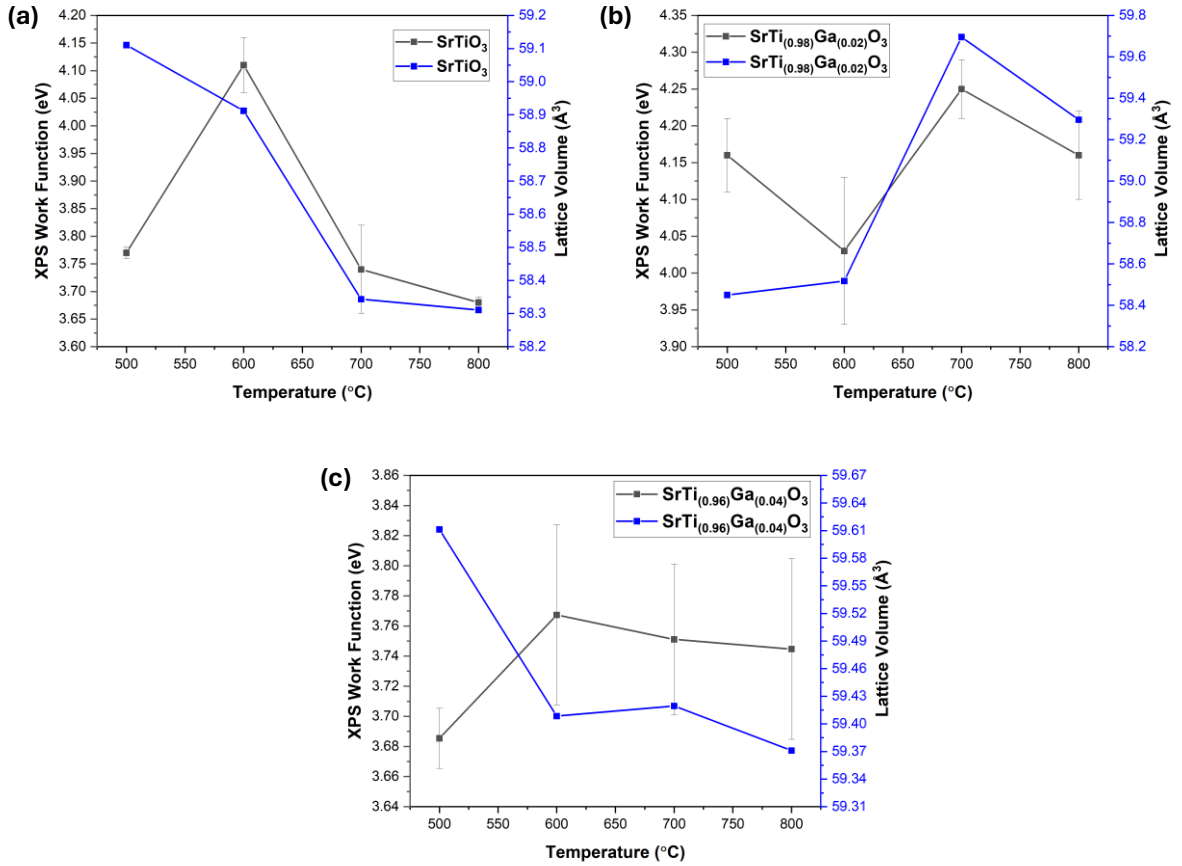


Figure 4.22: *Temperature Dependent Correlation between Microstructural (Cell Volume) and Electronic (XPS Work Function) properties (a.) Undoped (b.) 2 mol% Ga (c.) 4 mol% Ga doped $SrTiO_3$. The correlation between the two material properties can be linked to the formation of oxygen vacancies.*

Note: *In Figure 4.22, the work function shown is measured with the XPS. This is discussed in detail in Chapter 2.*

Aidhy, D.S. et al. [60] reported two scenarios that correlated the presence of oxygen vacancies

with the lattice volumes and lattice strains. In a strained system, the volume expansion and contraction behave oppositely than expected. They reported the following:

1.) Neutral Oxygen Vacancies: Such vacancies lead to volume expansion, and they are stable under tensile strained systems
2.) +2 Charged Oxygen Vacancies: This type of vacancy has lower volumes than oxygen atoms and hence they have contracted volumes. Such vacancies are stable under compressive strains

From Figure 4.12, the undoped and the 4 mol% Ga doped $SrTiO_3$ show shifts to higher 2θ values which indicates compressive stresses. This leads to the contraction of lattice volumes as shown in Figure 4.22(a.) and (c.). This can be attributed to the charged oxygen vacancies as reported by Aidhy, D.S. et al. [60]. In the 2 mol% Ga doped $SrTiO_3$, the XRD peaks shifting towards lower 2θ angles indicate tensile stress acting over the lattice. This can be attributed to neutral oxygen vacancies which can expand the lattice in Figure 4.22(b). Formation of oxygen vacancies can therefore significantly alter the microstructure.

The oxygen vacancies can also affect the opto-electronic parameters such as the work function of a material. Gayen, P. et al. [61] reported a decrease in work function in air-annealed $Pb_2Ru_2O_{7-x}$ due to an increase in oxygen vacancies. They reported a decrease in work function measured with UPS with an increase in annealing temperature which is also observed in this Ph.D. study more prominently with the Kelvin Probe (Figure 4.20 (b)). The undoped $SrTiO_3$ showed expansion between 500 °C and 600 °C. A significant decrease in volume was observed from 600 °C to 800 °C. A trend can be recognized here that when the work function decreased then the cell volume increased. The changes in work function and the cell volumes here could be a result of oxygen vacancies present. Wang, W. et al. [62] also observed a decrease in work function with an increase in oxygen vacancies.

From Figure 4.22, both microstructural and electronic properties therefore can be related to oxygen vacancies. The effect of change in these properties on other intrinsic properties such as electron affinity and ionization potential are discussed in the succeeding paragraph.

4.4.5 Influence of Temperature on Electron Affinity, Ionization Potential, and Charge Carrier Mobility

Figure 4.23 shows the key components of the band edge energy diagram. The energy diagram was calculated from three measurements- the work function for the fermi level, the band gap for the E_F-CB_{Min} separation, and the E_F-VB_M. The work function and the E_F-VB_M were measured from the XPS. The EA and the IP calculated the vacuum level which was fixed at 0 eV. From Figures 4.20 and 4.21 and the band edge energy diagram in Appendix Figures 1-6, the work function decreases with an increase in temperature. From the position of the fermi level (E_F) for the undoped samples in Appendix Figures 1-6, it is observed that E_F shifts closer to the conduction band minimum (CB_{Min}). This signifies an increase in the n-type nature as the temperature increases to 700 °C as shown in Figure 4.24 (a-d). All band edge energy diagram was done considering the direct band gap except the 2 mol% Ga^{3+} at 600 °C and 700 °C. The choice of the nature of band gap is explained in the section with the PL analysis.

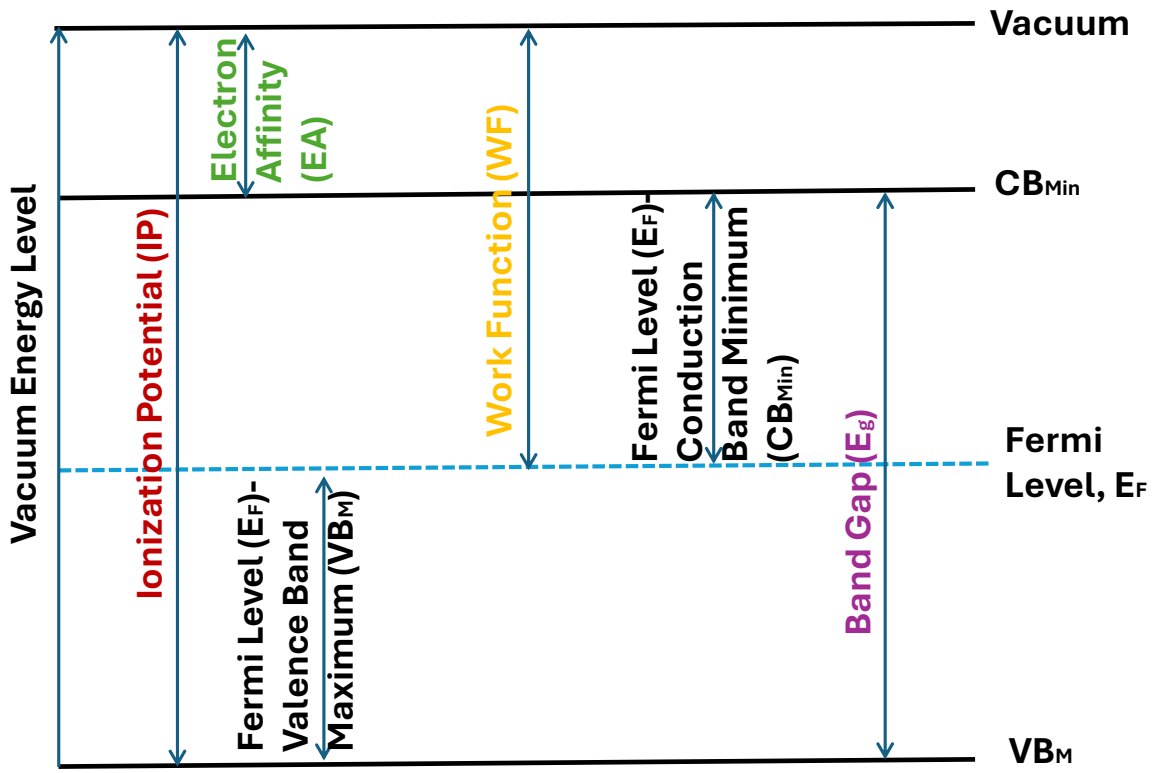


Figure 4.23: *Key components of the band edge energy diagram which were calculated from the direct band gap, the E_F- VB_M separation measured from the XPS, and the work function from the XPS. All values were referenced from the vacuum scale.*

Figure 4.24 (a) shows the band edge energy diagram of the undoped sample synthesized at 800 °C. Figure 4.24 (b-d) shows the comparison between the work functions and the E_F-CB_{Min} of the undoped and doped samples. The E_F-CB_{Min} demonstrates the position of the fermi level with respect to the conduction band minimum. The closer the E_F is to the $CB_{Min,\ the}$ higher the n-type conductivity. The n-type conductivity of the undoped samples increases as the temperature increases (Figure 4.24(b)). With the doped samples, the n-type nature is highest at 700 °C. This aligns with lower lifetimes at 700 °C as shown in Figure 4.15. The higher n-type nature and the lower lifetimes could be due to vacancies that are acting as traps for the charge carriers.

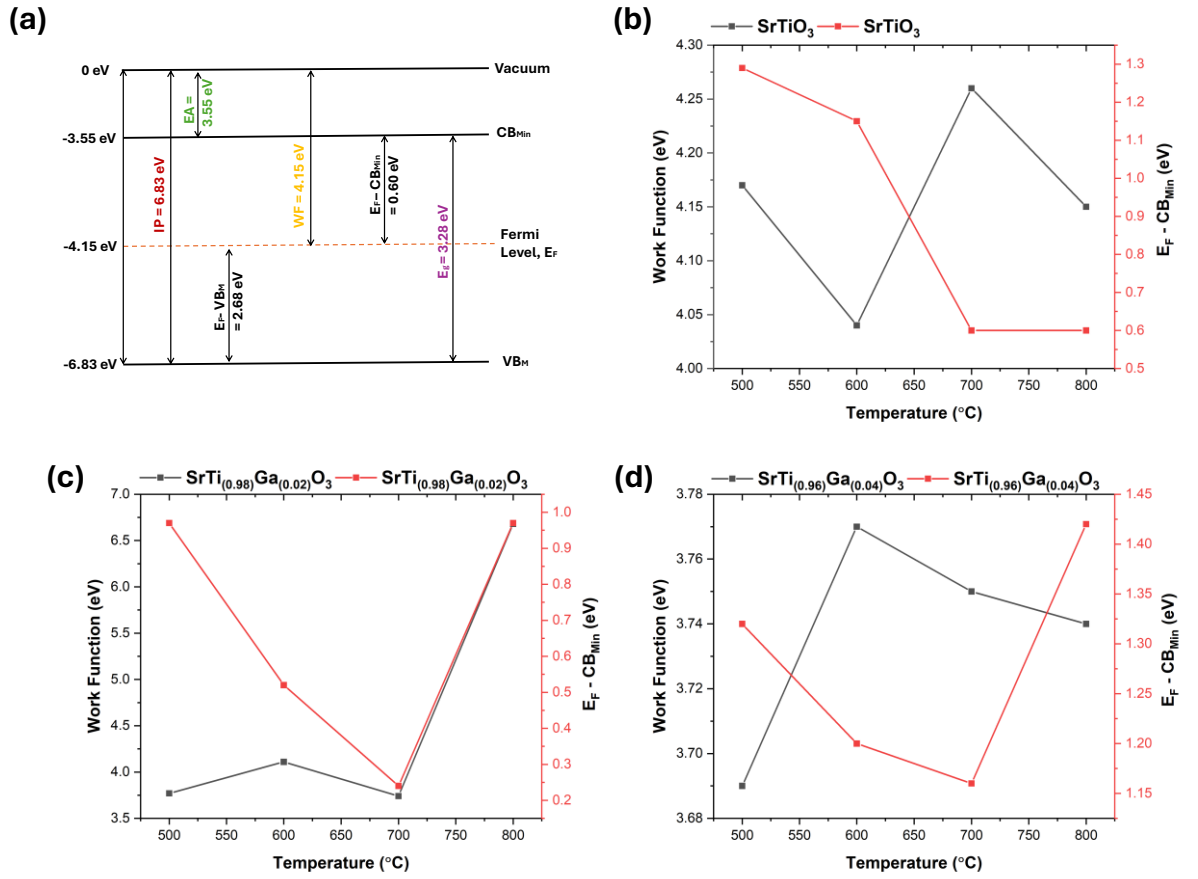


Figure 4.24: *(a) Band edge energy diagram of undoped $SrTiO_3$ synthesized at 800 °C. E_F-CB_{Min} separation at all temperatures (b) Undoped samples (c) 2 mol% Ga^{3+} (d) 4 mol% Ga^{3+} doped $SrTiO_3$ demonstrating the relation between the temperatures and n-type conductivity which is highest at 700 °C.*

From the previous section on lattice volumes and work functions, due to the probable doubly charged oxygen vacancies there is an excess of electrons in the 2 mol% Ga doped $SrTiO_3$. This can be represented by the Kröger-Vink notation given in Eq (4.1). Oxygen vacancies can act as shallow donor levels below the CB_{Min}. They increase the electron density in the conduction band, which increases the n-type nature of the samples. With the increase in temperature, the oxygen vacancy concentration can increase as explained in Chapter 3.

$$O_O^X = \ddot{V}_O + 2e^{`} + \frac{1}{2} O_2 \qquad (4.1)$$

Where,

O_O^X = An oxygen at an oxygen site

$\ddot{V}_O$ = Oxygen vacancy

EA and IP are important parameters that determine the charge carrier transport in semiconductors. From Figures 4.25-4.27, both IP and EA increase from 500 °C to 700 °C. At 800 °C there is a significant decrease in both IP and EA for all the samples. When relating to Figure 4.26 (b-c) with the TCSPC, for the undoped and 2 mol% Ga doped samples, the higher

lifetimes in these two categories are shown by the samples with the lowest EA and IP values. For the 4 mol% Ga doped samples, the lifetimes at 500 °C and 800 °C are within error at 0.54 ns and 0.52 ns (Figure 4.26(c)). Here, the IP and EA calculated with the XPS WF are similar and lower than the samples at 600 °C and 700 °C.

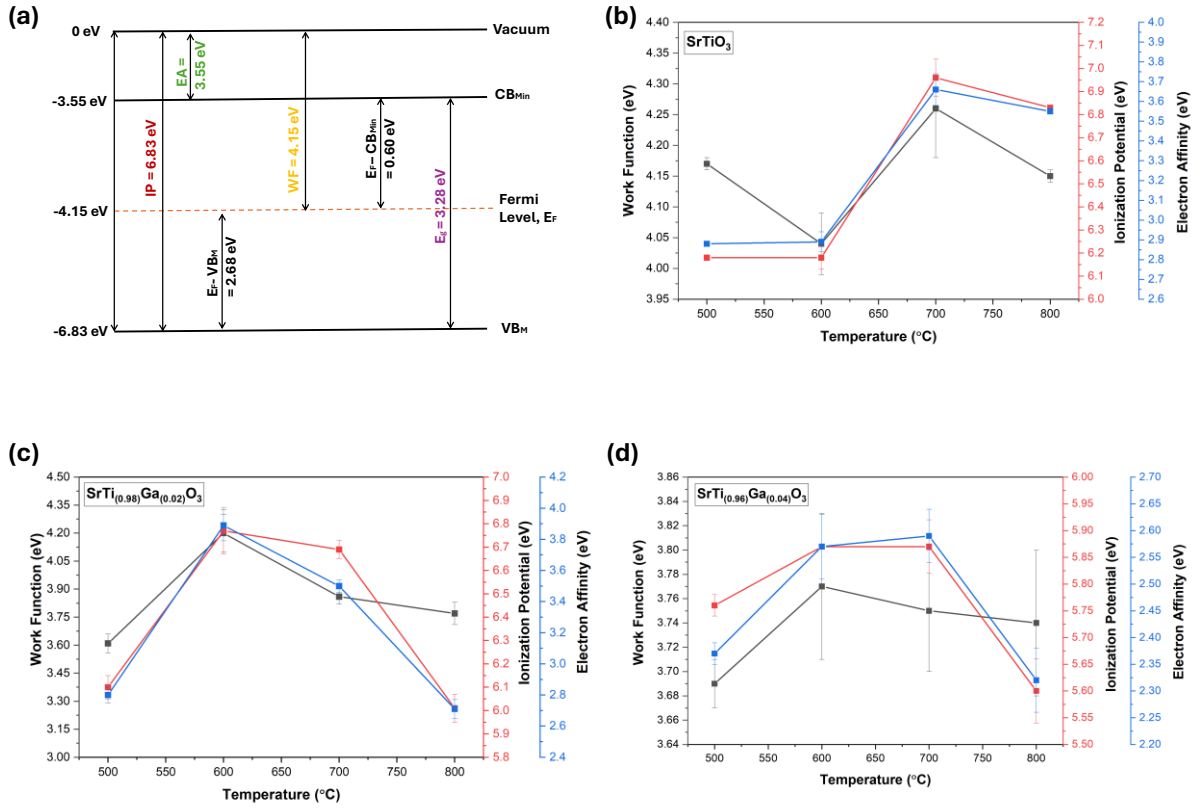


Figure 4.25: *(a) Band edge energy diagram of the undoped $SrTiO_3$ sample at 800 °C. Comparison of the IP and the EA with the work function at different temperatures. Doped samples show lower IP and EA at 500 °C and 800 °C. For the undoped samples, lower IP and EA are observed at 500 °C. The error bars in the IP and the EA were added after recalculating from the band edge alignment.*

For the 2 mol% and the 4 mol% of Ga^{3+} doping, samples with the highest lifetimes show lower microstrain. Lower microstrain indicates a decrease in defects which subsequently decreases any trap states that hinder charge mobility leading to higher lifetimes. These defects may be speculated to be acting as traps that restrict electrons (-ve charge) or holes (+ve charge). In the case of undoped $SrTiO_3$, the behavior observed is opposite to the doped samples. Here the sample at 500 °C with the highest microstrain demonstrates a higher lifetime. Here these defects might be facilitating the carrier mobility which enhances the lifetime.

Temperature variation in these samples has also affected their conductivity. From 500 °C -700 °C in the doped samples, the n-type nature and the defects increase as shown in the microstrain in Figure 4.11. These defects might be more inclined towards trapping holes leaving behind excess electrons. At 800 °C, there could be a change in the type of defects to electron trapping

which decreased the n-type nature. In the case of the undoped, there is a consistent increase of n-type nature indicating a more hole-trapping defect.

From the observations from the microstrain and the band energy diagrams, a hypothesis can be drawn where each catalyst possesses a window of minimum EA and maximum IP below and above which charge trapping can occur which decreases the carrier mobility to the surface of the photocatalyst. Hence, decreasing their efficiency. Figure 4.26 (a-c) shows the temperature-dependent relation between the IP, EA, and lifetimes of all the samples. Since 2 mol% Ga^{3+} doped $SrTiO_3$ showed the highest lifetime of 0.68ns, the window for maximum charge mobility for this concentration doping might be EA above 2.83 eV and IP below 6.01eV. Similar windows can be speculated for the different mol% dopings.

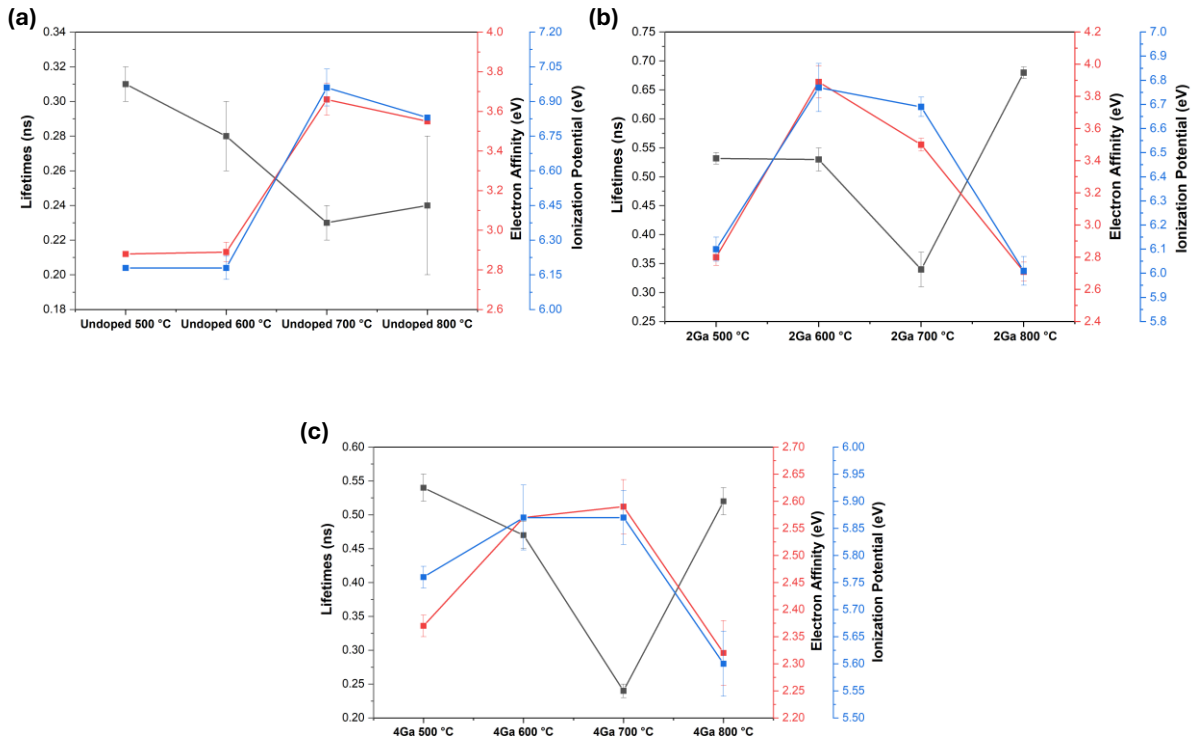


Figure 4.26: *Variation of IP, EA, and lifetimes in the samples with temperature (a) undoped (b) 2 mol% Ga doped (c) 4 mol% Ga doped $SrTiO_3$ samples. At 800 °C, both the doped samples show that decrease in the EA and the IP leading to an increase in lifetimes. The error bars in the IP and the EA were added after recalculating from the band edge alignment.*

Kotadiya, N.B. et al. [63] reported a window for trap-free charge transport in organic semiconductors. They reported that when IP surpasses 6 eV, hole transport is limited by hole traps and when EA is less than 3.6 eV, there will be trap-limited electron transport. Similar observations with organic semiconductors were reported by Enrique, L. et al. [64] where they argued the IP and EA are important parameters to consider while studying charge carrier

transport. Walsh, A. et al. [65] study and discuss the application of atomistic modelling techniques to study energy levels which they argue are necessary to develop water photolysis catalysts and solar cells. For the samples synthesized in this study, a parallel can be drawn. Here it can be hypothesized that in these samples as well an optimum value of EA and IP exists where trapping is minimal. EA and IP indicate a neutral atom's energy change when electrons are added or removed. As stated and established in the previous chapter, oxygen vacancies add localized states in the band gap which can act as traps. When EA is lower the likelihood of these defect states trapping electrons is also lower. Similarly, lower IP indicates lower energy to remove the electron from the defect site i.e. it is easier for the trapped electrons to escape. Therefore, a combination of lower EA and IP can be understood to influence the electronic structure of the defect states towards less trapping. This could lead to lower recombinations and hence, an increase in lifetimes.

The undoped at 500 °C, 2 mol% Ga doped $SrTiO_3$ sample at 800 °C and the 4 mol% Ga doped $SrTiO_3$ sample at 500 °C with the lower IP and EA might have provided a window where charge transports are not limited by traps. This might be a factor in higher lifetimes as observed with TCSPC in their group in Figure 4.15. It could be inferred here that since at 800 °C, both the doped samples showed higher lifetimes. Then for synthesizing Ga^{3+} doped $SrTiO_3$ with sol-gel Pechini, the ideal annealing temperature could be 800 °C considering other properties as well.

From the EA and IP, the positions of VB_M and CB_{Min} of the samples are determined. The positions of VB_M and CB_{Min} are crucial in understanding the activity of the photocatalysts. Figure 4.27 demonstrates these positions for water-splitting redox potentials.

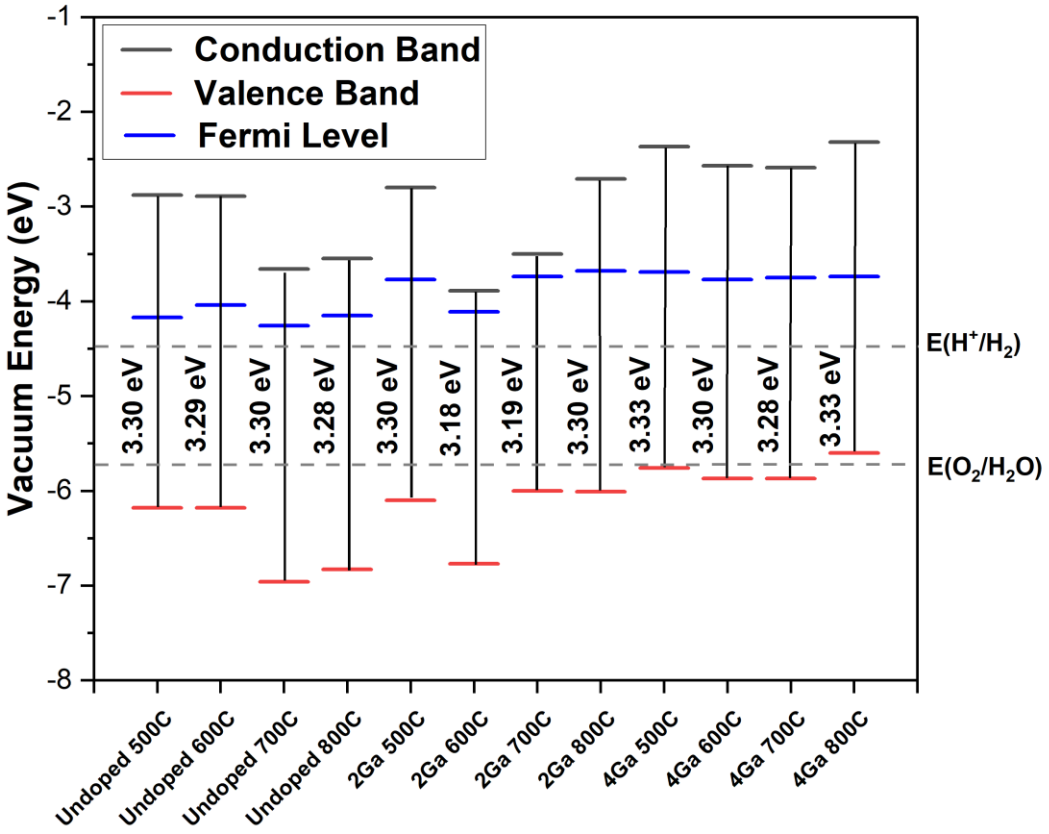


Figure 4.27: *Positions of CB_{Min} and VB_M of the synthesized samples at different temperatures with respect to vacuum.*

To be an efficient photocatalyst, the CB_{Min} should be more negative and the VB_M should be more positive with respect to the redox potentials. All the samples show sufficient capacity for reduction. In the case of the 4 mol% Ga^{3+} doped sample at 800 °C, the VB_M is above the oxidation potential. This condition is not conducive to oxidation even though the sample demonstrates ample reduction capacity. Other samples demonstrate sufficient oxidation capacity.

4.5 Elemental Analysis

In this section, the surface of the doped materials characterized by the XPS is discussed. The elemental analysis is done and quantified. This section also discusses the Ti^{3+} intrinsic defect which is widely regarded as detrimental to the material performance.

4.5.1 XPS

Sr3d

The surface of the undoped, 2 mol% Ga, and 4 mol% Ga doped $SrTiO_3$ was analyzed. To be concise only the samples with the highest lifetimes in their group are shown here All the peaks were charge-corrected with C1s at a binding energy of 284.8 eV. Figure 4.28 shows the deconvoluted Sr3d peaks with $Sr3d_{5/2}$ peak at 132.73 eV and $Sr3d_{3/2}$ peak at 134.49eV

attributed to Sr^{2+} in $SrTiO_3$ lattice. The split between the $d_{5/2}$ and the $d_{3/2}$ orbital in the case of the undoped $SrTiO_3$ is 1.76 eV. The sample shows two additional peaks at higher binding energies which can be attributed to $SrCO_3$. For the undoped sample, the ratio between the $SrCO_3$ $Sr3d_{5/2}$ and the C1s C=O is 1:1.3 which is close to the reported 1:1 carbonate ratio in the literature confirming the presence of $SrCO_3$[13]. Figure 4.29 shows the deconvoluted Sr3d peaks of the doped samples.

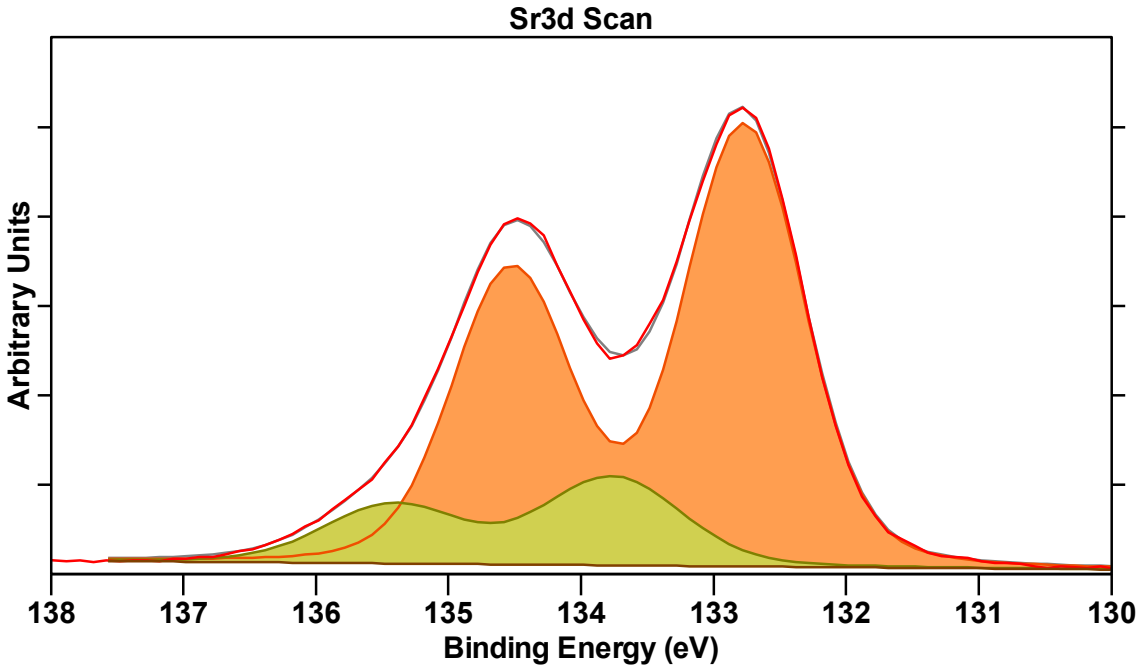


Figure 4.28: *Deconvoluted and charge-corrected Sr3d peaks of undoped $SrTiO_3$ at 500 °C at 132.73 eV and 134.49 eV with a trace amount of $SrCO_3$ (green doublet).*

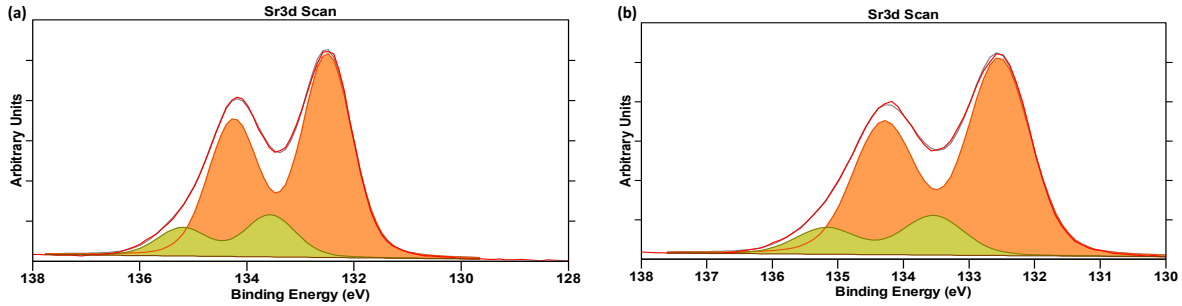


Figure 4.29: *Deconvoluted Sr3d peaks of (a) 2 mol% Ga^{3+} (b) 4 mol% Ga^{3+} doped $SrTiO_3$ synthesized at 800 °C and 500 °C.*

The binding energy positions of the $Sr3d_{5/2}$ and the $Sr3d_{3/2}$ of the lattice Sr^{2+} are presented in Table 7.

Table 4.8: Position of the $Sr3d_{5/2}$ and the $Sr3d_{3/2}$ of the doped samples

Sr No	Sample	$Sr3d_{5/2}$	$Sr3d_{3/2}$
1	Undoped $SrTiO_3$ (500 °C)	132.73	134.49
2	2 mol% Ga (800 °C)	133.43	134.18
3	4 mol% Ga (500 °C)	132.53	134.28

From the deconvolution of the Sr3d peaks in Figures 4.28-4.29, the presence of $SrCO_3$ at higher binding energies is apparent in the doped samples which are typical as reported by Cali, E. et al. [13]. For both the doped samples, the ratios between the $SrCO_3$ $Sr3d_{5/2}$ and the C1s C=O are 1:0.74 (4 mol%), and 1:1.15 (2 mol%), thereby confirming $SrCO_3$. The Sr3d peaks of all the doped samples show a shift to lower binding energies when compared to their undoped counterparts.

Ti2p

The $Ti2p_{3/2}$ peaks for the samples were analyzed and compared with the undoped in Figure 4.30. Ti^{3+} defects were detected for all the samples with varying degrees. The main components of the $Ti2p_{3/2}$ and $Ti2p_{1/2}$ peaks are at 458.13 eV and 463.87 eV which can be attributed to Ti^{4+}. The ratio of ($Sr3d_{5/2}$ + $Sr3d_{3/2}$): ($Ti2p_{3/2}$ + $Ti2p_{1/2}$) for the undoped at 500 °C is 1:1.0. In the 2 mol% Ga^{3+} doped sample, the (Sr3d): (Ti2p + Ga2p) ratio is 1:1.2 and in the 4 mol% Ga^{3+} doped sample, the (Sr3d): (Ti2p + Ga2p) is 1:0.9. The main components $Ti2p_{3/2}$ and $Ti2p_{1/2}$ in the 2 mol% sample is observed at 457.83 eV and 463.53 eV respectively. For the 4 mol% sample, the main peaks lie at 457.87 eV and 463.58 eV. Figure 4.31 (a-b) shows the $Ti2p_{1/2}$ for the doped samples.

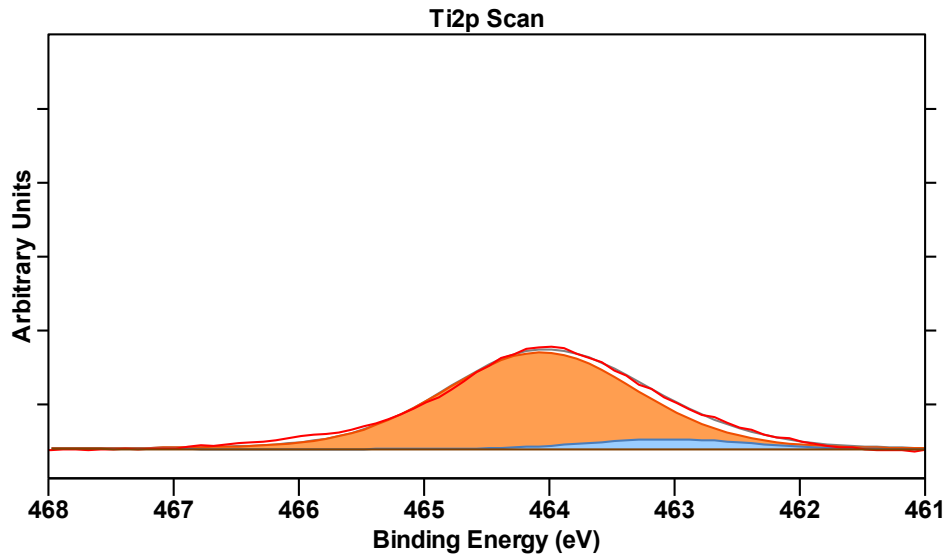


Figure 4.30: *XPS Ti2p Peak of Undoped $SrTiO_3$ with $Ti2p_{1/2}$ at 463.87 eV (orange) and Ti^{3+} (blue) towards lower binding energies.*

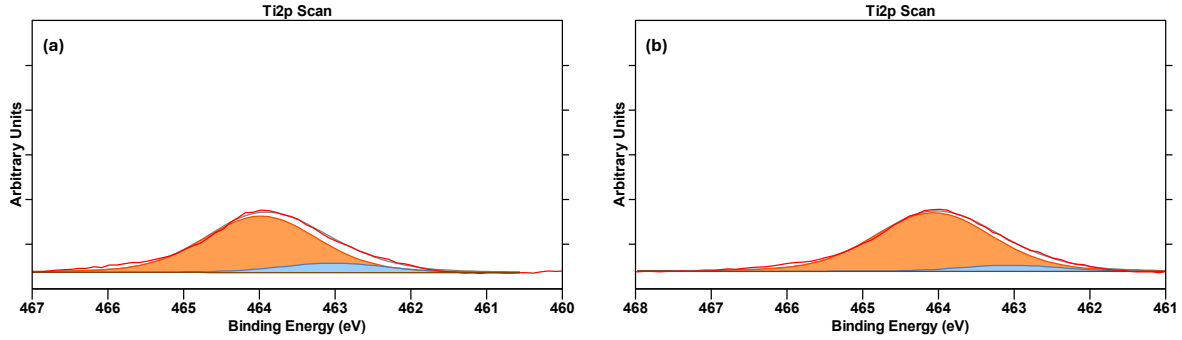


Figure 4.31: *XPS Ti2p peaks (orange) of (a) 2 mol% (800 °C) and 4 mol% (500 °C) Ga^{3+} doped samples with $Ti2p_{1/2}$ at lower binding energies as compared to undoped $SrTiO_3$. Deconvolution shows the presence of Ti^{3+} (blue) at varying concentrations.*

The $Ti2p_{3/2}$ and $Ti2p_{1/2}$ in all the doped samples show shifts to lower binding energies as compared to undoped samples.

O1s

The O1s peaks for the samples were analyzed and compared with the undoped in Figure 4.32. The deconvolution of all the samples showed secondary peaks at higher binding energies. In the case of the undoped sample, the main component of the O1s peak at 528.97 eV can be attributed to lattice oxygen. The spectrum also show another component at higher binding energy around 531 eV. This feature can be attributed to surface hydroxyl groups.

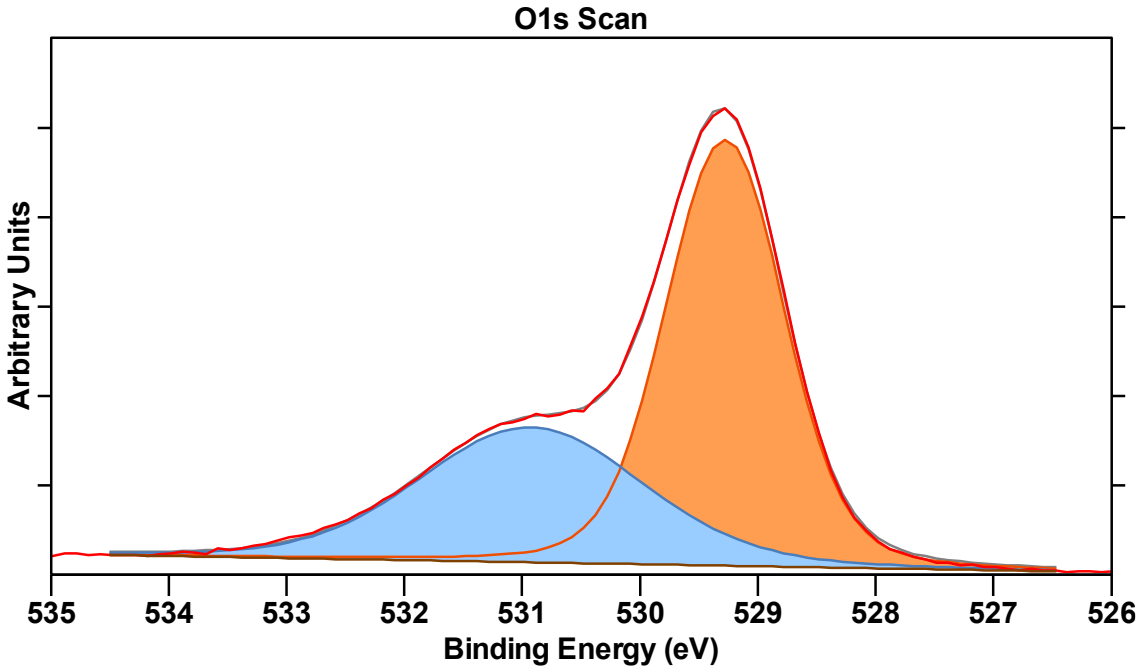


Figure 4.32: *XP spectrum of undoped $SrTiO_3$ synthesized at 500 °C peak with the main lattice component at 528.97 eV and surface -OH groups (blue) towards higher binding energies.*

The O1s peak of the doped samples as shown in Figure 4.33 show similar characteristics i.e., the presence of peaks at higher binding energies with surface carbonates (-C=O) around 529 - 530 eV and surface hydroxyls at around 531 eV. The main lattice peaks for 2 mol% and 4 mol% samples are found at 528.95 eV and 528.97 eV respectively.

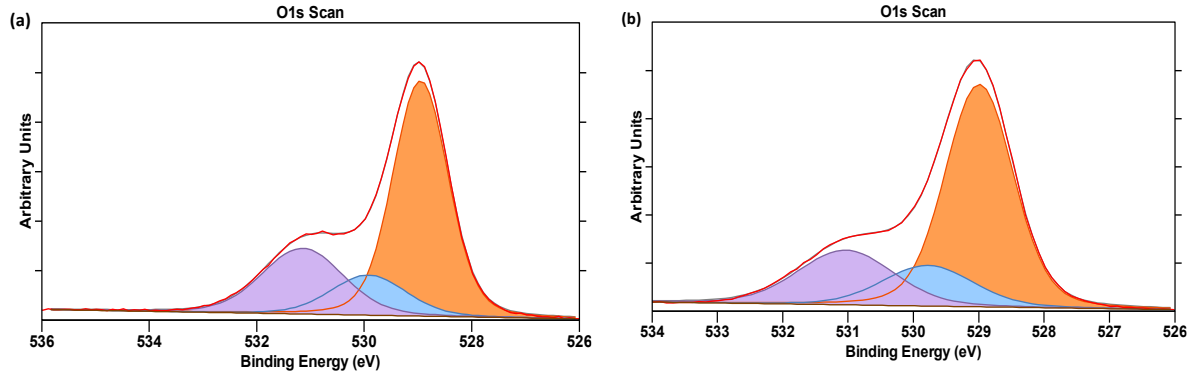


Figure 4.33: *XPS O1s (orange) peak deconvolution of (a) 2 mol% Ga^{3+} at 800 °C and (b) 4 mol% Ga^{3+} at 500 °C doped samples. Both the doped samples exhibit surface -OH groups (violet) and -C=O species (blue) at higher binding energies.*

The amount of -OH increased at the 4 mol% Ga doped sample. This could be due to the increased affinity for surface hydroxyls by the higher number of oxygen vacancies introduced with the % doping [66]. The shifts observed for all the peaks when compared to the undoped are within the error and do not indicate any fermi-level shifts [67].

Ga2p

From the XPS survey of the surface of 2 mol% Ga^{3+} doped and the 4 mol% Ga^{3+} doped $SrTiO_3$, the presence of Gallium is evident as shown in Figure 4.34. The main peaks of the $Ga2p_{3/2}$ are around 1117 eV for both samples.

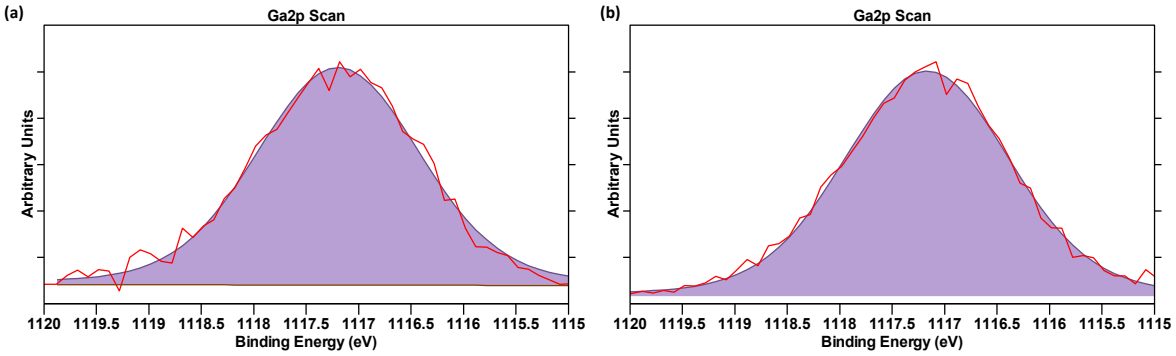


Figure 4.34: *XPS $Ga2p_{3/2}$ peak of (a) 2 mol% Ga^{3+} and (b) 4 mol% Ga^{3+} doped $SrTiO_3$ confirming the presence of Ga^{3+}.*

The atomic % of the elements in the samples are shown in Table 4.9. Here the actual doping mol% has been calculated with respect to Ti^{4+}.

Table 4.9: Atomic % of elements present in the samples

Sample	$Sr3d_{5/2}$ (At %)	O1s (At %)	$Ti2p_{3/2}$ (At %)	$Ti2p_{1/2}$ (At %)	$Ga2p_{3/2}$ (At %)	$Ga2p_{1/2}$ (At %)	(Ga2p)/(Ga2p+Ti 2p)	Ga^{3+} Doping %
Undoped $SrTiO_3$ (500 °C)	10.40	30.73	9.88	5.14	-	-	-	-
2 mol% Ga^{3+} $SrTiO_3$ (800 °C)	10.78	30.58	12.50	5.15	1.04	0.64	0.087	8.7%
4 mol% Ga^{3+} $SrTiO_3$ (500 °C)	12.02	27.33	9.86	5.05	0.56	0.36	0.058	5.8%

From Table 4.9, it can be observed that the undoped $SrTiO_3$ maintains the 1:1:3 stoichiometric

ratio between Sr^{2+}:Ti^{4+}:O^{2}–. In the doped samples, the stoichiometry around O^{2-} is not maintained. From here, it can be inferred that doping induces oxygen vacancies. At 800 °C, the higher temperature annealing can also lead to the creation of such vacancies. This observation regarding the presence of oxygen vacancies aligns with the previous results regarding the lattice expansion and contraction of the samples. Oxygen vacancies act as shallow electron donors to the conduction band [68]. This can result in the n-type conductivity exhibited by the samples with the fermi level lying close to the CB_{Min}. The presence of surface oxygen vacancies can be indicated by the -OH groups from the deconvolution of O1s peak around 531 eV. -OH groups can be adsorbed on these vacant sites on the surface [66]. A comparison between the samples regarding the amount of -OH groups is shown in Figure 4.35.

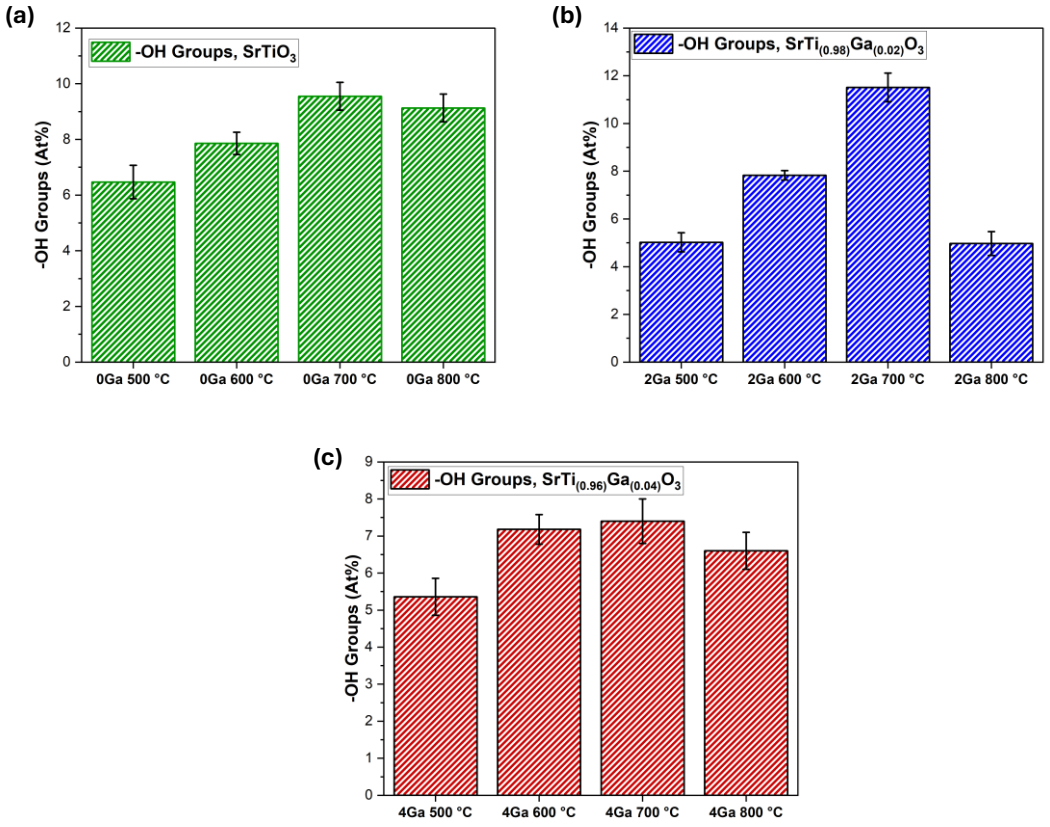


Figure 4.35: *Comparison of -OH groups adsorbed on the surface of the (a) undoped, (b) 2 mol%, and (c) 4 mol% Ga^{3+} doped samples synthesized at 500 °C- 800 °C. For the both undoped and the doped series, the sample synthesized at 700 °C shows the highest -OH groups.*

As discussed earlier oxygen vacancies are shallow donors to the conduction band which can increase the n-type nature of the samples. Figure 4.35 (a-c) can be correlated to the positions of the fermi levels band edge energy diagrams in Appendix Figures 1-6. In the undoped and the doped series, the sample synthesized at 700 °C shows the highest concentration of -OH groups. This aligns with the higher n-type conductivity determined from the E_F-CB_{Min} separation at this temperature in the band edge energy diagrams in Appendix figures 1-6. All the samples demonstrate varying degrees of n-type conductivity i.e. the fermi level lies closer to the CB_{Min}. The presence of these vacancies aligns with the observations from the

microstructural analysis. Here, however, it is difficult to pinpoint the type of vacancies whether neutral or charged are present.

Oxygen vacancies are point defects that are observed in the samples from the surface and the bulk characterizations. These point defects are either introduced via doping or at higher temperatures. To better understand these defects PL analysis was done which is discussed in the following sections. PL analysis can provide information regarding electronic and optical changes that are induced in the samples as the temperature is varied.

4.5.2 Doping and the Time-Temperature-Solubility Factor

Each mol% doped sample annealed at different temperatures was synthesized from the same polyesterized precursor batch. A peculiar trend was observed. Even though the same polyesterized material with intended mol% doping was calcined at different temperatures, the XPS revealed different doping levels. For the doped samples, at 500 °C the real mol% doping is close to the intended mol% doping at 2.1% and 5.8% for the 2 mol% and the 4 mol% samples respectively. The XPS surface analysis showed that this dopant concentration increased with temperature. This was observed for both of the mol% Ga^{3+} doping. Figure 4.36 (a, b) demonstrates this trend. **This phenomenon can be due to a time-temperature-solubility (T-T-S) factor**. At lower temperatures, Ga has greater solubility in the $SrTiO_3$ matrix. As the temperature increases, the solubility decreases and the dopant segregates on the surface. The time plays an important role in allowing the dopant to permeate the $SrTiO_3$. The effect of time can be observed more clearly in the batch synthesized at 900 °C for 6 h. This was discussed in the Chapter 3. For 10 h of calcination under compressed air, the doping levels are under 9 mol% whereas at 6 h the doping levels are 20 times higher than intended.

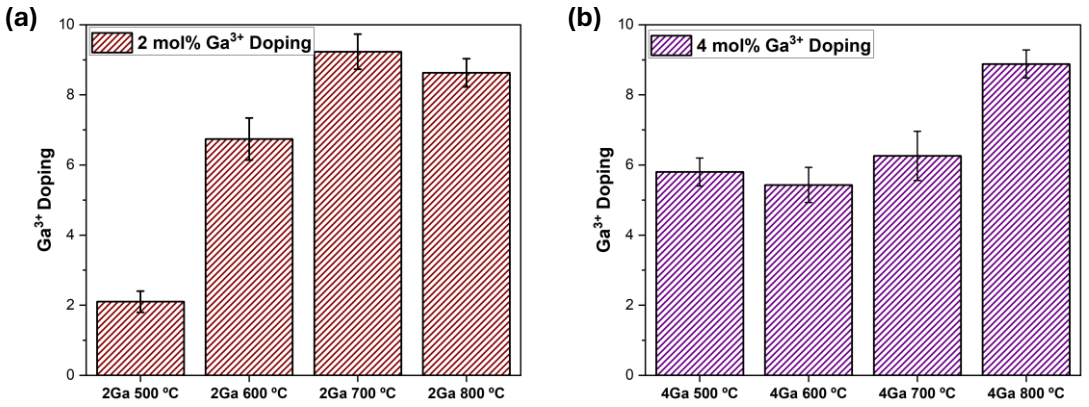


Figure 4.36: *Effect of increase in temperature on the doping levels for the (a) 2 mol% Ga^{3+} (b) 4 mol% Ga^{3+} doped $SrTiO_3$ from XPS. At 500 °C, the dopant concentration is close to the intended mol% doping which could indicate that the solubility of Ga dopant decreases with an increase in temperature in the $SrTiO_3$ matrix.*

4.5.3 Effect of Temperature on the Surface Composition of the Samples

Temperature change was observed to have an effect on the Sr^{2+} : Ti^{4+} on the doped samples as shown in Figure 4.37 (a, b). In the 2 mol% Ga^{3+} doped samples, most of the samples show slightly higher Ti^{4+} except at 600 °C (Figure 4.37 (a)). For the 4 mol% Ga^{3+} doped samples (Figure 4.37 (b)), the ratio is less than 1 indicating lower Ti^{4+}. The lower Ti^{4+} or Sr^{2+} content could indicate the site of incorporation of the dopants. Lower Sr^{2+} indicates the site of incorporation could be the A-site. While lower Ti^{4+} indicates the site of incorporation is the A-site.

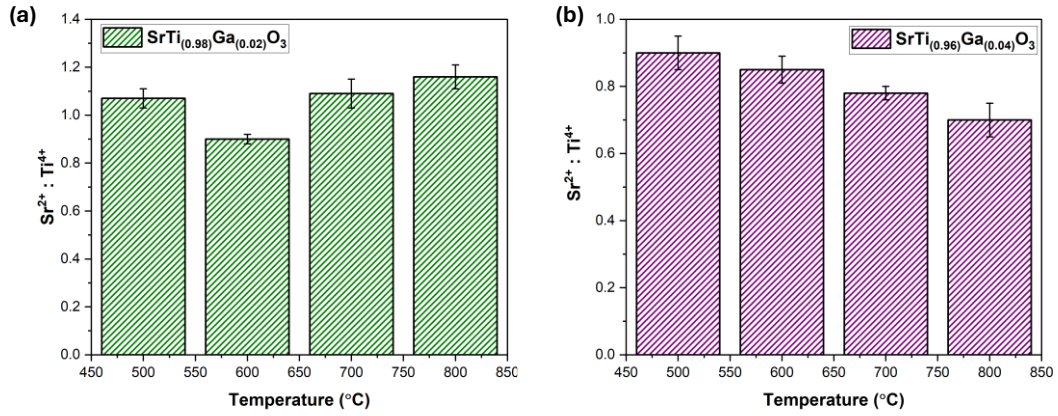


Figure 4.37: *Effect of increase in temperature on the doping levels for the (a) 2 mol% Ga^{3+} (b) 4 mol% Ga^{3+} doped $SrTiO_3$ from XPS. The ratio deviates from the 1:1 ratio in the doped samples indicating the incorporation of the dopant in the $SrTiO_3$ matrix.*

The samples synthesized at 800 °C were analyzed via the TEM as shown in Figure 4.38 (a, b). The samples were crystalline and did not show any exsolution.

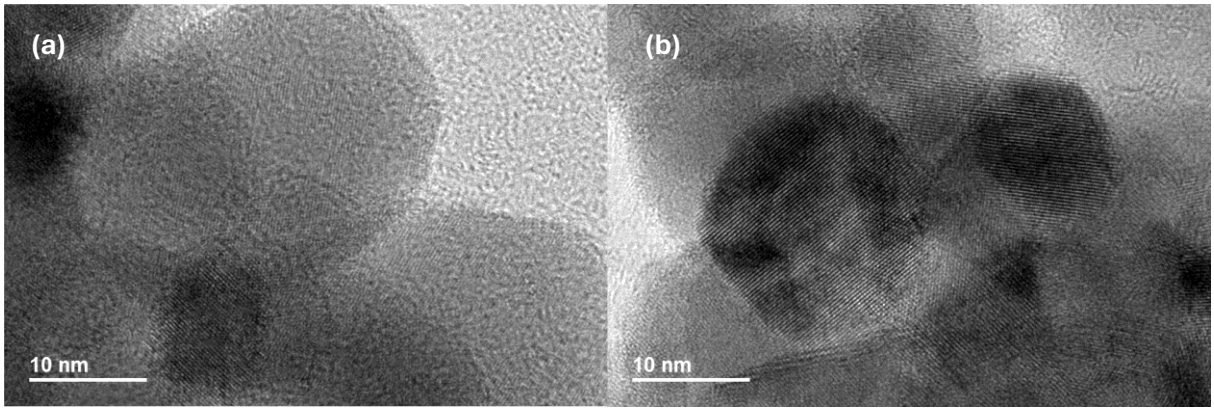


Figure 4.38: *Effect of increase in temperature on the (a) 2 mol% Ga^{3+} (b) 4 mol% Ga^{3+} doped $SrTiO_3$ synthesized at 800 °C from the TEM. The samples did not show any exsolution.*

4.6 Performance Assessment

In this section, the defect-related charge carrier recombination dynamics are studied via the PL to understand how it affects the PEC performance of the materials. The PEC analysis is done in a dopant-dependent sequence where undoped and doped samples are measured at a particular

temperature are compared. The PL is analyzed in both temperature-dependent and dopant dependent sequence.

4.6.1 Photoluminescence (PL) Analysis

PL analysis involves the emission of photons when a material is excited with light of a certain wavelength. Figure 4.39 (a-c) shows the comparison of the PL spectrum of the samples at different temperatures. The samples were excited at 295 nm (4.2 eV). A broad peak covering 350 nm to 430 nm with varying intensity can be observed. Excitation of samples at higher energy than the bandgap can allow emissions related to band-to-band transitions, defects, and dopant-induced luminescence.

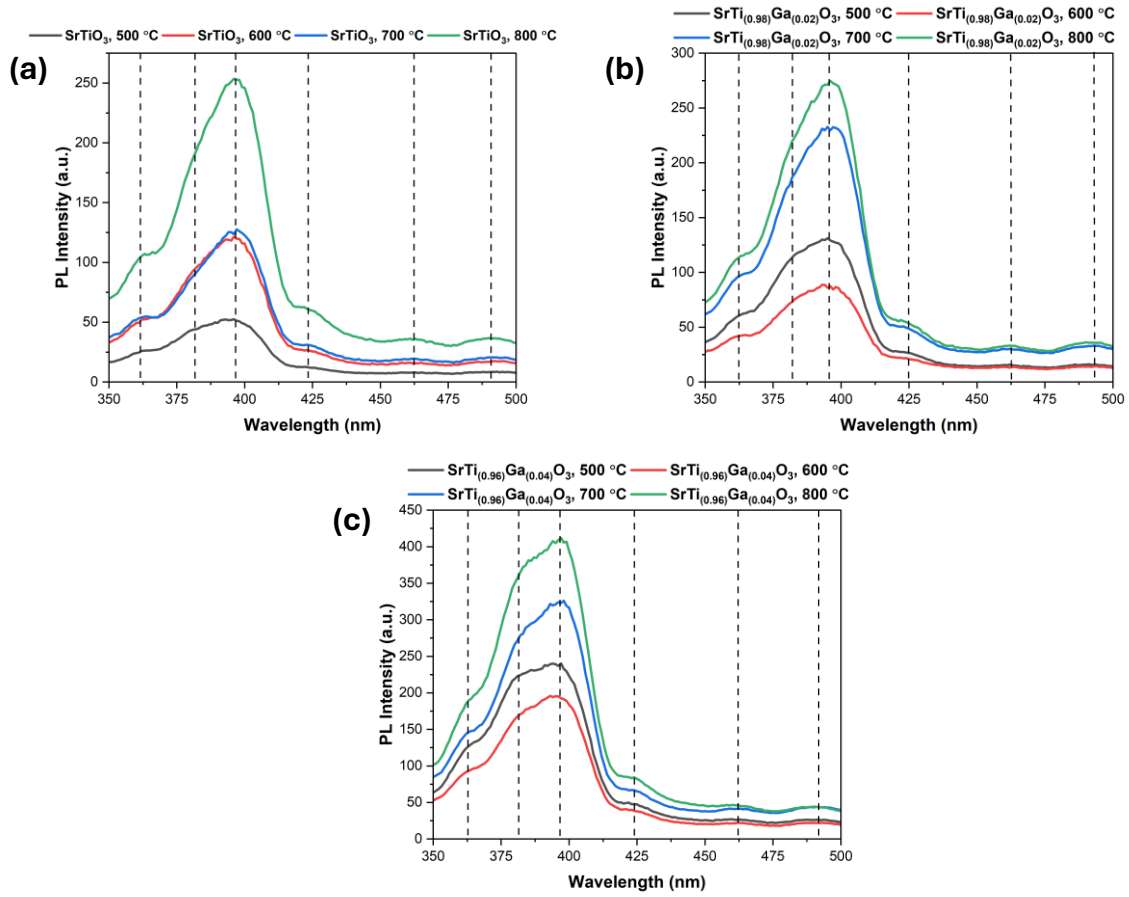


Figure 4.39: *Room temperature PL spectrum comparison of the samples (a) Undoped (b) 2 mol% and (c) 4 mol% Ga^{3+} doped $SrTiO_3$ samples synthesized at different temperatures. The 800 °C samples in the case of the undoped and the doped series show the highest intensity indicating the highest suppression of non-recombination pathways. The dotted lines show the emission peaks upon excitation.*

From PL peaks, the energy levels and transitions in a material can be studied. They represent the radiative recombination of electrons and holes with the emission of photons. The broad PL peaks for the samples in Figure 4.39 (a-c) indicate multiple recombination pathways. The presence of oxygen vacancies can create localized states within the bandgap of the samples [69]. When electrons transition from the conduction band to these states then recombination with holes can occur resulting in the emission spectrum.

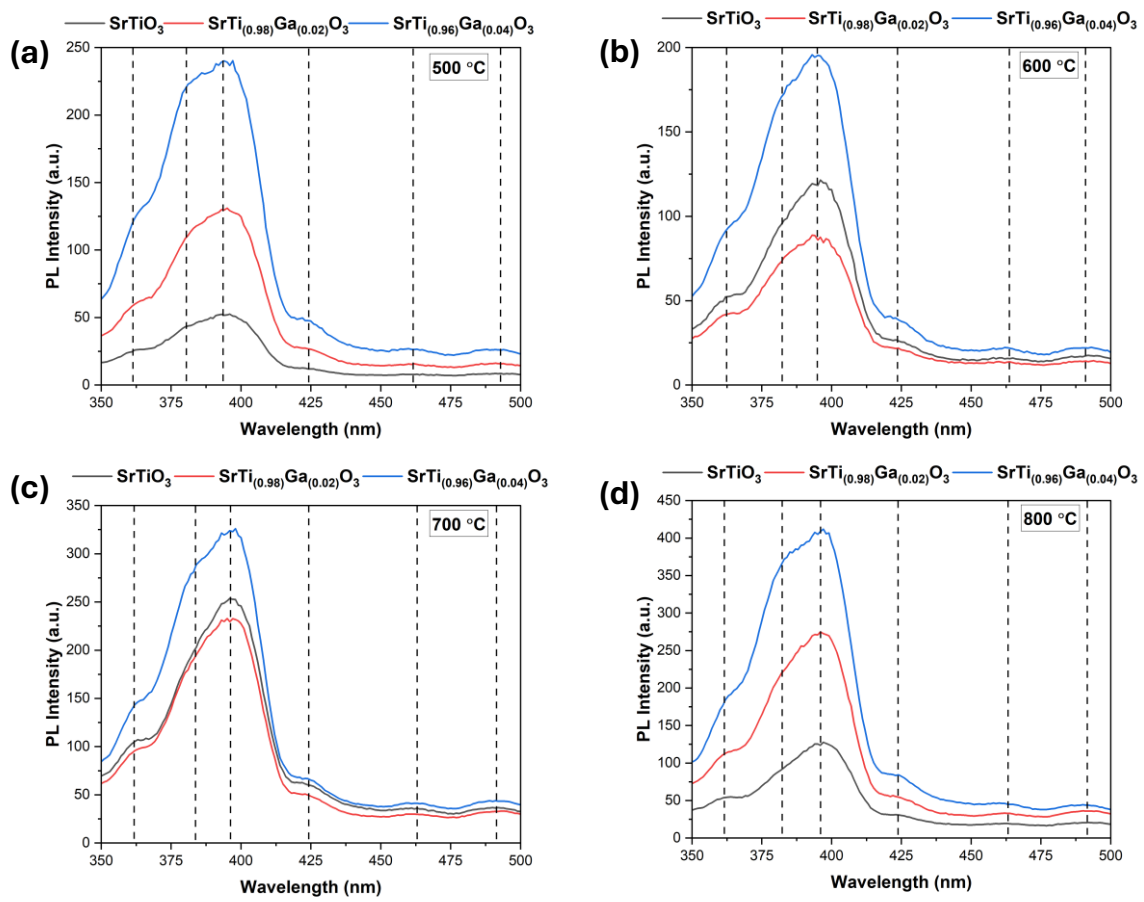


Figure 4.40: *Dopant dependent PL comparison of undoped and Ga^{3+} doped $SrTiO_3$ samples at (a) 500 °C (b) 600 °C (c) 700 °C (d) 800 °C. The 4 mol% doped samples at all temperatures show the highest PL intensity indicating the better suppression of non-radiative recombination pathways.*

In Figures 4.39-4.40, the emission spectrum of the samples can deconvoluted into 6 peaks (dotted lines in the figures) at 363 nm (3.43 eV), 385 nm (3.22 eV), 397 nm (3.12 eV), 424 nm (2.93 eV), 463 nm (2.68 eV) and 490 nm (2.53 eV). Each peak indicates a transition due to states induced via doping or defects. The peak around 385 nm is close to the band gap energy (Near Band Edge, NBE) of these materials. This could be speculated to be from phonon-assisted transitions from the conduction band to the valence band [70], [71]. The small peak at around 490 nm might be due to self-trapped excitons [72]. However, the emission peak from STE is only prominent at low temperatures. From the UV Vis analysis, no midgap states or visible light absorption was observed. Therefore, it can be inferred that Ga^{3+} doping can introduce states not within the bandgap but beyond the CB_{Min} and the $VB_{M.}$ From Figure 35 (a-d), the peak at 363 nm (3.43 eV) lies above the CB_{Min} which could indicate the states introduced with Ga^{3+} doping i.e. $Ga_{Ti}^{'}$. Lee, H. et al. [73] reported the presence of V_O-related cathodoluminescence peaks at 2.94 eV, 2.43 eV, and 2.15 eV in surface and bulk STO. In the samples synthesized for this Ph.D. work, therefore the two peaks at 2.93 eV and 2.53 eV can be related to oxygen vacancies. Neutral oxygen vacancies have been reported to act as shallow electron donors lying below the CB_{Min} [74]. From this, it can thus be inferred that the state at

3.12 eV could be related to neutral V_O^x. Mitra, C. et al. [68] reported that neutral V_O, $\dot{V}_O$, and $\ddot{V}_O$ in $SrTiO_3$ are present at 0.7 eV, 0.57 eV, and 0.28 eV below the CB_{Min} respectively. Therefore, it can be understood that the V_O, $\dot{V}_O$, and $\ddot{V}_O$ energy levels could lie at 0.77 eV, 0.62 eV, and 0.18 eV below the CB_{Min} for the synthesized samples. Hou, Z. et al. [68] have reported that V_O energetically prefers a single ionized state rather than a $\ddot{V}_O$ state. In the introduction of their work, Hou, Z. et al. [68] report that the V_O induces a delocalized state with a 3d-t_{2g} configuration in the conduction band. This could be the origin of the state 0.37 eV below the CB_{Min} observed for the synthesized samples. In Lim, H.H. et al. [73], a state above the CB was observed for ZnO from PL and PLE measurements. They attributed these states to zinc interstitial defects. All the defect levels as seen from the PL are shallow defects. Therefore, the possibility of Ti or Ga interstitials cannot be excluded. The defect energy level diagram from the PL of the doped samples is shown in Figure 4.41. The emission at 2.93 eV and 3.43 eV could be due to d-d transitions in the TiO_6 octahedron due to Ti^{3+} centers near oxygen vacancies [75].

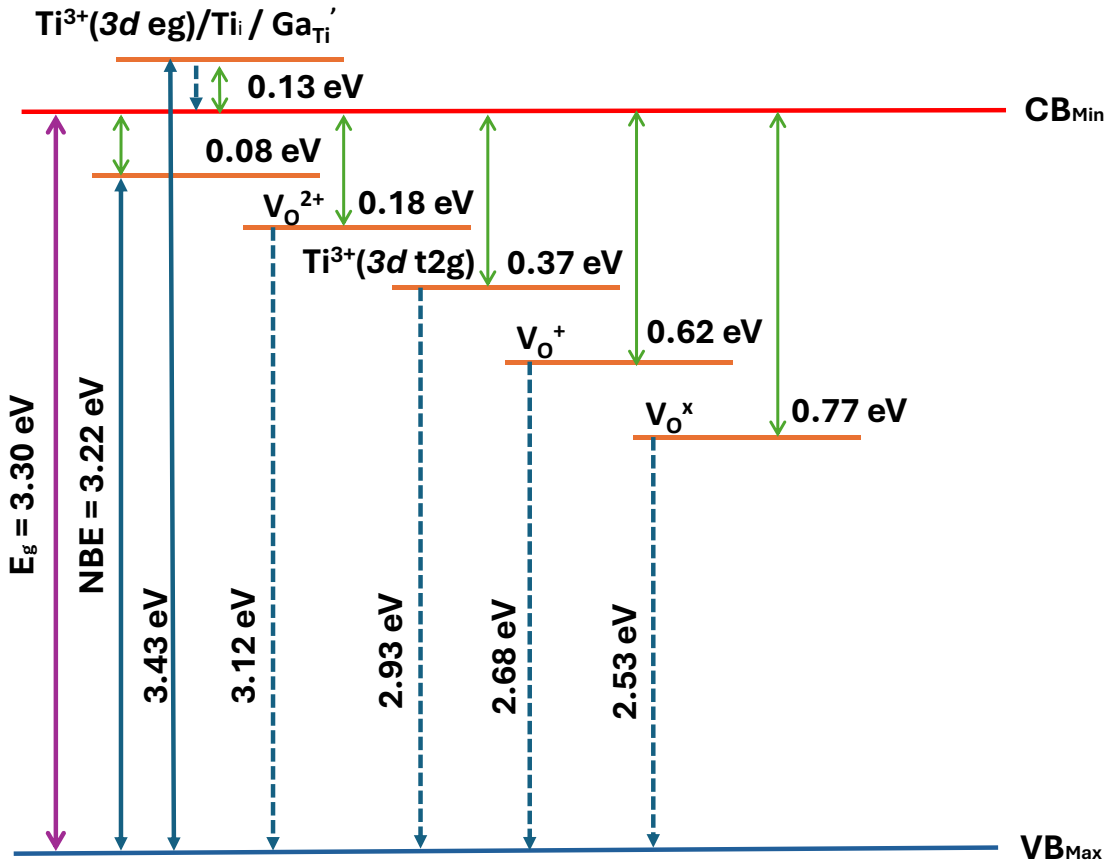


Figure 4.41: *Defect energy level diagram of Ga^{3+} doped $SrTiO_3$ from the PL analysis in Figures 4.39 and 4.40.*

Ionized oxygen vacancies i.e. $\dot{V}_O$ and $\ddot{V}_O$ are singly or doubly occupied with trapped electrons [76]. $\ddot{V}_O$ with two trapped electrons can reduce Ti^{4+} to Ti^{3+}. Ti^{3+} can act as traps for charge carriers and hence can be detrimental to the catalyst performance. An increase in the PL intensity indicates an increase in radiative recombination rates i.e. the suppression of non-

radiative pathways such as Ti^{3+} defects. A comparison of the Ti^{3+} defects between the samples is shown in Figure 4.42. The presence of Ti^{3+} was confirmed from the XPS Ti2p (Figures 4.30 and 4.31) peak analysis. At every temperature, the 4 mol% doped sample with higher PL intensity showed the lesser defects. At 600 °C and 700 °C, the 2 mol% doped sample has higher Ti^{3+} content than the undoped and the 4 mol% samples and lower PL intensity. Hence, the observations made in Figure 4.40 can positively correlate with the PL as suppression of Ti^{3+} defects in Figures 4.39-4.40.

As discussed earlier, charged oxygen vacancies with trapped electrons can reduce Ti^{4+} to Ti^{3+} at the B-site. Ti^{3+} has an ionic radius of 0.67 nm in 6-coordination which is higher than the 0.605 nm of Ti^{4+}. This can cause the lattice to expand as observed in the case of the temperature-dependent 2 mol% Ga^{3+} doped samples in Figure 4.13(b). At 800 °C, there is a decline in the Ti^{3+} for the 4 mol% doped sample at all temperatures. This could be why there is a contraction observed in the lattice of the 4 mol% samples as observed in Figure 4.13 (c). At 600-700 °C, the 2 mol% doped samples show the highest Ti^{3+} in their groups which aligns with two of the previous characterizations- the lower PL intensity in Figure 4.40 (b, c) and lattice expansions in Figure 4.13(b). The introduction of dopants increases the defect suppression in most cases as observed with the increased PL intensity. The 4 mol% Ga^{3+} doped $SrTiO_3$ shows the highest PL intensity according to Figures 4.39-4.40 at every temperature. In the doped catalysts, the samples that demonstrate higher lifetimes (Figures 4.14 and 4.15) do not necessarily demonstrate higher PL intensities. In these samples, other intrinsic parameters could be facilitating the charge separation and hence, the higher lifetimes.

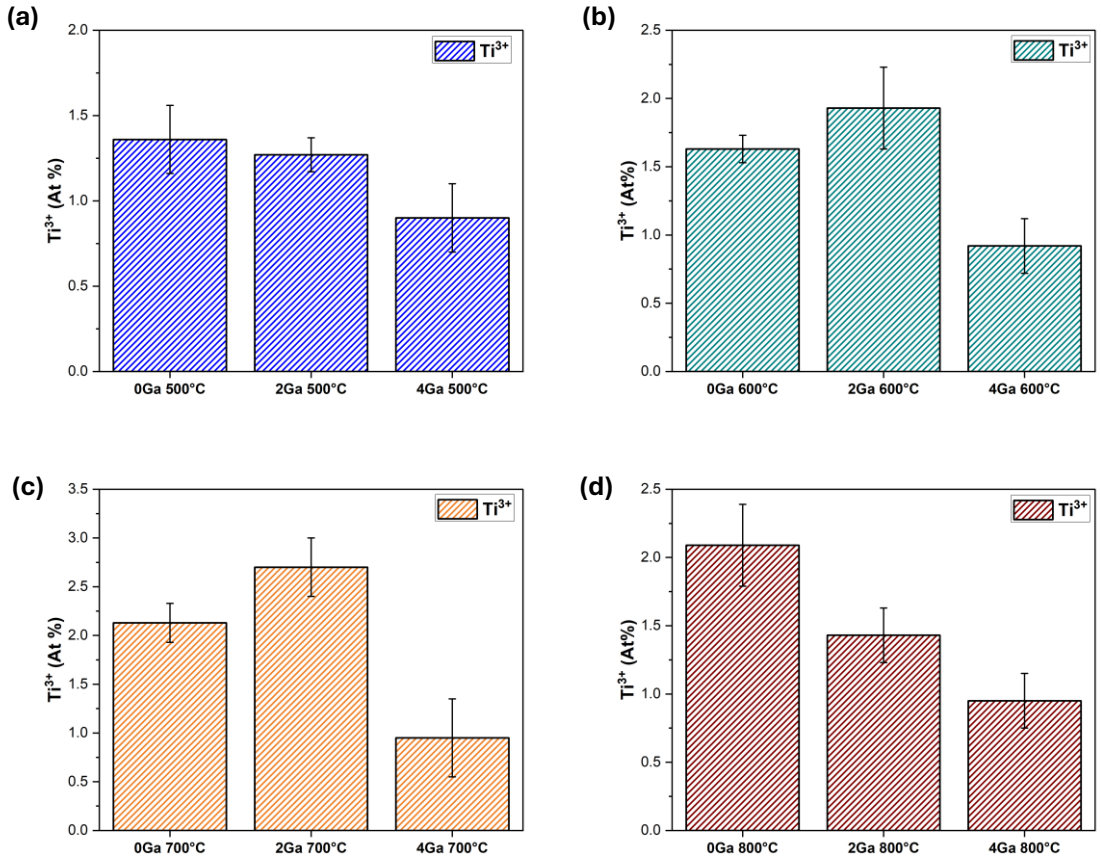


Figure 4.42: *Dopant dependent comparison of Ti^{3+} defects in the samples from the deconvolution of Ti2p peak from the XPS surface characterization at (a) 500 °C (b) 600 °C (c) 700 °C (d) 800 °C. The 4 mol% doped samples showed the highest Ti^{3+} defect suppression at all temperatures. The suppression of Ti^{3+} defects corresponds to the PL analysis in Figure 4.40.*

Overall, the increase in radiative recombination rates of the samples can also indicate a direct bandgap nature of the doped samples. This observation holds for most of the doped samples except the 2 mol% Ga^{3+} doped samples at 600 °C and 700 °C. Both of these samples show a lesser degree of radiative recombination than the undoped. Hence, in the band edge analysis in Appendix Figures 1-6, the 2 mol% Ga^{3+} doped samples are considered indirect band gap materials. The 4 mol% doped samples with greater suppression of defects also showed a decrease in the n-type nature in Figure 4.24 (b, c). The PL peaks do not show significant shifts in wavelengths which can be reflected in their similar bandgaps. From the PL analysis, we can determine what influences the performance of the samples. To correlate the suppression of defects, photoelectrochemical analysis was conducted which is discussed in detail in the next section.

4.6.2 Photoelectrochemical Performance of the Doped Samples

To compare the properties with the function of the materials, photoelectrochemical testing was performed. Linear sweep voltammetry tests were carried out in 1M KOH (pH= 13.6) with Ag/AgCl (Sat. KCl) as the reference electrode and the Pt wire as the counter electrode at 0.02

V/s scan rate. The samples were doctor-bladed on 2cm x 5cm FTO glass as working electrodes. Ga^{3+} doping in $SrTiO_3$ did not induce any visible light activity as shown in Figures 4.16-4.17. Therefore, UV irradiation was used to illuminate the samples. The irradiance of the light source was 40 W/cm^2. Figure 4.43 shows the PEC-LSV performances of the doped samples. All the samples showed better responses towards OER.

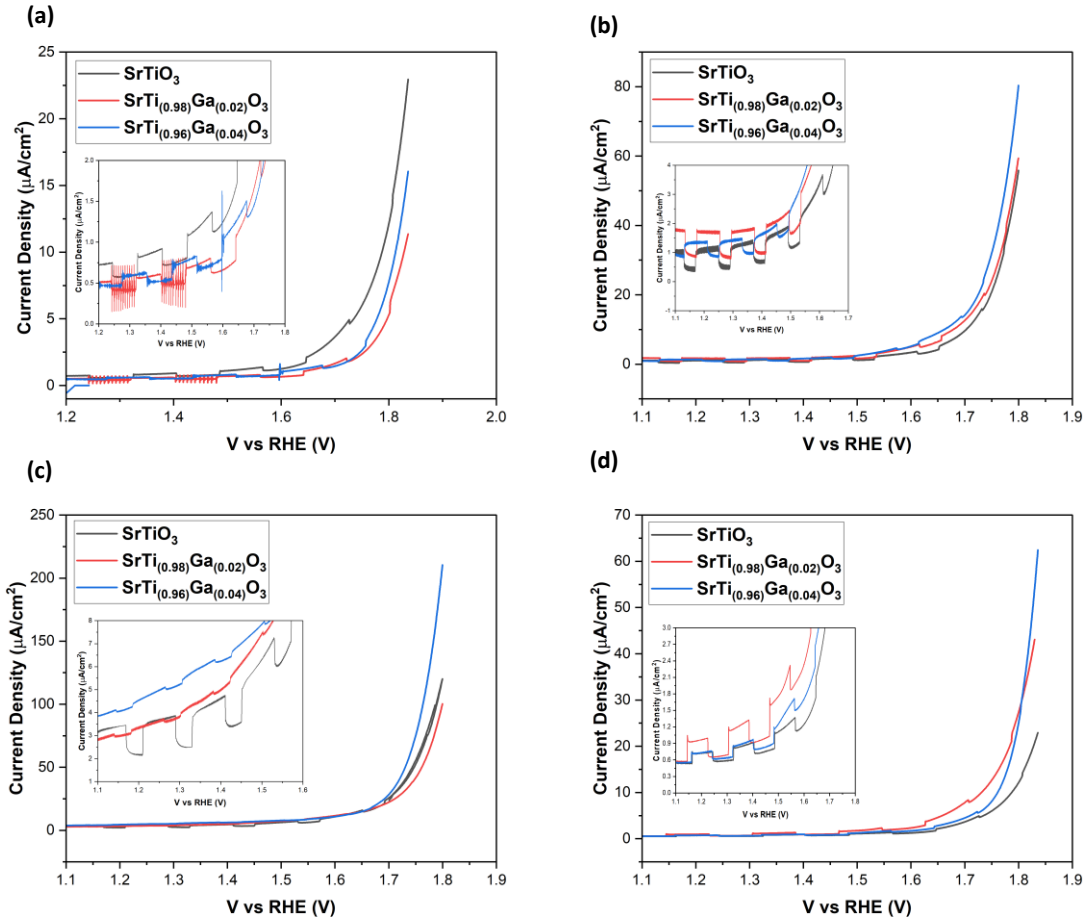


Figure 4.43: *PEC performance of Ga^{3+} doped $SrTiO_3$ synthesized at (a) 500 °C (b) 600 °C (c) 700 °C (d) 800 °C. At 500 °C, the undoped sample shows a higher performance towards OER and higher photoresponse.*

At 500 °C from Figure 4.43 (a), the photoresponse of the undoped is higher than both the doped samples. In terms of current density, the 4 mol% Ga^{3+} doped $SrTiO_3$ outperforms at all other temperatures. The photoresponse of the 2 mol% Ga^{3+} doped samples are higher for the samples synthesized at 600 °C and 800 °C (Figure 4.43 (b, d)). The onset potential decreases to 1.6 V for the undoped at 500 °C and the 2 mol% doped sample at 800 °C.

The higher current density of the 4 mol% doped samples at 600 °C -800 °C can be positively correlated with the PL intensity in Figure 4.40 (b-d). The exhibited performance can be attributed to the suppression of defects such as the Ti^{3+}. Even though the current density is higher for the 4 mol% Ga^{3+} doped samples from 600 °C- 800 °C, the photoresponse is higher for the 2 mol% doped sample at 600 °C and 800 °C. At 800 °C, the 2 mol% Ga^{3+} doped sample demonstrated the highest TCSPC lifetime (0.68ns) of all the samples indicating a better

charge carrier separation and mobility. At 600 °C, the 2 mol% Ga^{3+} doped sample has a higher TCSPC lifetime (0.53 ns) as seen in Table 4.6. At 500 °C, both the doped samples showed lower photoresponse and current density. At this temperature, the higher degree of crystallinity of the surface of undoped $SrTiO_3$ could have facilitated better charge migration leading to better performances. At 700 °C, all the samples show poor photoresponse (Figure 4.43(c)). This is due to the poor charge carrier lifetimes as indicated by the TCSPC lifetimes (Figure 4.15) due to higher trapping. *The 2 mol% doped samples show higher photoresponse at 600 and 800 °C compared to the other samples at those temperatures. The 4 mol% doped samples at temperatures 600-800 °C show the highest anodic performance aligning with the higher PL intensity due to suppression of non-radiative recombination pathways as shown in Figure (4.40(b-d)).*

In Figure 4.36, dopant segregation can be seen from the XPS as the temperature increases. This was also observed in the high-temperature samples studied in Chapter 3. Zhang, Z. et al. [77] reasons that dopant segregation takes place due to elastic or electrostatic interactions. This phenomenon is observed mostly in ionic oxides with aliovalent dopings [78]–[80]. In both the current chapter and Chapter 3, the samples (600 – 800 °C) and the 900 °C samples respectively a higher PEC performance can be observed. This can positively be linked to the dopant segregation as both the 2 mol% and 4 mol% doped samples at 500 °C underperformed when compared to the undoped. The dopant segregation in this case could have created more active sites for the OER by modifying the surface chemistry as observed with the intrinsic parameters such as the lifetimes, the IP, the EA, or the work function.

From this study, it was observed that Ga^{3+} doped $SrTiO_3$ improved the performance towards OER under UV irradiation without any significant changes to the bandgap. Ga^{3+} doping was found to have improved the UV absorption abilities of $SrTiO_3$. From the properties of the material, the performance of the catalysts was found to be due to many interrelated intrinsic and extrinsic factors. To understand dopants with d^{10} configuration, this chapter studies in detail the conditions, properties, and performances of Ga^{3+} doped $SrTiO_3$.

4.7 Conclusion

Ga^{3+} doped $SrTiO_3$ was synthesized via sol-gel Pechini at various annealing temperatures under compressed air. Varying temperatures impacted microstructural properties and opto-electronic properties. The linear sweep voltammetry (LSV) revealed higher current densities of the doped samples than the undoped ones at temperatures between 600 °C-800 °C. With the increase in temperatures, crystallinity and crystallite sizes increased. The microstrain was studied to correlate between the presence of defects and the TCSPC lifetimes. In the doped samples at 800 °C, the microstrain decreases and a subsequent increase in lifetimes can be observed as shown in Figure 4.44 (a-b). In general, the doped samples showed an inverse relation between the microstrain and the lifetimes. Higher microstrain in samples could mean lower lifetimes. In terms of suitable temperatures for synthesizing photocatalysts, 800 °C would be the ideal temperature due to the better material properties observed in the samples synthesized at this temperature. In the temperature-dependent samples, a time-temperature-solubility effect was observed where with an increase in temperature, more surface segregation of the dopant was observed with the XPS. This indicates that the solubility of Ga decreases with temperature.

This finding can be linked to the exsolution observed in Chapter 3 and hence, confirms that at higher temperatures Ga doping leaches out of the $SrTiO_3$ matrix as exsolution or surface segregates. This surface segregation as observed in the higher anodic currents which were observed in Chapter 3 as well could have led to increased active sites for the enhanced OER performances observed.

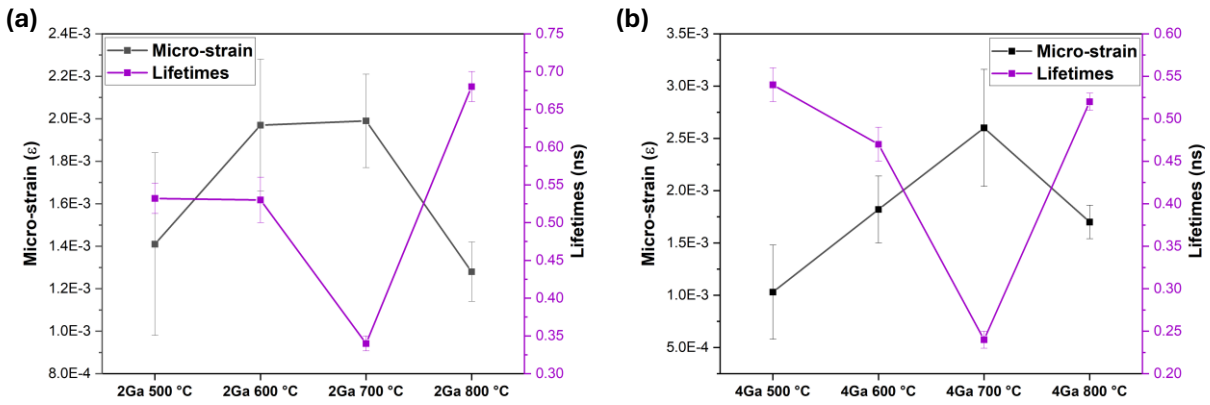


Figure 4.44: *Correlation between the microstrain and lifetimes of the samples for (a) 2 mol% Ga^{3+} and (b) 4 mol% Ga^{3+} doped $SrTiO_3$. In the doped samples, the microstrain shows an inverse relation to the lifetimes.*

Microstructural changes with temperature such as the lattice volume together with electronic properties like work function can be linked to the type of oxygen vacancies present in the samples. The presence of oxygen vacancies was indirectly validated from the XPS elemental ratios and with the PL. The role of defects in this work is both enhancing lifetimes in some samples and decreasing in others. No changes in bandgaps and visible light activity were observed. Measurement of work function, electron affinity, and ionization potential indicated the presence of traps that could limit the mobility of electrons and holes. From the materials synthesized, it was observed that the samples containing lower EA and IP demonstrated the highest lifetimes as shown in Figure 4.26. Hence, the idea of a window of EA and IP where these traps are low, and carrier mobility is high has been proposed. In summary, rigorous efforts should be made when designing a novel photocatalyst and the conditions under which the synthesis process takes place**. *The doped samples in this study showed n-type conductivity, which is indicative of oxygen vacancies and hence, is represented by the formula $SrTi_{(1-x)}Ga_xO_{3-y}$.*** The efficiency of a photocatalyst and how it performs depend on many interrelated factors that should be considered during the designing process. In this work, both the synthesis process and material properties were studied to understand Ga^{3+} doped $SrTiO_3$. The results obtained in this work can be used to understand how d^{10} dopants can be utilized to make an efficient photocatalyst and advance the field of photocatalytic clean fuel generation.

References

[1] M. Isaacs, J. Garcia-Navarro, W. J. Ong, and P. Jiménez-Calvo, “Is Photocatalysis the

Next Technology to Produce Green Hydrogen to Enable the Net Zero Emissions Goal?," *Glob. Challenges*, vol. 7, no. 3, pp. 1–5, 2023, doi: 10.1002/gch2.202200165.

[2] C. Avcıoğlu, S. Avcıoğlu, M. F. Bekheet, and A. Gurlo, "Photocatalytic Overall Water Splitting by $SrTiO_3$: Progress Report and Design Strategies," *ACS Appl. Energy Mater.*, vol. 6, no. 3, pp. 1134–1154, 2023, doi: 10.1021/acsaem.2c03280.

[3] R. Li, T. Takata, B. Zhang, C. Feng *et al.* , "Criteria for Efficient Photocatalytic Water Splitting Revealed by Studying Carrier Dynamics in a Model Al-doped $SrTiO_3$ Photocatalyst," *Angew. Chemie - Int. Ed.*, vol. 62, no. 49, 2023, doi: 10.1002/anie.202313537.

[4] M. Zhang, P. A. Salvador, and G. S. Rohrer, "Influence of particle size and shape on the rate of hydrogen produced by Al-doped SrTiO3 photocatalysts," *J. Am. Ceram. Soc.*, vol. 105, no. 8, pp. 5336–5346, 2022, doi: 10.1111/jace.18488.

[5] T. H. Chiang, H. Lyu, T. Hisatomi, Y. Goto *et al.* , "Efficient Photocatalytic Water Splitting Using Al-Doped $SrTiO_3$ Coloaded with Molybdenum Oxide and Rhodium-Chromium Oxide," *ACS Catal.*, vol. 8, no. 4, pp. 2782–2788, 2018, doi: 10.1021/acscatal.7b04264.

[6] A. N. Adeyemi, A. Venkatesh, C. Xiao, Z. Zhao *et al.* , "Synthesis of $SrTiO_3$ and Al-doped $SrTiO_3$ via the deep eutectic solvent route," *Mater. Adv.*, vol. 3, no. 11, pp. 4736–4747, 2022, doi: 10.1039/d2ma00404f.

[7] B. Moss, Q. Wang, K. T. Butler, R. Grau-Crespo *et al.* , "Linking in situ charge accumulation to electronic structure in doped $SrTiO_3$ reveals design principles for hydrogen-evolving photocatalysts," *Nat. Mater.*, vol. 20, no. 4, pp. 511–517, 2021, doi: 10.1038/s41563-020-00868-2.

[8] T. Takata and K. Domen, "Defect Engineering of Photocatalysts by Doping of Aliovalent Metal Cations for Efficient Water Splitting," *J. Phys. Chem. C*, vol. 113, pp. 19386–19388, 2009.

[9] D. Neagu and J. T. S. Irvine, "Enhancing electronic conductivity in strontium titanates through correlated A and B-site doping," *Chem. Mater.*, vol. 23, no. 6, pp. 1607–1617, 2011, doi: 10.1021/cm103489r.

[10] R. Moos and K. H. Härdtl, "Defect chemistry of donor-doped and undoped strontium titanate ceramics between 1000° and 1400°C," *J. Am. Ceram. Soc.*, vol. 80, no. 10, pp. 2549–2562, 1997, doi: 10.1111/j.1151-2916.1997.tb03157.x.

[11] J.-J. Wang, H.-B. Huang, T. J. M. Bayer, A.Moballegh *et al.* , "," *Acta Mater.*, vol. 108, pp. 229–240, 2016, doi: 10.1016/j.actamat.2016.02.022.

[12] B. L. Phoon, C. W. Lai, J. C. Juan, P. L. Show, and W. H. Chen, "A review of synthesis and morphology of $SrTiO_3$ for energy and other applications," *Int. J. Energy Res.*, vol. 43, no. 10, pp. 5151–5174, 2019, doi: 10.1002/er.4505.

[13] E. Calì, G. Kerherve, F. Naufal, K. Kousi *et al.* , "Exsolution of Catalytically Active Iridium Nanoparticles from Strontium Titanate," *ACS Appl. Mater. Interfaces*, vol. 12, no. 33, pp. 37444–37453, 2020, doi: 10.1021/acsami.0c08928.

[14] H. Y. Lin and L. T. Cian, "Microwave-assisted hydrothermal synthesis of $SrTiO_3$: Rh for photocatalytic Z-scheme overall water splitting," *Appl. Sci.*, vol. 9, no. 1, 2018, doi: 10.3390/app9010055.

[15] R. J. D. Tilley, "Perovskites: Structure–Property Relationships," *MRS Bull.*, vol. 42, no.

4, p. 325, 2017, doi: 10.1557/mrs.2017.81.

[16] W. Wang, G. Zhao, X. Wu, and Z. Zhai, "The effect of high temperature annealing process on crystallization process of polypropylene, mechanical properties, and surface quality of plastic parts," *J. Appl. Polym. Sci.*, vol. 132, no. 46, 2015, doi: 10.1002/app.42773.

[17] E. W. Fischer, "Effect Of Annealing And Temperature On The Morphological Structure Of Polymers," *Pure Appl. Chem.*, vol. 31, no. 1–2, pp. 113–132, 1972, doi: 10.1351/pac197231010113.

[18] A. Kudo, A. Tanaka, K. Domen, and T. Onishi, "The effects of the calcination temperature of $SrTiO_3$ powder on photocatalytic activities," *J. Catal.*, vol. 111, no. 2, pp. 296–301, 1988, doi: 10.1016/0021-9517(88)90088-7.

[19] C. J. Gommes, "Ostwald ripening of confined nanoparticles: Chemomechanical coupling in nanopores," *Nanoscale*, vol. 11, no. 15, pp. 7386–7393, 2019, doi: 10.1039/c9nr01349k.

[20] K. Kato, "Reactions of alkoxides toward nanostructured or multicomponent oxide films," *Handb. Sol-Gel Sci. Technol. Process. Charact. Appl.*, pp. 113–132, 2018, doi: 10.1007/978-3-319-32101-1_2.

[21] K. N. and T. Tsuchiya, "Sol-Gel Processing of Thin Films with Metal Salts," in *Handbook of Sol-Gel Science and Technology: Processing, Characterization and Applications*, 2018, p. ix.

[22] L.Dimesso, "Pechini Processes: An Alternate Approach of the Sol-Gel Method, Preparation, Properties, and Applications," in *Handbook of Sol-Gel Science and Technology: Processing, Characterization and Applications*, no. January, 2018, p. ix.

[23] A. E. Danks, S. R. Hall, and Z. Schnepp, "The evolution of 'sol-gel' chemistry as a technique for materials synthesis," *Mater. Horizons*, vol. 3, no. 2, pp. 91–112, 2016, doi: 10.1039/c5mh00260e.

[24] S. H. Wu and H. L. Chen, "The effects of heat-treatment temperature on the retention capacities of spinels prepared by the Pechini process," *J. Power Sources*, vol. 119–121, pp. 134–138, 2003, doi: 10.1016/S0378-7753(03)00142-3.

[25] A. J. Koller, S. Saini, I. V. Chaple, M. A. Joaqui-Joaqui, *et al.* , "A General Design Strategy Enabling the Synthesis of Hydrolysis-Resistant, Water-Stable Titanium(IV) Complexes," *Angew. Chemie - Int. Ed.*, vol. 61, no. 22, pp. 1–9, 2022, doi: 10.1002/anie.202201211.

[26] Y. Jia, S. Chen, D. Wang, X. Wang *et al.* , "Composite $Sr_2TiO_4/SrTiO_3$(La,Cr) heterojunction based photocatalyst for hydrogen production under visible light irradiation," *J. Mater. Chem. A*, vol. 1, no. 27, pp. 7905–7912, 2013, doi: 10.1039/C3TA11326D.

[27] B. Bradlyn, L. Elcoro, J. Cano, M. G. Vergniory *et al.* , "Topological quantum chemistry," *Nature*, vol. 547, no. 7663, pp. 298–305, 2017, doi: 10.1038/nature23268.

[28] M. G. Vergniory, B. J. Wieder, L. Elcoro, S.S.P. Parkin *et al.* , "All topological bands of all nonmagnetic stoichiometric materials," *Science (80-.).*, vol. 376, no. 6595, 2022, doi: 10.1126/science.abg9094.

[29] M. G. Vergniory, L. Elcoro, C. Felser, N. Regnault, B. A. Bernevig, and Z. Wang, "A complete catalogue of high-quality topological materials," *Nature*, vol. 566, no. 7745,

pp. 480–485, 2019, doi: 10.1038/s41586-019-0954-4.

[30] B. Zhao, W. Zhong, F. Chen, P. Wang, C. Bie, and H. Yu, "High-crystalline g-C3N4 photocatalysts: Synthesis, structure modulation, and H2-evolution application," *Chinese J. Catal.*, vol. 52, pp. 127–143, 2023, doi: 10.1016/S1872-2067(23)64491-2.

[31] J. Liu, W. Fu, Y. Liao, J. Fan, and Q. Xiang, "Recent advances in crystalline carbon nitride for photocatalysis," *J. Mater. Sci. Technol.*, vol. 91, pp. 224–240, 2021, doi: 10.1016/j.jmst.2021.03.017.

[32] S. Dolabella, A. Borzì, A. Dommann, and A. Neels, "Lattice Strain and Defects Analysis in Nanostructured Semiconductor Materials and Devices by High-Resolution X-ray Diffraction: Theoretical and Practical Aspects," *Small Methods*, vol. 6, no. 2, 2022, doi: 10.1002/smtd.202100932.

[33] G. Madhu, V. C. Bose, K. Maniammal, A. S. Aiswarya Raj, and V. Biju, "Microstrain in nanostructured nickel oxide studied using isotropic and anisotropic models," *Phys. B Condens. Matter*, vol. 421, pp. 87–91, 2013, doi: 10.1016/j.physb.2013.04.028.

[34] S. Kobayashi, Y. Ikuhara, and T. Mizoguchi, "Lattice expansion and local lattice distortion in Nb- and La-doped $SrTiO_3$ single crystals investigated by X-ray diffraction and first-principles calculations," *Phys. Rev. B*, vol. 98, no. 13, 2018, doi: 10.1103/PhysRevB.98.134114.

[35] N. Birkner, C. Li, S. L. Estes, and K. S. Brinkman, "Gallium-Doping Effects on Structure, Lithium-Conduction, and Thermochemical Stability of $Li_{7-3x}Ga_xLa_3Zr_2O_{12}$ Garnet-Type Electrolytes," *ChemSusChem*, vol. 14, no. 12, pp. 2621–2630, 2021, doi: 10.1002/cssc.202100526.

[36] R. Wagner, G.J. Redhammer, D. Rettenwander, A. Senyshyn *et al.* , "Crystal Structure of Garnet-Related Li-Ion Conductor $Li_{7-3x}Ga_xLa_3Zr_2O_{12}$: Fast Li-Ion Conduction Caused by a Different Cubic Modification?," *Chem. Mater.*, vol. 28, no. 6, pp. 1861–1871, 2016, doi: 10.1021/acs.chemmater.6b00038.

[37] G. Li, J. Boerio-Goates, B. F. Woodfield, and L. Li, "Evidence of linear lattice expansion and covalency enhancement in rutile TiO 2 nanocrystals," *Appl. Phys. Lett.*, vol. 85, no. 11, pp. 2059–2061, 2004, doi: 10.1063/1.1790596.

[38] L. R. V. Buizza, T.W. Crothers, Z. Wang, J. B. Patel *et al.* , "Charge-Carrier Dynamics, Mobilities, and Diffusion Lengths of 2D–3D Hybrid Butylammonium–Cesium–Formamidinium Lead Halide Perovskites," *Adv. Funct. Mater.*, vol. 29, no. 35, 2019, doi: 10.1002/adfm.201902656.

[39] Y. Matsumoto, "Energy positions of oxide semiconductors and photocatalysis with iron complex oxides," *J. Solid State Chem.*, vol. 126, no. 2, pp. 227–234, 1996, doi: 10.1006/jssc.1996.0333.

[40] K. P. O'Donnell and X. Chen, "Temperature dependence of semiconductor band gaps," *Appl. Phys. Lett.*, vol. 58, no. 25, pp. 2924–2926, 1991, doi: 10.1063/1.104723.

[41] J. Bhosale, A. K. Ramadass, A. Burger, A. Mũnoz *et al.* , "Temperature dependence of band gaps in semiconductors: Electron-phonon interaction," *Phys. Rev. B - Condens. Matter Mater. Phys.*, vol. 86, no. 19, pp. 1–10, 2012, doi: 10.1103/PhysRevB.86.195208.

[42] Y. Zhang, Z. Wang, J. Xi, and J. Yang, "Temperature-dependent band gaps in several semiconductors: From the role of electron-phonon renormalization," *J. Phys. Condens. Matter*, vol. 32, no. 47, 2020, doi: 10.1088/1361-648X/aba45d.

[43] T. Ma, R. Jacobs, J. Booske, and D. Morgan, "Understanding the interplay of surface structure and work function in oxides: A case study on $SrTiO_3$," *APL Mater.*, vol. 8, no. 7, 2020, doi: 10.1063/1.5143325.

[44] M. T. Greiner, L. Chai, M. G. Helander, W. M. Tang, and Z. H. Lu, "Transition metal oxide work functions: The influence of cation oxidation state and oxygen vacancies," *Adv. Funct. Mater.*, vol. 22, no. 21, pp. 4557–4568, 2012, doi: 10.1002/adfm.201200615.

[45] R. Jacobs, J. Booske, and D. Morgan, "Understanding and Controlling the Work Function of Perovskite Oxides Using Density Functional Theory," *Adv. Funct. Mater.*, vol. 26, no. 30, pp. 5471–5482, 2016, doi: 10.1002/adfm.201600243.

[46] Z. Zhong and P. Hansmann, "Tuning the work function in transition metal oxides and their heterostructures," *Phys. Rev. B*, vol. 93, no. 23, pp. 1–9, 2016, doi: 10.1103/PhysRevB.93.235116.

[47] S. A. Chambers and P. V. Sushko, "Influence of crystalline order and defects on the absolute work functions and electron affinities of TiO_2 - And SrO-terminated n-$SrTiO_3$(001)," *Phys. Rev. Mater.*, vol. 3, no. 12, 2019, doi: 10.1103/PhysRevMaterials.3.125803.

[48] Y. W. Chung and W. B. Weissbard, "Surface spectroscopy studies of the $SrTiO_3$ (100) surface and the platinum-$SrTiO_3$ (100) interface," *Phys. Rev. B*, vol. 20, no. 8, pp. 3456–3461, 1979, doi: 10.1103/PhysRevB.20.3456.

[49] T. Susaki, A. Makishima, and H. Hosono, "Work function engineering via $LaAlO_3$/$SrTiO_3$ polar interfaces," *Phys. Rev. B - Condens. Matter Mater. Phys.*, vol. 84, no. 11, pp. 2–6, 2011, doi: 10.1103/PhysRevB.84.115456.

[50] L. F. Zagonel, M. Bäurer, A. Bailly, O. Renault *et al.* , "Orientation-dependent work function of in-situ annealed strontium titanate," *J. Phys. Condens. Matter*, vol. 21, no. 31, 2009, doi: 10.1088/0953-8984/21/31/314013.

[51] M. Yoshitake, 'Work Function and Band Alignment of Electrode Materials: The Art of Interface Potential for Electronic Devices, Solar Cells, and Batteries′, 1st ed. Springer Tokyo.ISBN: 978-4-431-56896-4, 20 December, 2020. DOI: https://doi.org/10.1007/978-4-431-56898-8

[52] I. Brodie, S. H. Chou, and H. Yuan, "A general phenomenological model for work function," *Surf. Sci.*, vol. 625, pp. 112–118, 2014, doi: 10.1016/j.susc.2014.03.002.

[53] A. R. Zeradjanin, A. Vimalanandan, G. Polymeros, A. A. Topalov, K. J. J. Mayrhofer, and M. Rohwerder, "Balanced work function as a driver for facile hydrogen evolution reaction - Comprehension and experimental assessment of interfacial catalytic descriptor," *Phys. Chem. Chem. Phys.*, vol. 19, no. 26, pp. 17019–17027, 2017, doi: 10.1039/c7cp03081a.

[54] A. Kiejna, K. F. Wojciechowski, and J. Zebrowksi, "The temperature dependence of metal work functions," *J. Phys. F Met. Phys.*, vol. 9, no. 7, pp. 1361–1366, 1979, doi: 10.1088/0305-4608/9/7/016.

[55] R. Rahemi and D. Li, "Variation in electron work function with temperature and its effect on the Young's modulus of metals," *Scr. Mater.*, vol. 99, pp. 41–44, 2015, doi: 10.1016/j.scriptamat.2014.11.022.

[56] M. G. Helander, M. T. Greiner, Z. B. Wang, and Z. H. Lu, "Pitfalls in measuring work

function using photoelectron spectroscopy," *Appl. Surf. Sci.*, vol. 256, no. 8, pp. 2602–2605, 2010, doi: 10.1016/j.apsusc.2009.11.002.

[57] C. H. Phuong and V. Van Hung, "Study of the thermodynamic properties of $SrTiO_3$ perovskite under pressure by the statistical moment method with the improved interatomic potential," *Comput. Condens. Matter*, vol. 31, no. 3, pp. 38–47, 2022, doi: 10.1016/j.cocom.2022.e00683.

[58] D. de Ligny and P. Richet, "High-temperature heat capacity and thermal expansion of and perovskites," *Phys. Rev. B - Condens. Matter Mater. Phys.*, vol. 53, no. 6, pp. 3013–3022, 1996, doi: 10.1103/PhysRevB.53.3013.

[59] J. Mizusaki, "Relationship of Crystal Structure, Lattice Parameters and Thermal Expansion to Nonstoichiometry in $La_{1-x}MnO_{3+d}$ and $La_{1-x}Sr_xMnO_{3+d}$ Determined by High-Temperature X-ray Diffraction Under Controlled Oxygen Partial Pressures," *ECS Proc. Vol.*, vol. 1995–1, no. 1, pp. 444–453, 1995, doi: 10.1149/199501.0444pv.

[60] D. S. Aidhy, B. Liu, Y. Zhang, and W. J. Weber, "Chemical expansion affected oxygen vacancy stability in different oxide structures from first principles calculations," *Comput. Mater. Sci.*, vol. 99, pp. 298–305, 2015, doi: 10.1016/j.commatsci.2014.12.030.

[61] P. Gayen, S. Saha, K. Bhattacharyya, and V. K. Ramani, "Oxidation State and Oxygen-Vacancy-Induced Work Function Controls Bifunctional Oxygen Electrocatalytic Activity," *ACS Catal.*, vol. 10, no. 14, pp. 7734–7746, 2020, doi: 10.1021/acscatal.0c01541.

[62] W. Wang, P. J. Strohbeen, D. Lee, C. Zhou *et al.* , "The Role of Surface Oxygen Vacancies in $BiVO_4$," *Chem. Mater.*, vol. 32, no. 7, pp. 2899–2909, 2020, doi: 10.1021/acs.chemmater.9b05047.

[63] N. B. Kotadiya, A. Mondal, P. W. M. Blom, D. Andrienko, and G. J. A. H. Wetzelaer, "A window to trap-free charge transport in organic semiconducting thin films," *Nat. Mater.*, vol. 18, no. 11, pp. 1182–1186, 2019, doi: 10.1038/s41563-019-0473-6.

[64] E. Louis, E. San-Fabián, M. A. Díaz-García, G. Chiappe, and J. A. Vergés, "Are Electron Affinity and Ionization Potential Intrinsic Parameters to Predict the Electron or Hole Acceptor Character of Amorphous Molecular Materials?," *J. Phys. Chem. Lett.*, vol. 8, no. 11, pp. 2445–2449, 2017, doi: 10.1021/acs.jpclett.7b00681.

[65] A. Walsh and K. T. Butler, "Prediction of electron energies in metal oxides," *Acc. Chem. Res.*, vol. 47, no. 2, pp. 364–372, 2014, doi: 10.1021/ar400115x.

[66] H. Idriss, "On the wrong assignment of the XPS O1s signal at 531–532 eV attributed to oxygen vacancies in photo- and electro-catalysts for water splitting and other materials applications," *Surf. Sci.*, vol. 712, no. June, pp. 2–7, 2021, doi: 10.1016/j.susc.2021.121894.

[67] S. Chattopadhyay, A. B. Naden, W. S. J. Skinner, G. Kerherve, D. J. Payne, and J. T. S. Irvine, "Room Temperature Exsolution of Cds Nanodots on A-site Deficient Cotton-Ball Like Titanate Perovskite Nanoparticles for H_2 Production Under Visible Light," *Adv. Energy Mater.*, vol. 13, no. 47, pp. 1–9, 2023, doi: 10.1002/aenm.202301381.

[68] Z. Hou and K. Terakura, "Defect states induced by oxygen vacancies in cubic $SrTiO_3$: first-principles calculations," *J. Phys. Soc. Japan*, vol. 79, no. 11, pp. 1–6, 2010, doi: 10.1143/JPSJ.79.114704.

[69] C. Mitra, C. Lin, J. Robertson, and A. A. Demkov, "Electronic structure of oxygen

vacancies in SrTiO 3 and LaAlO 3," *Phys. Rev. B - Condens. Matter Mater. Phys.*, vol. 86, no. 15, 2012, doi: 10.1103/PhysRevB.86.155105.

[70] Y. Yamada and Y. Kanemitsu, "Band-to-band photoluminescence in $SrTiO_3$," *Phys. Rev. B - Phys Rev B*, vol. 82, Sep. 2010, doi: 10.1103/PhysRevB.82.121103.

[71] S. Dadgostar, J. L. Pura Ruiz, J. Serrano Gutierrez, B. Lepine, P. Schieffer, and J. Jimenez, "Luminescence in undoped and Nb-doped $SrTiO_3$ crystals: Bulk and surface emission," *Mater. Sci. Eng. B*, vol. 283, no. September 2021, p. 115830, 2022, doi: 10.1016/j.mseb.2022.115830.

[72] M. L. Crespillo, J. T. Graham, F. Agulló-López, Y. Zhang, and W. J. Weber, "Role of oxygen vacancies on light emission mechanisms in $SrTiO_3$ induced by high-energy particles," *J. Phys. D. Appl. Phys.*, vol. 50, no. 15, 2017, doi: 10.1088/1361-6463/aa627f.

[73] H. H. Kim, Y. Lee, Y.J. Lee, J. Jeong *et al.* , "Realization of Excitation Wavelength Independent Blue Emission of ZnO Quantum Dots with Intrinsic Defects," 2020, doi: 10.1021/acsphotonics.9b01587.

[74] K. Potzger, J. Osten, A.A. Levin, A. Shalimov *et al.* , "Defect-induced ferromagnetism in crystalline $SrTiO_3$," *J. Magn. Magn. Mater.*, vol. 323, no. 11, pp. 1551–1562, 2011, doi: 10.1016/j.jmmm.2011.01.018.

[75] M. L. Crespillo, J. T. Graham, F. Agulló-López, Y. Zhang, and W. J. Weber, "Isolated oxygen vacancies in strontium titanate shine red: Optical identification of Ti3+ polarons," *Appl. Mater. Today*, vol. 12, pp. 131–137, 2018, doi: https://doi.org/10.1016/j.apmt.2018.04.006.

[76] S. Yang, L. E. Halliburton, A. Manivannan, P. H. Bunton and D.B. Baker, "Photoinduced Electron Paramagnetic Resonance Study Of Electron Traps In TiO_2 Crystals : Oxygen Vacancies And Ti^{3+} Ions," 2009.

[77] Z. Zhang, T. Tsuchimochi, T. Ina, Y. Kumabe *et al.* , "Binary dopant segregation enables hematite-based heterostructures for highly efficient solar H_2O_2 synthesis," *Nat. Commun.*, vol. 13, no. 1, pp. 1–10, 2022, doi: 10.1038/s41467-022-28944-y.

[78] H. I. Yoon, D.-K. Lee, H. B. Bae, G.-Y. Jo *et al.* , "Probing dopant segregation in distinct cation sites at perovskite oxide polycrystal interfaces," *Nat. Commun.*, vol. 8, no. 1, pp. 1–7, 2017, doi: 10.1038/s41467-017-01134-x.

[79] K. L. Kliewer and J. S. Koehler, "Space charge in ionic crystals. I. General approach with application to NaCl," *Phys. Rev.*, vol. 140, no. 4A, 1965, doi: 10.1103/PhysRev.140.A1226.

[80] S. Y. Chung, S. Y. Choi, H. I. Yoon, H. S. Kim, and H. Bin Bae, "Subsurface Space-Charge Dopant Segregation to Compensate Surface Excess Charge in a Perovskite Oxide," *Angew. Chemie - Int. Ed.*, vol. 55, no. 33, pp. 9680–9684, 2016, doi: 10.1002/anie.201605561.

Appendix

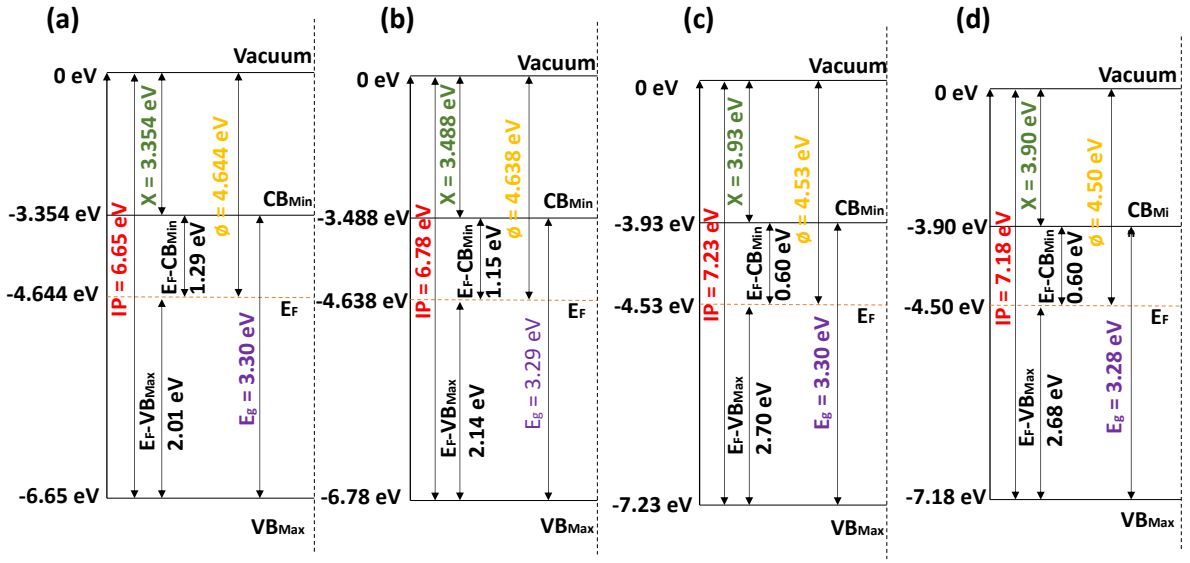


***Figure 4.A1**: Band Edge Alignment of undoped $SrTiO_3$ at a.) 500 °C b.) 600 °C c.) 700 °C d.) 800 °C with work function from Kelvin Probe*

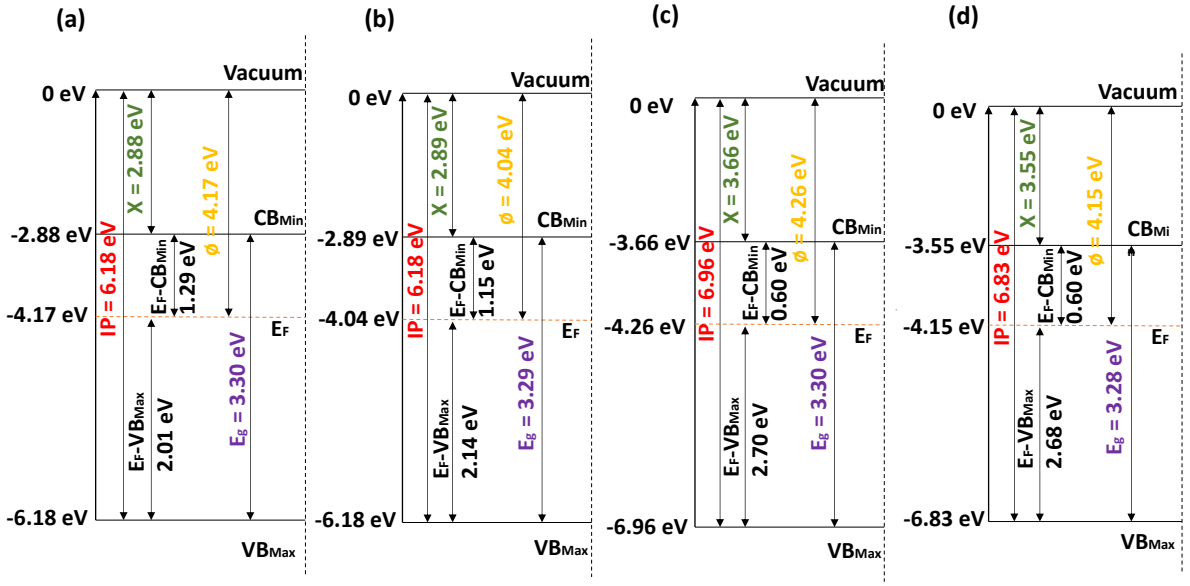


***Figure 4.A2:** Band Edge Alignment of undoped $SrTiO_3$ at a.) 500 °C b.) 600 °C c.) 700 °C d.) 800 °C with work function from the XPS*

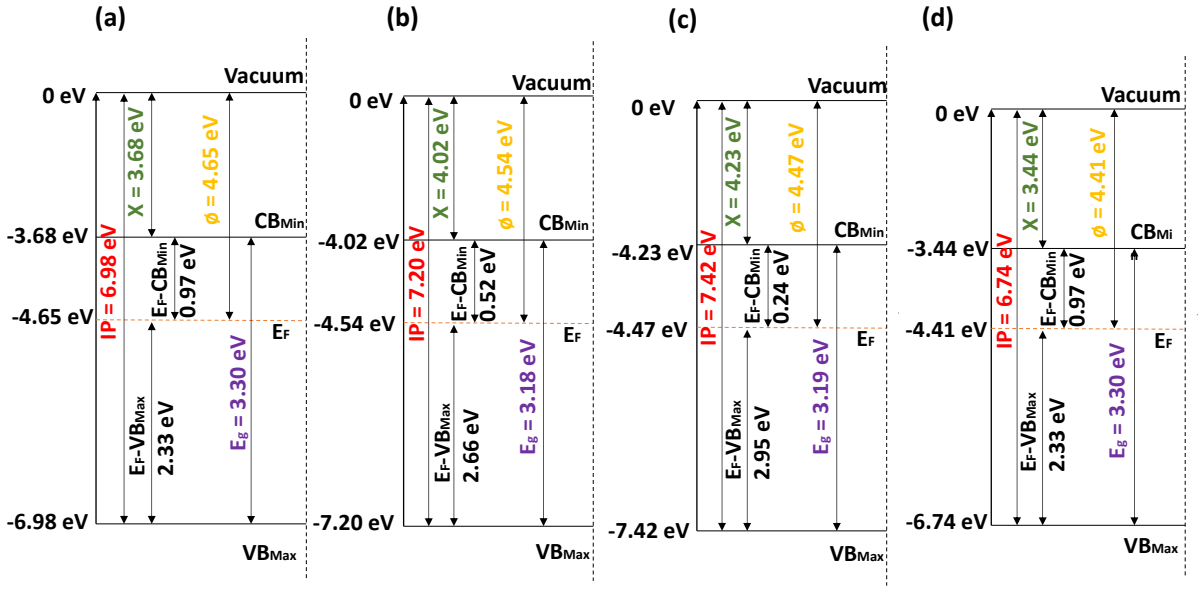


***Figure 4.A 3**: Band Edge Alignment of 2 mol% Ga doped $SrTiO_3$ at a.) 500 °C b.) 600 °C c.) 700 °C d.) 800 °C with work function from Kelvin Probe*

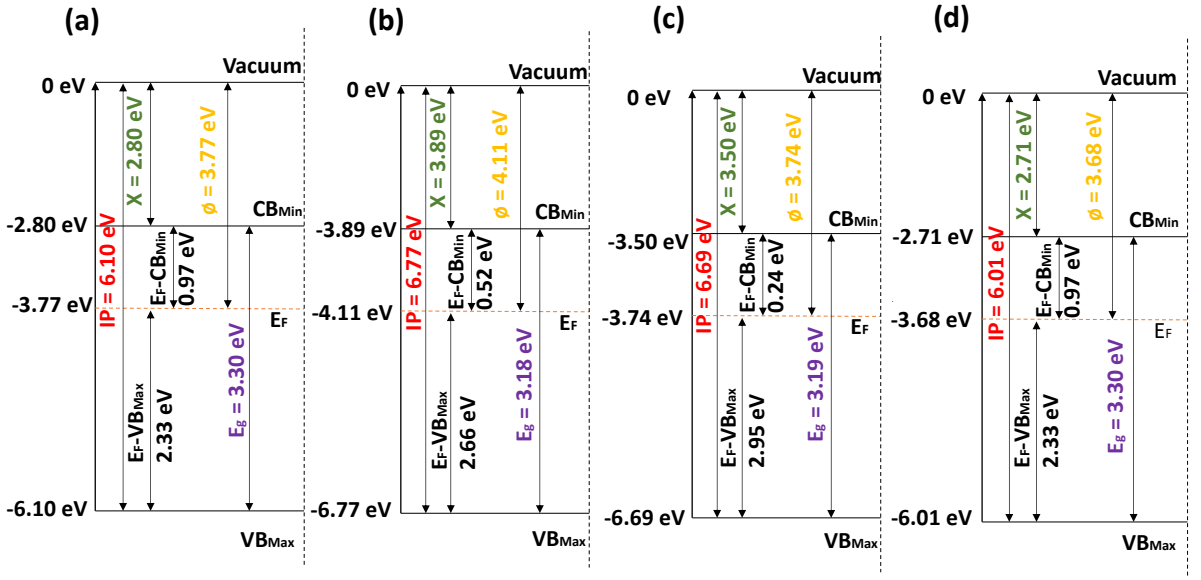


***Figure 4.A 4**:Band Edge Alignment of 2 mol% Ga doped $SrTiO_3$ at a.) 500 °C b.) 600 °C c.) 700 °C d.) 800 °C with work function from XPS*

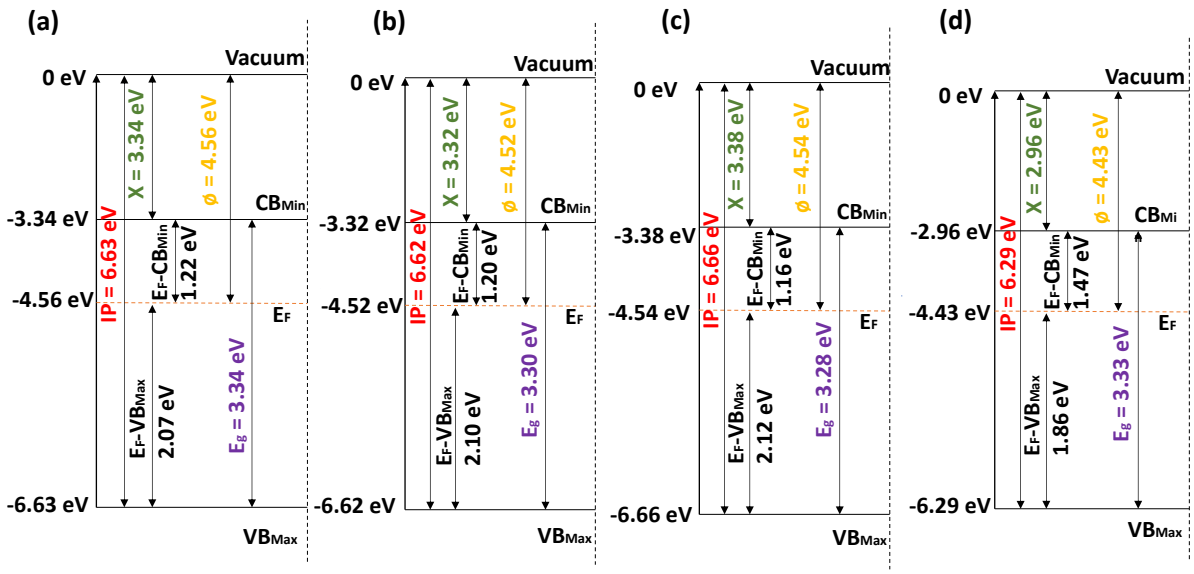


Figure 4.A5: *Band Edge Alignment of 4 mol% Ga doped $SrTiO_3$ at a.) 500 °C b.) 600 °C c.) 700 °C d.) 800 °C from the Kelvin Probe*

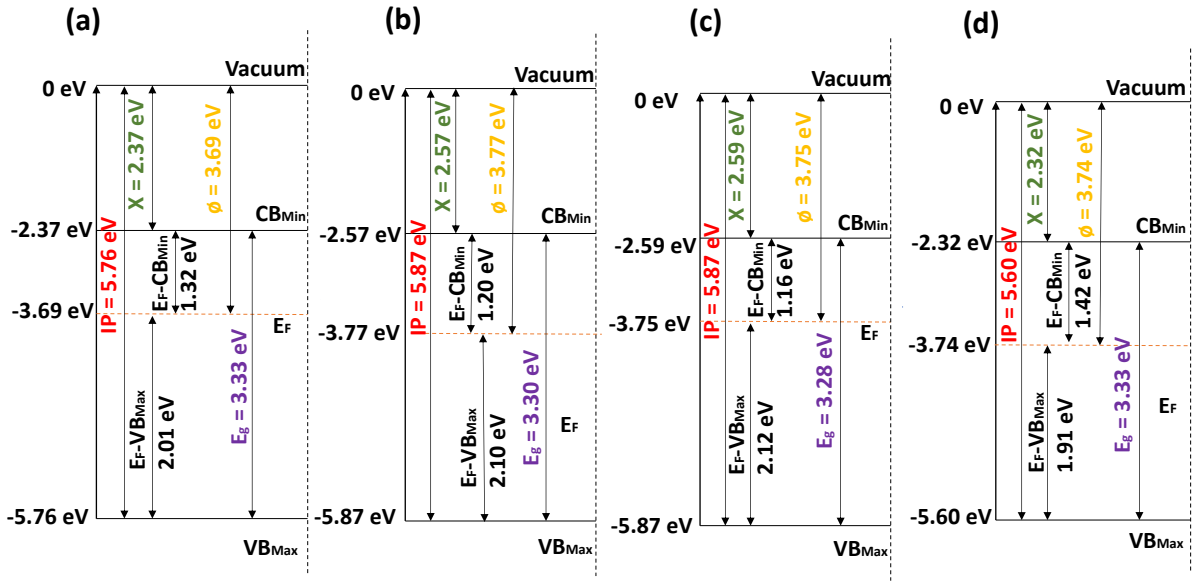
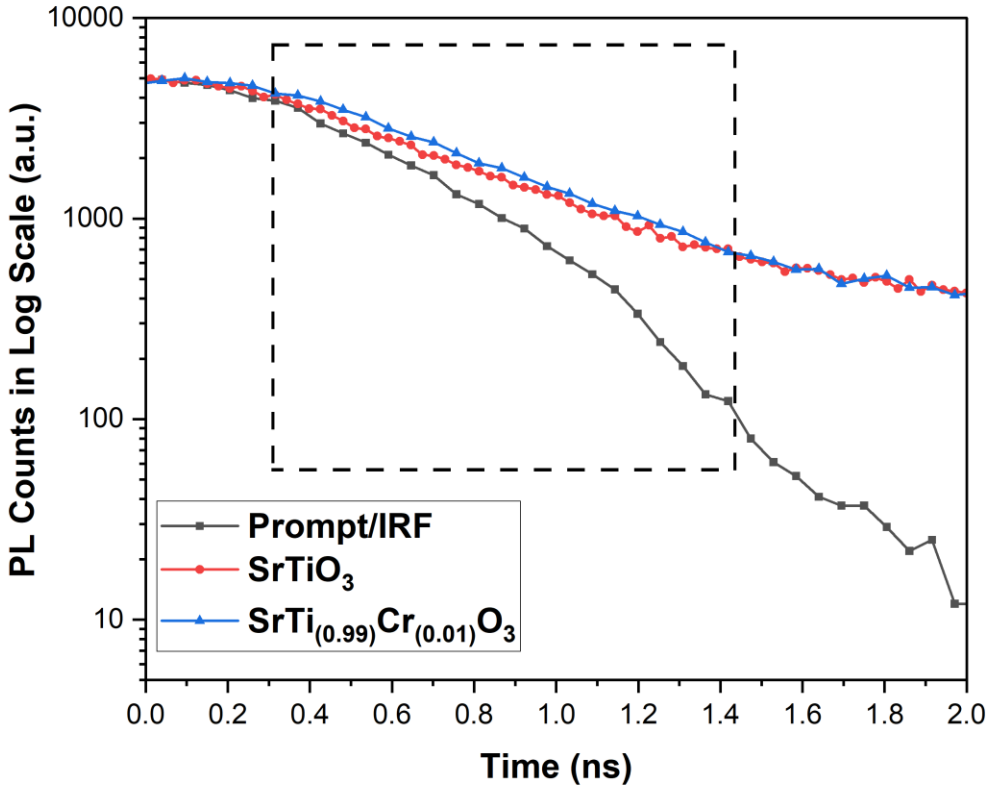


Figure 4.A6: *Band Edge Alignment of 4 mol% Ga doped $SrTiO_3$ at a.) 500 °C b.) 600 °C c.) 700 °C d.) 800 °C from the XP*

Chapter 5: Investigating the Role of the Cr^{3+}/Cr^{6+} in Determining the Photoactivity in Cr-(co-) doped $SrTiO_3$

Summary

In this work, a modification was introduced to the standard sol-gel Pechini process to study the effect of dopant incorporation. Co-doping methods were studied for their effect on midgap state suppression. Higher lifetimes were observed in 1 mol% Cr^{3+} doped $SrTiO_3$ sample prepared with the serial dilution method. No Cr^{6+} trap states were observed in this sample compared to the other doped samples.



5.1 Introduction

Doping with transition metal ions is a widely accepted strategy for narrowing band gaps and inducing visible light absorption in wide band gap $SrTiO_3$. One such material is Cr^{3+} (electronic configuration of $[Ar]3d^3$) which can narrow the band gap to induce visible light activity in $SrTiO_3$. Studies have shown that Cr^{3+} has better H_2 evolution than the undoped $SrTiO_3$ [1].[4]. Cr^{3+} doping can also result in Cr^{6+} states which can be detrimental to photocatalysis and co-doping with La might help suppress these states [1]. This study focuses on the incorporation route of the Cr dopants in $SrTiO_3$ and how it affects the performance of the catalysts. In this work, an attempt to understand how the Cr^{3+} and the Cr^{6+} affect the performance of the catalysts will be made. A detailed study will be made to understand which oxidation state facilitates photocatalytic performance and which state can be beneficial to electrocatalysis.

Motivation for Studying Cr-doped $SrTiO_3$

Cr^{3+} with d^3 configuration doping introduces states above the valence band that facilitate visible light absorption enabling a more efficient photocatalyst. With this objective, 2 mol% Cr^{3+} doped $SrTiO_3$ samples were synthesized at 800 °C and 900 °C. Figure 5. i (a, b) shows the absorption comparison spectrum between the synthesized undoped and Cr-doped $SrTiO_3$. The doped samples show an additional absorption feature around 550 nm tailing off around 900 nm. This behavior of extending the light absorption is analogous to other B-site transition metals such as Rh^{3+} doped $SrTiO_3$ as shown in Figure 5.i (c). These states in Rh-doped $SrTiO_3$ were attributed to Rh^{4+} trap states. Suppression of Rh^{4+} states can lead to an enhanced photocatalytic performance. To suppress these states, H_2 reduction or co-doping techniques can be employed. In this work, the study on the effect of co-doping was started with La^{3+}. This was followed by studying the effect of Cs^{+1} on the Cr^{6+} trap states. Another batch with monodoped Cr was prepared to study the effect of increasing controlled mono-doping on the Cr^{6+} states.

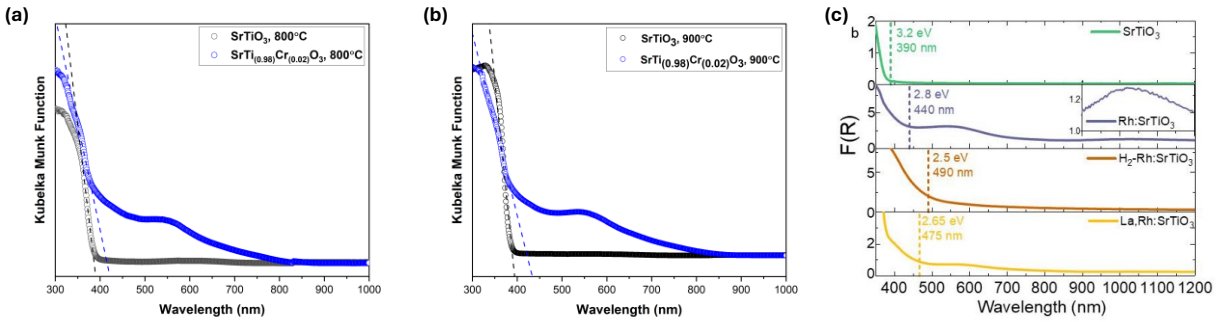


Figure 5.i: *Kubelka Munk function to study the mid-gap states around 550 nm in the absorption spectrum of 2 mol% Cr^{3+} doped $SrTiO_3$ at (a) 800 °C (b) 900 °C (c) Analogous behavior of Rh^{3+}: $SrTiO_3$ and the suppression of the Rh^{4+} trap states with La^{3+} and H_2 reduction reproduced from the work of Moss, B. et al. [5] (Copyright © 2021, The Author(s), under exclusive licence to Springer Nature Limited).*

In the previous chapters, a time-temperature-solubility (T-T-S) factor causing surface segregation of the dopants was discussed resulting in higher mol% doping than intended. Therefore, the samples were prepared via two dopant incorporation techniques to compare the effect of this factor on the amount of doping and their performance.

5.2 Experimental

Synthesis of Cr^{3+} mono- and co-doped $SrTiO_3$

Undoped, 2 mol% Cr^{3+} mono-, La^{3+}, and Cs^{1+} co-doped samples were synthesized via the sol-gel Pechini method as discussed in Chapter 2. The undoped, Cr monodoped, La^{3+} and Cs^{1+} co-doped $SrTiO_3$ samples yielded white, red, yellow, and violet fine powders respectively as shown in Figure 5.1 (a, b, and d). The SD series resulted in faint yellow samples at low doping concentrations to red powders at higher mol% doping as seen in Figure 5.1 (c).

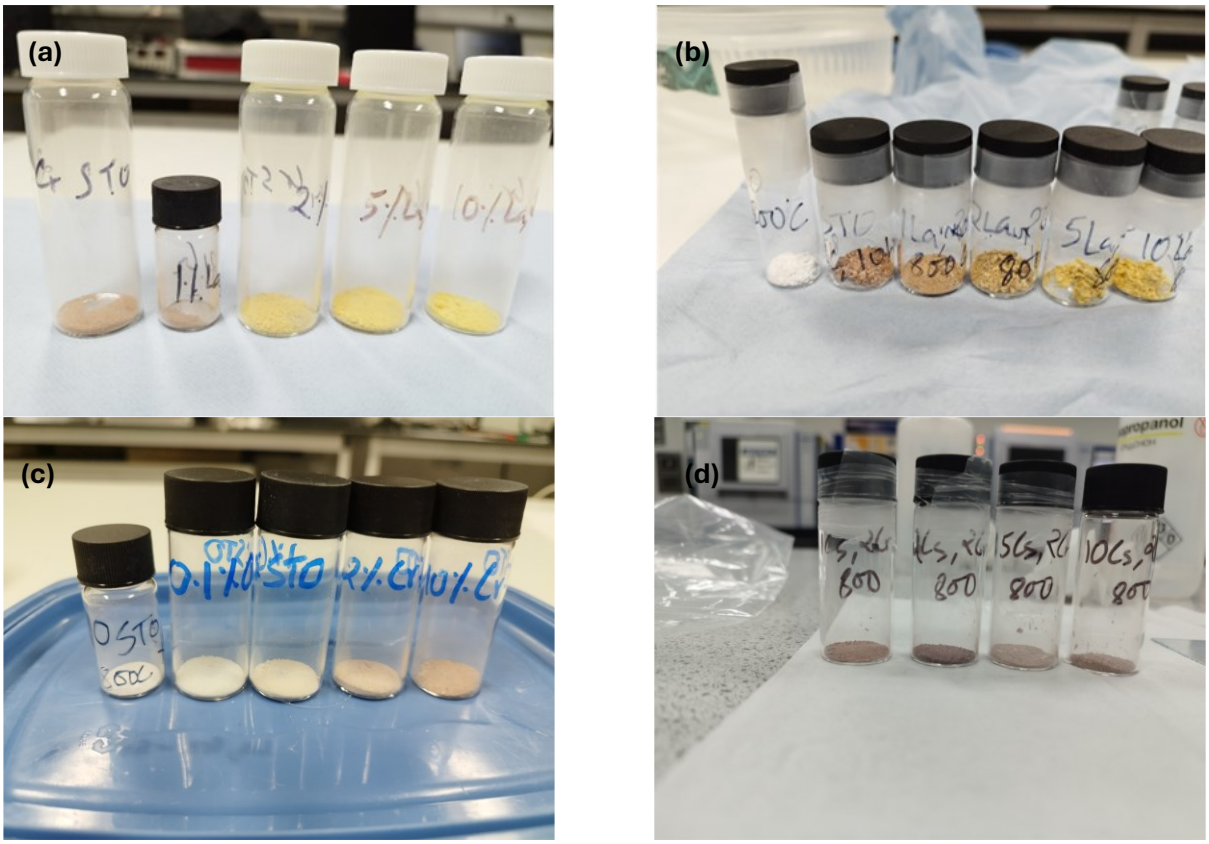


Figure 5.1: *Synthesized samples (a) La^{3+} co-doped samples 900 °C (b) La^{3+} co-doped samples 800 °C (c) Serial dilution Cr^{3+} monodoped series (d) Cs^{+1} co-doped sample at 800 °C.*

5.3 Goldschmidt's Tolerance Factor Consideration in the Structural Stability of the Samples

Goldschmidt's tolerance factor was calculated for the synthesized samples and is tabulated in Table 5.1.

Table 5.1: Goldschmidt's Tolerance Factor for undoped and doped $SrTiO_3$ samples

Sr No	Sample	Tolerance Factor, t
1	$SrTiO_3$	1.0000
2	$SrTi_{(0.999)}Cr_{(0.001)}O_3$	1.0016
3	$SrTi_{(0.99)}Cr_{(0.01)}O_3$	1.0015
4	$SrTi_{(0.98)}Cr_{(0.02)}O_3$	1.0015
5	$SrTi_{(0.9)}Cr_{(0.1)}O_3$	1.0011
6	$La_{(0.01)}Sr_{(0.99)}Ti_{(0.98)}Cr_{(0.02)}O_3$	1.0012
7	$La_{(0.02)}Sr_{(0.98)}Ti_{(0.98)}Cr_{(0.02)}O_3$	1.0009
8	$La_{(0.05)}Sr_{(0.95)}Ti_{(0.98)}Cr_{(0.02)}O_3$	1.0001
9	$La_{(0.1)}Sr_{(0.9)}Ti_{(0.98)}Cr_{(0.02)}O_3$	0.9987
10	$Cs_{(0.01)}Sr_{(0.99)}Ti_{(0.98)}Cr_{(0.02)}O_3$	1.0030
11	$Cs_{(0.02)}Sr_{(0.98)}Ti_{(0.98)}Cr_{(0.02)}O_3$	1.0046
12	$Cs_{(0.05)}Sr_{(0.95)}Ti_{(0.98)}Cr_{(0.02)}O_3$	1.0092
13	$Cs_{(0.1)}Sr_{(0.9)}Ti_{(0.98)}Cr_{(0.02)}O_3$	1.0170

From Table 5.1, the tolerance factor of the samples is 1 which is within the tolerance limit of 1 [6]. It can be inferred from Table 1, that most samples retain the cubic structure with no distortions upon doping. However, at 10 mol% Cs^{1+} co-doping, the tolerance factor (t) is slightly greater than 1. This could indicate distortions to the cubic structure.
Due to the similarities in the ionic radii of Ti^{4+} and Cr^{3+}, the dopant is expected to be in the B-site. In the work of Ichihara, F., the tolerance factor of undoped, Cr and La, Cr doped samples were reported to be 0.9986, 0.9981, and 0.9983 respectively [7]. This is quite close to the values calculated in the above table. The tolerance factor (t) of the samples was compared with the XRD patterns discussed in the following section.

5.4 Microstructural Analysis with the XRD

The diffraction patterns of the La^{3+} co-doped samples were phase pure, and no phase segregations were detected as shown in Figure 5.2 (a, b). For the Cr^{3+} monodoped samples synthesized via serial dilution doping method, the 10 mol% sample was not phase pure (Figure 5.2(e)). For both the Cs^{1+} co-doped batches synthesized at 800 °C and 900 °C, phase purity ceases beyond 5 mol% doping (Figure 5.2 (c, d)). La^{3+} co-doping could have increased the solubility of the Cr dopant in the $SrTiO_3$ matrix. Therefore, even at higher mol% the phase purity is maintained. La^{3+} enhancing dopant solubility was discussed in the previous chapter. All peaks were indexed after calculation and were found to be consistent with the $SrTiO_3$ ICSD 23076 file [8]–[10].

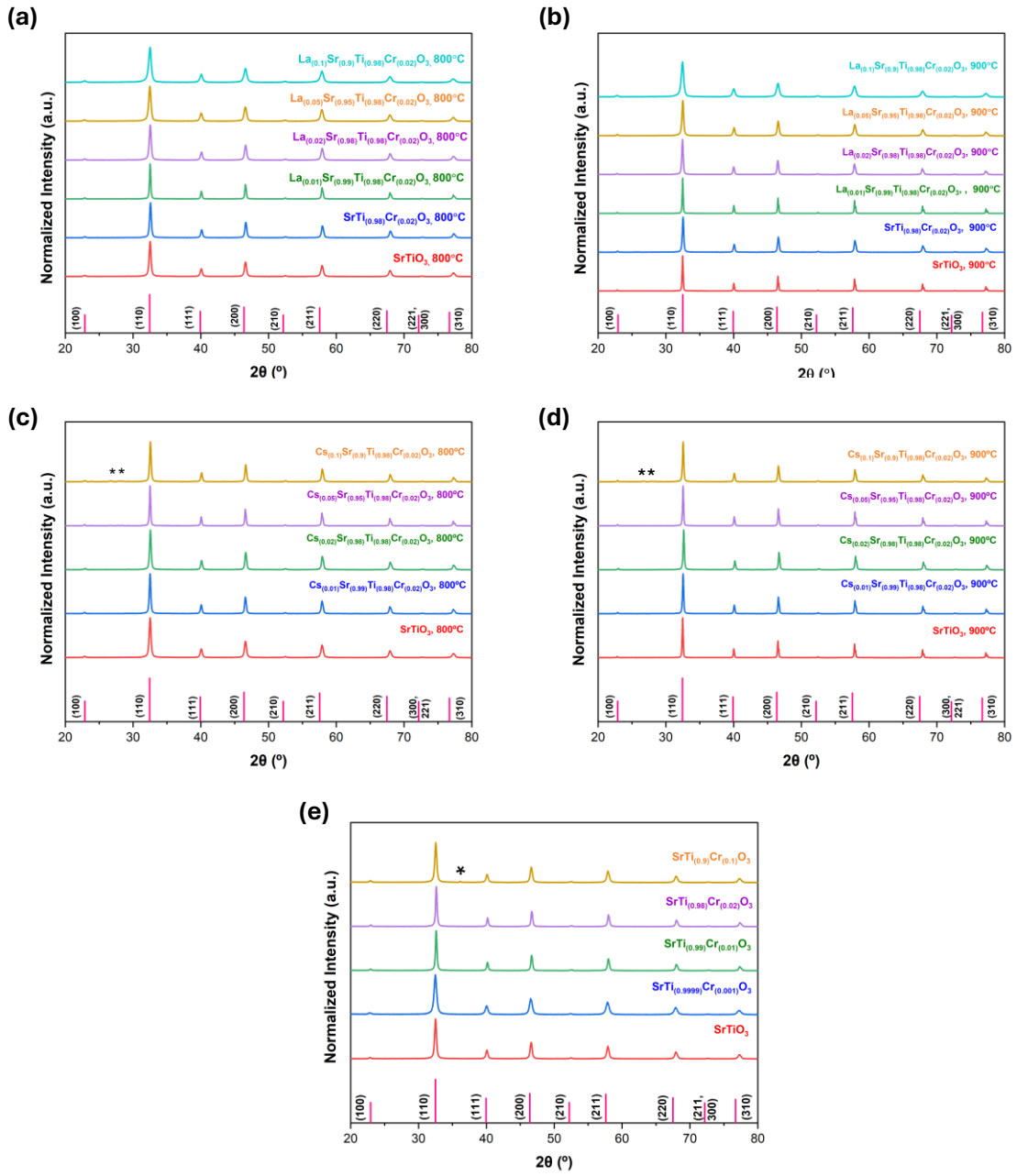


Figure 5.2: *XRD patterns of (a) La^{3+} co-doped batch at 800 °C (b) La^{3+} co-doped batch at 900 °C (c) Cs^{1+} co-doped batch at 800 °C (d) Cs^{1+} co-doped batch at 900 °C (e) Cr^{3+} monodoped batch with serial dilution synthesized at 800 °C compared with ICSD reference (pink) [8]-[10]. All patterns were measured with a PANanalytical X'pert MPD diffractometer with Cu Kα radiation source of λ = 0.15406 nm and were collected between 2θ range 20° to 80° and at 0.3s time/step.*

In photocatalysis, the size of the nanoparticles is fundamental in determining the efficiency of the photocatalytic activity [11], [12]. Smaller particles provide higher specific surface areas which promotes higher photoactivity. The coherently scattering domain size (crystallite sizes), the microstrain, and the lattice parameters were calculated from the XRD and the Rietveld refinements. These values are tabulated in Table 5.1A (Appendix) and the crystallite size comparison is shown in Figure 5.3 (a-c). The crystallite size of the samples was calculated by

the Debye-Scherrer equation and the microstrain with the W-H analysis as shown in Eqs (2.5) in Chapter 2.

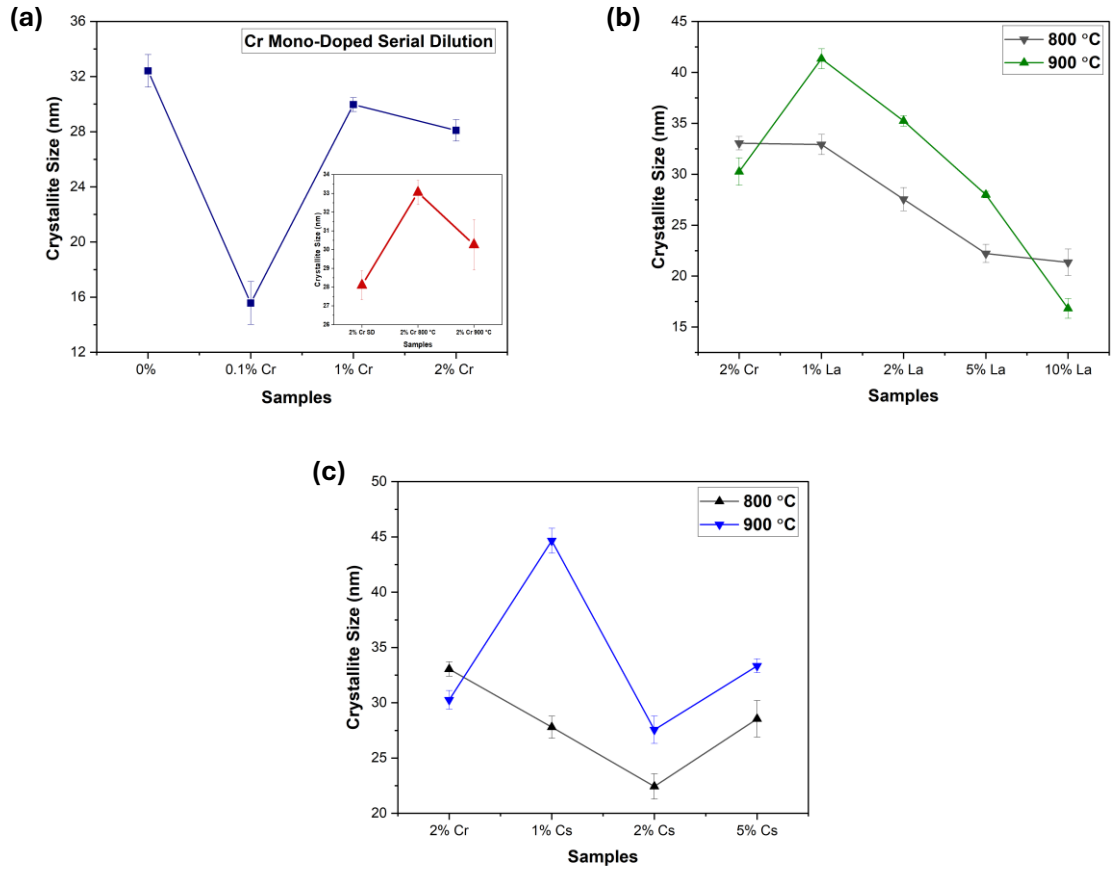


Figure 5.3: *Comparison of the crystallite sizes (a) Cr monodoped serial dilution samples with the inset comparing the 2 mol% Cr monodoped sample prepared by different methods (b) La^{3+} co-doped (800 °C, 900 °C) (b) La^{3+} co-doped (900 °C) (c) Cs^{1+} co-doped (800 °C, 900 °C).*

Note: * SD in Figure 5.3(a) inset denotes serial dilution.

Figure 5.3(a) shows the general trend in the crystallite sizes of the SD series with dopant in the B-site which decreases with increasing mol% doping. In this series, the 0.1 mol% sample significantly decreased compared to the undoped. The crystallite sizes of the 1 mol% and the 2 mol% are higher than the 0.1 mol% but lower than the undoped. The inset of 5.3(a) compares the 2 mol% Cr doped sample made with the serial dilution method and the sol-gel Pechini. The 2 mol% Cr doped sample made with the serial dilution shows the lowest crystallite size compared to the sol-gel Pechini samples made at 800 °C and 900 °C. In the La^{3+} co-doped series in 5.3(b), the samples made at 800 °C show a decrease compared to the monodoped sample. The samples made at 900 °C however show a more erratic trend. The 1 mol% La^{3+} co-doped samples show the highest crystallite size and increasing the co-doping from 1 mol% showed a decrease in the size. Similarly, in 5.3(c) the Cs^{+1} samples made at 900 °C behave more erratically with 1 mol% and 5 mol% Cs^{+1} co-doped samples showing higher crystallite size compared to the monodoped sample. The trend in the 800 °C samples shows decreasing

sizes up to 2 mol% and an abrupt increase in the 5 mol%. The decreasing sizes could be due to hindered grain growth or enhanced nucleation of smaller particles.

Another important aspect of the microstructure is the lattice volume. Lattice volume changes is an important parameter to understand the effect of oxygen vacancies on the microstructure [13]–[16]. The cell volume was calculated from the lattice parameters obtained after extracting the hkl values as per the method discussed in Chapter 2. The lattice volume was then calculated by the Eq (2.4) in Chapter 2.

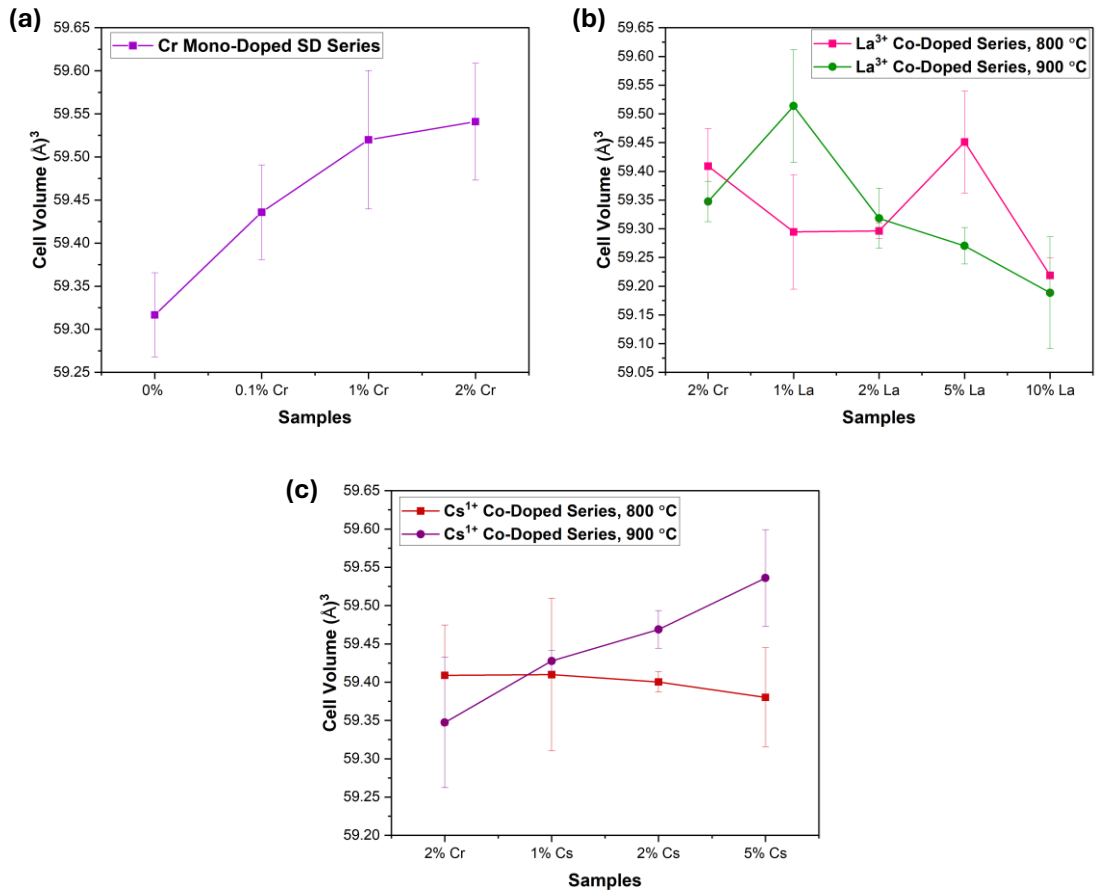


Figure 5.4: *Lattice volumes comparison (a) Cr monodoped SD series samples (b) La^{3+} co-doped samples (c) Cs^{1+} co-doped samples. An upward trend in the lattice volumes indicates an expansion and a downward trend indicates a contraction.*

Defects such as vacancies can be created through doping and high-temperature annealing. In Chapters 4 and 5, a detailed analysis of how lattice expansions and contractions are a result of the types of charged oxygen vacancies is discussed. Here, the Kröger Vink notations can be used to understand the type of charged defects present in the lattice. Figure 5.4 (a-c) demonstrates the cell volume changes in the doped batches. The SD series Cr monodoped samples in Figure 5.4(a) show a monotonic increase in volume as the mol% doping increases. To understand the effect of doping the micro-structure and the type of defects present, two scenarios are discussed. In Figure 5.1(c), the colors of the 0.1 and 1 mol% samples are faint yellowish which could indicate that the presence of Cr^{3+} could be dominant. The presence of

Cr^{3+} in the B-site can be demonstrated by Eq (5.1). When Cr^{3+} substitutes Ti^{4+}, it creates a negatively charged defect. To maintain overall charge neutrality, oxygen vacancies can be created and these vacancies can also be created during the high temperature annealing as shown in Eq (5.2).

$$Cr_2O_3 + 2Ti_{Ti}^{X} \longrightarrow 2Cr_{Ti}^{'} + \ddot{V}_O + 3O_O^X \quad (5.1$$

$$O_O^X \longrightarrow \tfrac{1}{2} O_2 + \ddot{V}_O + 2e^{'} \quad (5.2)$$

In the second scenario, predominantly in the 2 mol% and higher doped SD samples, the colors change from faint yellow to reddish as seen in Figure 5.1(c). This could be due to the increase in Cr^{6+} on increasing mol% doping. In this case, when Cr^{6+} replaces Ti^{4+}, it forms a positively charged defect as shown in Eq (5.3). In this scenario, charge compensation can occur with electronic compensation, and in Eq (5.4) the electrons from the electronic compensation can reduce the Ti^{4+} leading to the formation of Ti^{3+} ($Ti_{Ti}^{'}$). The overall defect Eq with both Cr^{3+} and Cr^{6+} in the B-site is shown in Eq (5.5).

$$CrO_3 + Ti_{Ti}^{X} \longrightarrow \ddot{C}r_{Ti} + 2e' + 3O_O^X \quad (5.3)$$

$$Ti_{Ti}^{X} + e' \longrightarrow Ti_{Ti}^{'} \quad (5.4)$$

$$Cr_2O_3 + CrO_3 + Ti_{Ti}^{X} \longrightarrow Cr_{Ti}^{'} + \ddot{C}r_{Ti} + Ti_{Ti}^{'} + 6O_O^X \quad (5.5)$$

The presence of Ti^{3+} with a higher ionic radius could also contribute to the increase in lattice volume in the SD series. The La^{3+} co-doped samples in Figure 5.4(b) show an increase in cell volume at 5 mol% co-doping compared to the monodoped sample for the 800 °C batch. This batch shows a monotonic decrease in cell volume from 2 mol% co-doping. For the La^{3+} co-doped samples at 900 °C, a monotonic decrease in cell volumes is also observed except at the 1 mol% co-doped sample which shows an increase in volume. The purpose of co-doping is to suppress the Cr^{6+} states. Therefore, in this batch two scenarios can be examined. The first scenario considers only Cr^{3+} states as seen in Eq (5.6) and the scenario with incomplete suppression of Cr^{6+} as seen in Eq (5.7). Cr^{3+} substitution forms a negatively charged defect ($Cr_{Ti}^{'}$)and Cr^{6+} forms a double positively charged defect ($\ddot{C}r_{Ti}$). Charge compensation is achieved with electronic and vacancy compensation in both scenarios. Both cases take into account the formation of Ti^{3+} defects.

$$Cr_2O_3 + La_2O_3 + 2Sr_{Sr}^{X} + 2Ti_{Ti}^{X} \longrightarrow 2Cr_{Ti}^{'} + 2\dot{La}_{Sr} + 2Ti_{Ti}^{'} + \ddot{V}_O + 5O_O^X \quad (5.6)$$

$$2Cr_2O_3 + CrO_3 + La_2O_3 + 2Sr_{Sr}^{X} + 2Ti_{Ti}^{X} \longrightarrow 4Cr_{Ti}^{'} + \ddot{C}r_{Ti} + 2\dot{La}_{Sr} + \ddot{V}_O + 2Ti_{Ti}^{'} + 11O_O^X \quad (5.7)$$

For the Cs^{1+} co-doped samples in Figure 5.4(c), the 800 °C batch shows a decrease and the 900 °C batch shows an increase with an increase in mol% co-doping. Similarly, the two scenarios with complete and incomplete Cr^{6+} states are shown in equations (5.8) and (5.9).

$$Cr_2O_3 + Cs_2O + 2Sr_{Sr}^{X} + 2Ti_{Ti}^{X} \longrightarrow 2Cr_{Ti}^{'} + 2Cs_{Sr}^{'} + 2Ti_{Ti}^{'} + 2\ddot{V}_O + 2O_O^X \quad (5.8)$$

$$Cr_2O_3 + CrO_3 + Cs_2O + 3Sr_{Sr}^{X} + 3Ti_{Ti}^{X} \longrightarrow 2Cr_{Ti}^{'} + 2\ddot{C}r_{Ti} + 2Cs_{Sr}^{'} + 2Ti_{Ti}^{'} + \ddot{V}_O + 6O_O^{X} \quad (5.9)$$

Both Eq (5.7) and (5.9), indicate double positively charged oxygen vacancies which could lead to lattice contractions which can be observed for most of the La^{3+} co-doped samples and the Cs^{1+} samples made at 800 °C. The Cs^{1+} samples made at 900 °C show lattice expansion, which could be due to other intrinsic defects such as the Ti^{3+}. Volume changes can also be caused by substituting larger Cs^{+1} ions in the B-site and the smaller Cr ions in the A-site. Cr substitution in the Ti^{4+} site can be understood based on oxygen-rich and poor conditions. In an oxygen-rich environment, the Cr_2O_3 undergoes oxidation to form Cr_{Ti}^{x} as shown in Eq (5.10). Eq (5.11) shows the case of an oxygen-poor environment where more vacancies are created.

$$Cr_2O_3 + 1/2\ O_2 \longrightarrow 2Cr_{Ti}^{x} + 4O_O^{X} \quad (5.10)$$

$$Cr_2O_3 \longrightarrow 2Cr_{Ti}^{'} + 2O_O^{X} + \ddot{V}_O \quad (5.11)$$

Figure 5.5(a-d) compares the relative crystallinity of the sample batches. From the intensity of the peak (110) of the samples, it is evident that the 900 °C samples have better crystallinity than those at 800 °C. From the (110) peaks in Figure 5.5 (a-d), the FWHM and 2θ of the samples can be correlated as per the Scherrer equation. Where the FWHM decreases, the crystallite size shows an increase. A shift to lower 2θ angles indicates an expansion and to lower 2θ angles indicates a contraction. The ionic size of La^{3+} (1.36 Å) in 12 co-ordination to oxygen atoms is smaller than the Sr^{2+} cation (1.44 Å) [17]. The ionic size of Cr^{3+} (0.615 Å) in 6 co-ordination to oxygen atoms is larger than the Ti^{4+} cation (0.605 Å) [17]. Shift to lower 2θ values resulting in the expansion of the lattice may be due to the substitution of larger dopants in the B-site. The reverting of 2θ values close to the undoped in the case of La^{3+} co-doped samples might be attributed to the substitution of the smaller-sized La dopant in the A site. Similar results related to the XRD peak analysis have been reported by Jiang, D. et al. [2]. Wang, D. et al. [18] and Bi, Y. et al. [19] both reported the peak shifts to higher 2θ values indicating the substitution of Cr^{3+} at the A site.

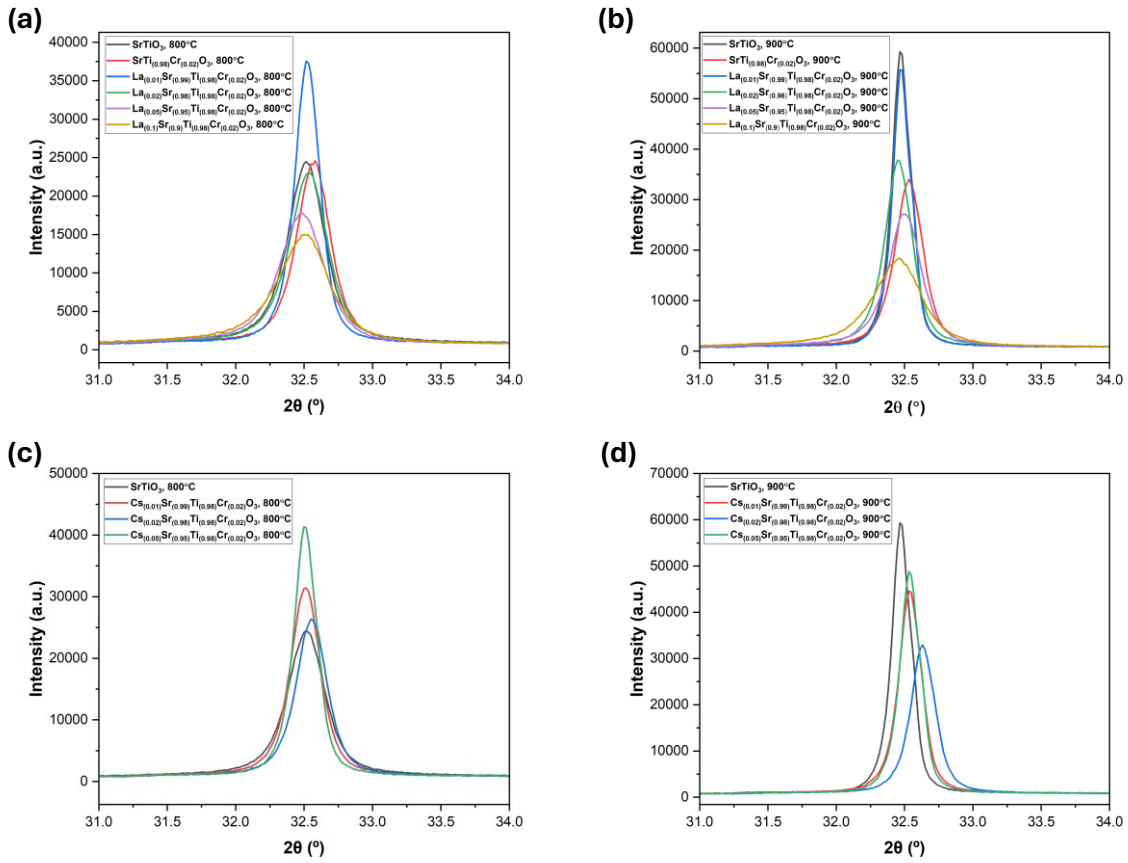


Figure 5.5: *Degree of relative crystallinity comparison w.r.t to (110) in (a) La^{3+} 800 °C co-doped (b) La^{3+} 900 °C co-doped (c) Cs^{1+} 800 °C co-doped (d) Cs^{1+} 900 °C co-doped $SrTiO_3$ samples. The 1 mol% La co-doped sample at 800 °C shows higher relative crystallinity than the undoped and other doped samples. All the Cs doped samples (800 °C) in (c) show higher relative crystallinity as compared to the undoped.*

Note: In Figure 5.5, some of the Cs^{1+} samples show discrepancies in the direction of shifts when compared with lattice volumes after Rietveld refinements. Here, the calculated lattice volumes are deemed accurate compared to the XRD peak shifts as these could be affected by how the samples are loaded on the sample holder.

In Figure 5.5(b), the undoped $SrTiO_3$ has the highest crystallinity whereas the co-doped samples have a steady decrease in crystallinity as the mol% of La^{3+} doping increased. In the case of the 800 °C batch in Figure 5.5(a), the 1 mol% La^{3+} co-doped showed the highest crystallinity. The undoped and the 2 mol% Cr^{3+} have similar degrees of crystallinity. Between 2 mol% to 10 mol% La^{3+} co-doped samples, the degree of crystallinity decreased steadily. At 800 °C, the 5 mol% Cs^{1+} co-doped sample has a higher degree of crystallinity than the other samples (Figure 5.5(c)). At 900 °C, the undoped $SrTiO_3$ has a higher degree of crystallinity than the co-doped samples (Figure 5.5(d)).

Along with the lattice volumes, Table 5.1A also lists the microstrain. The microstrain is defined as the strain that is localized in some lattice spacings. These types of strains are associated with defects such as dislocations, faults, and grain boundaries [20]. For the 900 °C batch, the

microstrain variation between the undoped $SrTiO_3$ and the 1 mol% La^{3+} co-doped samples is low. The 2 mol% Cr^{3+} doped sample shows a slight increase in the microstrain. For the 800 °C batch, the microstrain increases sharply for the Cr^{3+} monodoped samples which then decreases for the 1 mol% and 2 mol% La^{3+} co-doping and again shows a slight increase for the 1 mol% and 2 mol% La^{3+} co-doped samples. The microstrain comparison between different batches are shown in Figure 5.6 (a-c). The microstrain was calculated via the Williamson Hall Method assuming a uniform deformation model (UDM). Instrumental broadening was considered during both Scherrer and W-H analysis.

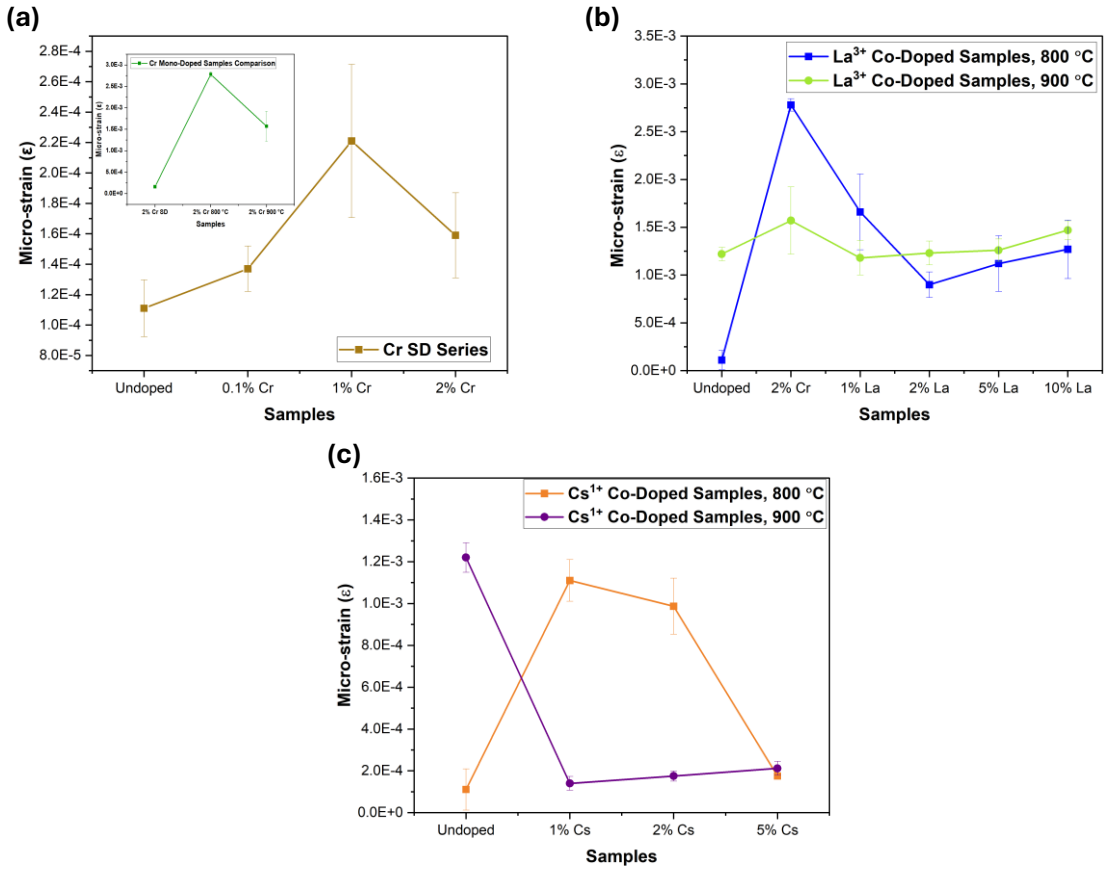


Figure 5.6: *Microstrain comparison (a) Cr monodoped SD series samples. The inset shows the comparison between the 2 mol% Cr doped samples synthesized with the serial dilution method and the standard sol-gel Pechini method (b) La^{3+} co-doped samples (c) Cs^{1+} co-doped samples. Microstrain is an indirect indicator of defects present in crystal lattices.*

Since the microstrain exists in the vicinity of defects, therefore this can be studied to understand the occurrence of defects in these samples. At both 800 °C and 900 °C (Figure 5.6 (a)), the Cr^{3+} monodoped samples show an increase in the presence of defects. These defects are subsequently decreased with the co-doping. Amongst the doped samples at 800 °C (Figure 5.6 (b)), 2 mol% La^{3+} co-doped samples showed a higher decrease in microstrain as compared to other doped samples. Here, the smaller increment of change in the 900 °C batch might be due to higher temperatures improving the crystallinity of the samples and decreasing the presence of defects. In the case of the Cs^{+1} co-doped 800 °C (Figure 5.6 (b)), the microstrain increased

against the undoped reference peaking at 1 mol%. For the 900 °C batch (Figure 5.6 (b)), the microstrain decreased. The serial dilution series also reported higher microstrain as compared to the undoped $SrTiO_3$.

From the microstructural analysis, with increasing the mol% of doping or changing the annealing conditions significant changes are introduced in the samples. Microstructural parameters can significantly affect the performance of the catalysts as was observed in the previous chapters. To facilitate the understanding of which batch of photocatalysts could perform better further, surface and opto-electronic analysis was done which are discussed in the subsequent sections.

5.5 Elemental Analysis with X-ray Photoemission Spectroscopy (XPS) and Site of Substitution of the Dopants with EPR

The oxidation states and the site of dopant substitution is important to understand the behaviour of the synthesized materials. In this section, XPS analysis is studied to confirm the elements and the oxidation states. To further the XPS results, EPR studies were conducted. The EPR measurements and data analysis in this Ph.D. work were done by Dr. Arnau Bertran under the guidance of Prof. Ludmilla Steier, St. Catherine's, University of Oxford. Dr. Bertran shared his expertise in this field and helped in understanding and writing this section.

5.5.1 XPS Analysis

Sr3d

The surface of the undoped, and the Cr^{3+} (co-) doped $SrTiO_3$ samples were investigated. For the samples Sr3d, Ti2p, Cr2p, La3d and O1s were analysed. All the peaks were charge-corrected for C1s at a binding energy of 284.8 eV. Figure 5.7 shows the deconvoluted Sr3d peaks with $Sr3d_{5/2}$ peak at 133.77 eV and $Sr3d_{3/2}$ peak at 134.49 eV attributed to Sr^{2+} in $SrTiO_3$ lattice. The split between the $d_{5/2}$ and the $d_{3/2}$ orbital in the case of the undoped $SrTiO_3$ is 1.72 eV. The sample shows two additional peaks corresponding to $SrCO_3$. For the undoped sample, the ratio between the $SrCO_3$ $Sr3d_{5/2}$ and the C1s C=O is 1:1.1 which is close to the reported 1:1 carbonate ratio in literature confirming the presence of $SrCO_3$. The calculated amount of $SrCO_3$ from the XPS analysis is 0.08% in the undoped sample.

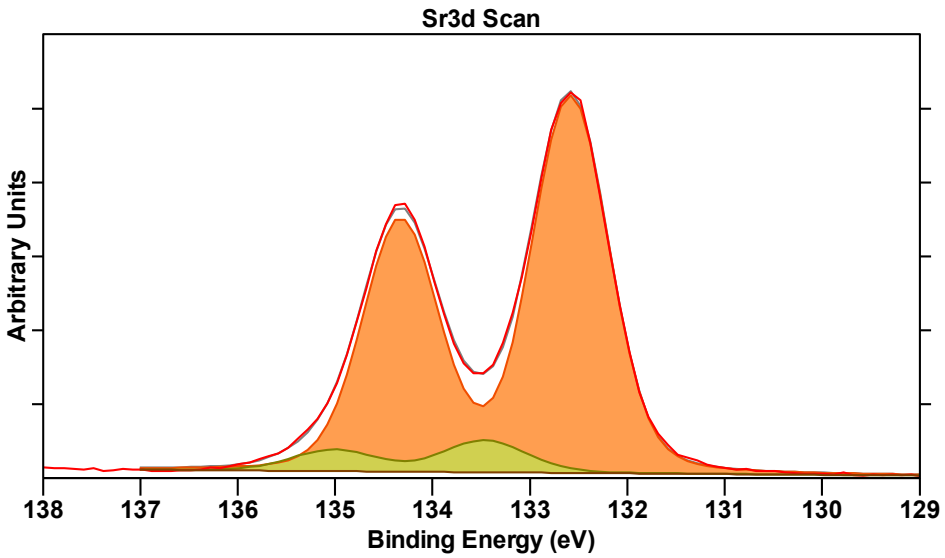


Figure 5.7: *Deconvoluted and charge-corrected Sr3d peaks of Undoped $SrTiO_3$ (900 °C) at 132.77 eV and 134.49 eV with trace amount of $SrCO_3$.*

The charge-corrected Sr3d peaks for the Cr-doped samples at 900 °C and 800 °C are shown in Figures 5.8-5.9. At 800 °C, the sample showed a higher amount of $SrCO_3$ at 2.45 atomic % compared to the 0.88 atomic % of the 900 °C sample.

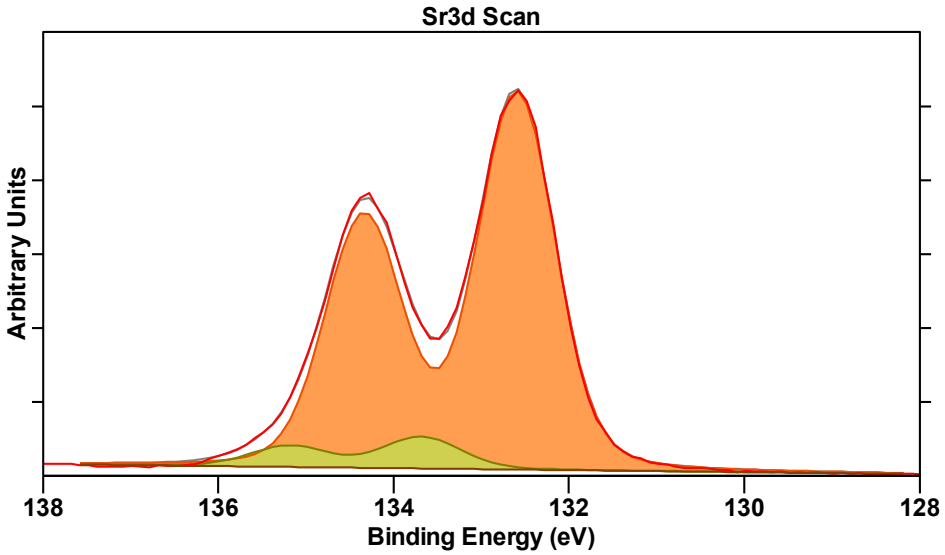


Figure 5.8: *Deconvoluted and charge-corrected Sr3d peaks of 2 mol% Cr^{3+} doped $SrTiO_3$ (900 °C) at 132.59 eV and 134.34 eV with trace amount of $SrCO_3$.*

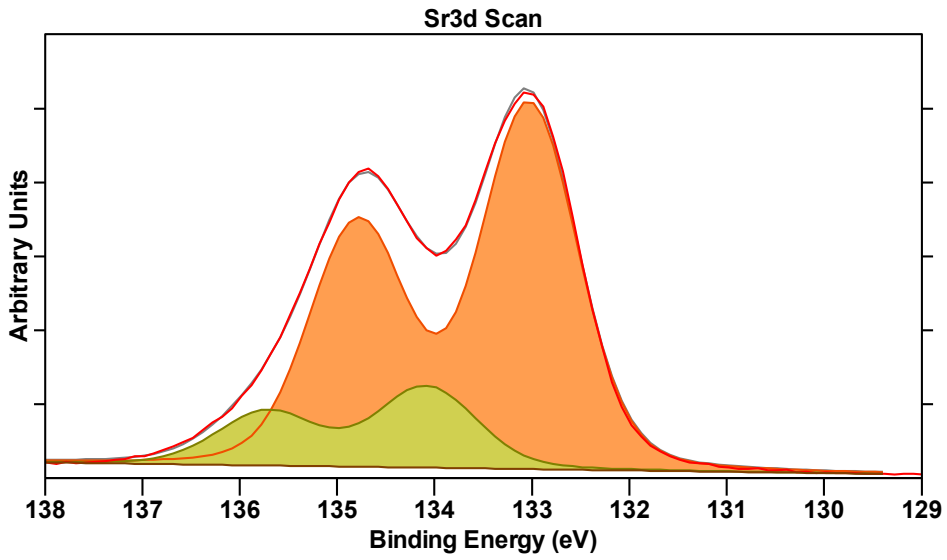


Figure 5.9: *Deconvoluted and charge-corrected Sr3d peaks of 2 mol% Cr^{3+} doped $SrTiO_3$ (800 °C) at 133.01 eV and 134.77 eV with a trace amount of $SrCO_3$.*

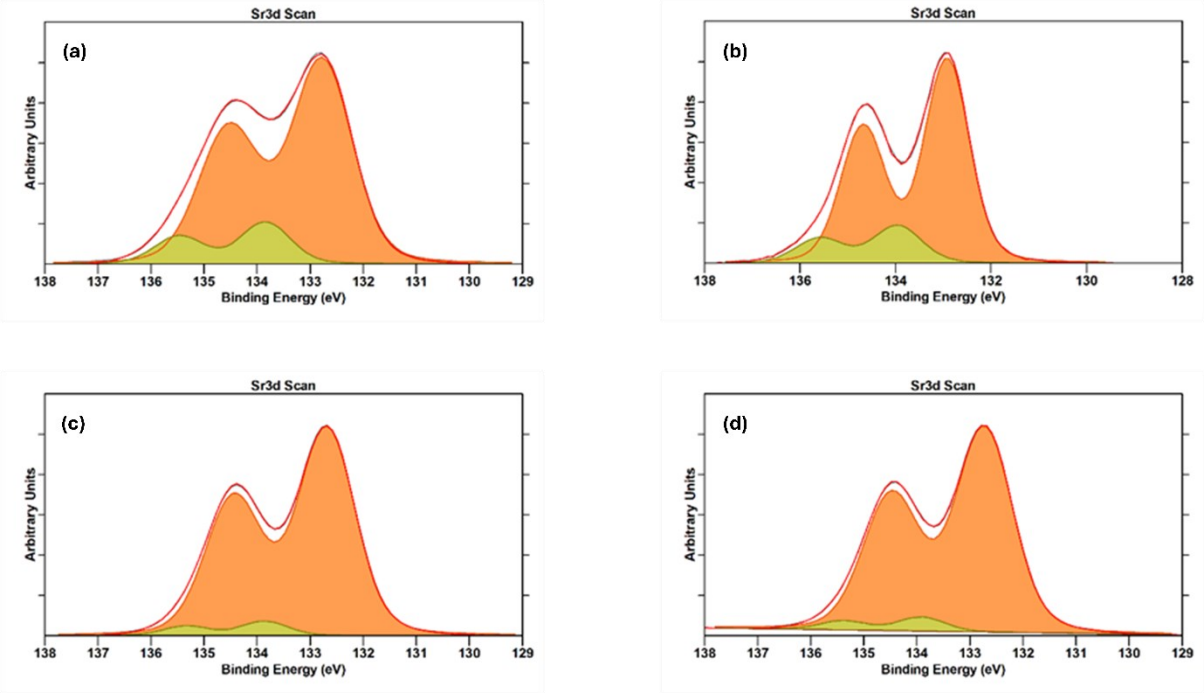


Figure 5.10: *Deconvoluted and charge corrected Sr3d peaks of 1 mol%, 2 mol%, 5 mol% and 10 mol% La, 2 mol% Cr doped $SrTiO_3$ synthesized at 900 °C with additional peaks of $SrCO_3$.*

From the deconvolution of the Sr3d peaks in Figures 5.7-5.10, the presence of $SrCO_3$ is apparent in the doped samples which are typical as reported by Cali, E. et al. [21]. For the 1 mol%, 2 mol%, 5 mol% and 10 mol% La^{3+}, 2 mol% Cr^{3+} doped $SrTiO_3$ co-doped samples at 900 °C, the ratios between the $SrCO_3$ $Sr3d_{5/2}$ and the C1s C=O are 1:0.91, 1:1.3, 1:1.4, 1:1.13

and 1:1.1 respectively, thereby confirming $SrCO_3$. The amount of $SrCO_3$ decreases for the 2 mol% Cr^{3+} sample and increases for the La co-doped samples. Figure 5.11 shows the Sr3d peaks for the La^{3+} co-doped samples at 800 °C.

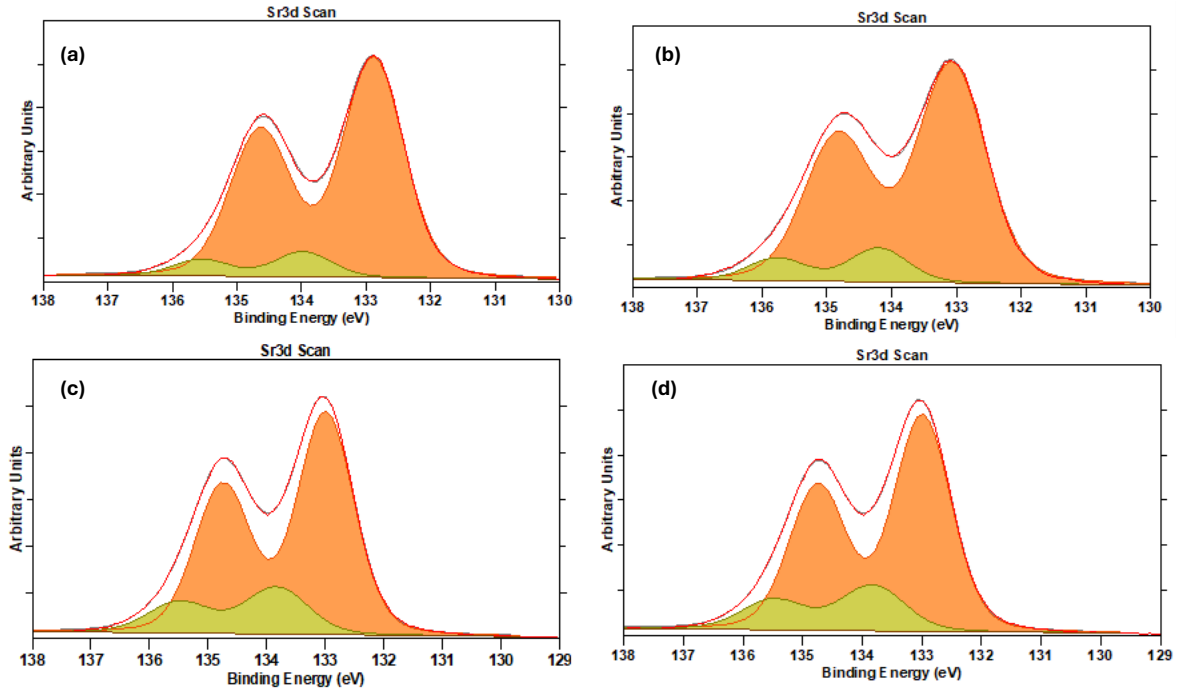


Figure 5.11: *Deconvoluted and charge corrected Sr3d peaks of (a) 1 mol% (b) 2 mol% (b) 5 mol% and (d) 10 mol% La, 2 mol% Cr doped $SrTiO_3$ synthesized at 800 °C with additional peaks of $SrCO_3$.*

Figure 5.12 shows the Sr3d peaks for the samples prepared with the SD method. The $SrCO_3$ $Sr3d_{5/2}$ and the C1s C=O ratio are close to 1:1 confirming the presence of $SrCO_3$ with the lowest amount in 1 mol%.

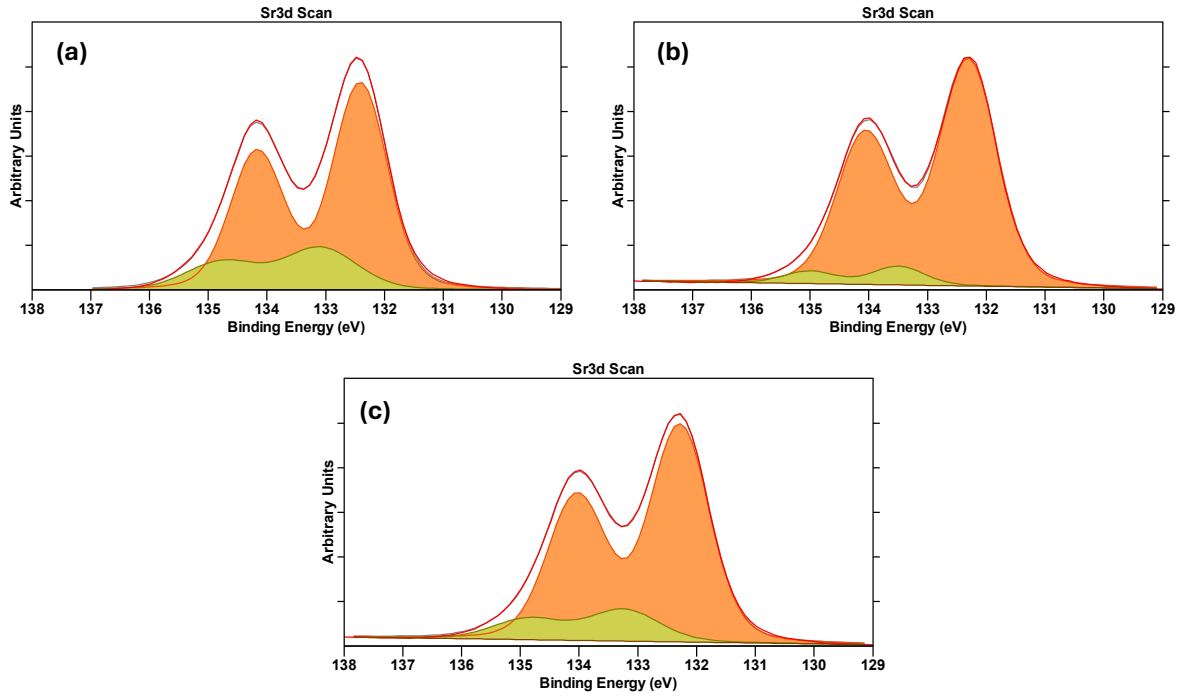


Figure 5.12: *Deconvoluted and charge corrected Sr3d peaks of (a) 0.1 mol% (b) 1 mol% and 2 mol% Cr doped $SrTiO_3$ prepared with the serial dilution method.*

The $SrCO_3$ amount decreased for the samples at 900 °C as the La^{3+} mol% doping increased as seen in Figure 5.10. For 800 °C, $SrCO_3$ increased with mol% co-doping as seen in Figure 5.11. For the 900 °C samples, $Sr3d_{5/2}$ and the $Sr3d_{3/2}$ peaks show shifts to 0.18 eV and 0.15 eV lower binding energies in the Cr^{3+} doped sample. The $Sr3d_{5/2}$ and the $Sr3d_{3/2}$ peaks in the 1 mol% (132.95 eV,134.70 eV), 2 mol% (132.96 eV, 134.71 eV), 5 mol% (132.94 eV, 134.69 eV) and 10 mol% (132.85 eV, 134.60 eV) La^{3+} co-doped samples show shifts to higher binding energies as compared to undoped $SrTiO_3$. Whereas in the 800 °C samples, $Sr3d_{5/2}$ and the $Sr3d_{3/2}$ peaks show shifts to 0.19 eV higher binding energies in the Cr^{3+} doped sample. The $Sr3d_{5/2}$ and the $Sr3d_{3/2}$ peaks in the 1 mol% (132.85 eV,134.60 eV), 2 mol% (133.00 eV, 134.75 eV), 5 mol% (133.05 eV, 134.79 eV) and 10 mol% (132.93 eV, 134.68 eV) La^{3+} co-doped samples show shifts to higher binding energies as compared to undoped $SrTiO_3$ at 800 °C. For the SD series, the 0.1 mol% (132.48 eV, 134.23 eV) and the 2 mol% shift (132.54 eV, 134.29 eV) to lower binding energies whereas the 1 mol% (132.95 eV, 134.72 eV) shift to higher binding energies.

The direction of shifts of the XPS peaks may indicate at which site the dopant has been incorporated. It has been reported that when Cr^{3+} substitutes the A site, a shift to higher energy is observed [19][22]**.** A shift to lower binding energies might indicate the substitution at the B-site. The split between the $d_{5/2}$ and the $d_{3/2}$ orbital in the case of the doped $SrTiO_3$ samples also shows an increase at 1.75 eV.

Ti2p

The $Ti2p_{3/2}$ peaks for the samples were analyzed and compared with the undoped. The main component of the undoped (900 °C) XPS $Ti2p_{3/2}$ and $Ti2p_{1/2}$ peaks are at 458.24 eV and 463.94

eV which can be attributed to Ti^{4+} in Figure 5.13. The samples showed the presence of additional Ti^{3+} defects. The ratio of Ti^{3+} are listed in Table 6. The main component of Ti2p is shown in orange and the Ti^{3+} is shown in blue. The ratio of $Sr3d_{5/2}$: $Ti2p_{3/2}$ in the case of the undoped is 1:0.98. In the 2 mol% Cr doped sample, the $Sr3d_{5/2}$: $Ti2p_{3/2}$ ratio is 1:1 shown in Figure 5.14. In the co-doped samples (900 °C), the $Sr3d_{5/2}$: $Ti2p_{3/2}$ are 1:1.11, 1:0.99, 1:0.98, 1:1.07 respectively in 1 mol%, 2 mol%, 5 mol% and 10 mol% co-doped sample (Figure 5.16(a-d)). The $Ti2p_{3/2}$ (458.08eV) and $Ti2p_{1/2}$ (463.78 eV) in the 2 mol% Cr doped sample show shifts to lower binding energy as shown in Figure 5.14. For the 900 °C samples, $Ti2p_{3/2}$ and $Ti2p_{1/2}$ move to higher binding energies in the case of the 1 mol% and 2 mol% co-doped samples as compared to undoped samples as shown in Figure 5.16 (a-b). The $Ti2p_{3/2}$ and $Ti2p_{1/2}$ move to lower binding energies in the case of the 5 mol% and 10 mol% co-doped samples shown in Figure 5.16(c-d). The binding energies are listed in Table 5.2.

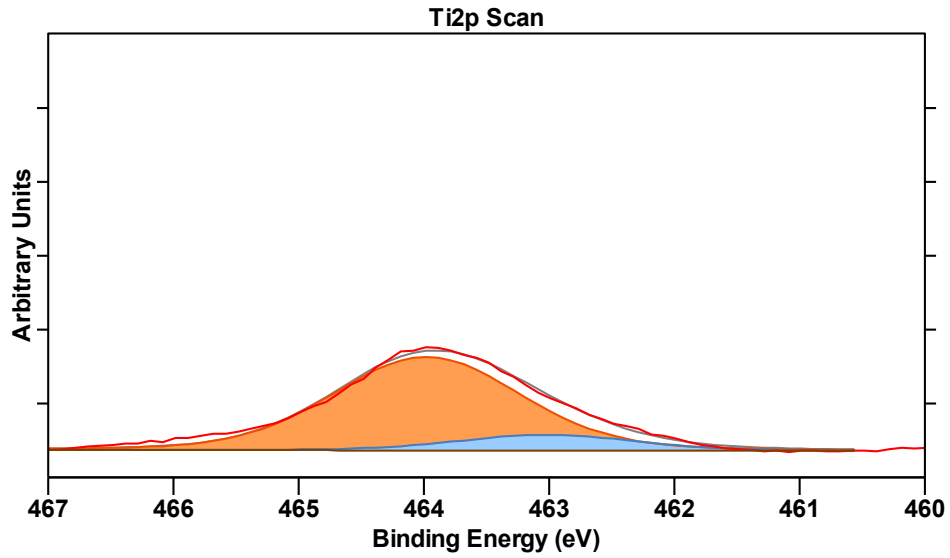


Figure 5.13: *XPS Ti2p Peak of Undoped $SrTiO_3$ with $Ti2p_{1/2}$ at 463.94 eV with Ti^{3+} (blue) at lower binding energies.*

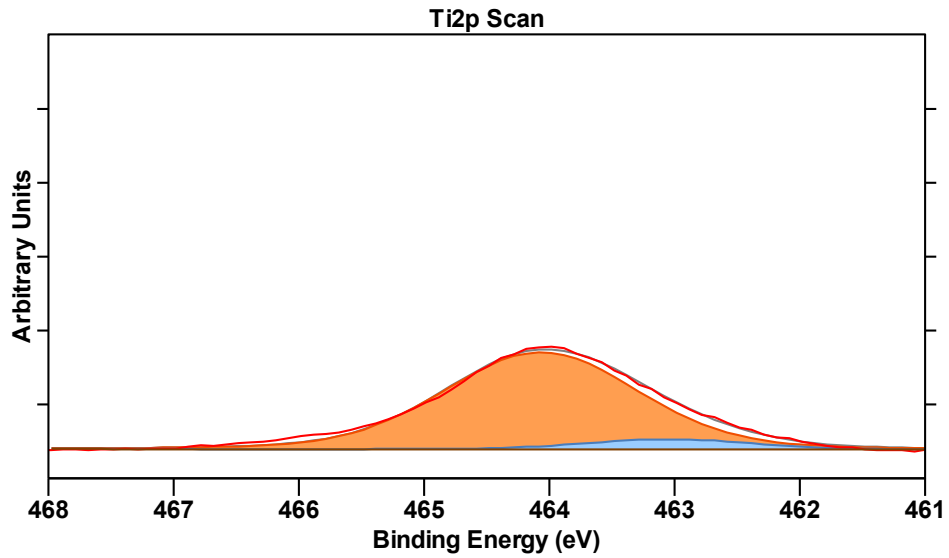


Figure 5.14: *Deconvoluted and charge- corrected $Ti2p_{1/2}$ peaks of 2 mol% Cr^{3+} doped $SrTiO_3$ (900 °C) at 463.78 eV and Ti^{3+} (blue).*

In the co-doped samples (800 °C), the $Sr3d_{5/2}$: $Ti2p_{3/2}$ are 1:1.11, 1:1.18, 1:1.08, 1:1.22 and 1:1.12 respectively in 2 mol% Cr^{3+}, 1 mol%, 2 mol%, 5 mol% and 10 mol% co-doped samples. The $Ti2p_{3/2}$ (458.34 eV) and $Ti2p_{1/2}$ (464.05 eV) in the 2 mol% Cr^{3+} doped sample show shifts to higher binding energy as compared to the undoped at 800 °C as shown in Figure 5.15. The $Ti2p_{3/2}$ and $Ti2p_{1/2}$ move to higher binding energies for 2 mol% co-doped samples as compared to undoped samples as shown in Figure 5.17 (b). The $Ti2p_{3/2}$ and $Ti2p_{1/2}$ move to lower binding energies in the case of the 1 mol%, 5 mol%, and 10 mol% co-doped samples shown in Figure 5.17 (a, c-d). The binding energies are listed in Table 5.2.

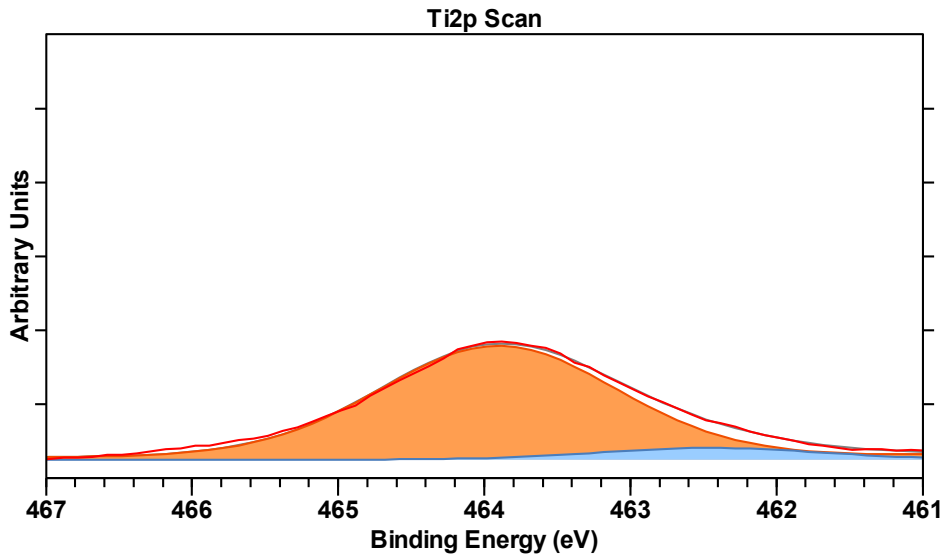


Figure 5.15: *Deconvoluted and charge corrected $Ti2p_{1/2}$ peaks of 2 mol% Cr^{3+} doped $SrTiO_3$ (800 °C) at 464.05 eV with Ti^{3+} defects.*

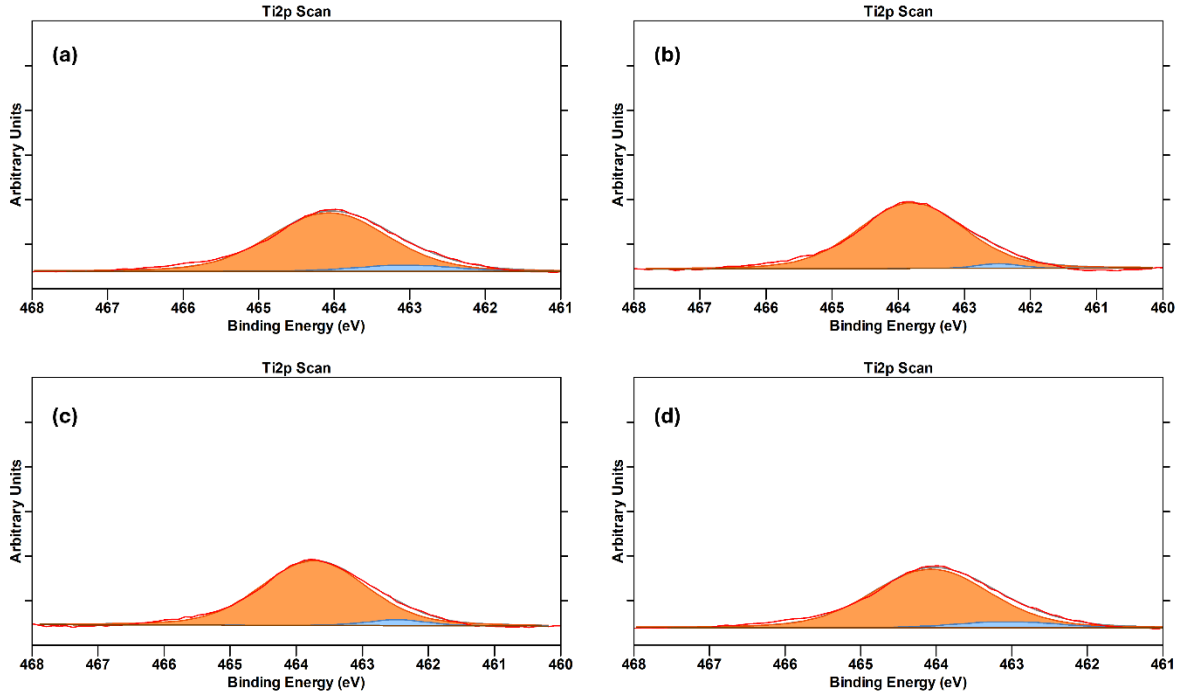


Figure 5.16: *Deconvoluted and charge corrected $Ti2p_{1/2}$ peaks of (a) 1 mol% (b) 2 mol% (c) 5 mol% and (d) 10 mol% La, 2 mol% Cr doped $SrTiO_3$ at 900 °C. All samples in this exhibit varying concentrations of Ti^{3+}.*

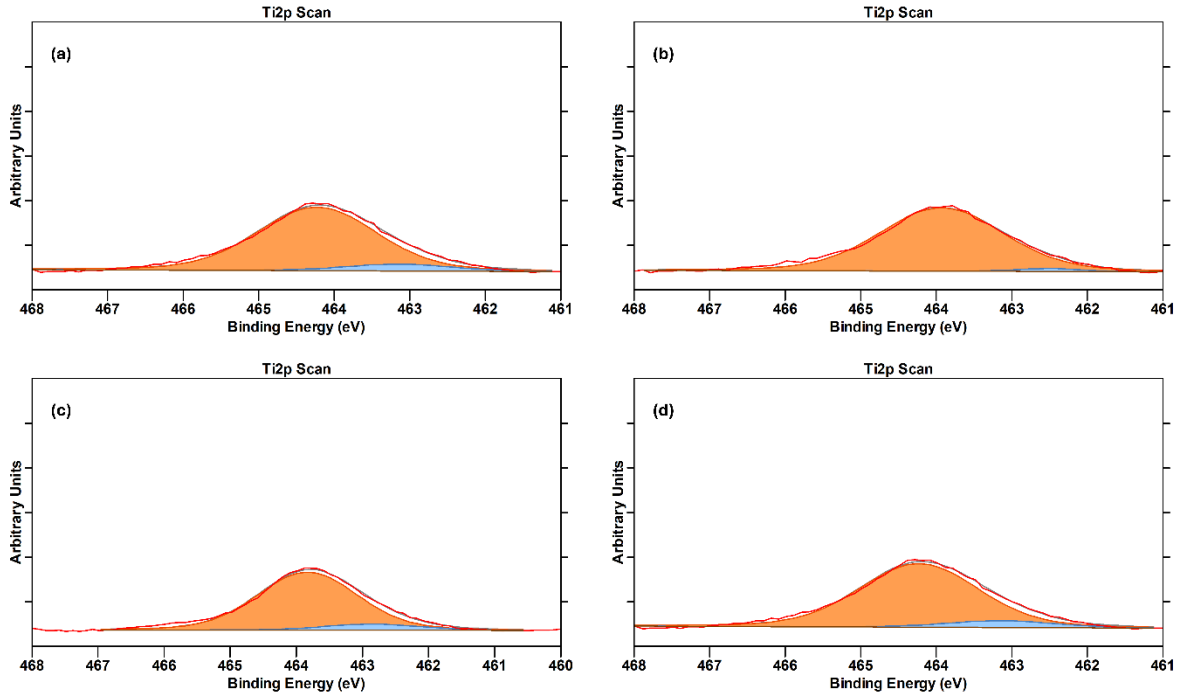


Figure 5.17: *Deconvoluted and charge corrected $Ti2p_{1/2}$ peaks of (a) 1 mol% (b) 2 mol% (c) 5 mol% and (d) 10 mol% La, 2 mol% Cr doped $SrTiO_3$ at 800 °C with Ti^{3+} present in all samples in this batch.*

Figure 5.18 (a-c) shows the Ti2p analysis of the monodoped samples prepared with the serial dilution method. The ratio of $Sr3d_{5/2}$: $Ti2p_{3/2}$ are 1:1.08, 1: 0.8 and 1:1.01 for the 0.1 mol%, 1 mol% and 2 mol% doped samples. These samples also show the presence of Ti^{3+} defects with the 1 mol% having the least amount. The ratio is listed in Table 5.2.

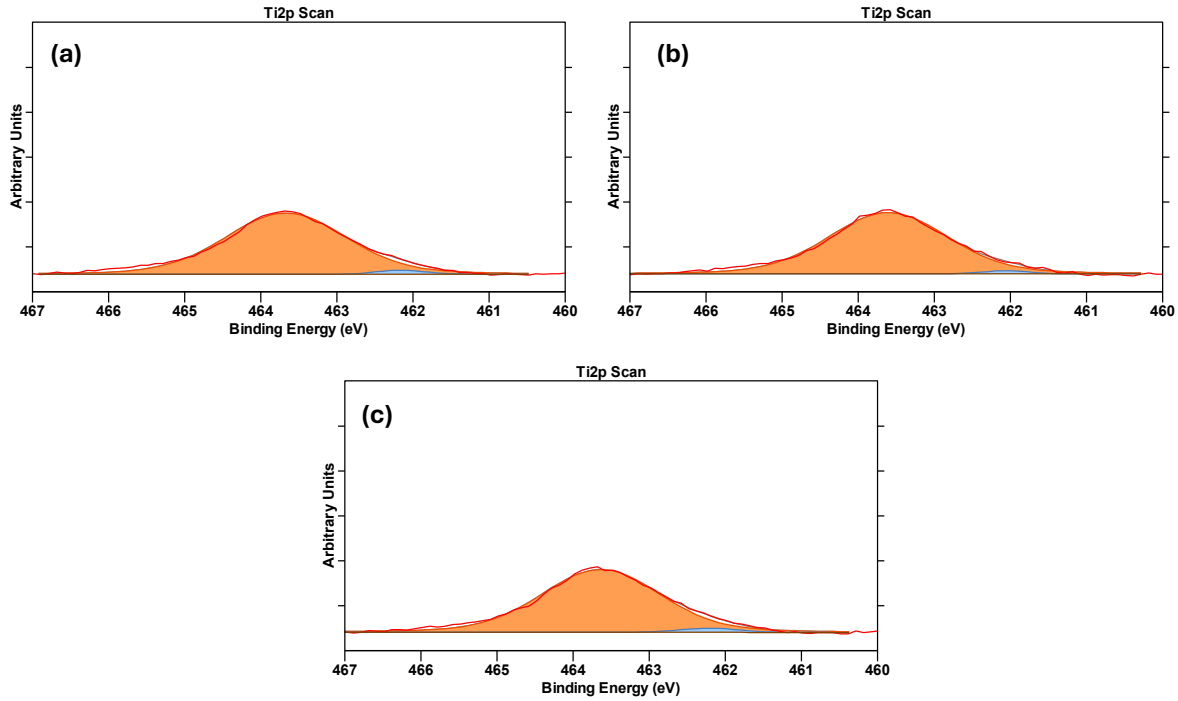


Figure 5.18: *Deconvoluted and charge-corrected $Ti2p_{1/2}$ peaks of (a) 0.1 mol% (b) 1 mol% and (c) 2 mol% Cr doped $SrTiO_3$ synthesized with the serial dilution series. 1 mol% SD samples exhibit the lowest Ti^{3+} in all the Cr (co-) doped samples prepared with different methods.*

Table 5.2: Ti2p peak position of the (co-) doped samples

Samples	$Ti2p_{3/2}$	$Ti2p_{1/2}$	Ti^{3+} / (Ti^{3+} + Ti^{4+})
$SrTiO_3$, 800 °C	458.25 eV	464.19 eV	0.27
$SrTiO_3$, 900 °C	458.24 eV	458.24 eV	0.30
$SrTi_{(0.999)}Cr_{(0.001)}O_3$, Serial Dilution	458.08 eV	463.94 eV	0.26
$SrTi_{(0.99)}Cr_{(0.01)}O_3$, Serial Dilution	457.82 eV	463.65 eV	0.12
$SrTi_{(0.98)}Cr_{(0.02)}O_3$, Serial Dilution	457.84 eV	463.64 eV	0.27
$SrTi_{(0.98)}Cr_{(0.02)}O_3$, 800 °C	458.34 eV	464.16 eV	0.27
$SrTi_{(0.98)}Cr_{(0.02)}O_3$, 900 °C	458.08 eV	463.94 eV	0.30
$La_{(0.01)}Sr_{(0.99)}Ti_{(0.98)}Cr_{(0.02)}O_3$, 900 °C	458.38 eV	464.04 eV	0.21
$La_{(0.02)}Sr_{(0.98)}Ti_{(0.98)}Cr_{(0.02)}O_3$, 900 °C	458.30 eV	464.02 eV	0.24
$La_{(0.05)}Sr_{(0.95)}Ti_{(0.98)}Cr_{(0.02)}O_3$, 900 °C	457.89 eV	463.89 eV	0.28

$La_{(0.1)}Sr_{(0.9)}Ti_{(0.98)}Cr_{(0.02)}O_3$, 900 °C	457.92 eV	463.63 eV	0.14
$La_{(0.01)}Sr_{(0.99)}Ti_{(0.98)}Cr_{(0.02)}O_3$, 800 °C	458.09 eV	463.80 eV	0.27
$La_{(0.02)}Sr_{(0.98)}Ti_{(0.98)}Cr_{(0.02)}O_3$, 800 °C	458.28 eV	463.99 eV	0.23
$La_{(0.05)}Sr_{(0.95)}Ti_{(0.98)}Cr_{(0.02)}O_3$, 800 °C	458.19 eV	463.89 eV	0.30
$La_{(0.1)}Sr_{(0.9)}Ti_{(0.98)}Cr_{(0.02)}O_3$, 800 °C	458.11 eV	463.84 eV	0.28

In Ga^{3+} doped $SrTiO_3$ (Chapters 3-4), Ti^{3+} suppression led to higher performances. For the Cr: $SrTiO_3$ the performance of the samples is influenced by the presence of factors other than oxygen vacancies and Ti^{3+} which led to the activity observed. This can be observed from Table 5.2 where even though the 1 mol% La^{3+} co-doped sample had a lesser Ti^{3+} than the undoped at 900 °C, the PL intensity of undoped is higher. This shows that there are other non-radiative pathways affecting the doped materials. Most samples show lower Ti^{3+} ratios than the undoped and lower PL intensities. Cali, E. et al. [21] reported that an equal amount of shift (0.15 eV) to lower binding energy in Sr3d and Ti2p might indicate the presence of oxygen vacancies. The Sr3d and Ti2p peaks of the 2 mol% Cr^{3+} doped (900 °C) sample show almost similar values (0.21-0.23 eV) of a shift to lower binding energies. This might indicate the presence of oxygen vacancies. In Wang, D. et al. [18], raises the possibility of partial Cr^{3+} substitution in the A-site with shifts to higher binding energies and at the B-site with shifts to higher binding energies. This can be further invested with the Cr2p peak.

Cr2p

From the XPS survey of the surface of 2 mol% Cr^{3+} doped and 1 mol%, 2 mol%, 5 mol%, and 10 mol% La, Cr co-doped $SrTiO_3$, the presence of Cr is evident as shown in Figures 5.19-5.23. The main peaks of the Cr can be identified as $Cr2p_{3/2}$ and $Cr2p_{1/2}$.

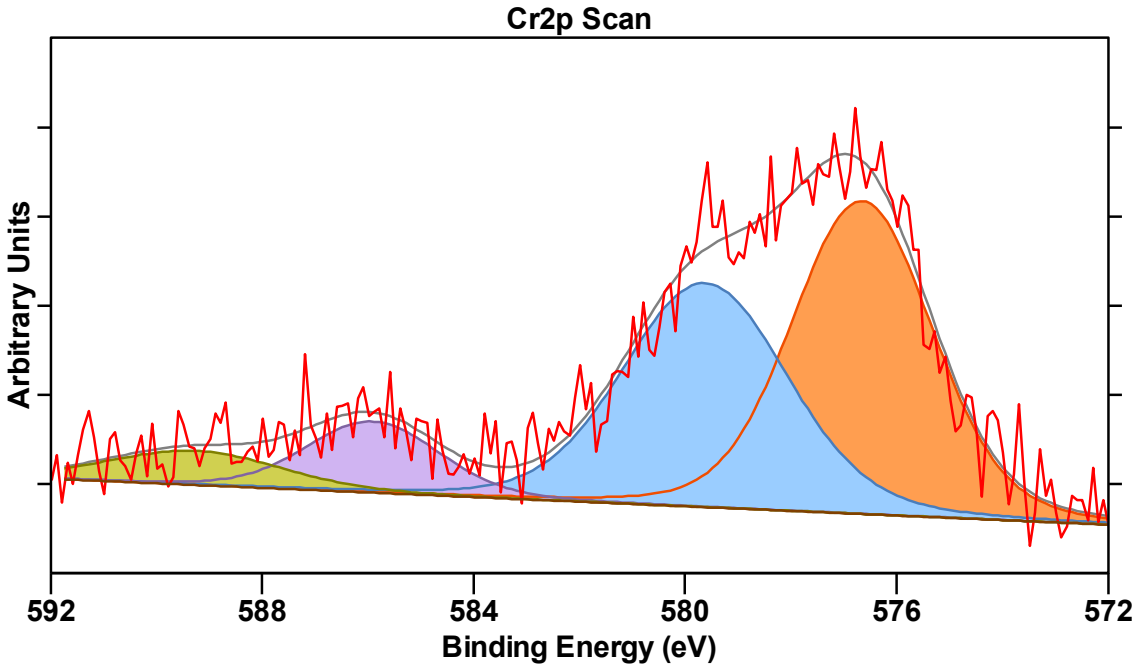


Figure 5.19: *XP spectrum of $Cr2p_{1/2}$ and $Cr2p_{3/2}$ of peaks of 2 mol% Cr^{3+} doped $SrTiO_3$ (900 °C). XPS reveals the presence of both Cr^{3+} (orange) at around 576 eV binding energy and Cr^{6+} (blue)at around 580 eV binding energy.*

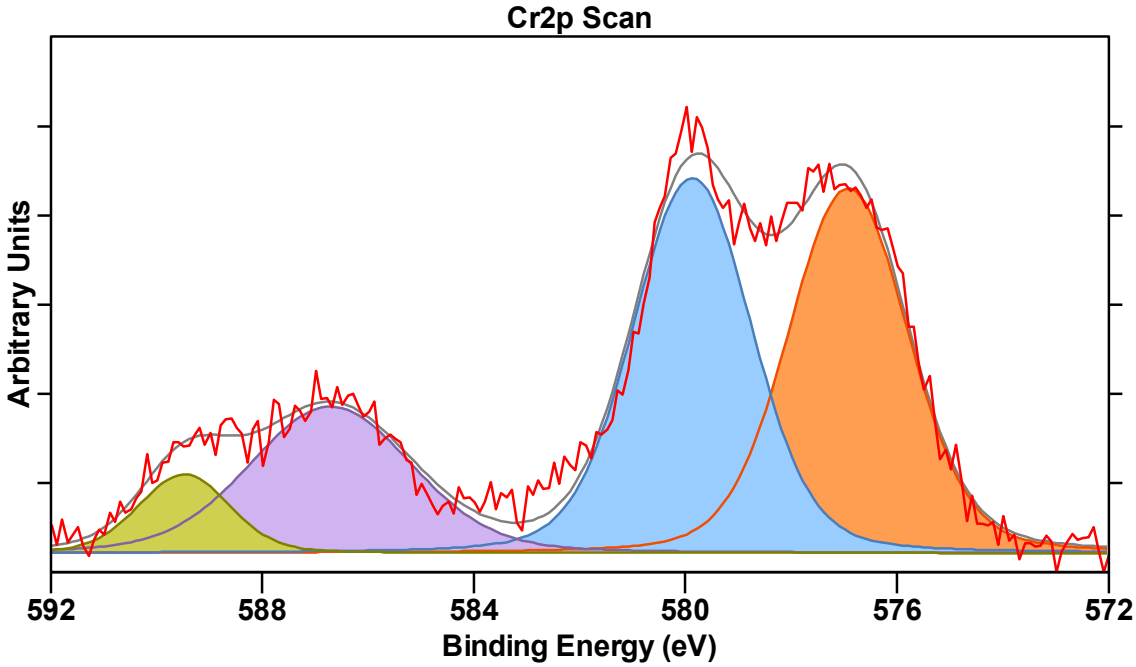


Figure 5.20: *XP spectrum of $Cr2p_{1/2}$ and $Cr2p_{3/2}$ of peaks of 2 mol% Cr^{3+} doped $SrTiO_3$ (800 °C) with both Cr^{3+} (orange) and Cr^{6+} (blue).*

In the 2 mol% Cr^{3+} monodoped samples at 900 °C and 800 °C Figures 5.19-5.20, the Cr2p multiplet can be deconvoluted into two doublet pairs. The La^{3+} co-doped samples are deconvoluted into two doublet pairs between 576 eV to 590 eV.

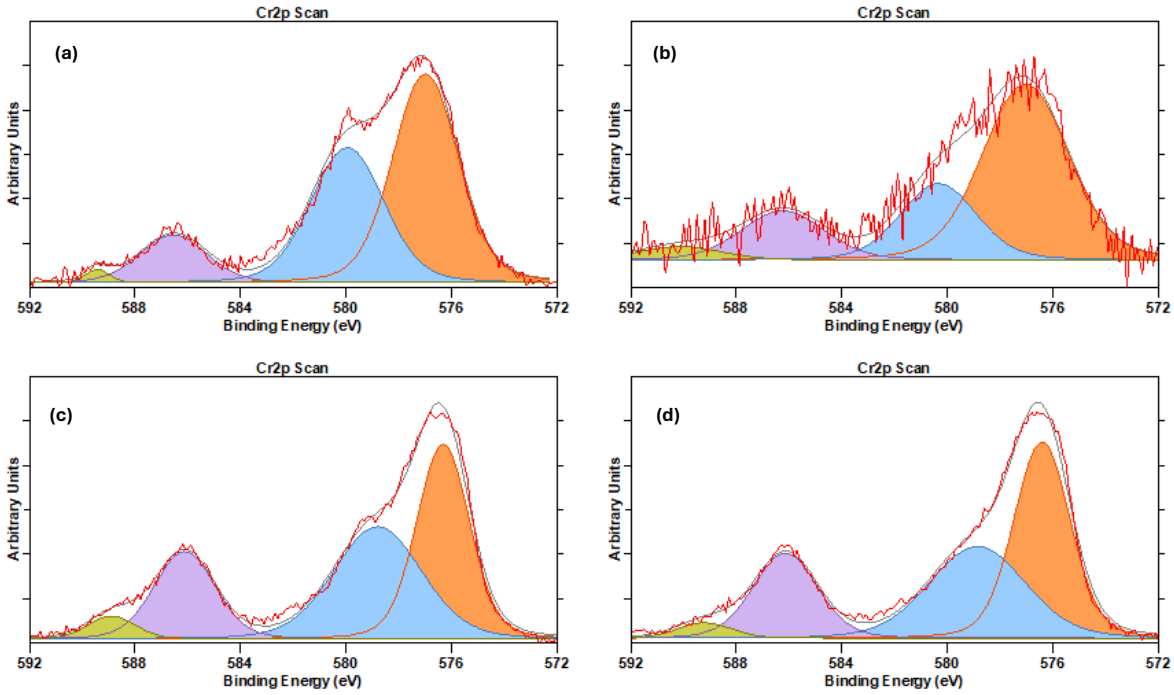


Figure 5.21: *XP spectrum of $Cr2p_{1/2}$ and $Cr2p_{3/2}$ of peaks of (a) 1 mol% (b) 2 mol% (c) 5 mol% and (d) 10 mol% La, 2 mol% Cr doped $SrTiO_3$ at 900 °C displaying both Cr^{3+} (orange)and Cr^{6+} (blue). The 2 mol% La co-doped show the highest suppression of the Cr^{6+} states in this batch.*

In Figures 5.19-5.22 alongside the Cr^{3+} the presence of Cr^{6+} can also be detected. Cr^{3+} is depicted in orange and Cr^{6+} in blue. Both 2 mol% Cr^{3+} and co-doped samples show the Cr^{6+} peaks around 577-579 eV and Cr^{3+} around 575-577 eV respectively [3],[4]. XPS confirms the oxidation states to be Cr^{3+} and Cr^{6+}.

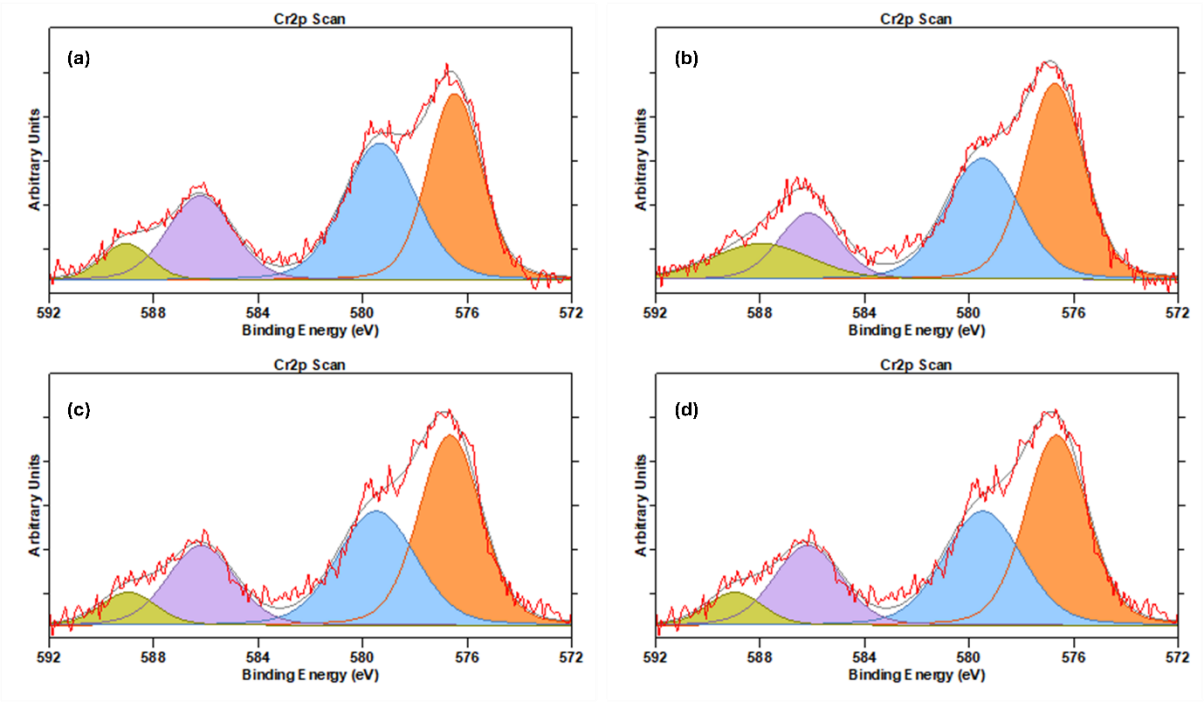


Figure 5.22: *XP spectrum of $Cr2p_{1/2}$ and $Cr2p_{3/2}$ of peaks of Cr^{3+} (orange) and Cr^{6+} (blue) (a) 1 mol% (b) 2 mol% (c) 5 mol% and (d) 10 mol% La, 2 mol% Cr doped $SrTiO_3$ at 800 °C. In this batch, the suppression of Cr^{6+} states is higher in the 5 mol% (co-) doped sample.*

Figure 5.23(a-c) shows the XPS analyzed Cr peak of the SD series samples. At nominal Cr mol% of 0.1 and 1, Cr^{6+} cannot be detected. This corresponds to the increasing yellow colour of these samples. With the increase in mol% doping to 2, the red colour predominates. This denotes the increase in Cr^{6+} states which was detected in the multiplet splitting in the XPS data.

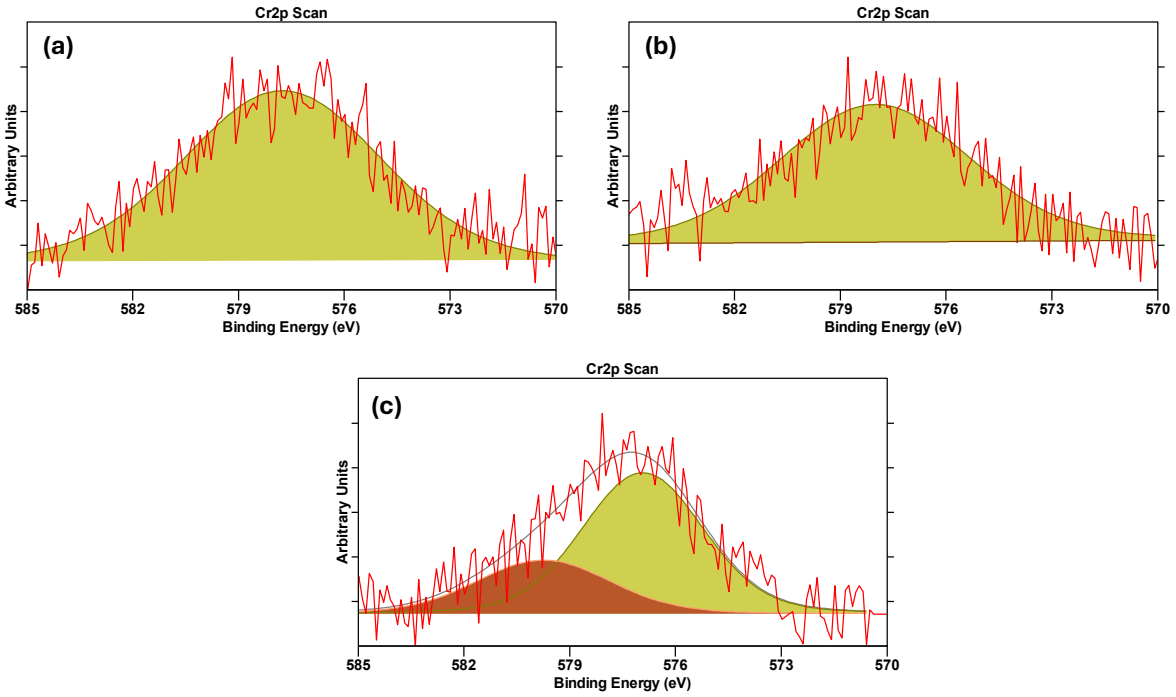


Figure 5.23: *XP spectrum of $Cr2p_{1/2}$ and $Cr2p_{3/2}$ of peaks of (a) 0.1 mol% (b) 1 mol% and (c) 2 mol% Cr doped $SrTiO_3$ of the SD series. Cr^{6+} states in this batch is prominent at higher mol% doping. The 0.1 and 1 mol% monodoped samples do not exhibit any Cr^{6+} states towards higher binding energies.*

The binding energies of the Cr peaks are listed in Table 5.3. Co-doping with La^{3+} was found to have suppressed the Cr^{6+} in the co-doped samples. Suppression of Cr^{6+} has also been reported with Ta, Cr co-doped $SrTiO_3$[3] and Sb, Cr co-doped $SrTiO_3$ [23]. A detailed discussion of the significance of Cr^{6+} and its subsequent suppression is provided in the next section.

Table 5.3: Binding energies of $Cr2p_{3/2}$ and $Cr2p_{3/2}$ peaks

Samples	Cr^{3+}	Cr^{6+}
$SrTi_{(0.999)}Cr_{(0.001)}O_3$, Serial Dilution	577.62 eV	-
$SrTi_{(0.99)}Cr_{(0.01)}O_3$, Serial Dilution	576.97 eV	-
$SrTi_{(0.98)}Cr_{(0.02)}O_3$, Serial Dilution	576.77 eV	579.68 eV
$SrTi_{(0.98)}Cr_{(0.02)}O_3$, 900 °C	576.62 eV	579.49 eV
$La_{(0.01)}Sr_{(0.99)}Ti_{(0.98)}Cr_{(0.02)}O_3$, 900 °C	577.07 eV	579.91 eV
$La_{(0.02)}Sr_{(0.98)}Ti_{(0.98)}Cr_{(0.02)}O_3$, 900 °C	576.74 eV	579.53 eV
$La_{(0.05)}Sr_{(0.95)}Ti_{(0.98)}Cr_{(0.02)}O_3$, 900 °C	576.29 eV	578.87 eV
$La_{(0.1)}Sr_{(0.9)}Ti_{(0.98)}Cr_{(0.02)}O_3$, 900 °C	575.87 eV	577.16 eV
$SrTi_{(0.98)}Cr_{(0.02)}O_3$, 800 °C	577.03 eV	579.94 eV
$La_{(0.01)}Sr_{(0.99)}Ti_{(0.98)}Cr_{(0.02)}O_3$, 800 °C	576.57 eV	579.47 eV
$La_{(0.02)}Sr_{(0.98)}Ti_{(0.98)}Cr_{(0.02)}O_3$, 800 °C	576.74 eV	579.49 eV
$La_{(0.05)}Sr_{(0.95)}Ti_{(0.98)}Cr_{(0.02)}O_3$, 800 °C	576.70 eV	579.46 eV
$La_{(0.1)}Sr_{(0.9)}Ti_{(0.98)}Cr_{(0.02)}O_3$, 800 °C	576.54 eV	579.09 eV

In Figure 5.21, the $Cr2p_{3/2}$ and $Cr2p_{1/2}$ peaks of 1 mol% and 2 mol% La, Cr co-doped sample show a peak shift to higher binding energies whereas the 5 mol% and 10 mol% La, Cr shift to lower binding energies. For the co-doped samples at 800 °C in Figure 5.22, the shift is towards the lower binding energies when compared to the monodoped sample. Following the trends of shifts to higher binding energies of Sr3d and Ti2p peaks, the case at 900 °C might be due to the dopant substituting partially the A-site. Shifts to lower binding energies might indicate the dopant incorporation at the B-site in the 800 °C samples. Similar observations can be made for the 1 mol% and 2 mol% Cr doped $SrTiO_3$ samples of the SD series.

Stoichiometric Ratio of Cr^{3+} Doped in the Synthesized Samples

From the XPS Cr2p and Ti2p peaks, the ratio of the amount of Cr^{3+} doped in the samples was calculated and shown in Table 5.4.

Table 5.4: Calculated Cr^{3+} doping from XPS for the synthesized samples

Samples	**Cr^{3+}**	**Ti^{4+} ($Ti2p_{3/2}$)**	**Ti^{4+} ($Ti2p_{1/2}$)**	**$Cr^{3+}/(Cr^{3+} + Ti2p_{3/2} + Ti2p_{1/2})$**	**Cr^{3+} Doping %**
$SrTi_{(0.999)}Cr_{(0.001)}O_3$, Serial Dilution	0.47	10.93	4.90	0.03	2.9%
$SrTi_{(0.99)}Cr_{(0.01)}O_3$, Serial Dilution	0.49	9.07	4.29	0.04	3.5%
$SrTi_{(0.98)}Cr_{(0.02)}O_3$, Serial Dilution	0.58	9.71	4.83	0.04	3.8%
$SrTi_{(0.98)}Cr_{(0.02)}O_3$, 900 °C	0.61	11.56	6.48	0.03	3.3%
$La_{(0.01)}Sr_{(0.99)}Ti_{(0.99)}Cr_{(0.02)}O_3$, 900 °C	0.61	9.97	6.34	0.04	3.6%
$La_{(0.02)}Sr_{(0.98)}Ti_{(0.98)}Cr_{(0.02)}O_3$, 900 °C	0.75	11.78	6.09	0.04	4.0%
$La_{(0.05)}Sr_{(0.95)}Ti_{(0.95)}Cr_{(0.02)}O_3$, 900 °C	0.92	10.01	5.59	0.06	5.6%
$La_{(0.1)}Sr_{(0.9)}Ti_{(0.95)}Cr_{(0.02)}O_3$, 900 °C	0.49	9.91	5.46	0.03	3.1%
$SrTi_{(0.98)}Cr_{(0.02)}O_3$, 800 °C	1.16	10.97	5.82	0.07	6.5%
$La_{(0.01)}Sr_{(0.99)}Ti_{(0.99)}Cr_{(0.02)}O_3$, 800 °C	1.06	10.17	5.40	0.06	6.4%
$La_{(0.02)}Sr_{(0.98)}Ti_{(0.98)}Cr_{(0.02)}O_3$, 800 °C	1.08	11.22	5.93	0.06	5.9%
$La_{(0.05)}Sr_{(0.95)}Ti_{(0.95)}Cr_{(0.02)}O_3$, 800 °C	1.07	9.80	5.04	0.07	6.7%
$La_{(0.1)}Sr_{(0.9)}Ti_{(0.95)}Cr_{(0.02)}O_3$, 800 °C	0.92	9.82	4.95	0.06	5.9%

Suppression of Cr^{6+} with La^{3+} co-doping

The Cr dopant exists in predominantly two states- Cr^{3+} and Cr^{6+}. Cr^{6+} states act as trapping centres for the photoinduced electrons and lead to a decrease in photocatalytic or PEC performances [1], [22]. Cr^{3+} has a d^3 configuration which can give off photo-induced electrons that can take part in the surface redox reactions. Whereas Cr^{6+} with its d^0 configuration is unable to participate in the surface redox reactions due to its inability to give any electrons. Hence, the presence of Cr^{6+} is detrimental to the performance of the catalysts. Jing, J. et al. [22] reported the use of hydrogen treatment to decrease the Cr^{6+} and increase the carrier concentrations. There is reported literature using Ta and Sb as A-site co-dopants to decrease the Cr^{6+} states [3], [23]. Amongst co-dopants, La^{3+} is reported to perform better at decreasing the Cr^{6+} states [1]. In the scope of this Ph.D., La^{3+} and Cs^{1+} were studied as a co-dopant. It was observed that with the introduction of La^{3+} co-dopant, the Cr^{6+} states were suppressed maximum at 2 mol% co-doping. The ratios of Cr^{3+} and Cr^{6+} are listed in Table 5.5.

Table 5.5: Amount of Cr^{6+} after La^{3+} co-doping

Samples	Cr^{3+} (Atomic %)	Cr^{6+} (Atomic %)	$Cr^{6+}/(Cr^{3+} + Cr^{6+})$
$SrTi_{(0.98)}Cr_{(0.02)}O_3$, Serial Dilution (without co-doping)	0.58	0.28	0.33
$SrTi_{(0.98)}Cr_{(0.02)}O_3$, 900 °C	0.61	0.61	1
$La_{(0.01)}Sr_{(0.99)}Ti_{(0.99)}Cr_{(0.02)}O_3$, 900 °C	0.61	0.59	0.49
$La_{(0.02)}Sr_{(0.98)}Ti_{(0.98)}Cr_{(0.02)}O_3$, 900 °C	0.75	0.51	0.40
$La_{(0.05)}Sr_{(0.95)}Ti_{(0.95)}Cr_{(0.02)}O_3$, 900 °C	0.92	0.61	0.40
$La_{(0.1)}Sr_{(0.9)}Ti_{(0.95)}Cr_{(0.02)}O_3$, 900 °C	0.49	0.41	0.46
$SrTi_{(0.98)}Cr_{(0.02)}O_3$, 800 °C	1.16	0.92	0.44
$La_{(0.01)}Sr_{(0.99)}Ti_{(0.99)}Cr_{(0.02)}O_3$, 800 °C	1.06	0.82	0.44
$La_{(0.02)}Sr_{(0.98)}Ti_{(0.98)}Cr_{(0.02)}O_3$, 800 °C	1.06	0.79	0.43
$La_{(0.05)}Sr_{(0.95)}Ti_{(0.95)}Cr_{(0.02)}O_3$, 800 °C	1.07	0.62	0.37
$La_{(0.1)}Sr_{(0.9)}Ti_{(0.95)}Cr_{(0.02)}O_3$, 800 °C	0.92	0.55	0.37

It was observed that the Cr^{6+} states were suppressed the most in the 2 mol% and 5 mol% La^{3+} co-doped sample of the 900 °C batch. In the 800 °C, 5 mol% and 10 mol% of the co-doped batch showed the highest suppression. Ichihara, F. et al. [1] stated in their paper that the

appearance of the multiplet splitting of Cr2p signifies that most of the states are in Cr^{3+} states which is also observed with Cr samples in this study as shown in Figures 5.19-5.22. The suppression of the Cr^{6+} from 2 mol% to 10 mol% co-doped samples is evident in the colour of these samples as shown in Figure 5.1(a, b). These samples are yellow. In the other samples where the Cr^{6+} are dominant, the colour of these samples is red.

O1s

The O1s peaks for the samples were analysed and compared with the undoped in Figure 5.24. The deconvolution of all the samples showed secondary peaks at higher binding energies. In the case of the undoped sample, the main component of the O1s peak at 529.36 eV can be attributed to lattice oxygen. The spectrum show another component at a higher binding energy of 529.91 eV. This feature can be attributed to being a C=O group. The feature at 531.26 eV can be attributed to a surface OH group.

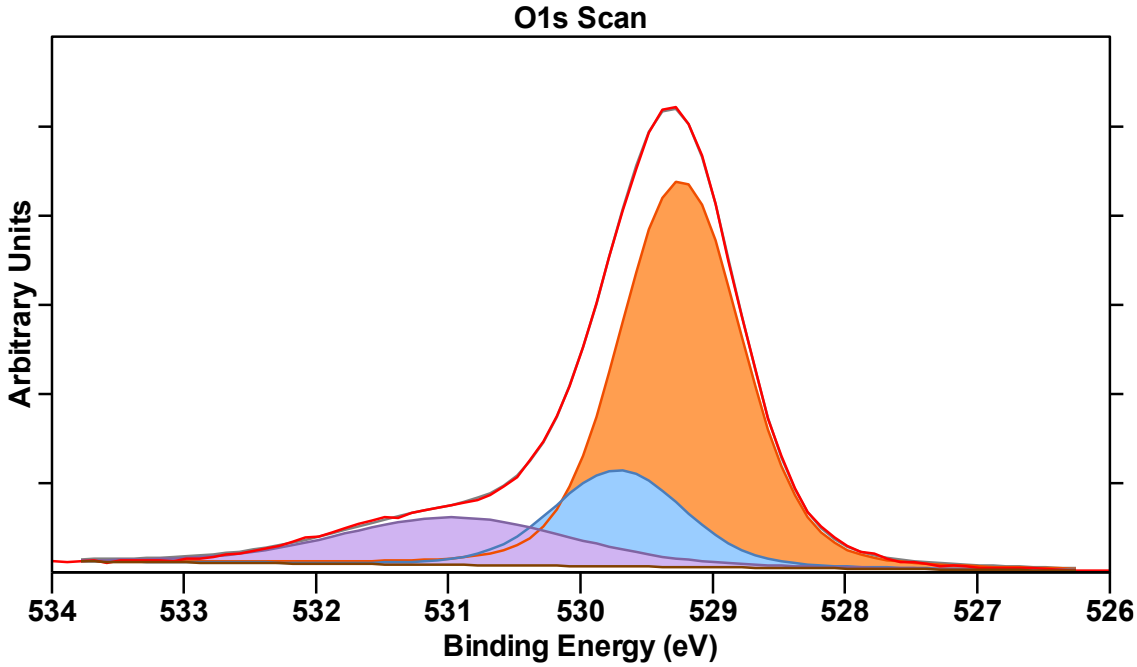


Figure 5.24: *XP spectrum of O1s peak with the main component at 529.36 eV at 900 °C with -C=O (blue) and -OH species (violet).*

The doped samples on the O1s peak deconvolution gave similar three peaks that were assigned to lattice O1s, C=O and OH (Figures 5.25- 5.29). The binding energies of the doped samples with respect to O1s are listed in Table 5.6.

Table 5.6: Binding energies of O1s deconvoluted peaks

Samples	Lattice O1s	-C=O	-OH
$SrTi_{(0.999)}Cr_{(0.001)}O_3$, Serial Dilution	529.12 eV	529.60 eV	531.05 eV
$SrTi_{(0.99)}Cr_{(0.01)}O_3$, Serial Dilution	528.20 eV	528.60 eV	530.18 eV

$SrTi_{(0.98)}Cr_{(0.02)}O_3$, Serial Dilution	528.95 eV	529.26 eV	530.94 eV
$SrTi_{(0.98)}Cr_{(0.02)}O_3$, 900 °C	529.18 eV	529.73 eV	531.08 eV
$La_{(0.01)}Sr_{(0.99)}Ti_{(0.98)}Cr_{(0.02)}O_3$, 900 °C	529.30 eV	529.99 eV	531.71 eV
$La_{(0.02)}Sr_{(0.98)}Ti_{(0.98)}Cr_{(0.02)}O_3$, 900 °C	529.43 eV	529.95 eV	530.94 eV
$La_{(0.05)}Sr_{(0.95)}Ti_{(0.98)}Cr_{(0.02)}O_3$, 900 °C	528.96 eV	529.45 eV	530.82 eV
$La_{(0.1)}Sr_{(0.9)}Ti_{(0.98)}Cr_{(0.02)}O_3$, 900 °C	529.07 eV	529.34 eV	530.87 eV
$SrTi_{(0.98)}Cr_{(0.02)}O_3$, 800 °C	529.43 eV	-	530.57 eV
$La_{(0.01)}Sr_{(0.99)}Ti_{(0.98)}Cr_{(0.02)}O_3$, 800 °C	529.12 eV	529.62 eV	531.07 eV
$La_{(0.02)}Sr_{(0.98)}Ti_{(0.98)}Cr_{(0.02)}O_3$, 800 °C	529.38 eV	530.21 eV	531.39 eV
$La_{(0.05)}Sr_{(0.95)}Ti_{(0.98)}Cr_{(0.02)}O_3$, 800 °C	529.25 eV	529.77 eV	531.10 eV
$La_{(0.1)}Sr_{(0.9)}Ti_{(0.98)}Cr_{(0.02)}O_3$, 800 °C	529.14 eV	529.66 eV	530.88 eV

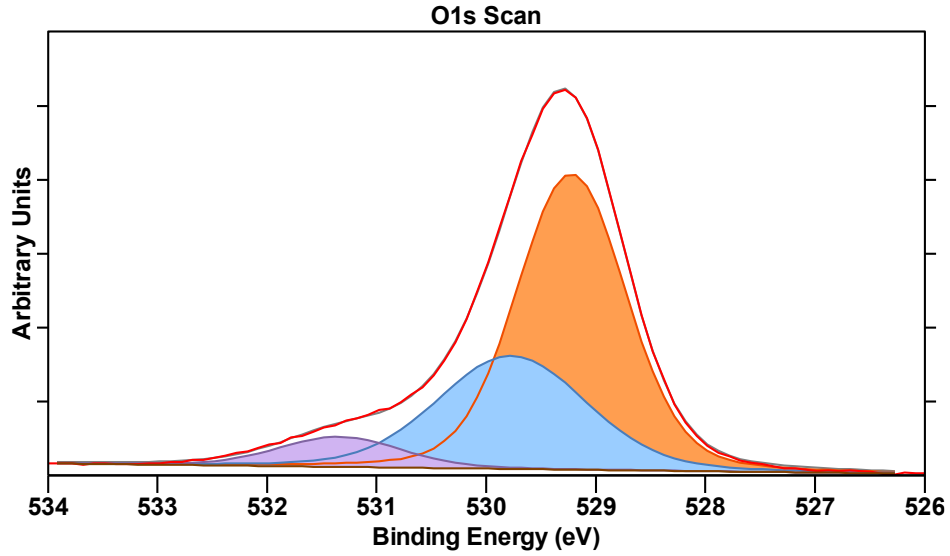


Figure 5.25: *XP spectrum of O1s (orange) of peaks of 2 mol% Cr^{3+} doped $SrTiO_3$ at 900 °C and -C=O (blue) and -OH (violet) towards higher binding energies.*

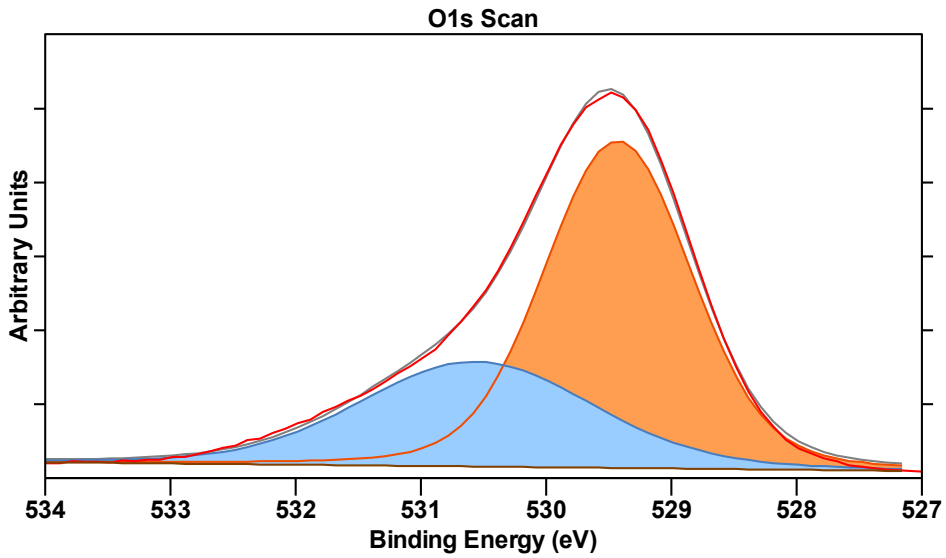


Figure 5.26: *XP spectrum of O1s (orange) of peaks of 2 mol% Cr^{3+} doped $SrTiO_3$ at 800 °C*

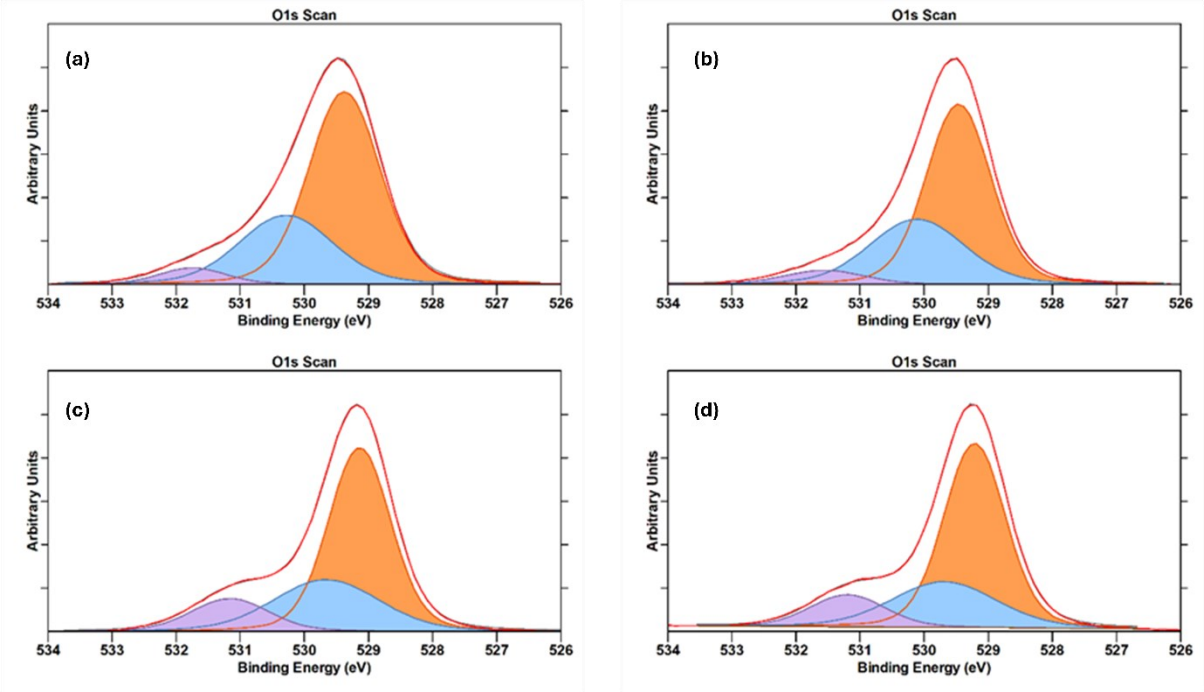


Figure 5.27: *XPS O1s (orange) peak deconvolution of (a) 1 mol% (b) 2 mol% (c) 5 mol% (d) 10 mol% La, 2 mol% Cr co-doped $SrTiO_3$ at 900 °C with varying concentrations of -C=O (blue) and -OH (violet).*

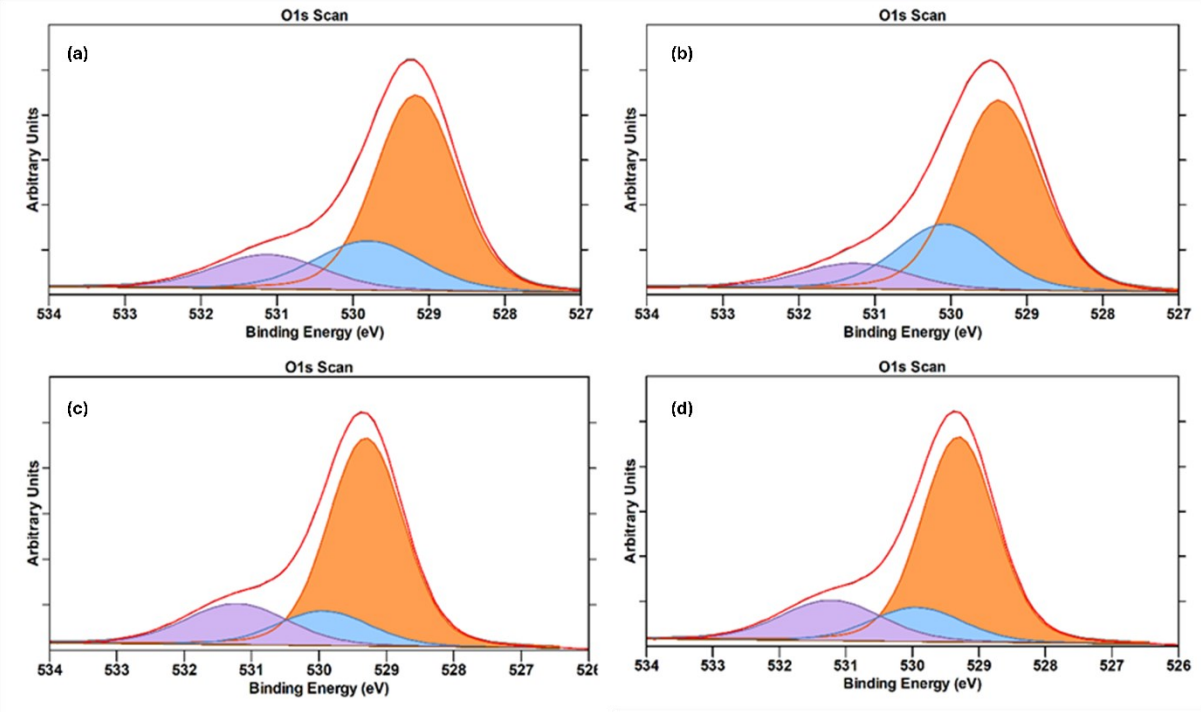


Figure 5.28: *XPS O1s peak (orange) deconvolution of (a) 1 mol% (b) 2 mol% (c) 5 mol% (d) 10 mol% La, 2 mol% Cr doped $SrTiO_3$ at 800 °C with*

From Table 5.6, it can be observed that the trend in shifting of the binding energies is consistent with the Sr3d, Ti2p, and Cr2p as discussed in the previous sections. Here again, this trend can be speculated to be due to the site of incorporation of the dopants.

From Figures 5.24-5.28, another crucial observation regarding the secondary peaks can be made. With the increase in La^{3+} co-doping, the amount of -OH increases for the 900 °C synthesized La^{3+} co-doped samples which are shown in Table 5.7. The 2 mol% La^{3+} co-doped sample at 800 °C has the lowest surface hydroxyl groups. Idriss, H. et al. [24] argues that the peak around 531.5 eV is due to the surface hydroxyls which is also acknowledged in the XPS analysis in the Ph.D. study. Idriss, H. et al. [24] reports that the formation of these groups could be due to exposure to the ambient. As highlighted in the previous chapters, oxygen vacancies acting as shallow donors can affect the n-type conductivity of the materials. Similar peaks were observed for the monodoped samples prepared with the serial dilution method as shown in Figure 5.29.

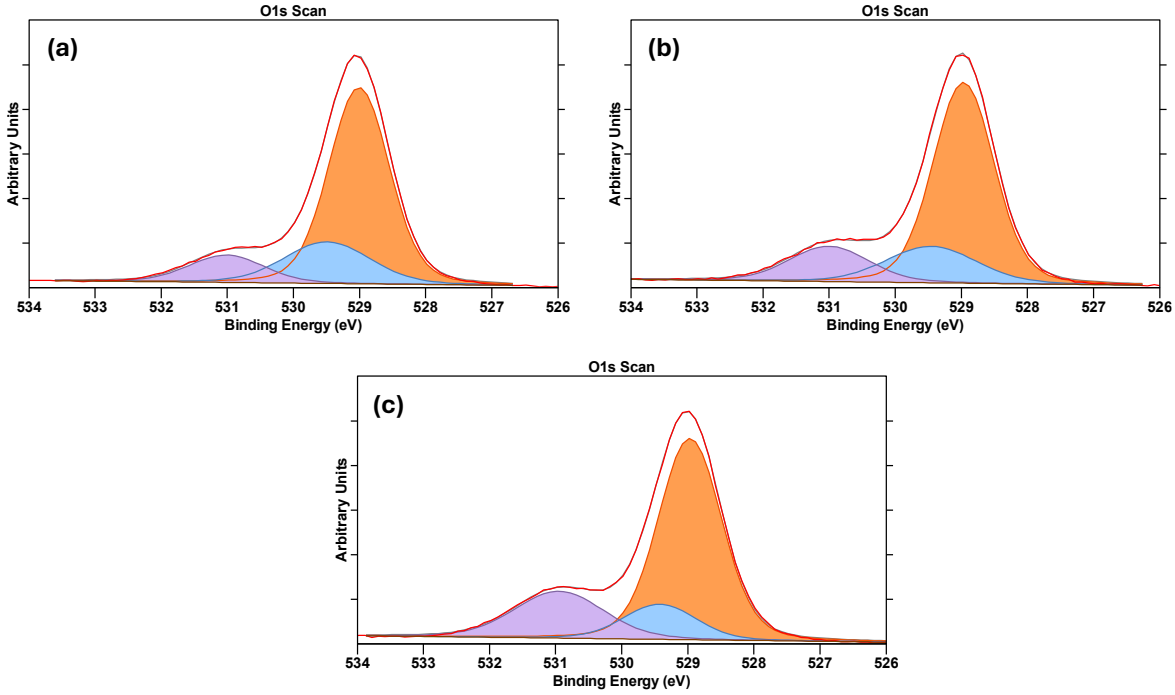


Figure 5.29: *XPS O1s peak (orange) deconvolution of (a) 0.1 mol% (b) 1 mol% and (c)2 mol% Cr doped $SrTiO_3$ prepared with the SD series with -C=O (blue) and -OH (violet) at higher binding energies.*

Table 5.7: -C=O and -OH concentrations comparison

Sample	-C=O Atomic %	-OH Atomic %
$SrTiO_3$, 900 °C	8.78	5.99
$SrTi_{(0.98)}Cr_{(0.02)}O_3$, 900 °C	14.44	13.08
$La_{(0.01)}Sr_{(0.99)}Ti_{(0.98)}Cr_{(0.02)}O_3$, 900 °C	15.02	11.91
$La_{(0.02)}Sr_{(0.98)}Ti_{(0.98)}Cr_{(0.02)}O_3$, 900 °C	12.13	15.41
$La_{(0.05)}Sr_{(0.95)}Ti_{(0.98)}Cr_{(0.02)}O_3$, 900 °C	11.59	11.57
$La_{(0.1)}Sr_{(0.9)}Ti_{(0.98)}Cr_{(0.02)}O_3$, 900 °C	11.56	11.54
$SrTi_{(0.98)}Cr_{(0.02)}O_3$, 800 °C	8.00	14.14
$La_{(0.01)}Sr_{(0.99)}Ti_{(0.98)}Cr_{(0.02)}O_3$, 800 °C	13.71	5.06
$La_{(0.02)}Sr_{(0.98)}Ti_{(0.98)}Cr_{(0.02)}O_3$, 800 °C	13.83	12.05
$La_{(0.05)}Sr_{(0.95)}Ti_{(0.98)}Cr_{(0.02)}O_3$, 800 °C	7.97	17.48
$La_{(0.1)}Sr_{(0.9)}Ti_{(0.98)}Cr_{(0.02)}O_3$, 800 °C	9.77	14.50
$SrTi_{(0.999)}Cr_{(0.001)}O_3$, Serial Dilution	7.13	11.53
$SrTi_{(0.99)}Cr_{(0.01)}O_3$, Serial Dilution	7.63	8.94
$SrTi_{(0.98)}Cr_{(0.02)}O_3$, Serial Dilution	10.22	8.67

La3d

From the XPS survey of the surface of the co-doped samples, the presence of Lanthanum is evident as shown in Figures 5.30-5.31. La3+ co-doping aimed to suppress the Cr^{6+} states which has been reported to be detrimental to photocatalysis. The Cr^{6+} suppression effect has been enlisted in Table 5.5. La^{3+} ion due to its similar size with Sr^{2+}, is expected to be in the A site of $SrTiO_3$.

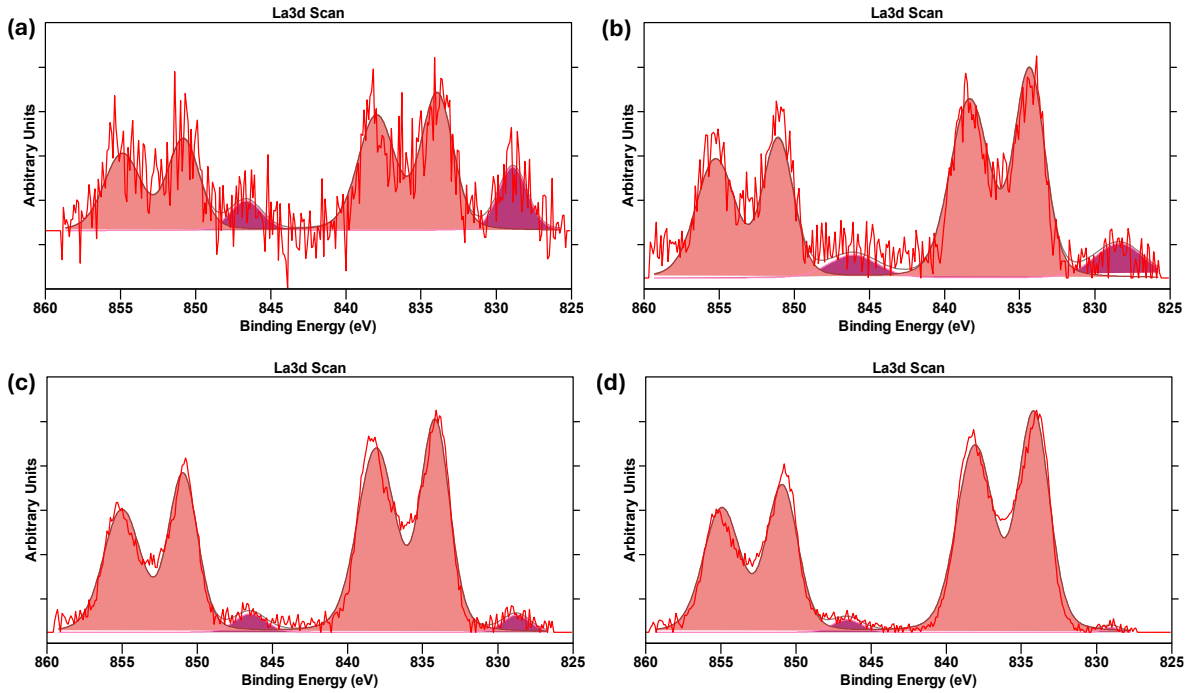


Figure 5.30: *XP spectrum of $La3d_{3/2}$ and $La3d_{5/2}$ peaks of 1 mol%, 2 mol%, 5 mol% and 10 mol% La, 2 mol% Cr doped $SrTiO_3$ at 800 °C.*

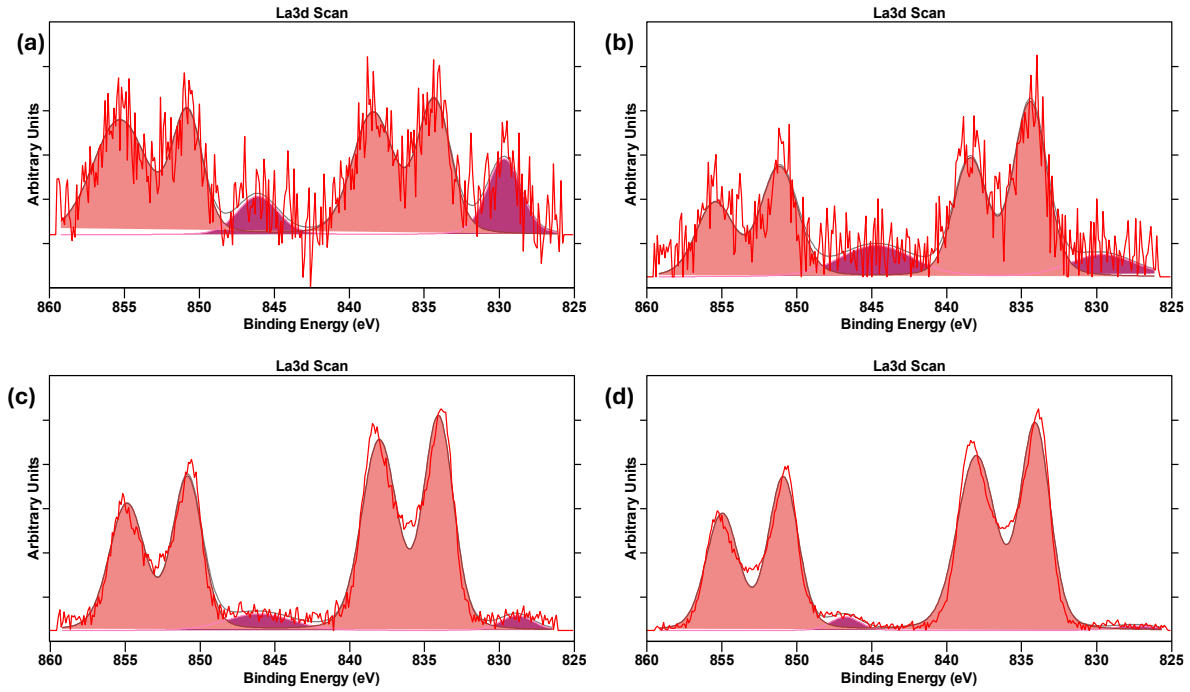


Figure 5.31: *XP spectrum of $La3d_{3/2}$ and $La3d_{5/2}$ peaks of (a) 1 mol% (b) 2 mol% (c) 5 mol% and (d) 10 mol% La, 2 mol% Cr doped $SrTiO_3$ at 900 °C.*

La3d shows two satellites at lower binding energies than the d5/2 and the d3/2 peaks at 829.65 eV and 846.04 eV in the co-doped samples at both temperatures. These satellites are called shake-down satellites as they appear towards lower binding energies of the main peaks. These satellites result from the relaxation process when an electron fills a hole created by an ejected photoelectron. The binding energies of the La3d peaks of the co-doped samples are listed in Table 5.8. The shifts in binding energies follow similar trends as observed for Sr3d, Ti2p, Cr2p, and O1s.

Table 5.8: Binding energies of the La3d peaks

Samples	$La3d_{5/2}$	$La3d_{3/2}$	$La3d_{5/2}$	$La3d_{3/2}$
$La_{(0.01)}Sr_{(0.99)}Ti_{(0.98)}Cr_{(0.02)}O_3$, 900 °C	834.32 eV	850.94 eV	838.49 eV	855.30 eV
$La_{(0.02)}Sr_{(0.98)}Ti_{(0.98)}Cr_{(0.02)}O_3$, 900 °C	834.36 eV	850.96 eV	838.41 eV	855.04 eV
$La_{(0.05)}Sr_{(0.95)}Ti_{(0.98)}Cr_{(0.02)}O_3$, 900 °C	833.99 eV	850.63 eV	837.97 eV	854.67 eV
$La_{(0.1)}Sr_{(0.9)}Ti_{(0.98)}Cr_{(0.02)}O_3$, 900 °C	834.05 eV	850.66 eV	838.00 eV	854.78 eV
$La_{(0.01)}Sr_{(0.99)}Ti_{(0.98)}Cr_{(0.02)}O_3$, 800 °C	833.96 eV	850.74 eV	838.12 eV	854.84 eV
$La_{(0.02)}Sr_{(0.98)}Ti_{(0.98)}Cr_{(0.02)}O_3$, 800 °C	834.33 eV	851.10 eV	838.35 eV	855.17 eV

$La_{(0.05)}Sr_{(0.95)}Ti_{(0.98)}Cr_{(0.02)}O_3$, 800 °C	834.22 eV	850.82 eV	838.13 eV	854.88 eV
$La_{(0.1)}Sr_{(0.9)}Ti_{(0.98)}Cr_{(0.02)}O_3$, 800 °C	834.20 eV	850.80 eV	838.08 eV	854.80 eV

The amount of La^{3+} co-doping to Sr^{2+} is calculated in Table 5.9.

Table 5.9: Amount of La^{3+} co-doping with respect to Sr^{2+}

Samples	**La3d$_{5/2}$**	**La3d $_{5/2}$**	**La3d $_{3/2}$**	**La3d $_{3/2}$**	**Sr3d $_{5/2}$**	**Sr3d$_{3/2}$**	**La3d/(La3d+Sr3d)**	**La^{3+} Doping %**
$La_{(0.01)}Sr_{(0.99)}Ti_{(0.98)}Cr_{(0.02)}O_3$, 900 °C	0.06	0.09	0.06	0.09	9.01	9.02	0.02	1.6
$La_{(0.02)}Sr_{(0.98)}Ti_{(0.98)}Cr_{(0.02)}O_3$, 900 °C	0.16	0.17	0.16	0.16	11.87	11.86	0.03	2.7
$La_{(0.05)}Sr_{(0.95)}Ti_{(0.98)}Cr_{(0.02)}O_3$, 900 °C	0.57	0.42	0.58	0.43	10.17	10.18	0.09	8.9
$La_{(0.1)}Sr_{(0.9)}Ti_{(0.98)}Cr_{(0.02)}O_3$, 900 °C	1.35	0.87	1.38	0.89	9.25	9.26	0.19	19.5
$La_{(0.01)}Sr_{(0.99)}Ti_{(0.98)}Cr_{(0.02)}O_3$, 800 °C	0.07	0.07	0.08	0.08	12.01	12.02	0.01	1.2
$La_{(0.02)}Sr_{(0.98)}Ti_{(0.98)}Cr_{(0.02)}O_3$, 800 °C	0.20	0.20	0.16	0.17	10.36	10.37	0.03	3.4
$La_{(0.05)}Sr_{(0.95)}Ti_{(0.98)}Cr_{(0.02)}O_3$, 800 °C	0.54	0.55	0.45	0.45	13.06	13.06	0.07	7.1
$La_{(0.1)}Sr_{(0.9)}Ti_{(0.98)}Cr_{(0.02)}O_3$, 800 °C	1.16	1.18	1.00	1.01	10.97	10.98	0.17	16.5

Note: The XPS analysis was conducted on the La^{3+} co-doped samples and the Cr monodoped SD series. La^{3+} series showed evidence of Cr^{6+} suppression. The dopant concentration was aimed to be controlled with the SD series samples.

5.5.2 Site of Cr^{3+} doping: EPR Studies

The site of Cr^{3+} doping in the A or B site is an important parameter that affects the activity of the photocatalysts [18], [25]. Wang, D. et al. [18] reported a higher photocatalytic H_2 evolution with Cr^{3+} doped in the A-site against a barely seen activity when doped in the B-site. They reported that when doped in the A site, the valence state of Cr is only +3 whereas B site doping has both the detrimental +6 and +3 states. In this report, they however also stated that when photogenerated electrons upon UV light irradiation, reduced the +6 states to +3 states and saw a highly enhanced performance. From the XPS analysis and absorption spectrum, the Cr2p

peak deconvolution showed the presence of both Cr^{3+} and Cr^{6+} in both the co-doped series. Hence, it can be speculated from the work of Wang, D. et al. [18] that Cr has been doped in the B-site in the standard sol-gel samples. This speculation can also be made due to the similarity in the ionic size of Cr^{3+} and Ti^{4+}. To maintain charge neutrality and suppress Cr^{6+} states, La^{3+} with similar ionic radii as Sr^{2+} is speculated to be in the A site.

To further confirm the effect of oxidation states and the site of the dopants, EPR was done on the samples. The 2 mol% Cr samples annealed at 800 °C and 900 °C show Cr^{3+} signals. These signals consist of a weak 4-line signal from Cr (I = 3/2, 9.5% abundance) with a strong single-line signal from the Cr isotopes with zero nuclear spin as shown in Figure 5.32. The samples showed no change under UV illumination. The g value at 1.9784 and the hyperfine splitting at 46.8 MHz are consistent with literature with Cr in the B-site [26]–[30].

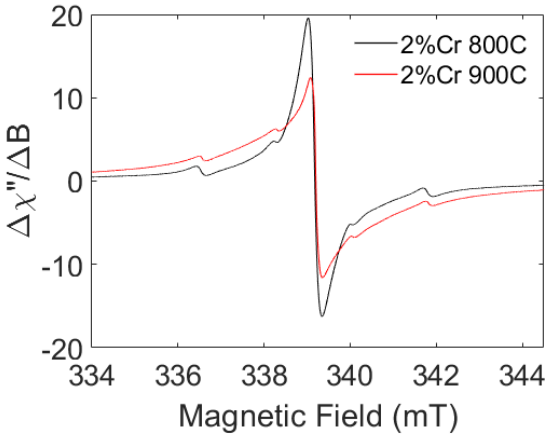


Figure 5.32: *EPR spectrum of samples 2 mol% Cr-STO 800 °C (black) and 2 mol% Cr-STO 900 °C (red), measured at 100 K with a microwave power of 50 µW and a field modulation amplitude of 0.025 mT. The plot shows only the central part of the measured spectrum, but the integration was carried out using the full magnetic field range at the edges of which the EPR intensity would go to zero.*

The monodoped samples in Figure 5.32 at different temperatures show however greater broadening than the reported literature. The 900 °C sample shows 1.75 times higher signal broadening (intensity) than the 800 °C sample indicating higher Cr^{3+} content in the higher temperature sample. To confirm this the 2 mol% Cr doped sample at 800 °C was compared with the simulation of the Cr signal as shown in Figure 5.33.

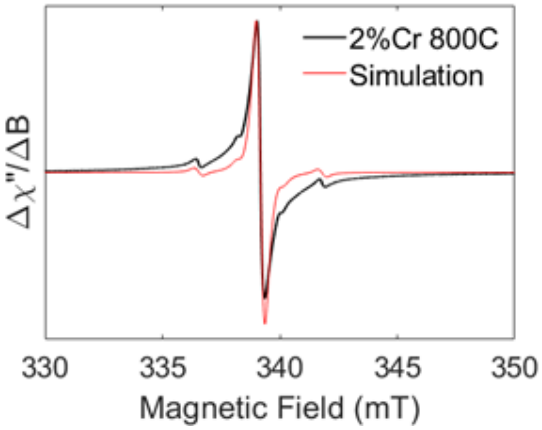


Figure 5.33: *Measurement (black) and simulation (red) of the Cr(III) signal in 2 mol% Cr-STO 800 °C. The spectrum was simulated considering an isotropic Cr(III) (S = 3/2, I = 3/2 (9.5% abun.), I = 0 (90.5% abun.), g = 1.9784, g-Strain = 0.001, A = 48.6 MHz, Lorentzian linewidth = 0.55 mT. The inclusion of zero-field splitting interaction did not improve the agreement with the experiment, and it was therefore neglected, making the simulation identical to that of the corresponding S = 1/2 ion.*

Extensive broadening of the Cr signal in $SrTiO_3$ was reported by Lehuta, K.A et al. [27] at higher temperatures upon reduction with $NaBH_4$. This was attributed to the increased conversion of Cr^{6+} to Cr^{3+} leading to strong interactions between the paramagnetic ions. From the XPS, the concentration of the Cr^{3+} is higher than the intended level of doping in the standard sol-gel Pechini samples. This could lead to the observed signal broadening. To check the possibility of higher Cr^{3+} leading to signal broadening, the monodoped serial dilution series were measured as shown in Figure 5.34 (a, b).

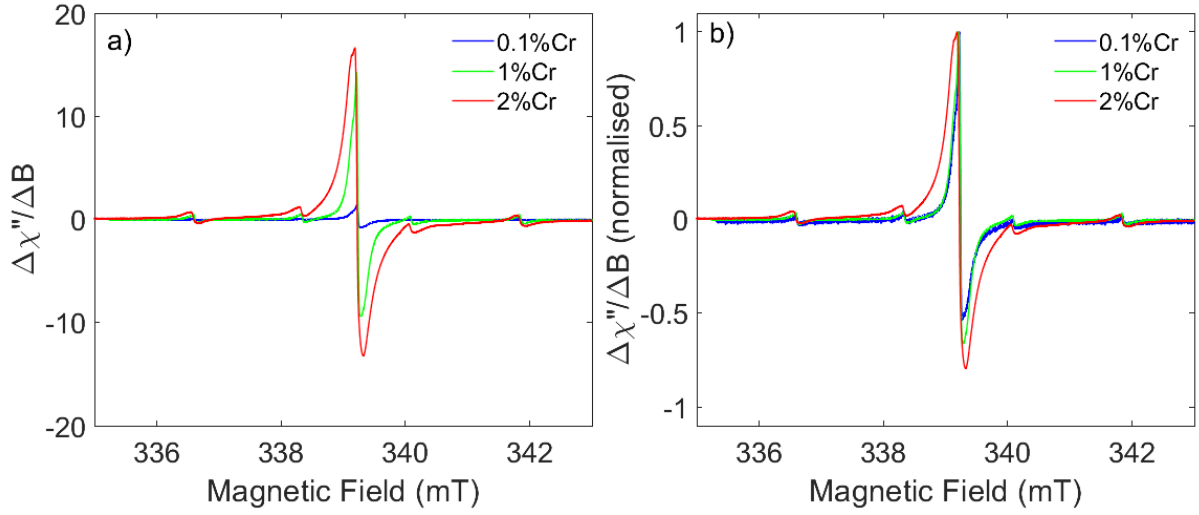


Figure 5.34: *Raw (a) and normalised (b) EPR spectrum of Cr-STO samples prepared with the serial dilution method. 2 mol% Cr-STO 900 °C (red), 1 mol% Cr-STO 800 °C (green), and 0.1 mol% Cr-STO 800 °C (blue). The spectrum was measured at 100 K with a microwave power of 50 μW and a field modulation amplitude of 0.025 mT for 2 mol% Cr and 0.015 mT for 0.1 mol% Cr and 1 mol% Cr.*

In Figure 5.34 (b), the 0.1 mol% and the 1 mol% Cr monodoped samples show signals consistent with the reported literature [26], [31]. The 2 mol% Cr doped sample made by the serial dilution series has 0.66 times lower Cr^{3+} signal intensity than the samples made via the standard sol-gel Pechini method. Asymmetric broadening has been reported in Cr-doped $SrTiO_3$ samples with $Ti^{3+}$with lower g values (1.92-1.97) [28], [32], [33]. This aligns with the presence of Ti^{3+} as was observed with the XPS.

Co-doping 2 mol% Cr samples with Cs^{1+} led to narrower and weaker Cr^{3+} signals with increasing Cs content as shown in Figure 5.35 (a, b). Similar effects were seen for both the samples at 800 °C and 900 °C. The narrower and weaker signals of the Cs co-doped samples indicate the oxidation of Cr^{3+} to Cr^{6+} due to charge compensation when replacing Sr^{2+} by Cs^{1+} in the A-site.

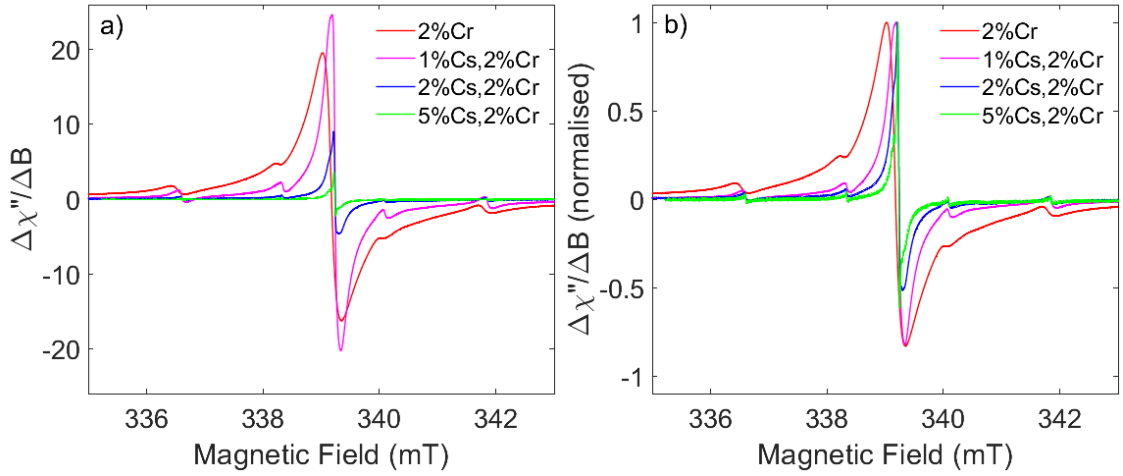


Figure 5.35: *Raw (a) and normalised (b) EPR spectrum of 2 mol% Cr-STO 800 °C (red), 1 mol% Cs,2 mol% Cr-STO 800 °C (magenta), 2 mol% Cs,2 mol% Cr-STO 800 °C (blue) and 5 mol% Cs,2 mol% Cr-STO 800 °C (green). The samples were measured at 100 K with a microwave power of 50 µW and a field modulation amplitude of 0.025 mT. The field modulation for sample 5 mol%Cs,2 mol% Cr-STO 800 °C was 0.01 mT.*

Co-doping a 2 mol% Cr sample with 1 mol% La^{3+}, increases both the signal intensity and broadening as shown in Figure 5.36 (a-d). This aligns with the fact that La^{3+} in the A-site via charge compensation leads to the reduction of Cr^{6+} to Cr^{3+}. However, with an increase in La^{3+} co-doping, the signal broadening is accompanied with a decrease in signal intensity.

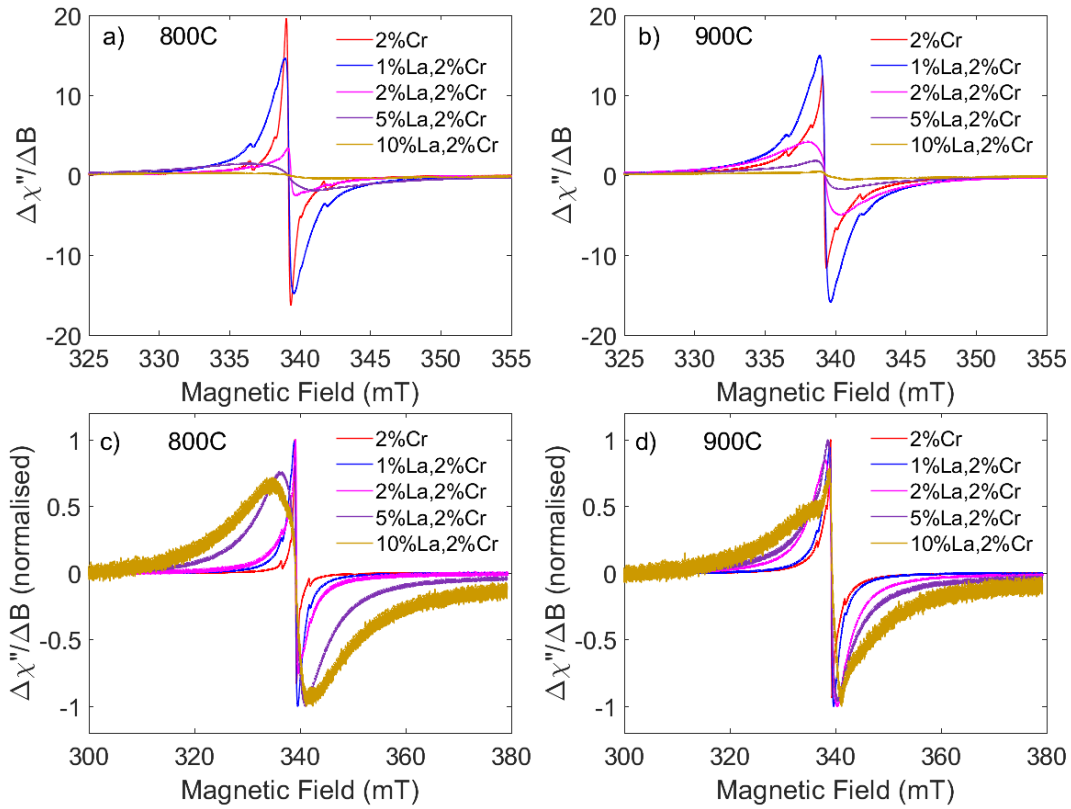


Figure 5.36: *EPR spectrum of the sample sets annealed at 800 °C (a) 900 °C (b), consisting of 2 mol% Cr-SrTiO₃ (red), 1 mol% La,2 mol% Cr-SrTiO₃ (blue), 2 mol% La, 2 mol %Cr-SrTiO₃ (magenta), 5 mol% La,2 mol% Cr-SrTiO₃ (purple) and 10 mol% La,2 mol% Cr-SrTiO₃ (yellow). The samples were measured at 100 K with a microwave power of 50 µW and a field modulation amplitude of 0.025 mT. (c, d) Normalization of panels a and b.*

The EPR studies show that Cr is in the B-site for all the samples with the g-value and the hyperfine splitting values consistent with the literature on Cr doped in the B-site of $SrTiO_3$. Cr^{3+} shows strong interactions between the paramagnetic ions above 1 mol% doping, leading to the signal broadening. Co-doping with Cs^{1+} or higher than 1 mol% La^{3+} decreases the Cr^{3+} content.

5.6 Opto-Electronic Analysis

In this section, the opto-electronic behaviour of the materials is studied. The techniques discussed are the DRS for the bandgaps and absorption wavelengths, the XPS for the valence band, work function and band edge energy diagrams, and the TCSPC and the PL for the charge carrier dynamics.

5.6.1 Diffuse Reflectance Spectroscopy (DRS) Analysis

Transition metals with partially filled d-orbitals can introduce mid-gap states or electronic states in the band gap that can act as recombination centres[5],[34]. Moss, B. et al. [5] in their work on Rh doping reported the presence of both Rh^{4+} traps and Rh^{3+} as shown in Figure 5.37(a). They reported the La^{3+} co-doping to fix Rh^{3+} which adds states above the VB leading to visible light absorption. Wang, D. et al. [18] reported in their study the existence of both

Cr^{6+} and Cr^{3+} when the dopant is substituted in the B-site. They observed that the Cr^{6+} levels are added as shallow donors below the CB shown in Figure 5.37(b). In contrast, the Cr^{3+} is added above the O2p levels (VB). Diffuse reflectance spectroscopy measurements were carried out in a Shimadzu UV-vis Instrument using an integrating sphere to study whether such mid-gap states exist in the samples. The direct and indirect band gaps were measured via the Kubelka-Munk function and the Tauc plots. The steps involving the Kubelka Munk function have been discussed in detail in Chapter 2.

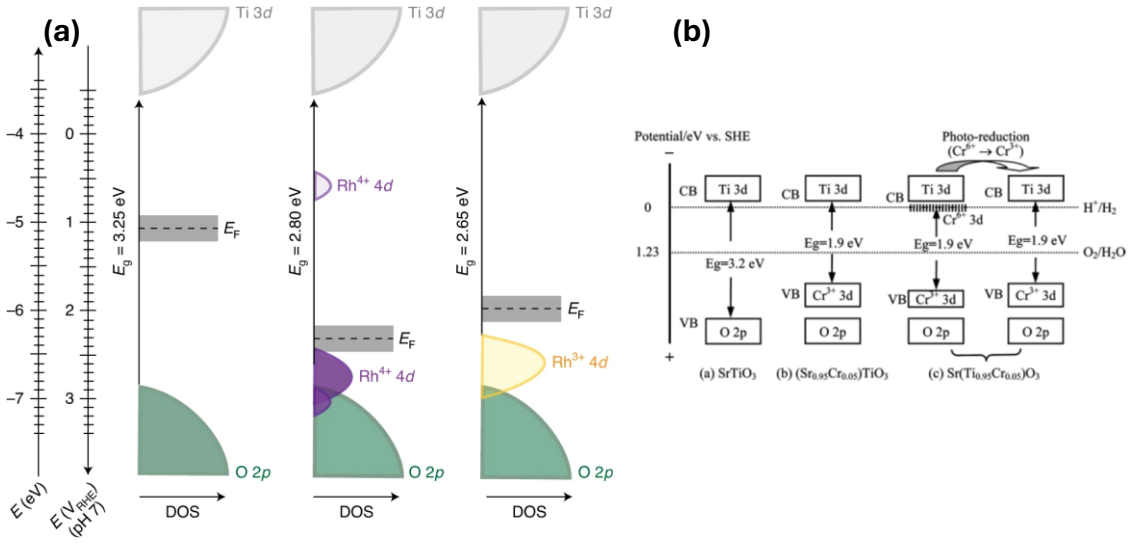


Figure 5.37: *(a) Suppression of Rh^{4+} states by La^{3+} co-doping which the Rh^{3+} states above the O2p level (VB) reproduced with permission from the work of Moss, B. et al. [5] (Copyright © 2021, The Author(s), under exclusive licence to Springer Nature Limited) (b) Shallow Cr^{6+} states below the CB and Cr^{3+} states above the VB upon site-specific Cr doping in $SrTiO_3$ reproduced with permission from Wang, D. et al. [18] (Copyright © 2006 American Chemical Society).*

The indirect and direct bandgaps of the samples are compared and shown in Figures 5.38-5.39. The doped samples retaining the parent bandgap of $SrTiO_3$ also demonstrated an increase in absorption in the visible light region up to > 800nm. The first indication of visible light absorption was observed from the colours of the doped materials. In Figure 5.38 (a-d), an absorption feature around 2 eV is prominent in the indirect band gaps of most co-doped samples. This feature is suppressed in the 2 mol% La^{3+} co-doped samples synthesized at 800 °C and 900 °C (Figure 5.38 (b, c)). In the Cr monodoped serial dilution samples (Figure 5.38(a)), it can be observed that this feature becomes more prominent with an increase in mol% doping. For scattering samples, the calculation of the band gaps is not straightforward due to the presence of the inter-band states [35]. For accurate measurements of the indirect bandgaps, background subtraction was applied while analysing the reflectance data. The values of indirect and direct bandgaps are listed in Table 5.10.

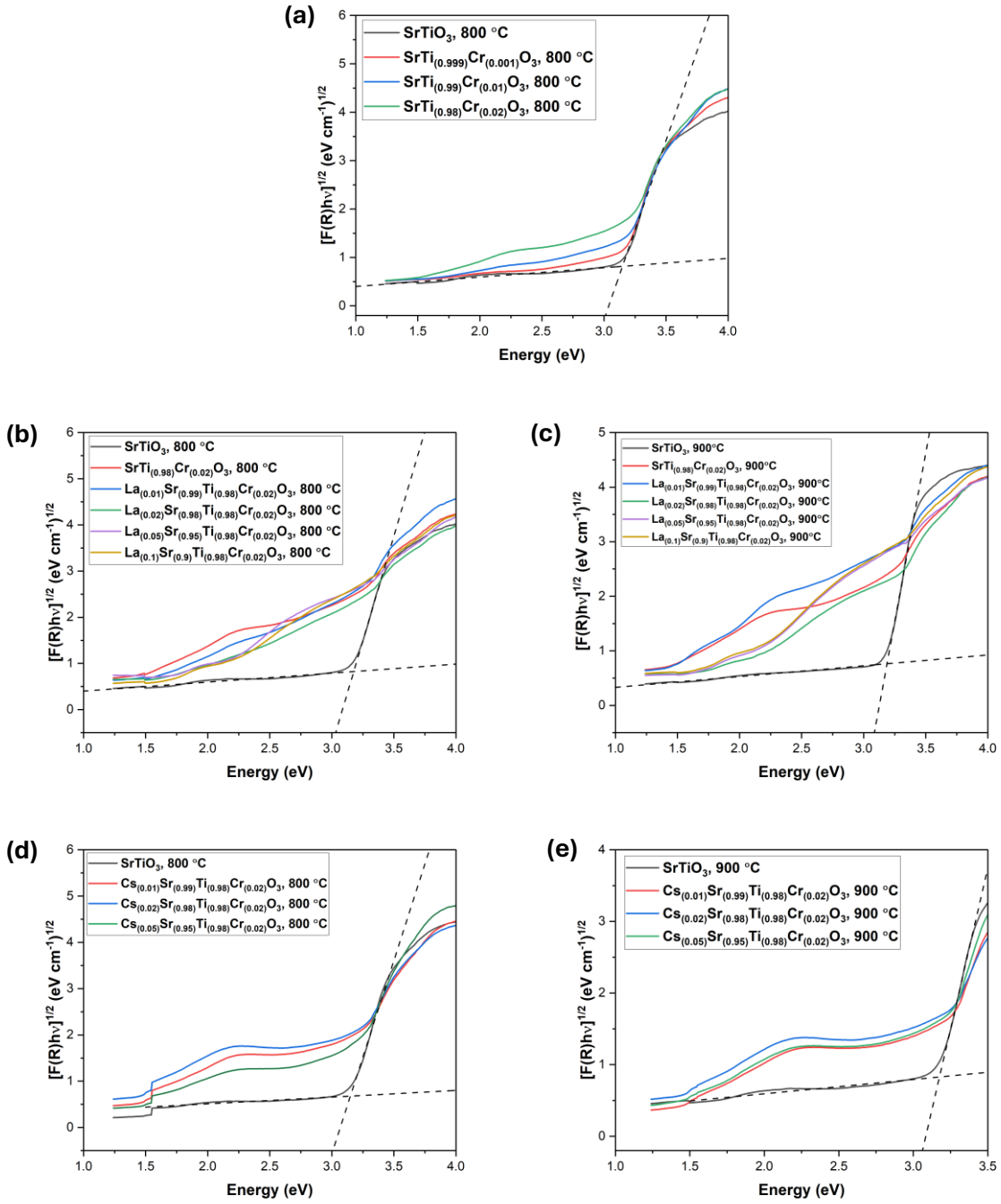


Figure 5.38: *Indirect band gaps of (a) Cr monodoped serial dilution $SrTiO_3$ samples (b) La^{3+} co-doped 800 °C (c) La^{3+} co-doped 900 °C (d) Cs^{1+} co-doped 800 °C (e) Cs^{1+} co-doped 900 °C. All the doped samples show midgap states. These states are suppressed to the maximum for both the 2 mol% La^{3+} (co-) doped samples. Cs co-doping did not show any suppression of these states.*

Both types of co-doping prepared at 900 °C and 800 °C showed a decrease in the parent $SrTiO_3$ band gaps as shown in Table 3. The direct band gaps did not show significant changes (Figure 5.39). In the Cr monodoped serial dilution samples, both the direct and indirect band gaps do not show significant changes. However, for strongly scattering samples, analysing the band

gaps from Tauc plots is not straightforward [5]. The Kubelka Munk function, F(R) was further analysed to understand the absorption dynamics of the doped samples as shown in Figures 5.40-3.44. The undoped showed an absorption edge at 387 nm (UV region). The Kubelka Munk absorption demonstrates the extension into the visible light region > 400 nm in the case of the co-doped samples. The 5 mol% Cs^{+1} co-doped sample at 900 °C and 2 mol% Cr (SD) monodoped samples show absorption < 400nm.

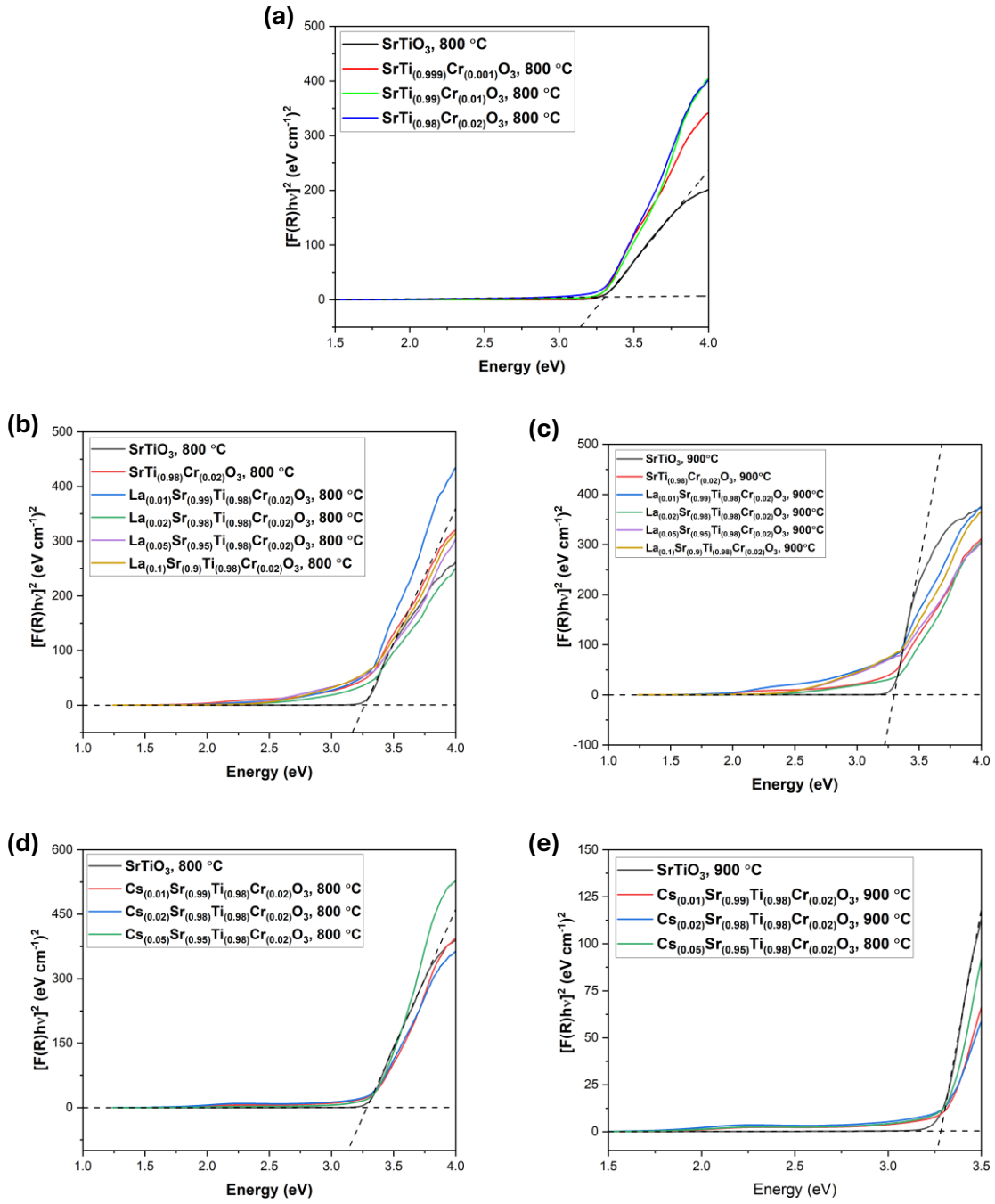


Figure 5.39: *Direct band gaps with midgap states of (a) Cr monodoped serial dilution $SrTiO_3$ samples (b) La^{3+} co-doped 800 °C (c) La^{3+} co-doped 900 °C (d) Cs^{1+} co-doped 800 °C (e) Cs^{1+} co-doped 900 °C. The midgap state suppression are analogous to the indirect bandgaps.*

Table 5.10: Indirect, Direct Band Gaps and Absorption Wavelengths of the parent $SrTiO_3$ Edge

% Doping	$SrTiO_3$ Edge Indirect Band Gaps (eV)	$SrTiO_3$ Edge Direct Band Gaps (eV)	$SrTiO_3$ Edge Absorption Wavelength (nm)
$SrTiO_3$, 800 °C	3.17	3.29	387
$SrTi_{(0.999)}Cr_{(0.001)}O_3$, 800 °C (Serial Dilution)	3.17	3.27	400.20
$SrTi_{(0.99)}Cr_{(0.01)}O_3$, 800 °C (Serial Dilution)	3.18	3.29	398.80
$SrTi_{(0.98)}Cr_{(0.02)}O_3$, 800 °C (Serial Dilution)	3.21	3.29	402.30
$SrTi_{(0.98)}Cr_{(0.02)}O_3$, 800 °C	2.96	3.21	419.32
$La_{(0.01)}Sr_{(0.99)}Ti_{(0.99)}Cr_{(0.02)}O_3$, 800 °C	2.93	3.24	411.31
$La_{(0.02)}Sr_{(0.98)}Ti_{(0.98)}Cr_{(0.02)}O_3$, 800 °C	2.81	3.21	427.33
$La_{(0.05)}Sr_{(0.95)}Ti_{(0.95)}Cr_{(0.02)}O_3$, 800 °C	2.31	3.21	442.34
$La_{(0.1)}Sr_{(0.9)}Ti_{(0.95)}Cr_{(0.02)}O_3$, 800 °C	2.31	3.21	437.33
$SrTiO_3$, 900 °C	3.17	3.29	387
$SrTi_{(0.98)}Cr_{(0.02)}O_3$, 900 °C	2.91	3.23	416.31
$La_{(0.01)}Sr_{(0.99)}Ti_{(0.98)}Cr_{(0.02)}O_3$, 900 °C	2.88	3.17	444.05
$La_{(0.02)}Sr_{(0.98)}Ti_{(0.98)}Cr_{(0.02)}O_3$, 900 °C	2.69	3.28	411.22
$La_{(0.05)}Sr_{(0.95)}Ti_{(0.98)}Cr_{(0.02)}O_3$, 900 °C	2.18	3.16	442.68
$La_{(0.1)}Sr_{(0.9)}Ti_{(0.98)}Cr_{(0.02)}O_3$, 900 °C	2.44	3.20	419.43
$Cs_{(0.01)}Sr_{(0.99)}Ti_{(0.98)}Cr_{(0.02)}O_3$, 800 °C	2.99	3.37	407.30
$Cs_{(0.02)}Sr_{(0.98)}Ti_{(0.98)}Cr_{(0.02)}O_3$, 800 °C	3.05	3.34	411.31
$Cs_{(0.05)}Sr_{(0.95)}Ti_{(0.98)}Cr_{(0.02)}O_3$, 800 °C	3.09	3.36	401.30
$Cs_{(0.01)}Sr_{(0.99)}Ti_{(0.98)}Cr_{(0.02)}O_3$, 900 °C	3.13	3.31	401.40
$Cs_{(0.02)}Sr_{(0.98)}Ti_{(0.98)}Cr_{(0.02)}O_3$, 900 °C	3.09	3.29	405.30
$Cs_{(0.05)}Sr_{(0.95)}Ti_{(0.98)}Cr_{(0.02)}O_3$, 900 °C	3.15	3.30	393.54

Most of the doped samples show visible light absorption. Wang, D. et al. [18] reported the significance of site-specific Cr doping in $SrTiO_3$ in photocatalytic performance. They reported two systems with Cr doped in the A-site (Sr^{2+}) and the B-site (Ti^{4+}). When Cr is doped in the B-site, it exists as both Cr^{6+} and Cr^{3+}. Cr in the A-site evolves 100 times more H_2 as compared to when in the B-site. In the case of the co-doped samples synthesised in this study, the presence of Cr^{6+} is evident. Therefore, it can be inferred that for the La^{3+} and Cs^{+1} co-doped and the 2 mol% monodoped Cr: $SrTiO_3$ synthesised via the sol-gel Pechini method, the site of doping is the B-site. For the Cr monodoped serial dilution series, the Cr^{6+} states increase with doping. This can be observed from Figure 5.44 (a-c). At 0.1 and 1 mol% Cr doping, no absorption features around 550 nm can be observed. This can also be physically observed when the colour of these samples' changes from faint yellow to deeper yellow to red. This could signify the

increase in Cr^{6+} states. From this, it could be inferred that in the case of the 0.1 and 1 mol% Cr monodoped sample, the dopant could be in the A-site wholly or partially. The other samples in the serial dilution series show Cr^{6+} states in the absorption spectrum (Figures 5.40-5.44). Therefore, the dopants are substituted in the B-site of $SrTiO_3$.

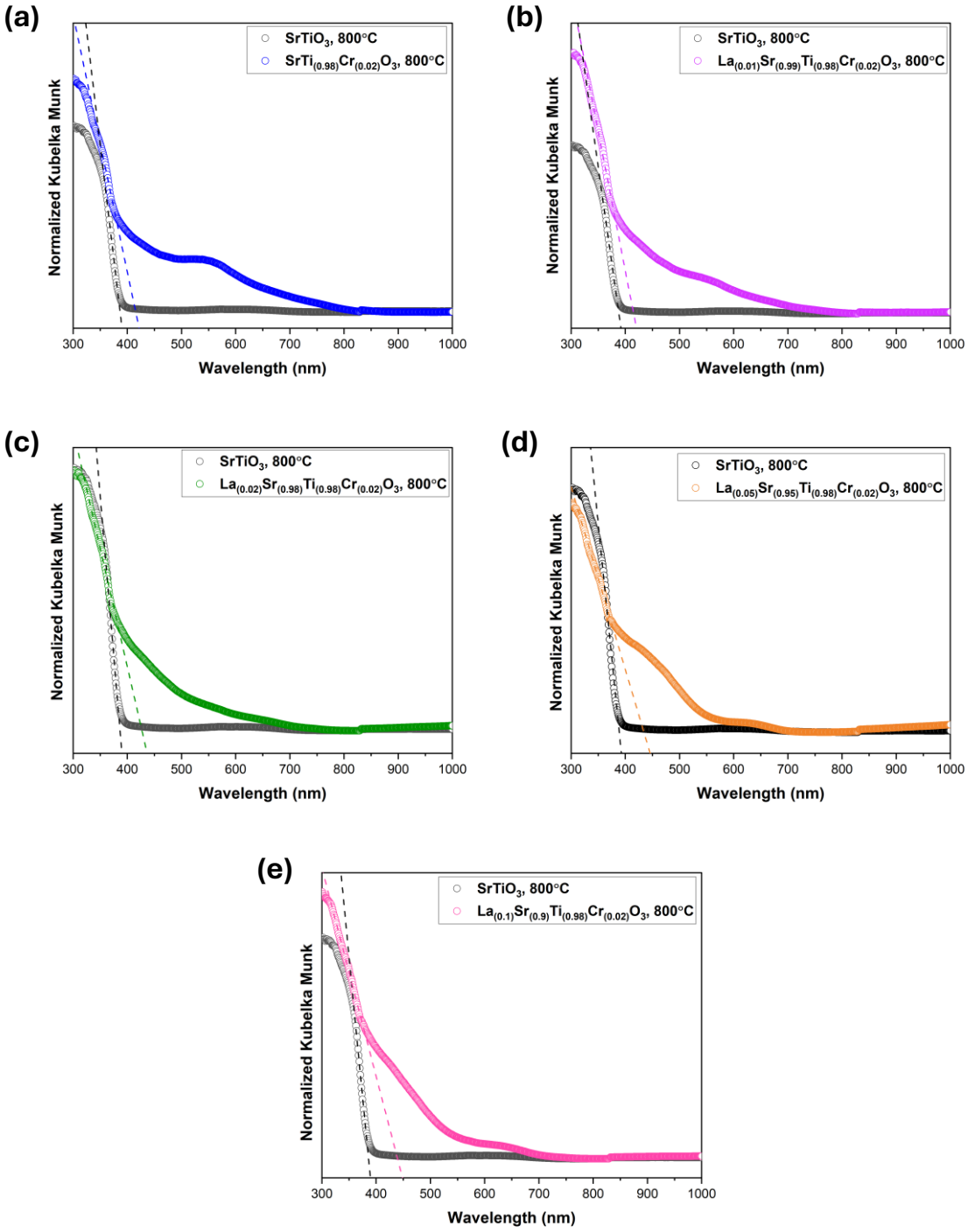


Figure 5.40: *Comparison of absorption wavelengths from the Kubelka Munk function of the La^{3+} co-doped samples synthesized at 800 °C with the undoped. These samples show the*

extension of the absorption into the visible light region and tailing off at 750 nm. The absorption feature around 450 – 500 nm is highly suppressed for the 2 mol% co-doped sample.

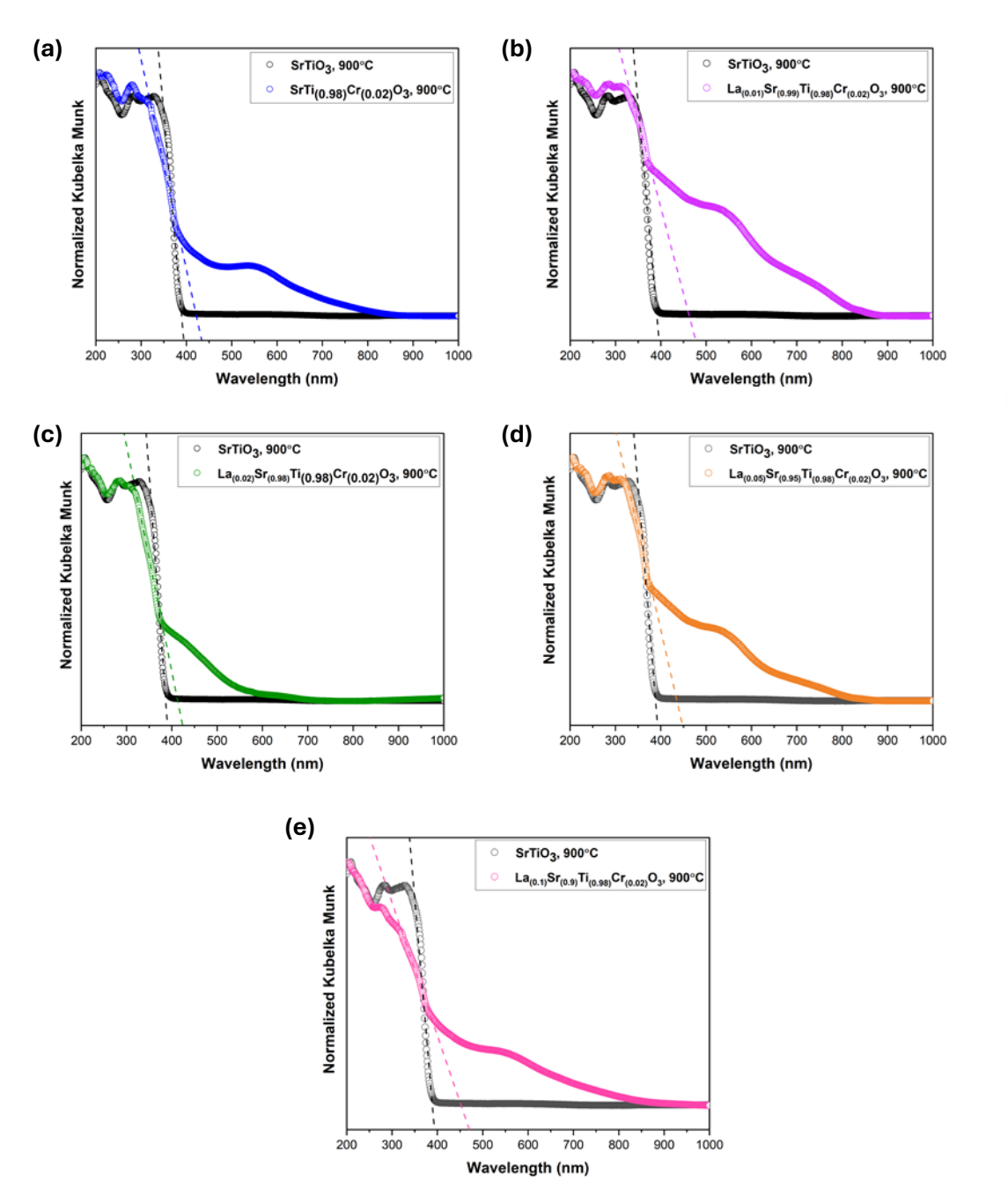


***Figure 5.41**: Comparison of absorption wavelength from the Kubelka Munk function of the La^{3+} co-doped samples synthesized at 900 °C with absorption in the doped samples extending beyond 800 nm in most cases. The 2 mol% co-doped sample tails off at 700 nm and shows the highest suppression of the absorption feature around 500 nm.*

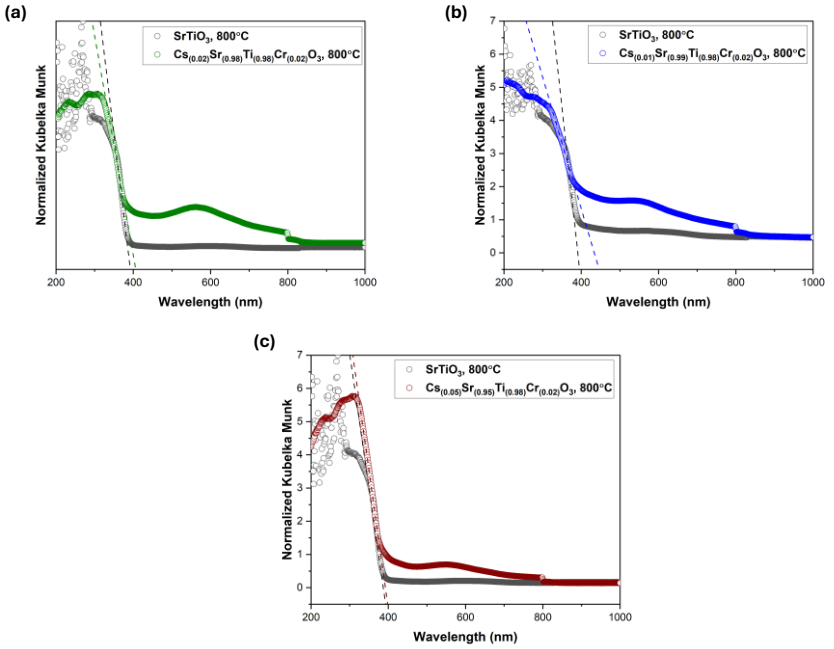


Figure 5.42: *Comparison of absorption wavelength from the Kubelka Munk function of the Cs^{+1} samples synthesized at 800 °C with the increase in absorption beyond 800 nm with an increase in co-doping. No suppression of the absorption feature in any of the co-doped samples.*

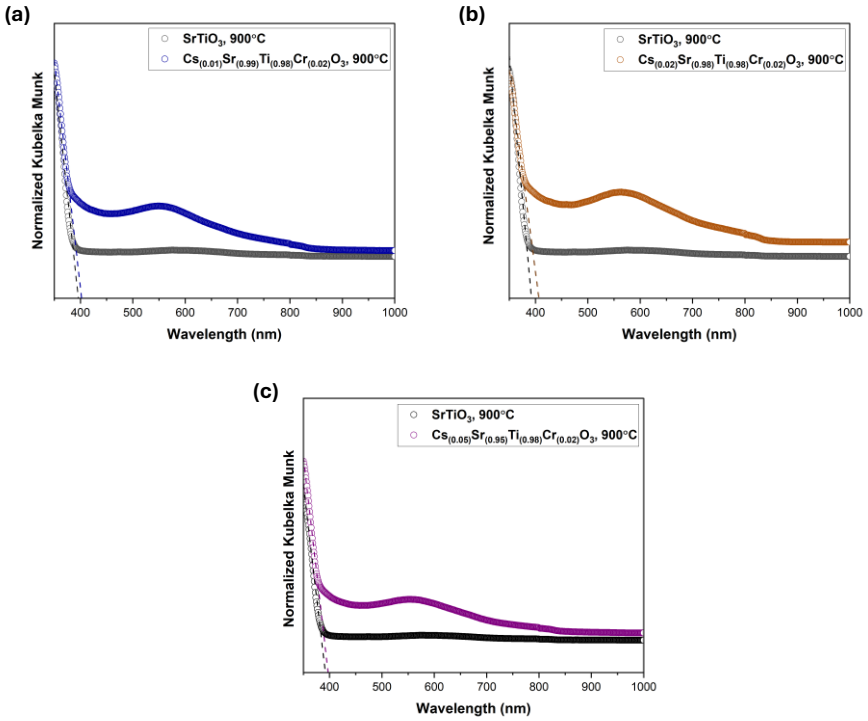


Figure 5.43: *Comparison of absorption wavelength from the Kubelka Munk function of the Cs^{+1} samples synthesized at 900 °C behaving similarly to the batch at 800 °C.*

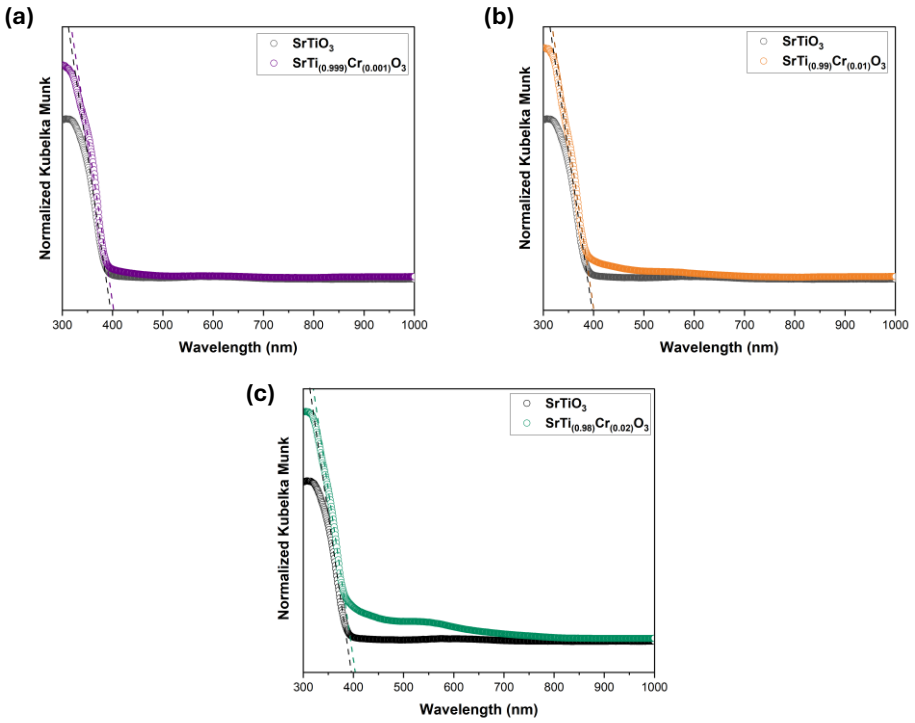


Figure 5.44: *Comparison of absorption wavelength from the Kubelka Munk function of the (a) 0.1 mol% (b) 1 mol% and (c) 2 mol% Cr monodoped serial dilution series synthesized at 800 °C. The absorption into the visible light region and the absorption feature around 550 nm increase with doping.*

The doped samples though retained the $SrTiO_3$ intrinsic absorption edges (Figures 5.40-5.44), they showed additional absorption band tails from 400 nm to 800 nm wavelengths of the visible light region in the case of most of the doped samples. The 2 mol% Cr^{3+} doped samples synthesized with the sol-gel Pechini method showed an absorption feature around 550 nm and the tail extended to 850 nm of the spectrum. All the doped samples exhibit some mid-gap states. The absorption feature at 550nm introduced with 2 mol% Cr^{3+} doping is completely suppressed with 2 mol% La^{3+} co-doping in both temperature cases in Figures 5.40 (c)-5.41 (c). In Ichihara, F. et al. [1] it has been reported that the absorption band edge from 400 nm to 600 nm corresponds to a charge transfer absorption of Cr^{3+} to Ti^{4+} and absorption between 600 nm to 700 nm indicates a transition between $^4A_{2g}$ to $^4t_{2g}$ in octahedral Cr^{3+} units. Similar observations were made by Ischii, T. et al. [3]. The absorption beyond the 700 nm region has been attributed to Cr^{6+} [3][1]. Absorption beyond 700nm is greatly suppressed in the 2 mol% La^{3+} co-doped samples. This indicates a suppression of the Cr^{6+} states as seen in Figures 5.40(c)-5.41(c). This result can be corroborated by the XPS $Cr2p_{3/2}$ peak analysis which showed the decrease in in Cr^{6+} states upon La co-doping discussed in later sections. In most of the doped samples, the absorption intensity is higher as shown in Figures 5.40-5.44. This could be due to a higher number of occupied Cr3d t_{2g} valence states available for electron-hole excitations [36].

Another important facet of this study is the colours of the doped samples as demonstrated by Figure 5.1. Jiang, D. et al. [2] reported the colour of the 2 mol% Cr^{3+} doped sample to be yellow. At 2 mol%, the Cr monodoped serial dilution sample is red indicating higher Cr^{6+}.

However, the sol-gel synthesised monodoped samples in this study are red at both temperatures. The red colour of the sample might be from the extended absorption above 500 nm wavelength resulting from the Cr^{6+} states which can be corroborated with the XPS results. Similarly, the 1 mol% La^{3+} co-doped samples are also red. The colours of the samples from 2 mol% to 10 mol% La^{3+} are yellow. This could be speculated to be from suppression of the Cr^{6+} states and absorption of light in the 420 nm – 430 nm region which aligns with wavelengths. Łąnz, A. et al. speculated the similar red colour in their samples to be due to higher Cr^{6+} states [37]. The Cs^{+1} co-doped samples show a deepening of the violet colour as the mol% doping increased. This could be too related to the suppression of Cr^{6+} with doping and absorption of light beyond 570 nm in the visible region.

Cr mono-doping and La-Cs co-doping have significant effects on the absorption dynamics of $SrTiO_3$. The bandgap is an intrinsic material property that affects the overall performance of the photocatalyst. In this study, the bandgap along with other intrinsic parameters is studied in detail in the subsequent sections to measure the band edge energy diagrams to understand the activity of Cr-doped $SrTiO_3$.

5.6.2 Valence Band Analysis

All the y-axes in Figures 5.43-5.48 have been measured in counts/sec from the XPS with arbitrary units (a.u.).

The valence band analysis of the samples was performed alongside the XPS survey scan. In Cr-doped $SrTiO_3$, the top of the valence band comprises the O2p, and the bottom of the conduction band consists of Ti3d [18]. The analysis of the undoped samples, the linear extrapolation fittings gave a valence band maximum and the Fermi level separation to be at 2.68 eV (800 °C) and 2.21 eV (900 °C) at the intersection of the two fitted lines as shown in Figure 5.45. The E_F-VB_M at 900 °C is close to the reported value in the literature of 1.8 -1.9 (± 0.2) eV [5],[36].

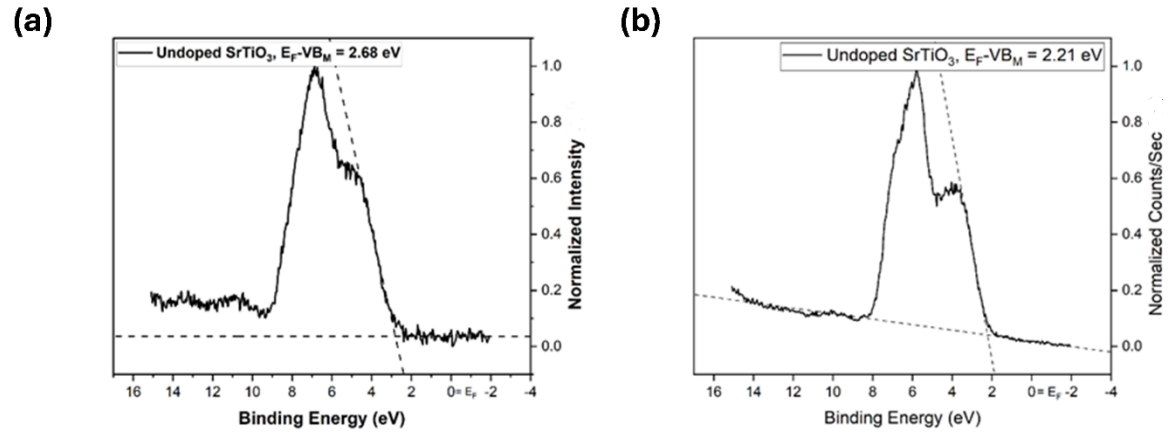


Figure 5.45: *VB_M - Fermi level separation of undoped $SrTiO_3$ at (a) 800 °C (2.68 eV) and (b) 900 °C (2.21 eV).*

The VB_M analysis of the monodoped samples synthesized via the sol-gel Pechini at 900 °C and 800 °C gave a separation of 2.05 eV and 2.01 eV respectively as shown in Figure 5.46 (a, b).

For the Cr^{3+} monodoped samples, the E_F-VB_M separation decreases as compared to the undoped samples as shown in Figure 5.45 (a, b). The VB_M edges of the batch doped at 800 °C shift towards 0 eV compared to the undoped as shown in Figure 5.47 (a-d), hence becoming more p-type

For the 2 mol% and the 5 mol% La^{3+} co-doped samples (900 °C), the E_F-VB_M separation increases to 2.39 eV (Figure 5.48 (b, c)). Whereas, for the 1 mol% and the 10 mol% La^{3+} co-doped samples the E_F-VB_M separation to 1.98 eV and 1.95 eV respectively (Figure 5.48 (a, d)). An n-type nature is expected when the E_F-VB_M becomes larger and a p-type nature when it shifts towards 0 eV i.e. the E_F.

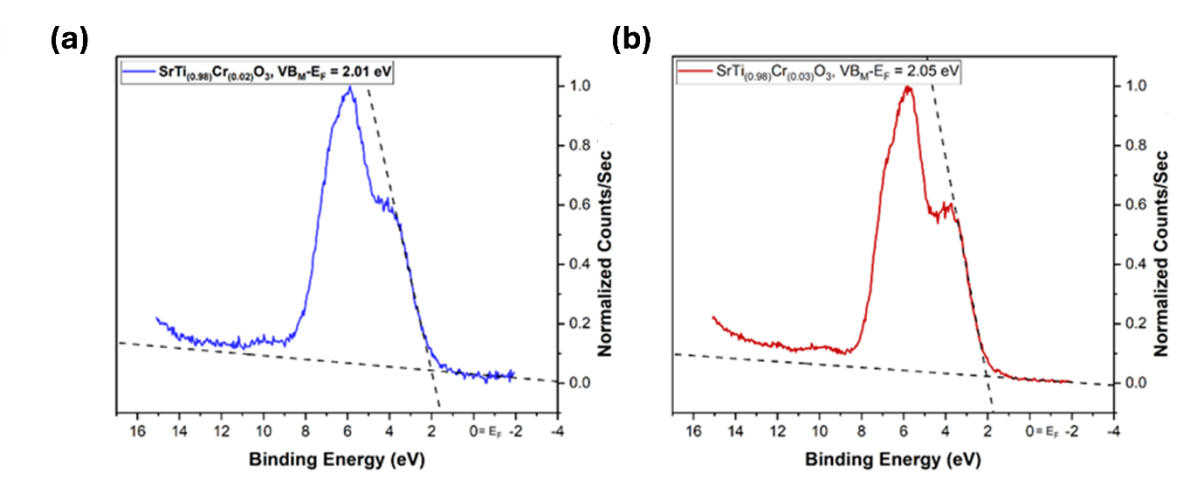


Figure 5.46: *VB_M – E_F separation decreases for the sol-gel Pechini synthesized 2 mol% Cr^{3+} doped $SrTiO_3$ at (a) 800 °C (2.01 eV) (b) 900 °C (2.05 eV) as compared to the undoped samples.*

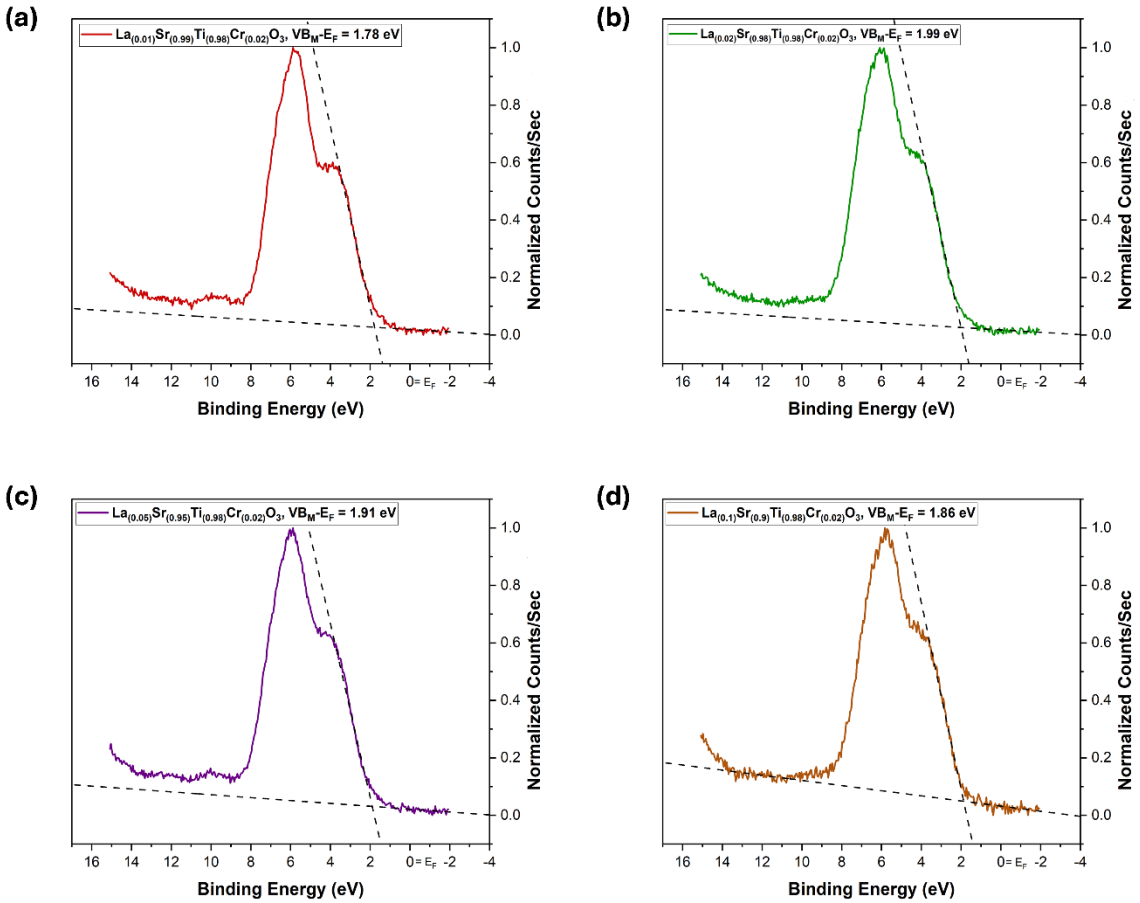


Figure 5.47: *VB_M-Fermi level separation further decreases of (a) 1 mol% (1.78 eV) (b) 2 mol% (1.99 eV) (c) 5 mol% (1.91 eV) (d) 10 mol% (1.86 eV) La^{3+} co-doped $SrTiO_3$ synthesized at 800 °C compared to the 2 mol% Cr monodoped and the undoped samples.*

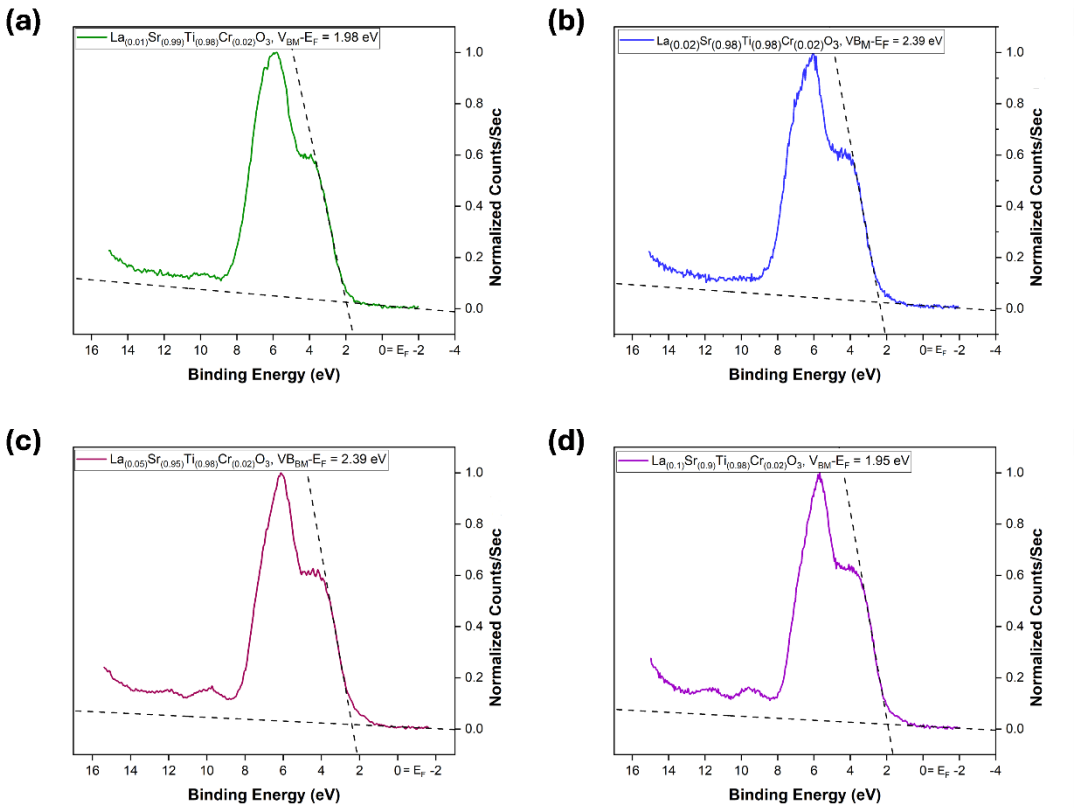


Figure 5.48: *VB_M-Fermi level separation of (a) 1 mol% (1.98 eV) (b) 2 mol% (2.39 eV) (c) 5 mol% (2.39 eV) (d) 10 mol% (1.95 eV) La^{3+} co-doped $SrTiO_3$ synthesized at 900 °C. The 1 mol% and the 10 mol%* decrease *and the 2 mol% and the 5 mol%* increase *compared to the 2 Cr monodoped samples.*

Both the standard sol-gel Pechini synthesized doped samples at 800 °C and 900 °C show similarly shaped VB spectrum with shifts in positions (Figures 5.47 – 5.48). However, no additional features were observed in these batches. The SD batch however showed some additional features in the lower energy side of the VB spectrum. The previous section discussed a possibility where Cr could have been substituted in the A-site. Comes, R. et al. [36] report that when Cr is substituted in the A-site, an additional feature assigned to Cr3d t_{2g} towards lower binding energy is observed in the valence band spectrum at the O2p edge shown in Figure 5.49(a). They stated this feature became more prominent in higher doping regimes. Such a feature was observed in the 1 mol% Cr^{3+} doped SD series samples shown in Figure 5.49 (b).

The Cr monodoped serial dilution series shows shifts towards 0 eV compared to the undoped at 800 °C as shown in Figure 5.49. The decrease in the VB_M-E_F happens systematically for these samples with an increase in mol% doping.

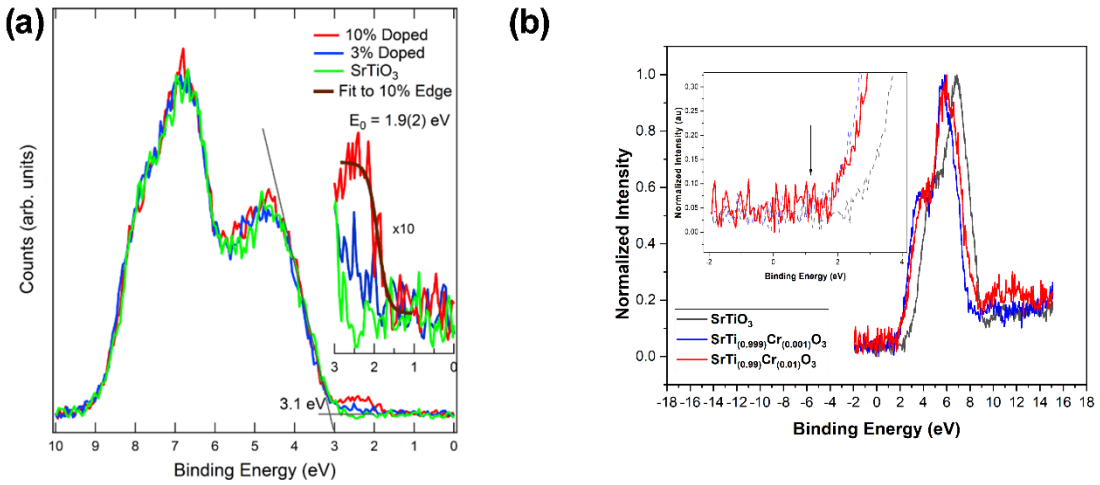


Figure 5.49: *(a) Appearance of Cr3d t_{2g} states when Cr is doped at the A-site of $SrTiO_3$ reproduced with permission from the work of Comes, R. B. et al. [36] (Copyright © 2014, American Chemical Society) (b) 0.1 mol% and 1 mol% Cr^{3+} synthesized during the Ph.D. hinting the presence of Cr3d t_{2g} states in the inset at the edge of the O2p of the VB spectrum.*

In the 1 mol% Cr^{3+} doped samples, the Cr3d t_{2g} states are not very prominent. This could be either due to a low-energy flood gun used for the XPS experiments or low doping levels. The appearance of these states pinpoints the substitution either wholly or partially in the A-site. With the increase in doping for the SD series, the VB_M-E_F difference decreases compared to the undoped at 800 °C. The observation here is contradictory to the results with the EPR in Figure 5.34 where it indicates the substitution in the B-site.

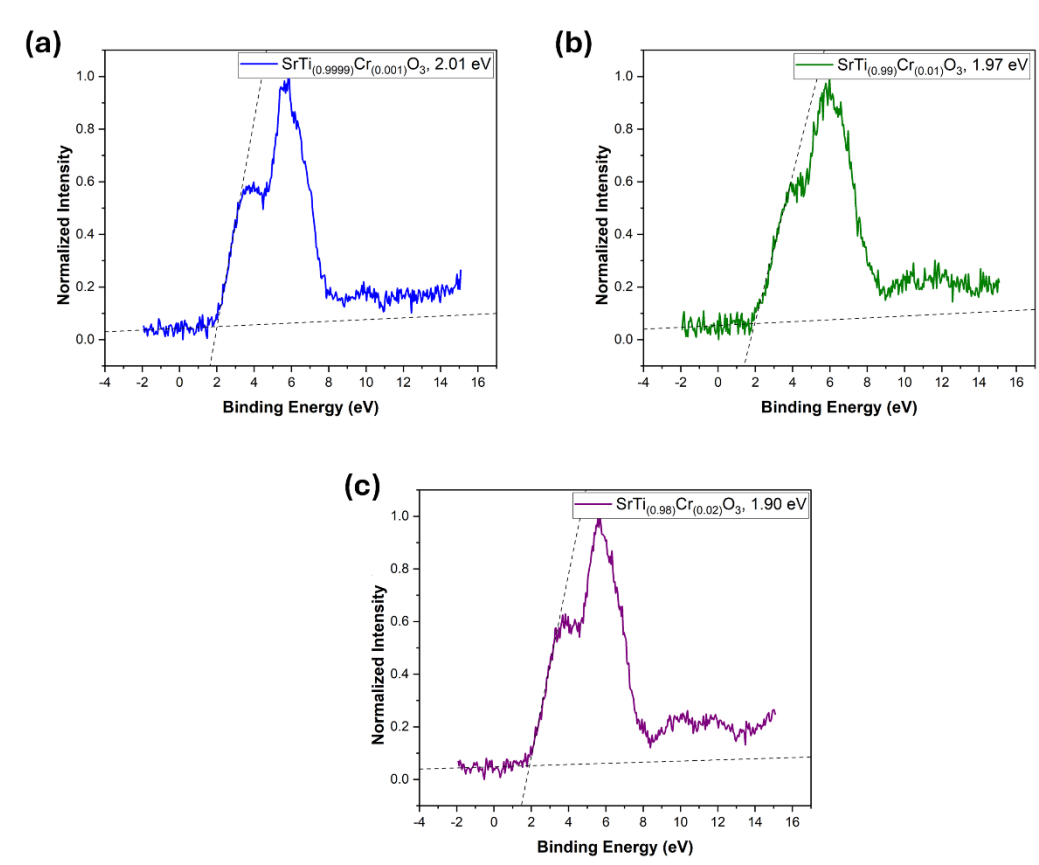


Figure 5.50: *VB_M-Fermi level separation decreases of (a) 0.1 mol% (b) 1 mol% (c) 2 mol% Cr doped $SrTiO_3$ synthesized via the serial dilution method at 800 °C compared to the undoped samples.*

The VB_M position together with the work function are the intrinsic parameters required for the determination of the Band edge energy diagrams of the catalysts. The VB_M-E_F separation values are listed in Table 5.11. The measurement of work function is discussed in detail in the following section.

5.6.3 Work Function

The intensity of the y-axes in figures 5.50-5.54 was measured in counts/sec with arbitrary units (a.u.) from the XPS.

The surface work function of the samples was investigated with the XPS. The doped samples were compared with the undoped $SrTiO_3$. The work function of the undoped $SrTiO_3$ at 900 °C and 800 °C was measured to be measured at 4.18 eV and 4.16 eV respectively on a kinetic energy scale as shown in Figure 5.51. The Cut-off Energy ($E_{cut\text{-}off}$) is the region in the graph which was linearly fitted. The samples were subjected to a bias/photon energy (hν) of 29.47 eV and Eq (2.23) as described in Chapter 2 was used to calculate the work function.

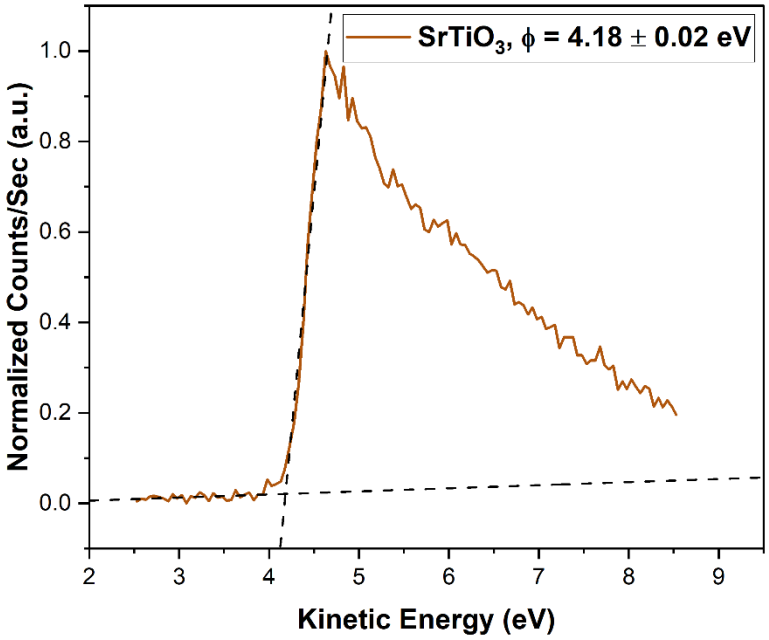


Figure 5.51: *Work function of the undoped $SrTiO_3$ synthesized at 900 °C at 4.18 (± 0.02) eV.*

In the case of the 800 °C and 900 °C annealed sol-gel Pechini monodoped batch, the 2 mol% Cr^{3+} doped sample, the work function shifts to higher kinetic energies as shown in Figure 5.52 (a, b). The co-doped samples for the 800 °C showed only slight variations in work functions as shown in Figure 5.53 (a-d). For the 1 mol% and the 2 mol% La^{3+} co-doped samples at 900 °C, the work functions shift to higher kinetic energies to the undoped sample as shown in Figure 5.54 (a, b). The work function shifts to lower kinetic energies for the 5 mol% and 10 mol% co-doped samples as shown in Figure 5.54 (c, d). The Cr monodoped serial dilution batch shows an increase in work function for the 1 mol% and 2 mol% as shown in Figure 5.55 (b-c). The 0.1 mol% monodoped sample works similarly to the undoped at 800 °C.

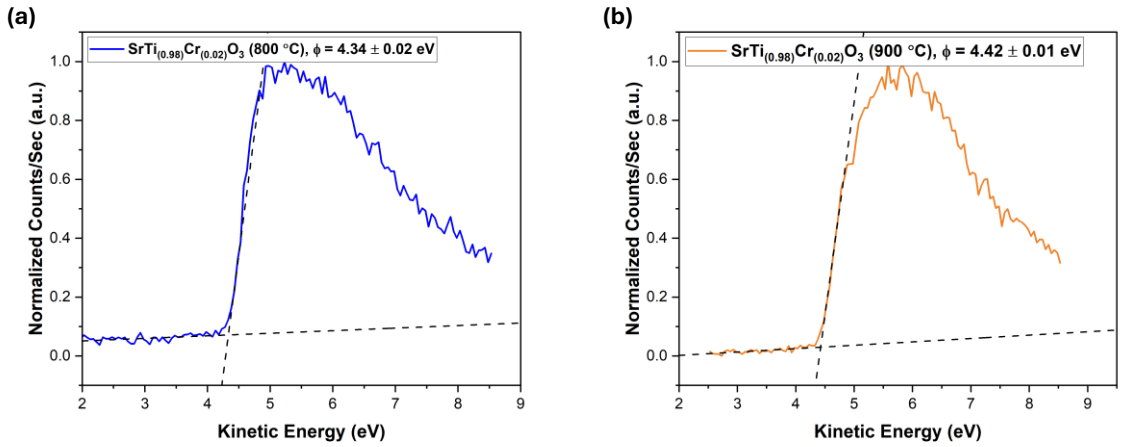


Figure 5.52: *Work function of the 2 mol% Cr^{3+} doped sample synthesized at (a) 800 °C (4.34 ± 0.02 eV) and (b) 900 °C (4.42 ± 0.01 eV) increased compared to the undoped.*

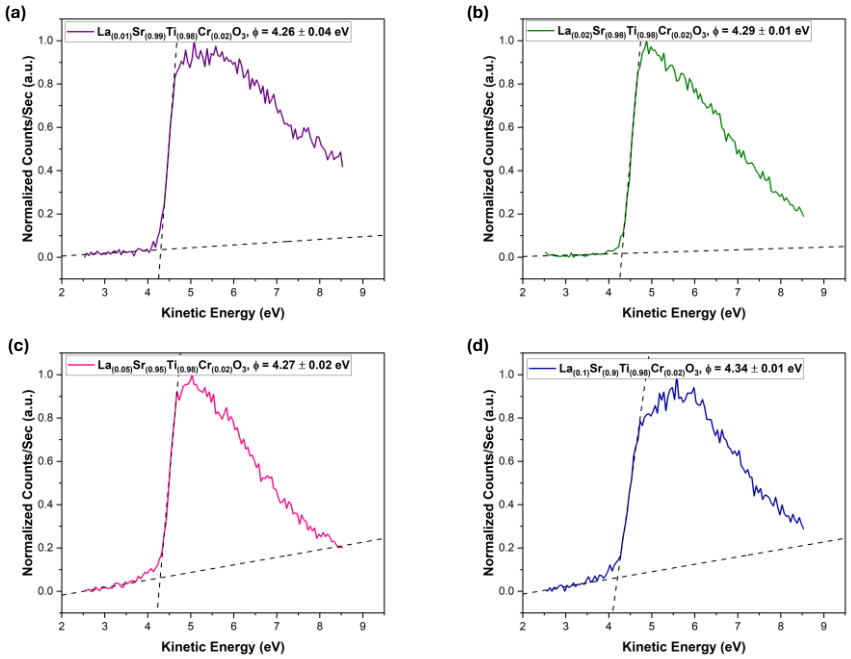


Figure 5.53: *Work function of the (a) 1 mol% (4.26 ± 0.04 eV) (b) 2 mol% (4.29 ± 0.01 eV) (c) 5 mol% (4.27 ± 0.02 eV) (d) 10 mol% La^{3+} co-doped (4.34 ± 0.01 eV) samples synthesized at 800 °C decreases in most samples compared to the 2 mol% Cr monodoped sample at the same temperature.*

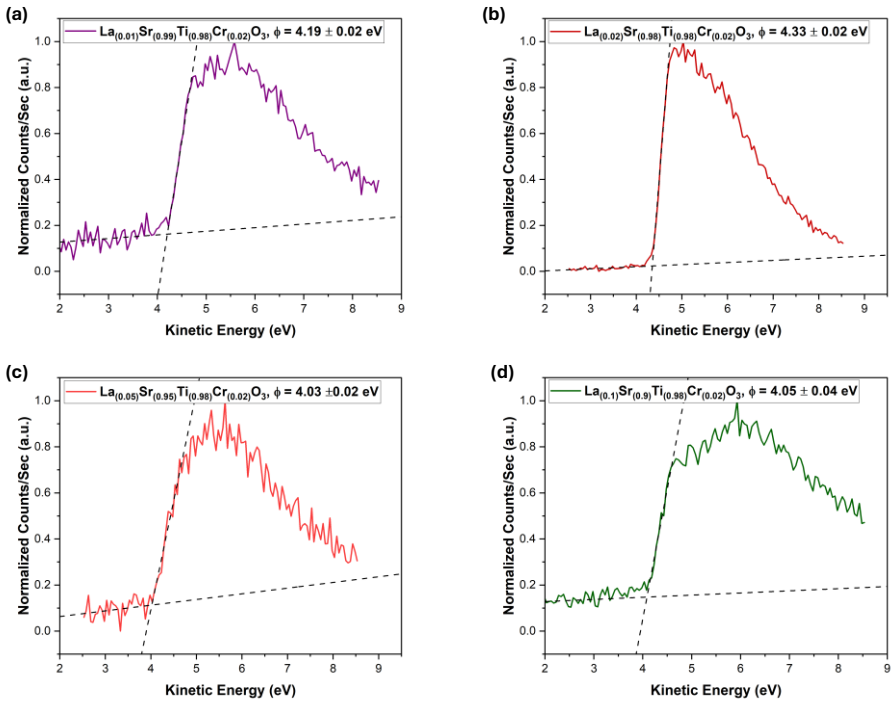


Figure 5.54: *Work function of these samples decreases with (a) 1 mol% (4.19 ± 0.02 eV) (b) 2 mol% (4.33 ± 0.02 eV) (c) 5 mol% (4.03 ± 0.02 eV) (d) 10 mol% La^{3+} (4.05 ± 0.04 eV) co-*

doped samples synthesized at 900 °C compared to the 2 mol% Cr monodoped sample at 900 °C.

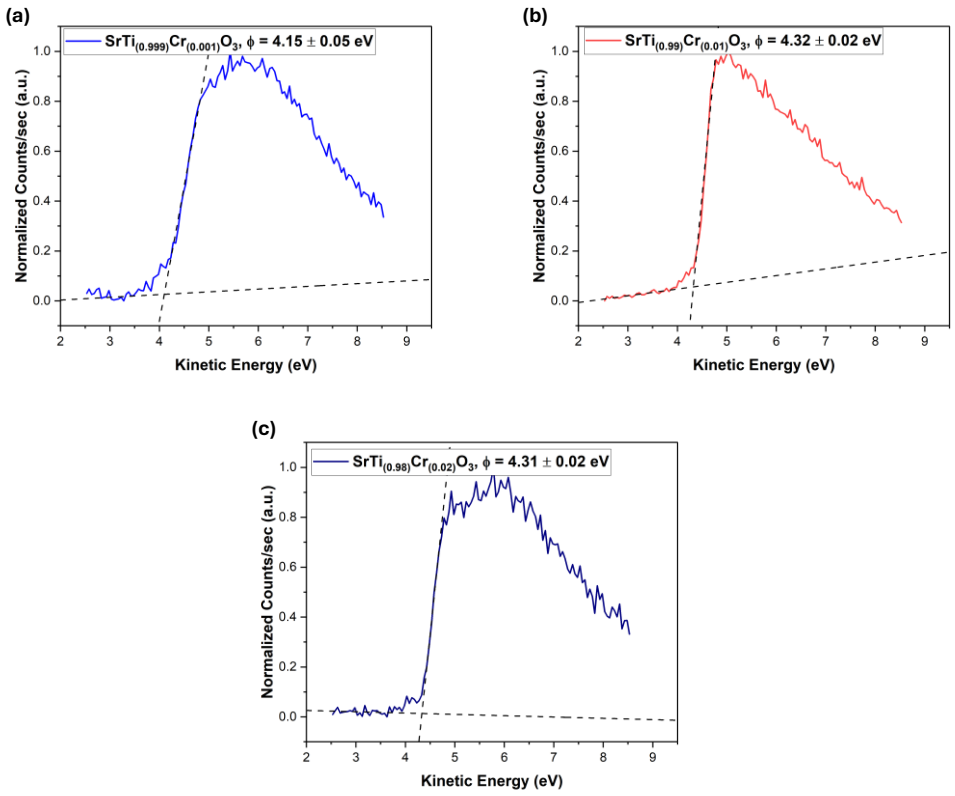


Figure 5.55: *Work function of the (a) 0.1 mol% decreases (b) 1 mol% (c) 2 mol% Cr^{3+} doped samples synthesized at 800 °C with the serial dilution method increases compared to the undoped.*

In both types of doped samples, the work function changed when compared to the undoped. All the samples show one secondary cut-off edge. The work functions of the samples are listed in Table 5.11. The shapes of the work function spectrum also vary from the undoped to the doped samples. The sharp peak for the undoped sample in Figure 5.51 could indicate a clean surface with a homogenous work function distribution throughout the sample [38]. The doped samples (Figures 5.52-5.55) exhibit a more rounded spectrum which could be due to inhomogeneity in the work function distribution in the sample. These inhomogeneities could arise due to the localized states, surface defects or varying surface dipoles introduced upon Cr doping. The effect of surface dipoles on the work function has been discussed in Chapter 2.

The work function of the samples was measured to study the position of the Fermi levels and how they might affect the photocatalytic performance of the samples. To further understand how the work function affects the overall behaviour of the samples, the Band edge energy diagrams were calculated and discussed in the following section.

5.6.4 Band Edge Energy Diagrams from the Work Function, the Band Gap, and the Valence Band Analysis

The band edge energy diagrams of the samples were made from the band gap (E_g) measurements, work function (ϕ) and valence band analysis. From the alignment, the electron affinity (X), and the ionisation potential (IP) were calculated which are depicted in Table 5.11. All the values were calculated from the vacuum level. All band alignment diagrams of the doped samples were made with the indirect band gaps extrapolated from the shifts in the parent $SrTiO_3$ absorption edge of the doped samples as shown in Figures 5.56-5.60.

Table 5.11: Measurement of Work Function (ϕ), Ionisation Potential (IP), and VB_M-E_F Separation from the Band Edge Energy Diagrams in Figures 5.56 – 5.60

Sample	ϕ (eV)	IP (eV)	VB_M-E_F (eV)
$SrTiO_3$, 800 °C	4.18	6.86	2.68
$SrTi_{(0.999)}Cr_{(0.001)}O_3$, Serial Dilution	4.15	6.16	2.01
$SrTi_{(0.99)}Cr_{(0.01)}O_3$, Serial Dilution	4.33	6.30	1.97
$SrTi_{(0.98)}Cr_{(0.02)}O_3$, Serial Dilution	4.31	6.21	1.90
$SrTi_{(0.98)}Cr_{(0.02)}O_3$, 800 °C	4.34	6.35	2.01
$La_{(0.01)}Sr_{(0.99)}Ti_{(0.98)}Cr_{(0.02)}O_3$, 800 °C	4.26	6.04	1.78
$La_{(0.02)}Sr_{(0.98)}Ti_{(0.98)}Cr_{(0.02)}O_3$, 800 °C	4.29	6.28	1.99
$La_{(0.05)}Sr_{(0.95)}Ti_{(0.98)}Cr_{(0.02)}O_3$, 800 °C	4.27	6.18	1.91
$La_{(0.1)}Sr_{(0.9)}Ti_{(0.98)}Cr_{(0.02)}O_3$, 800 °C	4.34	6.20	1.86
$SrTiO_3$, 900 °C	4.18	6.39	2.21
$SrTi_{(0.98)}Cr_{(0.02)}O_3$, 900 °C	4.41	6.46	2.05
$La_{(0.01)}Sr_{(0.99)}Ti_{(0.98)}Cr_{(0.02)}O_3$, 900 °C	4.19	6.17	1.98
$La_{(0.02)}Sr_{(0.98)}Ti_{(0.98)}Cr_{(0.02)}O_3$, 900 °C	4.33	6.72	2.39
$La_{(0.05)}Sr_{(0.95)}Ti_{(0.98)}Cr_{(0.02)}O_3$, 900 °C	4.03	6.42	2.39
$La_{(0.1)}Sr_{(0.9)}Ti_{(0.98)}Cr_{(0.02)}O_3$, 900 °C	4.05	6.00	1.95

From Table 4, the position of CB_{Min} and VB_M were calculated, and the band edge energy diagrams were made. The EA and the IP increased for the 5 mol% and the 10 mol% La^{3+} co-doped (800 °C) samples as compared to the undoped $SrTiO_3$ at 800 °C. These parameters

decreased for the 1 mol% and 2 mol% co-doped samples. For the doped batch at 800 °C, the 2 mol% Cr-doped sample showed the lowest EA and the 1 mol% La^{3+} co-doped sample showed the lowest IP. The EA and IP are the intrinsic parameters that influence the charge carrier mobility. This concept has been discussed in detail in Chapter 4. The EA below a certain limit will give rise to trap limited electron flow and the IP above a certain threshold will give rise to trap limited hole transport.

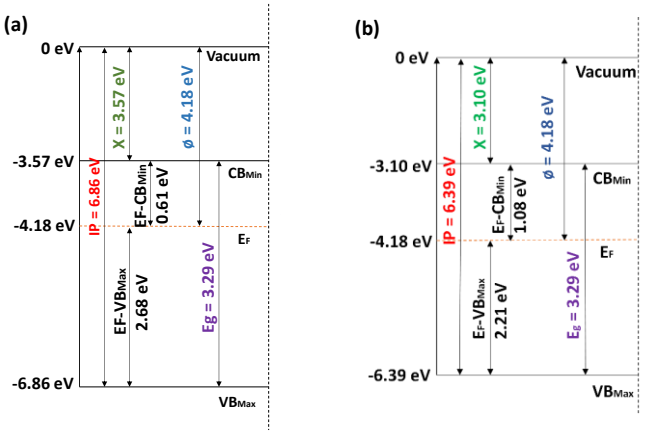


Figure 5.56: *Band edge energy diagrams of undoped $SrTiO_3$ synthesized at (a) 800 °C (b) 900 °C.*

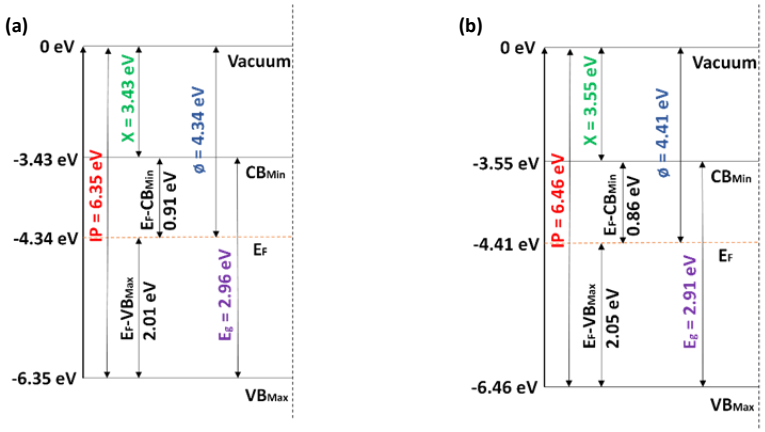


Figure 5.57: *Band edge energy diagrams of 2 mol% Cr^{3+} doped $SrTiO_3$ synthesized via sol-gel Pechini at (a) 800 °C for 10 h (b) 900 °C for 6 h.*

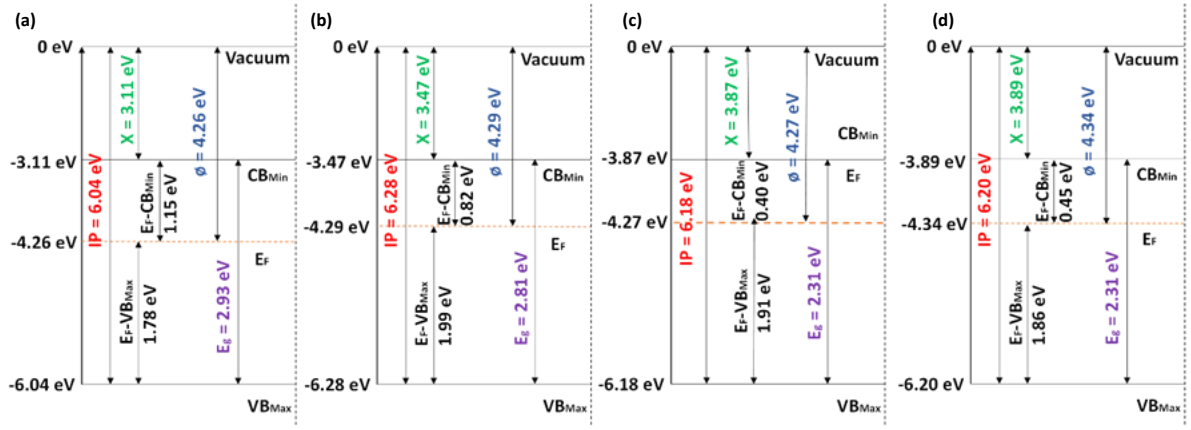


Figure 5.58: *Band edge energy diagrams of (a) 1 mol% La^{3+} (b) 2 mol% La^{3+} (c) 5 mol% La^{3+} (d) 10 mol% La^{3+} co-doped $SrTiO_3$ synthesized at 800 °C (10 h).*

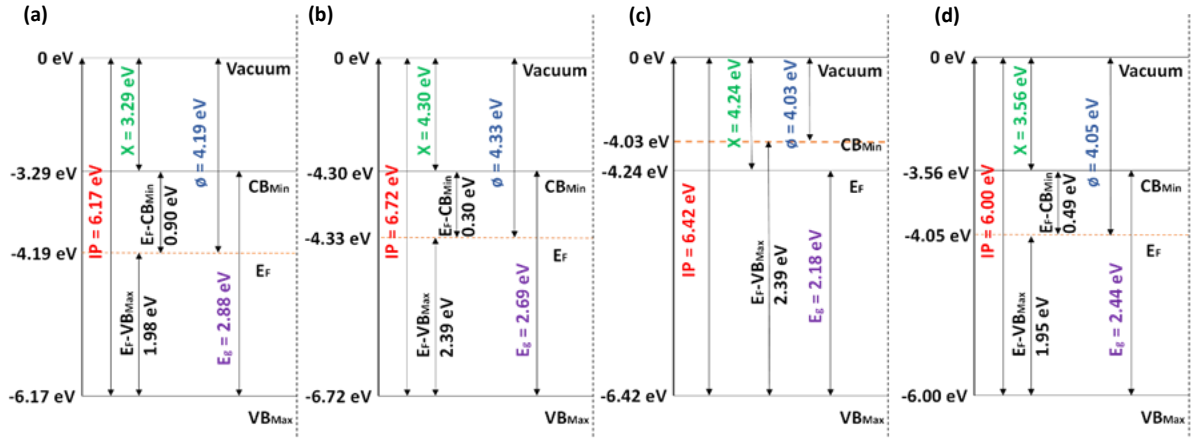


Figure 5.59: *Band edge energy diagrams of (a) 1 mol% La^{3+} (b) 2 mol% La^{3+} (c) 5 mol% La^{3+} (d) 10 mol% La^{3+} co-doped $SrTiO_3$ synthesized at 900 °C (6 h).*

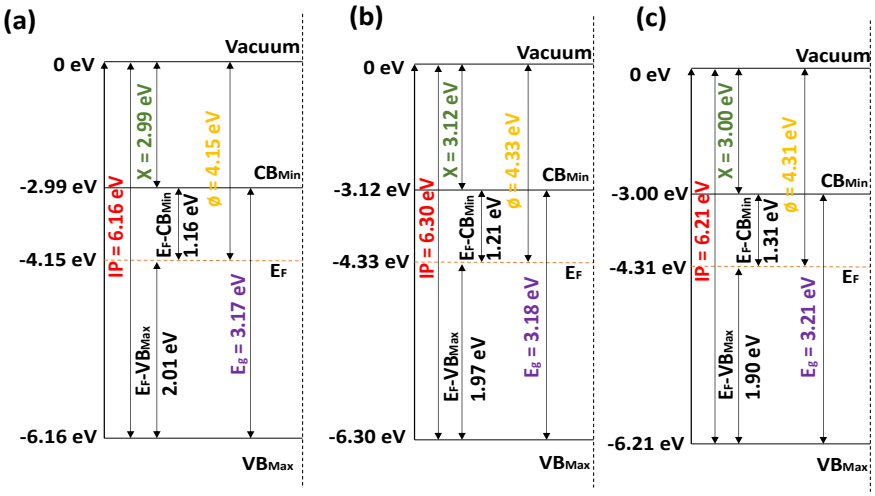


Figure 5.60: *Band edge energy diagrams of (a) 0.1 mol% (b) 1 mol% (c) 2 mol% Cr^{3+} doped $SrTiO_3$ synthesized via the serial dilution method at 800 °C (10 h).*

From the 800 °C batch, the 5 mol% co-doped sample showed the highest n-type conductivity (Figure 5.58). In Figure 5.59 (c), for the 5 mol% co-doped (900 °C) sample, the Fermi level lies above the $CB_{Min.}$ This indicates that the 5 mol% co-doped sample will likely be a degenerate semiconductor. Repeat characterizations confirmed the observed degeneracy in this sample. Hence, the low TCSPC lifetime compared to the other samples (discussed in the subsequent section). All the doped samples exhibit a shift in band positions as seen in the above diagrams. From the band positions, it is apparent that the samples exhibit n-type conductivity though with varying degrees (Figures 5.56-5.60). The 2 mol% La^{3+}:$SrTiO_3$ shows the highest n-type conductivity in the 900 °C co-doped batch (Figure 5.59). At 900 °C, the 2 mol% Cr^{3+} doped sample exhibits a lesser n-type nature than the co-doped samples. With the increase in La^{3+} co-doping, the Fermi level is pushed towards the $CB_{Min.}$ Reunchan, P. et al. [39] in their DFT study on Cr-doped $SrTiO_3$ concluded that a lower oxidation state of Cr is desirable for higher photocatalytic activity due to the absence of electron trapping centres near the CB_{Min}. This happens when the shifting of the Fermi level towards the CB_{Min} stabilizes the Cr at the Ti site. From Figures 5.56-5.60, Cr and La, Cr doped samples exhibit n-type conductivity. Under such conditions, the Cr at the Ti (i.e. Cr_{Ti}^{-}) site acts as an acceptor with fully occupied t_{2g} states above the VB_M. These act as electron sources upon photo-excitation. In the 2 mol% Cr monodoped and the 1 mol% La^{3+} co-doped samples of both temperature batches, the Fermi level lies away from the CB_{Min} as compared to the other doped samples. In these samples, the Cr_{Ti} might be present as the neutral Cr_{Ti}^{0} state which causes the ti_{2g} to split and be partially occupied. This might facilitate the formation of Cr^{6+} states [39]. Hence, the 2 mol% monodoped and 1 mol% La^{3+} co-doped samples are red. For the serial dilution series (Figure 5.60 (a-c)), the Fermi level shifts away from the CB_{Min} with an increase in mol% doping with the E_F-CB_{Min} of the 2 mol% sample being the highest. The colour of this sample (red) corresponds to the 2 mol% Cr and 1 mol% La^{3+} co-doped samples prepared via the sol-gel Pechini. The splitting and the partial occupation of the t_{2g} facilitating the Cr^{6+} states can be inferred in the 2 mol% monodoped SD sample. The higher n-type conductivity in the other samples could be from the oxygen vacancies (V_O) acting as electron donors. The presence of V_O will be discussed in detail in the PL analysis section.

5.6.5 Band Edge Alignment for Water Redox Potential

Band edge alignment is required to determine the photocatalytic activity. For the best photoelectrocatalytic water splitting, the band gap of the material should be straddling the water redox potential of 1.23V. The redox water potentials are at -4.5 eV for $E(H^+/H_2)$ and -5.73 eV for $E(O_2/H_2O)$ on the vacuum scale [5]. The band edge alignment for the water redox potentials was calculated as shown in Figure 5.60 with data from Figures 5.56-5.60. The Cr^{3+} and Cr^{6+} states were added to the alignment from the Kubelka Munk analysis in Figures 5.40-5.44.

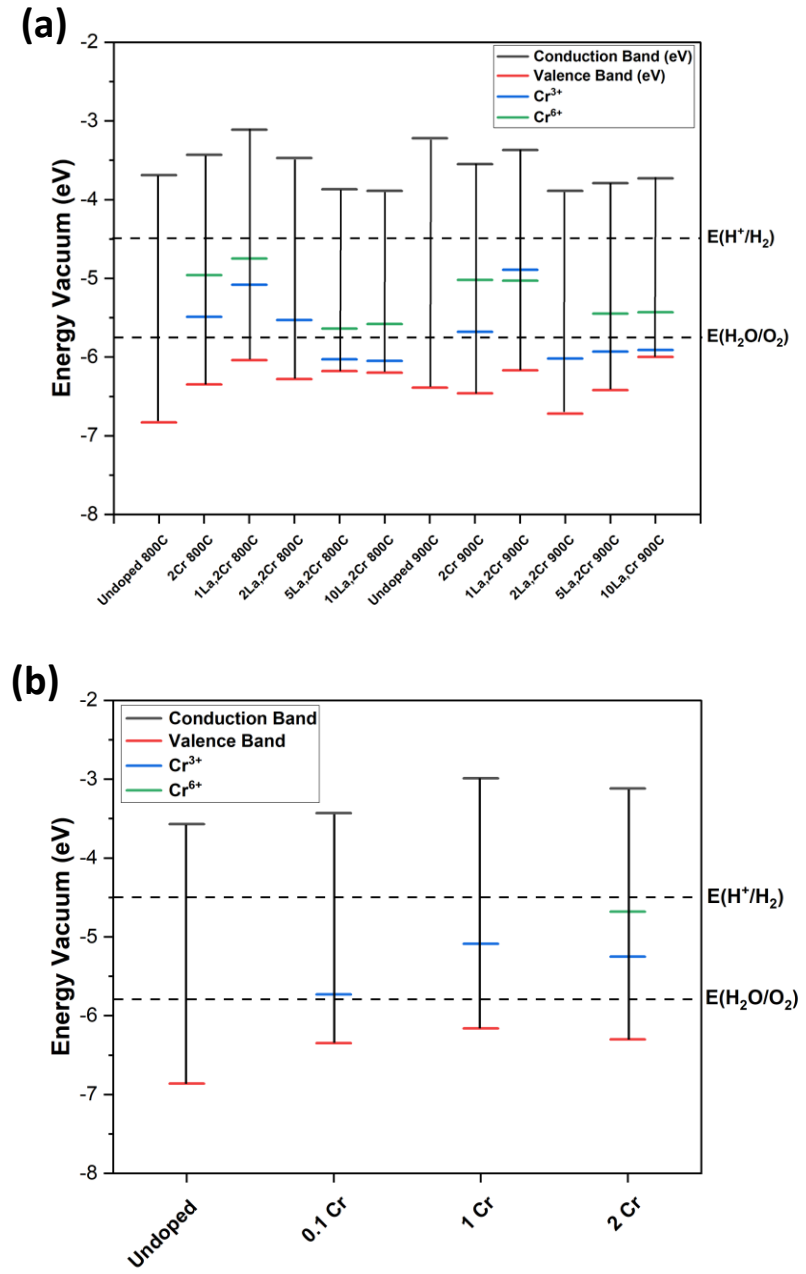


Figure 5.61: *Band Edge Alignment for Water Redox Potentials of (a) undoped and Cr^{3+}-La^{3+} doped samples synthesized at 800 °C and 900 °C (b) Cr monodoped $SrTiO_3$ prepared via the serial dilution method at 800 °C.*

On Cr doping, new states were introduced in the band gap as seen in Figure 5.61 (a, b). Cr^{3+} occupies a state around 2 eV below the CB_{Min} [18], [19], [22]. In the Ph.D. study, in most of the Cr-La co-doped samples, the Cr^{3+} has occupied around 2 ± 0.14 eV below the CB_{Min} consistent with the literature. Empty Cr^{6+} with d^0 configuration are present above the Cr^{3+} in the band gap. These states behave as traps for electrons moving from Cr^{3+} to Ti^{4+}. In the 2 mol% La^{3+} co-doped samples, these trap states are suppressed. In the 1 mol% La^{3+} co-doped sample, the Cr^{3+} state is found higher than the trap state and therefore, could facilitate easier charge migration to CB. All the doped samples exhibit bandgap reduction. For the serial

dilution samples in Figure 5.61(b), the 0.1 mol% and 1 mol% doped sample exhibit only Cr^{3+} states about 2 ± 0.18 eV below the CB_{Min}. The 2 mol% doped sample shows the existence of the Cr^{6+} states above the Cr^{3+} within the bandgap of the material. The presence of Cr^{6+} (d^0 configuration) could act as a trap for the charge transfer from the Cr^{3+} level to the CB.

The presence of trap states can be detrimental to the mobility of the charge carriers. To understand the charge carrier mobility and dynamics, TCSPC and the room temperature steady-state PL spectroscopy were carried out. The findings of these characterization techniques are discussed in the following section.

5.6.6 Time Co-related Single Photon Counting (TCSPC)

Time-resolved PL spectroscopy via TCSPC is essential for measuring the recombination lifetimes of the samples. The weighted average lifetimes of the samples were measured from the exponential fitting via the TCSPC software Horiba DA.6 which are tabulated below in Table 5.12 and shown in Figures 5.62-5.63.

Table 5.12: Average lifetime of the Cr (co-) doped samples

Samples	T_1 (s)	T_2 (s)	T_3 (s)	Average Lifetimes (ns)	χ^2
$SrTiO_3$, 800 °C	1.92E-09	3.60E-08	7.52E-11	0.16 ± 0.04	1.31
$SrTi_{(0.999)}Cr_{(0.001)}O_3$, Serial Dilution	5.50E-09	2.01E-10	2.49E-07	0.68 ± 0.02	1.66
$SrTi_{(0.99)}Cr_{(0.01)}O_3$, Serial Dilution	5.48E-09	2.54E-07	1.98E-10	0.77 ± 0.01	1.77
$SrTi_{(0.98)}Cr_{(0.02)}O_3$, Serial Dilution	1.59E-10	5.14E-09	2.31E-07	0.43 ± 0.02	1.45
$SrTi_{(0.98)}Cr_{(0.02)}O_3$, 800 °C	1.79E-09	8.37E-11	8.37E-11	0.16 ± 0.03	1.28
$La_{(0.01)}Sr_{(0.99)}Ti_{(0.99)}Cr_{(0.02)}O_3$, 800 °C	1.43E-09	3.26E-08	1.11E-10	0.25 ± 0.02	1.35
$La_{(0.02)}Sr_{(0.98)}Ti_{(0.98)}Cr_{(0.02)}O_3$, 800 °C	1.74E-09	3.46E-08	8.60E-11	0.19 ± 0.01	1.38
$La_{(0.05)}Sr_{(0.95)}Ti_{(0.95)}Cr_{(0.02)}O_3$, 800 °C	1.70E-09	3.31E-08	7.88E-11	0.15 ± 0.03	1.38
$La_{(0.1)}Sr_{(0.9)}Ti_{(0.95)}Cr_{(0.02)}O_3$, 800 °C	1.58E-09	3.31E-08	9.56E-11	0.21 ± 0.01	1.34
$SrTiO_3$, 900 °C	1.94E-09	8.41E-11	3.54E-08	0.18 ± 0.03	1.32
$SrTi_{(0.98)}Cr_{(0.02)}O_3$, 900 °C	1.31E-09	3.19E-08	1.04E-10	0.24 ± 0.01	1.37
$La_{(0.01)}Sr_{(0.99)}Ti_{(0.98)}Cr_{(0.02)}O_3$, 900 °C	1.73E-09	3.22E-08	9.54E-11	0.19 ± 0.01	1.28

$La_{(0.02)}Sr_{(0.98)}Ti_{(0.98)}Cr_{(0.02)}O_3$, 900 °C	1.85E-09	3.38E-08	8.93E-11	0.18 ± 0.02	1.42
$La_{(0.05)}Sr_{(0.95)}Ti_{(0.98)}Cr_{(0.02)}O_3$, 900 °C	7.99E-11	1.50E-09	3.19E-08	0.16 ± 0.01	1.39
$La_{(0.1)}Sr_{(0.9)}Ti_{(0.98)}Cr_{(0.02)}O_3$, 900 °C	1.81E-09	3.39E-08	8.69E-11	0.18 ± 0.01	1.37
$Cs_{(0.01)}Sr_{(0.99)}Ti_{(0.98)}Cr_{(0.02)}O_3$, 800 °C	1.24E-09	1.04E-08	3.28E-11	0.05 ± 0.08	1.07
$Cs_{(0.02)}Sr_{(0.98)}Ti_{(0.98)}Cr_{(0.02)}O_3$, 800 °C	1.24E-09	4.25E-11	1.02E-08	0.06 ± 0.10	1.12
$Cs_{(0.05)}Sr_{(0.95)}Ti_{(0.98)}Cr_{(0.02)}O_3$, 800 °C	1.22E-09	1.06E-08	3.65E-11	0.06 ± 0.12	1.04
$Cs_{(0.01)}Sr_{(0.99)}Ti_{(0.98)}Cr_{(0.02)}O_3$, 900 °C	7.90E-11	1.38E-09	2.13E-08	0.12 ± 0.01	1.16
$Cs_{(0.02)}Sr_{(0.98)}Ti_{(0.98)}Cr_{(0.02)}O_3$, 900 °C	1.43E-09	8.02E-11	1.99E-08	0.11 ± 0.01	1.22
$Cs_{(0.05)}Sr_{(0.95)}Ti_{(0.98)}Cr_{(0.02)}O_3$, 900 °C	8.34E-11	1.51E-09	2.19E-08	0.13 ± 0.02	1.22

From Table 5.12 and Figure 5.62 (a-d), the 1 mol% La^{3+} co-doped sample synthesized at 800 °C shows the highest lifetime at 0.25 ns in that series. The 2 mol% Cr^{3+} doped $SrTiO_3$ synthesized at 900 °C closely follows the 1 mol% co-doped sample at 0.24 ns. All the Cr monodoped samples synthesized via the serial dilution method show higher lifetimes compared to the undoped and co-doped samples as shown in Figure 5.63 (a-d). A longer lifetime generally indicates a better probability of charge migration to catalytically active regions before recombination occurs. This increases the efficiency of the photocatalyst. Hence, from this analysis, it could be speculated that the serial dilution series doped samples might better perform than the rest. All the Cs^{+1} co-doped samples exhibit lower lifetimes than the undoped as seen in Figure 5.63(c, d).

From the TCSPC analysis, a contradictory result can be observed from that of the literature. As discussed above, the presence of Cr^{6+} suppresses photocatalytic performance. From Figure 5.62(a) and (b), the 1 mol% La^{3+} at 800 °C and 2 mol% Cr^{3+} at 900 °C doped samples show higher lifetimes. The occurrence of Cr^{6+} states in both samples is higher than in the other doped samples.

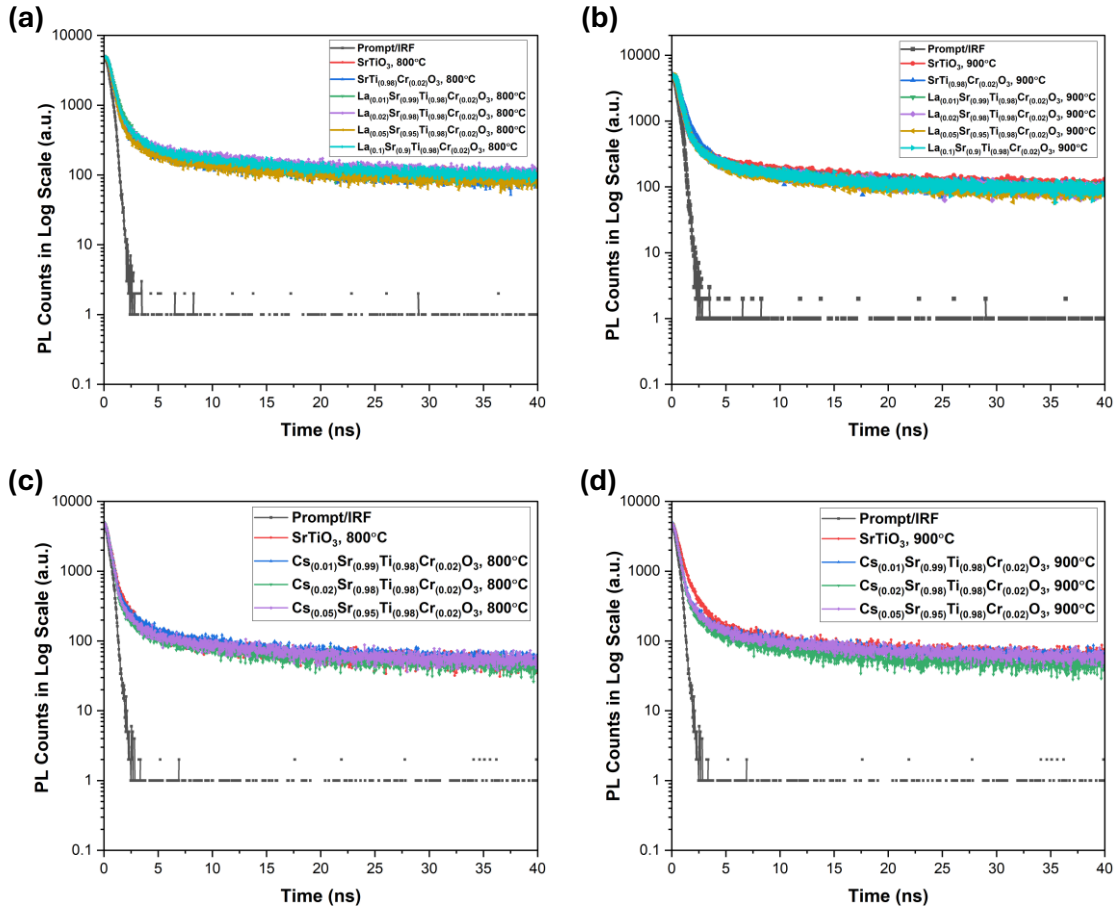


Figure 5.62: *Average Lifetimes of the doped samples (a) La^{3+}, Cr^{3+} samples annealed at 800 °C for 10 h (b) La^{3+}, Cr^{3+} samples annealed at 900 °C for 6 h (c) Cs^{1+}, Cr^{3+} samples annealed at 800 °C for 10 h (d) Cs^{1+}, Cr^{3+} annealed at 900 °C for 6 h. Most of the co-doped samples did not show significant changes in lifetimes compared to the undoped samples.*

For the Cr-doped sample from the serial dilution series, the 0.1 mol% and 1 mol% samples have the highest lifetimes of all the samples as seen in Figure 5.63 (a, b). Neither of these samples demonstrates Cr^{6+}. The 2 mol% doped sample (Figure 5.63 (c)) with lower lifetimes exhibits Cr^{6+} trap states which could obstruct the mobility of the charge carriers leading to faster recombinations.

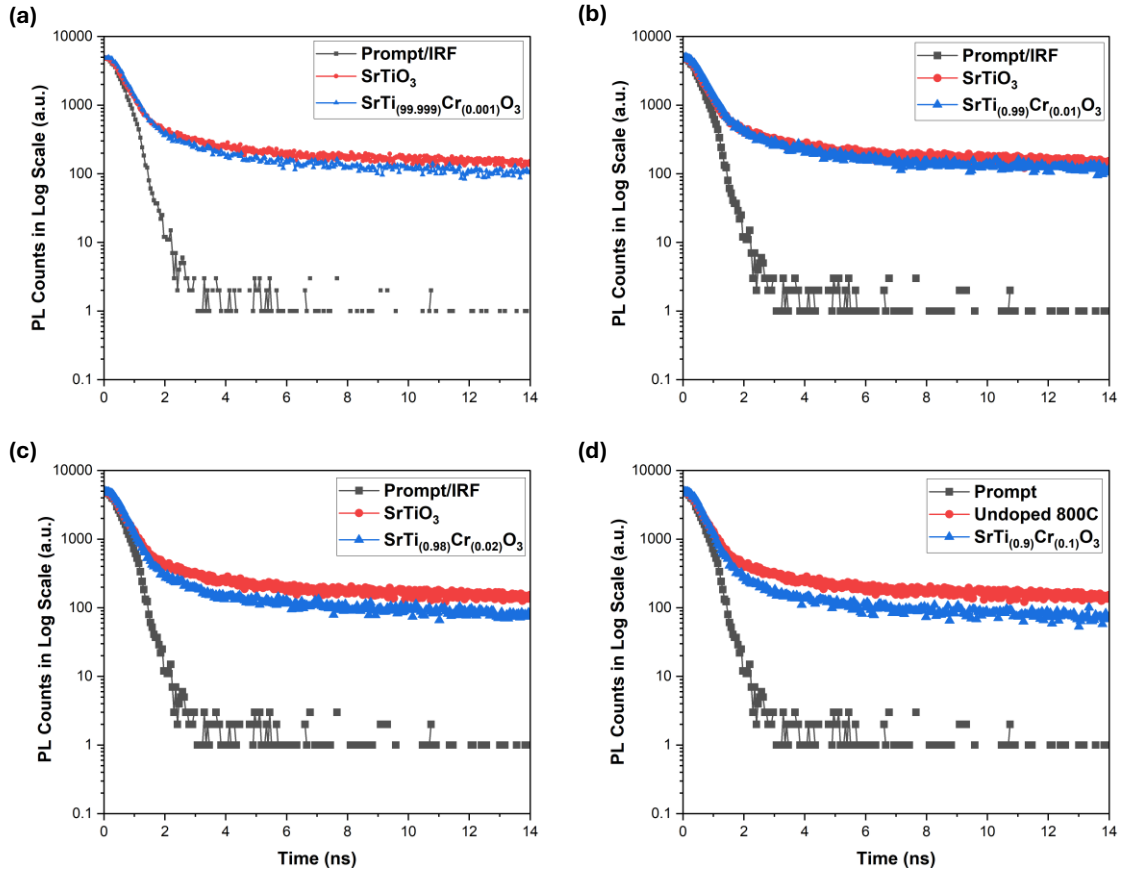


Figure 5.63: *Average lifetimes of the (a) 0.1 mol% (b) 1 mol% (c) 2 mol% (d) 10 mol% monodoped serial dilution series. This batch showed a significant increase in the lifetimes of the doped samples with 1 mol% showing the longest.*

To facilitate the understanding of the recombination dynamics in the Cr monodoped and co-doped samples, steady-state PL was performed at room temperature and is discussed in the following section.

5.6.7 Room Temperature Steady State Photoluminescence Analysis (PL)

PL analysis of the samples was carried out to understand the defects and the recombination dynamics of the samples. The PL was carried out with excitation at 282 nm (4.4 eV). The main emission spectrum of the doped samples consist of the parent $SrTiO_3$ broad peak but with decreasing PL intensity. The decrease in the PL intensity as shown in Figure 5.64 (a-f) indicates the suppression of radiative pathways and an increase in non-radiative recombinations. The non-radiative pathways could be from Cr^{6+} trap states or intrinsic $SrTiO_3$ defects such as Ti^{3+} and oxygen vacancies. Between the Cr monodoped samples, the 900 °C synthesized sample shows a lower PL intensity (figure 5.64 (a)). In the La^{3+} co-doped series, 1 mol% La^{3+} co-doped samples show the lowest PL intensity in their respective temperature group (Figure 5.64 (b, c)). In the Cs^{+1} co-doped series, the 2 mol% co-doped samples at 800 °C and 900 °C show a lower PL intensity (Figure 5.64 (d, e)). The PL intensity decreases linearly with increased mol% doping for the SD series samples (Figure 5.64(f)). In the previous chapters, the type of bandgap of the materials was determined from the PL. Here, the doped samples with higher

non-radiative recombination pathways demonstrate indirect bandgaps. The band edge energy diagrams of the doped samples were calculated considering an indirect bandgap.

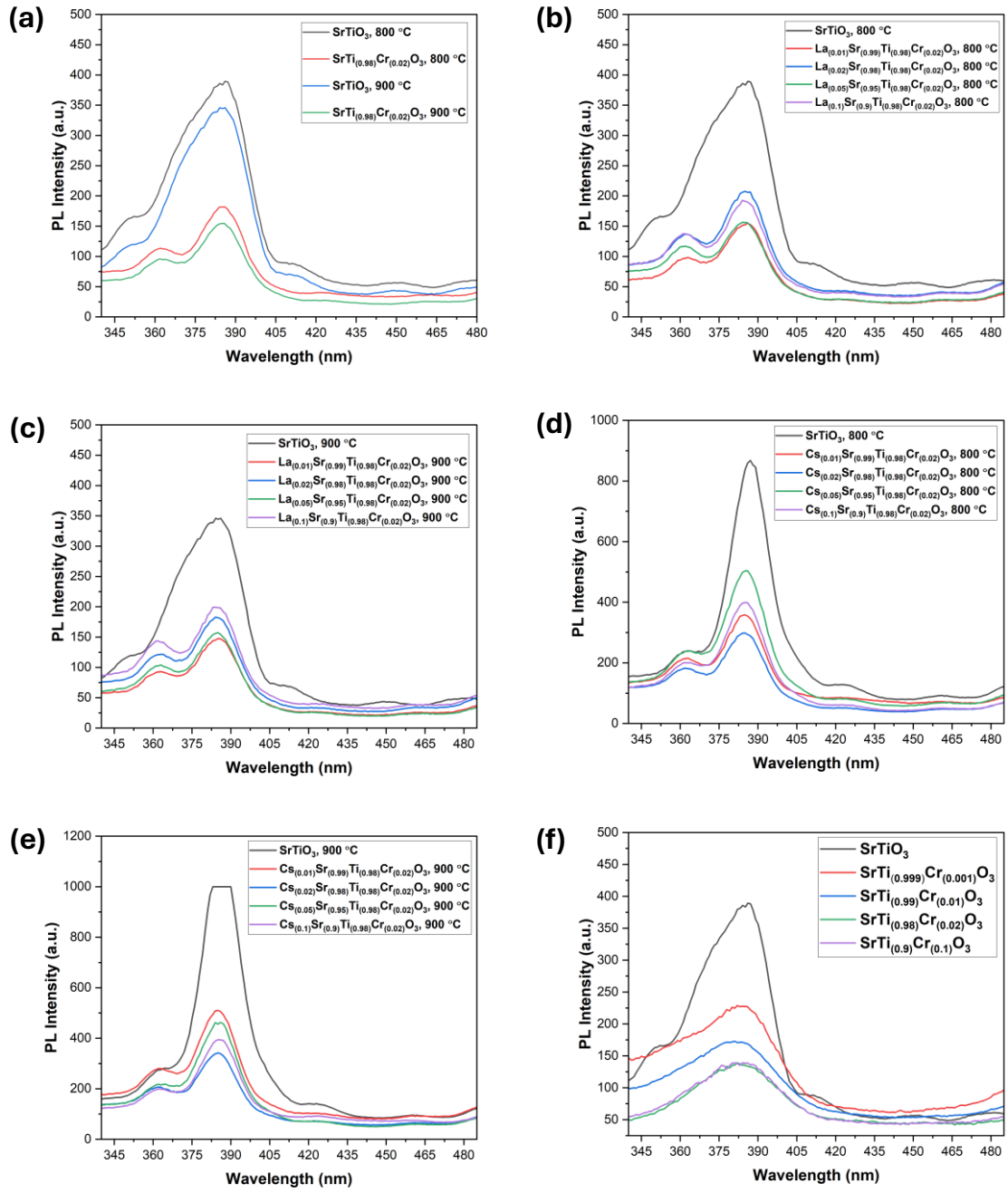


Figure 5.64: *Room temperature PL spectrum of (a) Cr monodoped samples synthesized with the sol-gel Pechini at 800 °C and 900 °C (b) La^{3+} co-doped at 800 °C (c) La^{3+} co-doped at 900 °C (d) Cs^{1+} co-doped at 800 °C (e) Cs^{1+} co-doped at 900 °C (f) Cr monodoped samples synthesized with the serial dilution method at 800 °C. All the (co-) doped samples (a-f) synthesized with the standard sol-gel Pechini showed lower PL intensity indicating higher non-radiative recombination pathways.*

Deconvolution of the PL spectrum of the undoped $SrTiO_3$ exhibits the multiple peaks related to the oxygen vacancies as discussed in the previous chapters. The doped samples show clear bifurcation between peaks at 363 nm (3.43 eV) and 385 nm (3.22 eV). The other oxygen vacancy-related peaks are present at 424 nm (2.93 eV), 463 nm (2.68 eV), and 490 nm (2.53 eV). The n-type conductivity from the band edge energy diagrams (Figures 5.56-5.60) aligns with the presence of oxygen vacancies and can create localized states within the bandgap of the samples[40]. The PL peak around 385 nm in all the samples may indicate the phonon-assisted transition between the valence to conduction band as near band edge emission (NBE). In the Ga^{3+} doped $SrTiO_3$ samples (Chapters 3-4), the emission around 363 nm was speculated to be due to the e_g states of Ti^{3+}. The presence of intrinsic defects such as the Ti^{3+} aligns with the increase in the non-radiative recombination pathways (or decrease in PL intensity). The chosen excitation wavelength for the samples gives information regarding the inherent defect levels of the parent $SrTiO_3$.

In Figure 5.61, the band edge alignment show the impurity levels introduced in the band gap from extrapolation from the Kubelka Munk absorption diagrams (Figures 5.40-5.44). Cr^{6+} (d^0 configuration) added states ~ 1.6 eV (±0.1 eV) below the CB_{Min} in the synthesized samples. The Cr^{3+} (d^3 configuration) added states ~ 2 eV (±0.14 eV) or 1 eV (±0.15 eV) respectively above the VB_M. As discussed previously, the 600 nm to 700 nm region in the absorption spectrum indicates a transition between $4A_{2g}$ to $4t_{2g}$ in octahedral Cr^{3+} units. Vibronic coupling allows the forbidden d-d transition by breaking the Laporte selection rules when the crystal field gets momentarily distorted by lattice vibrations. This could be why the transitions between $4A_{2g}$ to $4t_{2g}$ in Cr^{3+} (600nm to 700nm absorption region) are observed. This transition allows weak absorption and PL spectrum.

The weaker emission peak around 363nm in the PL spectrum could be due to shallow, e_g states of Cr^{6+} from the octahedral splitting of the d-orbital. Due to their proximity to the CB_{Min}, these states can facilitate the trapping of electrons and releasing them back to the CB_{Min}. Therefore, these states could be inferred to be promoting the transport of electrons which led to the increase in performance towards OER in the PEC performances discussed in the next section. The presence of non-radiative recombination pathways observed with the decrease in PL intensity in the doped samples could also justify the presence of t_{2g} states from defect states such as Ti^{3+}. In this case, there is a possibility of overlap of t_{2g} states from the Cr^{6+} and Ti^{3+} states. The PL defect energy level is shown in Figure 5.64.

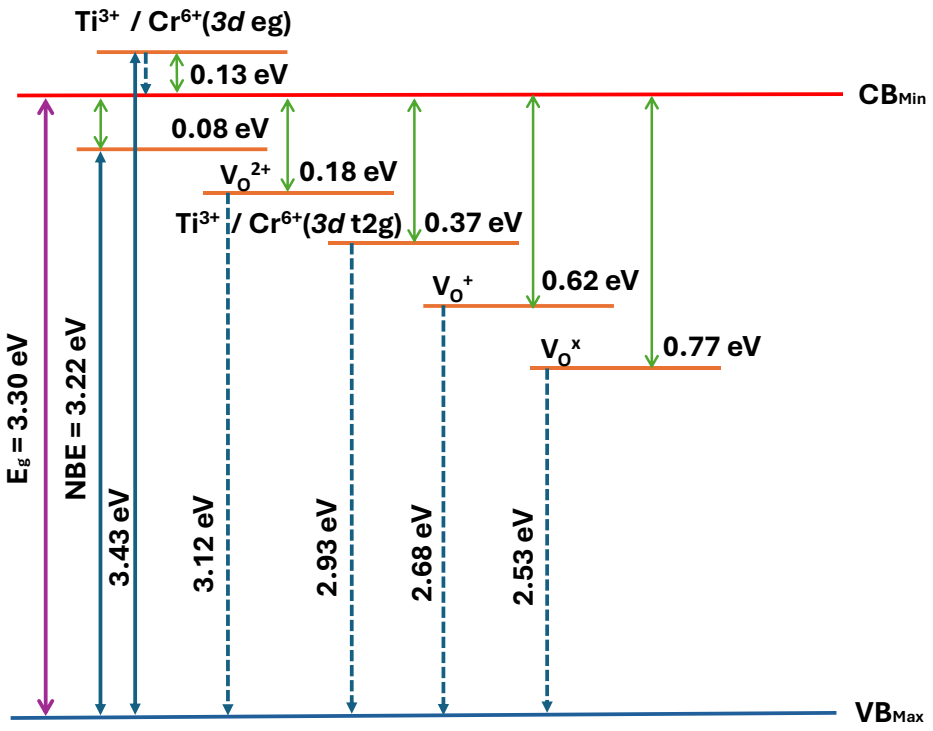


Figure 5.65: *PL Defect Energy Level in Cr: $SrTiO_3$.*

5.7 Performance Assessments

In this section, the PEC measurements were studied to assess how the materials perform. The properties of the materials were determined from the characterization techniques and correlated to the PEC analysis.

5.7.1 Photoelectrochemical Measurements

Cr^{3+} doping can induce visible light absorption and increase the performance of the photo-electrocatalysts. Cr^{6+} trap states which can be detrimental to photocatalysis are often formed along with the Cr^{3+} states. In the Cr samples synthesized in this Ph.D. work, there is ample evidence of the formation of these trap states**.** PEC testing was done to understand how Cr with different oxidation states affects the performance. Linear sweep voltammetry tests were carried out in 1M KOH (pH= 13.6) with Ag/AgCl (Sat. KCl) as the reference electrode and the Pt wire as the counter electrode at a 0.02 V/s scan rate under chopped AM1.5G illumination. No UV filters were used and the backside (FTO) of the electrodes was illuminated. The samples were doctor-bladed on 2cm x 5cm FTO glass as working electrodes. For the PEC, 10 samples from two batches i.e. La^{3+} and SD series were selected. From the La^{3+} co-doped series at each temperature, the 2 mol% Cr and 2 mol% La, Cr were selected as shown in Figure 5.66(a, b). These two samples provide suitable conditions that fulfil the objective of this study of oxidation state effects on equivalent mono- and co-doping effects. All the samples of the SD series were studied for the nominal doping effects as shown in Figure 5.67 (a, b).

The photoresponse and the anodic current density show the effect of Cr^{6+} on the synthesized samples. Figure 5.66(a, b) shows the higher current density of the 2 mol% Cr doped $SrTiO_3$ towards OER. As discussed earlier, a higher concentration of Cr^{6+} (d^0-configuration) can harm

the photocatalytic activity. In the 2 mol% Cr samples (800 °C and 900 °C) from Table 5.5, the ratio of Cr^{6+} is higher than the co-doped samples. From the absorption spectrum in Figures 5.40(c) and 5.41(c), the 2 mol% La^{3+} co-doped samples showed the highest suppression of these states.

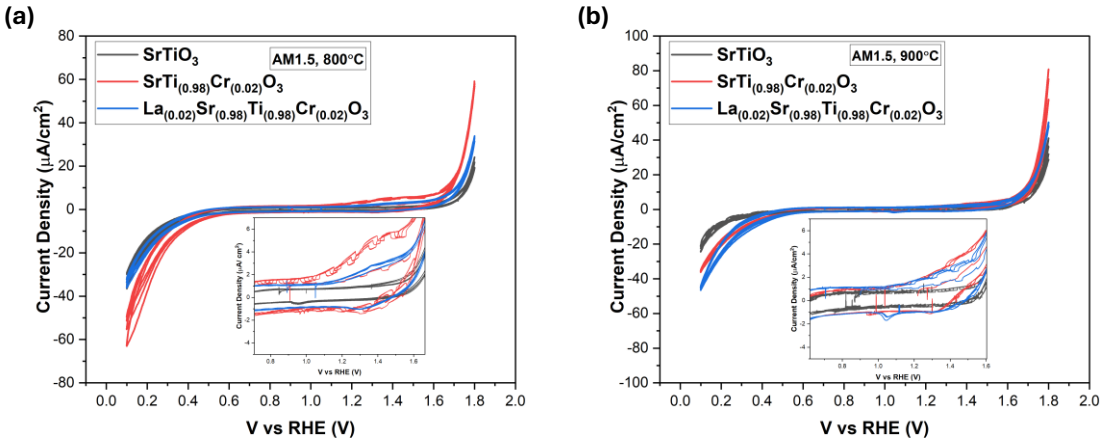


Figure 5.66: *(a) CV of Cr and La co-doped samples synthesized at 800 °C (b) CV of Cr and La co-doped samples synthesized at 900 °C. All the samples were illuminated with chopped AM1.5G light. In both cases, the 2 mol% showed higher anodic OER performance. The doped samples do not show significant photoresponse due to insufficient suppression of the Cr^{6+} and intrinsic defects.*

In both the temperature cases, the 2 mol% Cr showed higher performance in current density towards oxidation. The 2 mol% Cr sample at 800 °C also shows higher performance towards HER. The Cr monodoped samples have a higher Cr^{6+} ratio. These samples however show lower photoresponse. The Cr monodoped samples with nominal doping (SD series) were then tested to verify these findings and the results are shown in Figure 5.67 (a, b).

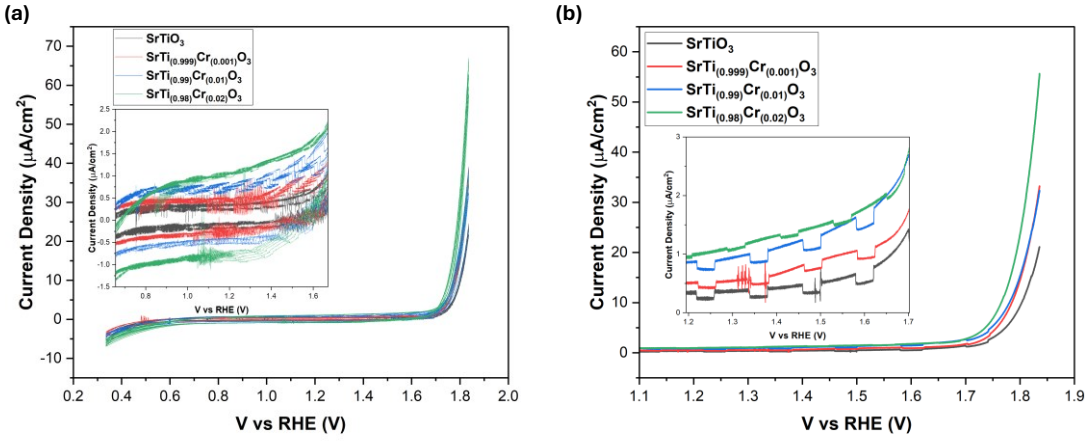


Figure 5.67: *(a) CV of Cr SD series synthesized at 800 °C (b) LSV of the samples. All the samples were illuminated with AM1.5G light and demonstrated higher anodic performance with an increase in doping the 1 mol% Cr monodoped SD sample (highest TCSPC lifetime,*

Figure 5.62 (b)) showed the highest photoresponse due to the absence of Cr^{6+} states and maximum suppression of Ti^{3+} states.

2 mol% Cr monodoped sample in the SD series shows higher current density than the 0.1 mol% and the 1 mol% doped sample (Figure 5.67(a, b)). From the XPS analysis, the 2 mol% doped sample shows a higher presence of Cr^{6+} as seen in Figure 5.23(c). This confirms that the presence of Cr^{6+} facilitated the performance of the samples. The photoresponse of the 1 mol% sample is the highest among all the samples. The calculated photocurrents of the undoped, 0.1 mol%, 1 mol%, and 2 mol% Cr doped samples are 0.17, 0.14, 0.22, and 0.10 μA. The higher photoresponses of the 1 mol% sample can be due to the better charge carrier separation and mobility as confirmed by the TCSPC lifetimes in Table 5.12. This SD sample showed the highest lifetime with 0.773 ns aligning with the higher photoresponse in this series. The lifetimes of the standard sol-gel Pechini samples are significantly lower. The inferior charge carrier separation and mobility in these samples could result in lower photoresponses. In the case of this Ph.D. study, the samples with Cr^{6+} showed lower photoresponses in both series. The 1 mol% SD series Cr monodoped sample also shows the lowest Ti^{3+} defect states as calculated in Table 5.2.

The presence of Cr^{6+} states on one hand suppressed the light response and on the other resulted in higher anodic current density. The higher current density can be rationalized by three main characterization results discussed earlier. They are:

1.) Increased electron mobility: The empty Cr^{6+} t_{2g} as seen in Figure 5.60(b) below CB_{Min} can act as shallow intermediate states. These states can facilitate the mobility of electrons to the conduction band. This theory aligns with the concept of either low EA or low IP or both (discussed in Chapter 3) facilitating the electrons to reach the conduction band. This can be rationalized in the SD series where lower EA and IP were observed as shown in Figure 5.60 (a-c). Lower EA and IP can easily detrap the electrons and transfer them to the conduction band.
2.) Increase in visible light absorption: From the absorption spectrum discussed in Figures 5.40-5.44, Cr mono and co-doping extend the light absorption to > 800 nm. This can lead to more efficient generation of charge carriers when illuminated with simulated solar irradiation.
3.) Reduced recombination: As discussed Cr^{6+} introduces states very close above the $CB_{Min.}$ These can act as traps that can separate electrons and holes, thereby decreasing recombinations and increasing lifetimes.

The higher anodic current of the samples aligns with their n-type conductivity as shown in Figures 5.55-5.59. Similar findings were also observed by Haryński, L. et al. [41] in their work on Cr thin film sputtered in TiO_2 nanotubes as shown in Figure 5.68 (a, b). They reported that when illuminated with UV irradiation, the bare TiO_2 showed better photoresponse which decreased with higher Cr loadings as shown in Figure 5.68 (a). They used a UV filter when measuring the catalysts under visible light. The photoresponse under visible light demonstrated higher performance by the Cr samples as seen in Figure 5.68 (b).

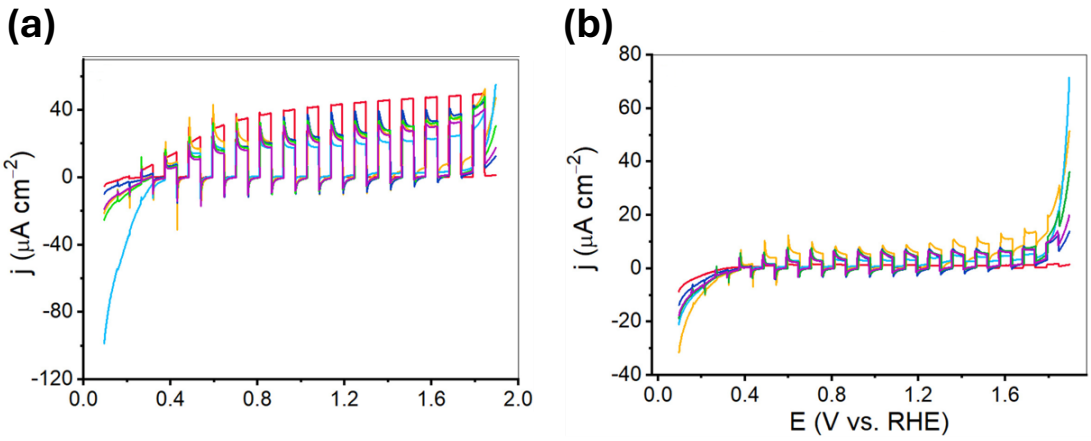


Figure 5.68: *Cr sputtered on TiO_2 nanotubes (a) without UV filter and (b) with UV filter reproduced with permission from the work of Haryński, L. et al. [41] (Copyright © 2021 Elsevier B.V).*

In the Cr-doped $SrTiO_3$ samples, the 1 mol% of the SD series shows the highest photoresponse. This sample from the XPS analysis demonstrates no Cr^{6+} states, the least Ti^{3+} states, and the highest TCSPC lifetime. In both types of dopants i.e. in Ga^{3+} and Cr^{3+}, intrinsic and extrinsic defects play a determining role in the performance. Ga^{3+} doping suppressed defect states such as the Ti^{3+} at most of the measured conditions. In the Cr-doped samples, even though the co-doping method suppressed the Cr^{6+} states with La^{3+} and at 2 mol%, this was not enough to increase the photoresponse. Even though at 0.1 mol% and 1 mol% of the SD series no Cr^{6+} was detected, only 1 mol% showed higher suppression of intrinsic $SrTiO_3$ defects such as the Ti^{3+}. Therefore, it can be inferred that even though Cr^{6+} states are suppressed, it is equally possible to suppress Ti^{3+} states for better photoresponse. The presence of Cr^{6+} can be inferred from the higher current density to make these samples better electro-catalysts.

5.8 Conclusion

In this work, Cr (co-) doped samples were synthesized investigating two dopant incorporation routes and their potential to be photocatalysts were studied. The 1 mol% Cr monodoped sample prepared via serial dilution showed the highest photoresponse from the PEC measurements. The inferences that can be drawn from this study are as follows:

1.) For incorporation of dopants at lower concentrations, the serial dilution method (800 °C) can be deemed more efficient as the standard method leads to excess Cr^{3+} which can result in strong paramagnetic interactions as confirmed by the EPR. Even though reported literature confirms that Cr^{3+} is beneficial for Photoelectrocatalysis/ photocatalysis, this study confirms that the optimal value of performance is for nominal mol% doping levels (≤ 1 mol%). This is supported by the highest photoresponse as observed in the 1 mol% Cr-doped samples prepared with the SD method.
2.) Cr^{6+} due to their d^0 configurations can act as trap states hindering the performances. For the samples in this study, it was observed that the effect of these trap states was twofold. On one hand, they suppressed the photoresponse and on the other, they increased the

current density towards the OER. Therefore, Cr^{6+} can enhance the ability of the samples as electrocatalysts.

3.) Suppression of intrinsic $SrTiO_3$ defects such as the Ti^{3+} should also be considered when synthesizing Cr-doped $SrTiO_3$. These can act as recombination centers for the charge carriers which can decrease the performance. The 1 mol% Cr doped sample with the highest photoresponse was prepared via serial dilution and exhibited the lowest Ti^{3+} trap states.

4.) The effect of two co-dopants on the oxidation states of Cr-doped $SrTiO_3$ was studied. Even though the 2 mol% La^{3+} co-doped samples were the only samples that showed higher suppression of the Cr^{6+} states compared to the Cs^{1+} or other La^{3+} co-doped samples, the photoresponse did not however show a significant increase.

5.) From the band edge energy diagrams, the standard sol-gel samples show n-type nature for both the monodoped and co-doped samples. ***Hence, these samples can be represented with the formulae, $SrTi_{(1-x)}Cr_xO_{3-y}$ and $La_{(1-a)}Sr_{(a)}Ti_{(1-x)}Ga_xO_{3-y}$ where a and x represent the mol% co-dopant and the mono-dopant respectively.*** For the SD series, the n-type nature decreased with an increase in mol% mono-doping.

References

[1] S. Ouyang, H. Tong, N. Umezawa, J. Cao *et al.*, "Surface-alkalinization-induced enhancement of photocatalytic H 2 evolution over SrTiO 3-based photocatalysts," *J. Am. Chem. Soc.*, vol. 134, no. 4, pp. 1974–1977, 2012, doi: 10.1021/ja210610h.

[2] D. Jiang, X. Sun, X. Wu, L. Shi, and F. Du, "Hydrothermal synthesis of single-crystal Cr-doped $SrTiO_3$ for efficient visible-light responsive photocatalytic hydrogen evolution," *Mater. Res. Express*, vol. 7, no. 1, 2020, doi: 10.1088/2053-1591/ab660d.

[3] T. Ishii, H. Kato, and A. Kudo, "H2 evolution from an aqueous methanol solution on $SrTiO_3$ photocatalysts codoped with chromium and tantalum ions under visible light irradiation," *J. Photochem. Photobiol. A Chem.*, vol. 163, no. 1–2, pp. 181–186, 2004, doi: 10.1016/S1010-6030(03)00442-8.

[4] J. Shi, S. Shen, Y. Chen, L. Guo, and S. S. Mao, "Visible light-driven photocatalysis of doped SrTiO_3 tubular structure," *Opt. Express*, vol. 20, no. S2, p. A351, 2012, doi: 10.1364/oe.20.00a351.

[5] B. Moss, Q. Wang, K. T. Butler, R. Grau-Crespo *et al.* , "Linking in situ charge accumulation to electronic structure in doped $SrTiO_3$ reveals design principles for hydrogen-evolving photocatalysts," *Nat. Mater.*, vol. 20, no. 4, pp. 511–517, 2021, doi: 10.1038/s41563-020-00868-2.

[6] Y. Sun, J. Peng, Y. Chen, Y. Yao, and Z. Liang, "Triple-cation mixed-halide perovskites: Towards efficient, annealing-free and air-stable solar cells enabled by Pb(SCN) 2 additive," *Sci. Rep.*, vol. 7, no. April, pp. 1–7, 2017, doi: 10.1038/srep46193

[7] F. Ichihara, F. Sieland, H. Pang, D. Philo, A.-T. Duong *et al.* , "Photogenerated Charge Carriers Dynamics on La- and/or Cr-Doped $SrTiO_3$ Nanoparticles Studied by Transient Absorption Spectroscopy," *J. Phys. Chem. C*, vol. 124, no. 2, pp. 1292–1302, Jan. 2020,

doi: 10.1021/acs.jpcc.9b09324

[8] M. G. Vergniory, L. Elcoro, C. Felser, N. Regnault, B. A. Bernevig, and Z. Wang, "A complete catalogue of high-quality topological materials," *Nature*, vol. 566, no. 7745, pp. 480–485, 2019, doi: 10.1038/s41586-019-0954-4.

[9] B. Bradlyn, L. Elcoro, J, Cano, M. G. Vergniory *et al.*, "Topological quantum chemistry," *Nature*, vol. 547, no. 7663, pp. 298–305, 2017, doi: 10.1038/nature23268.

[10] M. G. Vergniory, B. J. Wieder, L. Elcoro, S. S. P. Parkin *et al.* , "All topological bands of all nonmagnetic stoichiometric materials," *Science (80-.).*, vol. 376, no. 6595, 2022, doi: 10.1126/science.abg9094.

[11] T. Tatarchuk, A. Peter, B. Al-Najar, J. Vijaya, and M. Bououdina, "Photocatalysis: Activity of Nanomaterials," *Nanotechnol. Environ. Sci.*, vol. 1–2, pp. 209–292, 2018, doi: 10.1002/9783527808854.ch8.

[12] C. Dong, C. Lian, S. Hu, Z. Deng *et al.* , "Size-dependent activity and selectivity of carbon dioxide photocatalytic reduction over platinum nanoparticles," *Nat. Commun.*, vol. 9, no. 1, pp. 1–11, 2018, doi: 10.1038/s41467-018-03666-2.

[13] M. Tyunina, O. Pacherova, T. Kocourek, and A. Dejneka, "Anisotropic chemical expansion due to oxygen vacancies in perovskite films," *Sci. Rep.*, vol. 11, no. 1, pp. 1–6, 2021, doi: 10.1038/s41598-021-93968-1.

[14] D. S. Aidhy, B. Liu, Y. Zhang, and W. J. Weber, "Chemical expansion affected oxygen vacancy stability in different oxide structures from first principles calculations," *Comput. Mater. Sci.*, vol. 99, pp. 298–305, 2015, doi: 10.1016/j.commatsci.2014.12.030.

[15] M. P. Mueller, F. Gunkel, S. Hoffmann-Eifert, and R. A. De Souza, "The importance of singly charged oxygen vacancies for electrical conduction in monoclinic HfO2," *J. Appl. Phys.*, vol. 129, no. 2, 2021, doi: 10.1063/5.0036024.

[16] H. L. Tuller and S. R. Bishop, "Point defects in oxides: Tailoring materials through defect engineering," *Annu. Rev. Mater. Res.*, vol. 41, pp. 369–398, 2011, doi: 10.1146/annurev-matsci-062910-100442.

[17] R. D. Shannon, "Revised effective ionic radii and systematic studies of interatomic distances in halides and chalcogenides," *Acta Crystallogr. Sect. A*, vol. 32, pp. 751–767, 1976.

[18] D. Wang, J. Ye, T. Kako, and T. Kimura, "Photophysical and photocatalytic properties of $SrTiO_3$ doped with Cr cations on different sites," *J. Phys. Chem. B*, vol. 110, no. 32, pp. 15824–15830, 2006, doi: 10.1021/jp062487p.

[19] Y. Bi, M. F. Ehsan, Y. Huang, J. Jin, and T. He, "Synthesis of Cr-doped $SrTiO_3$ photocatalyst and its application in visible-light-driven transformation of CO2 into CH4," *J. CO2 Util.*, vol. 12, pp. 43–48, 2015, doi: 10.1016/j.jcou.2015.10.004.

[20] S. Dolabella, A. Borzì, A. Dommann, and A. Neels, "Lattice Strain and Defects Analysis

in Nanostructured Semiconductor Materials and Devices by High-Resolution X-ray Diffraction: Theoretical and Practical Aspects," *Small Methods*, vol. 6, no. 2, 2022, doi: 10.1002/smtd.202100932.

[21] E. Calì, G. Kerherve, F. Naufal, K. Kousi *et al.* , "Exsolution of Catalytically Active Iridium Nanoparticles from Strontium Titanate," *ACS Appl. Mater. Interfaces*, vol. 12, no. 33, pp. 37444–37453, 2020, doi: 10.1021/acsami.0c08928.

[22] J. Jing, Z. Chen, Y. Bu, M. Sun, W. Zheng, and W. Li, "Significantly enhanced photoelectrochemical cathodic protection performance of hydrogen treated Cr-doped SrTiO 3 by Cr 6+ reduction and oxygen vacancy modification," *Electrochim. Acta*, vol. 304, pp. 386–395, 2019, doi: 10.1016/j.electacta.2019.03.020.

[23] H. Kato and A. Kudo, "Visible-Light-Response and Photocatalytic Activities of TiO2 and $SrTiO_3$ Photocatalysts Codoped with Antimony and Chromium," *J. Phys. Chem. B*, vol. 106, no. 19, pp. 5029–5034, May 2002, doi: 10.1021/jp0255482.

[24] H. Idriss, "On the wrong assignment of the XPS O1s signal at 531–532 eV attributed to oxygen vacancies in photo- and electro-catalysts for water splitting and other materials applications," *Surf. Sci.*, vol. 712, no. June, pp. 2–7, 2021, doi: 10.1016/j.susc.2021.121894.

[25] H. Yu, S. Ouyang, S. Yan, Z. Li, T. Yu, and Z. Zou, "Sol-gel hydrothermal synthesis of visible-light-driven Cr-doped SrTiO 3 for efficient hydrogen production," *J. Mater. Chem.*, vol. 21, no. 30, pp. 11347–11351, 2011, doi: 10.1039/c1jm11385b.

[26] D. V. Azamat, A. Dejneka, J. Lančok, V. A. Trepakov, L. Jastrabik, and A. G. Badalyan, "Pulse-electron paramagnetic resonance of Cr3+ centers in $SrTiO_3$," *J. Appl. Phys.*, vol. 113, no. 17, 2013, doi: 10.1063/1.4804062.

[27] K. A. Lehuta and K. R. Kittilstved, "Speciation of Cr(iii) in intermediate phases during the sol-gel processing of Cr-doped $SrTiO_3$ powders," *J. Mater. Chem. A*, vol. 2, no. 17, pp. 6138–6145, 2014, doi: 10.1039/c3ta14475e.

[28] K. A. Lehuta and K. R. Kittilstved, "Reversible control of the chromium valence in chemically reduced Cr-doped $SrTiO_3$ bulk powders," *Dalt. Trans.*, vol. 45, no. 24, pp. 10034–10041, 2016, doi: 10.1039/c6dt00706f.

[29] W. L. Harrigan, S. E. Michaud, K. A. Lehuta, and K. R. Kittilstved, "Tunable Electronic Structure and Surface Defects in Chromium-Doped Colloidal $SrTiO_{3-\delta}$ Nanocrystals," *Chem. Mater.*, vol. 28, no. 2, pp. 430–433, 2016, doi: 10.1021/acs.chemmater.6b00049.

[30] A. A. Sukhanov, I. V. Yanilkin, V. F. Valeev, V. I. Nuzhdin *et al.*, "Features of Formation of Cr^{3+} Paramagnetic Centers in Strontium Titanate ($SrTiO_3$) Implanted with Chromium Ions," *J. Surf. Investig.*, vol. 14, no. 3, pp. 551–554, 2020, doi: 10.1134/S1027451020030398.

[31] D. V Azamat, A. Dejneka, J. Lancok, L. Jastrabík *et al.*, "EPR investigation of the trivalent chromium complexes in $SrTiO_3$," *J. Phys. Chem. Solids*, vol. 75, no. 2, pp. 271–

275, 2014, doi: https://doi.org/10.1016/j.jpcs.2013.10.003.

[32] W. L. Harrigan and K. R. Kittilstved, “Reversible Modulation of the Cr3+ Spin Dynamics in Colloidal $SrTiO_3$ Nanocrystals,” *J. Phys. Chem. C*, vol. 122, no. 46, pp. 26652–26657, 2018, doi: 10.1021/acs.jpcc.8b08680.

[33] A. C. Wardhana, A. Yamaguchi, S. Shoji, M. Liu *et al.*, “Visible-light-driven photocatalysis via reductant-to-band charge transfer in Cr(III) nanocluster-loaded $SrTiO_3$ system,” *Appl. Catal. B-environmental*, vol. 270, p. 118883, 2020, [Online]. Available: https://api.semanticscholar.org/CorpusID:216281706.

[34] M. Beck, P. Bornhauser, B. Visser, G. Knopp, J. A. va. Bokhoven, and P. P. Radi, “Spectroscopic disentanglement of the quantum states of highly excited Cu_2,” *Nat. Commun.*, vol. 10, no. 1, 2019, doi: 10.1038/s41467-019-11156-2.

[35] P. Makuła, M. Pacia, and W. Macyk, “How To Correctly Determine the Band Gap Energy of Modified Semiconductor Photocatalysts Based on UV-vis Spectrum,” *J. Phys. Chem. Lett.*, vol. 9, no. 23, pp. 6814–6817, 2018, doi: 10.1021/acs.jpclett.8b02892.

[36] R. B. Comes, P. V. Sushko, S. M. Heald, R. J. Colby, M. E. Bowden, and S. A. Chambers, “Band-gap reduction and dopant interaction in epitaxial La, Cr Co-doped $SrTiO_3$ thin films,” *Chem. Mater.*, vol. 26, no. 24, pp. 7073–7082, 2014, doi: 10.1021/cm503541u.

[37] A. Łącz, Ł. Łańcucki, R. Lach, B. Kamecki, and E. Drożdż, “Structural and electrical properties of Cr-doped $SrTiO_3$ porous materials,” *Int. J. Hydrogen Energy*, vol. 43, no. 18, pp. 8999–9005, 2018, doi: 10.1016/j.ijhydene.2018.03.180.

[38] M. G. Helander, M. T. Greiner, Z. B. Wang, and Z. H. Lu, “Pitfalls in measuring work function using photoelectron spectroscopy,” *Appl. Surf. Sci.*, vol. 256, no. 8, pp. 2602–2605, 2010, doi: 10.1016/j.apsusc.2009.11.002.

[39] P. Reunchan, N. Umezawa, S. Ouyang, and J. Ye, “Mechanism of photocatalytic activities in Cr-doped $SrTiO_3$ under visible-light irradiation: An insight from hybrid density-functional calculations,” *Phys. Chem. Chem. Phys.*, vol. 14, no. 6, pp. 1876–1880, 2012, doi: 10.1039/c2cp23348g.

[40] C. Mitra, C. Lin, J. Robertson, and A. A. Demkov, “Electronic structure of oxygen vacancies in $SrTiO_3$ and $LaAlO_3$,” *Phys. Rev. B - Condens. Matter Mater. Phys.*, vol. 86, no. 15, 2012, doi: 10.1103/PhysRevB.86.155105.

[41] Ł. Haryński, J. Karczewski, J. Ryl, K. Grochowska, and K. Siuzdak, “Rapid development of the photoresponse and oxygen evolution of TiO2 nanotubes sputtered with Cr thin films realized via laser annealing,” *J. Alloys Compd.*, vol. 877, 2021, doi: 10.1016/j.jallcom.2021.160316.

Appendix

Table 5.1A: Average crystallite sizes, Microstrain, and Lattice Volumes

% Doping	Average Crystallite Size (nm)	Microstrain	Cell Volume (Å^3)
$SrTiO_3$, 800 °C	32.41 ± 1.19	1.11E-04 ± 1.87E-05	59.3167 ±0.05
$SrTi_{(0.999)}Cr_{(0.001)}O_3$, 800 °C (Serial Dilution)	15.57 ±1.55	1.37E-04 ± 1.49E-05	59.4359 ±0.06
$SrTi_{(0.99)}Cr_{(0.01)}O_3$, 800 °C (Serial Dilution)	29.97 ±0.50	2.21E-04 ± 5.032E-05	59.5199 ± 0.08
$SrTi_{(0.98)}Cr_{(0.02)}O_3$, 800 °C (Serial Dilution)	28.10 ±0.78	1.59E-04 ± 2.79E-05	59.5410 ± 0.07
$SrTi_{(0.98)}Cr_{(0.02)}O_3$, 800 °C	33.05 ±0.66	2.78E-03 ± 6.57E-05	59.4089 ± 0.07
$La_{(0.01)}Sr_{(0.99)}Ti_{(0.99)}Cr_{(0.02)}O_3$, 800 °C	32.92 ±0.99	1.66E-03 ± 3.96E-04	59.2944 ± 0.01
$La_{(0.02)}Sr_{(0.98)}Ti_{(0.98)}Cr_{(0.02)}O_3$, 800 °C	27.55 ±1.13	8.99E-04 ± 1.34E-04	59.2962 ± 0.01
$La_{(0.05)}Sr_{(0.95)}Ti_{(0.95)}Cr_{(0.02)}O_3$, 800 °C	22.22 ±0.89	1.12E-03 ± 2.91E-04	59.4510 ± 0.01
$La_{(0.1)}Sr_{(0.9)}Ti_{(0.95)}Cr_{(0.02)}O_3$, 800 °C	21.36 ±1.31	1.27E-03 ± 3.06E-04	59.2187 ± 0.03
$SrTiO_3$, 900 °C	47.51 ± 0.83	1.22E-03 ± 7.03E-04	59.5045 ± 0.05
$SrTi_{(0.98)}Cr_{(0.02)}O_3$, 900 °C	30.26 ±1.35	1.57E-03 ± 3.52E-04	59.3473 ±0.04
$La_{(0.01)}Sr_{(0.99)}Ti_{(0.98)}Cr_{(0.02)}O_3$, 900 °C	41.34 ±0.98	1.18E-03 ± 1.80E-04	59.5136 ± 0.01
$La_{(0.02)}Sr_{(0.98)}Ti_{(0.98)}Cr_{(0.02)}O_3$, 900 °C	35.23 ±0.53	1.23E-03 ± 1.25E-04	59.3181 ± 0.05
$La_{(0.05)}Sr_{(0.95)}Ti_{(0.98)}Cr_{(0.02)}O_3$, 900 °C	28.00 ±0.32	1.26E-03 ± 1.17E-04	59.2702 ± 0.03
$La_{(0.1)}Sr_{(0.9)}Ti_{(0.98)}Cr_{(0.02)}O_3$, 900 °C	16.83 ±0.97	1.47E-03 ± 9.72E-05	59.1886 ± 0.01
$Cs_{(0.01)}Sr_{(0.99)}Ti_{(0.98)}Cr_{(0.02)}O_3$, 800 °C	27.79 ±1.00	1.11E-03 ± 9.96E-05	59.4099 ± 0.01
$Cs_{(0.02)}Sr_{(0.98)}Ti_{(0.98)}Cr_{(0.02)}O_3$, 800 °C	22.43 ±1.13	9.87E-04 ± 1.34E-04	59.4003 ± 0.01
$Cs_{(0.05)}Sr_{(0.95)}Ti_{(0.98)}Cr_{(0.02)}O_3$, 800 °C	28.54 ±1.65	1.75E-04 ± 2.46E-05	59.3802 ± 0.06
$Cs_{(0.01)}Sr_{(0.99)}Ti_{(0.98)}Cr_{(0.02)}O_3$, 900 °C	44.65 ±1.13	1.4E-04 ± 1.33E-05	59.4277 ± 0.01
$Cs_{(0.02)}Sr_{(0.98)}Ti_{(0.98)}Cr_{(0.02)}O_3$, 900 °C	27.56 ±1.25	1.75E-04 ± 2.46E-05	59.4688 ± 0.02
$Cs_{(0.05)}Sr_{(0.95)}Ti_{(0.98)}Cr_{(0.02)}O_3$, 900 °C	33.34 ±0.63	2.12E-04 ± 6.32E-05	59.5360 ± 0.06

Chapter 6: A New Method to Quantify Photocatalysis Data and the Effect of an Intermediate N_2 annealing Before Calcination on the Crystallite Sizes

This work is an ongoing study with Ms. Baliana Shani, Steier Group, Oxford University who is currently working on the photocatalytic measurements in a new setup in the Steier Laboratory.

Summary

Preliminary photocatalytic CO_2 hydrogenation data shows an increase in CO generation with an increase in mol% Ga^{3+} doping**.** A new method to report photocatalysis data is discussed here. In this work, an intermediate N_2 annealing step was introduced in the standard sol-gel Pechini route. It was observed that this step leads to lower crystallite sizes**.**

6.1 Introduction

Photocatalytic CO_2 hydrogenation is an up-and-coming method to harvest solar energy to produce clean fuels [1]. $SrTiO_3$ as discussed previously due to the high photochemical stabilities and suitable band positions is an ideal photocatalyst for such reactions. Doping aliovalent metal ions such as Ga^{3+} in $SrTiO_3$ has been found to have a positive impact on the properties of the parent material as discussed in Chapters 3 and 4. The photocatalytic activity also depends on the synthesis route of these doped materials which affects the particle size and specific surface areas [2]. In this study, the sol-gel Pechini synthesis route of doped $SrTiO_3$ has been found to control the particle size with a high specific surface area that aids surface catalysis. The core objective of this work is to study how the synthesis route and doping d^{10} Ga^{3+} in the Ti^{4+} site of $SrTiO_3$ affect specific surface areas. This study also focuses on a method to quantify photocatalysis data.

Enhanced photocatalytic performance of Ga^{3+} doped $SrTiO_3$ was observed with CO_2 hydrogenation to CO. Among different Ga mol% doping, 4% doped samples showed the highest activity. The doped samples were observed to be highly crystalline, and most particles were less than 25 nm in distribution. Three methods were employed to examine the crystallite sizes. The correlation of the crystallite sizes with the Scherrer equation, Williamson Hall Analysis, and TEM show a decreasing trend. No contribution of the band gap to the performance of the catalysts was observed. In this study, we conclude that the enhanced photocatalytic performance was due to the decreasing crystallite size, decreasing Ti^{3+} defects, and subsequent increasing surface area.

6.2 Experimental Method

The sol-gel Pechini route was used for the synthesis of two batches of Ga^{3+} doped $SrTiO_3$. The synthesis route is discussed in Chapter 2. The new optimized batch was annealed in N_2 for 3 h at 350 °C at 5 °C/min heating rate at 10 sscm N_2 flow which resulted in a charred material as shown in Figure 6.1.

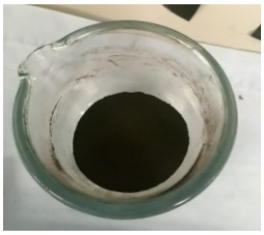


Figure 6.1: *Finely ground charred material after N_2 annealing at 350°C.*

These charred materials were then ground to fine powders. The ground mixture was then calcined at 900 °C for 3 h under 10 sscm of compressed air at a heating rate of 5 °C/min. The white flaky material obtained is further ground to get fine powders. The standard sol-gel Pechini Ga^{3+} doped samples were resynthesized for this work and are different than those studied in Chapter 3. The La^{3+}, Ga^{3+} co-doped samples are the same as those discussed in Chapter 3.

6.3 Results and Discussion

6.3.1 Preliminary Photocatalytic CO_2 Hydrogenation Results

The XRD pattern shows that all the synthesized Ga^{3+} monodoped samples were phase pure as shown in Figure 6.2(a). The Scherrer equation (Chapter 2, Eq 2.5) showed that the crystallite sizes decreased with an increase in mol% doping. Similar observations were made in the case of the La^{3+} co-doped samples as discussed in Chapter 3 Table 3.2. The optical absorption of the monodoped samples did not change and was limited to the UV region as the undoped (Figure 6.3 (b)).

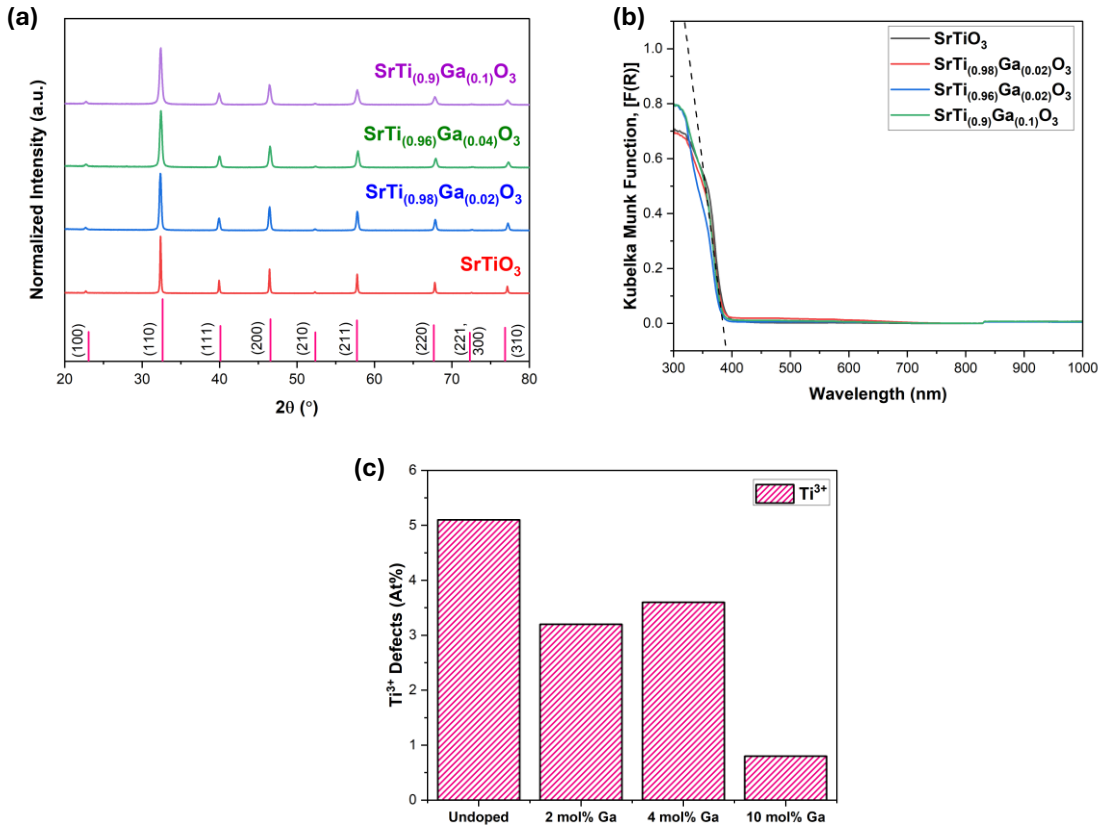


Figure 6.2: *(a) Phase pure XRD pattern of Ga^{3+} monodoped samples compared to the ICSD standard $SrTiO_3$ (pink). The XRD parameters used for the pattern are described in Table 2.2 in Chapter 2. (b) The Kubelka Munk spectrum of the doped samples shows absorption in the UV region similar to the undoped sample. (c) Decrease in Ti^{3+} defects with increase in mol% doping which is consistent with the findings in Chapters 3 and 4.*

The La^{3+} (2 and 4 mol%) co-doped samples show absorption features around the 515 nm region and show an extended absorption into the NIR region as shown in Figures 3.24 (a-d) in Chapter 3. Since no such features were observed for the monodoped samples, one of the major variations was in the decreasing crystallite sizes, and for the co-doped samples, both optical and crystallite size changes were observed. The decrease in Ti^{3+} defects as observed with the XPS in Figure 6.2 (c) is also consistent with the findings in Chapters 3 and 4.

A decrease in crystallite sizes leads to an increase in the specific surface area. This correlation was further verified with the BET and the analysis of the N_2 and CO_2 isotherms as shown in Figure 6.3 (a) and (b). The monodoped samples show a gradual increase in adsorption of both N_2 (Figure 6.3 (a)) and CO_2 (Figure 6.3 (b)) compared to the undoped. The co-doped samples in both cases show lower adsorption than the undoped samples. The BET surface areas and the crystallite sizes are listed in Table 6.1.

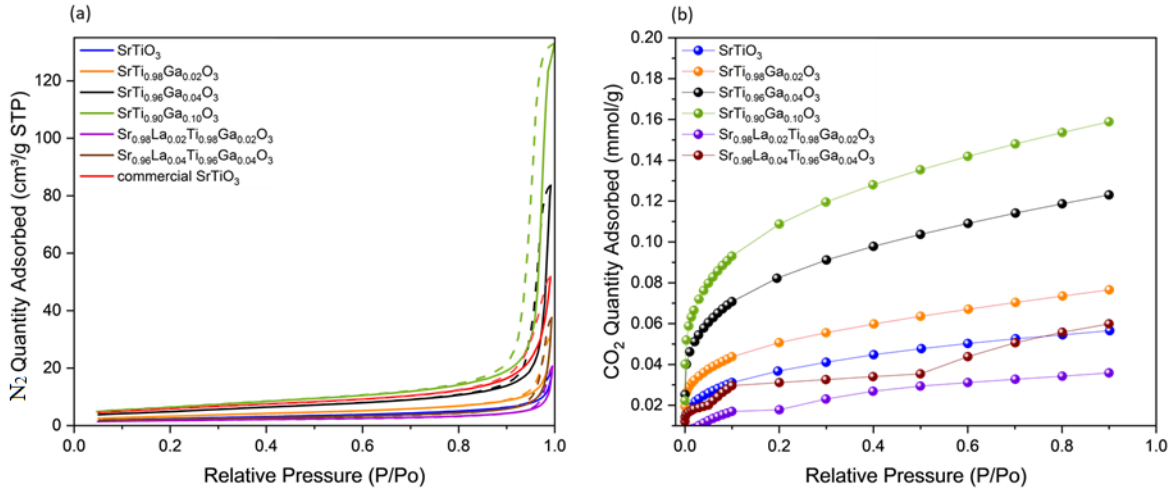


Figure 6.3: *(a) N_2 physisorption curves collected at -195.85 °C for the samples. They are all mesoporous with type IV isotherm with an H1 hysteresis loop (multilayer adsorption and capillary condensation of the nitrogen in the mesopores) according to IUPAC[3]. Pore sizes are in the range between 20 and 37 nm. The BET data obtained aligns with the surface area of $SrTiO_3$ between 8 and 13 m^2/g as reported in literature. (b) CO_2 adsorption isotherms of all samples collected at 25 °C.*

Table 6.1: The crystallite sizes and the BET surface areas from the N_2 and the CO_2 physisorption measurements

Samples	Crystallite Size (Scherrer equation)	N_2 BET area of all samples (m^2/g) (value ± 2)	CO_2 surface area of all samples with BET method (m^2/g) (value ± 2)
Commercial $SrTiO_3$	33	-	-
$SrTiO_3$	67	9	2
$SrTi_{0.98}Ga_{0.02}O_3$	55	12	3
$SrTi_{0.96}Ga_{0.04}O_3$	42	18	6
$SrTi_{0.90}Ga_{0.10}O_3$	27	23	7
$Sr_{0.98}La_{0.02}Ti_{0.98}Ga_{0.02}O_3$	37.50	6	2
$Sr_{0.96}La_{0.04}Ti_{0.96}Ga_{0.0}O_3$	26.52	8	3

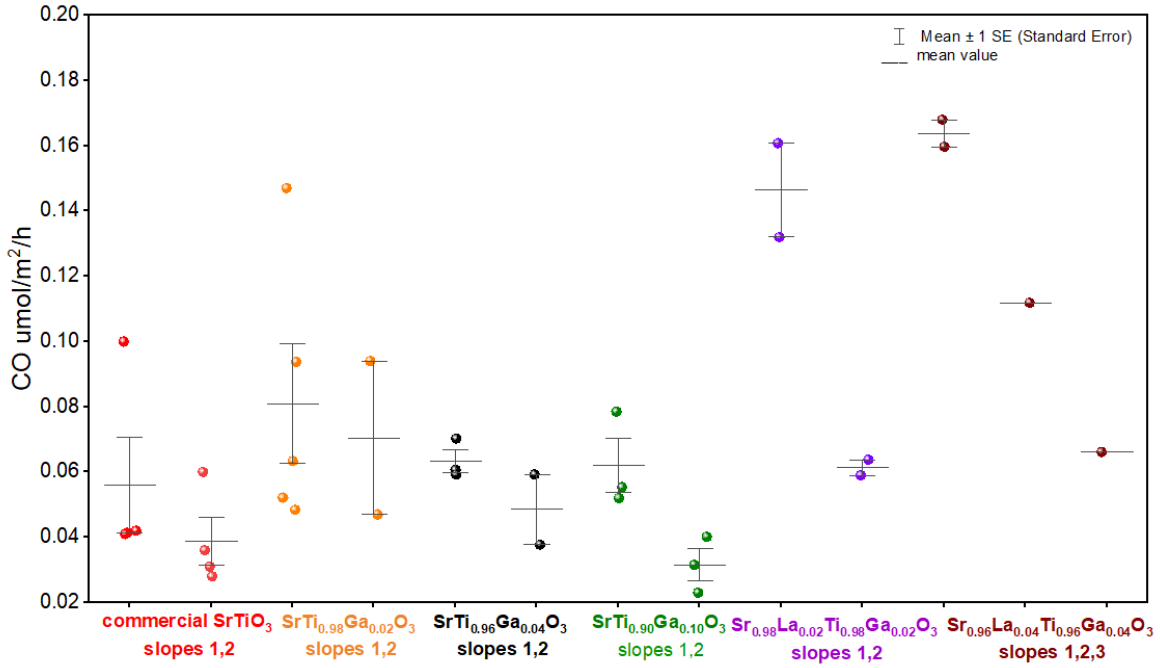


Figure 6.4: *Preliminary CO evolution from photocatalytic CO_2 hydrogenation over Ga^{3+} and La^{3+}, Ga^{3+} co-doped $SrTiO_3$ samples expressed in micromoles normalized per surface area obtained with the BET N_2 physisorption. The photocatalytic setup and sample preparation have been discussed in Chapter 2.*

As discussed earlier in the thesis, the specific surface area can be an important determinant of photocatalytic activity. A higher specific surface provides more active sites for the redox reactions to take place. Therefore, with the established decrease in crystallite sizes and the increase in the BET-specific surface areas with the Ga^{3+} mono-doping, we wanted to account for the surface area in photocatalysis. In this work, we report a novel technique to quantify photocatalysis data in terms of the micromoles of CO evolved per BET N_2-surface area exposed normalized per gram loaded vs mol% doping assuming that the entire area exposed is active in photocatalysis. Preliminary photocatalysis results in Figure 6.4 show that when normalizing per active BET surface area, the Ga^{3+}-doped samples showed comparable activity towards CO production with the undoped. For the La^{3+} co-doped samples on the other hand, where the absorption features in the visible region and exsolutions were observed, the activity normalized by the surface area showed an enhancement in CO evolution. For the data analysis, the rate of CO evolution expressed as µmols g^{-1} h^{-1} was calculated from the slopes after linear fitting of the trends in the graph as shown in Figure 6.5. This was normalized by the BET N_2 physisorption surface area (m^2/g). Here we want to emphasize the surface-specific activity of the photocatalysts which is shown in Figure 6.4. A second slope was observed after 6-7 h of activity, as shown in Figures 6.4 and 6.5. Preliminary analysis suggests being due to catalyst poisoning with CO. However, this is still ongoing research and the exact reason for this behavior is yet to be found. The slopes and the samples' N_2 BET surface areas are recorded in Table 6.2.

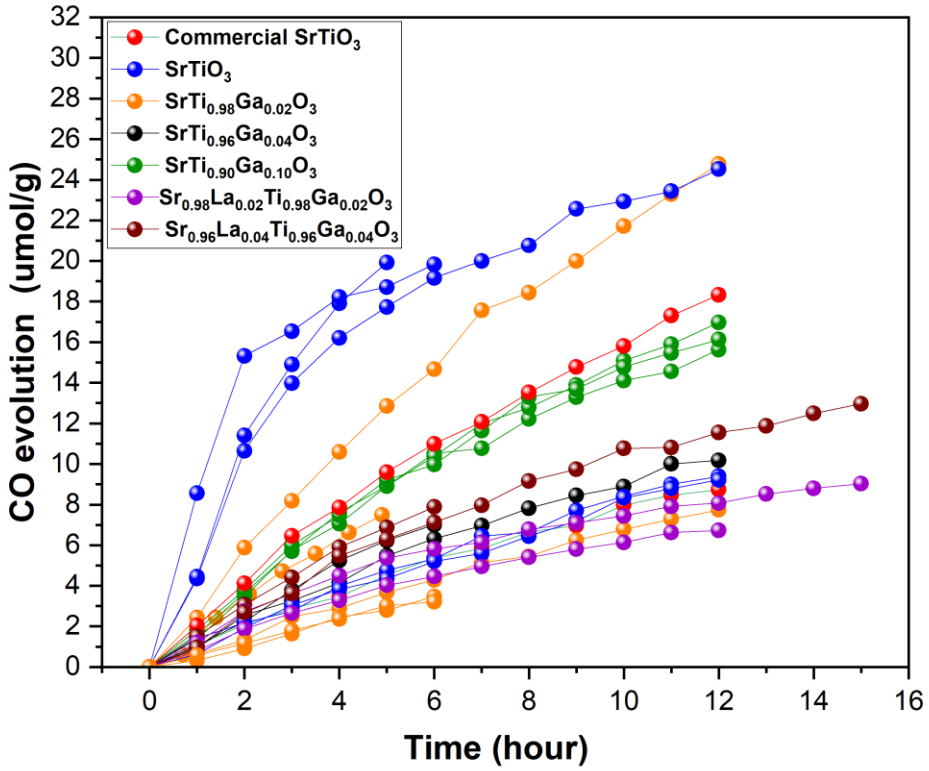


Figure 6.5**:** *The CO evolved after photocatalytic reaction expressed as micromoles per gram of catalyst as a function of time for all samples. The synthesized $SrTiO_3$ has an evolution that differs from all the other samples. Therefore, the origin of this behavior is being studied separately and has not been analyzed further. Figure 6.4 compares the doped samples with the commercial $SrTiO_3$.*

Table 6.2: The µmoles/m^2/h for each fitted sample, the amount of catalyst (mg) loaded, and the N_2 BET-specific surface areas used for the experiments.

Samples	**µmols/m^2/h fit of first 6-7 h (±0.005) [a]**	**µmols/m^2/h fit of the second slope (±0.005) [a]**	**mg loaded (±0.01)[b]**	**N_2-BET surface area m^2/g (±2)[c]**
Commercial $SrTiO_3$	0.100	0.060	1.35	21
Commercial $SrTiO_3$	0.041	0.028	1.35	
Commercial $SrTiO_3$	0.041	0.031	2.43	
Commercial $SrTiO_3$	0.042	0.036	2.43	
$SrTiO_3$ (900 °C annealed)	0.560	0.110	1.19	8
$SrTiO_3$ (900 °C annealed)	0.890	0.130	1.42	8

$SrTi_{0.90}Ga_{0.10}O_3$ (900 °C annealed)	0.078	0.041	1.59	22
$SrTi_{0.90}Ga_{0.10}O_3$	0.055	0.032	2.51	32
$SrTi_{0.96}Ga_{0.04}O_3$ (900 °C annealed)	0.061	0.038	1.63	17
$SrTi_{0.96}Ga_{0.04}O_3$ (900 °C annealed)	0.070	-	1.38	
$SrTi_{0.96}Ga_{0.04}O_3$ (900 °C annealed)	0.059	0.059	1.78	
$SrTi_{0.98}Ga_{0.02}O_3$ (900 °C annealed)	0.063	0.047	1.6	11
$SrTi_{0.98}Ga_{0.02}O_3$ (900 °C annealed)	0.052	-	1.71	11
$SrTi_{0.98}Ga_{0.02}O_3$ (900 °C annealed)	0.048	-	2.34	11
$Sr_{0.98}La_{0.02}Ti_{0.98}Ga_{0.02}O_3$ (900 °C annealed)	0.130	0.064	2.47	6
$Sr_{0.98}La_{0.02}Ti_{0.98}Ga_{0.02}O_3$ (900 °C annealed)	0.180	0.059	1.40	6
$Sr_{0.96}La_{0.04}Ti_{0.96}Ga_{0.0}O_3$ (900 °C annealed)	0.160	0.110 and 0.066 (3 slopes)	1.49	8
$Sr_{0.96}La_{0.04}Ti_{0.96}Ga_{0.0}O_3$ (900 °C annealed)	0.170	-	1.6	8

[a] The error refers to the fit reported from Origin

[b] The error refers to the accuracy of the balance

[c] The error is estimated as an average deviation between two measurements

The results obtained so far will be confirmed after multiple repeats and testing in a new photocatalytic system. The current setup with the McCulloch group (setup discussed in Chapter 2) allows for the manually controlled ratios of CO_2 and H_2 gases which can increase errors due to inaccuracies in the mass flow controllers, and the measurements. Therefore, to rectify these errors, Baliana Shani (Steier Group) is designing/working on a more advanced photocatalytic setup as part of her Ph.D. where these samples will be remeasured. Preliminary results show a novel method to quantify photocatalysis data per normalized N_2 BET surface areas in inorganic photocatalyst materials such as $SrTiO_3$. Most literatures so far report the data in terms of moles of product generated per gram of catalyst per hour [4]–[6]. Morruzzi, F. et al. [7] in their work on gas-phase CO_2 photoreduction studies on solution-processable polymers have reported their CO data normalized to BET surface area (μmols/m^2/h) which remains one of the few studies to do so. Robatjazi, H. et al. [8] has reported their photocatalytic CO evolution as a function of visible light intensity under ambient conditions.

So far smaller crystallite size leading to higher specific surface areas has been established to facilitate higher photocatalysis rates. Therefore, as a motivation for further study, the synthesis method was optimized with an additional N_2 annealing step at 350 °C to see the effect on the particle sizes. From the XRD data of the samples (with N_2 annealing), all the doped samples were phase pure except the undoped as shown in Figure 6.6 with all peaks compared with the data in $SrTiO_3$ ICSD file 23076 [9]–[11].

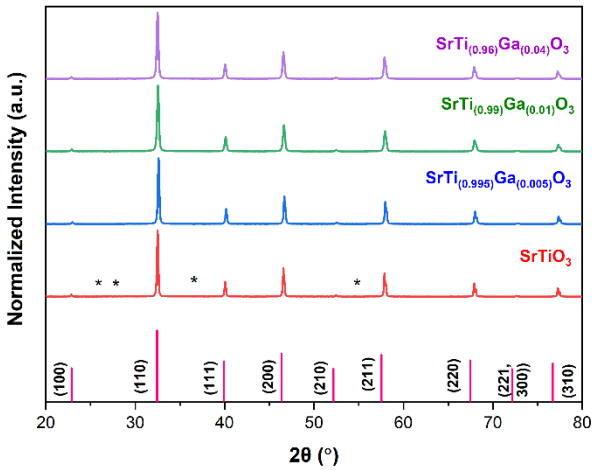


Figure 6.6: *XRD pattern of samples with N_2 annealing intermediate step in the synthesis process compared to the ICSD reference $SrTiO_3$ pattern (pink) [9]-[11]. The XRD conditions used are discussed in Chapter 2 in Table 2.2. The * indicates the presence of secondary phases in the undoped sample.*

The microstructural parameters such as the crystallite sizes, the lattice parameters, and the cell volume were calculated as discussed in the previous chapters and are shown in Table 6.3.

Table 6.3: Average crystallite sizes, and Lattice Parameters of the synthesized samples with N_2 annealing

Sr No	% Doping	Average Crystallite Size from Scherrer equation (nm)	Average Crystallite Size from W-H Analysis (nm)	Lattice Parameter (Å)	Unit Cell Volume (Å^3)
1	Commercial $SrTiO_3$*	24.71 ± 3.27	33.21 ± 2.00	3.8811 ± 0.002	58.4604 ± 0.09
2	0.5 mol% Ga	21.75 ± 1.50	29.65 ± 1.78	3.8782 ± 0.002	58.3289 ± 0.09
3	1 mol% Ga	16.36 ± 2.00	29.14 ± 1.50	3.8816 ± 0.001	58.4809 ± 0.05
4	4 mol% Ga	15.11 ± 2.00	25.36 ± 1.50	3.8840 ± 0.002	58.5931 ± 0.09

* Since the Undoped of the N_2 annealed batch is impure, therefore comparison with commercial $SrTiO_3$ is being done

Both batches of Ga^{3+} doped samples in Tables 6.1 and 6.3 show differences in crystallite sizes. The N_2 annealed batch is observed to be smaller than the batch without N_2 in Table 6.1. This could be because N_2 annealing completes the drying of the polyesterized which makes the resin easy to finely grind. The crystallite sizes with the W-H analysis in Table 6.3 are larger than those with the Scherrer equation. This discrepancy might arise from the irregular arrangement

of data due to the elastic anisotropy in each plane [12]. To eradicate this issue, there is a simplified modified version of the W-H analysis. The modified W-H analysis is built on the work of Thomas Ungar where they proposed a modification of the original method to take into account the dislocation arrangement and dislocation density [13].To correlate the sizes obtained from the XRD, TEM analysis on the N_2 annealed batch as shown in Figure 6.7 (a, b). Most particles were observed to be less than 25 nm in distribution. The EDX pattern shows Ga^{3+} incorporation, the crystalline nature of the materials with the diffraction pattern, and the correlation of the lattice planes with the XRD is shown in Appendix Figure 6.2A and Table 6.1A.

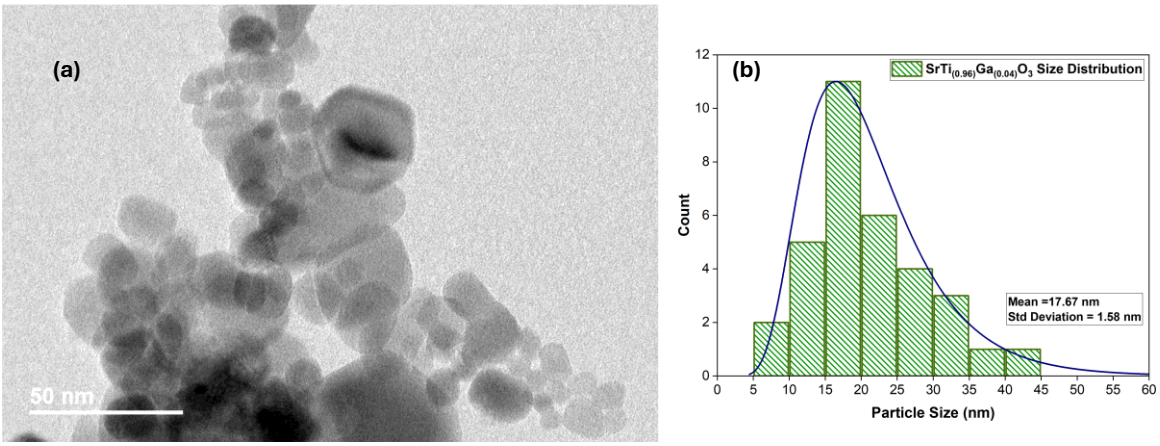


Figure 6.7: *TEM (a) Nanoparticle cluster (b) Size distribution of 4 mol% Ga^{3+} doped $SrTiO_3$ with N_2 annealing indicating most particles below 25 nm.*

TEM analysis was done on the N_2 annealed batch and correlation was made with the Scherrer and W-H analysis as shown in Figure 6.8. Even though there are discrepancies in the sizes, all the size comparison methods point towards a decreasing trend. With W-H analysis and Scherrer methods, an attempt to study the bulk of the nanoparticles was made. With the TEM, it was more of a localized observation.

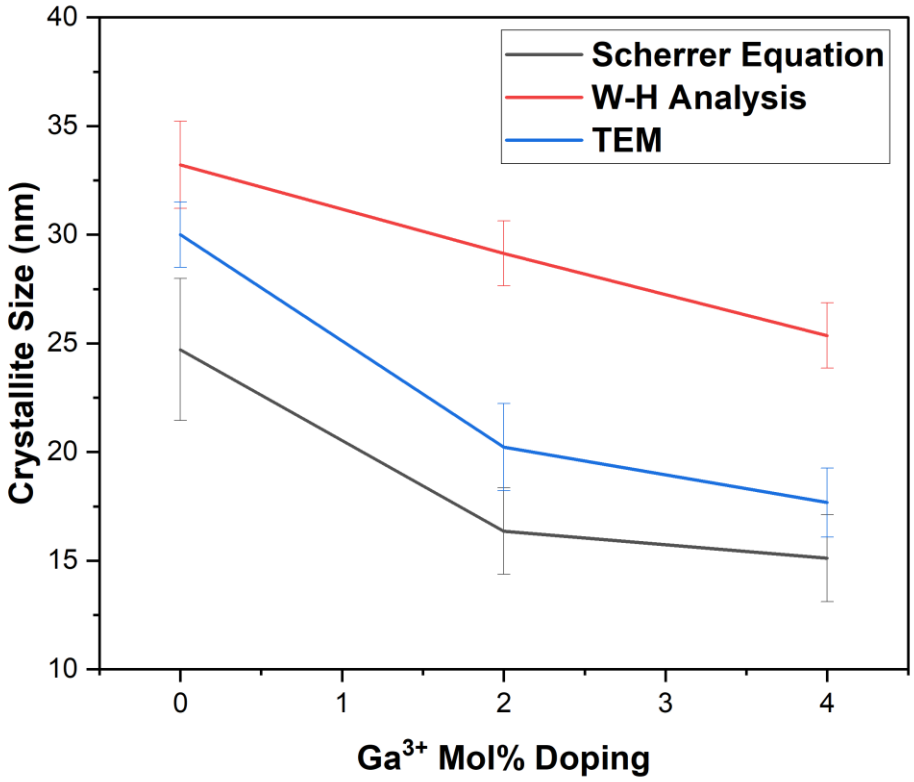


Figure 6.8: *Size comparison of particles with XRD (Scherrer equation and W-H analysis) and the TEM. These methods point towards a common trend of decreasing crystallite sizes with an increase in mol% Ga^{3+} doping.*

The XPS analysis was done for these samples to confirm the elemental ratios and the oxidation states. The Sr3d, Ga2p, and O1s are shown in Appendix Figures 6.3A-6.7A. Here, the Ti2p peak is discussed due to the presence of Ti^{3+} defects and their effect on the performance of the materials. The $Ti2p_{3/2}$ peaks for the samples were analyzed and compared with the undoped in Figure 6.9. The deconvolution of the peaks shows the presence of Ti^{3+} defects and some TiO_2. In the undoped sample, the ratio of Ti^{3+}: (Ti^3 + Ti^{4+}) is 0.13:1. In the N_2 annealed batch, 1 mol% Ga showed the presence of Ti^{3+} defects with the ratio of Ti^{3+}: (Ti^3 + Ti^{4+}) of 0.045:1. The 4 mol% Ga doped samples did not show any defects. The main component of the XPS $Ti2p_{3/2}$ peak is at 458.32 eV which can be attributed to Ti^{4+}. In Figure 6.10 (a, b), in the 1 mol% Ga^{3+} doped sample, the ($Sr3d_{5/2}$): (Ti + Ga) ratio is 1:0.9 and in the 4 mol% Ga^{3+} doped sample, the ($Sr3d_{5/2}$): (Ti + Ga) is 1:1.2. The $Ti2p_{3/2}$ and $Ti2p_{1/2}$ in 1 mol% Ga^{3+} doped sample of the N_2 annealed batch show shifts to higher and the 4 mol% to lower binding energies compared to undoped samples as shown in Figure 6.10. However, they remain within the error.

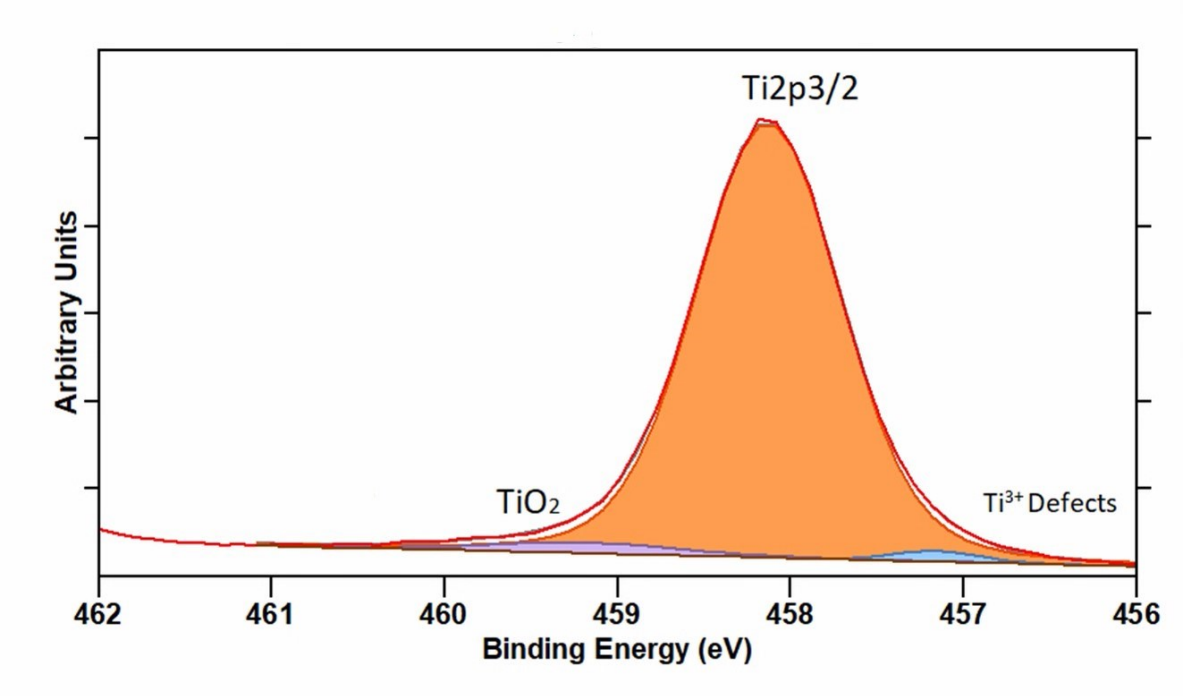


Figure 6.9: *XPS Ti2p Peak of undoped $SrTiO_3$ with $Ti2p_{3/2}$ at 458.32 eV with Ti^{3+}(blue) and TiO_2 (violet).*

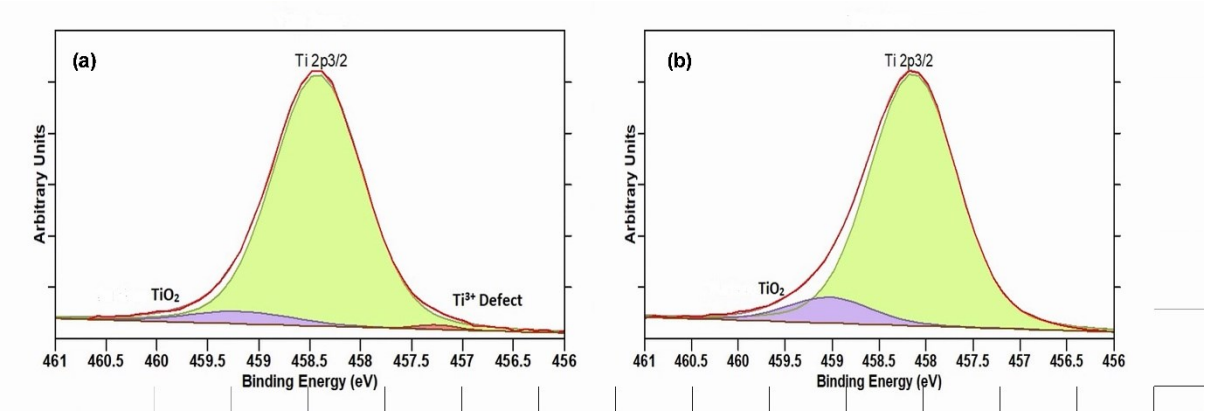


Figure 6.10: *XPS Ti2p peaks of (a) 1 mol% Ga^{3+} (N_2) (b) 4 mol% Ga^{3+} (N_2) doped samples with $Ti2p_{3/2}$ at lower binding energies compared to undoped $SrTiO_3$ with Ti^{3+}(red) and TiO_2 (violet).*

The Kubelka Munk, [F(R)] of the samples was measured to understand the absorption pattern of the samples. The onset of absorption in the N_2 annealed samples is earlier than the commercial $SrTiO_3$ as shown in Figure 6.11. However, no visible light absorption is observed, and they are analogous to the previous Ga^{3+} doped samples.

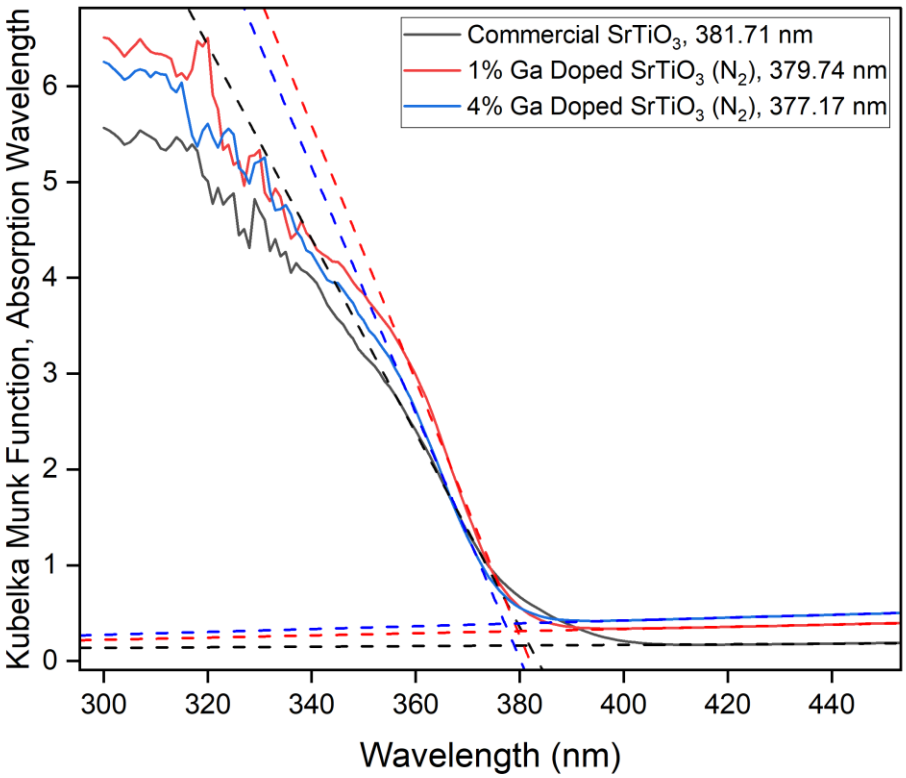


Figure 6.11: *Kubelka Munk function of the samples annealed under N_2 showing absorption in the UV region and no additional optical features.*

The samples synthesized with the additional N2 annealing step retain similar characteristics as the standard sol-gel Pechini samples. The only variable so far in these samples is the still smaller particle sizes which is beneficial in providing higher specific areas that increase photocatalytic rates [14]. The results obtained so far with this batch will be confirmed with repeats and the effect of the surface area on the performance will be measured with the photocatalytic setup in the Steier Laboratory in St. Catherine's College, Oxford.

6.4 Conclusion and Future Work

Preliminary photocatalytic results show that Ga^{3+} doping enhances the photocatalytic CO_2 hydrogenation rates. With this work, we are trying to establish the reasons why Ga^{3+}doping works. The two reasons we have established so far are the decrease in $Ti^{3+}$and the decrease in crystallite sizes with increasing specific surface areas. To achieve even smaller crystallite sizes, an intermediate N_2 annealing step was introduced before calcination. Preliminary results showed that although Ga did not induce any significant changes in the band gap, we observed an increasing trend of CO produced during our CO_2 photo hydrogenation experiments. A thorough analysis of crystallinity led us to pursue the effect of crystallite/particle size and hence, the effect of the specific surface area on our catalytic rates. Indeed, if we account for the specific surface area, we see that upon doping with d^{10} Ga, we do not observe a significant increase in our catalytic rate of CO production. This study highlights that the reports of

photocatalytic rates in the literature are better off leaning more toward the way photo-electrochemical and electrochemical rates are reported (per specific or (electro)chemically active surface area) instead of the traditional thermochemical way of reporting yields (per gram catalyst). In conclusion, with this work, we are trying to establish a new method (first of its kind) to quantify photocatalytic data in terms of normalized BET N_2 specific surface area to be expressed as μmols per m^2 per h in oxide materials such as the $SrTiO_3$. This chapter also raises the need for optimizing the synthesis conditions which could be beneficial for the photocatalytic performance. As a scope for future work, more work is being done to correlate the specific areas to report PEC, electrocatalysis, and photocatalysis data.

References

[1] L. Guo, X. Guo, Y. He, and N. Tsubaki, "CO2 heterogeneous hydrogenation to carbon-based fuels: recent key developments and perspectives," *J. Mater. Chem. A*, vol. 11, no. 22, pp. 11637–11669, 2023, doi: 10.1039/d3ta01025b.

[2] U. P. I, U. S. Shenoy, and D. K. Bhat, "Nanocubic Copper-Doped $SrTiO_3$ for Photoreduction of Cr(VI) and Photodegradation of Methyl Violet," *ACS Appl. Nano Mater.*, Sep. 2023, doi: 10.1021/acsanm.3c02997.

[3] M. Thommes, K. Kaneko, A. V. Neimark, J. P. Olivier *et al.* , "Physisorption of gases, with special reference to the evaluation of surface area and pore size distribution (IUPAC Technical Report)," *Pure Appl. Chem.*, vol. 87, no. 9–10, pp. 1051–1069, 2015, doi: doi:10.1515/pac-2014-1117.

[4] H. Zhou, J. Guo, P. Li, T. Fan, D. Zhang, and J. Ye, "Leaf-architectured 3D hierarchical artificial photosynthetic system of perovskite titanates towards CO_2 photoreduction into hydrocarbon fuels," *Sci. Rep.*, vol. 3, no. i, pp. 1–9, 2013, doi: 10.1038/srep01667.

[5] D. Li, S. Ouyang, H. Xu, D. Lu *et al.*, "Synergistic effect of Au and Rh on $SrTiO_3$ in significantly promoting visible-light-driven syngas production from CO_2 and H_2O," *Chem. Commun.*, vol. 52, no. 35, pp. 5989–5992, 2016, doi: 10.1039/c6cc00836d.

[6] Y. Shen, S. Ren, L. Zheng, X. Xu *et al.*, "Room-temperature photosynthesis of propane from CO_2 with Cu single atoms on vacancy-rich TiO_2," *Nat. Commun.*, vol. 14, no. 1, 2023, doi: 10.1038/s41467-023-36778-5.

[7] F. Moruzzi, W. Zhang, B. Purushothaman *et al.*, "Solution-processable polymers of intrinsic microporosity for gas-phase carbon dioxide photoreduction," *Nat. Commun.*, vol. 14, no. 1, pp. 1–11, 2023, doi: 10.1038/s41467-023-39161-6.

[8] H. Robatjazi, H. Zhao, D. F. Swearer, N. J. Hogan *et al.*, "Plasmon-induced selective carbon dioxide conversion on earth-abundant aluminum-cuprous oxide antenna-reactor nanoparticles," *Nat. Commun.*, vol. 8, no. 1, pp. 1–9, 2017, doi: 10.1038/s41467-017-00055-z.

[9] B. Bradlyn, L. Elcoro, J. Cano, M.G. Vergniory *et al.*, "Topological quantum chemistry," *Nature*, vol. 547, no. 7663, pp. 298–305, 2017, doi: 10.1038/nature23268.

[10] M. G. Vergniory, B.J. Wieder, L. Elcoro, S.S.P. Parkin *et al.*, "All topological bands of all nonmagnetic stoichiometric materials," *Science (80-.).*, vol. 376, no. 6595, 2022, doi: 10.1126/science.abg9094.

[11] M. G. Vergniory, L. Elcoro, C. Felser, N. Regnault, B. A. Bernevig, and Z. Wang, "A complete catalogue of high-quality topological materials," *Nature*, vol. 566, no. 7745, pp. 480–485, 2019, doi: 10.1038/s41586-019-0954-4.

[12] S. Takaki, T. Masumura, and T. Tsuchiyama, "Proposal of simplified modified Williamson-Hall Eq," *ISIJ Int.*, vol. 58, no. 12, pp. 2354–2356, 2018, doi: 10.2355/isijinternational.ISIJINT-2018-517.

[13] T. Ungár and A. Borbély, "The effect of dislocation contrast on X-ray line broadening: A new approach to line profile analysis," *Appl. Phys. Lett.*, vol. 69, no. 21, pp. 3173–3175, 1996, doi: 10.1063/1.117951.

[14] C. Dong, C. Lian, S. Hu, Z. Deng *et al.*, "Size-dependent activity and selectivity of carbon dioxide photocatalytic reduction over platinum nanoparticles," *Nat. Commun.*, vol. 9, no. 1, pp. 1–11, 2018, doi: 10.1038/s41467-018-03666-2.

[15] H. Idriss, "On the wrong assignment of the XPS O1s signal at 531–532 eV attributed to oxygen vacancies in photo- and electro-catalysts for water splitting and other materials applications," *Surf. Sci.*, vol. 712, no. June, pp. 2–7, 2021, doi: 10.1016/j.susc.2021.121894.

Appendix

Aging and High-Temperature XRD

It is observed that Ga^{3+} doped $SrTiO_3$ starts to form oxides like SrO and TiO_2 with time. This might be due to the aging of the samples. This process was studied via the HT-XRD on the 3 mol% Ga^{3+} doped $SrTiO_3$ as shown in Figure 6.1A. The catalyst was heated from room temperature with a 200 °C temperature ramp and then cooled down to room temperature. It was observed that all the oxide phases disappeared after 800 °C, and it demonstrated a cubic structure and maintained it after cooling down to room temperature. From this experiment, we get a clear idea of the safe temperature to which we can heat up before running photocatalysis measurements on synthesized older samples.

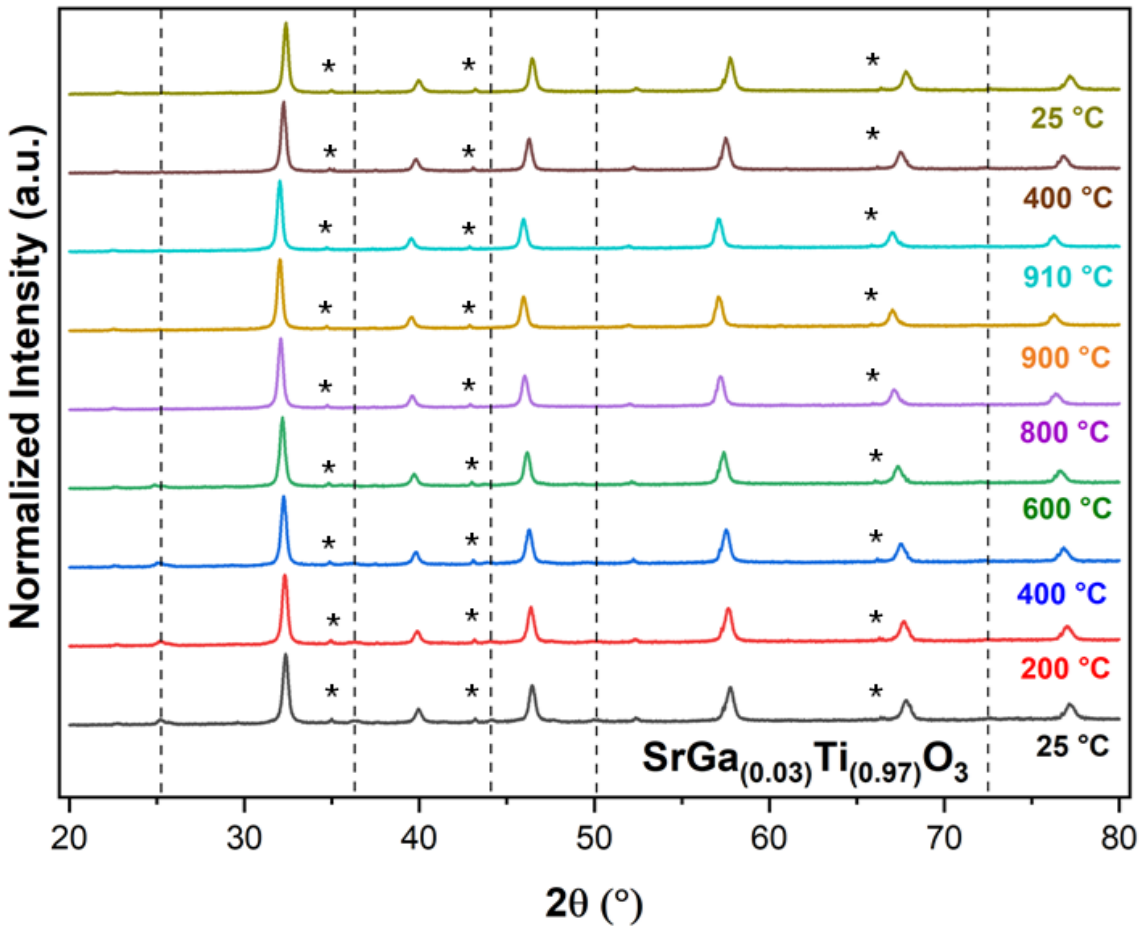


Figure 6.1A: HT-XRD pattern of 3 mol% Ga doped $SrTiO_3$ with the * indicating oxide phases and dashed line indicating the alumina crucible's reflection. This experiment aimed to understand how the oxides in the aged samples behave when subjected to heating. It was observed that these samples regained their phase pure cubic structure when heated at ≥ 800 °C and maintained it upon cooling to room temperature.

The nanoparticles demonstrate high crystallinity as demonstrated in Figure 6.6. Due to their shapes, the particles were observed to be variedly oriented.

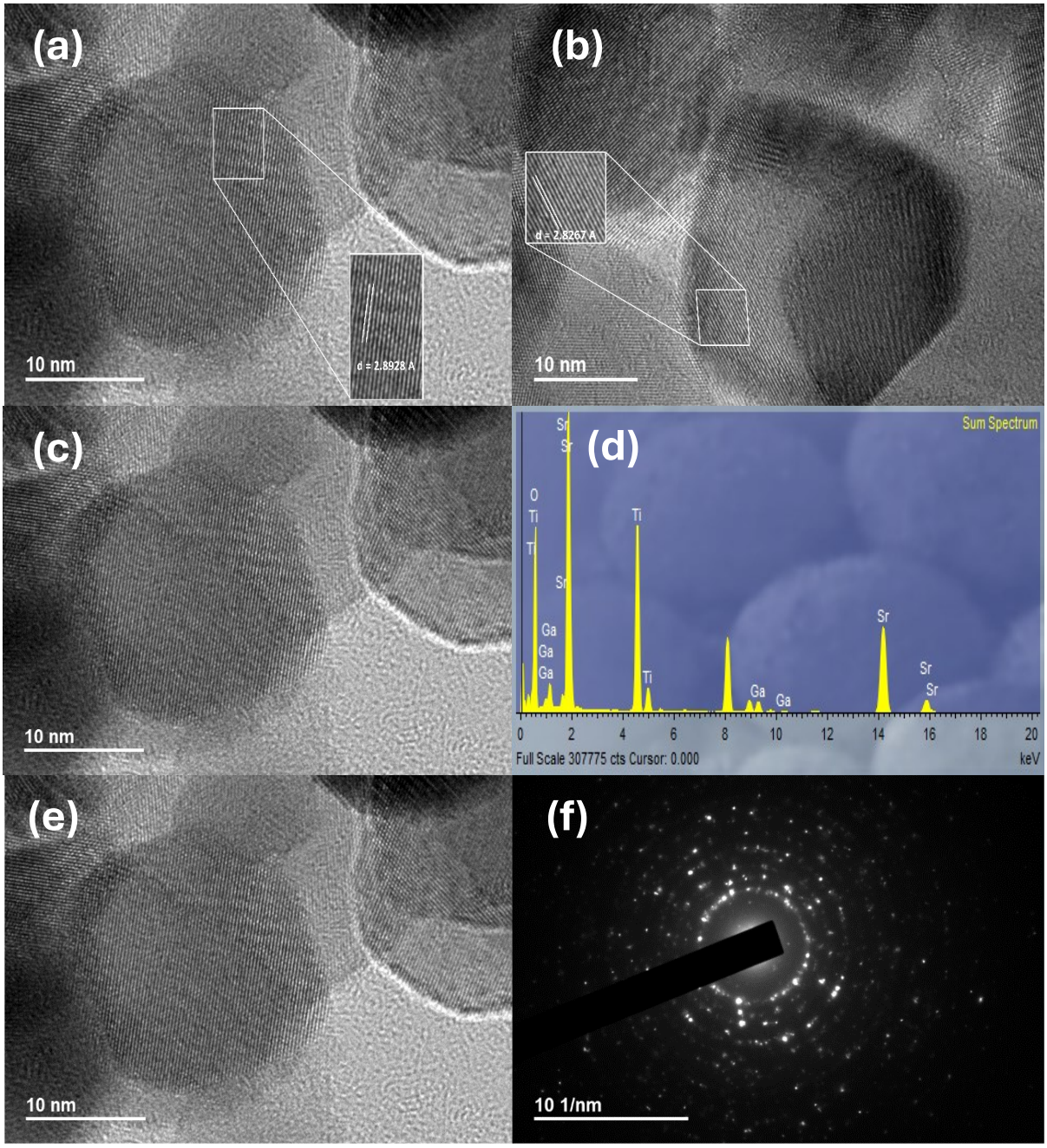


Figure 6.2A: d-spacings of the particles of 4 mol% Ga Doped $SrTiO_3$ with sizes (a, c, e) 21.89 nm in (110) (b) 23.94 nm oriented in (110) (c) EDX Pattern showing the incorporation of Ga (f) Diffraction of the Particles

From Figure 6.2A(f), the (hkl) was calculated and tabulated for the 4 mol% Ga (N_2) doped sample which has a lattice parameter of 3.88403 Å.

Table 6.1A: Calculated (hkl) from Diffraction Pattern

(hkl)	d-spacings (Å)
100	3.57143
110	2.75748
111	2.24517
200	1.93817
211	1.60013
220	1.37542
221	1.21102
222	1.13372

The (hkl) values obtained from the diffraction pattern in Table 6.4 corroborate with the XRD pattern.

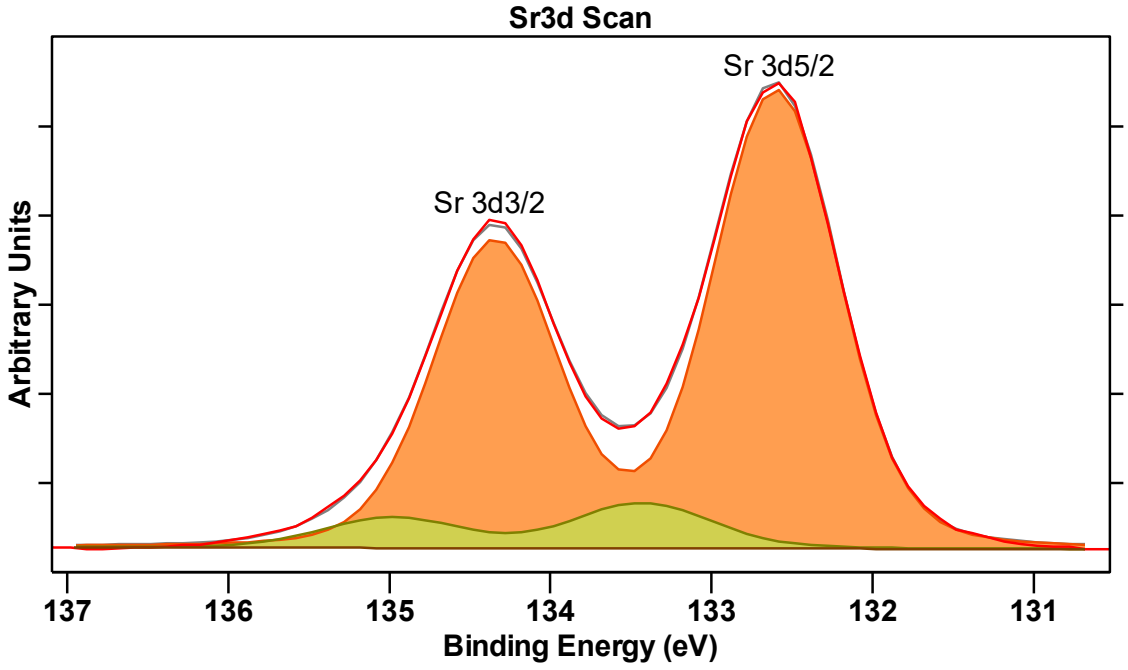


Figure 6.3A: Deconvoluted and charge corrected Sr3d Peaks of undoped $SrTiO_3$ at 132.77 eV and 134.49 eV with trace amount of $SrCO_3$

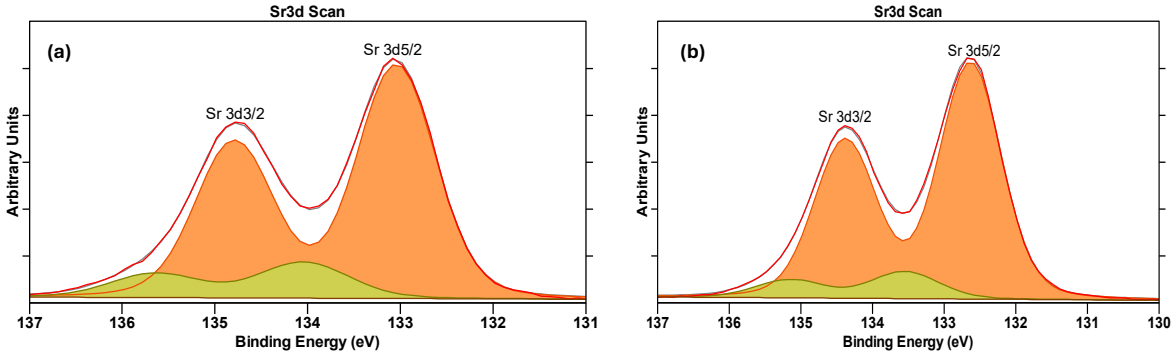


Figure 6.4A: Clockwise from top a.) 1 mol% Ga^{3+} (N_2) b.) 4 mol% Ga^{3+} (N_2) doped $SrTiO_3$ samples

The binding energy positions of the $Sr3d_{5/2}$ and the $Sr3d_{3/2}$ of the lattice Sr^{2+} is presented in Table 6.2A.

Table 6.2A: Position of the $Sr3d_{5/2}$ and the $Sr3d_{3/2}$ of the doped samples

Sr No	Sample	$Sr3d_{5/2}$	$Sr3d_{3/2}$
1	Undoped $SrTiO_3$	132.77	134.49
2	1 mol% Ga (N_2)	133.06	134.75
3	4 mol% Ga (N_2)	132.63	134.39

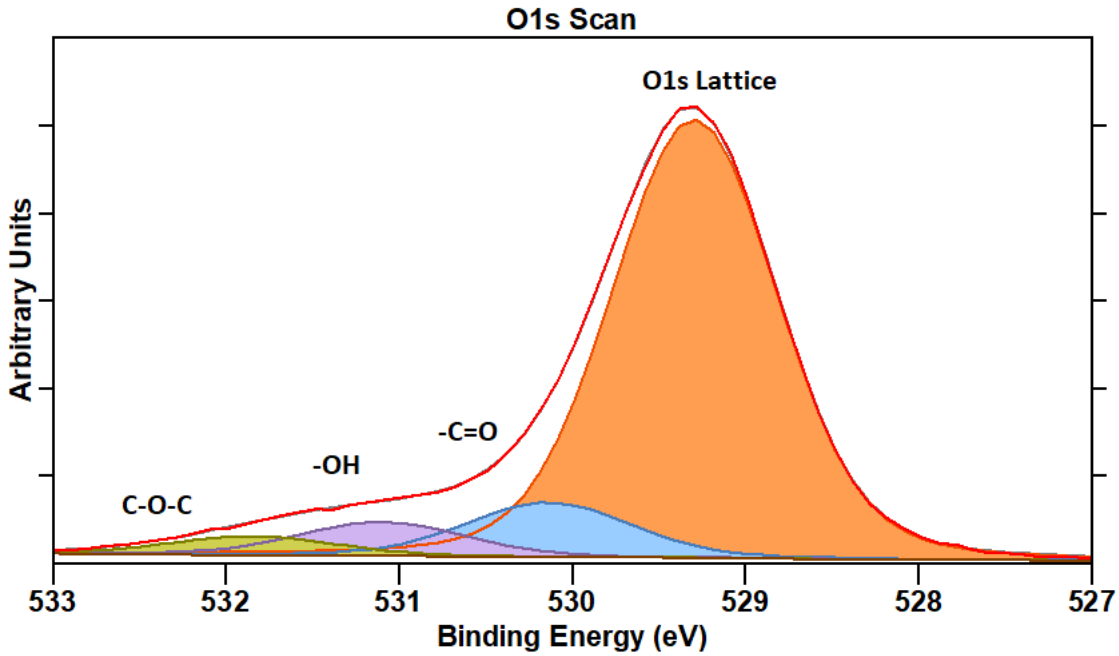


Figure 6.5A: XP spectrum of undoped O1s peak with the main component at 529.48 eV with -C=O (blue), -OH (violet) and -C-O-C (green)

The O1s peak of the doped samples as shown in Figure 6.6A shows similar characteristics i.e., the presence of four peaks. However, all the peaks show shifts to lower binding energies.

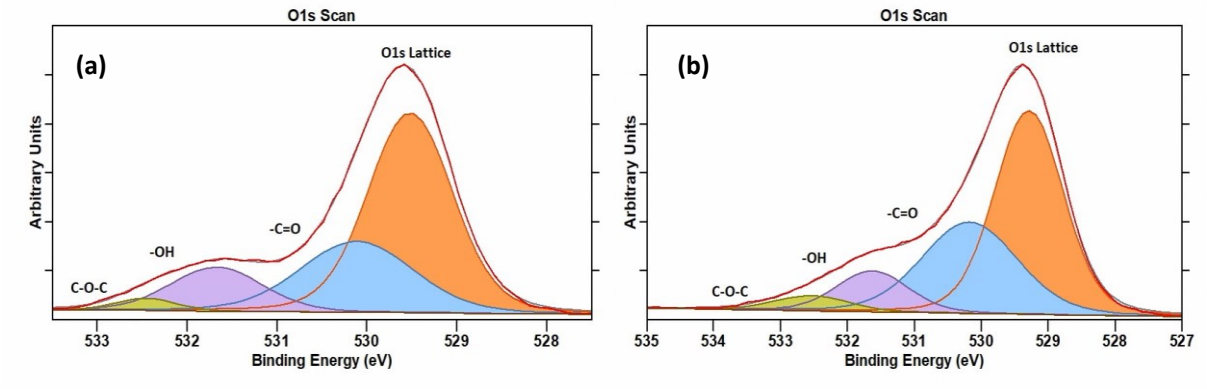


Figure 6.6A: XPS O1s peak (deconvolution of (a) 1 mol% Ga^{3+} (N_2) (b) 4 mol% Ga^{3+} (N_2) doped samples with -C=O (blue) , -OH (violet) and C-O-C groups (green)

The peak positions of the O1s of the doped samples are given in Table 6.3A.

Table 6.3A: Peak Positions of the O1s

Sr No	Samples	Lattice	-C=O	-OH	C-O-C
1	Undoped	529.50 eV	530.40 eV	530.91 eV	531.68 eV
2	1 mol% Ga^{3+} Doped	529.52 eV	530.12 eV	531.64 eV	532.44 eV
3	4 mol% Ga^{3+} Doped	529.28 eV	530.19 eV	531.64 eV	532.57 eV

The presence of carbonate peaks is quite consistent with the Sr3d peaks which showed the presence of $SrCO_3$. The -OH peak of the 1 mol% Ga doped sample with N_2 annealing is the highest among all the doped samples. This could be due to the increased affinity for surface hydroxyls by the higher number of oxygen vacancies introduced with the % doping [15].

Ga2p

From the XPS survey of the surface of 1 mol% Ga^{3+} doped, and 4 mol% Ga^{3+} doped $SrTiO_3$, the presence of Gallium is evident as shown in Figure 6.7A. For the N_2 annealed batch, the 1 mol% and 4 mol% doped samples the main $Ga2p_{3/2}$ peak at 1117.89 eV and 1117.96 eV respectively.

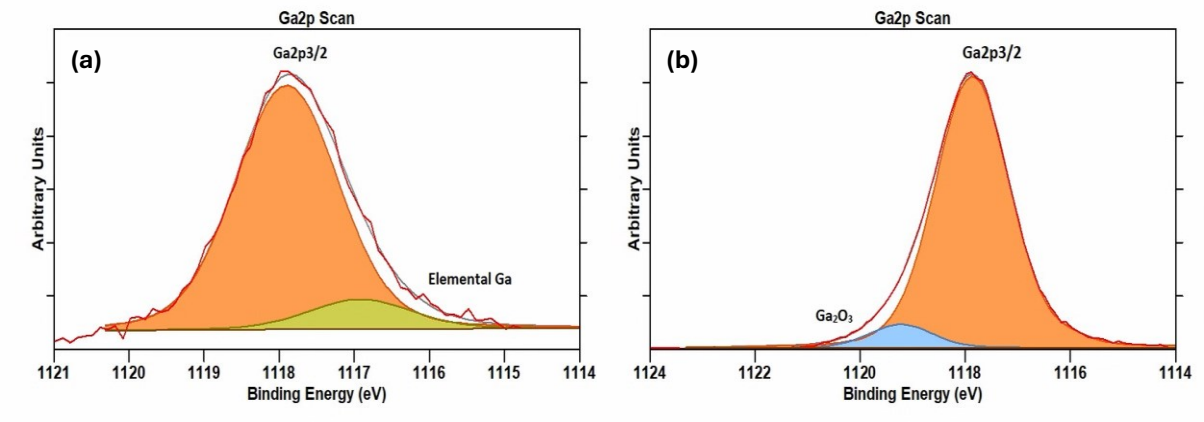


Figure 6.7A: XPS $Ga2p_{3/2}$ peak deconvolution of (a) 1 mol% Ga^{3+} (N_2) (b) 4 mol% Ga^{3+} (N_2) doped samples with elemental peak (green) and Ga_2O_3 (blue)

Chapter 7: Conclusion and Future Work

7.1 Conclusion

The Ph.D. work studied the effect of d- and p-block dopants in the material and the PEC/photocatalytic properties of $SrTiO_3$. Initially, the synthesis route which was assumed to be a straightforward process was found to have a profound effect on the properties of the materials. Detailed investigations showed that synthesis parameters such as the temperature influenced the distribution and the behavior of the dopants such as surface segregation and exsolution. These effects highlight the importance of controlling synthesis parameters to optimize the materials' catalytic performance. The Ph.D. work aims to improve the performance of $SrTiO_3$ via doping with ions having d^{10} (Ga^{3+}) and d^3 (Cr^{3+}) configurations. The thesis work tried to study whether doping is a feasible strategy to increase the efficiency of $SrTiO_3$. Both Ga^{3+} and Cr^{3+} dopants showed the suppression of intrinsic Ti^{3+} defects that were found to have affected the performance of catalysts. Oxygen vacancies particularly in the Ga^{3+} doped samples were found to have facilitated the PEC performances. Lifetimes of the samples were found to have been affected by charge trappings as reflected in the TCSPC measurements. Another important parameter that can facilitate higher performances is the specific surface areas as indicated by the decreasing crystallite sizes with an increase in the mol% doping concentration.

In Chapter 3, a series of Ga^{3+} and La^{3+} (co-) doped $SrTiO_3$ samples were synthesized via the standard sol-gel Pechini method at 900 °C. *Ga^{3+} doping was found to have increased the n-type conductivity of the catalysts which deviated from their expected behavior (Figures 3.31-3.32).* With La^{3+} co-doping, the fermi level was found to have shifted away from the CB_{Min} (Figures 3.31-3.32). The n-type conductivity was found to have most likely resulted from oxygen vacancies acting as shallow donors to the CB. In the co-doped series, two samples- 2 mol% and 4 mol% deviated from the other samples in color (bluish grey) and opto-electronic properties. These samples showed oxygen vacancy-related absorption features (Figure 3.23) and exsolution (Figure 3.8). The 2 mol% and the 4 mol% in the mono- and the co-doped series showed higher PEC performance than the undoped sample towards OER (Figures 3.36-3.37). *In the monodoped samples, the primary factor resulting in the higher performance was the suppression of Ti^{3+} defects and the increase of surface oxygen vacancies (Figure 3.33)*. For the La^{3+} co-doped samples, the higher performance was found to be due to a combination of factors with the exsolution being one of them. This study also tries to understand the role of crystallographic 1D (dislocations) and 2D (grain boundaries) defects in the performance of these catalysts. *It was found in this study that the exsolution of the nanoparticles can occur along the grain boundaries which acted as nucleation pathways (Figure 3.9(a)).* This study also highlights a *Time-Temperature-Solubility Factor* that affects how the dopants incorporate into the host matrix and their surface segregation.

In Chapter 4, a study of Ga^{3+} doped $SrTiO_3$ synthesized at different temperatures (500 °C-800 °C) was undertaken. This work builds on Chapter 3 where high-temperature synthesis led to crystallographic defects such as dislocations and grain boundaries which were found to have influenced the performances. To understand how the samples would perform if synthesized at

lower temperatures, this Chapter focuses on the synthesis route and finding an optimum temperature for the best photocatalytic performance. It was observed that samples synthesized at different temperatures behaved differently in their microstructural such as the increasing crystallite sizes with temperature (Figures 4.10-4.11) and electronic aspects such as the lifetimes (Figure 4.14) which were in turn influenced by oxygen vacancies (charged or neutral). The presence of oxygen vacancies was found to have influenced the n-type conductivity. The 2 mol% Ga^{3+} doped $SrTiO_3$ sample synthesized at 800 °C showed the highest lifetimes among all the samples (Figure 4.15). *A hypothesis was proposed where a window of lower EA and IP exists when charge trapping is minimal. In this window, the lifetimes are higher (Figure 4.26).* The 2 mol% Ga^{3+} doped $SrTiO_3$ also reported a higher photoresponse. The PEC performance of the doped samples was higher towards OER from 600 °C onwards (Figure 4.43). The suppression of Ti^{3+} and increase in surface oxygen vacancies were found to have affected the performances of the catalysts (Figure 4.42). The *Time-Temperature-Solubility Factor* was found to have influenced the Ga^{3+} doping in the $SrTiO_3$ matrix. There is an increased surface segregation of dopants with an increase in temperature (Figure 4.36). This finding concludes both chapters 3 and 4 that surface segregation can be beneficial to the performance of the catalysts as observed with the higher OER in the samples synthesized from 600 – 900 °C. The samples synthesized at 500 °C where the doping level was close to the intended mol% doping underperformed in the PEC which further confirmed that the segregation could be beneficial to the performance.

In Chapter 5, 2 mol% Cr doped $SrTiO_3$ was synthesized at 800 °C and 900 °C. Even though the Cr monodoped samples showed absorption into the visible light region, these samples also exhibited Cr^{6+} states (red-colored samples) which are detrimental to the photoactivity. *The effect of Cr^{6+} states was found to be twofold. Cr^{6+} states on the one hand were found to have inhibited the photoresponse and on the other hand, increased the anodic current towards OER (Figure 5.66)*. To suppress these trap states, co-doping with La^{3+} (yellow-colored samples) and Cs^{1+} (violet-colored samples) was tried. Cs^{1+} co-doping did not suppress the Cr^{6+} states (Figures 5.42-5.43) and was found to have decreased the Cr^{3+} content as the mol% co-doping increased as confirmed by the EPR and diffuse reflectance measurements (Figure 5.35). Even though 2 mol% La^{3+} co-doping showed the highest suppression of the Cr^{6+} states, it did not significantly affect the photoresponse. *Due to the Time-Temperature-Solubility Factor as discussed in the previous chapter, another technique was employed to incorporate the dopants into the* $SrTiO_3$ *matrix with the serial dilution method.* The 1 mol% Cr monodoped sample synthesized with this method showed the highest photoresponse (Figure 5.67) and no Cr^{6+} states (Figure 5.44 (b)). Therefore, confirming that even though Cr^{6+} inhibits the photoresponse, these states facilitate the Cr-doped $SrTiO_3$ to be better electrocatalysts. Suppression of intrinsic defects such as the Ti^{3+} also enhanced the performances.

In Chapter 6, preliminary photocatalytic CO_2 hydrogenation with Ga^{3+} doped $SrTiO_3$ showed a decrease in crystallite sizes (Table 6.1), increasing BET-specific surface areas (Figure 6.3), and decreasing Ti^{3+} defects (Figure 6.2 (c)) show an increasing trend in CO generation. *This study proposes a new method to report PEC or photocatalysis data considering the normalized BET N_2 specific active surface areas for the first time in titanate-based materials such as the* $SrTiO_3$ *(Figure 6.4).* In this work, an attempt was made to optimize the sol-gel Pechini method

with an intermediate N_2 annealing step. *The primary motivation was to achieve smaller coherently scattering domain (or crystallite) sizes which could provide a higher specific surface area for higher photocatalytic performances.*

To conclude, even though doping $SrTiO_3$ is not the most efficient method to enhance the performance of the photocatalyst, it can be explored as a viable option. To achieve this, it is important to choose the right synthesis method and tailor the conditions according to the dopants used. From the work done in the Ph.D., it can be inferred this step is crucial as to control the amount of doping being incorporated in the host matrix and the intrinsic defect concentration.

7.2 Future Work

The work done in the Ph.D. study lays the framework for some unfounded research avenues. Each primary result, chapters 3-6, tries to propose a hypothesis still in the nascent research stage. In photocatalysis, the effect of crystallographic (extrinsic) defects such as dislocations and grain boundaries is still limited. In this Ph.D. work, an attempt was made to understand how these defects could have facilitated exsolution and therefore, affected the performance of the catalysts. The second hypothesis that needs to be understood is the possibility of the existence of a window of EA and IP where charge trapping is low resulting in higher lifetimes. This could be an important aspect in the future for designing high-performing photocatalysts. For the Cr-doped $SrTiO_3$ samples, other co-dopants such as Sb and Ta should be considered to suppress Cr^{6+} trap states. In the study on the Cr doping, the position of Cr^{3+} and Cr^{6+} were speculated from the diffuse reflectance data. To fully understand where the positions of these states are, a DFT simulation can be helpful. In the Ph.D. study, a *Time-Temperature-Solubility Factor* has been discussed which could have affected how the dopants interact with the host matrix. Here, it can be understood that different dopants have unique solubility rates in the $SrTiO_3$ matrix and therefore the time of synthesis should be tailored to the dopants being used. In the future, techniques such as TOF-SIMS could be used to understand how dopants if segregated on the surface of the host matrix could affect the performance. XAFS is another technique to understand the site where dopants without paramagnetic ion species can occupy. Another important aspect to understand while synthesizing photocatalysts is their nature of conductivity. Even though both Ga^{3+} and Cr^{3+} are dopants with expected p-type conductivity, in this study both types of dopants are n-type in nature. To reverse the nature of conductivity in these dopants, more experimental techniques such as oxygen (function of partial pressures) annealing should be undertaken. Different types of oxygen vacancies were found to have affected the microstructural parameters such as the lattice volumes and lattice strains in the samples, therefore it is equally important to be able to quantify these and understand their effect on the catalyst performances. For the specific surface area normalized PEC/ photocatalytic data, more research is being ongoing in the current Ph.D. group in terms of BET and gas phase photocatalytic CO_2 hydrogenation.

Copyright Permissions

[1] "Semiconductor-based photocatalysts and photoelectrochemical cells for solar fuel generation: a review. Authors: J. Li and N. Wu. License No. 1 572087-1," pp. 5–11, 2025.

[2] "Tuning the electronic and optical properties of $SrTiO_3$ for optoelectronic and photocatalytic applications by plasmonic-metal doping: a DFT- computation. Authors: Ashish Raturi et al. License No. 5956850957840," pp. 4–9, 2025.

[3] "Solar Water Splitting Using Semiconductor Photocatalyst Powders. Authors: Kazuhiro Takanabe. License No. 5956860763430," pp. 3–8, 2025.

[4] "In situ growth of nanoparticles through control of non-stoichiometry. Authors: Dragoes Neagu et al. License No. - 5956920740485.," pp. 1–6, 2025.

[5] "Tuning the electronic and optical properties of $SrTiO_3$ for optoelectronic and photocatalytic applications by plasmonic-metal doping: a DFT- computation Ashish. Authors: Ashish Raturi et al. License No. : 5957000164043," pp. 1–6, 2025.

[6] "Linking in situ charge accumulation to electronic structure in doped $SrTiO_3$ reveals design principles for hydrogen-evolving photocatalysts. Authors: Benjamin Moss et al. License No. : 5956930339958," pp. 2–7, 2025.

[7] "Rapid development of the photoresponse and oxygen evolution of TiO_2 nanotubes sputtered with Cr thin films realized via laser annealing. Authors: Łukasz Haryński,Jakub Karczewski,Jacek Ryl,Katarzyna Grochowska,Katarzyna Siuzdak. License Number: 5956930977," pp. 1–7, 2025.

[8] "Chapter 8- Transmission Electron Microscope, Membrane Characterization. Authors: C. Y. Tang and Z. Yang. License Number: 5957021109589," pp. 1–7, 2025.